Nucleation Theory and Applications

Edited by
Jürn W. P. Schmelzer

WILEY-VCH Verlag GmbH & Co. KGaA

Editor

Dr. Jürn W. P. Schmelzer
Universitaet Rostock
Fachbereich Physik
juern-w.schmelzer@physik.uni-rostock.de

Library of Congress Card No.: applied for
British Library Cataloging-in-Publication Data:
A catalogue record for this book is available from the British Library

Bibliographic information published by Die Deutsche Bibliothek
Die Deutsche Bibliothek lists this publication in the Deutsche Nationalbibliografie; detailed bibliographic data is available in the Internet at <http://dnb.ddb.de>.

Printed in the Federal Republic of Germany
Printed on acid-free paper

Printing Strauss GmbH, Mörlenbach
Bookbinding Litges & Dopf Buchbinderei GmbH, Heppenheim

ISBN-13 978-3-527-40469-8
ISBN-10 3-527-40469-4

Contents

Preface

Norwegen ist ein großes Land, das Volk ist ungestüm und es ist nicht gut, es mit einem unzureichenden Heer anzugreifen.
Snorri Sturloson, Heimskringla (about 1230)
cited after D.M. Wilson (Ed.):
Die Geschichte der Nordischen Völker,
Orbis-Verlag, München, 2003

The present book consists of contributions, which have been presented and discussed in detail in the course of the research workshops *Nucleation Theory and Applications* organized jointly by scientists from the Bogoliubov Laboratory of Theoretical Physics of the Joint Institute for Nuclear Research in Dubna, Russia, and the Department of Physics of the University of Rostock, Germany, involving colleagues from Russia, Belorussia, Ukraine, Kazakhstan, Estonia, Bulgaria, Czech Republic, Brazil, United States, and Germany. These workshops have been conducted yearly for about one month in Dubna, Russia, starting in 1997. The intention of these workshops was and is to unite research activities aimed at a proper understanding of both fundamental problems and a variety of applications of the theory of first-order and second-order phase transitions, in particular, and of the typical features of processes of self-organization of matter, in general. The meetings in Dubna have been supplemented hereby by mutual research visits of the participants in the course of the year in order to continue and extend the work performed during the workshops.

By such a combination of the common attempts, the search for solutions to the highly complex problems occurring in this field could be stimulated in a very effective way, and a number of problems could be solved which would otherwise have remained unsolved. The results of these efforts have been published in a variety of journal articles, which will be partly cited in the contributions in the present book. Some of the results have already been reflected in detail in the preceding monograph, *J. Schmelzer, G. Röpke, R. Mahnke (Eds.): Aggregation Phenomena in Complex Systems*, published in 1999 also by Wiley-VCH. It is also planned to continue the series of research workshops in the coming years. Relevant information will be given at the homepage *http://thsun1.jinr.ru* of the Bogoliubov Laboratory of Theoretical Physics of the Joint Institute for Nuclear Research and can also be requested via electronic mail from the editor of the present book (juern-w.schmelzer@physik.uni-rostock.de).

These workshops could be carried out for such prolonged times only through continued support from a variety of organizations. We would like to mention here in particular, the Bundesministerium für Bildung, Wissenschaft, Forschung und Technologie (BMBF) (via Research projects, the TRANSFORM and Heisenberg-Landau programs), the Deutsche Forschungsgemeinschaft (DFG) (via Research projects, travel and conference grants), the Deutscher Akademischer Austauschdienst (DAAD), the Russian Foundation for Basic Research (RFBR), the UNESCO, the BASF-AG Ludwigshafen, the SOROS-Foundation, the State of São Paulo Research Foundation (FAPESP), and the host institution, the Bogoliubov Laboratory of Theoretical Physics of the Joint Institute for Nuclear Research in Dubna. To all the

above-mentioned organizations and to those not mentioned explicitly, we would like to express our sincere thanks. We would also like to express our gratitude to all the colleagues who helped us in the organization of the workshops.

It also gives us particular pleasure to thank the coworkers of the Vitreous Materials Laboratory (LAMAV) of the Federal University of São Carlos (UFSCar), Brazil, and, especially, the Head of the Department, Professor Edgar D. Zanotto, for their cordial hospitality and the excellent working conditions during the course of the stay of the editor of the present monograph at their laboratory allowing to bring this book to completion.

Rostock, Germany – Dubna, Russia – São Carlos, Brazil
August 2004 Jürn W. P. Schmelzer

List of Contributors

- *Alexander S. Abyzov* *Ch. 3*

  Kharkov Institute of Physics
  and Technology
  Academician Str. 1,
  61 108 Kharkov,
  Ukraine

- *Vladimir G. Baidakov* *Ch. 5, 11*

  Institute of Thermal Physics,
  Ural Branch of the Russian Academy of Sciences,
  Amundsen Str. 106
  620016 Ekaterinburg,
  Russia

- *Grey Sh. Boltachev* *Ch. 11*

  Institute of Thermal Physics,
  Ural Branch of the Russian Academy of Sciences,
  Amundsen Str. 106
  620016 Ekaterinburg,
  Russia

- *Helga Dunken* *Ch. 8*

  Institut für Physikalische Chemie,
  Friedrich-Schiller Universität Jena,
  Lessingstr. 10,
  07743 Jena,
  Germany

- *Mars Z. Faizullin* *Ch. 2*

  Institute of Thermal Physics,
  Ural Branch of the Russian Academy of Sciences
  Amundsen Str. 106,
  620016 Ekaterinburg,
  Russia

- *Vladimir M. Fokin* *Ch. 4*

  Vavilov State Optical Institute
  ul. Babushkina 36-1,
  193171 St. Petersburg
  Russia

- *Alexander P. Grinin* *Ch. 9*

  Department of Statistical Physics, Institute of Physics,
  St. Petersburg State University
  Ulyanovskaya 1, Petrodvoretz,
  198 504 St. Petersburg
  Russia

- *Victoria Guencheva* *Ch. 8*

  Institute of Physical Chemistry,
  Bulgarian Academy of Sciences,
  Acad. Bonchev Street,
  Sofia 1113,
  Bulgaria

- *Andriy M. Gusak* *Ch. 10*

  Cherkasy State University,
  Shevchenko Str. 81
  18017 Cherkasy,
  Ukraine

- *Ivan Gutzow* *Ch. 8*

  Institute of Physical Chemistry,
  Bulgarian Academy of Sciences,
  Acad. Bonchev Street,
  Sofia 1113,
  Bulgaria

• *Fiqiri Hodaj* *Ch. 10*

LTPCM, UMR CNRS – Institute National Polytechnique de Grenoble,
Universite Joseph Fourier
BP 75, 38402 Saint Martin d' Heres,
France

• *Lyubomir Kostadinov* *Ch. 8*

Institute of Physical Chemistry,
Bulgarian Academy of Sciences,
Acad. Bonchev Street,
Sofia 1113,
Bulgaria

• *Sergey A. Kukushkin* *Ch. 7*

Institute of Problems of Mechanical Engineering,
Russian Academy of Sciences,
Bolshoy pr. 61,
199178 St. Petersburg,
Russia

• *Fedor M. Kuni* *Ch. 9*

Department of Statistical Physics
Institute of Physics,
St. Petersburg State University
Ulyanovskaya 1, Petrodvoretz,
198 504 St. Petersburg
Russia

• *Andrey V. Osipov* *Ch. 7*

Institute of Problems of Mechanical Engineering,
Russian Academy of Sciences,
Bolshoy pr. 61,
199178 St. Petersburg,
Russia

• *Christian Rüssel* *Ch. 8*

Otto-Schott Institut für Glaschemie
Friedrich-Schiller Universität Jena,
Fraunhoferstr. 6
07743 Jena,
Germany

• *Anatoly I. Rusanov* *Ch. 9*

Department of Colloid Chemistry
St. Petersburg State University
Petrodvoretz, Universitetskii prospekt 2
198 504 St. Petersburg,
Russia

• *Jürn W. P. Schmelzer* *Ch. 1, 3, 11, 12*

Fachbereich Physik der Universität Rostock
Universitätsplatz, 18051 Rostock,
Germany

• *Alexander K. Shchekin* *Ch. 9*

Department of Statistical Physics
Institute of Physics, St. Petersburg State University
Ulyanovskaya 1, Petrodvoretz,
198 504 St. Petersburg
Russia

• *Vladimir Ya. Shur* *Ch. 6*

Institute of Physics & Applied Mathematics
Ural State University,
Lenin Avenue
620083 Ekaterinburg,
Russia

• *Vladimir P. Skripov* *Ch. 2*

Institute of Thermal Physics,
Ural Branch of the Russian Academy of Sciences
Amundsen Str. 106,
620016 Ekaterinburg,
Russia

• *Vitali V. Slezov* *Ch. 3*

Kharkov Institute of Physics and Technology
Academician Str. 1,
61 108 Kharkov,
Ukraine

• *Emil Stoyanov* *Ch. 8*

Institute of Physical Chemistry,
Bulgarian Academy of Sciences,
Acad. Bonchev Street,

Sofia 1113,
Bulgaria

• *Snejana Todorova* *Ch. 8*

Institute of Geophysics,
Bulgarian Academy of Sciences,
Acad. Bonchev Street,
Sofia 1113,
Bulgaria

• *Günther Völksch* *Ch. 8*

Otto-Schott Institut für Glaschemie
Friedrich-Schiller Universität Jena,
Fraunhoferstr. 6
07743 Jena,
Germany

• *Nikolay S. Yuritsyn* *Ch. 4*

Grebenshchikov Institute of Silicate Chemistry
Russian Academy of Sciences
ul. Odoevskogo 24/2,
199155 St. Petersburg
Russia

• *Edgar D. Zanotto* *Ch. 4*

Department of Materials Engineering
Federal University of São Carlos, UFSCar
13565-905 São Carlos-SP, Brazil

1 Introductory Remarks

Jürn W.P. Schmelzer

If God will send me readers, then, may be,
it will be interesting for them ...
Alexander S. Pushkin
cited after: B.S. Cantor: Talks on Minerals
(Astrel, Moscow, 1997) (in Russian)

Clustering processes in first-order phase transformations play an important role in a huge variety of processes in nature, and in scientific and technological applications. An adequate theoretical description of such processes is therefore of considerable interest. One of the tools allowing the theoretical description of such processes is the nucleation theory. The theoretical approach predominantly employed so far in the interpretation of experimental results of nucleation-growth processes is based on the classical nucleation theory, its extensions and modifications. It is supplemented by density functional computations, statistical mechanical model analyses, and computer modeling of model systems allowing us to gain additional insights into the respective processes and to specify the possible limitations of the classical approaches.

Although the basic concepts of the classical approach to the description of nucleation processes were developed about 80 years ago, a number of problems remain, however, unsettled till now which are partly of fundamental character. Several of these problems are analyzed in the present book. One of these analyzes is directed to the method of determination of the coefficients of emission in nucleation theory avoiding the concept of constraint equilibrium distributions (Chap. 3). A second such topic is the proper determination of the work of critical cluster formation for the different processes under investigation. It is discussed in detail in Chaps. 4 (in application to crystallization) and 5 (in application to boiling of binary liquid–gas solutions). A third topic, a relatively recent development of the nucleation theory with a wide spectrum of possible applications, consists in the theoretical description of nucleation and growth processes in solid solutions with sharp concentration gradients (Chap. 10).

The majority of theoretical approaches to the description of nucleation and growth processes rely, as far as thermodynamic aspects are involved, on Gibbs' classical thermodynamic theory of interfacial phenomena. In recent years it has been shown that, by generalizing Gibbs' thermodynamic approach, a number of problems of the classical theory can be resolved. In particular, as is shown in Chap. 11, the generalized Gibbs' approach leads to predictions for the properties of the critical clusters and the work of critical cluster formation, which are equivalent to the results of van der Waals' square gradient and more sophisticated density functional approaches. Some additional new insights, which have been obtained recently employing the generalized Gibbs' approach, are sketched in Chap. 12.

The nucleation theory has the unique advantage that its basic principles are equally well applicable to quite a variety of different systems. As a reflection of this general applicability, the spectrum of analyses, presented in the monograph, includes condensation and boiling, crystallization and melting, self-organization of ferroelectric domains and nanofilms, for-

Nucleation Theory and Applications. edited by J. W. P. Schmelzer

ISBN: 3-527-40469-4

mation of micellar solutions, formation and growth of diamonds from vitreous carbon. The analysis of different types of phase equilibria and different applications of the nucleation theory starts with a comparison of similarities and differences of solid–liquid and liquid–vapor phase transitions (Chap. 2). It is followed by an extended review of the state of knowledge in the field of nucleation and crystallization kinetics in silicate glasses (Chap. 4) as a particular example of the phase transition liquid–solid. An overview of the kinetics of boiling of binary liquid–gas solutions is given in Chap. 5. In Chap. 6, it is shown that nucleation concepts can be applied successfully to the description of the polarization reversal phenomenon in ferroelectric materials allowing the treatment of different modes of domain evolution from a single universal point of view. Of similar current direct technological significance are the analyses of formation and growth processes of nanofilms on surfaces reviewed in Chap. 7. Chapter 8 deals with an overview on traditional and novel methods of diamond synthesis, while Chap. 9 employs nucleation theory methods to the description of micellization processes. Some summary of the results and outlook on possible future developments is given in Chap. 12.

All of the chapters included in the present book are written by internationally outstanding scientists in their respective fields. It is of particular pleasure to have among the authors the Corresponding Member of the Ukrainian Academy of Sciences, Vitali V. Slezov (Slyozov), one of the authors of the well-known L(ifshitz)S(lezov)W(agner)-theory of coarsening, the description of the late stages of first-order phase transitions being till now one of the corner stones of the theory of first-order phase transformation processes, the Member of the Russian Academy of Sciences, Vladimir P. Skripov, well known for his enormous work devoted, in particular, to the kinetics of boiling processes and reflected in part in his book *Metastable Liquids*, published also by Wiley in 1974 [3], the member of the Russian Academy of Sciences, Anatoli I. Rusanov, well known for his monographs devoted to the thermodynamics of heterogeneous systems which has served as a comprehensive introduction to theses topics for decades, and the Member of the Bulgarian Academy of Sciences, Ivan S. Gutzow, who continued with his colleagues and coworkers the traditions of the Bulgarian school of nucleation theory originated by Ivan Stranski and Rostislav A. Kaischew.

As already mentioned in the preface, the contributions, included in the present book, have been presented and discussed in detail at the Research Workshops *Nucleation Theory and Applications* in Dubna, Russia, in the course of the years 1997–2003. Of course, neither all the contributions presented nor all of the results obtained in the common research can be reflected in one book. Some other highly interesting topics are contained in the specialized workshop proceedings [1] and in the publications [2–15] of the participants of the meetings and the authors of the present book we refer to for a more detailed outline of some of the topics discussed here and related aspects.

References

[1] J.W.P. Schmelzer, G. Röpke, and V.B. Prieezhev (Eds.), *Nucleation Theory and Applications*, Proceedings of the Research Workshops Nucleation Theory and Applications held at the Joint Institute for Nuclear Research in Dubna/Russia, JINR Publishing Department, Dubna, 1999 (covering the period 1997–1999) and 2002 (for the period 2000–

2002). Copies of the proceedings can be ordered via the editor of the present book by electronic mail (Email: juern-w.schmelzer@physik.uni-rostock.de).

[2] J.W.P. Schmelzer, G. Röpke, and R. Mahnke (Eds.), *Aggregation Phenomena in Complex Systems* (Wiley-VCH, Weinheim, 1999).

[3] V.P. Skripov, *Metastable Liquids* (Nauka, Moscow, 1972 (in Russian); Wiley, New York, 1974 (in English)).

[4] A.I. Rusanov, *Phasengleichgewichte und Grenzflächenerscheinungen* (Akademie-Verlag, Berlin, 1978).

[5] V.P. Skripov and V.P. Koverda, *Spontaneous Crystallization of Superheated Liquids* (Nauka, Moscow, 1984) (in Russian).

[6] V.G. Baidakov, *Thermophysical Properties of Superheated Liquids*, Soviet Technology Reviews, Section B, Thermal Physics Reviews (Harwood Academic, New York, 1994) vol. 5, part 4.

[7] V.G. Baidakov, *The Interface of Simple Classical and Quantum Liquids* (Nauka, Ekaterinburg, Russia, 1994) (in Russian).

[8] V.G. Baidakov, *Superheating of Cryogenic Liquids* (Ural Branch of the Russian Academy of Sciences Publishers, Ekaterinburg, Russia, 1995) (in Russian).

[9] I. Gutzow and J. Schmelzer, *The Vitreous State: Thermodynamics, Structure, Rheology, and Crystallization* (Springer, Berlin, 1995).

[10] V.V. Slezov, *Theory of Diffusive Decomposition of Solid Solutions*. In: Soviet Scientific Reviews/Section A, Physics Reviews, Ed. I. M. Khalatnikov (Harwood Academic, London, 1995).

[11] S.A. Kukushkin and V.V. Slezov, *Disperse Systems on Solid Surfaces* (Nauka, St. Petersburg, 1996) (in Russian).

[12] B.M. Smirnov, *Clusters and Small Particles in Gases and Plasmas*, Graduate Texts in Contemporary Physics (Springer, New York, Berlin, Heidelberg, 2000).

[13] F.M. Kuni, A.K. Shchekin, and A.P. Grinin, Phys.-Usp. **171**, 331 (2001).

[14] B.M. Smirnov, *Physics of Atoms and Ions*, Graduate Texts in Contemporary Physics (Springer, New York, Berlin, Heidelberg, 2003).

[15] V.P. Skripov and M.Z. Faizullin, *Crystal–Liquid–Gas Phase Transitions and Thermodynamic Similarity* (Fizmatlit Publishers, Moscow, 2003) (in Russian).

2 Solid–Liquid and Liquid–Vapor Phase Transitions: Similarities and Differences

Vladimir P. Skripov and Mars Z. Faizullin

Every theory, whether in the physical or biological or social sciences, distorts reality in that it oversimplifies. But if it is a good theory, what is omitted is outweighted by the beam of light and understanding thrown over diverse facts.
Paul A. Samuelson

A comparison has been made between the behavior of the thermodynamic properties of simple substances along the curves of solid–liquid and liquid–vapor phase equilibrium. Hereby the attention is concentrated on the internal pressure p_i, the isothermal elasticity $-(\partial p/\partial v)_T$, the surface energy of the interfacial boundary σ, and the viscosity of the liquid, η. The mentioned curves have been extended beyond the triple point into the region of coexistence of metastable phases. Both phase transitions considered approach here the boundaries of stability of the liquid, but in opposite directions from the triple point with respect to variations of temperature and pressure. Among other consequences, the difference in the thermodynamic behavior of one-component systems for both types of phase transformations, as established in the analysis, gives support to the theoretical idea of the absence of a critical point for the solid–liquid phase equilibrium curve.

2.1 Introduction

From a thermodynamic point of view, liquid–vapor (LV) and solid–liquid (SL) first-order phase transitions have much in common. In both cases, the equilibrium of coexisting phases is determined via equality of the chemical potentials, μ, of the coexisting phases. For a solid–liquid equilibrium, we have for example

$$\mu_S(T, p) = \mu_L(T, p) \; . \tag{2.1}$$

The differential form of this equality leads to the Clausius–Clapeyron equation

$$\frac{dp}{dT_{SL}} = \frac{\Delta s_{SL}}{\Delta v_{SL}} \; , \tag{2.2}$$

where $\Delta s_{SL} = s_L - s_S$, $\Delta v_{SL} = v_L - v_S$ are entropy and volume changes during melting, respectively.

But there are also significant qualitative distinctions between the behavior of the liquid–vapor and solid–liquid equilibrium coexistence curves. One of them consists in the fact that the phase coexistence curve for liquid–vapor equilibrium $p = p_{LV}(T)$ has a lower limit at pressure $p = 0$, whereas the solid–liquid coexistence curve may be extended into the region

Nucleation Theory and Applications. edited by J. W. P. Schmelzer

ISBN: 3-527-40469-4

of negative pressures, where both coexistent phases are metastable. This extension has, at $T \to 0$, no universal low pressure limiting value, p_*. Differences in the behavior of liquid–vapor and solid–liquid coexistence curves are also observed for high values of temperature, T, and pressure, p.

A fundamental fact, concerning the properties of liquid–vapor phase equilibria, has been established long ago by Andrews [1]: There exists an upper end point for the equilibrium coexistence of both fluid phases – the critical point. It is characterized by the well-defined values of the parameters T_c, p_c, and v_c, denoted as critical temperature, pressure, and volume. With increasing temperature and pressure (both having initially values lower than T_c and p_c) the properties of the different coexisting phases move closer and become indistinguishable at the critical point itself. This feature of the coexistence curve allows for the possibility of performing a continuous (without change of homogeneity of the substance) liquid–vapor phase transition by choosing a path around the critical point. In such a continuous transition, the trajectory in the space of thermodynamic variables intersects neither the line of phase equilibrium (binodal) nor the region of unstable states, where the elasticity $-(\partial p/\partial v)_T$ is negative. The main difference between the solid–liquid from the liquid–vapor transition consists in the absence of a critical point. This result can be considered as a well-established fact as well [2]. New physical information is permanently accumulated supporting the point of view as outlined above and so far no indications are found requiring for its revision.

The above-mentioned difference of solid–liquid and liquid–vapor phase transitions leads to a number of thermodynamic consequences, which manifest themselves in the thermodynamic behavior of the different systems and, consequently, in the theoretical dependences describing them. One of such generalizations of experimental data for phase coexistence is the Simon equation for the description of the melting line in temperature–pressure variables [3]. It reads

$$1 + \frac{p}{p_*} = \left(\frac{T}{T_0}\right)^c \quad . \tag{2.3}$$

Here $p_* = -p(T \to 0) > 0$ is an individual parameter which may vary in dependence of the substance considered. Generally it stands for the limiting (for $T \to 0$) value of pressure (taken with the opposite sign) on the extension of the melting line, T_0 is the temperature at which the melting line intersects the isobar $p = 0$ and c is another individual parameter of the system under consideration.

From the paper of 1929 by Simon and Glatzel [3] one can see that, in processing experimental data, the authors had to discard any possible analogy in the interpretation of experimental results on liquid–solid equilibria as compared with liquid–vapor equilibrium, where the relationship between pressure and temperature is close to a semi-logarithmic one. The power-type dependence, as given by Eq. (2.3), proved to give a satisfactory description. It can further be simplified and generalized by the introduction of a *shifted* pressure scale, p^+, via

$$p^+ = p + p_*. \tag{2.4}$$

The introduction of the pressure p^+ allows a transformation of Eq. (2.3) into the canonical form

$$\frac{p_1^+}{p_2^+} = \left(\frac{T_1}{T_2}\right)^c \quad , \tag{2.5}$$

not containing any more the individual parameter p_*. It emphasizes the automorphism of the melting lines and the meaning of the individual exponent c as the parameter of thermodynamic similarity of different groups of substances.

Since c is a constant, we can derive the following estimate for its possible values. First, we rewrite Eq. (2.3) in the differential form as

$$\frac{\mathrm{d}p}{\mathrm{d}T} = p_* \frac{c}{T} \left(\frac{T}{T_0} \right)^{c-1} . \tag{2.6}$$

Further, from the third law of thermodynamics, we have the condition $(\mathrm{d}p/\mathrm{d}T) \to 0$ at $T \to 0$. Consequently, in order to get finite values of c in the whole range of temperatures (including $T \to 0$), Eq. (2.6) yields the inequality $c > 1$.

Equation (2.3) has not got any additional theoretical substantiation so far similar, e.g., to the van der Waals equation of state for liquid–vapor phase equilibria. Its advantage (and justification) is that it reproduces satisfactorily the relationship between temperature and pressure [4] along the line of phase equilibrium. Another difference to van der Waals' and similar equations of state is that it does not contain the densities of coexisting phases. In his note [5], Simon discussed briefly the relation between Eq. (2.3) and the van der Waals equation, but this direction of research was not developed further by him.

We emphasize that the absence of the critical point of solid–liquid equilibrium makes the solid–liquid different from the liquid–vapor phase transition in the sense that there is no continuous equation of state $f(T, p, v) = 0$ of the type of the van der Waals equation, which would include the description of three states of aggregation. In particular, at $T < T_\mathrm{c}$ in the (v, p) plane there is no common isotherm for solid and fluid states (see Fig. 2.1). It is well known that not only the van der Waals equation, but also other existing more sophisticated continuous equations of state do not allow for a combined description of the T, p, and v properties of a fluid and a crystal.

Figure 2.1 represents the following common peculiarity of fluid states. At $T < T_\mathrm{c}$, there are two branches of the spinodal. These two curves are determined by the equation

$$\left(\frac{\partial p}{\partial v} \right)_T = 0 . \tag{2.7}$$

They merge at the critical point. One of the branches refers to a superheated (stretched) liquid, the other – to a supercooled (supercompressed) gas, but there is no spinodal for supercompressed (supercooled) liquid states [6,7], i.e., no other extremum exists on the extension *BA* of each isotherm for high pressures. The point F in Fig. 2.1 specifies the location of the spinodal (for the given value of temperature) of the stretched (superheated) crystal.

If in the (T, p) plane we construct a family of isochores for the liquid and the vapor phases extending them up to the spinodal, we can reveal an exciting feature: each of the branches of the spinodal curve turns out to be the envelope of the corresponding group of isochores [8]. Formally it means that, at any arbitrary point of the spinodal, the condition

$$\left(\frac{\mathrm{d}p}{\mathrm{d}T} \right)_{Sp} = \left(\frac{\partial p}{\partial T} \right)_v \tag{2.8}$$

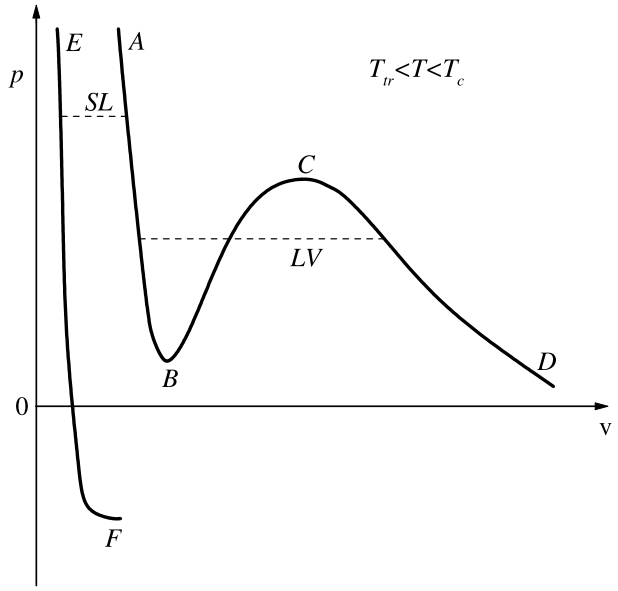

Figure 2.1: Crystalline (EF) and fluid (ABCD) branches of the isotherm in the range $T_{\mathrm{tr}}<T<T_{\mathrm{c}}$, where T_{tr} is the temperature of the triple point, T_{c} the critical point and F, B, and C are the spinodal points on the plane $T = \mathrm{const}$ for solid, liquid, and vapor. The dashed lines (SL) and (LV) correspond to equilibrium phase transitions

is fulfilled. In Fig. 2.2, the results of such a construction are shown for argon [9] employing experimental $(T,\ p,\ v)$ data and the extrapolation of the isochores beyond the binodal curve AC.

Employing the van der Waals or similar equations of state for liquid–vapor phase equilibria, the binodal curve can be determined via the Maxwell rule. This method of determination of the points along the binodal curve is not applicable for solid–liquid phase coexistence. In searching for alternative methods of determination of the binodal curves for liquid–solid phase equilibria, one has to guarantee agreement of Eq. (2.3) with the condition $\mu_{\mathrm{S}}(T,\ p) = \mu_{\mathrm{L}}(T,\ p)$, and therefore with the Clausius–Clapeyron equation (2.2).

The aim of the present contribution consists in the analysis of the behavior of some basic thermodynamic quantities reflecting the specific character of phase transitions on the solid–liquid and liquid–vapor phase equilibrium lines extended beyond the triple point. Hereby experimental $(T,\ p, v)$ data are employed for liquids in the stable state and their extrapolation along chosen isolines into the region of metastability. We have restricted ourselves here to the consideration of normally melting substances, for which the relations $\mathrm{d}p/\mathrm{d}T_{\mathrm{SL}} > 0$ and $\Delta v_{\mathrm{SL}} > 0$ hold.

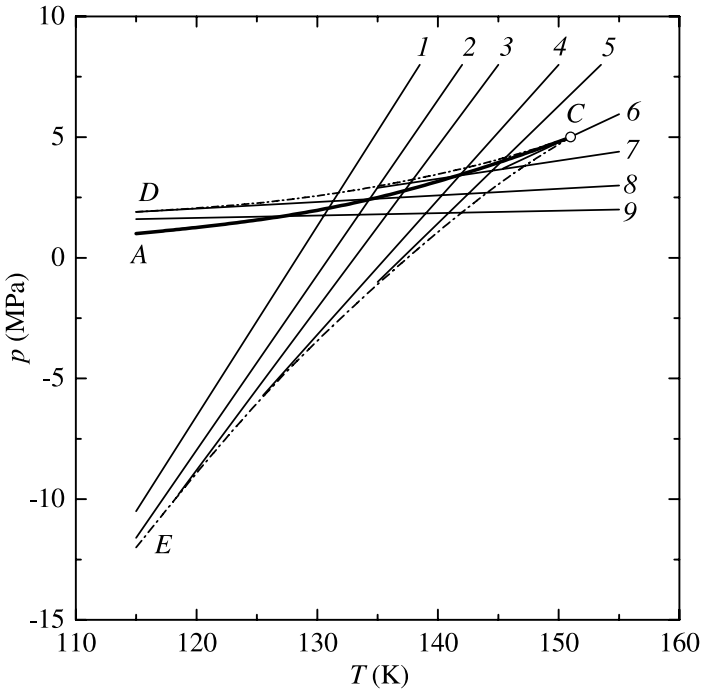

Figure 2.2: Phase diagram of fluid states of argon: *AC* is the binodal curve, *EC* is the spinodal of the liquid, *DC* is the vapor spinodal, (1–5) are a set of liquid phase isochores, (6) is the critical isochore ($v_c = 1.867 \times 10^{-3} m^3/kg$), (7–9) are isochores of the vapor

2.2 Behavior of the Internal Pressure

The internal pressure, p_i, of an isotropic phase is determined by the derivative of the internal energy, u, with respect to the volume, i.e.,

$$p_i = \left(\frac{\partial u}{\partial v}\right)_T \ . \tag{2.9}$$

In a thermodynamic equilibrium state, the internal (p_i) and the external (p) pressures are related by the following equation

$$p_i = T\left(\frac{\partial p}{\partial T}\right)_v - p = p_t - p \ , \tag{2.10}$$

where

$$p_t = T\left(\frac{\partial p}{\partial T}\right)_v \tag{2.11}$$

is called the thermal or total pressure. The behavior of the internal pressure during changes of the state of the system reflects the variations in the relationship between the forces of attraction

($p_\mathrm{i} > 0$) and repulsion ($p_\mathrm{i} < 0$) with position averaging over all particles. The values of the pressures p_t and p_i in the different states of the system under consideration can be calculated by Eqs. (2.10) and (2.11), if the thermal equation of state of the substance is known.

With Eq. (2.2) and the relation

$$T\,\Delta s = \Delta h = \Delta u + p\Delta v\ , \tag{2.12}$$

where h is the enthalpy, we can introduce another quantity $\hat{p}$. This quantity has the dimension of pressure as well and is another important characteristic of the phase transition. For the liquid–vapor phase transition, we have then

$$\hat{p}_\mathrm{LV} \equiv \left(\frac{\Delta u}{\Delta v}\right)_\mathrm{LV} = T\,\frac{\mathrm{d}p}{\mathrm{d}T_\mathrm{LV}} - p\ . \tag{2.13}$$

The respective notations for the solid–liquid phase transition may be introduced in a similar way. Equations (2.10) and (2.13) are close to each other in form. However, the specific volumes, v, of the liquid along the liquid–vapor and solid–liquid coexistence curves change differently with increasing temperature: In the first case $\mathrm{d}v_\mathrm{L}/\mathrm{d}T_\mathrm{LV} > 0$ holds, whereas $\mathrm{d}v_\mathrm{L}/\mathrm{d}T_\mathrm{SL} < 0$. There is also a difference in the relative slope of the phase transition line on the (T, p) plane and the family of isochores at the points of attachment of isochores to this line: For the solid–liquid line we have

$$\frac{\mathrm{d}p}{\mathrm{d}T_\mathrm{SL}} > \left(\frac{\partial p}{\partial T}\right)_v\ , \tag{2.14}$$

whereas

$$\frac{\mathrm{d}p}{\mathrm{d}T_\mathrm{LV}} < \left(\frac{\partial p}{\partial T}\right)_v\ . \tag{2.15}$$

These results mean that, if we take into account Eqs. (2.10) and (2.13), the quantity $\hat{p}_\mathrm{SL}$ is larger and $\hat{p}_\mathrm{LV}$ is smaller than the corresponding internal pressures p_i in the liquid at the lines of phase equilibrium. Including into consideration the low-temperature range of metastable states of the coexisting phases we note that the relations $\hat{p}_\mathrm{LV},\ p_\mathrm{i,LV} \to 0$ at $T \to 0$ hold for liquid–vapor equilibrium, whereas in the same limit $\hat{p}_\mathrm{SL},\ p_\mathrm{i,SL} \to p_*$. This result follows from Eqs. (2.10), (2.13), and (2.3). At any arbitrary point of the melting line, we have

$$\hat{p}_\mathrm{SL} = cp_* + (c-1)p\ . \tag{2.16}$$

The lines $p_\mathrm{i,LV}(T)$ and $p_\mathrm{i,SL}(T)$, pertaining to the liquid, intersect at the triple point.

Figure 2.3 shows the behavior of the quantities p_SL and p_LV as well as p_i and $\hat{p}$ for the liquid phase along the lines of the liquid–solid and liquid–vapor equilibrium for argon (a) and sodium (b). To construct the $p_\mathrm{i}(T)$ and $\hat{p}(T)$ curves the (T, p, v) data were used from Ref. [10] for argon and Refs. [11, 12] for sodium. Melting lines have been extended into the region $p < 0$ by Eq. (2.3).

From the constructions in Fig. 2.3 it can be seen that the values of $\hat{p}_\mathrm{SL}$ and $p_\mathrm{i,SL}$ diverge rapidly with increasing temperature and pressure. This property is connected with the absence

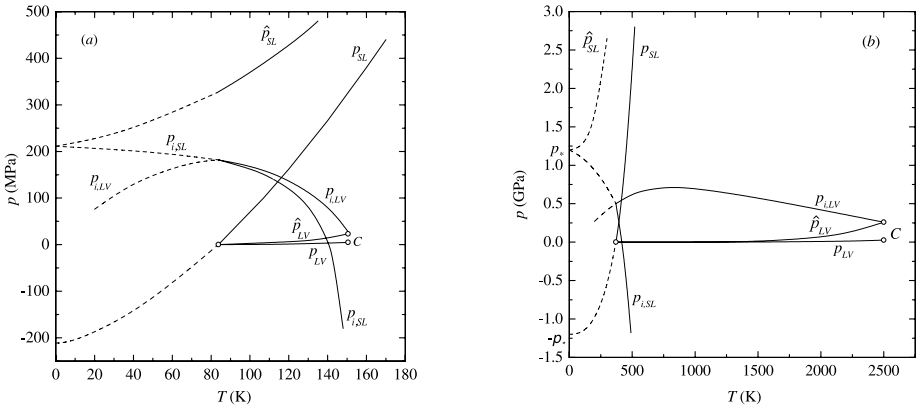

Figure 2.3: Behavior of the internal pressure, p_i, in the liquid and of the quantity, $\hat{p}$, given by Eq. (2.13), on the lines of solid–liquid ($p_\mathrm{SL}(T)$) and liquid–vapor ($p_\mathrm{LV}(T)$) phase equilibrium for argon (a) and sodium (b), C is the critical point. The dashed sections of the curves show the extension beyond the triple point into the region of metastable states

of an end point for solid–liquid equilibrium of critical-point type. The existence of a critical point for liquid–vapor equilibrium leads above the triple point to an approach of the $p_\mathrm{i,LV}$ and $\hat{p}_\mathrm{LV}$ lines with increasing temperature and their convergence at the critical point. For solid–liquid equilibrium the values of $\hat{p}$ and p_i coincide only at $T \to 0$.

On the whole line of liquid–vapor equilibrium the internal pressure is positive, $p_\mathrm{i} > \hat{p}_\mathrm{LV} > 0$, whereas on the melting line the internal pressure passes, with increasing temperature, through zero and becomes negative. Note that, according to the van der Waals equation of state, we have $p_\mathrm{i} = a/v^2$, i.e., everywhere $p_\mathrm{i} > 0$ holds. This result indicates the inadequacy of the van der Waals equation at high densities of the fluids. In addition, the above considerations also give support to the well-known point of view that a liquid–solid phase transition is not connected with the predominance of attractive forces in the molecular system as is the case in the phenomenon of gas condensation.

2.3 The Boundaries of Stability of a Liquid

The coexistence of two phases presupposes stability of each of them with respect to local perturbations of density or entropy. The condition of mechanical stability

$$-\left(\frac{\partial p}{\partial v}\right)_T > 0 \tag{2.17}$$

has to be fulfilled for each of the phases on the liquid–vapor and solid–liquid coexistence curves including the metastable sections of these lines. Thus, Eq. (2.7) corresponds to the boundary of stability – the spinodal.

It is interesting to reveal the tendency in the relative position of the low-temperature sections of the melting line and the liquid spinodal. For these purposes, a (T, p) diagram

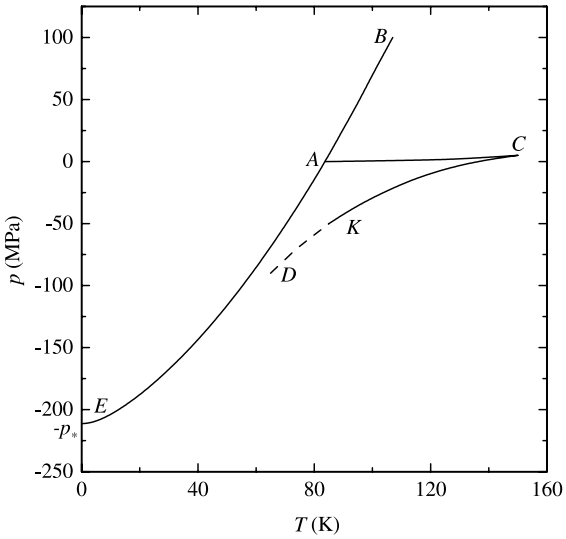

Figure 2.4: Melting line (AB) of argon with a metastable extension (AE) into the region of negative pressures; (AC) is the line of liquid–vapor phase equilibrium; (CKD) is the spinodal of a stretched liquid; A is the triple point

of the state of argon is shown in Fig. 2.4. The extension AE of the melting line BA beyond the triple point corresponds to the Simon equation (2.3) with the following parameters: $p_* = 211.4$ MPa, $c = 1.593$, and $T_0 = 83.8$ K. The liquid spinodal CK has been constructed employing experimental (T, p, v) data [13] in the region of stable and metastable states of liquid argon. The extension KD of the spinodal is less reliable.

From Fig. 2.4, a qualitative conclusion can be derived concerning the approach of the melting line and the liquid spinodal to each other with increasing tensile stress applied to the coexisting liquid and crystal. The crystalline phase also decreases its stability. This result can be reconfirmed by the pressure dependence of the elasticity $-(\partial p/\partial v)_T$ on the melting line of argon as shown in Fig. 2.5. A similar behavior of the elasticity is also observed for sodium (see also Fig. 2.5). It can be seen from the figures that the boundaries of stability of the liquid and crystalline phases $-(\partial p/\partial v)_T = 0$ are reached in the vicinity of the initial point ($p^+ = 0$, $T = 0$) of the melting line. In Fig. 2.5, use is made of a shifted pressure scale $p^+ = p + p_*$. For the preparation of the figures, data from Refs. [11,14] were employed in order to construct the liquid and crystalline branches of the elasticity curves for argon and sodium.

The general character of the tendency mentioned above is confirmed for different substances by comparison of the values of the limiting pressure $-p_* = p(0)$ on the melting line, and the limiting pressure $p_{\mathrm{sp}}(0)$ on the liquid spinodal for $T \to 0$. To retain uniformity in the approach to the evaluation of $p_{\mathrm{sp}}(0)$ for substances of different nature, the present authors [15, 16] turned to the van der Waals equation, according to which $p_{\mathrm{sp}}(0) = -27\,p_{\mathrm{c}}$. This result reveals the same order of magnitude and the correlated character of the quantities p_* and $27\,p_{\mathrm{c}}$ in the series of such substances as inert and two-atomic gases, organic liquids,

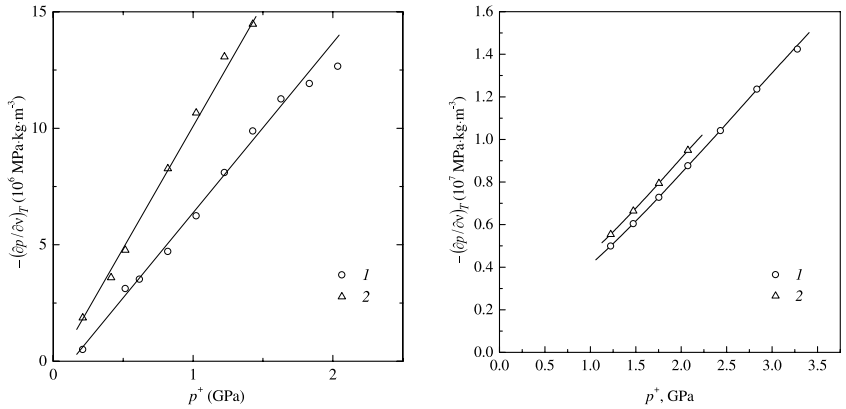

Figure 2.5: Behavior of the elasticity of liquid (1) and solid (2) argon (left) and sodium (right) along the melting line

metals [4, 16]. The quantities p_* and $27p_c$ themselves change in this series by two decimal orders going over from neon, argon to copper and nickel.

Thus, one can establish the following pattern of behavior for coexisting solid and liquid with respect to their stability. At $p > 0$, both phases increase their stability with increasing temperature as evidenced by the increase in elasticity $-(\partial p/\partial v)_T$. Here no manifestation of any spinodal peculiarity is observed, which would be noticeable in the case of existence of a critical point of the solid–liquid type in analogy to the liquid–vapor phase equilibrium. If the melting line is extended into the region of stretched states of both phases, then, as seen from Figs. 2.4 and 2.5, the stability of a coexisting solid and liquid decreases approaching the boundary as given by Eq. (2.7). The region of this coexistence is restricted by the low-temperature limit. For the line of liquid–vapor equilibrium the upper limit is the critical point.

The difference in the degree of stability of solid–liquid and liquid–vapor phase equilibria is demonstrated for argon in Fig. 2.6. Here one can see the variation with temperature of the elasticity of the liquid phase, which is in equilibrium with vapor (LV line) and solid (SL line), C is the critical point. The zero line for $(\partial p/\partial v)_T$ refers to the spinodal. The discrepancy between the spinodal and the extended SL line at $T = 0$ may reflect the approximate character of the description of these lines in the low-temperature limit.

The construction in Fig. 2.6 shows that the spinodal seems to connect the limiting states on the liquid–vapor and solid–liquid lines. Both of the mentioned states are located at the boundary of stability of the coexisting phases. With respect to stability, there is a certain analogy between the critical point of a liquid–vapor equilibrium and the metastable limit $T = 0$ of the solid–liquid equilibrium.

2.4 The Surface Energy of the Interfacial Boundary

The behavior of the surface tension, $\sigma_{LV}(T)$, for liquid–vapor equilibria in pure substances has been studied thoroughly. Available experimental methods allow us to determine the val-

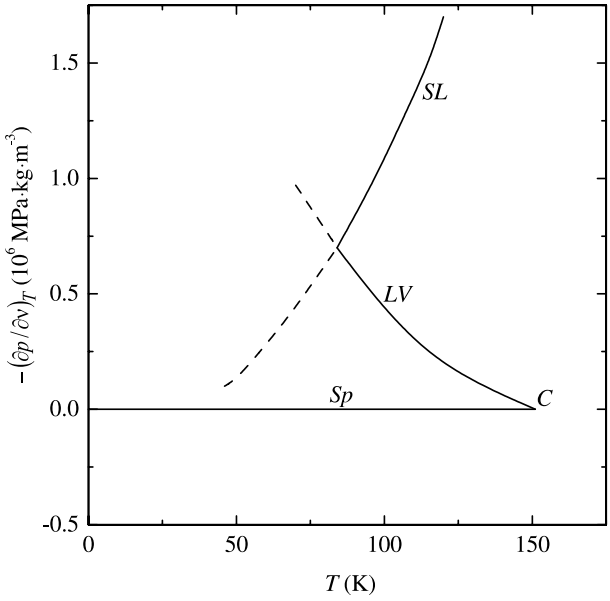

Figure 2.6: Elasticity of liquid argon along the lines of solid–liquid (SL) and liquid–vapor (LV) equilibrium, the *Sp* line is the liquid spinodal, and *C* is the critical point. The intersection of the SL and LV lines corresponds to the triple point

ues of σ_{LV} with high precision. As one of the results, it turns out that the surface tension monotonically decreases, as the temperature increases, and tends to zero at the critical point. The approach to zero can be described by the power law [17]

$$\sigma_{\mathrm{LV}} \sim \left(1 - \frac{T}{T_{\mathrm{c}}}\right)^{\mu} , \tag{2.18}$$

where T_{c} is the critical temperature of the substance considered and the parameter $\mu \approx 1.25$.

Molecular-kinetic approaches to the description of the surface properties of liquids imply the existence of a correlation between surface tension, σ_{LV}, and specific heat of vaporization of a substance, Δh_{LV}. An analysis of the experimental data led to the formulation of several empirical equations interrelating these properties [17, 18]. The application of the thermodynamic similarity methodology for describing the surface tension of normal (nonassociated) liquids resulted in the discovery of a one-parametric relation for σ in reduced variables of the form [19]

$$\sigma^*_{\mathrm{LV}} = \sigma^*_{\mathrm{LV}}(\Delta h^*_{\mathrm{LV}}, A) \tag{2.19}$$

with

$$\sigma^*_{\mathrm{LV}} = \sigma_{\mathrm{LV}} k_{\mathrm{B}}^{-\frac{1}{3}} T_{\mathrm{c}}^{-\frac{1}{3}} p_{\mathrm{c}}^{-\frac{2}{3}} , \quad \Delta h^*_{\mathrm{LV}} = \frac{\Delta h_{\mathrm{LV}}}{RT} . \tag{2.20}$$

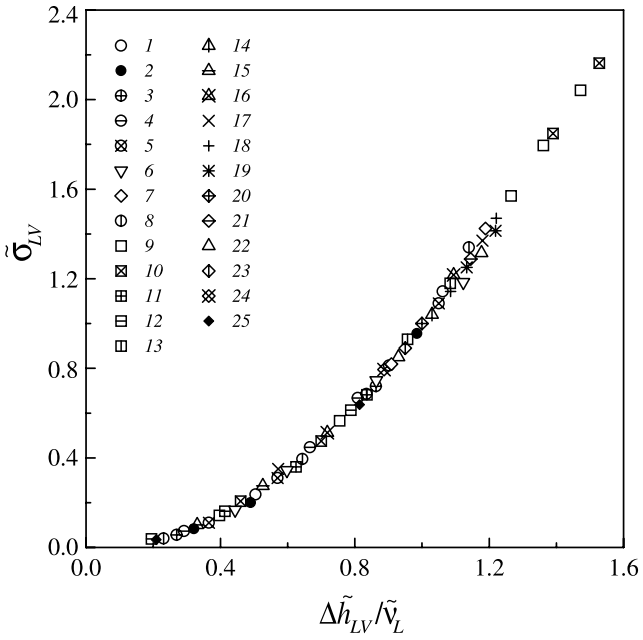

Figure 2.7: Relationship between the dimensionless quantities $\widetilde{\sigma}_{\mathrm{LV}}$ and $\Delta\widetilde{h}_{\mathrm{LV}}/\widetilde{v}_{\mathrm{L}}$ for normal liquids. The numbers refer to different substances as specified in Table 2.1

Here A is the thermodynamic similarity parameter characterizing individual properties of the molecules of the particular substance considered, p_{c} is the pressure at the critical point, k_{B} is the Boltzmann constant, and R is the universal gas constant.

An analysis of the relation between σ_{LV} and the enthalpy of vaporization (referred to a unit volume of the liquid phase), $\Delta h_{\mathrm{LV}}/v_{\mathrm{L}}$, allowed us to discover new simple relationships containing no individual parameters for the description of normal liquids in the context of thermodynamic similarity. Here v_{L} is the specific volume of the liquid in equilibrium with the vapor.

Let us introduce dimensionless values for σ_{LV} and Δh_{LV} by choosing as scales the corresponding quantities at the temperature $\widetilde{T} = T/T_{\mathrm{c}} = 0.6$

$$\widetilde{\sigma}_{\mathrm{LV}} = \frac{\sigma_{\mathrm{LV}}}{\sigma_{\mathrm{LV}}(\widetilde{T}=0.6)}\,, \quad \frac{\Delta\widetilde{h}_{\mathrm{LV}}}{\widetilde{v}_{\mathrm{L}}} = \left(\frac{\Delta h_{\mathrm{LV}}}{v_{\mathrm{L}}}\right) \Big/ \left(\frac{\Delta h_{\mathrm{LV}}}{v_{\mathrm{L}}}\right)_{\widetilde{T}=0.6}\,. \tag{2.21}$$

Figure 2.7 shows the relation between the quantities $\widetilde{\sigma}_{\mathrm{LV}}$ and $\Delta\widetilde{h}_{\mathrm{LV}}/\widetilde{v}_{\mathrm{L}}$ for a large group of nonassociated liquids in the temperature range from the triple to the critical point. Tables 2.1 and 2.2 give the scale values for the calculation of these dimensionless variables. A separate column presents references to the literature from which the experimental data for Δh_{LV} and v_{L}, and also the critical parameters T_{c} and p_{c} have been taken.

Table 2.1: Main quantities determining the thermodynamic similarity of vapor–liquid equilibria for nonassociated liquids

No.	Substance	T_c	p_c	$\sigma_{\tilde{T}=0.6}$	$\sigma^*_{\tilde{T}=0.6}$
		K	MPa	mJ/m^2	
1	Argon	150.7	4.86	11.75 [17]	3.192
2	Krypton	209.4	5.49	14.28 [17]	3.221
3	Xenon	289.7	5.83	16.87 [21]	3.281
4	Nitrogen	126.3	3.40	9.20 [22]	3.381
5	Oxygen	154.7	5.09	12.50 [17]	3.281
6	Carbon monoxide	132.9	3.50	9.95 [17]	3.532
7	Diborane	289.9	4.00	14.37 [25]	3.589
8	Methane	190.6	4.60	12.36 [17]	3.243
9	Ethane	305.4	4.88	16.31 [17]	3.508
10	Propane	369.8	4.26	16.66 [17]	3.681
11	Butane	425.2	3.80	16.90 [17]	3.846
12	Isobutane	408.1	3.65	16.40 [17]	3.864
13	Pentane	469.6	3.37	17.30 [25]	4.130
14	Isopentane	461.0	3.33	16.83 [25]	4.027
15	Hexane	507.9	3.03	17.26 [25]	4.365
16	Heptane	540.2	2.74	17.32 [25]	4.529
17	Octane	569.4	2.49	17.05 [25]	4.667
18	Nonane	595.2	2.28	17.01 [25]	4.842
19	Decane	619.2	2.10	16.89 [25]	5.035
20	Cyclopentane	511.9	4.51	20.64 [25]	3.908
21	Cyclohexane	553.1	4.03	20.83 [25]	4.036
22	Benzene	562.6	4.92	23.09 [25]	4.036
23	Toluone	594.0	4.05	21.61 [25]	4.178
24	Monofluorotrichloromethane	471.2	4.41	19.65 [28]	3.908
25	Hexafluorobenzene	516.8	3.26	19.98 [29]	4.699

As is evident from Fig. 2.7, points for different substances fall well onto a common curve in a wide range of values of the variables. The point (0, 0) in the plot corresponds to the critical point of the respective substances.

The data in Fig. 2.7 may be expressed by the following simple relation

$$\widetilde{\sigma}_{LV} = \left(\frac{\Delta \widetilde{h}_{LV}}{\widetilde{v}_L} \right)^m . \tag{2.22}$$

The average value of the exponent m for different substances is equal to $m = 2.15$. The correlation equation (2.22) gives an adequate description of the experimental data at temperatures $\widetilde{T}$ from 0.6 to 1 and makes it possible to evaluate the surface tension of liquids using known data of Δh_{LV} and v_L. This discovered relation is an example of the law of corresponding states containing no substance dependent parameters and may be regarded as a zeroth-order

Table 2.2: Main quantities determining the thermodynamic similarity of vapor–liquid equilibria for nonassociated liquids (continuation)

No.	Substance	$\left(\frac{\Delta h_{LV}}{v_L}\right)_{\widetilde{T}=0.6}$	$\left(\frac{\Delta h_{LV}}{v_L p_c}\right)_{\widetilde{T}=0.6}$	References
		10^3 kJ/m^3		
1	Argon	217.7	44.59	[20]
2	Krypton	248.7	45.30	[20]
3	Xenon	269.3	46.19	[20]
4	Nitrogen	165.5	48.69	[23]
5	Oxygen	235.3	46.24	[24]
6	Carbon monoxide	174.4	49.77	[25]
7	Diborane	230.3	57.54	[25]
8	Methane	211.1	45.90	[26]
9	Ethane	265.5	54.41	[27]
10	Propane	257.8	60.51	[27]
11	Butane	245.9	64.70	[27]
12	Isobutane	232.0	63.56	[27]
13	Pentane	242.8	72.05	[25]
14	Isopentane	229.8	67.92	[25]
15	Hexane	234.7	74.13	[25]
16	Heptane	228.7	83.37	[25]
17	Octane	225.5	90.57	[25]
18	Nonane	222.1	96.61	[25]
19	Decane	214.8	102.3	[25]
20	Cyclopentane	294.5	64.42	[25]
21	Cyclohexane	276.1	67.92	[25]
22	Benzene	335.8	68.53	[25]
23	Toluone	308.1	74.99	[25]
24	Monofluorotrichloromethane	283.6	64.27	[25]
25	Hexafluorobenzene	288.6	88.51	[29]

approximation in describing the thermodynamic similarity of substances of different nature in reduced variables as determined by Eq. (2.21).

The use of the critical parameters of the substances in constructing reduced variables revealed the existence of a relation between the dimensionless quantities σ^*_{LV} and $\Delta h_{LV}/v_L p_c$. This dependence is shown in Fig. 2.8 in logarithmic coordinates for a temperature $\widetilde{T} = 0.6$. Tables 2.1 and 2.2 give the numerical values of the dimensionless variable. According to Fig. 2.8, the dependence between $\log(\sigma^*_{LV})_{\widetilde{T}=0.6}$ and $\log(\Delta h_{LV}/v_L p_c)_{\widetilde{T}=0.6}$ is close to a linear one.

It has been found that the dependence remains linear and its slope does not change at other temperatures $\widetilde{T}$ up to the critical point ($\widetilde{T} = 1$). This means that for approximation of data

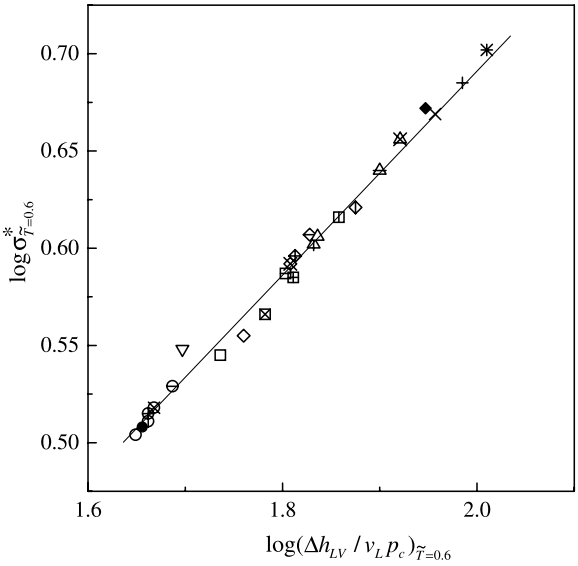

Figure 2.8: Correlation between the quantities $\log \sigma^*_{\tilde{T}=0.6}$ and $\log(\Delta h_{\mathrm{LV}}/v_{\mathrm{L}} p_{\mathrm{c}})_{\tilde{T}=0.6}$ for normal liquids. The different substances are specified in the same way as done in Fig. 2.7

one may use the function

$$\sigma^*_{\mathrm{LV}} = N \left(\frac{\Delta h_{\mathrm{LV}}}{v_{\mathrm{L}} p_{\mathrm{c}}} \right)^n , \tag{2.23}$$

where the exponent n is of the order $n \cong 0.55$. The factor N is a function of temperature, and $N(\widetilde{T}) \to 0$ holds for $\widetilde{T} \to 1$.

At a given temperature the dimensionless complex

$$N = \sigma^*_{\mathrm{LV}} \left(\frac{v_{\mathrm{L}} p_{\mathrm{c}}}{\Delta h_{\mathrm{LV}}} \right)^n = \sigma^*_{\mathrm{LV}} \left[\left(\frac{p_{\mathrm{c}}}{T_{\mathrm{c}}} \right) \frac{v_{\mathrm{L}}}{\widetilde{T}\, \Delta s_{\mathrm{LV}}} \right]^n \tag{2.24}$$

characterizes the similarity of substances with respect to the liquid–vapor phase transition. It follows from Eq. (2.24) that the behavior of the surface energy of a liquid–vapor interface is determined to a large extent by the ratio of the entropy difference between liquid and vapor and the specific volume of the liquid phase.

Table 2.3 gives the values of the quantity $N(\widetilde{T})$ as calculated from experimental data for several temperatures $\widetilde{T}$. The calculations were done by employing the method of least squares. The variation of N along the vapor pressure curve can be described by the relation

$$\widetilde{T} - 1 = aN + bN^2 \tag{2.25}$$

with values of the coefficients equal to $a = -0.870$ and $b = -0.357$.

Similar to Eq. (2.22), Eq. (2.23) does not contain substance-dependent parameters and may be used for calculating the surface tension values using the vaporization enthalpy and the

Table 2.3: Variation of the factor $N(\tilde{T})$ in Eq. (2.23) along the vapor pressure curve

$\tilde{T}$	0.5	0.6	0.7	0.8	0.9	0.95	1
$N(\tilde{T})$	0.481	0.395	0.308	0.211	0.111	0.057	0

saturated liquid density data at the phase equilibrium point. A comparison with experimental data shows a high accuracy of the correlations derived here.

In contrast to the liquid–vapor equilibrium there is no simple and reliable method for measuring the solid–liquid surface tension, σ_{SL}, along the $p_{SL} = f(T)$ melting curve at different temperatures [30]. Theoretical (computational) surface tension estimates for the crystal–melt interface are very approximate. This conclusion is supported, for example, by the results of σ_{SL} calculations for metals reported by various authors and summarized in Ref. [31]. There are no data on the temperature dependence of σ_{SL}. The absence of a singular point of the critical point type for crystal–liquid phase equilibria makes predictions of $\sigma_{SL}(T)$ uncertain.

For normally melting substances ($\Delta v_{SL} > 0$) the volume jump decreases as the temperature increases, but, in contrast to the liquid–vapor equilibrium, the densities of both phases, $\rho_L = 1/v_L$ and $\rho_S = 1/v_S$, increase. In addition, the increase in temperature is accompanied by an increase in elasticity $(\partial p/\partial \rho)_T$; that is, an increase in the thermodynamic stability of the coexisting crystalline and liquid phases. The approach to the liquid–vapor critical point not only decreases the difference of phase densities but also destabilizes the phases with respect to small homophase perturbations, whereas crystal–liquid equilibria show a similar tendency in the low temperature limit $T \to 0$ along the metastable melting curve continuation below the triple point [4]. These considerations led us to expect a more complex behavior of the surface tension of simple substances along the melting curve as compared with its behavior along the boiling curve, $p_{LV} = f(T)$. In Refs. [32,33], the surface energy of the crystal–liquid interface was estimated from experiments on spontaneous crystallization of supercooled liquid drops employing the classical theory of homogeneous nucleation [34,35]. For stationary conditions, the theory predicts the following dependence of the rate of nucleation, J (in s^{-1} cm^{-3}), on critical crystalline nucleus formation W_*

$$J = N_1 B \exp\left(-\frac{W_*}{k_B T}\right) , \tag{2.26}$$

where N_1 is the number of molecules in a unit volume of the liquid, B is a kinetic factor, and k_B is the Boltzmann constant. For low-viscosity melts, B changes insignificantly as the degree of supercooling $\Delta T = T_0 - T$ increases. In the order of magnitude, we have $N_1 \approx 10^{22}$ cm^{-3} and $B \approx 10^{10}$–10^{11} s^{-1}. The thermodynamic factor containing the Gibbs number, Gi, in the exponent

$$Gi = \frac{W_*}{k_B T} \tag{2.27}$$

plays then the determining role in the kinetics of nucleation [36].

The homogeneous nucleation theory was developed in a thermodynamic approximation. A supercooled liquid and a crystalline nucleus are treated as volume phases, and interface

effects are introduced via the surface tension. For a spherical nucleus of radius, r, in unstable equilibrium with the surrounding ambient phase we have

$$W_* = \frac{4\pi}{3} r^2 \sigma_{SL} = \frac{16\pi}{3} \frac{\sigma_{SL}^3 v_S^2}{(\Delta\mu)^2} = \frac{16\pi}{3} \frac{\sigma_{SL}^3 v_S^2}{(\Delta s_{SL})^2 (\Delta T)^2} \,. \tag{2.28}$$

Equation (2.28) is obtained with an accuracy to first-order terms in the expansion of the chemical potential $\mu(T, p)$ in powers of temperature, T, and pressure, p [36]. The right-hand side of Eq. (2.28) allows us to express Eq. (2.27) as

$$Gi = \frac{16\pi}{3} \frac{\sigma_{SL}^3 v_S^2}{k_B T \, (\Delta s_{SL})^2 \, (\Delta T)^2} \,. \tag{2.29}$$

Small changes in supercooling, ΔT, have a strong effect on the nucleation rate, J. An increase in supercooling by 10 K, increases J by nine orders of magnitude for mercury and four orders of magnitude for tin at $\Delta T = 52$ and 122 K, respectively, for $J \approx 10^5$ s^{-1} cm^{-3} [36].

A comparison of experiments on spontaneous crystallization with the homogeneous nucleation theory makes it possible to estimate the surface tension, which is the only significant adjustment parameter in Eqs. (2.26) and (2.28). This approach was applied in Ref. [32] to organic liquids and in Ref. [33] to metals. The most serious difficulty was premature crystallization on impurity particles, which decreased σ_{SL} and resulted in a strong temperature dependence of surface tension. "Pure" conditions are easier to attain in small samples. For this reason, submillimeter drops were used in the experiments.

The condition $Gi = 62$ employed in Ref. [32] corresponds to $J \approx 10^6$ s^{-1} cm^{-3}. A more detailed study of the homogeneous nucleation of metals, water, and several organic liquids was performed in a series of measurements reviewed in the monograph [36]. All these experiments were, however, performed at atmospheric and lower pressures and gave σ_{SL}-values at a single melting curve point close to $p = 0$. The scaling pressure value for the solid–liquid equilibrium p_* in Eq. (2.3) is equal to several GPa for metals. Experimental studies of the kinetics of spontaneous crystallization at such pressures are a long way to go in a future.

It is possible to evaluate the surface tension of a solid–liquid interface for different substances in a large range along the melting line with information on homogeneous nucleation only in the vicinity of $p = 0$. For this purpose, we shall return to considerations on thermodynamic similarity basing the analysis on the available data on the kinetics of spontaneous crystallization.

The melting line of tin, approximated by the Simon equation, is shown in Fig. 2.9 with $T_0 = 505$ K, $p_* = 5.70$ GPa, and $c = 3.4$ [37]. This line contains its metastable continuation to negative pressures and low temperatures $(T/T_0) < 1$. The supercoolings $\Delta T = T_0 - T$, used in the experiments on the kinetics of homogeneous nucleation [36], are labeled by squares. The group of points on the right was detected in experiments with submillimeter drops in a neutral medium [38], and the group of points on the left corresponds to crystallization of tin in island films (submicron drops) [39, 40].

Data processing reveals two circumstances [36]: (i) The $J(T)$ dependence is satisfactorily described by the homogeneous nucleation theory with a constant σ_{SL}-value (for tin, $\sigma_{SL} \approx 60$ mJ/m^2), and (ii) the dome-shaped $J(T)$ dependence is linearized in the log J vs.

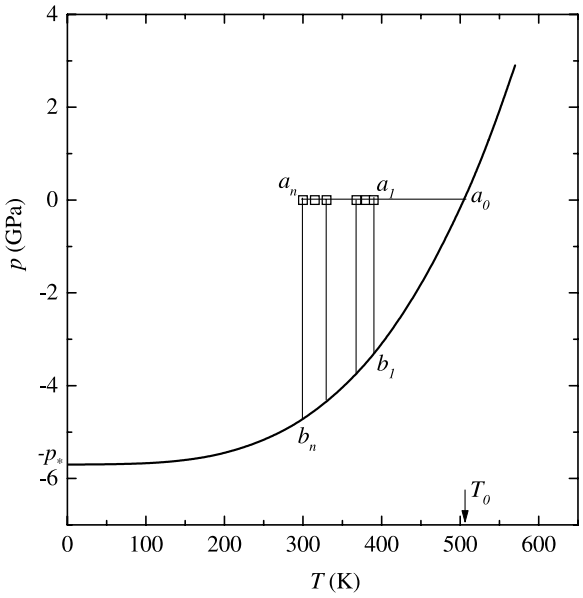

Figure 2.9: Melting curve of tin with a metastable continuation to negative pressures. Points a_1–a_n correspond to homogeneous nucleation experiments on supercooled drops and island films

$[T(\Delta T)^2]^{-1}$ coordinates at $T > T_{\max}$, where $T_{\max}$ is the temperature of the maximum of the dome (see Fig. 2.10). This result implies the constancy of the complex

$$Z = \frac{\sigma_{\mathrm{SL}}^3 \upsilon_{\mathrm{S}}^2}{k_{\mathrm{B}} (\Delta s_{\mathrm{SL}})^2} \,, \tag{2.30}$$

which determines the slope of the dependence of $\log J$ on $[T(\Delta T)^2]^{-1}$, if it is assumed that $\ln J = \text{const} - Gi$; that is, if variations in $\ln(N_1 B)$ are ignored as compared with variations in Gi.

At $p = \text{const}$, the $(a_1, a_2, \ldots, a_n)$ experimental data are referred to one point (a_0) of the melting curve (see Fig. 2.9). The specific volume, υ_{S}, and the entropy of melting, Δs_{SL}, are taken for this point. It follows that if Z remains constant under increasing supercooling at fixed υ_{S}- and Δs_{SL}-values, then σ_{SL} is also constant.

The condition $Z = \text{const}$ can be interpreted more broadly if the a_i points are referred to different points, b_i, of the melting curves as shown in Fig. 2.9. Here the points a_i, b_i correspond to the same temperatures. Each b_i-point is characterized by Δs_{SL}- and υ_{S}-values of its own. Generally, the condition $Z = \text{const}$ gives then different σ_{SL}-values for the points b_1, b_2, ... The linearization, mentioned above, means that the σ_{SL}-, Δs_{SL}-, and υ_{S}-values are correlated by the condition $Z = \text{const}$, where Z has the form as given by Eq. (2.30).

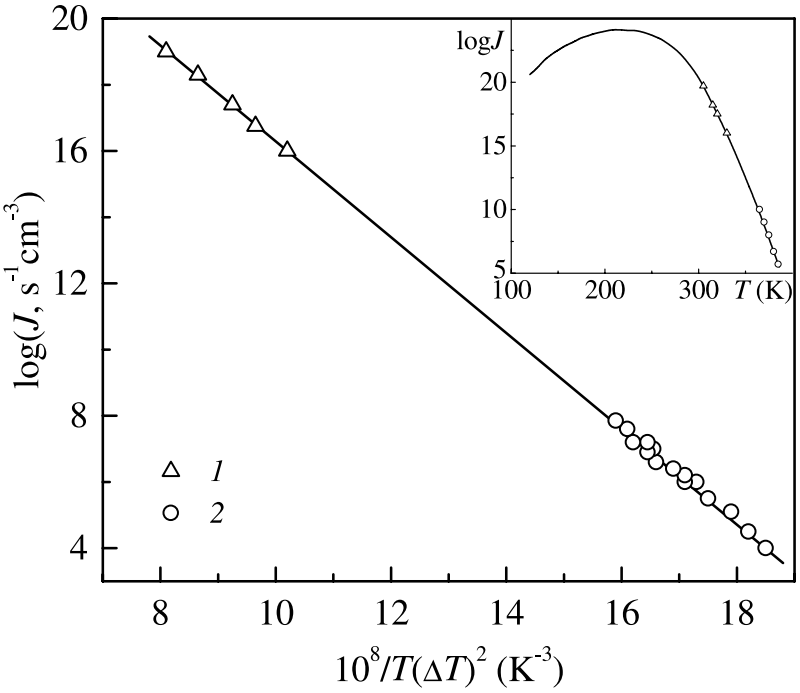

Figure 2.10: Temperature dependence of the nucleation rate in supercooled liquid tin: (1) experiments with island films $d = 4$–100 nm in diameter and (2) experiments with drops ($d = 20$–400 μm); the solid line corresponds to computations by homogeneous nucleation theory

The Z-complex can be brought into a dimensionless form $Nc = Z/T_0^3$ by dividing it by T_0^3. Here T_0 is the temperature on the melting curves of different substances at the corresponding points for $p = 0$

$$Nc = \frac{\sigma_{\mathrm{SL}}^3 v_{\mathrm{S}}^2}{k_{\mathrm{B}} T_0^3 (\Delta s_{\mathrm{SL}})^2} \,. \tag{2.31}$$

It was found that the $(Nc)^{1/3}$-values for different substances differ insignificantly from each other (see Table 2.4). The use of the complexes as defined via Eqs. (2.30) and (2.31) for determination of σ_{SL} at the solid–liquid interface implies the use of phenomenological thermodynamic similarity concepts. Surface tension is assumed to be an explicit function only of temperature. The value of pressure corresponds to this temperature along the melting curve or its metastable continuation into the $p < 0$ region.

Our next step in the analysis consists in the assumption that the condition, $Nc = \mathrm{const}$, holds not only close to $p = 0$ but also over a wide range of the melting curve of the different substances. In order to calculate the $\sigma_{\mathrm{SL}}(T)$ dependence, we have to know then the entropy or

Table 2.4: Values of thermodynamic parameters characterizing solid–liquid equilibria for different substances at atmospheric pressure; Nc is a dimensionless complex determined via Eq. (2.31)

Substance	T_0	v_S	Δh_{SL}	$(\sigma_{SL})_{T_0}$	$(Nc)^{\frac{1}{3}}$
	K	10^{-3} m^3/kg	kJ/kg	mJ/m^2	
Lithium	453.8	1.902	428.6	30	0.44
Sodium	370.8	1.019	115.2	20	0.50
Copper	1 356	0.119	203.1	200	0.54
Silver	1 235	0.102	104.7	143	0.55
Indium	429.8	0.139	28.4	31	0.49
Tin	505.0	0.139	60.7	60	0.54
Mercury	234.3	0.070	11.5	23	0.51
Lead	600.0	0.091	22.6	40	0.50
Argon	83.8	0.608	29.8	7	0.5
Tetrachloromethane	250.6	0.570	16.4	6.7	0.47
Benzene	278.6	0.990	128.2	21.7	0.54
Gallium	302.9	0.175	80.3	40	0.41
Antimony	903.7	0.152	163.9	101	0.41
Bismuth	544.5	0.103	52.6	69	0.55
Water	273.2	1.090	334.4	28.7	0.41

enthalpy jump, Δs_{SL} or $\Delta h_{SL} = T\,\Delta s_{SL}$, and the specific volume of the crystalline phase, v_S, at different points of the melting curve, $p_{SL} = f(T)$.

Table 2.4 contains the values that determine Nc for several simple substances at the corresponding melting curve points at zero (atmospheric) pressure. The values of T_0, v_S, and Δh_{SL} were taken from Ref. [41] for lithium and sodium and from Ref. [42] for the other substances. For $(\sigma_{SL})_{T_0}$, the data from the monograph [36] were used for all substances except sodium and lithium [31] and argon. For argon, the value of $(\sigma_{SL})_{T_0}$ was obtained from the condition $(Nc)^{1/3} = 0.5$. Such choice corresponds to the mean value of the dimensionless complex for normally melting substances.

The calculated $\sigma_{SL}(T)$ dependences are shown in Fig. 2.11 for mercury and argon and for tin, lead, and sodium. The values of Δs_{SL} and v_S were taken from the literature for $p_{SL} > 0$ and obtained from approximations correlated with the Simon equation for $p_{SL} < 0$ [4]. The σ_{SL}-values in the temperature region of experimental studies of nucleation kinetics [36] are marked by squares. Circles correspond to the values calculated from the condition $Nc = \text{const}$ and the experimental Δh_{SL}- and v_S-values. Continuous curves were obtained by extrapolating the Δh_{SL}- and v_S-values. For mercury and tin, the temperature T_0 is marked by an arrow. For the other substances in Fig. 2.11, T_0 corresponds to the leftmost points (circles). The σ_{SL}-values, marked by squares, correspond to negative pressures, because spontaneous crystallization was observed [36] at a finite supercooling of the liquid ($T < T_0$), and the projection of the figurative point at this temperature falls onto the melting curve section, where $p < 0$. This result does not contradict the conditions of the nucleation kinetics experiments, in which

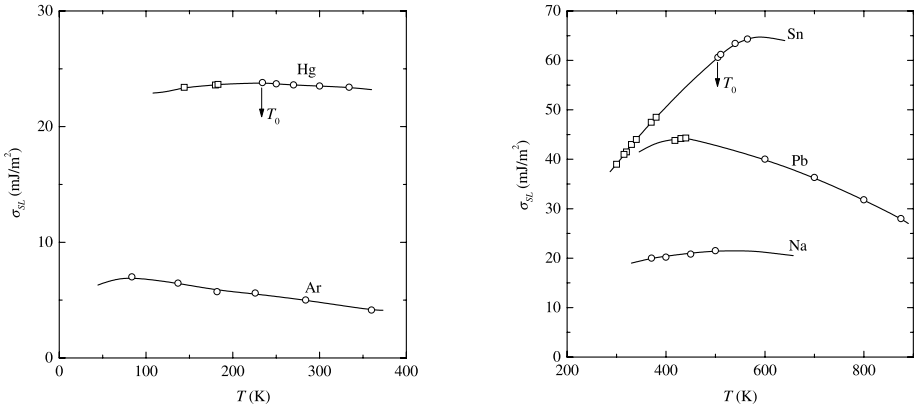

Figure 2.11: Temperature dependences of the surface tension of argon and mercury (left) and tin, lead, and sodium (right) along the melting lines

measurements of σ_{SL} were performed at fixed Δh_{SL}- and υ_S-values corresponding to T_0. The width of the temperature range of σ_{SL} variations in Fig. 2.11 depends on the availability of the data of Δh_{SL} and υ_S at high pressures. For argon, mercury, tin, lead, and sodium, the extreme right points correspond to 1.77 [14], 2.00 [43], 2.60 [44], 5.00 [45,46], and 2.20 GPa [47], respectively. The method, employed by us for estimating $\sigma_{SL}(T)$ along the melting curve, leads to values of the surface tension which decrease as temperature increases at $p > 0$. At the same time, the dependences contain a maximum, and $\sigma_{SL}(T)$ tends to decrease as the temperature becomes lower in the region of negative pressures.

More reliable determinations of surface tension were obtained from homogeneous nucleation experiments for the liquid–vapor phase transitions as compared to the case of spontaneous crystallization considered above. Spontaneous boiling was studied systematically at different pressures and in a wide range of nucleation rates [8,48]. Independent determinations of σ_{LV} by the capillary rise method substantiated the validity of surface tension estimates obtained by utilizing the homogeneous nucleation theory. It was simultaneously shown that the curvature corrections to the surface tension of the interfacial boundary for bubbles containing 10^2–10^3 molecules did not exceed 2–5% of the σ_{LV}-values for a planar interface.

Surface tension depends on the temperature of measurement. This fact is an important circumstance, because an unstable-equilibrium (critical) bubble is characterized by three pressure values at a given temperature, $p_L < p_V < p_{LV}$ (p_L is the pressure in the liquid, p_V is the pressure in the bubble, and p_{LV} is the saturation pressure at a planar interface, $p_{LV} = g(T)$). We also follow the $\sigma = \sigma(T)$ rule in estimating the surface tension at the solid–liquid interface. At this interface, the inequalities $p_{SL}(T) < p_L(T) < p_S(T)$ hold, where p_S is the pressure in the crystalline nucleus. The p_{SL}, p_L, and p_S pressures are essentially different, but the $p_L - p_{SL}$ and $p_S - p_L$ differences can be considered to be small as compared with the scaling pressure, p_*.

The limitations of the approach, employed in estimating $\sigma_{SL}(T)$ in this work, are connected with the narrowness of the experimentally studied spontaneous crystallization intervals. All data on the kinetics of nucleation virtually refer to one pressure ($p = 0 + \delta p$). We

are therefore unable to check whether property (ii) (linearization, see above) holds at other pressures as well. The condition $Nc = \text{const}$, employed here for a large part of the melting curve, is therefore an assumption that has to be substantiated further. Physics and mechanics, however, exhibit many examples when the introduction of dimensionless complexes of essentially interrelated variables helps to determine the functional dependence between them. In this work, the Nc-complex, as defined via Eq. (2.31), plays a similar role.

The dependence of $\sigma_{\mathrm{SL}}(T)$ on temperature along the melting curve, as obtained in this work, has a maximum determined by the behavior of the ratio $(\Delta s_{\mathrm{SL}}/v_{\mathrm{S}})^{2/3}$. Most importantly, a decrease in the Δs_{SL}-entropy jump at $T/T_0 \ll 1$ follows from the Nernst theorem. Equation (2.3) satisfies, for $c > 1$, the condition $\mathrm{d}p/\mathrm{d}T_{\mathrm{SL}} \to 0$ for $T \to 0$, which implies that the Δs_{SL}-entropy jump vanishes when T tends to zero at a finite Δv_{SL}-value. According to Eq. (2.3), Δs_{SL} begins to decrease noticeable at $T > T_{\mathrm{D}}$, where T_{D} is the Debye temperature. At high temperatures ($T > T_0$), the derivative $(\mathrm{d}\sigma_{\mathrm{SL}}/\mathrm{d}T)$ is negative because of an increase in the amplitude of atomic oscillations. This effect results in a swelling of the interface and a decrease in σ_{SL}.

2.5 Viscosity of a Liquid along the Curves of Equilibrium with Crystalline and Vapor Phases

The coefficient of dynamic viscosity, η (hereinafter termed viscosity), is defined via the linear relationship between the shear rate, $\dot{\varepsilon}$, of a liquid and the tangential component of the force acting between the liquid layers at shear stress. In the cases, when η is independent of $\dot{\varepsilon} = \mathrm{d}u_x/\mathrm{d}y$, where u_x is the component of velocity in the direction of shear stress, a fluid is called a Newtonian liquid. The quantity η characterizes the intensity of a momentum flux in the normal direction to the plane of slip. The energy dissipated per unit volume and unit time due to viscosity is defined by the product $\eta\dot{\varepsilon}^2$. The quantity η^{-1} is referred to as fluidity.

Depending on the nature of the substance, on temperature T and pressure p, the range of viscosity variation is extremely wide, for example, from $\eta = 10^{-3}$ Pa · s (water under normal conditions) to 10^{12} Pa · s in the range where fluids undergo the process of vitrification. The wide variation in the possible values of η suggest that the Newtonian liquid approximation presupposes a corresponding space-time scale of experiment or transition to a more complex description of the medium as a viscoelastic body. The relaxation time, τ, of shear stresses is defined (in the order of magnitude) by the ratio of viscosity coefficient to the "instantaneous" shear modulus, G, in Hooke's law via

$$\tau = \frac{\eta}{G} \,. \tag{2.32}$$

Presently, there does not exist a consistent molecular theory of viscosity and simple empirical dependences are commonly employed to describe the behavior of viscosity of liquids ranging from a high-fluid to the vitrified state. Of particular interest are supercooled liquid states (at $T < T_{\mathrm{SL}}$). This interest is connected with the problem of homogeneous nucleation [36] and with the conditions of preparing solid-amorphous samples, including metallic glasses. The main difficulty consists in choosing the dependence of viscosity on the thermodynamic para-

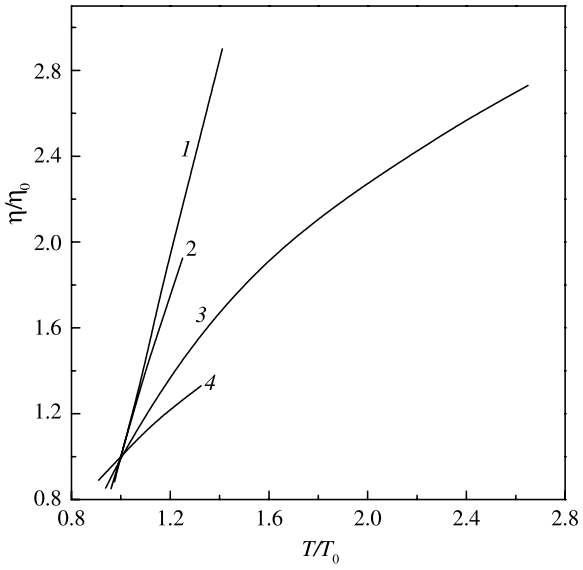

Figure 2.12: Behavior of the viscosity of liquids along the melting line (η_0 and T_0 denote the viscosity and temperature, respectively, at the melting point under atmospheric pressure): (1) benzene [53], (2) carbon dioxide [54], (3) argon [55], and (4) carbon tetrachloride [56]

meters of the liquid and internal consistency of the T, p, v, and η-data when using "far-away" extrapolations into the region of metastable states.

We shall consider the behavior of the viscosity of a melt along the line of solid–liquid phase equilibrium, both for high pressure and for states of coexisting phases ($p < 0$) on the metastable continuation of the melting line beyond the triple point. For normally melting substances, $\mathrm{d}p/\mathrm{d}T_{\mathrm{SL}}$ is positive. Increasing temperature and pressure leads to an opposite change in viscosity, and the resulting effect depends on the steepness of the melting line.

A preliminary treatment [49–52] has demonstrated that, in moving along the melting line, the liquid becomes more viscous with increase in temperature. For several substances, the behavior of η in the initial segment of the melting line is shown in Fig. 2.12. The persistence of this tendency may lead to the vitrification of the melt in the high-temperature segment of the continued melting line rather than in its low-temperature segment. By definition, the value of the viscosity equal to $\eta(T_{\mathrm{g}}, p) = 10^{12}$ Pa · s corresponds to the vitrification temperature T_{g}. We shall study the experimental data for the viscosity of different liquids and extrapolation of the values of η along isobars into the region of supercooled states. For the specification of the melting line we shall use the Simon approximation (2.3).

Two approaches are popularly employed for describing the viscosity. In accordance with Frenkel [57], the viscosity of a liquid is related to the activation energy, E, of a local molecular regrouping via

$$\eta = A \exp\left(\frac{E}{k_{\mathrm{B}}T}\right) , \tag{2.33}$$

where A is a weak function of temperature and pressure as compared to the exponential term. The activation energy increases as the temperature decreases and the pressure rises. On approaching the glass-transition region, under atmospheric pressure, the parameter E increases by an order of magnitude as compared to its value for low-viscosity states [36].

Another approach was developed by Batchinskii [58]. The essence of this approach is expressed as "The viscosity of a liquid is defined by its specific volume v_{L}." The formula

$$\eta = \frac{C}{v_{\mathrm{L}} - \omega} \tag{2.34}$$

was suggested by him. In this relation, C and ω are individual constants of the respective liquids. Although the subsequent test revealed the inadequacy of Eq. (2.34) for a wide range of viscosities, its heuristic significance is retained. Frenkel examined the possibility of matching formulas like Eqs. (2.33) and (2.34) from the viewpoint of the hole theory of liquids [57].

In our analysis, we used initially the following two equations for the decription of the dependence of viscosity on the thermodynamic state parameters, i.e.,

$$\eta = A \exp\left(\frac{B}{T - T_1}\right) , \tag{2.35}$$

and

$$\eta = a \exp\left(\frac{b}{v_{\mathrm{L}} - v_1}\right) . \tag{2.36}$$

Equation (2.35) is commonly known as the Vogel–Fulcher–Tammann formula [59, 60] and Eq. (2.36) as the Doolittle formula [61]. Both relations may be treated as modifications of Eqs. (2.33) and (2.34).

The introduction of the parameter values T_1 and v_1 a priori into the description defines zero fluidity by the conditions $T = T_1$ or $v_{\mathrm{L}} = v_1$; however, the quantities T_1 and v_1 depend on pressure. Furthermore, the parameters A and b are taken to be functions of pressure, while B and a are taken to be individual constants. In this approximation, we treated the experimental data on the viscosity of liquids along isobars using the glass transition temperature of each substance under atmospheric pressure. At low temperatures, we discovered a mismatch of the data on viscosity calculated by using Eq. (2.36) and via the p, v_{L}, and T properties of the liquids, extrapolated to the region of high supercoolings. Thus, further on Eq. (2.35) was assumed as the basic one.

The quantities $A(p)$ and $T_1(p)$ in Eq. (2.35) were described with the aid of the following approximations

$$A = \alpha \left(\frac{p}{\beta} + 1\right)^m \tag{2.37}$$

and

$$T_1 = \gamma \left(\frac{p}{\delta} + 1\right)^n , \tag{2.38}$$

where α, β, γ, δ, m, and n are constants.

Table 2.5: The values of the parameters in Eqs. (2.35), (2.37), and (2.38) used for the calculation of viscosity

Substance	B	α	β	m	γ	δ	n
	K	10^{-4} Pa · s	MPa		K	MPa	
Benzene	469	0.430	182	1.068	120	403	0.677
Dodecane	394	0.860	203	1.314	150	697	0.675
Octadecane	529	0.772	243	1.828	167	1254	1.0
Argon	202	0.145	80	1.201	16	75	0.377
Carbon dioxide	724	0.045	340	2.064	36	–	–
Carbon tetrachloride	992	0.202	191	1.768	35	–	–

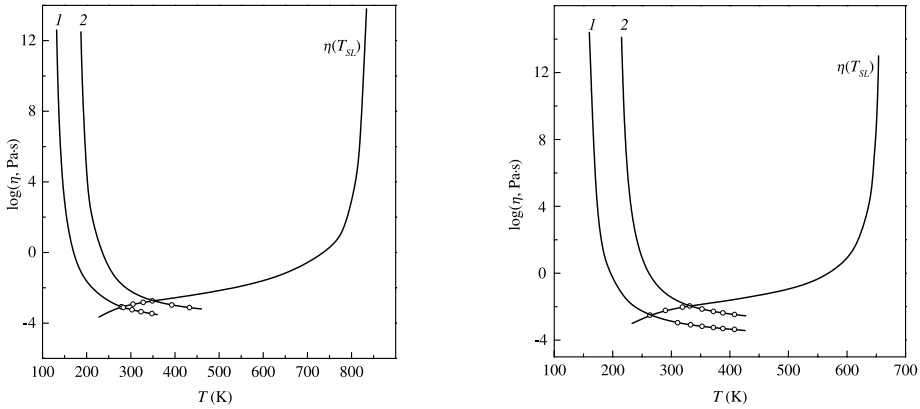

Figure 2.13: Change in the viscosity of benzene (left) and dodecane (right) along the melting line $\eta(T_{\mathrm{SL}})$ and along the isobars $p = 0.1$ and 300 MPa (curves (1) and (2)). The points correspond to experimental data. The solid lines indicate the results of calculation by Eq. (2.35)

For the analysis, we have chosen substances for which experimental data on viscosity are available in a wide range of pressures for several isotherms. The data for the following liquids were analyzed: argon [55], carbon tetrachloride [56], benzene [53], dodecane [62], octadecane [62], and carbon dioxide [54]. The range of pressure variation given in [62] was 360 MPa for dodecane; for other substances the pressure variation range was 200 to 300 MPa.

Table 2.5 gives the values of the parameters of Eqs. (2.35), (2.37), and (2.38), which were employed in the calculation. For carbon dioxide and carbon tetrachloride, we did not succeed in finding the dependence of temperature T_1 on pressure. Therefore, the values of δ and n entering Eq. (2.38) are not included into the table for these substances, and we assume $T_1 =$ const.

Figure 2.13 shows, in a semilogarithmic scale, the variation of viscosity with temperature for benzene on two isobars and on the melting line. In accordance with our estimates, the glass transition of benzene on the melting line takes place at a temperature of 830 K and pressure of 6.5 GPa. The behavior of the viscosity of dodecane is similar.

Although the viscosity on the melting line increases with temperature, one still cannot be sure that the melt would undergo glass transition on the melting line. In this case the mutual arrangement on the $(T,\ p)$ plane of the glass transition line $\eta(T,\ p) = 10^{12}$ Pa · s and of the melting line for different substances, as well as the possibility of their intersection, are of importance.

As an additional verification of the degree of consistency of the data for η, calculated by Eqs. (2.35) and (2.36), we consider the conditions of explosive crystallization [36] during the heating of amorphous layers of a number of organic substances. Under atmospheric pressure, the temperature of explosive crystallization, T_*, is higher than that of the glass transition by approximately 15 K with a viscosity ranging from 10^7 to 10^8 Pa · s corresponding to T_* [36]. For the substances, given in Table 2.5, the calculation by Eq. (2.35) results in $T_* - T_g \simeq 6-8$ K.

With an increase in temperature, an increase in the viscosity of a liquid along the melting line is connected with a decrease in the specific volume, υ_L, of the liquid. This result is expressed by the local condition [4, 15]

$$Ml_L = \frac{\beta_T}{\alpha_p}\frac{\mathrm{d}p}{\mathrm{d}T_{SL}} = \frac{\dfrac{\mathrm{d}p}{\mathrm{d}T_{SL}}}{\left(\dfrac{\partial p}{\partial T}\right)_\upsilon} > 1\ , \tag{2.39}$$

where $\beta_T = -(1/\upsilon_L)(\partial\upsilon_L/\partial p)_T$ is the isothermal compressibility coefficient and $\alpha_p = (1/\upsilon_L)(\partial\upsilon_L/\partial T)_p$ is the coefficient of thermal expansion of the liquid phase. The inequality (2.39) holds for normally melting substances for which the melting line has a slope $\mathrm{d}p/\mathrm{d}T_{SL}$ steeper than that of the isochore of a liquid at the point of intersection with the melting line.

Table 2.6 gives the values of the characteristic number Ml_L of a liquid calculated for several substances in the vicinity of the melting temperatures at atmospheric pressure employing data for the quantities α_p, β_T, and $\mathrm{d}p/\mathrm{d}T_{SL}$ taken from the literature. For most substances, the values of α_p and β_T were computed utilizing p, υ, and T data close to the triple point (references to literary sources are given in the table) or taken from a reference book [63]. To determine β_T for liquid lithium, rubidium, and caesium, use was made of an extrapolation to the corresponding melting temperatures of data for the compressibility determined employing the results of measurements of the velocity of sound in melts. The third column lists the references from which data for the derivative $\mathrm{d}p/\mathrm{d}T_{SL}$ were taken. If we assume that the condition $Ml_L > 1$ holds along the whole melting curve, including its low-temperature extension (at $T < T_0$) into the region of stretched (metastable) states of the coexisting phases, it will make liquid vitrification on such an extension unlikely.

The behavior of the parameter Ml_L on the melting line of argon, shown in Fig. 2.14, may serve as an illustration. The values of Ml_L were calculated employing experimental data for α_p, β_T, and $\mathrm{d}p/\mathrm{d}T_{SL}$ taken from the paper [76]. The dashed line in the figure shows the extension of the temperature dependence of the number Ml_L into the region of negative pressures. As shown in the figure, for argon the complex Ml_L does not change practically along the melting line.

Table 2.6: Values of the parameter Ml_{L} for the liquid along the melting line in the vicinity of the triple point of some substances

Substance	Ml_{L}	Reference
Hydrogen	3.0 [64]	[65]
Neon	2.4 [20]	[65]
Argon	1.9 [20]	[65]
Krypton	2.1 [20]	[65]
Xenon	2.0 [20]	[65]
Oxygen	4.3 [66]	[65]
Nitrogen	2.6 [67]	[65]
Carbon dioxide	2.9 [68]	[69]
Ammonia	4.0 [70]	[37]
Benzene	2.5 [53]	[71]
Lithium	15.0 [72]	[65]
Sodium	8.2 [11]	[65]
Potassium	8.8 [73]	[65]
Rubidium	6.9 [74]	[65]
Caesium	8.2 [75]	[65]
Mercury	4.1 [43]	[65]

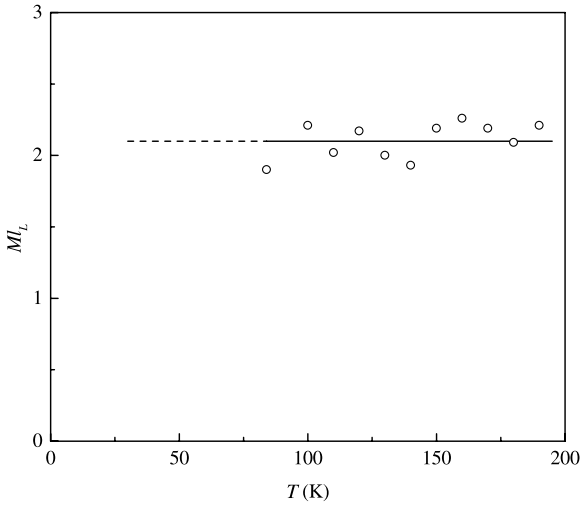

Figure 2.14: Behavior of the complex Ml_{L} on the melting line for argon

A different pattern is observed for a liquid–vapor phase transition. The value of the dimensionless complex $(\beta_T/\alpha_p)(\mathrm{d}p/\mathrm{d}T_{\mathrm{LV}})$ for the liquid phase on the saturation line is less than one in the range from the triple point to the critical point. For example, in the order of magnitude, in the vicinity of the triple point the value of this complex is $\sim 10^{-3}$ for argon and

$\sim 10^{-11}$ for sodium. The fulfillment of the inequality

$$\frac{\dfrac{\mathrm{d}p}{\mathrm{d}T_{\mathrm{LV}}}}{\left(\dfrac{\partial p}{\partial T}\right)_{v}} < 1 \tag{2.40}$$

along the liquid–vapor phase transition line (see Fig. 2.2) implies that the viscosity of the liquid phase along the saturation curve decreases with increasing temperature.

It is possible to obtain another local criterion which yields $\mathrm{d}\eta/\mathrm{d}T_{\mathrm{SL}} > 0$, i.e.,

$$\frac{\dfrac{\mathrm{d}p}{\mathrm{d}T_{\mathrm{SL}}}}{\left(\dfrac{\partial p}{\partial T}\right)_{\eta}} > 1 \,. \tag{2.41}$$

This criterion correlates, in variables T and p, the slope of the melting line and that of the line of constant viscosity. In fact, assuming that viscosity is a single-valued function of temperature and pressure, we have the following relation for the derivatives:

$$\left(\frac{\partial \eta}{\partial T}\right)_{p}\left(\frac{\partial T}{\partial p}\right)_{\eta}\left(\frac{\partial p}{\partial \eta}\right)_{T} = -1 \,. \tag{2.42}$$

Note that the inequality $(\partial p/\partial T)_{\eta} > 0$ follows from Eq. (2.42) when one takes into account the relations $(\partial \eta/\partial T)_{p} < 0$ and $(\partial \eta/\partial p)_{T} > 0$ as known from the experiment.

We write the derivative $\mathrm{d}\eta/\mathrm{d}T_{\mathrm{SL}}$, defining the sign of change in the viscosity along the melting line, as

$$\frac{\mathrm{d}\eta}{\mathrm{d}T_{\mathrm{SL}}} = \left(\frac{\partial \eta}{\partial T}\right)_{p} + \left(\frac{\partial \eta}{\partial p}\right)_{T}\frac{\mathrm{d}p}{\mathrm{d}T_{\mathrm{SL}}} \,. \tag{2.43}$$

At $\mathrm{d}p/\mathrm{d}T_{\mathrm{SL}} > 0$, the terms on the right-hand side of the equation have opposite signs. For the sake of definitiveness, it is appropriate to express the derivative $(\partial \eta/\partial p)_{T}$ in Eq. (2.43) via Eq. (2.42). We obtain then

$$\frac{\mathrm{d}\eta}{\mathrm{d}T_{\mathrm{SL}}} = \left(\frac{\partial \eta}{\partial T}\right)_{p}\left[1 - \frac{\dfrac{\mathrm{d}p}{\mathrm{d}T_{\mathrm{SL}}}}{\left(\dfrac{\partial p}{\partial T}\right)_{\eta}}\right] \,. \tag{2.44}$$

Hence, in view of Eq. (2.41), it follows that $\mathrm{d}\eta/\mathrm{d}T_{\mathrm{SL}} > 0$.

Figure 2.15 shows, plotted for dodecane with the experimental data given in [62] at pressures up to 400 MPa, the melting line $T_{\mathrm{SL}}(p)$, the isoviscous curves and the isochore having the common point of attachment to the melting line with the curve $\eta(T, p) = 3$ mPa·s, as well as the calculated dependence of the vitrification temperature on pressure $T_{\mathrm{g}}(p)$. The qualitative behavior of the viscosity of the liquid along the melting line is indicative both of the increase

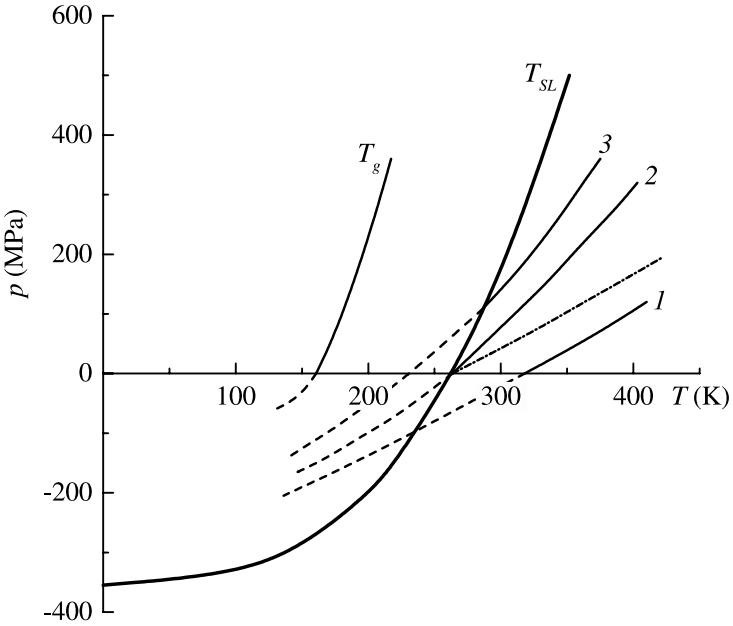

Figure 2.15: The melting line of dodecane $T_{\mathrm{SL}}(p)$, the lines of constant viscosity (1–3) ((1): 1, (2): 3, (3): 5 mPa · s), and the glass transition line $\eta(T, p) = 10^{12}$ Pa · s. The dashed lines represent the continuation into the region of negative pressures. The dashed–dotted curve is the isochore of the liquid corresponding to $v_{\mathrm{L}} = 1.3\ \mathrm{cm}^3/\mathrm{g}$

in η with an increase of temperature and of the conservation of low values of η on the metastable continuation of the melting line into the region of low temperatures, i.e., at $(T/T_0) < 1$. This result follows from the monotonicity of the isoviscous curves $\eta(T, p) = \mathrm{const}$ and from the condition that these curves do not intersect (see Fig. 2.15).

Table 2.7 gives, for each of the treated substances, the melting point T_0, the viscosity of the liquid at T_0 and atmospheric pressure, and the glass transition temperature $T_{\mathrm{g,at}}$ at this pressure. Moreover, the values of the viscosity of the melt, calculated for temperatures $T/T_0 = 0.8$ and 1.5, are given, and the pressure $p_{\mathrm{SL,g}}$ on the melting line is estimated, at which the melt vitrifies.

For one and the same substance, the data of different authors on $T_{\mathrm{g,at}}$ may differ strongly. So for carbon tetrachloride, we took the data for $T_{\mathrm{g,at}} = 61$ K from [77], where the vitrification point was estimated from the results of experiments on the crystallization of amorphous layers. Angell et al. [78] gave a different value of $T_{\mathrm{g,at}} = 129$ K, obtained by extrapolating the vitrification temperatures of carbon tetrachloride–ethyl benzene solutions to zero concentration of the second component. At $T_{\mathrm{g,at}} = 61$ K, the ratio $T_{\mathrm{g,at}}/T_0$ is 0.25, which is much lower than the analogous ratio for organic substances with a more complex molecular configuration. For dichloroethane, we have$T_{\mathrm{g,at}}/T_0 = 0.40$ [36]; for thiophene, 0.39 [36]; and for benzene, 0.47 [78]. The values of $T_{\mathrm{g,at}}$ for argon and carbon dioxide, given in Table 2.7, were obtained by assuming that $T_{\mathrm{g,at}}/T_0 = 0.25$. For dodecane and octadecane, this ratio was assumed to be 0.6.

Table 2.7: The viscosity of liquids at different points of the melting line, the glass transition temperature $T_{g,at}$ under atmospheric pressure, and the temperature $T_{SL,g}$ and pressure $p_{SL,g}$ of the glass transition of the liquid along the melting line

Substance	T_0	p_*	$T_{g,at}$	$\eta(T = 0.8T_0)$	$\eta(T = T_0)$	$\eta(T = 1.5T_0)$	$T_{SL,g}$	$p_{SL,g}$
		MPa	K	MPa · s	MPa · s	MPa · s	K	GPa
Carbon tetrachloride	250.6	292	61	1.8	2.0	2.7	–	–
Benzene	278.6	360	131	0.1	0.82	3.2	830	6.5
Dodecane	263.7	355	160	0.6	2.8	14	650	5.3
Octadecane	301.0	345	181	1.3	4.0	55	570	2.7
Carbon dioxide	216.6	400	54	0.2	0.25	0.6		
Argon	83.8	211	21	0.1	0.28	0.5		

From the constructed isoviscous curves (Fig. 2.15), one can expect their nonlinearity in the region of negative pressures; it is only in this case that their intersection is impossible. At high pressures of the order $p \simeq p_*$, the lines of constant viscosity in the $(T,\ p)$ coordinates are close to straight lines. This property was experimentally proven for the glass transition line as well [79].

In analyzing the question of the glass transition of a liquid on the melting line, we take the parameter p_* in the Simon equation (2.3) to be the scaling value of pressure. The value of p_* is a characteristic of the internal pressure in the condensed phase [3, 4] of each substance at $T/T_0 \leq 1$. We assume the liquid to vitrify on the melting line if the vitrification line $\eta(T, p) = 10^{12}$ Pa·s intersects in its continuation the melting line $T_{SL} = f(p)$ at a pressure of $p/p_* < 20$. Otherwise, the question remains open, because the procedure employed becomes rather unreliable. Out of the substances listed in Table 2.7, argon, carbon dioxide, and carbon tetrachloride are covered under this case.

2.6 Conclusions

The comparison of the two types of phase transitions, as performed in the present investigation, is based on the thermodynamic consideration not only of stable but also of metastable states of each of the phases. This procedure requires some explanations. Diamond may serve here as a well-known example for illustration. Under ordinary conditions diamond is the metastable phase of solid carbon. There are no doubts as to the applicability of the methods of equilibrium thermodynamics for describing the properties of diamond. This possibility is allowed by the fact that the characteristic times of an experiment on diamonds, t_{exp}, is always much shorter than the mean time of expectation of diamond transformation $\langle \tau \rangle$ into the stable phase (graphite). Not only for diamonds, but also for any similar example the conditions

$$\{t_i\} < t_{exp} < \langle \tau \rangle \tag{2.45}$$

have to be fulfilled (where t_i is the characteristic time of relaxation of a system under investigation by the ith state parameter (temperature, pressure, etc.)) if one would like to speak about the so-called *well-defined* or *pure* metastable states [8, 9].

Two phases, metastable with respect to a third one, may coexist if their chemical potentials are equal. For water in a quasistatic experiment it has been shown to be possible to extend the melting line [80] to a negative pressure of −24 MPa. The metastable state is destroyed by nucleation and the growth of nuclei of a more stable phase at a given temperature and pressure. In a system free of initiating impurities, nucleation takes place owing to thermal fluctuations. This case (homogeneous nucleation) has been studied in detail theoretically beginning with the papers [34, 81] and experimentally [8, 9, 36]. The main contribution to the value of $\langle \tau \rangle$ in Eq. (2.45) can be made by the time of expectation of the first nucleus. The observed kinetics of formation of crystalline nuclei in supercooled pure liquids [33, 36] corresponds to theoretical predictions and supports confidence in the reality of the melting line extension far beyond the triple point of a substance. It should be mentioned, however, that the evaluations of the behavior of the quantities $p_{\mathrm{i,SL}}$, $\hat{p}_{\mathrm{SL}}$, and the melting line p_{SL} itself at very high tensile stresses, which are presented in this contribution, have been made asymptotically going beyond the limits achieved in experiment. This extension made it possible not only to supplement the indications of a considerable difference in solid–liquid and liquid–vapor phase transitions, but also to advance the hypothesis about the position of the phase stability boundary with respect to the lines of these two phase transitions. Both phase transitions approach the stability boundary (Eq. (2.7)), but in opposite directions from the triple point in temperature and pressure. For normally melting substances the mechanical stability of coexisting solid and liquid increases with increasing T and p. One can say that, when moving along the line of solid–liquid phase equilibrium, a system passes a wide range of degrees of stability, the low-temperature limiting temperature range of the melting line corresponding to the lower limit of stability.

Another remark should be made concerning Eq. (2.3). It is in agreement with the experimental data for $\{T, p\}_{\mathrm{SL}}$ in a wide, but finite range of $p > 0$. The quantities p_* and c, considered here, make it possible to construct an unambiguous extension of the melting line to $T = 0$ and $p = -p_*$. The agreement of this extension with the main part is determined by the length of the main (observed) part in temperature and pressure.

In accordance with the problem to be solved, we established above the similarities and differences between solid–liquid and liquid–gas phase transitions in the vicinity of the equilibrium lines of these states of aggregation. Common is the condition of equilibrium (2.1) at a flat boundary of coexistent phases and the Clausius–Clapeyron equation (2.2), which relates the slope $\mathrm{d}p/\mathrm{d}T$ of the equilibrium line with the jumps of the volume and the entropy of a substance at the intersection of this line. But even in the behavior of the temperature dependence of Δv and Δs one can observe a considerable difference. The derivatives $\mathrm{d}(\Delta v_{\mathrm{LV}})/\mathrm{d}T$ and $\mathrm{d}(\Delta s_{\mathrm{LV}})/\mathrm{d}T$ at the liquid–vapor phase transition are negative everywhere, and the values Δv_{LV} and Δs_{LV} vanish at the critical point. On the line of normal melting ($\Delta v_{\mathrm{SL}} > 0$) the derivative $\mathrm{d}(\Delta v_{\mathrm{SL}})/\mathrm{d}T < 0$, and the derivative $\mathrm{d}(\Delta s_{\mathrm{SL}})/\mathrm{d}T$ changes sign and becomes positive at low temperatures in the metastable part of the melting line. Distinct from the liquid–vapor transition, the specific volumes of both coexistent phases – solid and liquid – decrease with increasing temperature.

In the (T, p) plane the lines of liquid–vapor and solid–liquid phase transitions are located differently with respect to the family of isochores $v = f(T, p) = \mathrm{const}$. The melting line moves more steeply than the isochores at the place of their intersection with this line, $\mathrm{d}p/\mathrm{d}T_{\mathrm{SL}} > (\partial p/\partial T)_v$. Such a behavior is connected with an increase of the viscosity, η, of the liquid along the melting line with increasing temperature.

The liquid retains a high fluidity, $(1/\eta)$, in the low-temperature (metastable) segment of the melting line, which is due to a uniform extension of coexisting phases. As the temperature rises, the viscosity of the melt monotonically increases, and the liquid phase may vitrify in the vicinity of some point on the melting line $\{T,\ p\}_{\mathrm{SL,g}}$. This observed behavior of viscosity is of both cognitive and practical importance (for example, in metallurgy and geophysics). In Ref. [52], the extrapolation of the melting line of iron to $p \simeq 300$ GPa led to the conclusion about the vitreous state of the Earth's core. For the liquid–vapor phase transition one can observe the reverse: the liquid isochores move more steeply than the equilibrium curve, $\mathrm{d}p/\mathrm{d}T_{\mathrm{LV}} < (\partial p/\partial T)_{\upsilon}$ (see Fig. 2.2), and the liquid viscosity decreases when moving along the binodal from the triple point to the critical point.

Coexisting phases behave quite differently with respect to stability at liquid–vapor and solid–liquid phase equilibria. In the first case, the stability of the liquid and the vapor decreases with increasing temperature. Both phases loose stability on reaching the critical point, where $(\partial p/\partial \upsilon)_T = 0$ holds. The reverse tendency of increase of stability of both liquid and crystal, on varying the state along the melting line toward high temperatures, indicates the absence of a critical point for the melting line. This conclusion can be derived from the behavior of the elasticity $-(\partial p/\partial \upsilon)_T$ or inverse compressibility $\beta_T^{-1} = -\upsilon(\partial p/\partial \upsilon)_T$ (cf. Fig. 2.5). At the same time, on analyzing the stability one can reveal a certain analogy of liquid–vapor and solid–liquid phase transitions if one takes into account the metastable part of the melting lines ($p < 0$). The coexisting crystal and liquid approach, via stretching and decreasing temperature, the boundary of phase stability (cf. Fig. 2.5).

The point $\{T = 0,\ p = -p_*\}$, where $p_* > 0$ is the pressure pole, each substance having a pole of its own, serves as the peculiar point of a melting line of the normal type. The second characteristic point $\{T = T_0,\ p = 0\}$ is the corresponding point for different substances. The use of these two points and the introduction of the shifted pressure scale $p^+ = p + p_*$ make it possible to go over to dimensionless variables $\widetilde{p}$, $\widetilde{T}$, and $\widetilde{\upsilon}$, similar as the application of another particular point (the critical point) in a liquid–vapor phase transition leads to the possibility of presenting various relations pertaining to this phase transition in a reduced form. Thus, instead of looking for a high-temperature peculiar point of the critical type, one can turn to low-temperature asymptotics. This approach was favored by the appearance of the Simon equation (2.3) [3] and the concepts of metastability on which this paper is based.

The position of the critical point $(T_{\mathrm{c}},\ p_{\mathrm{c}},\ \upsilon_{\mathrm{c}})$ is determined experimentally with a sufficiently high accuracy. The same statement holds with respect to the behavior of thermophysical properties as one approaches the critical point. For the vicinity of the peculiar point of the melting line ($T = 0,\ p = -p_* < 0$) one has to rely on an extrapolation of both this line itself and the properties of the liquid and the solids. For instance, one cannot be sure of the position of the intersection point of the melting line and the spinodals of the liquid and the crystal. If the liquid spinodal "cuts" the melting line at $T > 0$, $-p < p_*$, then a further coexistence of the phases is impossible. A crystal can retain internal stability in this case. But the above-mentioned approach of coexisting phases to the spinodal state at $T \to 0$ exists irrespective of more subtle details in the behavior of the metastable liquid and crystal close to $T = 0$.

Molecular concepts, advanced for an understanding of the mechanism of phase transitions accompanied by changes of the states of aggregation, rely on taking into account attractive and repulsive forces in the presence of the thermal motion of the ensemble of particles. The phenomenon of condensation may be explained in a simple model and qualitatively described

by continuous equations of state (of the van der Waals equation type). A change to an ordered regular structure is accompanied by the "switching-on" of more subtle mechanisms (anisotropy of the molecular field, allowance for multiple interactions, collective vibrational modes). The equation of state for a crystal $p = f(v, T)$ forms a separate branch with respect to the gas–liquid branch. Isolated likewise are phases that originate owing to polymorphism: There cannot exist any continuous transition in between them [35].

Acknowledgement

The work was supported by the Russian Foundation for Basic Research (Grant no. 00-02-16227).

References

[1] T. Andrews, Phil. Trans. Roy. Soc. London **159**, 575 (1869).

[2] A.R. Ubbelohde, *Melting and Crystal Structure* (Clarendon, Oxford, 1965).

[3] F. Simon and G. Glatzel, Z. Anorg. Allg. Chem. **178**, 309 (1929).

[4] V.P. Skripov and M.Z. Faizullin, Teplofiz. Vys. Temp. **37**, 814 (1999) (Engl. Transl.: High Temp. **37**, 784 (1999)).

[5] F. Simon, Trans. Farad. Soc. **33**, 65 (1937).

[6] V.P. Skripov, *Equations of State of Gases and Liquids* (Nauka, Moscow, 1975) (in Russian).

[7] V.P. Skripov and V.G. Baidakov, Teplofiz. Vys. Temp. **10**, 1226 (1972) (Engl. Transl.: High Temp. **10**, 1102 (1972)).

[8] V.P. Skripov, *Metastable Liquids* (Wiley, New York, 1974).

[9] V.P. Skripov, E.N. Sinitsyn, P.A. Pavlov, G.V. Ermakov, G.N. Muratov, N.V. Bulanov, and V.G. Baidakov, *Thermophysical Properties of Liquids in the Metastable (Superheated) State* (Gordon and Breach, London, 1988).

[10] Ch. Tegler, R. Span, and W. Wagner, J. Phys. Chem. Ref. Data **28**, 779 (1999).

[11] I.N. Makarenko, A.M. Nikolaenko, V.A. Ivanov, and S.M. Stishov, Zh. Eksp. Teor. Fiz. **69**, 1723 (1975) (Engl. Transl.: Sov. Phys.-JETP **42**, 875 (1975)).

[12] M.A. Pokrasin, V.V. Roschupkin, L.R. Fokin, N.E. Handamirova, *Thermophysical Properties of Substances and Materials* (Izdatelstvo Standartov, Moscow, 1983), Vol. 19 (in Russian).

[13] V.G. Baidakov, V.P. Skripov, and A.M. Kaverin, Zh. Eksp. Teor. Fiz. **67**, 676 (1974) (Engl. Transl.: Sov. Phys.-JETP **40**, 335 (1975)).

[14] P.H. Lahr and W.G. Eversole, J. Chem. Eng. Data **7**, 42 (1962).

[15] V.P. Skripov, Teplofiz. Vys. Temp. **19**, 85 (1981) (Engl. Transl.: High Temp. **19**, 66 (1981)).

[16] V.P. Skripov and M.Z. Faizullin, High Temp. – High Press. **18**, 1 (1986).

[17] V.G. Baidakov, *The Interface of Simple Classical and Quantum Liquids* (Nauka, Ekaterinburg, 1994) (in Russian).

[18] M. Keeney and J. Heicklen, J. Inorg. Nucl. Chem. **41**, 1755 (1979).
[19] L.P. Filippov, J. Phys. Chem. (Russian) **54**, 2979 (1980).
[20] V.A. Rabinovich, A.A. Vasserman, V.I. Nedostup, and L.S. Veksler, *Thermophysical Properties of Neon, Argon, Krypton and Xenon*. Edited by T.B. Selover Jr., Monograph of the National Standard Reference Data Service of the USSR (Hemisphere, New York, 1988) (Translated from Russian).
[21] B.L. Smith, P.R. Gardner, and H.C. Parker, J. Chem. Phys. **47**, 1148 (1967).
[22] D. Stensfield, Proc. Phys. Soc. **72**, 854 (1958).
[23] R.T. Jacobsen, R.B. Stewart, and M. Jahangiri, J. Phys. Chem. Ref. Data **15**, 735 (1986).
[24] *IUPAC International Thermodynamic Tables of the Fluid State – 9, Oxygen* (Blackwell, Oxford, London, Edinburgh, Boston, Palo Alto, Melbourne, 1987).
[25] N.B. Vargaftik, *Tables on the Thermophysical Properties of Liquids and Gases* (Wiley, New York, 1975), 2nd ed.
[26] U. Zetzmann and W. Wagner, J. Phys. Chem. Ref. Data **20**, 1061 (1991).
[27] B.A. Younglove and J.F. Ely, J. Phys. Chem. Ref. Data **16**, 577 (1987).
[28] G.N. Muratov, E.N. Sinitsyn, and V.P. Skripov, *Atomic and Molecular Physics* (Nauka, Sverdlovsk, 1972).
[29] E.N. Sinitsyn, L.A. Mikhalevich, O.P. Yankovskaya, I.F. Guletskaya, V.B. Ivakin, G.N. Muratov, and G.V. Ermakov, *Thermal Properties of Liquid Fluoroorganic Compounds* (Nauka, Ekaterinburg, 1995).
[30] *Physics and Chemistry of the Organic Solid State* (Wiley, New York, London, 1965), Vol. 1.
[31] M.P. Dohov, Metals (Russian) **4**, 28 (1999).
[32] D.G. Thomas and L.A.K. Staveley, J. Chem. Soc. **12**, 4569 (1952).
[33] H. Hollomon and D. Turnbull, *Nucleation. Progress in Metal Physics* (Pergamon, London, 1953).
[34] Ya.B. Zeldovich, Zh. Eksp. Teor. Fiz. (Russian) **12**, 525 (1942).
[35] L.D. Landau and E.M. Lifshitz, *Statistical Physics* (Academy of Sciences Publishing House, Berlin, 1987).
[36] V.P. Skripov and V.P. Koverda, *Spontaneous Crystallization of Supercooled Liquids* (Nauka, Moscow, 1984) (in Russian).
[37] S.E. Babb, Rev. Mod. Phys. **35**, 400 (1963).
[38] V.P. Skripov, V.P. Koverda, and G.T. Butorin, Crystallogr. (Russian) **15**, 1219 (1970).
[39] G.S. Zhdanov, Phys. Solid State (Russian) **18**, 1415 (1976).
[40] V.P. Koverda, V.N. Skokov, and V.P. Skripov, Crystallogr. (Russian) **27**, 358 (1982).
[41] Ye.Yu. Tonkov, *Phase Diagrams of Compounds at High Pressure* (Nauka, Moscow, 1983) (in Russian).
[42] Ye.Yu. Tonkov, *Phase Transformations of Compounds at High Pressure* (Nauka, Moscow, 1988) (in Russian).
[43] M.P. Vukalovich, A.I. Ivanov, L.R. Fokin, and A.T. Yakovlev, *Thermophysical Properties of Mercury* (Izdatelstvo Standartov, Moscow, 1971) (in Russian).
[44] M.E. Cavalery, T.G. Plymate, and J.H. Stout, J. Phys. Chem. Solids **49**, 945 (1988).

[45] V.D. Urlin, Zh. Eksp. Teor. Fiz. (Russian) **49**, 485 (1965).

[46] P.W. Mirwald and G.C. Kennedy, J. Phys. Chem. Solids **37**, 795 (1976).

[47] V.A. Ivanov, I.N. Makarenko, A.M. Nikolaenko, and S.M. Stishov, Phys. Lett. **A 47**, 75 (1974).

[48] V.G. Baidakov, *Superheating of Cryogenic Liquids* (Publishing House of the Ural Branch of the Russian Academy of Sciences, Ekaterinburg, 1995) (in Russian).

[49] V.P. Skripov, Teplofiz. Vys. Temp. (Russian) **19**, 85 (1981).

[50] V.P. Skripov and M.Z. Faizullin, High Temp. – High Press. **18**, 1 (1986).

[51] V.E. Lyusternik, Teplofiz. Vys. Temp. (Russian) **28**, 686 (1990).

[52] V.V. Brazhkin and A.G. Lyapin, Usp. Fiz. Nauk. (Russian) **170**, 535 (2000).

[53] H.J. Parkhurst and J. Jonas, J. Chem. Phys. **63**, 2705 (1975).

[54] S.A. Ulybin and W.I. Makarushkin, in *Proceedings of the 7th Symposium on Thermophysical Properties* Gaithersburg, Md., N.Y., USA (1977).

[55] N.J. Trappeniers, P.S. van der Gulik, and H. van den Hooff, Chem. Phys. Lett. **70**, 438 (1980).

[56] M.A. Mc Cool and L.A. Woolf, J. Chem. Soc. Farad. Trans. I. **10**, 1971 (1972).

[57] Ya.I. Frenkel, *Introduction into the Theory of Metals* (Nauka, Leningrad, 1972) (in Russian).

[58] A.I. Batchinskii, *Selected Papers* (Academy of Sciences of the USSR Publishing House, Moscow, 1960) (in Russian).

[59] G. Tammann, *The Vitreous State* (ONTI-Publishers, Moscow, Leningrad, 1935) (in Russian).

[60] O.V. Mazurin, *Vitrification* (Nauka, Leningrad, 1986) (in Russian).

[61] A.K. Doolittle, J. Appl. Phys. **22**, 1471 (1951).

[62] D.L. Hogenboom, W. Webb, and J.A. Dixon, J. Chem. Phys. **46**, 2586 (1967).

[63] *Thermophysical Properties*. Reference book. edited by I.K. Kikoin (Atomizdat, Moscow, 1976) (in Russian).

[64] L.S. Serdyuk, Thermodynamic properties of normal hydrogen at temperatures up to 1500 K and pressures up to 5000 bar, in: *Thermophysical Properties of Substances and Materials* (Izdatelstvo Standartov, Moscow, 1973), vol. 6 (in Russian).

[65] Ye.Yu. Tonkov, *Phase Diagrams of the Elements at High Pressure* (Nauka, Moscow, 1979) (in Russian).

[66] V.V. Sychev, A.A. Vasserman, A.D. Kozlov, G.A. Spiridonov, and V.A. Zymarnii, *Thermodynamical Properties of Oxygen* (Izdatelstvo Standartov, Moscow, 1981) (in Russian).

[67] V.V. Sychev, A.A. Vasserman, A.D. Kozlov, G.A. Spiridonov, and V.A. Zymarnii, *Thermodynamical Properties of Nitrogen* (Izdatelstvo Standartov, Moscow, 1977) (in Russian).

[68] V.V. Altunin, *Thermophysical Properties of Carbon Dioxide* (Izdatelstvo Standartov, Moscow, 1975) (in Russian).

[69] A. Michels, B. Blaisse, and J. Hoogschagen, Physica **9**, 565 (1942).

[70] I.F. Golubev, V.P. Kiyashova, I.I. Perelshtein, and E.B. Parushin, *Thermophysical Properties of Ammonia* (Izdatelstvo Standartov, Moscow, 1978) (in Russian).

[71] M.K. Zhohovskii and V.C. Bogdanov, J. Phys. Chem. (Russian) **39**, 2520 (1965).
[72] I.I. Novikov, Yu.S. Trelin, and T.A. Zyganova, Teplofiz. Vys. Temp. (Russian) **7**, 1220 (1969).
[73] P.M. Kesselman and V.P. Onischenko, *Thermophysical Properties of Substances and Materials* (Izdatelstvo Standartov, Moscow 1977), vol. 11.
[74] I.I. Novikov, Yu.S. Trelin, and T.A. Zyganova, Teplofiz. Vys. Temp. (Russian) **10**, 1114 (1972).
[75] I.I. Novikov, Yu.S. Trelin, and T.A. Zyganova, Teplofiz. Vys. Temp. (Russian) **8**, 450 (1970).
[76] R.K. Crawford and W.B. Daniels, J. Chem. Phys. **50**, 3171 (1969).
[77] H. Suga and S. Seki, J. Non-Cryst. Solids **16**, 171 (1974).
[78] C.A. Angell, J.M. Sare, and E.J. Sare, J. Phys. Chem. **82**, 2622 (1978).
[79] T. Atake and C.A. Angell, J. Phys. Chem. **83**, 3218 (1979).
[80] S.J. Henderson and R.J. Speedy, J. Phys. Chem. **91**, 3069 (1987).
[81] M. Volmer, *Kinetik der Phasenbildung* (Steinkopff, Dresden-Leipzig, 1939).

3 A New Method of Determination of the Coefficients of Emission in Nucleation Theory

Vitali V. Slezov, Jürn W. P. Schmelzer, and Alexander S. Abyzov

Nobody knows what entropy really is and when you use the word "entropy" in an argument, you will win every time.
John von Neumann

A new method of determination of the emission coefficients of single particles from clusters of arbitrary sizes – being an essential ingredient of the kinetic equations describing nucleation and growth processes – is developed. This method does not require the application of the so-called equilibrium or constraint equilibrium distributions and the principle of detailed balancing to nonequilibrium states. It is applicable generally to any kind of phase transformation processes (condensation of gases, segregation processes in solid and liquid solutions, bubble formation in liquids, pore formation in solids, crystallization in melts, etc.) both for one-component and multicomponent systems. As it turns out from the analysis, the final equations obtained are quite similar to those employed traditionally in the classical nucleation theory, where these relations are utilized without a sufficient theoretical foundation. The approach developed here gives thus a theoretical foundation of some basic assumptions of the classical approach in the description of nucleation-growth processes. Based on the method outlined, the kinetic equations describing nucleation-growth processes are formulated and some further consequences are discussed. It is shown, in particular, that, under quite general conditions, the set of kinetic equations describing nucleation-growth processes in multicomponent systems can be reduced to relations for the description of these processes in one-component systems. However, the thermodynamic and kinetic parameters in the resulting set of kinetic equations depend on the kinetic and thermodynamic parameters of all of the components involved in the process. The respective expressions are derived and outlined in the contribution as well.

3.1 Introduction

Phase transformations play an important role in a variety of processes ranging from nucleation and growth in the atmosphere [1, 2], nucleation and growth in expanding gases [3, 4], bubble formation in liquids [5, 6] and phase formation in solids [7–10] to phase transitions in nuclear matter [11–14] and in the early universe [15]. Despite a number of the modern developments [16–20], the theoretical interpretation of the experimental results on phase transformations is carried out till now, by methods which are widely based on the classical nucleation theory, its modifications and extensions (see, e.g., Refs. [5, 21–23]). According to the classical picture, the phase transformation proceeds via the formation of clusters representing precursors of the newly evolving phase. Hereby it is assumed in a sufficiently accurate approximation that the growth or dissolution of the clusters proceeds via incorporation or emission of single atoms or molecules.

Nucleation Theory and Applications. edited by J. W. P. Schmelzer

ISBN: 3-527-40469-4

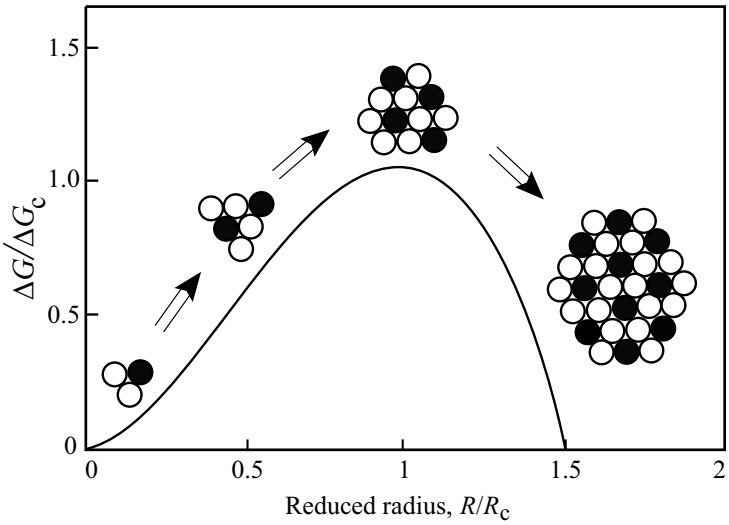

Figure 3.1: Work of cluster formation (or change in the Gibbs free energy, ΔG) in dependence on cluster size (R is the radius of the cluster) as it is assumed commonly in the classical nucleation theory. Nucleation is the process of formation of supercritical clusters with sizes $R > R_c$ capable of a further deterministic growth. In the calculations it is assumed in accordance with the classical approach that bulk and surface properties of the clusters are widely same as the respective properties in the newly evolving macroscopic phase. The work of cluster formation can be expressed then via Eq. (3.16)

In order to develop a kinetic description of nucleation-growth processes in the framework of the classical approach, one has to know, consequently, the values of the coefficients of aggregation and emission of single particles for clusters of arbitrary sizes. Moreover, one has to develop appropriate expressions for the so-called work of formation of clusters of arbitrary sizes, i.e., one has to determine the change of the characteristic thermodynamic potential if a cluster is formed in the system. A particular example for the dependence of the work of cluster formation on cluster size, as it is assumed commonly in the classical nucleation theory, is shown in Fig. 3.1. However, although the classical theory was formulated in its basic premises in the 1930s, till now a number of problems both of fundamental character and with respect to possible applications are not solved finally. The present analysis is directed to the solution of some of such problems.

One of the most debated points in the nucleation theory is the method of determination of the emission coefficients. These coefficients are specified commonly by deriving the so-called equilibrium or constraint equilibrium distributions with respect to cluster sizes and applying the principle of detailed balancing to thermodynamic nonequilibrium states (cf. Refs. [24, 25] and references cited therein). Such an approach is, however, highly questionable [12, 13, 26]. In application to thermodynamic nonequilibrium states such distributions are artificial constructs; they are not realized in nature. Moreover, the principle of detailed balancing holds for equilibrium but not for nonequilibrium states. Thus, various attempts have been made to

overcome such difficulties. The most straightforward solution to the problem of determination of the emission coefficients would consist, of course, in the application of microscopic statistical-mechanical approaches (cf., e.g., Refs. [27, 28]). Due to the enormous problems in applying this method to real systems it is, however, till now more an interesting possibility rather than a practical tool (cf. also Ref. [24]).

Macroscopic approaches, like the traditional method discussed above, have the advantage that specific properties of the system under consideration enter the description only via the specific expressions for the characteristic thermodynamic functions. These or other thermodynamic characteristics applied can be determined more easily. Thus, it is of use to develop further the macroscopic methods for the determination of the emission coefficients retaining the advantages but avoiding questionable arguments. One of such approaches was developed by Katz et al. (cf., e.g., Refs. [29–33]) both in application to vapor condensation as well as to nucleation and growth in condensed media. In this approach, the coefficients of emission of single particles are determined first for the state of a saturated system. In a next step, by applying appropriate expressions for the cluster size distributions evolving in saturated systems and certain additional assumptions (e.g., independence of the emission coefficients on the state of the ambient phase [29–31]) the emission coefficients for the supersaturated systems are determined. In another development, which goes back to Becker and Döring [34], the emission rates are determined by applying the Gibbs–Thomson (or Kelvin's) equation (cf. Refs. [24, 32] and [33]).

The problem described was discussed some years ago in detail by Wu [35]. He came to similar conclusions and mentioned: "The constrained equilibrium hypothesis (CEH) formulated as an extrapolation of fluctuation thermodynamics is ... not valid. A different justification is required ... Since CEH is central to nucleation theory, it is not likely to go away until something better comes along ..." It is one of the aims of the present chapter to show that these mentioned approaches may be generalized arriving, indeed, at some justification of the methods commonly employed. We show that a mesoscopic statistical–mechanical method of determination of the coefficients of emission can be developed without relying on such questionable concepts like constraint equilibrium distributions and the application of the principle of detailed balancing to nonequilibrium states. This method does not involve the assumption that the emission rates are independent of the state of the ambient phase. It is applicable quite generally to a variety of phase transformation processes in gases as well as in condensed matter both for one-component and multicomponent systems. It allows a straightforward generalization to nonisothermal phase formation processes as well.

The chapter is organized as follows. After a brief introduction of the basic kinetic equations (Sect. 3.2), the newly developed method of determination of the emission coefficients is outlined. It is shown that the method is applicable both to one-component (Sect. 3.3) and multicomponent (Sect. 3.4) systems. As an example, here the derivation of the respective dependences is given in detail for the case that external pressure, p, and temperature, T, are kept constant. It is shown further that the method can also be applied with minor modifications if phase formation at any other boundary conditions is considered (Sect. 3.5). The resulting relations for the determination of the emission coefficients are independent of the constraints applied. Employing these results, the basic sets of kinetic equations describing nucleation-growth processes both in one- and multicomponent systems are completed, the initial conditions for their solution are specified (Sect. 3.6) and some further consequences are discussed

(Sect. 3.7). For the first time, this approach was outlined in [36, 37] and elaborated in more detail in [38]. The present contribution contains both a comprehensive outline of the basic ideas and results of the approach developed and an analysis of some further developments.

3.2 Basic Kinetic Equations

We first discuss here the processes of formation of a new phase in an ambient phase with a high thermal conductivity. In this case heat sources, connected with transitions of the basic elementary units of the system (atoms, molecules, aggregates of a given stoichiometric composition, etc.) from one phase to another, practically do not change the temperature T of the part of the system, where the aggregate of the new phase evolves. Therefore, with a sufficiently high accuracy, the nucleation-growth process may be considered as isothermal. Moreover, in addition, constancy of the pressure p is supposed. To be precise, the discussion focuses on the application to condensation processes in gases (in an inert carrier gas). However, the basic assumptions are applicable quite generally. Thus, the results are equally valid for a variety of different phase formation processes as discussed above, e.g., for segregation in solid or liquid solutions, crystallization of melts or bubble formation in liquids.

As generally assumed in nucleation theory, the condensation or evaporation of the clusters (or droplets) occurs by aggregation or emission of single particles, only. Therefore, the kinetic equation will be of the standard form [36–39], i.e.,

$$\begin{aligned}\frac{\partial f\,(n,t)}{\partial t} &= w^{(+)}_{n-1,n} f\,(n-1,t) - w^{(-)}_{n,n-1} f\,(n,t) \\ &\quad + w^{(-)}_{n+1,n} f\,(n+1,t) - w^{(+)}_{n,n+1} f\,(n,t)\ .\end{aligned} \tag{3.1}$$

Here $f(n,t)$ is the distribution function of clusters of the new phase, containing n single particles; $w^{(+)}_{n-1,n}$ and $w^{(+)}_{n,n+1}$ are the average number of events that per unit time one particle is absorbed and the number of particles in a cluster is increased from $(n-1)$ to n and n to $(n+1)$, respectively; $w^{(-)}_{n,n-1}$ and $w^{(-)}_{n+1,n}$ are the average number of events for a cluster to release one particle per unit time and to be transferred to the states with $(n-1)$ and n particles, respectively.

By introducing fluxes J_n, we may rewrite Eq. (3.1) in the form of an ordinary continuity equation in cluster size space as

$$\frac{\partial f}{\partial t} = J_{n-1} - J_n\ , \tag{3.2}$$

where the fluxes J_n are determined by

$$J_{n-1} = w^{(+)}_{n-1,n} f\,(n-1,t) - w^{(-)}_{n,n-1} f\,(n,t)\ , \tag{3.3}$$

$$J_n = w^{(+)}_{n,n+1} f\,(n,t) - w^{(-)}_{n+1,n} f\,(n+1,t)\ . \tag{3.4}$$

Once we have derived the kinetic equations in the general form, we have, now, to determine the kinetic coefficients.

3.3 Ratio of the Coefficients of Absorption and Emission of Particles

The condensation or absorption coefficients $w^{(+)}_{n-1,n}$ and $w^{(+)}_{n,n+1}$ are determined by the kinetic mechanism the droplets (or, in general, clusters of the new phase) grow, they are, in general, well-known. As will be shown later, they can be determined directly from the macroscopic growth rates. To complete the determination of the kinetic coefficients it is necessary, consequently, to have at one's disposal methods for the determination of the emission coefficients, $w^{(-)}$. For such purposes, let us note that the particles of the new phase may be divided into two groups: for the particles with number of atoms less than the critical cluster size, $n < n_c$, the ambient phase is undersaturated. Here n_c is the critical cluster size in nucleation. In a macroscopic deterministic description, such clusters shrink and disappear. In other words, the concentration of single particles in the ambient phase, capable of being incorporated into the clusters of the newly evolving phase, is too small to retain a dynamic equilibrium (cf. Fig. 3.1).

For drops with supercritical sizes, $n > n_c$, the ambient phase is supersaturated and, in a deterministic description, the clusters of the new phase grow. In this case, the concentration of single particles has such values that the average number of aggregation processes per unit time interval exceeds the respective value for emission from a given cluster of the new phase. Particles with critical sizes, $n = n_c$, are in (unstable) thermodynamic equilibrium with the ambient phase of the given composition (here the vapor phase). Hence, for critical clusters the average number of aggregation and emission processes coincide.

The methods of determination of the coefficients $w^{(-)}$ differ in our approach depending on the range of cluster sizes considered, i.e., which class of clusters is considered. However, before we go over to the explanation of our method, the traditional approach is briefly revisited and discussed. In addition, some general thermodynamic relationships are derived which will be employed in the subsequent analysis.

3.3.1 Traditional Approach

In thermodynamic equilibrium states, a time-independent statistical cluster size distribution is established in the course of time. This distribution is described by Eq. (3.1) with $(\partial f/\partial t) = 0$. Thus, in order to find the equilibrium cluster size distributions we have to find the time-independent solutions of the set of equations (3.1).

In the search for these solutions, we may follow a different path as well. The equilibrium distribution of clusters, $f^{(\mathrm{eq})}(n)$, may be determined by the general methods of statistical physics [40]

$$f^{(\mathrm{eq})}(n) = A \exp\left(-\frac{R_{\mathrm{rev}}(n)}{k_{\mathrm{B}}T}\right) . \tag{3.5}$$

Here k_{B} is the Boltzmann constant and T the absolute temperature. $R_{\mathrm{rev}}(n)$ is the work of formation of a cluster of size n performed in a reversible process [40]. For processes proceeding at constant values of pressure and temperature (as it is assumed here), it equals the change in Gibbs free energy, ΔG [40]. This quantity can be expressed, generally, as

$$\Delta G(n) = G_{\mathrm{d}}(n) - n\mu_{\mathrm{v}}(p, T) . \tag{3.6}$$

Here $G_d(n)$ is the contribution of the cluster (drop) of size n to the value of the thermodynamic potential of the whole system, $\mu_v(p, T)$ is the chemical potential per particle in the ambient bulk (vapor) phase and n is the number of atoms in the cluster. In other words, $\Delta G\,(n)$ is the difference in the thermodynamic potentials of the system consisting of a cluster in the vapor compared with the homogenous initial state.

In Eq. (3.6) the particular expression for $G_d(n)$ remains unspecified, so this relation is valid quite generally. If, for example, the capillarity approximation and certain additional assumptions are employed [23, 41] for the determination of $\Delta G(n)$, Eq. (3.6) gets the form

$$\Delta G\,(n) = n\left[\mu_d(p, T) - \mu_v(p, T)\right] + 4\pi\sigma\left(\frac{3}{4\pi}\omega_d\right)^{2/3} n^{2/3}\,. \tag{3.7}$$

Here $\mu_d(p, T)$ is the chemical potential of one single particle in the bulk liquid phase at pressure p and temperature T, ω_d is the volume per atom in the newly evolving phase, and σ is the surface tension at the (planar) interface between ambient phase (vapor) and the newly evolving phase. For the particular case as expressed by Eq. (3.7) we have, consequently,

$$G_d\,(n) = n\mu_d(p, T) + 4\pi\sigma\left(\frac{3}{4\pi}\omega_d\right)^{2/3} n^{2/3}\,. \tag{3.8}$$

Note, however, that the further derivation is independent of any particular choice of the expression for $G_d(n)$.

Substituting the expression for the work of cluster formation, as given by Eq. (3.6), into the relation describing heterophase fluctuations (Eq. (3.5)) into the time-independent form of the kinetic equations (Eq. (3.1)) we get (by applying the principle of detailed balancing $J_n = 0$, $n > 1$)

$$\frac{w^{(+)}_{n,n+1}}{w^{(-)}_{n+1,n}} = \frac{f^{(\mathrm{eq})}\,(n+1)}{f^{(\mathrm{eq})}\,(n)} \tag{3.9}$$

or

$$\frac{w^{(+)}_{n,n+1}}{w^{(-)}_{n+1,n}} = \exp\left(-\frac{[\Delta G(n+1) - \Delta G(n)]}{k_B T}\right)\,. \tag{3.10}$$

It is evident that the knowledge of the specific form of the preexponential coefficient A in Eq. (3.5) is, in general, not required. It has to be supposed only that its dependence on the size and the composition of the cluster is weak as compared with the exponential term in Eq. (3.5).

With the general relation (3.6) we may write further

$$-\left[\Delta G(n+1) - \Delta G(n)\right] = \mu_v(p, T) - \left.\frac{\partial G_d(n)}{\partial n}\right|_{n=n+1} = \mu_v - \mu_d(n+1)\,. \tag{3.11}$$

Here $\mu_d(n)$ is the chemical potential per atom of the drop of size n including surface energy and other possible size effects. It is defined by

$$\mu_d(n) = \frac{\partial G_d(n)}{\partial n}\,. \tag{3.12}$$

For the special choice of $G_d(n)$, as expressed by Eq. (3.8), we have, in particular,

$$\mu_d(n) = \frac{\partial G_d(n)}{\partial n} = \mu_d(p,T) + \frac{8\pi\sigma}{3}\left(\frac{3}{4\pi}\omega_d\right)^{2/3} n^{-1/3} . \tag{3.13}$$

Generally, with Eq. (3.11) we may also write

$$\frac{w^{(+)}_{n,n+1}}{w^{(-)}_{n+1,n}} = \exp\left(\frac{\mu_v - \mu_d\,(n+1)}{k_B T}\right) . \tag{3.14}$$

In this way, it has been shown that in thermodynamic equilibrium states the relation between the coefficients of emission and absorption is given either by Eqs. (3.9), (3.10), or (3.14).

In application to thermodynamic equilibrium states, the function $f^{(eq)}(n)$ has a real physical meaning. It represents the equilibrium distribution of heterophase fluctuations. Moreover, in equilibrium the principle of detailed balancing holds. Therefore, for the states considered so far the method of derivation of the emission coefficients is fully satisfactory. However, even in this region of applicability some uncertainty remains connected with the properties of the preexponential factor A in Eq. (3.5).

However, considering thermodynamically unstable, nonequilibrium states, where nucleation-growth processes may occur, the situation becomes quite different. Distributions of the type as given by Eq. (3.5) can be derived in a correct way only for equilibrium but not for nonequilibrium states. This remark refers both to the classical thermodynamic and the statistical–thermodynamic approaches. Frenkel [22] derived his well-known distribution based on the assumption of a minimum of the Gibbs free energy (cf. also the more detailed discussion given below). However, this condition is applicable only to equilibrium states. Fisher [42] obtained similar slightly modified expressions by applying the methods of equilibrium statistical physics. Thus, the extrapolation of these results to thermodynamic nonequilibrium states is, again, not correct. Generally, the application of methods of equilibrium statistical mechanics for a description of fluctuation processes [40] is valid in thermodynamic equilibrium states, only.

For the determination of the emission rates of single particles from the clusters and the steady-state nucleation rate, in general, a somewhat artificial model is commonly utilized introduced originally by Szilard (see Fig. 3.2). It is assumed that, once a cluster reaches an upper limiting size, $g \gg n_c$, it is instantaneously removed from the system. Moreover, according to Szilard's model, simultaneously to the removal of a g-sized cluster, g single particles are added to the system. In this way, the total number of particles is kept constant. Starting with a state consisting of single particles only, after some time interval (denoted commonly as time-lag in nucleation) a time-independent steady-state cluster size distribution is established in the system. Assuming that (i) clusters of different sizes can be considered as different components in a multicomponent perfect solution (or a mixture of perfect gases for vapor condensation), (ii) the number of particles aggregated in the clusters is small as compared with the total number of solute particles, (iii) conservation of the total number of solute particles is fulfilled, (iv) the change of the cluster size is possible by emission or aggreation of monomers, only,

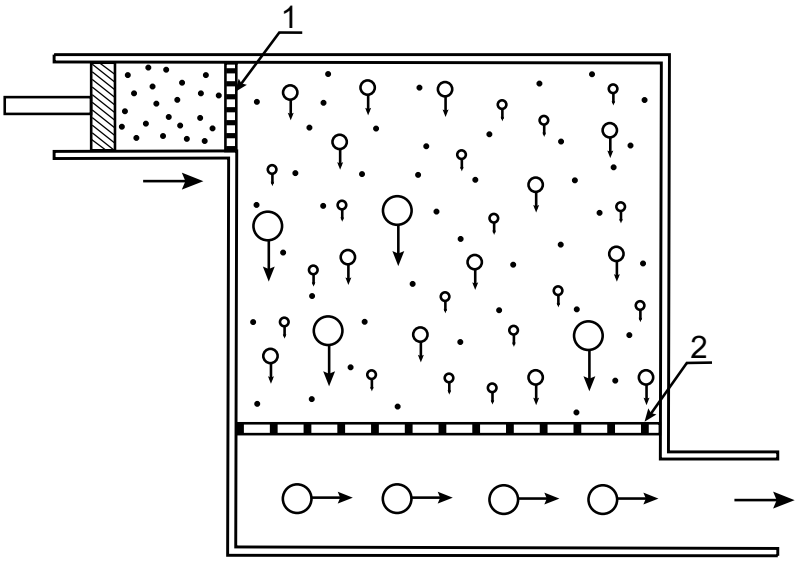

Figure 3.2: Schematic representation of Szilard's model used in the classical nucleation theory. Clusters (or droplets) with numbers of monomers $g \gg n_c$ are instantaneously removed from the chamber via a membrane (2) impermeable for clusters of smaller sizes. Simultaneously to the removal of such a cluster, g monomers are added to the chamber (1). In this way, a constant supersaturation is sustained in the system and a steady state with a constant nucleation rate may be established in the course of time

Frenkel [22] obtained an expression for the stationary cluster size distribution function $f^{(e)}(n)$ as

$$f^{(e)}(n) = f(1) \exp\left\{-\frac{\Delta G(n)}{k_B T}\right\} , \tag{3.15}$$

quite similar to Eq. (3.5). Indeed, for the thermodynamic boundary conditions chosen, the work of cluster formation is given by $\Delta G(n)$. Here $f(1)$ is the concentration (number per unit volume) of single particles which will be also denoted as c.

The distribution equation (3.15) is commonly denoted as equilibrium or constraint equilibrium distribution with respect to cluster sizes [1,2,24,25,35]. Note, however, that this notation is misleading. The time-independent state in the model system, it was derived for, is not an equilibrium but a nonequilibrium steady state. Therefore, the procedure applied to the derivation of Eq. (3.15) lacks any thermodynamic foundation. Moreover, one has to take into account that the distribution refers to Szilard's artificial model system which is not realized in nature (except for artificial conditions or by assuming some kind of "Szilard's demon" in analogy to Maxwell's demon (cf. e.g. [29–33])). Therefore, the identification of the so-called equilibrium distribution with respect to cluster sizes with real distributions evolving in nucleation-growth processes in thermodynamically unstable systems is, in general, incorrect. Even in interpreting such expressions in terms of Szilard's model (cf., e.g., Refs. [12, 13]), the resulting distribu-

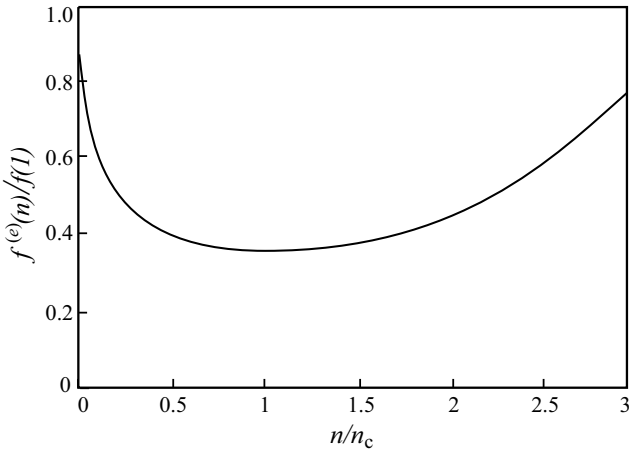

Figure 3.3: *Equilibrium* cluster size distribution $f^{(e)}(n)/f(1)$ of the classical nucleation theory in relative coordinates (n/n_c) for thermodynamically unstable initial states (according to Eq. (3.17)). $(\Delta G_{(c)}/k_B T)$ was chosen equal to one for convenience. Fisher's statistical droplet model [42] leads to a widely equivalent dependence except in the immediate vicinity of the critical point

tions refer not to equilibrium but to stationary nonequilibrium steady states. For such states, the principle of detailed balancing also does not hold, in general.

For thermodynamically unstable initial states, ΔG may be written, employing certain approximations, as (e.g. [23])

$$\frac{\Delta G}{\Delta G_{(c)}} = 3\left(\frac{n}{n_c}\right)^{2/3} - 2\left(\frac{n}{n_c}\right) . \tag{3.16}$$

The so-called equilibrium distribution function $f^{(e)}(n)$ (cf. Eq. (3.15)) gets in this case the form

$$\left(\frac{f^{(e)}(n)}{f(1)}\right) = \exp\left\{-\frac{\Delta G_{(c)}}{k_B T}\left[3\left(\frac{n}{n_c}\right)^{2/3} - 2\left(\frac{n}{n_c}\right)\right]\right\} . \tag{3.17}$$

It is qualitatively presented in Fig. 3.3. The function has a minimum for $n = n_c$ and diverges for larges values of (n/n_c).

Based on the methods of equilibrium statistical physics, Fisher [42] developed an alternative derivation of dependences quite similar to Eq. (3.15). Fisher did not employ the second of mentioned Frenkel's assumptions. As a consequence, the expression for the preexponential factor remains undefined in his approach. Fisher introduced, in addition, a term $(k_B T \tau \ln n)$ into the expression for the work of cluster formation resulting thus in

$$\Delta G(n) = -n\Delta\mu + \alpha_2 n^{2/3} + k_B T \tau \ln n . \tag{3.18}$$

The actual value of τ depends on specific properties of the substance considered. It can vary, according to Fisher's approach, in the range $2.0 < \tau < 2.5$ [42, 43].

In the vicinity of the liquid–gas critical point the differences between the liquid and the gas vanish, the relations $\Delta\mu \to 0$, $\alpha_2 \to 0$ hold and Fisher's model yields

$$\Delta G(n)|_{T\to T_c} = k_B T \tau \ln n \ , \quad f_F^{(e)}(n)\Big|_{T\to T_c} \propto n^{-\tau} \ . \tag{3.19}$$

The occurrence of such dependences in the vicinity of the liquid–gas or percolation critical points was reconfirmed by alternative approaches [44–48] giving in this way support to Fisher's proposal. Moreover, for thermodynamic equilibrium states Fisher's model is equivalent, again, to the Boltzmann type heterophase fluctuations with a somewhat modified expression for the work of cluster formation as compared with the classical result. However, in thermodynamically unstable states (i.e., below T_c) beyond (i.e., at a sufficiently large distance from) the critical point, with respect to Fisher's model the same conclusions have to be drawn as done in the analysis of the so-called equilibrium distribution of the classical nucleation theory. Fisher's model is inappropriate to describe real cluster size distributions evolving in thermodynamically unstable initial states beyond the liquid–gas critical point.

This conclusion follows from the method applied in the derivation which is based on the equilibrium statistical physics. Moreover, on physical grounds it is also evident. For thermodynamically unstable states beyond the critical point, Fisher's model results, again, in qualitatively similar dependences as shown in Fig. 3.3. However, the only (time-independent) equilibrium distribution evolving in the course of time consists of one large cluster (the newly evolving bulk phase in the ambient phase) surrounded eventually by a distribution of small clusters (monomers, dimers, etc.).

The same conclusions can be drawn with respect to any other similar expressions resulting from different approaches in the determination of the work of cluster formation, ΔG (cf. [1, 2]). Such distributions may be of use in order to determine the emission coefficients from the expressions for the coefficients of aggregation by applying the principle of detailed balancing to an artificial model state (with all the problems involved in such a procedure (cf. [36–49])). However, the application of these expressions to the description of real cluster size distributions formed in nucleation-growth processes is, in general, incorrect. To some extent, the results can be considered, however, as a reasonable approximation also for thermodynamic nonequilibrium states, but here only for clusters of subcritical sizes $n < n_c$. Since the system is undersaturated for these aggregates, they are in similar conditions as heterophase fluctuations in thermodynamic equilibrium states. This statement means that the relations between the coefficients of absorption $w_{n,n-1}^{(+)}$ and emission $w_{n,n+1}^{(-)}$ for these aggregates may be the same as in the case of heterophase fluctuations in equilibrium states.

This idea gets additional support by a comparison between the distribution given with Eq. (3.5) and the steady-state cluster size distribution (cf. e.g. [23, 50, 51]). The latter distribution is the asymptotic solution of the set of kinetic equations provided the concentration of single particles is kept constant by some appropriate mechanism (cf., e.g., Ref. [39]). In the range of cluster sizes $n < n_c$, both distributions coincide with an accuracy to a factor in the range 0.5–1. However, the degree to which such an extrapolation leads to correct results remains unclear. The situation gets even more complex for new phase aggregates with $n > n_c$, because in this case we have a fully developed nonequilibrium situation. A reference to heterophase fluctuations is impossible for such clusters and another approach has to be employed for the determination of the emission coefficients $w^{(-)}$.

3.3.2 A New Method of Determination of the Coefficients of Emission

General Remarks: Real and Virtual States of the Ambient Phase

After the discussion of the limitations of the traditionally employed approach, we go over, now, to the description of a new general method of solution of the problem of the determination of the emission coefficients. This method (i) avoids the application of the so-called equilibrium distributions of classical nucleation theory to nonequilibrium states (i.e., to the states of interest in nucleation-growth processes), and (ii) does not employ the principle of detailed balancing, which is valid for thermodynamic equilibrium but not for nonequilibrium states. As mentioned already in the introduction, it is our aim to develop a macroscopic method of determination of the emission coefficients retaining its advantages but avoiding the application of not well-founded or even incorrect (for the considered nonequilibrium states) concepts.

One of the basic assumptions, central to our method, is that we assume that the clusters of the newly evolving and the ambient phases are both in states of internal thermodynamic equilibrium. Such an assumption resembles the concept of a local equilibrium widely employed in the thermodynamics of irreversible processes [52]. It is the basis for an appropppriate description of the thermodynamics of heterogeneous systems [53], in general, and a thermodynamic (macroscopically based) analysis of cluster formation processes [54, 55], in particular. Moreover, it gives also the foundation to speak about well-defined values of the kinetic coefficients. This way, this first assumption is not a serious restriction but the precondition of any mesoscopic approach to the analysis of cluster formation and growth processes. It makes the problem well-defined. Remember, however, that the system as a whole is in a nonequilibrium state. The clusters are, in general, not in equilibrium with the surrounding ambient phase.

As a second ingredient in the analysis, we employ the concept of *virtual* and real states of the ambient phase. (cf. Fig. 3.4) A virtual state is an idealized model state. It is constructed in the following way: provided we have a cluster of a given size. The question is what the state of the ambient phase should be in order to attain a thermodynamic equilibrium between the cluster considered and the ambient phase. Such *virtual* or possible states of the ambient phase will differ, in general, from the real state of the system. Moreover, for clusters of different sizes, the possible *virtual* states of the ambient phase are different. The coefficients of emission will be determined in our approach by considering the differences between real and virtual states of the system. Hereby it plays no role, as in many other applications of thermodynamics, whether the different *virtual* states may be realized in practice or not. One only has to take care that the models employed do not contradict in their consequences the basic laws of thermodynamics, in particular, or physics, in general. This property is fulfilled by our model.

This concept is a generalization of the application of Kelvin's equation in the determination of the coefficients of emission for vapor condensation [23]. In this method, the same question is asked, i.e., what the (virtual) state of the gas phase should be that a drop of given size is in equilibrium with the vapor. From such considerations, then conclusions are derived concerning the values of the coefficients of evaporation for drops of a given size (aggregation and emission rates have to coincide for the *virtual* state of the vapor). While from the basic idea our approach resembles the mentioned one, it is much more general and applicable to condensation in nonideal one- and multicomponent gas systems as well as to phase formation processes in condensed media both for isothermal and nonisothermal conditions.

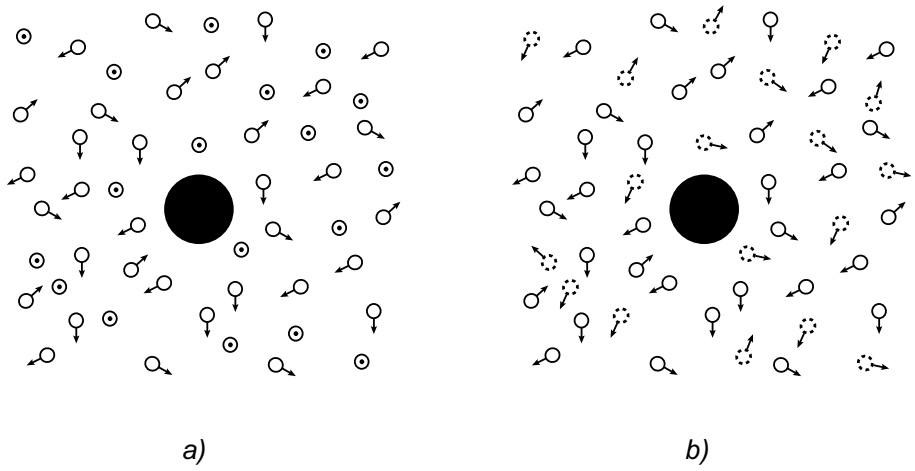

Figure 3.4: Illustration of the model of virtual states (see text). (a) Supercritical clusters: Particles marked with a dot are made immobile in order to retain a dynamic equilibrium. (b) Subcritical clusters: A number of additional particles (specified by dotted circles) are added in order to retain a dynamic equilibrium

The Alternative Approach: Clusters of Supercritical Sizes

Going over, now, to a more detailed outline of our method of determination of the emission coefficients, we start with the region of supercritical cluster sizes. (cf. Fig. 3.4a) In order to proceed with our task we consider, as mentioned, in addition to the real also a *virtual* state of the ambient (vapor) phase. This *virtual* state of the ambient phase is defined in such a way that the chemical potential of the condensing particles is equal to the chemical potential of the building units in the considered aggregate of the new phase. The *virtual* state of the ambient phase depends thus on the size of the cluster (drop) considered. For clusters of different sizes, different *virtual* states of the ambient phase have to be introduced. Since we are considering, in application to vapor condensation, drops with sizes $n > n_c$, the chemical potential per particle μ in the real vapor is larger than in the assumed *virtual* states ($\mu > \widetilde{\mu}$). Here and subsequently, the parameters of the virtual state are specified by a tilde. Therefore, in order to attain a dynamic equilibrium, a certain part of the gas particles has to be fixed in its spatial positions. Consequently, the real and virtual vapor (or, generally, the different real and virtual states of the ambient phase) differ in the number of single particles fixed in the latter ones.

For the determination of the ratio between the coefficients of aggregation and emission and the specification of the virtual state of the ambient phase, we consider a reference system connected with the chosen cluster. The immobile particles are fixed in their spatial positions with respect to the chosen cluster (drop). Such a choice of the reference system also allows us to apply the method to systems like droplets in gases, where the motion of the clusters affects the aggregation rates.

It is required only in subsequent considerations that the state of the ambient phase in the vicinity of the chosen cluster is at any time in a local thermodynamic equilibrium. This

condition implies that the characteristic time scales of changes of the state of the system (including the motion of the cluster) have to be large as compared to the respective times of aggregation or emission of single particles. The assumption of a local equilibrium is inherent in most methods of determination of the coefficients of aggregation. Therefore, we stay here inside the range of commonly accepted quite reasonable approximations. For large drops and most applications of the nucleation theory in condensed matter physics, the clusters practically do not move. In these cases, the reference system coincides with the usual laboratory system.

If we describe vapor as a perfect gas, then the *virtual* vapor state coincides with a state of the gas at a density of mobile particles corresponding to the equilibrium concentration of the vapor for a droplet of the given size. In dense vapors, one has to take into account also the interaction of the gas particles. In both cases, the fixed part of the gas particles in the virtual states creates the environment for the mobile particles, identical to the environment in the real vapor state. It follows that the condensing particles (in both actually existing and *virtual* vapor states) have the same energetic barriers for condensation. More generally, the kinetic conditions for aggregation are the same in both the real and virtual states.

By definition of the *virtual* vapor state, the gas must contain such a number of mobile ambient phase particles that their chemical potential, taking into account the interaction also with the fixed gas atoms, is equal to the chemical potential of a particle in a drop (or cluster) of size n, i.e., $\widetilde{\mu} = \mu_{\mathrm{d}}(n)$ holds. At such conditions, the virtual gas (or ambient) phase is in a dynamic equilibrium with a chosen drop (cluster) of the liquid (newly evolving) phase, i.e., the relation $w^{(-)}_{n,n-1} = \widetilde{w}^{(+)}_{n-1,n}$ is fulfilled. Note that this relation is a consequence of the definition of the *virtual* states. It is thus quite different from Eq. (3.9) where rates of aggregation and emission of clusters of different sizes in thermodynamic equilibrium states are compared. Moreover, the virtual vapor state is characterized by equal probabilities per unit time for one selected mobile atom to be added to the liquid drop as compared to a particle at the same state (position and velocity) in the real vapor at the same overall concentration. This property is due to the fact that the environment of the mobile atoms, by definition, is the same as the one in the real vapor phase, or, in other words, in both virtual and real vapors, the kinetic conditions for condensation are the same for the mobile atoms. It follows that the probabilities $w^{(+)}_{n-1,n}$ of aggregation in the real and $\widetilde{w}^{(+)}_{n-1,n}$ in the virtual vapor have the same kinetic preexponential factors. They differ only by the probabilities p_r and $\widetilde{p}_r$ of occurrence of favorable configurations for the realization of these processes with respect to a given mobile particle.

As already mentioned, with sufficiently high precision we may assume that both real and virtual states of the ambient phase (vapor) are in an internal thermodynamic equilibrium. Hence, applying the conditions $w^{(-)}_{n,n-1} = \widetilde{w}^{(+)}_{n-1,n}$ and the above-given considerations, we get

$$\frac{w^{(+)}_{n-1,n}}{w^{(-)}_{n,n-1}} = \frac{w^{(+)}_{n-1,n}}{\widetilde{w}^{(+)}_{n-1,n}} = \frac{p_r}{\widetilde{p}_r} \,. \tag{3.20}$$

Here p_r and $\widetilde{p}_r$ are the probabilities of occurrence of a favorable configuration for incorporation of one mobile particle to a drop from the real and virtual vapors at a given average (thermodynamic) energy of these subsystems (cluster or drop surrounded by a sufficiently large part of the ambient phase). Since in the virtual state of the ambient phase some part of

the atoms is fixed in their positions, the probabilities of occurrence of favorable configurations obey the condition $\widetilde{p}_r < p_r$.

Further on, we employ a basic relationship of statistical thermodynamics [40], i.e.,

$$S = k_{\mathrm{B}} \ln W \ . \tag{3.21}$$

Here S is the entropy of a given macrostate of a system and W the number of microstates (or thermodynamic probability) referring to the respective macrostate. In application to the considered problem we may write

$$\frac{p_r}{\widetilde{p}_r} = \exp\left[\frac{\left(\Delta S - \Delta\widetilde{S}\right)}{k_{\mathrm{B}}}\right] \ . \tag{3.22}$$

Here $\Delta\widetilde{S}$ and ΔS are the entropies per mobile particle in the virtual and real vapor (real or virtual states of the ambient phase) for each of the subsystems considered. The macrostates refer here to those configurations which allow the incorporation of a single mobile particle to the cluster.

As mentioned, both the virtual and the real states of the ambient phase may be considered to be in an internal thermodynamic equilibrium at the respective concentrations of their mobile particles. Moreover, the temperature of both systems is the same. The latter condition implies that the difference of the entropies $\Delta S - \Delta\widetilde{S}$ is equal to the change of the entropy ΔS_n, resulting from the transfer of one mobile particle from the virtual to the real state of the ambient phase. Moreover, the number of configurations allowing the incorporation of a mobile particle to a given cluster is larger in the real state of the ambient phase than in the virtual one. Therefore, in the range of cluster sizes $n > n_{\mathrm{c}}$ the relation

$$\Delta S - \Delta\widetilde{S} = \Delta S_n > 0 \tag{3.23}$$

holds. In addition, one can always add to ΔS and $\Delta\widetilde{S}$ the entropies S_0 and $\widetilde{S}_0$, respectively, of the rest of the subsystems (we consider, now and hereinafter, only the respective parts of the ambient phase in the real and the virtual states). These contributions do not change in the course of the transfer of a mobile particle between both states. ΔS_n may also be treated, therefore, as the total change of entropy in such a transfer resulting from the respective changes ΔS and $\Delta\widetilde{S}$ in both subsystems.

At given values of the external thermodynamic parameters, the change in entropy of a thermodynamic subsystem may be connected with the work R_{rev}. R_{rev} is the work one has to perform in a reversible process to create the same changes of the state of the subsystem (the same change of entropy). Generally, we may write (cf., e.g., Ref. [40])

$$\Delta S = \left(\frac{\Delta S}{\Delta U}\right) R_{\mathrm{rev}} = \frac{1}{T} R_{\mathrm{rev}} \ . \tag{3.24}$$

Here the thermodynamic relation

$$\frac{\partial S}{\partial U} = \frac{1}{T} \tag{3.25}$$

has been employed, in addition, U in Eqs. (3.24) and (3.25) is the internal energy of the considered subsystem.

For a subsystem at fixed values of the external pressure, p, and temperature, T, the work performed in a reversible process equals the change of the Gibbs free energy Δg in the respective process. Taking into account, moreover, that the temperatures are same both in the real and the virtual states of the ambient phase, we obtain from Eqs. (3.24) and (3.23)

$$\Delta S_n = \frac{1}{T} R_{\text{rev}} = \frac{\Delta g}{T} \ . \tag{3.26}$$

Here Δg is the total change in Gibbs free energy in the transfer of the considered particle from the virtual to the real state.

For one-component systems, we may write immediately

$$\Delta g = \mu_{\text{v}} - \widetilde{\mu} \ . \tag{3.27}$$

Taking into account the relation $\widetilde{\mu} = \mu_{\text{d}}(n)$, we have

$$\Delta S_n = \frac{\mu_{\text{v}} - \mu_{\text{d}}(n)}{T} \ . \tag{3.28}$$

Here, as earlier, μ_{v} is the chemical potential of a particle in the real state of the ambient phase, and $\mu_{\text{d}}(n)$ is its value in a cluster of size n (including interfacial and other possible finite size effects).

Combining Eqs. (3.20), (3.22), (3.23), (3.26), (3.27), and (3.28), we get the result for the ratio of absorption and emission coefficients as

$$\frac{w^{(+)}_{n-1,n}}{w^{(-)}_{n,n-1}} = \exp\left(\frac{\Delta S_n}{k_{\text{B}}}\right) = \exp\left(\frac{\mu_{\text{v}} - \mu_{\text{d}}\,(n)}{k_{\text{B}} T}\right) \ . \tag{3.29}$$

It follows that the relation between the coefficients of aggregation and emission for supercritical clusters is same as obtained earlier by applying the traditional method for thermodynamic equilibrium states (cf. Eq. (3.14)), i.e.,

$$\boxed{\frac{w^{(+)}_{n,n+1}}{w^{(-)}_{n+1,n}} = \exp\left(\frac{\mu_{\text{v}} - \mu_{\text{d}}\,(n+1)}{k_{\text{B}} T}\right) \ .} \tag{3.30}$$

However, in the present derivation, no reference was made to the so-called equilibrium distributions and the principle of detailed balancing (nonapplicable in nonequilibrium states).

Moreover, taking into account the generally valid thermodynamic relationships (3.11), we may also write

$$\frac{w^{(+)}_{n,n+1}}{w^{(-)}_{n+1,n}} = \exp\left(-\frac{[\Delta G(n+1) - \Delta G(n)]}{k_{\text{B}} T}\right) \ . \tag{3.31}$$

This relation is identical to Eq. (3.10). By introducing an auxiliary function $f^{(*)}(n)$ as

$$f^{(*)} = \exp\left(-\frac{\Delta G(n)}{k_{\mathrm{B}}T}\right) , \tag{3.32}$$

we may express the relation between the considered coefficients in another equivalent form as the ratio of the functions $f^{(*)}(n+1)$ and $f^{(*)}(n)$, again, i.e., (cf. Eq. (3.9)),

$$\frac{w^{(+)}_{n,n+1}}{w^{(-)}_{n+1,n}} = \frac{f^{(*)}(n+1)}{f^{(*)}(n)} . \tag{3.33}$$

Note that here these functions do not have any physical meaning, however. They have to be considered as auxiliary mathematical quantities.

The Alternative Approach: Clusters of Subcritical Sizes

In the first case considered, a certain part of the particles in the ambient phase was fixed in its positions. The kinetic conditions for aggregation for the remaining mobile particles remain thus same as in the real state of the ambient phase. For clusters of subcritical sizes the concentration of aggregating particles in the ambient phase is too small to reach a dynamic equilibrium. Thus, in order to construct the virtual state of the ambient phase we have to add, now, mobile particles. (cf. Fig. 3.4b) The total concentration of mobile particles is defined, again, by the condition $\widetilde{\mu} = \mu_{\mathrm{d}}(n)$. However, to retain, again, the requirement that the kinetic conditions for aggregation have to be same for any arbitrary particle, the newly added particles do not interact among themselves and with the particles present in the real state of the ambient phase. All further derivations then can be carried out step by step in the same way as explained in detail for the range of cluster sizes $n > n_{\mathrm{c}}$. Therefore, Eqs. (3.30), (3.31), and (3.33) hold equally well for clusters of subcritical sizes.

Summarizing this part, we may conclude that we have developed a method of determination of the coefficients of emission in terms of a macroscopic approach to the description of cluster properties in nucleation-growth processes. The basic result (3.30) can be brought into coincidence with expressions like Eqs. (3.31) and (3.33) used widely in the nucleation theory but so far without any satisfactory theoretical foundation. The development of a theoretical foundation of this widely employed approach is one of the basic results of the present analysis. Further, we will analyze some applications, derive generalizations, and find out the consequences of this result.

3.3.3 Applications

Once the kinetic coefficients $w^{(-)}$ have been determined, they may be substituted into the kinetic equations (3.1). Finally, for the solution of particular problems, the coefficients $w^{(+)}$ have to be specified. Instead of applying the set of kinetic equations (3.1)–(3.4), we may also go over to a continous description in the form of a Fokker–Planck equation. It provides a sufficiently accurate description of the initial stages of the condensation process. During the initial stage, for $1 \leq n \leq n_{\mathrm{c}}$, the second derivative of the distribution function $\left(\partial^2 f/\partial n^2\right)$ is

important, because it determines the rise of the nucleus from the size $n < n_c$ to a size $n > n_c$. The higher order derivatives are smaller than the second-order ones, if $n_c \gg 1$. It means that the basic spectrum of the nuclei is also found then in the range $n \gg 1$. The spectrum of droplet sizes in the range $n \sim 1$ may also be well-described by this differential equation. This is due to the fact that the character of the solution provides qualitatively correct results, even if we apply the differential equation. Having introduced $f^{(*)}(n) = \exp(-\Delta G(n)/k_B T)$ we get

$$\begin{aligned} J_{n-1} &= w^{(+)}_{n-1,n} f^{(*)}(n-1)\left[\frac{f(n-1,t)}{f^{(*)}(n-1)} - \frac{f(n,t)}{f^{(*)}(n)}\right] \\ &= J_n - \frac{\partial}{\partial n}\left\{w^{(+)}_{n,n+1} f^{(*)}(n)\left[\frac{f(n,t)}{f^{(*)}(n)} - \frac{f(n-1,t)}{f^{(*)}(n-1)}\right]\right\} \\ &= J_n + \frac{\partial}{\partial n}\left\{w^{(+)}_{n,n+1}\left[\frac{1}{k_B T}\frac{\partial \Delta G(n)}{\partial n} f(n,t) + \frac{\partial f(n,t)}{\partial n}\right]\right\} . \end{aligned} \tag{3.34}$$

Therefore, the difference equation (3.2) acquires the form

$$\frac{\partial f(n,t)}{\partial t} = \frac{\partial}{\partial n}\left\{w^{(+)}_{n,n+1}\left[\frac{1}{k_B T}\frac{\partial \Delta G(n)}{\partial n} f(n,t) + \frac{\partial f(n,t)}{\partial n}\right]\right\} . \tag{3.35}$$

A comparison with the ordinary continuity equation shows that the deterministic growth rate may be expressed as

$$\frac{\mathrm{d}n}{\mathrm{d}t} = -w^{(+)}_{n,n+1}\left\{\frac{1}{k_B T}\left(\frac{\partial \Delta G(n)}{\partial n}\right)\right\} . \tag{3.36}$$

This equation allows us to determine the coefficients of aggregation $w^{(+)}$ if the macroscopic growth rates $\mathrm{d}n/\mathrm{d}t$ of the clusters are known.

3.4 Generalization to Multicomponent Systems

Assume that both the ambient and the newly evolving phases are composed of k different components. The distribution function with respect to cluster sizes is then a function of all numbers n_j of particles of the different components j ($j = 1, 2, \ldots, k$) in the cluster, i.e., $f = f(n_1, n_2, \ldots, n_k, t)$ holds. Instead of the kinetic equation (3.2), we have now

$$\frac{\partial f(n_1, n_2, \ldots, t)}{\partial t} = -\sum_{j=1}^{k}[J(n_j, t) - J(n_j - 1, t)] \tag{3.37}$$

with

$$\begin{aligned} J(n_j, t) = {} & w^{(+)}_{n_j, n_j+1} f(n_1, n_2, \ldots, n_j \ldots, n_k, t) \\ & - w^{(-)}_{n_j+1, n_j} f(n_1, n_2, \ldots, n_j + 1, \ldots, n_k, t) . \end{aligned} \tag{3.38}$$

As a next step, again, the coefficients of emission have to be specified. This procedure can and will be carried out in the same way as done so far for one-component systems.

3.4.1 Traditional Approach

For thermodynamic equilibrium states in multicomponent systems, the cluster size distribution may be approximated by the expression for heterophase fluctuations as (cf., again, Ref. [40])

$$f^{(\mathrm{eq})}\,(n_1, n_2, \ldots, n_k) = A \exp\left(-\frac{\Delta G\,(n_1, n_2, \ldots, n_k)}{k_\mathrm{B} T}\right)\,. \tag{3.39}$$

Here $\Delta G(n_1, n_2, \ldots, n_k)$ is the work of formation of a cluster consisting of the respective number of particles of the different components. Assuming that the preexponential factor A depends only weakly on the composition and size of the clusters, we obtain similarly to the one-component case

$$\frac{w^{(+)}_{n_j;n_j+1}}{w^{(-)}_{n_j+1;n_j}} = \exp\left\{-\frac{[\Delta G(n_j+1) - \Delta G(n_j)]}{k_\mathrm{B} T}\right\}\,. \tag{3.40}$$

Here all values of the number of particles of the different components in the cluster, except for the component j are fixed.

As a next step, we introduce the difference of the Gibbs free energy ΔG, when, at constant values of the external pressure, p, and temperature, T, a cluster of a given composition is formed. We have

$$\Delta G(n_1, n_2, \ldots, n_k) = G_\mathrm{d}(n_1, n_2, \ldots, n_k) - \sum_{j=1}^{k} n_j \mu_{j\upsilon}\,. \tag{3.41}$$

$G_\mathrm{d}(n_1, n_2, \ldots, n_k)$ is the contribution of the cluster to the thermodynamic potential including interfacial and other possible correction terms. With Eq. (3.41), we get for example

$$\begin{aligned} -\big[\Delta G(n_1, n_2, \ldots, n_j+1, \ldots, n_k) - \Delta G(n_1, n_2, \ldots, n_j, \ldots, n_k)\big] \\ = \mu_{j\upsilon} - \mu_{jd}(n_1, n_2, \ldots, n_j+1, \ldots, n_k)\,. \end{aligned} \tag{3.42}$$

Indeed, we may write

$$\begin{aligned} \Delta G(n_j+1) - \Delta G(n_j) &= G_\mathrm{d}(n_j+1) - \sum_i n_i \mu_{i\upsilon} - \mu_{j\upsilon} - \left[G_\mathrm{d}(n_j) - \sum_i n_i \mu_{i\upsilon}\right] \\ &= G_\mathrm{d}(n_j+1) - G_\mathrm{d}(n_j) - \mu_{j\upsilon} \\ &= \left(\frac{\partial G_\mathrm{d}(n_j+1)}{\partial n_j}\right) - \mu_{j\upsilon} = \mu_{jd}(n_j+1) - \mu_{j\upsilon}\,. \end{aligned} \tag{3.43}$$

The dependences (3.42) allow us to reformulate Eq. (3.40) as

$$\frac{w^{(+)}_{n_j,n_j+1}}{w^{(-)}_{n_j+1,n_j}} = \exp\left\{\frac{[\mu_{j\upsilon} - \mu_{jd}(n_1, n_2, \ldots, n_j+1, \ldots, n_k)]}{k_\mathrm{B} T}\right\}\,. \tag{3.44}$$

Again, for systems in thermodynamic equilibrium states this approach is quite satisfactory provided the additional assumption (weak dependence of the prefactor A on cluster size) is fulfilled. The method cannot be applied, as discussed in detail earlier, to thermodynamic nonequilibrium states.

3.4.2 Alternative Approach

The alternative method of determination of the relation between the kinetic coefficients in application to thermodynamically unstable initial states relies, again, on the consideration of the probabilities of formation of favorable configurations for a single particle to be incorporated into the cluster (both in the real and virtual states). The derivations as outlined above can also be applied without any qualitative modification to multicomponent systems. Consequently, as will be shown, qualitatively the same results are obtained as derived in Sect. 3.3 for phase formation processes in one-component systems. In particular, similarly to Eq. (3.29) we arrive at

$$\frac{w^{(+)}_{n_j-1,n_j}}{w^{(-)}_{n_j,n_j-1}} = \exp\left(\frac{\Delta S_n}{k_\mathrm{B}}\right) = \exp\left(\frac{\Delta g}{k_\mathrm{B}T}\right) . \tag{3.45}$$

Remember that Δg is the total change in Gibbs free energy of both subsystems (real and virtual ones) if a mobile particle is transferred from the virtual to the real state. Taking into account this meaning of Δg, we have

$$\Delta g = g_\mathrm{final} - g_\mathrm{initial} , \tag{3.46}$$

$$\Delta g = \widetilde{g}(n_j - 1) - g(n_j + 1) - \left[\widetilde{g}(n_j) + g(n_j)\right] \tag{3.47}$$

or

$$\Delta g = -\frac{\partial \widetilde{g}}{\partial n_j} + \frac{\partial g}{\partial n_j} = \mu_{jv} - \widetilde{\mu}_j . \tag{3.48}$$

Here g or $\widetilde{g}$ are the Gibbs free energies of the ambient phase in the two considered states, and n_j is the number of particles of the component j in the subsystems. Moreover, the well-known relations

$$\mu_j = \frac{\partial g}{\partial n_j} , \quad \widetilde{\mu}_j = \frac{\partial \widetilde{g}}{\partial n_j} \tag{3.49}$$

are employed. With $\widetilde{\mu}_j = \mu_{jd}$ (consequence of the definition of the *virtual* states), we obtain immediately

$$\boxed{\frac{w^{(+)}_{n_j,n_j+1}}{w^{(-)}_{n_j+1,n_j}} = \exp\left\{\frac{[\mu_{jv} - \mu_{jd}(n_1, n_2, \ldots, n_j + 1, \ldots, n_k)]}{k_\mathrm{B}T}\right\}} \tag{3.50}$$

and as a result

$$\frac{w^{(+)}_{n_j,n_j+1}}{w^{(-)}_{n_j+1,n_j}} = \exp\left\{-\frac{[\Delta G(n_j + 1) - \Delta G(n_j)]}{k_\mathrm{B}T}\right\} . \tag{3.51}$$

In Eq. (3.50), μ_{jv} is the chemical potential of a particle of the jth component in the ambient vapor phase, while $\mu_{jd}(n_1, n_2, \ldots, n_j + 1, \ldots, n_k)$ is its value in a cluster of the specified

composition. As in the one-component case, the value of μ_{jd} accounts for surface and other possible finite size effects. In Eq. (3.51), the values of $n_i, i \neq j$ are kept constant, again.

By the introduction of an auxiliary function $f^{(*)}(n_1, n_2, \ldots, n_k)$ via

$$f^{(*)}(n_1, n_2, \ldots, n_k) = \exp\left\{-\frac{\Delta G(n_1, n_2, \ldots, n_k)}{k_B T}\right\} , \tag{3.52}$$

Eqs. (3.40) and (3.51) may be written, generally, in the form

$$\frac{w^{(+)}_{n_j;n_j+1}}{w^{(-)}_{n_j+1;n_j}} = \frac{f^{(*)}(n_j+1)}{f^{(*)}(n_j)} . \tag{3.53}$$

Here $f^{(*)}$ is an auxiliary mathematical function without any physical meaning, again. Thus, the method of derivation of the rates of emission of single particles from clusters of the newly evolving phase can be extended to multicomponent systems.

3.4.3 Applications

Once the coefficients $w^{(-)}$ are specified, they can be substituted into the kinetic equations. Moreover, one can go over, again, to a continous description in the form of a Fokker–Planck equation. By the same method as demonstrated in Sect. 3, we obtain

$$\frac{\partial f}{\partial t} = \sum_j \frac{\partial}{\partial n_j}\left\{ w^{(+)}_{n_j,n_j+1}\left[\frac{1}{k_B T}\frac{\partial \Delta G(n_1, n_2, \ldots, n_k)}{\partial n_j} f(n_1, n_2, \ldots, n_k, t) + \frac{\partial f(n_1, n_2, \ldots, n_k, t)}{\partial n_j}\right]\right\} \tag{3.54}$$

or, equivalently,

$$\frac{\partial f(n_1, n_2, \ldots, n_k, t)}{\partial t} = -\sum_j \frac{\partial J(n_j, t)}{\partial n_j} , \tag{3.55}$$

$$J(n_j, t) = -\left\{ w^{(+)}_{n_j,n_j+1}\left[\frac{1}{k_B T}\frac{\partial \Delta G(n_1, n_2, \ldots, n_k)}{\partial n_j} f(n_1, n_2, \ldots, n_k, t) + \frac{\partial f(n_1, n_2, \ldots, n_k, t)}{\partial n_j}\right]\right\} . \tag{3.56}$$

An inspection of Eqs. (3.55) and (3.56) leads to the conclusion that the macroscopic (deterministic) growth rates are given by

$$v_j = \frac{\mathrm{d}n_j}{\mathrm{d}t} = -w^{(+)}_{n_j,n_j+1}\left[\frac{1}{k_B T}\frac{\partial \Delta G(n_1, n_2, \ldots, n_k)}{\partial n_j}\right] , \tag{3.57}$$

while the diffusion coefficients $D_j^{\{n\}}$ in the space of independent variables $\{n_j\}$ are determined by

$$D_j^{\{n\}} = w_{n_j,n_{j+1}}^{(+)} \; . \tag{3.58}$$

Note that the theory of Langer [16] results in similar dependences for the description of the evolution of the characteristic parameters of a system undergoing a first-order phase transformation. Differences between his and the theoretical approach employed here occur only in the way the macroscopic parameters of the system are introduced, and the way the critical cluster size in nucleation and the steady-state nucleation rate are determined.

3.5 Generalization to Arbitrary Boundary Conditions

Summarizing the results obtained so far we come to the following conclusions: It follows from the analysis outlined that the basic relationships between the coefficients of aggregation and emission are given by Eqs. (3.30) (for the one-component case) and (3.50) (for a multicomponent system). By applying thermodynamic identities, these relations can be transformed into Eqs. (3.31) and (3.51). In these expressions, the ratio of the kinetic coefficients is expressed via the differences of the thermodynamic potentials. Further, one may introduce auxiliary functions $f^{(*)}$ (Eqs. (3.32) and (3.52)) in order to express the ratio of the kinetic coefficients as the ratio of these auxiliary functions (Eqs. (3.33) and (3.53)). The latter results are similar in the form to the respective dependences obtained by the traditional approach. However, in our method no reference is made to the so-called equilibrium distributions and the principle of detailed balancing is not applied to nonequilibrium states. As an additional advantage, the problem of determination of the coefficient A in the expressions for the distributions of heterophase fluctuations does not occur so far at all.

In order to extend the range of applicability of the method, we have to show that similar results can also be obtained for other boundary conditions such as constancy of pressure and temperature. In order to proceed in this direction we start with the basic intermediate result of our approach, i.e., with Eq. (3.26) or

$$\Delta S_n = \frac{1}{T} R_{\text{rev}} \; . \tag{3.59}$$

Assume, now, that instead of external pressure and temperature another set of thermodynamic parameters are fixed. Then the work R_{rev} one has to perform in a reversible process to create the same change in entropy ΔS_n is given not by Δg but by $\Delta\phi$. Here ϕ is the appropriate thermodynamic potential for the selected (arbitrary) boundary conditions. Instead of Eq. (3.26) we obtain then

$$\Delta S_n = \frac{1}{T} \Delta\phi \; . \tag{3.60}$$

Now, proceeding in the same way as in the derivation of Eq. (3.26), we get (cf. Eqs. (3.46)–(3.49))

$$\Delta S_n = \frac{1}{T} \left[\mu_{jv} - \mu_{jd} \right] \; . \tag{3.61}$$

Here it was taken into account, again, that the relation

$$\mu_j = \frac{\partial \phi}{\partial n_j} \tag{3.62}$$

holds, provided the other appropriate variables except n_j are kept constant. As a result, we obtain Eqs. (3.30) or (3.50), again.

Similar to Eq. (3.41), we may express the change in the characteristic thermodynamic function in cluster formation as

$$\Delta\Phi(n_1, n_2, \ldots, n_k) = \Phi_d(n_1, n_2, \ldots, n_k) - \sum_{j=1}^{k} n_j \mu_{jv} \, . \tag{3.63}$$

Proceeding in the same way as earlier, we arrive at

$$-\left[\Delta\Phi(n_1, n_2, \ldots, n_j + 1, \ldots, n_k) - \Delta\Phi(n_1, n_2, \ldots, n_j, \ldots, n_k)\right] = \mu_{jv} - \mu_{jd}(n_1, n_2, \ldots, n_j + 1, \ldots, n_k) \tag{3.64}$$

with similar consequences.

Finally, in the derivation of the basic equations for determination of the emission coefficients it was not utilized that the temperature in the cluster has to be the same as in the surrounding ambient phase. Therefore, the method is equally well applicable to phase formation under nonisothermal conditions. In this case, the values of the chemical potential have to be taken at the respective temperatures of the clusters and the ambient phase. In addition, the basic kinetic equations have to be supplemented by relations describing the heat flow between the clusters and the ambient phase (cf., e.g., Ref. [38]).

In this way, a regular method of formulation of the kinetic equations for the description of nucleation-growth processes is developed. The method does not depend on the boundary conditions applied, and it can be employed both for isothermal and nonisothermal nucleation. Moreover, since the derivation of the relation between the kinetic coefficients does not rely on any specific feature of vapor condensation but only on very general thermodynamic arguments, it is equally well applicable generally to the description of first-order phase formation processes proceeding via nucleation and growth.

3.6 Initial Conditions for the Cluster Size Distribution Function

The method of determination of the kinetic coefficients, developed here, can be employed without any reference to the so-called constraint equilibrium distributions. Such distributions may, nevertheless, enter the description but in a reduced much less significant way via the determination of the initial conditions for the solutions of the kinetic equations describing nucleation and growth. Indeed, it can be assumed in a variety of applications that the initial cluster size distribution after the quench into the unstable state corresponds to some extent to the spectrum of heterophase fluctuations existing in the initial equilibrium system before the

quench took place. Alternatively, one may suppose that for small cluster sizes the distribution is more or less well-expressed by the respective expressions for heterophase fluctuations even in thermodynamically unstable states.

For the determination of the initial conditions, following such an argumentation, only the value of the preexponential factor A in the expressions for heterophase fluctuations [40]

$$f(n_1, n_2, \ldots, n_k) = A \exp\left(-\frac{\Delta G(n_1, n_2, \ldots, n_k)}{k_B T}\right) \tag{3.65}$$

has to be known or, in other words, the limit of the respective distributions for very small cluster sizes $n_j \to 0$. Once the initial cluster size distribution is determined the further evolution is governed by the kinetic equations themselves. It is also only the value of A, i.e., the limit of the distribution for small sizes of the clusters of the newly evolving phase, which has to be known in order to derive expressions for the steady-state nucleation rate and the steady-state cluster size distribution (cf., e.g., Ref. [39]). From such a point of view, limiting consistency has to be considered as a fundamental property, i.e., the cluster size distributions at small cluster sizes have to be expressed accurately, while the shape of the expressions, like those given by Eq. (3.65), for large cluster sizes is of no relevance for nucleation (cf. also [35]).

Moreover, since relations of the type as given by Eq. (3.65) do not reflect real equilibrium distributions which may evolve in thermodynamically unstable states, they are applied exclusively in order to determine possible initial states for real cluster size distributions in the considered nonequilibrium states. The fulfilment of the mass action law has not to be considered, in our opinion, as a necessary fundamental condition for the validity of the respective distribution any more (see, in contrast, Refs. [24,25]). The coefficients A may or may not obey such property, in part, depending on whether these distributions are determined mainly by the initial equilibrium state before the quench took place or by the way the system is transferred into the considered nonequilibrium state. From such a point of view, the fulfilment of the mass action law is not an appropriate starting point for a possible redetermination of the value of the parameter A and the formulation of different specific versions of the nucleation theory.

In order to have a guide for the determination of possible initial conditions for the cluster size distributions, let us summarize, finally, some attempts in the determination of the parameter A for different special cases (cf. also [35]).

(i) For one-component systems, following Frenkel [22], the parameter A may be determined from the limiting condition as (cf. Eq. (3.5))

$$A = c \ . \tag{3.66}$$

Here c is the volume concentration of single particles in the ambient phase.

(ii) For clusters of arbitrary composition, following Reiss [56], the relation

$$A = c = \sum_{j=1}^{k} c_j \tag{3.67}$$

could be taken as a first approximation. Here, c_j is the volume concentration of the different components in the ambient phase, able to enter the new phase. Equation (3.67)

can be derived, similar to Eq. (3.66), based on the basic ideas of the fluctuation theory, as representing the number of particles able to act as centers of condensation. The probability that, indeed, a cluster of some definite but arbitrary composition is formed at a given nucleation site, is determined then by the exponential term.

(iii) An extended discussion of the different attempts for a proper determination of this coefficient for one-component and binary systems was given by Wilemski and Wyslouzil [24, 25]. They proposed (in application to binary systems) the relation

$$A = c \prod_{j=1}^{k} (x_{j\beta})^{x_{j\alpha}} \tag{3.68}$$

as a better approximation. This expression fulfils the limiting conditions for one-component clusters and, in addition, the mass action law. In Eq. (3.68), $x_{j\beta}$ is the molar fraction of the different components in the ambient phase, while $x_{j\alpha}$ is the molar fraction of the different components in the cluster considered. It is determined as

$$x_{j\alpha} = \frac{n_j}{\sum_{i=1}^{k} n_i} \ . \tag{3.69}$$

(iv) For clusters of a given stoichiometric composition (cf. also Refs. [36, 37]) the total number of nucleation sites is equal to the number of particles in the system able to enter the new phase. We have for that number

$$c = \sum_{j=1}^{k} c_j \ . \tag{3.70}$$

A heterophase fluctuation with a given composition can be formed in the ambient phase if a favorable configuration of particles of the different components is developed. Considering the motion of the different particles as independent, the probability of such an event is equal to the product of the molar fractions $x_{i\beta}$ of the different components i in the ambient phase each of them taken to the power $x_{i\alpha}$. As a result, we obtain the following expression for A (cf. Refs. [36, 37])

$$A = c \prod_{j=1}^{k} x_{j\beta}^{x_{j\alpha}} \ . \tag{3.71}$$

Most of the above-mentioned considerations concerning the initial state of the cluster size distribution function can be carried out equally well without any reference to expressions like Eq. (3.65). Therefore, even for the determination of the initial conditions the reference to distributions like that given by Eq. (3.65) may be completely avoided.

3.7 Description of Cluster Ensemble Evolution Along a Given Trajectory

3.7.1 Motivation

The set of kinetic equations as outlined above allows us to determine the evolution of the cluster size distribution function for phase formation in multicomponent systems in a complete way. However, with an increase in the number of components in the system, the computation times increase dramatically. Due to this reason, a comprehensive description of the whole course of nucleation-growth processes based on the numerical solution of the sets of kinetic equations is possible presently for one-component and binary systems only (cf. e.g. [57]).

In a number of cases, the problems can be reduced significantly. Indeed, following the classical approach to nucleation-growth processes, one can distinguish the case that the clusters of the newly evolving phase have widely the same composition and structure as the newly evolving macroscopic phase. In these cases, which are illustrated in Fig. 3.1, the task to be solved is reduced to a one-dimensional problem. The clusters consist here of units with a given well-defined composition, $\{x_{i\alpha}\}$. This problem has been analyzed in detail for the first time in [36, 37]. However, in general, the composition and state of the clusters will change with cluster size and variations of the state of the ambient phase. By this reason, the classical assumption that the state of the clusters is independent of their sizes can be considered, in general, as a crude approximation only.

Quite recently, a new general approach to the description of nucleation-growth processes has been developed [58–60] (cf. also Chapters 11 and 12). This approach allows one a theoretically founded determination of the path of evolution of the clusters in the space of cluster parameters or, in other words, a description of the changes in the state parameters of the clusters with their sizes. The respective situation is illustrated in Fig. 3.5. The details of this approach are outlined in the papers cited and in the chapters mentioned. Here it is only of importance that in this very general case a reduction of the description from the determination of the distribution function, $f(n_1, n_2, \ldots, n_k, t)$, to a description in terms of a distribution function $f(n, t)$ is possible as well. The respective transformations are described below.

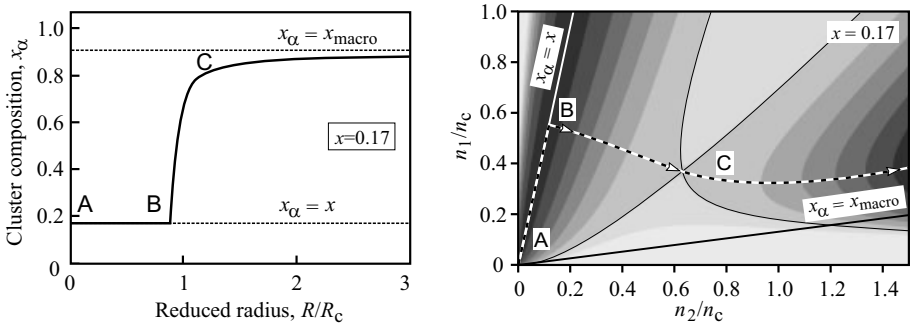

Figure 3.5: Illustration of the evolution of the cluster in the space of cluster parameters for segregation processes in regular solutions (for the details see [58–60])

3.7.2 Effective Diffusion Coefficients

The variation of the number of particles of the i-th component in the cluster is determined via (cf. Eq. (3.57))

$$\frac{\mathrm{d}n_i}{\mathrm{d}t} = -4\pi R^2 j_i = -w^{(+)}_{n_i,n_i+1}\left[\frac{1}{k_\mathrm{B}T}\frac{\partial \Delta G(n_1, n_2, \ldots, n_k)}{\partial n_i}\right] . \tag{3.72}$$

Moreover, the relations

$$n_i = n n_b x_{i\alpha} , \quad V_\alpha = n\omega_\alpha , \quad \omega_\alpha = \sum_{i=1}^{k} n_b x_{i\alpha}\omega_{i\alpha} \tag{3.73}$$

hold. Here, $\omega_{i\alpha}$ is the volume per particle of the ith component in the cluster, n is the total number of structural units of the newly evolving phase in the cluster of volume, V_α, or radius, R, and n_b is the number of particles in a structural unit of the newly evolving macrophase in equilibrium with the ambient phase, and ω_α is the volume of a structural unit of the newly evolving phase in a cluster of radius, R, or volume, V_α. For the case that the clusters can be considered as multiples of a basic unit of the newly evolving phase, n_b can be identified with the number of particles in such a unit. If the clusters change their composition with cluster sizes, n_b loses its definite physical meaning and will be determined such as to allow an expression of the basic kinetic equations in the most simple form. In any of the considered cases, it is a constant parameter.

Further, based on Eq. (3.73) (we take the derivative of the identity $n_i = n n_b x_{i\alpha}$ with respect to time) and taking into account that the composition of the clusters depends uniquely on the cluster radius, R, or on the particle number, n, in the cluster we may write

$$\frac{\mathrm{d}n}{\mathrm{d}t} = -4\pi R^2\left(\frac{j_i}{\nu_{i\alpha}}\right) , \quad \nu_{i\alpha} = n_b\left(x_{i\alpha} + n\frac{\mathrm{d}x_{i\alpha}}{\mathrm{d}n}\right) . \tag{3.74}$$

Since the left-hand side of the first of Eq. (3.74) does not depend on the particular component considered, the right-hand side must have the same value for each of the components. This way, we get

$$\frac{j_i}{\nu_{i\alpha}} = \frac{j_k}{\nu_{k\alpha}} \quad \text{for} \quad i = 1, 2, \ldots, k-1 . \tag{3.75}$$

As it is evident from the derivation, we assume here that the different components may move, in principle, independently. Nevertheless, the motion is coupled by the requirement that the composition of the clusters is a well-defined function of its size.

Equation (3.74) allows us to express the change in the number of ambient phase units, n, via the fluxes of any of the components in the system. Now, as the next step, the terms $(\partial \Delta G/\partial n_i)$ in Eq. (3.72) will be replaced by the change of the characteristic thermodynamic potential $G(n+1) - G(n)$, if the cluster size is increased from n to $(n+1)$. Instead of $G(n)$ and $G(n+1)$, we will use here the differences $\Delta G(n) = G(n) - G_\mathrm{hom}$ between the respective heterogeneous and homogeneous initial states. This procedure will be performed here for the case where pressure and temperature are kept constant. As can be checked easily, the

derivation can be repeated in a similar form for any other boundary conditions with identical results.

The change of the thermodynamic potential in such a process can be written as

$$G(n+1) - G(n) = \frac{\mathrm{d}\Delta G(n)}{\mathrm{d}n}\Delta n = \sum_{i=1}^{k}\left(\frac{\partial \Delta G(n_1, n_2, \ldots, n_k)}{\partial n_i}\right)\Delta n_i \ . \tag{3.76}$$

Here, the values of Δn_i cannot be chosen arbitrarily, but are uniquely determined via Δn as

$$\Delta n_i = \nu_{i\alpha}\,\Delta n \ . \tag{3.77}$$

With the condition $\Delta n = 1$ and Eq. (3.77), we arrive at

$$\frac{\mathrm{d}\Delta G(n)}{\mathrm{d}n} = \sum_{i=1}^{k}\left(\frac{\partial \Delta G(n_1, n_2, \ldots), n_k}{\partial n_i}\right)\nu_{i\alpha} \ . \tag{3.78}$$

Finally, Eq. (3.72) yields

$$\frac{4\pi R^2}{w^{(+)}_{n_i,n_i+1}} j_i = \frac{1}{k_\mathrm{B}T}\frac{\partial \Delta G(n_1, n_2, \ldots, n_k)}{\partial n_i} \ . \tag{3.79}$$

Multiplying both sides of Eq. (3.79) with $\nu_{i\alpha}$ and taking the sum over all components, we get from Eqs. (3.74), (3.75), and (3.78)

$$4\pi R^2\left(\frac{j_i}{\nu_{i\alpha}}\right)\sum_{i=1}^{k}\frac{\nu_{i\alpha}^2}{w^{(+)}_{n_i,n_i+1}} = \frac{1}{k_\mathrm{B}T}\frac{\mathrm{d}\Delta G(n)}{\mathrm{d}n} \tag{3.80}$$

and

$$\frac{\mathrm{d}n}{\mathrm{d}t} = -\frac{1}{\sum_{i=1}^{k}\left(\dfrac{\nu_{i\alpha}^2}{w^{(+)}_{n_i,n_i+1}}\right)}\frac{1}{k_\mathrm{B}T}\frac{\mathrm{d}\Delta G(n)}{\mathrm{d}n} \ . \tag{3.81}$$

A comparison with Eq. (3.36) shows that the growth rates for the clusters can be written, again, in one-dimensional form as

$$\frac{\mathrm{d}n}{\mathrm{d}t} = -w^{(+)}_{n,n+1}\left\{\frac{1}{k_\mathrm{B}T}\left(\frac{\mathrm{d}\Delta G\,(n)}{\mathrm{d}n}\right)\right\} \tag{3.82}$$

with

$$\boxed{w^{(+)}_{n,n+1} = \frac{1}{\sum_{i=1}^{k}\left(\dfrac{\nu_{i\alpha}^2}{w^{(+)}_{n_i,n_i+1}}\right)} \ .} \tag{3.83}$$

Similarly, we can also express the change in the volume of a cluster of the new phase consisting of n ambient phase units. The change in the volume of a cluster of the new phase can be written generally as

$$\frac{\mathrm{d}V_\alpha}{\mathrm{d}t} = -4\pi R^2 \sum_{i=1}^{k} \omega_{i\alpha} j_i \ . \tag{3.84}$$

From Eq. (3.72), we get

$$\frac{\mathrm{d}V_\alpha}{\mathrm{d}t} = \sum_{i=1}^{k} \omega_{i\alpha} \frac{\mathrm{d}n_i}{\mathrm{d}t} \ . \tag{3.85}$$

Equation (3.73) yields further

$$\frac{\mathrm{d}n_i}{\mathrm{d}t} = \nu_{i\alpha} \frac{\mathrm{d}n}{\mathrm{d}t} \tag{3.86}$$

resulting in

$$\frac{\mathrm{d}V_\alpha}{\mathrm{d}t} = \frac{\mathrm{d}n}{\mathrm{d}t} \left\{ \sum_{i=1}^{k} \omega_{i\alpha} \nu_{i\alpha} \right\} \ . \tag{3.87}$$

Following Refs. [36, 37], one can now obtain expressions for the rates of growth of the aggregates of the new phase or the kinetic coefficients, $w^{(+)}_{n_i,n_i+1}$, for the different mechanisms of cluster growth of interest. Taking into account that D_i^*/a_β^2 is the frequency with which a particle of the ith component hits the interface of a cluster of radius R and $4\pi R^2 a_\beta c_{i\beta}^{(\mathrm{s})}$ is the number of particles of the considered component capable of reaching the interface in one step of motion, we obtain

$$w^{(+)}_{n_i,n_i+1} = \frac{D_i^*}{a_\beta^2} \left(4\pi R^2 c_{i\beta}^{(\mathrm{s})} \right) \ . \tag{3.88}$$

Here D_i^* are the partial diffusion coefficients of the different components in the ambient solution near the interface while a_β is a characteristic length scale of the ambient phase defined via

$$\omega_\beta = \sum_{i=1}^{k} \omega_{i\beta} x_{i\beta} \ , \quad a_\beta = \left(\frac{3\omega_\beta}{4\pi} \right)^{1/3} \ . \tag{3.89}$$

The parameters $\omega_{i\beta}$ describe the characteristic volumes of the different components in the ambient phase. They are connected with the respective size parameters, $a_{i\beta}$, via

$$\omega_{i\beta} = \frac{4\pi}{3} a_{i\beta}^3 \ . \tag{3.90}$$

Assuming steady-state conditions, the volume concentration of particles of the ith component near the interface, $c_{i\beta}^{(s)}$, can be determined by the balance of diffusional fluxes and fluxes from the ambient phase to the cluster. We get after some algebraic calculations

$$c_{i\beta}^{(s)} = c_{i\beta} \left\{ \frac{1}{1 + \left[\left(\frac{D_i^*}{D_i} \right) \left(\frac{R}{a_\beta} \right) \right]} \right\} . \tag{3.91}$$

Here $c_{i\beta}$ is the average volume concentration of the respective component in the ambient phase. D_i are the partial diffusion coefficients of the respective components in the bulk. The diffusion coefficients D_i^* and D_i are connected by the relations $D_i^* = D_i \alpha_i$, where α_i obeys the inequality $\alpha_i \leq 1$. With Eq. (3.73) and $a_\alpha = (3\omega_\alpha/4\pi)^{1/3}$ or $R = a_\alpha n^{1/3}$, respectively, we can express the coefficients $w_{n_i,n_i+1}^{(+)}$ in the form (see also [13])

$$w_{n_i,n_i+1}^{(+)} = 4\pi D_i^* c_{i\beta} a_\alpha n^{1/3} \left\{ \frac{\left(\frac{a_\alpha}{a_\beta} \right) n^{1/3}}{1 + \left[\left(\frac{D_i^*}{D_i} \right) \left(\frac{a_\alpha}{a_\beta} \right) n^{1/3} \right]} \right\} . \tag{3.92}$$

Finally, the volume concentration of the ith component in the ambient phase, $c_{i\beta}$, can be expressed as

$$c_{i\beta} = \frac{n_{i\beta}}{V} = c_\beta x_{i\beta} , \quad c_\beta = \frac{n_\beta}{V} , \quad x_{i\beta} = \frac{n_{i\beta}}{n_\beta} , \quad n_\beta = \sum_{j=1}^{k} n_{j\beta} . \tag{3.93}$$

In the general form, the expression for $w_{n,n+1}^{(+)}$ is given then via

$$w_{n,n+1}^{(+)} = \frac{4\pi c_\beta a_\alpha^2 n^{2/3}}{a_\beta} \left\{ \sum_{i=1}^{k} \frac{\nu_{i\alpha}^2 \left[1 + \left(\frac{D_i^*}{D_i} \right) \left(\frac{a_\alpha}{a_\beta} \right) n^{1/3} \right]}{D_i^* x_{i\beta}} \right\}^{-1} . \tag{3.94}$$

Equation (3.94) represents the most general expression for the determination of the quantity $w_{n,n+1}^{(+)}$. It is a rather nontrivial function of the kinetic and thermodynamic parameters of the different components in the multicomponent solution considered.

As already mentioned, in the case of formation of a new phase with a given stoichiometric composition, the value of the total number of particles, n_b, in a basic unit of the new phase is well-defined. For the more general case considered here the composition of the cluster changes with cluster size, such well-defined units does not exist. By this reason, we will set n_b equal to one (cf. Eq. (3.73)). With this definition, n gets the meaning of the total number of particles in a cluster. We have then

$$w_{n,n+1}^{(+)} = \frac{4\pi c_\beta a_\alpha^2 n^{2/3}}{a_\beta \sum_{i=1}^{k} \left\{ \frac{\widetilde{\nu}_{i\alpha}^2 \left[1 + \left(\frac{D_i^*}{D_i} \right) \left(\frac{a_\alpha}{a_\beta} \right) n^{1/3} \right]}{D_i^* x_{i\beta}} \right\}} \tag{3.95}$$

with (cf. Eq. (3.74))

$$\widetilde{\nu}_{i\alpha} = \left(x_{i\alpha} + n \frac{\mathrm{d}x_{i\alpha}}{\mathrm{d}n} \right) \tag{3.96}$$

or, equivalently,

$$w_{n,n+1}^{(+)} = \frac{4\pi\, D_{\mathrm{eff}} c_\beta a_\alpha^2 n^{2/3}}{a_\beta} \,, \tag{3.97}$$

$$\frac{1}{D_{\mathrm{eff}}} = \sum_{i=1}^{k} \left\{ \frac{\widetilde{\nu}_{i\alpha}^2 \left[1 + \left(\frac{D_i^*}{D_i} \right) \left(\frac{a_\alpha}{a_\beta} \right) n^{1/3} \right]}{D_i^* x_{i\beta}} \right\} \,. \tag{3.98}$$

For the case of kinetic limited growth (if the condition $1 \gg (D_i^*/D_i) n^{1/3}$ is fulfilled for any of the components), we have

$$w_{n,n+1}^{(+)} = \frac{4\pi\, D_{\mathrm{eff}}^* c_\beta a_\alpha^2 n^{2/3}}{a_\beta} \,, \quad \frac{1}{D_{\mathrm{eff}}^*} = \sum_{i=1}^{k} \frac{\widetilde{\nu}_{i\alpha}^2}{x_{i\beta} \alpha_i D_i} \,. \tag{3.99}$$

For diffusion limited growth of the clusters (if the condition $1 \ll (D_i^*/D_i) n^{1/3}$ is fulfilled for any of the components), we get similarly

$$w_{n,n+1}^{(+)} = 4\pi\, c_\beta a_\alpha D_{\mathrm{eff}}^{**} n^{1/3} \,, \quad \frac{1}{D_{\mathrm{eff}}^{**}} = \sum_{i=1}^{k} \frac{\widetilde{\nu}_{i\alpha}^2}{x_{i\beta} D_i} \,. \tag{3.100}$$

With $\omega_\beta = V/n_\beta = 1/c_\beta$, we can always make the replacement $4\pi c_\beta = 3/a_\beta^3$ in above equations.

3.7.3 Evolution of the Cluster Size Distribution Functions

According to the theoretical developments discussed, we may write down the following expressions for the determination of the evolution of the cluster size distribution with time:

$$\begin{aligned} \frac{\partial f(n,t)}{\partial t} &= w_{n-1,n}^{(+)} \left\{ f(n-1,t) - f(n,t) \exp\left[\frac{\Delta G(n) - \Delta G(n-1)}{k_{\mathrm{B}} T} \right] \right\} \\ &\quad + w_{n,n+1}^{(+)} \left\{ -f(n,t) + f(n+1,t) \exp\left[\frac{\Delta G(n+1) - \Delta G(n)}{k_{\mathrm{B}} T} \right] \right\} \,. \end{aligned} \tag{3.101}$$

For the distribution function $f(n=1,t)$ at $n=1$, we employ the relation

$$f(n=1,t) = c_\beta \prod_{j=1}^{k} x_{j\beta}^{x_{j\alpha}} \,, \quad c_\beta = \frac{3}{4\pi a_\beta^3} \,. \tag{3.102}$$

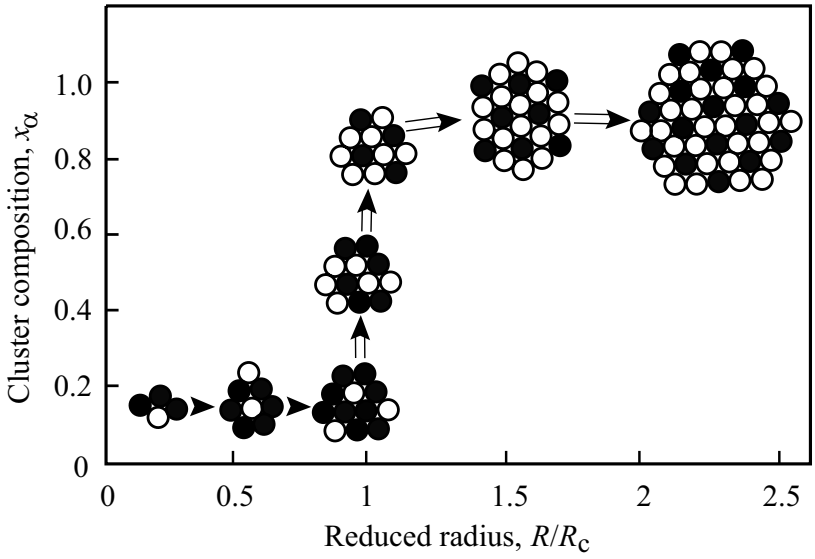

Figure 3.6: Illustration of the cluster evolution if the newly developed approach to nucleation-growth processes is utilized as outlined in detail in Refs. [58–60] (cf. also Chapters 11 and 12)

Here c_β is the total volume concentration of the particles of the different components in the ambient phase, $x_{j\beta}$ the molar fraction of the different components in the ambient phase, and $x_{j\alpha}$ the composition of the cluster phase in the limit $R \to 0$ (or $n \to 1$).

The effective values of the coefficients of aggregation, $w^{(+)}_{n,n+1}$, are given by Eqs. (3.97) and (3.98). Assuming, in addition, $D_i = D_i^*$, we get

$$w^{(+)}_{n,n+1} = \frac{4\pi D^{**} c_\beta a_\alpha^2}{a_\beta} \left\{ \frac{n^{2/3}}{1 + \left(\frac{a_\alpha}{a_\beta}\right) n^{1/3}} \right\} . \tag{3.103}$$

This expression is reduced to previously discussed cases under the well-defined limiting conditions.

According to the analysis of segregation processes in regular solutions illustrated partly in Fig. 3.5 (cf. [58–60]), initially the preferred cluster composition is equal to the composition of the ambient phase. In such cases, however, the cluster cannot be distinguished from the ambient phase. Thus, the real cluster evolution starts only when the parameters start to deviate from the respective values they have in the ambient phase. As evident from the figure, such processes start at cluster sizes near the critical one. In the further evolution the composition of the cluster changes then dramatically until values near to the respective macroscopic parameters are reached. This situation is illustrated in Fig. 3.6. It deviates dramatically from the classical picture of nucleation and cluster growth shown in Fig. 3.1.

3.8 Conclusions

In the discussion of our results we would like to stress two points. First, we would like to underline once more that a regular method has been developed allowing to determine the emission coefficients once the coefficients of aggregation are known. The basic equation (3.44) can be applied widely independent of the application and the boundary conditions considered. The method allows to eliminate such artificial constructs like constraint equilibrium distributions from the theory as well as the incorrect application of the principle of detailed balancing to nonequilibrium states.

Second, as an intermediate step in our analysis, we introduced an idealized model, as we called it, *virtual* states. According to the definition, *virtual* states are those states for which a dynamic equilibrium between cluster and ambient phase is established. This is the only property employed in addition to the widely accepted assumption of existence of a local equilibrium in the ambient phase in the vicinity of the clusters of the new phase. In this respect our approach is similar but more general as compared with the application of Kelvin's (or the Gibbs–Thomson) equation. In applying Kelvin's equation the same question is posed as in our analysis, i.e., what should be the state of the system be to attain dynamic equilibrium for a cluster of a given size. Starting with our basic equation (3.30) (e.g., in application to one-component systems)

$$\frac{w^{(+)}_{n,n+1}}{w^{(-)}_{n+1,n}} = \exp\left(\frac{\mu_{\mathrm{v}} - \mu_{\mathrm{d}}\,(n+1)}{k_{\mathrm{B}}T}\right)\,, \tag{3.104}$$

applying the perfect gas law

$$\mu_{\mathrm{v}}(p,T) = \mu^{(*)} + k_{\mathrm{B}}T\ln\left(\frac{p}{p^{(*)}}\right)\,, \tag{3.105}$$

and the equilibrium conditions for a drop of a given size in the gas

$$\mu_{\mathrm{d}}(n+1) = \mu_{\mathrm{v}}[p_v(n+1),T] = \mu^{(*)} + k_{\mathrm{B}}T\ln\left[\frac{p_v(n+1)}{p^{(*)}}\right]\,, \tag{3.106}$$

we arrive at

$$w^{(-)}_{n+1,n} = w^{(+)}_{n,n+1}(p)\left[\frac{p_v(n+1)}{p}\right] = w^{(+)}_{n,n+1}[p_v(n+1)]\,. \tag{3.107}$$

Here $p^{(*)}$ is the pressure in some refence state and $p_v(n+1)$ is the pressure in the vapor if a drop of size $(n+1)$ exists in dynamic equilibrium in the vapor phase. Similarly, condensation in multicomponent perfect gases or segregation in multicomponent perfect solutions may be discussed. Here approaches based on Kelvin's equation and on our method lead to equivalent results. The latter one is, however, more straightforward and also applicable directly to phase formation in nonideal vapors, nonideal solutions and beyond.

Finally, having developed a theoretical foundation of the expressions for the coefficients of emission in terms of a mesoscopic approach to nucleation-growth processes by general

thermodynamic methods, we have not even touched the problem of determination of the appropriate expressions for the chemical potential of a particle in a cluster of given size or, in other words, the work of formation of a cluster of given size. Such a step in the analysis is required to apply the theory to particular problems. Here a detailed thermodynamic analysis for each specific kind of phase transformation is further necessary. In the present contribution, we cannot and will not make the analysis more explicite but refer to the overviews given in Refs. [58–60] and in Chapters 11 and 12.

Acknowledgements

The authors would like to thank the Bundesministerium für Bildung, Wissenschaft, Forschung und Technologie (BMBF), and the Deutsche Forschungsgemeinschaft (DFG), Germany, for financial support.

References

[1] M. Kulmala and P.E. Wagner (Eds.), Nucleation and atmospheric aerosols 1996, in *Proceedings of the Fourteenth International Conference on Nucleation and Atmospheric Aerosols*, Helsinki, August, 1996, (Pergamon, London, 1996), pp. 26–30.

[2] B. Hale and M. Kulmala (Eds.), Nucleation and atmospheric aerosols 2000, in *Proceedings of the Fifteenth International Conference on Nucleation and Atmospheric Aerosols*, Rolla, Missouri, USA, August 6–11, 2000; AIP Conference Proceedings, Melville, New York, 2000, vol. 534.

[3] B.M. Smirnov, Usp. Fiz. Nauk **164**, 665 (1994) (in Russian).

[4] J.W.P. Schmelzer, D. Labudde, and G. Röpke, Physica A **254**, 389 (1998).

[5] V.P. Skripov, *Metastable Liquids* (Nauka, Moscow, 1972 (in Russian); Wiley, New York, 1974 (in English)).

[6] S.D. Lubetkin, *The Fundamentals of Bubble Evolution*, Chemical Society Reviews **243**, 1 (1995).

[7] J.W. Christian, *The Theory of Transformations in Metals and Alloys* (Oxford University Press, Oxford, 1975), 2nd ed.

[8] W.C. Johnson, J.M. Howe, D.E. Laughlin, and W.A. Soffa, (Eds.), Solid to solid phase transformations, in *Proceedings of the International Conference on Solid to Solid Phase Transformations in Inorganic Materials PTM94*, Nemacolin Woodlands, Farmington, July 1994.

[9] M. Koiwa, K. Otsuka, and T. Miyazaki (Eds.), Solid to solid phase transformations, in *Proceedings of the International Conference on Solid to Solid Phase Transformations in Inorganic Materials PTM99*, Kyoto, Japan, May 24–28, 1999 (The Japan Institute of Metals, 1999).

[10] A.G. Khachaturian, *Theory of Phase Transitions and Structure of Solid Solutions* (Nauka, Moscow, 1979) (in Russian).

[11] L.P. Csernai and J.L. Kapusta, Phys. Rep. **131**, 223 (1986).

[12] J.W.P. Schmelzer, G. Röpke, and F.-P. Ludwig, Phys. Rev C **1917**, 55 (1997).

[13] J.W.P. Schmelzer, G. Röpke, J. Schmelzer (Jr). , and V.V. Slezov, *Shapes of Cluster Size Distributions Evolving in Nucleation – Growth Processes*. In [14], pp. 82–129.

[14] J.W.P. Schmelzer, G. Röpke, and V.B. Priezzhev, *Nucleation Theory and Applications* (Joint Institute for Nuclear Research Publishing House, Dubna, Russia, 1999).

[15] B. Kämpfer, B. Lukasc, and G. Paal, *Cosmic Phase Transitions* (Teubner-Texte zur Physik, Bd. 29, Teubner, Leipzig, 1994).

[16] J.S. Langer, Ann. Phys. (NY) **41**, 108 (1967); **54**, 258 (1969).

[17] A.C. Zettlemoyer (Ed.), *Nucleation* (Dekker, New York, 1969); *Nucleation Phenomena*, Adv. Colloid Interface Sci. **7** (1977).

[18] J.D. Gunton, M. San Miguel, and P.S. Sahni, The dynamics of first-order phase transitions, in *Phase Transitions and Critical Phenomena*, edited by C. Domb and J.L. Lebowitz (Academic Press, London, New York, 1983), vol. 8.

[19] K. Binder and D. Stauffer, Adv. Phys. **25**, 343 (1976).

[20] K. Binder, Rep. Progr. Phys. **50**, 783 (1987).

[21] M. Volmer, *Kinetik der Phasenbildung* (Th. Steinkopff, Dresden, 1939).

[22] Ya.I. Frenkel, *Kinetic Theory of Liquids* (Oxford University Press, Oxford, 1946).

[23] I. Gutzow and J.W.P. Schmelzer, *The Vitreous State: Thermodynamics, Structure, Rheology, and Crystallization* (Springer, Berlin, 1995).

[24] G. Wilemski, J. Chem. Phys. **103**, 1119 (1995).

[25] G. Wilemski and B.E. Wyslouzil, J. Chem. Phys. **103**, 1127 (1995); **103**, 1137 (1995); **105**, 1090 (1996).

[26] J.W.P. Schmelzer, Dynamical approaches to cluster formation and nuclear multifragmentation, in *Proceedings of the 4th Catania Relativistic Ion Studies Conference CRIS 2002*, Catania, 10–14 July, 2002, AIP Conference Proceedings **644**, pp. 178–187, Melville, New York, 2002.

[27] E. Ruckenstein and B. Nowakowski, J. Colloid Interface Sci. **137**, 583 (1990).

[28] E. Ruckenstein and B. Nowakowski, J. Chem. Phys. **94**, 1397 (1991).

[29] J.L. Katz and H. Wiedersich, J. Colloid Interface Sci. **61**, 351 (1977).

[30] J.L. Katz and F. Spaepen, Phil. Mag. B **37**, 137 (1978).

[31] J.L. Katz and M.D. Donohue, Adv. Chem. Phys. **40**, 137 (1979).

[32] J.L. Katz, Pure Appl. Chem. **64**, 1661 (1992).

[33] J.L. Katz, J.A. Fisk, and M.M. Rudek, *Nucleation of Single-Component Supersaturated Vapors*, in [1] p. 1.

[34] R. Becker and W. Döring, Ann. Phys. **24**, 719 (1935).

[35] D.T. Wu, *Nucleation Theory*, in Solid State Physics: Advances in Research and Applications **50**, 37 (1997).

[36] V.V Slezov and J. Schmelzer, J. Phys. Chem. Solids **55**, 243 (1994).

[37] V.V. Slezov, Ya. Yu. Tkatch, and J. Schmelzer, J. Mater. Sci. **32**, 3739 (1997).

[38] V.V. Slezov and J. Schmelzer, J. Phys. Chem. Solids **59**, 1507 (1998).

[39] V.V. Slezov, J.W.P. Schmelzer, and Ya. Yu. Tkatch, J. Chem. Phys. **105**, 8340 (1996).

[40] L.D. Landau and I.M. Lifshitz, *Statistical Physics* (Nauka, Moscow, 1964).

[41] J.W.P. Schmelzer, *Comments on Curvature Dependent Surface Tension and Nucleation Theory*. In [14], pp. 268–289.

[42] M.E. Fisher, Physics **3**, 255 (1967).

[43] C.S. Kiang, Phys. Rev. Lett. **24**, 47 (1970).

[44] K. Binder, J. Physique (France) **41**, C4-51 (1980).

[45] H. Furukawa and K. Binder, Phys. Rev A **26**, 556 (1982).

[46] D. Stauffer, *Introduction into Percolation Theory* (Taylor and Francis, London, Philadelphia, 1985).

[47] J. Desbois, R. Boisgard, C. Ngo, and J. Nemeth, Z. Phys. A **328**, 101 (1987).

[48] J. Pan and S. Das Gupta, Phys. Lett. B **344**, 30 (1995); Phys. Rev. C **51**, 1384 (1995).

[49] V.V. Slezov, Phys. Rep. **288**, 389 (1998).

[50] V.V. Slezov and J.W.P. Schmelzer, *Kinetics of Nucleation-Growth Processes: The First Stages*, In [14], pp. 6–81.

[51] V.V. Slezov and J.W.P. Schmelzer, Phys. Rev. E **65**, 031506 (2002).

[52] R. Haase, *Thermodynamik der Irreversiblen Processe* (D. Steinkopf Publishers, Darmstadt, 1963).

[53] J.W. Gibbs, On the equilibrium of heterogeneous substances, Collected Works vol.1, *Thermodynamics* (Academic Press, New York, London, Toronto, 1928).

[54] J. Schmelzer, *Thermodynamics of Finite Systems and the Kinetics of First-Order Phase Transitions*, D.Sc. thesis (Habilarbeit), Rostock, 1985.

[55] J. Schmelzer and H. Ulbricht, J. Colloid Interface Sci. **117**, 325 (1987); **128**, 104 (1989).

[56] H. Reiss, J. Chem. Phys. **18**, 840 (1950).

[57] J. Schmelzer (Jr.), U. Lembke, and R. Kranold, J. Chem. Phys. **113**, 1268 (2000).

[58] J.W.P. Schmelzer, Phys. Chem. Glasses **45**(2), 116 (2004).

[59] J.W.P. Schmelzer, A.R. Gokhman, and V.M. Fokin, J. Colloid Interface Sci. **272**, 109 (2004).

[60] J.W.P. Schmelzer, A.S. Abyzov, and J. Möller, J. Chem. Phys. **121**, 6900 (2004).

4 Nucleation and Crystallization Kinetics in Silicate Glasses: Theory and Experiment

Vladimir M. Fokin, Nikolay S. Yuritsyn, and Edgar D. Zanotto

All truths are easy to understand once they are discovered;
the point is to discover them.
Galileo Galilei

Experimental data on internal homogeneous crystal nucleation in silicate glasses obtained in the last four decades are analyzed in detail in the framework of the classical nucleation theory (CNT). Despite the fact that reasonable qualitative interpretations of the temperature and time dependences of nucleation rates are given by CNT, it meets with serious problems in their quantitative description. Different reasons for this failure are tested and discussed. The main conclusion is that, in contrast to Gibbs' description of heterogeneous systems, the thermodynamic properties of critical nuclei which, to a large extent, govern nucleation kinetics, generally differ from those of the corresponding macrophase. A number of evidences based on the analysis of both crystal nucleation and growth data are given for a decreased thermodynamic driving force for crystallization and critical nuclei/liquid interfacial energy, as compared with the respective properties of the macro-phase. Special attention is devoted to the widespread and practically important type of heterogeneous nucleation – nucleation on glass surfaces. A comparative analysis of available data on surface and bulk nucleation rate data is performed.

4.1 Introduction

Glasses can be defined as noncrystalline solids that, in the course of their preparation, undergo a process commonly denoted as *glass transition*. One of the most important (but not the only) ways of vitrification consists in supercooling a liquid suppressing crystallization. When a liquid is cooled down with sufficiently high rates, crystallization may occur to a very limited degree or be completely absent down to temperatures corresponding to very high viscosities in the range $\eta \geq 10^{13}$–10^{12} Pa · s $\cong \eta(T_g)$, where T_g is defined as the glass transition temperature. Below this temperature, the viscosity is so high that large-scale atomic rearrangements in the system are no longer possible within the time-scale of the experiment, and the structure freezes-in, i.e., the structural rearrangements required to retain the liquid in the appropriate metastable equilibrium state cannot follow any more the changes of temperature. This process of freezing-in of the structure of an undercooled liquid is commonly denoted as glass transition and, as a result, the system is transformed into a glass. Typical glass-forming liquids, such as silicate melts, are commonly characterized by: (i) relatively high viscosities ($\eta > 100$ Pa · s) at the melting point (or *liquidus*), and (ii) a steep increase of the viscosity with decreasing temperature. These properties favor the process of transformation of a liquid into a glass. The above mechanism discussed leads to the conclusion that the glass structure is very similar to that of the parent (undercooled) liquid at temperatures near T_g.

Nucleation Theory and Applications. edited by J. W. P. Schmelzer

ISBN: 3-527-40469-4

Glass is thermodynamically unstable with respect to the undercooled metastable liquid. This way, processes of relaxation of the glass structure may occur aimed to reach a metastable liquid state for the given temperature and then, eventually, the crystalline state. Nevertheless, glasses can exist at room temperatures for extremely long periods of time because any structural rearrangements, including those required for crystal nucleation and growth, are inhibited by its high viscosity. However, when a glass is heated for sufficiently large time intervals to temperatures within or above the glass transition range, devitrification readily starts, as a rule, from the surface and sometimes via bulk nucleation.

Nucleation in glass-forming melts, or the process of formation of the precursors of the crystalline phases, may occur by different mechanisms. Commonly one distinguishes homogeneous and heterogeneous nucleation. Homogeneous nucleation is a stochastic process occurring with the same probability in any given volume (or surface) element. Alternatively, nucleation occurring on preferable nucleation sites, such as preexisting interfaces, solid impurities, previously nucleated phases, and surface defects is denoted as heterogeneous nucleation. Depending on the position where nucleation takes places, volume (bulk) and surface crystallization can be distinguished.

Glass-forming melts are highly interesting objects for model studies of nucleation phenomena. The high viscosities of glass-forming melts result in relatively low (measurable) rates of crystallization. This property sometimes permits detailed studies of nucleation kinetics. In addition, the rapid increase of viscosity with decreasing temperature makes it possible to "freeze-in" different states of the crystallization process by quenching previously heat-treated specimens to room temperature. Hence, as it was figuratively said in Ref. [1], "glasses did and may serve as the 'Drosophila' of nucleation theory in order to test different approaches." Moreover, silicate glass is one of the oldest materials produced by mankind, having its origin as early as 4000 years BC in ancient Mesopotamia [2], but they retain their technological importance up to the present date.

As is evident from the above discussion, crystallization and glass formation are competitive processes. This way, in order to avoid uncontrolled crystallization of glassy articles one needs to know the main factors governing nucleation and crystal growth. On the other hand, controlled nucleation and crystallization of glasses underlay the production of glass–ceramics invented in the mid 50s [3]. Glass–ceramics are widely used today in both domestic and high-technology applications. By both reasons, the investigation of glass crystallization kinetics is of great interest from both practical and theoretical points of view. Since, in many respects, the nucleation stage determines the pathways of overall crystallization, in this chapter we will focus our main attention on nucleation with particular emphasis on the analysis of relevant experimental results obtained with silicate glasses.

The present chapter is organized as follows: In Sect. 4.2 the basic equations of the classical nucleation theory (CNT) are given, which are employed then for nucleation data analysis. Section 4.3 presents the main methods which may be employed to experimentally determine nucleation rates. Section 4.4 is devoted to the experimental findings concerning transient and steady-state crystal nucleation in glasses. In particular, evidence for a strong correlation between nucleation rates and reduced glass transition temperature is given. An analysis of problems arising in the application of CNT to experimentally observed nucleation rate data is performed in Sect. 4.5. Section 4.6 deals with one of the forms of heterogeneous nucleation, nucleation on glass surfaces, which is especially important for practical applications. In this

section, the relatively few measurements of surface nucleation rates are presented, and the origin of preferential surface nucleation is discussed. The chapter is completed by some concluding remarks.

4.2 Basic Assumptions and Equations of Classical Nucleation Theory (CNT)

4.2.1 Historical Notes

In its original form, the CNT is based on the thermodynamic description of heterogeneous systems as developed by Gibbs [4]. Following Gibbs [4], the real inhomogeneous system is replaced by a model system consisting of two homogeneous phases divided by a mathematical surface of zero thickness. The properties of the respective macroscopic phases coexisting in equilibrium are chosen as reference states for the description of the two different homogeneous phases. The free energy of the system – consisting of a cluster of the newly evolving phase in the ambient phase – is expressed then as the sum of the bulk contributions of the nucleus and the ambient phase. These bulk terms are supplemented by interfacial contributions, the main one is given by the product of the interfacial area and specific surface energy.

Applying the theory to cluster formation, these surface terms result initially in an increase of the characteristic thermodynamic potential and the existence of a critical cluster size. Only clusters with sizes larger than the critical size are capable to grow up in a deterministic way to macroscopic sizes. The change of the characteristic thermodynamic potential resulting from the formation of a cluster of critical size is commonly denoted as work of critical cluster formation. This quantity reflects basically the thermodynamic or energetic aspects of nucleation.

In addition to the thermodynamic aspects of nucleation, the dynamics of cluster formation and growth has to be incorporated appropriately into the theory. Here different approaches are employed in dependence on the particular application analyzed. The application of CNT to condensed systems – which is of particular importance in the present analysis – originates from the work of Kaischew and Stranski [5]. These authors employed the approach, developed by Volmer and Weber [6] for vapor condensation, to crystal formation in condensed systems. Further, advances in CNT are connected with the work of Becker and Döring [7], Volmer [8], Frenkel [9], Turnbull and Fischer [10], Reiss [11], and others. Photographs of some of these pioneers of the nucleation theory are shown in Fig. 4.1.

According to CNT, the description of homogeneous and heterogeneous nucleation can be performed basically by the same methods. We will first present the results for homogeneous nucleation and discuss afterward the modifications required to account for the effect of impurities, etc. that lead to heterogeneous nucleation.

4.2.2 Homogeneous Nucleation

Homogeneous nucleation supposes the same probability of critical nucleus formation in any given volume or surface element of the system under study. According to CNT (see, e.g.,

Figure 4.1: From left top to right bottom: J.W. Gibbs, G. Tammann, M. Volmer, R. Kaischew, J. Frenkel, and D. Turnbull

Ref. [12]), the steady-state homogeneous volume nucleation rate can be written as

$$I_{\mathrm{st}} = I_0 \exp\left[-\frac{W_* + \Delta G_{\mathrm{D}}}{k_{\mathrm{B}} T}\right], \quad I_0 = 2N_1 \frac{k_{\mathrm{B}} T}{h}\left(\frac{a^2 \sigma_{\mathrm{cm}}}{k_{\mathrm{B}} T}\right)^{1/2}. \tag{4.1}$$

It determines the number of supercritical clusters formed per unit time in a unit volume of the system. The preexponential term I_0 in Eq. (4.1) depends weakly only on temperature (if compared to the exponential function) and varies between 10^{41} and 10^{43} m^{-3} s^{-1} for different condensed systems [14]. In Eq. (4.1), k_{B} and h are the Boltzmann and Planck constants, respectively; $N_1 \sim 1/a^3$ is the number of structural (formula) units, with a mean size a, per unit volume of melt; σ_{cm} is the specific free energy of the critical nucleus–melt interface; ΔG_{D} is the activation free energy for transfer of a "structural unit" from the melt to a nucleus (kinetic barrier). Alternatively, for glass-forming liquids, the kinetic factors affecting the process of crystallite formation have been expressed, in most practical applications of the theory, via the Newtonian viscosity, i.e., ΔG_{D} is replaced by the activation free energy for viscous flow, ΔG_η. In addition, W_* is the thermodynamic barrier of nucleation, i.e., the increase in the free energy of a system due to the formation of a nucleus with critical size, r_*.

The critical nucleus size can be determined from the condition

$$\frac{\partial W}{\partial r} = 0 \,, \quad W = c_1 r^2 \sigma_{\mathrm{cm}} - c_2 r^3 \Delta G_{\mathrm{V}} \,, \tag{4.2}$$

where $\Delta G_{\mathrm{V}} = G_{\mathrm{l}} - G_{\mathrm{c}}$ is the difference between the free energies of liquid and crystal per unit volume of the crystal (i.e., the thermodynamic driving force for crystallization) and c_1 and c_2 are the shape factors. In the case of a spherical nucleus, one gets

$$r_* = \frac{2\sigma_{\mathrm{cm}}}{\Delta G_{\mathrm{V}}} \tag{4.3}$$

and

$$W_* = \frac{16\pi}{3} \frac{\sigma_{\mathrm{cm}}^3}{\Delta G_{\mathrm{V}}^2} \,. \tag{4.4}$$

The thermodynamic driving force for crystallization is given by

$$\Delta G_{\mathrm{V}} V_{\mathrm{m}} = \frac{\Delta H_{\mathrm{m}}}{T_{\mathrm{m}}} (T_{\mathrm{m}} - T) + \int_T^{T_{\mathrm{m}}} \Delta C_{\mathrm{p}} \, \mathrm{d}T' - T \int_T^{T_{\mathrm{m}}} \frac{\Delta C_{\mathrm{p}}}{T'} \, \mathrm{d}T' \,, \tag{4.5}$$

where V_{m} is the molar volume, ΔH_{m} and T_{m} are the molar heat of melting and the melting temperature of the crystal, respectively, and $\Delta C_{\mathrm{p}} = C_{\mathrm{p}}^{\mathrm{l}} - C_{\mathrm{p}}^{\mathrm{c}}$ is the difference between the molar heat capacities of liquid and crystal at constant pressure. The experimental values of ΔG_{V} are normally bounded by the approximations usually assigned to Turnbull (Eq. (4.6)) and Hoffman (Eq. (4.7)) that assume $\Delta C_{\mathrm{p}} = 0$ and $\Delta C_{\mathrm{p}} =$ constant, respectively [13]

$$\Delta G_{\mathrm{V}}(T) = \Delta H_{\mathrm{V}} \left(1 - \frac{T}{T_{\mathrm{m}}} \right) \,, \tag{4.6}$$

$$\Delta G_{\mathrm{V}}(T) = \Delta H_{\mathrm{V}} \left(1 - \frac{T}{T_{\mathrm{m}}} \right) \frac{T}{T_{\mathrm{m}}} \,, \tag{4.7}$$

where ΔH_{V} is the melting enthalpy per unit volume of the crystal. One should note, however, that Eq. (4.6) was first employed already by J.J. Thomson and M. Volmer (cf. Ref. [8])

Equation (4.1) describes the so-called steady-state nucleation. Such nucleation regime can be realized if a stationary size distribution of the newly evolving subcritical ($r < r_*$) and critical ($r = r_*$) nuclei is established in the system. The cooling rates typically used for glass formation from the melt, and the rates of heating a glass up to a given temperature T under investigation, are commonly too high to maintain a steady-state distribution of nuclei in the system. Hence, some time period is needed for reconstruction of the initial nuclei distribution toward the time independent distribution corresponding to the temperature T. During this period the nucleation rate varies and approaches a steady-state value given by Eq. (4.1).

The time required to establish steady-state nucleation in the system is commonly denoted as the time-lag in nucleation, τ. It characterizes the duration for the onset of the steady-state distribution, and hence the evolution of the nucleation rate, $I(t)$, to a steady-state value, I_{st}. In

cases when the initial concentration of critical and subcritical nuclei may be neglected, τ and $I(t)$ can be expressed by Eqs. (4.8) and (4.9), respectively [15, 16],

$$\tau = \frac{16h}{\pi} \frac{\sigma_{\mathrm{cm}}}{\Delta G_{\mathrm{V}}^2 a^4} \exp\left(\frac{\Delta G_{\mathrm{D}}}{k_{\mathrm{B}} T}\right) , \tag{4.8}$$

$$I(t) = I_{\mathrm{st}} \left[1 + 2 \sum_{m=1}^{\infty} (-1)^m \exp\left(-\frac{m^2 t}{\tau}\right)\right] . \tag{4.9}$$

Integration of Eq. (4.9) results in the following expression for the time-dependence of the number of supercritical nuclei per unit volume of the system, N_{V},

$$\frac{N_{\mathrm{V}}(t)}{I_{\mathrm{st}}\tau} = \left[\frac{t}{\tau} - \frac{\pi^2}{6} - 2 \sum_{m=1}^{\infty} \frac{(-1)^m}{m^2} \exp\left(-m^2 \frac{t}{\tau}\right)\right] . \tag{4.10}$$

For large times, this expression can be approximately written as

$$N_{\mathrm{V}}(t) = I_{\mathrm{st}} \left(t - \frac{\pi^2}{6}\tau\right) \quad \text{for} \quad t \to \infty . \tag{4.11}$$

For the experimental estimation of τ, it is convenient to use the induction period, t_{ind}, defined via Eq. (4.12), as

$$\tau = \frac{6}{\pi^2} t_{\mathrm{ind}} . \tag{4.12}$$

This induction time, t_{ind}, is easily determined as the point of intersection of the asymptote (Eq. (4.11)) with the time axis.

4.2.3 Heterogeneous Nucleation

The existence of foreign solid particles, phase boundaries, etc., may favor nucleation. This effect is mainly due to the diminished thermodynamic barrier, as compared to that of homogeneous nucleation, owing to a decrease of the effective surface energy contributions to the work of critical cluster formation. This effect is the main distinguishing feature of heterogeneous nucleation. For example, the thermodynamic barrier for nucleation for condensation on planar interfaces is given by [12]

$$W_{\mathrm{het}}^* = W_* \Phi , \quad \Phi = \tfrac{1}{2} - \tfrac{3}{4}\cos\theta + \tfrac{1}{4}\cos^3\theta . \tag{4.13}$$

Depending on the value of the wetting angle, θ, the values of the parameter Φ may vary from zero to unity. Generally, for heterogeneous nucleation we can write $W_{\mathrm{het}}^* = W_* \Phi$. The values of Φ depend hereby on the mechanism of nucleation catalysis.

In order to adapt the expression for the steady-state nucleation rate, Eq. (4.1), to the description of heterogeneous nucleation, the number of "structural" units per unit volume, N_1, which appears in the preexponential term of Eq. (4.1), must be replaced by the number, N^{S}, of "structural units" in contact with the catalyzing surface per unit volume. Hence, in the

case of heterogeneous nucleation, the following equation can be written for the steady-state nucleation rate

$$I_{\mathrm{st}}^{\mathrm{het}} \cong N^{\mathrm{S}} \frac{k_{\mathrm{B}} T}{h} \exp\left[-\frac{W_* \Phi + \Delta G_{\mathrm{D}}}{k_{\mathrm{B}} T}\right] . \tag{4.14}$$

4.3 Experimental Methods to Estimate Nucleation Rates

4.3.1 General Problems

Since, at the high undercoolings corresponding to the range of measurable (homogeneous) volume nucleation rates in glass-forming liquids, the critical nuclei are undetectable by the common experimental techniques, they have first to be developed up to a visible size to allow one to determine (e.g., using a microscope) their number density, N, as a function of time and then to estimate the nucleation rate as $I = \mathrm{d}N/\mathrm{d}t$. In order to perform such task, different methods have been developed.

4.3.2 Double-Stage ("Development") Method

If the overlapping of nucleation and growth rate curves is weak (i.e., the crystal growth rates are very low at temperatures corresponding to high nucleation rates), the observation of the nucleated crystals and the estimation of the crystal number density is a quite difficult task. For these cases, about 100 years ago, Gustav Tammann (who was studying crystallization of organic liquids) proposed the following procedure, which is now known as the Tammann or "development" method [17]. Following this method, crystals nucleated at a low temperature, T_n, are grown up to microscopic sizes at a higher temperature, $T_{\mathrm{d}} > T_n$. The development temperature T_{d} has to meet the following conditions for nucleation (I) and growth (U) rates: $I(T_n) \gg I(T_{\mathrm{d}})$ and $U(T_{\mathrm{d}}) \gg U(T_n)$. After a lapse of 70 years, Ito et al. [18] and Filipovich and Kalinina [19] independently applied Tammann's method to study the crystal nucleation kinetics in lithium disilicate glasses. Since then, this method has been widely employed for the glass crystallization studies.

In employing Tammann's method one usually assumes that the "development" process includes only the growth of crystals that were nucleated at low temperature. However, since the critical nucleus size, r_*, increases with increasing temperature (due to the decrease in the thermodynamic driving force, see Eq. (4.3)), the crystals which do not achieve the size $r_*(T_{\mathrm{d}})$ during the heat treatment at T_n, i.e., crystals with sizes between $r_*(T_n)$ and $r_*(T_{\mathrm{d}})$, have a high probability of dissolving at T_{d}. Thus, T_{d} must be carefully chosen in such a way that there is no significant dissolution of subcritical nuclei at T_{d}. This is the case when most of them have reached the corresponding critical or supercritical sizes by growing at the temperature T_n. It will be shown in Sect. 4.4 that this effect results in a *shift* of the $N(t)$ curves along the time-axis, but does not affect its shape and, hence, does not change the value of the steady-state nucleation rate.

4.3.3 Single-Stage Methods

The Traditional Method

In cases of considerable overlaps of the $I(T)$ and $U(T)$ curves, the number density of crystals can be measured directly after single-stage heat treatments at T_n. Then, the obtained $N(T_n, t)$ curve will be shifted (with regard to the true one) to higher times by a period of time $t_0 = (r_{\text{res}} - r_*(T_n))/U(T_n) \cong r_{\text{res}}/U(T_n)$ that is needed to grow the crystals up to the microscope resolution, $\varepsilon = 2r_{\text{res}}$ [20]. Finally, one must correct the number densities to account for stereological errors. This procedure will be described in Sect. 4.3.4.

Köster's Method

Continuous nucleation and growth can result in a broad distribution of crystal sizes, i.e., the first nucleated crystal has the largest size and so on. If the crystal growth rate is known, one can calculate the "birth dates" of crystals belonging to different size groups and then plot an $N(t)$ curve. This method works also in the case of heterogeneous nucleation with a finite number of active centers, when the latter are depleted in a relative short time, and further advancement of crystallization occurs only via crystal growth. This method, proposed by Köster [21] for metallic glasses, has been successfully employed to study surface nucleation rates in silicate glasses (see Sect. 4.6).

4.3.4 Stereological Corrections

The use of reflected light microscopy can lead to large errors in the determination of the number of crystals per unit volume due to the use of stereological methods, since one has to calculate volume properties (size distributions, numbers, etc.) based on statistical evaluations performed on cross-sections through the specimens. So a significant fraction of the cutted crystals (in the cross sections) can be smaller than the resolution limit of the microscope used, which may lead to a underestimation of the numbers and, consequently, in the determined values of nucleation rates. In Ref. [22] equations were derived for the fractional underestimation, f, of the number of spherical particles per unit volume and of the nucleation rates, as obtained from the stereological techniques for reflected light microscopy or SEM, for typical cases of crystal nucleation in glasses. The following two cases bound the common experimental situations: (i) a monodisperse system of spherical particles that can result, e.g., from instantaneous heterogeneous nucleation; (ii) a uniform size distribution of spherical particles from the critical size to D_M, where D_M is the largest diameter. Such distribution is typical for simultaneous homogeneous nucleation and growth in a singlestage heat treatment. The equations for these cases are as follows:

Case (i) monodisperse systems:

$$f = \frac{2}{\pi} \arcsin(\sigma_1) \,, \tag{4.15}$$

Case (ii) uniform size distribution from the critical size to D_M:

$$f = 1 - \left\{ \frac{2}{\pi} [\cos\theta_1 [1 - \ln(1 + \sin\theta_1)] + \theta_1 + \sigma_1 \ln\sigma_1 - \sigma_1] \right\} \,. \tag{4.16}$$

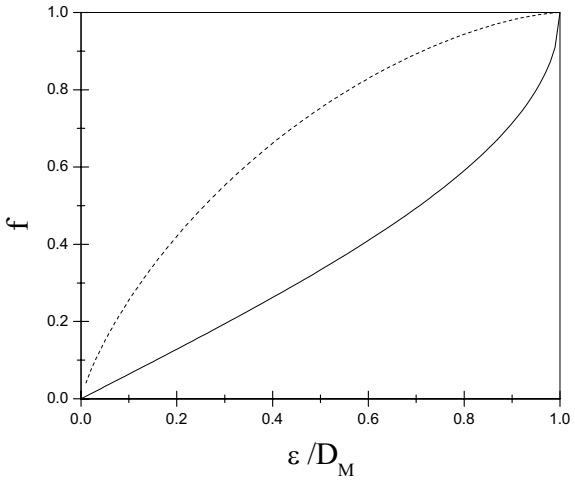

Figure 4.2: Fractional underestimations in the number of spherical particles versus the ratio between the resolution limit and the largest diameter. Solid and dashed curves refer to cases (i) and (ii), respectively

In the above equation, the notation $\theta_1 = \arccos \sigma_1$, $\sigma_1 = \varepsilon / D_M$ is employed and ε is the resolution limit of the microscope used. Comparison with experimental nucleation data for two silicate glasses demonstrated that these equations predict well the observed underestimations of nucleation rates. Figure 4.2 shows the fractional underestimations in the number of spherical particles versus the ratio between the resolution limit and the largest diameter.

To minimize these errors employing reflected light optical microscopy methods, one should use high magnification objective lenses or SEM. Alternatively, transmission methods could be used because they lead to much smaller errors than reflection techniques. Similar underestimates occur when one tries to determine volume fractions of the crystallized phase by microscopy methods. In Ref. [23] equations were derived to estimate systematic errors in experimental determinations of the volume fractions of the transformed part of the system by microscopy methods. For reactions that occur by continuous nucleation and growth, the experimental values of volume fractions of transformed substance may be subjected to significant errors when the largest grain size of the distribution is close to the microscope resolution limit. For transformations occurring from a fixed number of nuclei, the systematic errors are smaller than those observed in the continuous nucleation case, but can still be significant when reflected light microscopy methods are used. Transmission methods are more time consuming but lead to much smaller errors than reflection techniques.

4.3.5 Overall Crystallization Kinetics and Nucleation Rates

Crystal nucleation followed by subsequent growth results in overall crystallization. This process can be described by determining the volume fraction of the transformed phase, $\alpha(t)$. The formal theory of overall-crystallization kinetics under isothermal conditions was developed in

the late 30s by Kolmogorov [24], Johnson and Mehl [25], and Avrami [26], and is well known today as JMAK theory. According to this theory the volume fraction of the new phase is given by

$$\alpha(t) = 1 - \exp\left\{-g\int_0^t I(t')\left[\int_{t'}^t U(t'')\,\mathrm{d}t''\right]^3 \mathrm{d}t'\right\}\ , \tag{4.17}$$

where g is a shape factor, which is equal to $4\pi/3$ for spherical crystals. If the nucleation (I) and growth (U) rates are constant throughout the transformation (e.g., steady-state homogeneous nucleation), Eq. (4.17) can be rewritten as

$$\alpha(t) = 1 - \exp\left[-\frac{gIU^3t^4}{4}\right]\ . \tag{4.18}$$

When the number of growing crystals, N_0, does not change with time (as it is typical for fast heterogeneous nucleation on a finite number of active sites), Eq. (4.17) transforms to

$$\alpha(t) = 1 - \exp\left[-gN_0U^3t^3\right]\ . \tag{4.19}$$

Avrami proposed that generally the following relation should be used

$$\alpha(t) = 1 - \exp(-Kt^n)\ . \tag{4.20}$$

In typical applications, Eq. (4.20) is used in the form

$$\ln(-\ln(1-\alpha)) = \ln K + n\ln t\ . \tag{4.21}$$

The values of K and n can be estimated then by fitting the experimental data concerning the $\alpha(t)$ dependence to Eq. (4.21). Thus the coefficient K includes I and U, or N_0 and U. Therefore, the Avrami coefficient, n, depends on both nucleation and growth mechanisms, and can by written as

$$n = k + 3m\ . \tag{4.22}$$

Here k and m are taken from the formulas $N \sim t^k$ and $r \sim t^m$ describing the variation of crystal number (N) and crystal size (r) with time.

The knowledge of the Avrami coefficient, n, is helpful in order to understand the mechanism of phase transformation at a given temperature. When it is possible to measure independently the crystal growth rate, one can then calculate the nucleation rate from the coefficient K. This method is not as precise as direct measurements, but can give an information about nucleation in advanced stages of crystallization, when the application of other methods is confronted with difficulties (see Sect. 4.5).

For the simplest cases of constant nucleation rate (or constant number of crystals) and linear growth, Eqs. (4.18) and (4.19) were tested by using I_{st}, U, and N_0 data independently measured by optical microscopy in glasses of stoichiometric compositions $2Na_2O \cdot CaO \cdot 3SiO_2$ [27] and $Na_2O \cdot 2CaO \cdot 3SiO_2$ [28]. A reasonable agreement was obtained between the values of gIU^3 (or gN_0U^3), calculated from fitting the $\alpha(t)$ data to the JMAK equation, and directly measured values. Recently, the JMAK equation was also successfully employed, together with measured crystal growth rates, to estimate extremely high nucleation rates in a stoichiometric glass of fresnoite composition [29].

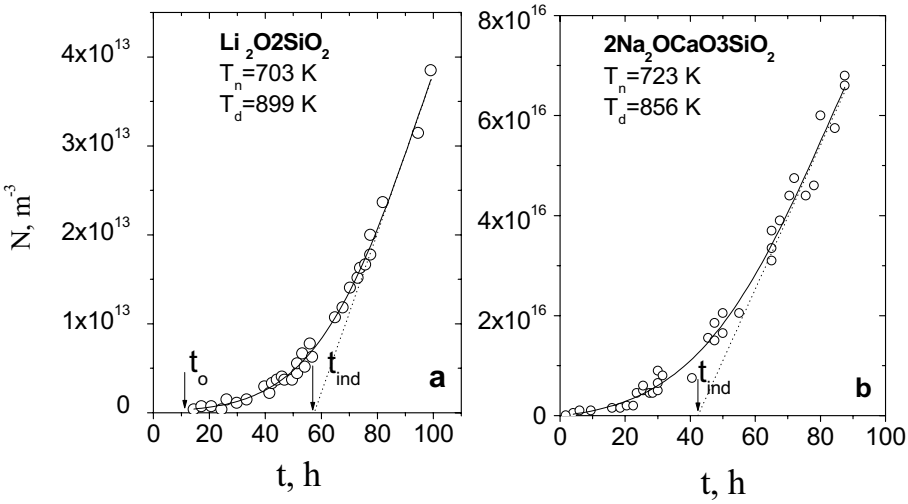

Figure 4.3: Typical curves of the number density of nucleated crystals versus time of nucleation obtained by the "development" method [30, 31]

4.4 Interpretation of Experimental Results by Classical Nucleation Theory

4.4.1 Nonsteady State (Transient) Nucleation

Estimation of the Time-Lag in Nucleation

Typical $N(T_n, T_\mathrm{d}, t)$ curves obtained with the "development" method are shown in Fig. 4.3. As already mentioned, only crystals that achieve the critical size, $r_*(T_\mathrm{d})$, during heat treatment at T_n can grow at the development temperature T_d. The other nuclei have a high probability to dissolve at T_d. The total number of supercritical crystals, N, nucleated at a temperature, T_n, in a time, t, is given by

$$N\left(T_n, r_*(T_n), t\right) = \int_0^t I(T_n, t')\ \mathrm{d}t' \ . \tag{4.23}$$

The number of crystals nucleated at the same conditions, but having a size larger than the critical size, $r_*(T_\mathrm{d})$, and which are, consequently, capable to grow at T_d, is given by

$$N\left(T_n, r_*(T_\mathrm{d}), t\right) = \int_0^{t-t_0} I(T_n, t')\ \mathrm{d}t' \ , \tag{4.24}$$

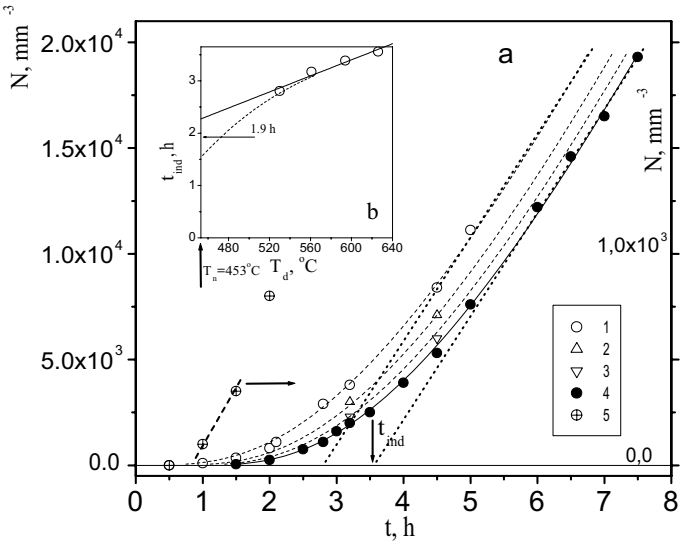

Figure 4.4: (a) Number density of $Li_2O \cdot 2SiO_2$ crystals developed at $T_d = 530$ °C (1, 5), 560 °C (2), 594 °C (3) and 626 °C (4) as a function of nucleation time at $T_n = 453$ °C [32]. (b) Induction time versus development temperature

where t_0 is the period of time that the critical nucleus with a size $r_*(T_n)$ needs to reach the size $r_*(T_d)$. This time interval is determined via

$$t_0(T_n, T_d) = \int_{r_*(T_n)}^{r_*(T_d)} \frac{dr}{U(T_n, r)} \ . \tag{4.25}$$

Equations (4.23) and (4.24) yield

$$N\,(T_n, r_*(T_n), t) = N\,(T_n, r_*(T_d), t + t_0) \ . \tag{4.26}$$

Hence, the $N(T_n, r_*(T_n), t)$ plots are similar to the $N(T_n, r_*(T_d), t)$ plots with the only difference that the latter is shifted along the time-axis by a time t_0. Thus, the development method can provide the correct value of the steady-state nucleation rate, but overestimates the induction time for nucleation by t_0.

The period during which the heat treatment at the nucleation temperature T_n does not influence crystallization at T_d can be identified with t_0 (given by Eq. (4.25)). This time is indicated by an arrow in Fig. 4.3a. According to Eq. (4.25), the higher the growth rates U at the temperature of nucleation T_n, and the closer is T_d to T_n($r_*(T_n)$ is correspondingly closer to $r_*(T_d)$), the lower is t_0. Hence, for a strong overlap of the nucleation and growth rate curves, the value of t_0 is not very high and can often be neglected. This result has been observed for the $2Na_2O \cdot CaO \cdot 3SiO_2$ glass, it is shown in Fig. 4.3b.

On the other hand, when the overlap of the nucleation and growth rate curves is weak, as observed for lithium disilicate glass, one has to correct (reduce) the measured value of

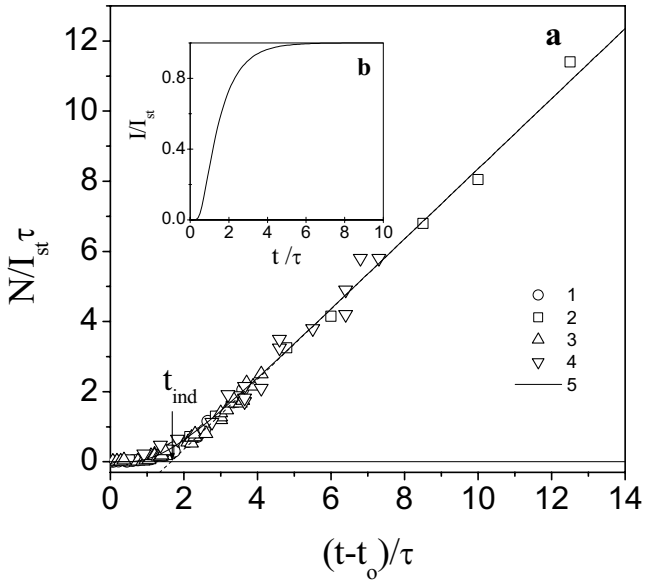

Figure 4.5: (a) $N/(I_{\mathrm{st}}\tau)$ versus reduced time for glasses $Li_2O \cdot 2SiO_2$ (1) and (2) and $2Na_2O \cdot CaO \cdot 3SiO_2$ (3) and (4) [30] for $T = 430$ (1), 465 (2), 465 (3) and 470 °C (4). Curve (5) was calculated from Eq. (4.10). (b) Reduced nucleation rate versus reduced time calculated from Eq. (4.9)

$t_{\mathrm{ind}}(T_n, T_{\mathrm{d}})$ by a time $t_0(T_n, T_{\mathrm{d}})$ (see Fig. 4.3(a)). The value of $t_{\mathrm{ind}}(T_n)$ can be roughly estimated via an extrapolation of the $t_{\mathrm{ind}}(T_n, T_{\mathrm{d}})$-values for the $N(T_n, T_{\mathrm{d}}, t)$ curves, obtained at different T_{d}, to t_{ind} corresponding to $T_{\mathrm{d}} = T_n$. Figure 4.4(a) presents, as examples, such $N(T_n, T_{\mathrm{d}}, t)$ curves for lithium disilicate glass. The values of t_{ind}, taken from these curves, versus development temperature are plotted in Fig. 4.4(b). When T_{d} approaches $T_n = 453$ °C, t_{ind} is about 1.9 h (the average value of the linear and quadratic polynomial extrapolations). Hence, one can approximately estimate t_0 as $t_0 = t_{\mathrm{ind}}(T_n, T_{\mathrm{d}}) - t_{\mathrm{ind}}(T_n)$, e.g., for $T_{\mathrm{d}} = 530$ °C the time interval t_0 is about 0.9 h. A value close to the given one was also obtained by extrapolating the initial section of the $N(t)$ curve (1) (see also curve (5)) to $N = 0$. Thus, according to Eq. (4.12), one can assume that Eq. (4.27) holds, i.e.,

$$\tau(T_n) = \frac{6}{\pi^2}\left(t_{\mathrm{ind}}(T_n, T_{\mathrm{d}}) - t_0(T_n, T_{\mathrm{d}})\right) \ . \tag{4.27}$$

Kinetic $N(t)$-curves, such as those presented by Fig. 4.3, can be plotted in dimensionless coordinates ($N(T, t - t_0)/I_{\mathrm{st}}(T)\tau(T)$ versus $(t - t_0)/\tau(T)$). These coordinates allow one to combine data for different glasses and different temperatures in the same plot, as shown in Fig. 4.5(a). Experimental points are quite close to the theoretical master curve calculated with Eq. (4.10). This kinetic curve corresponds to increasing nucleation rates toward the steady-state value, I_{st}. The evolution of the nucleation rate calculated by Eq. (4.9) is shown in Fig. 4.5(b).

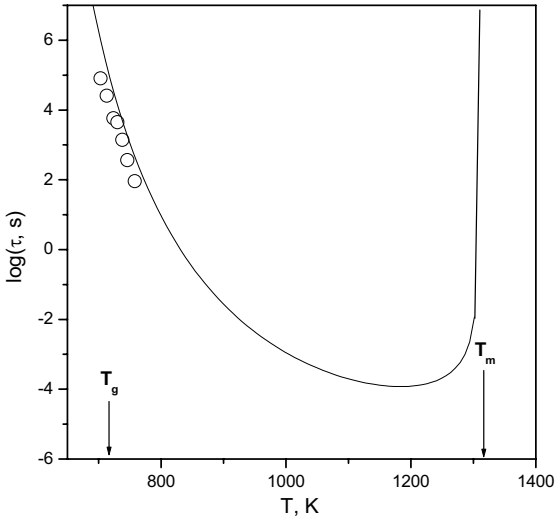

Figure 4.6: Temperature dependence of the time-lag for nucleation. Circles refer to experimental data for $Li_2O \cdot 2SiO_2$ glass [34]. The solid line was calculated by Eq. (4.8)

4.4.2 Temperature Dependence of the Time-Lag in Nucleation

According to Eq. (4.8), when the degree of undercooling increases, the time-lag τ has to pass through a minimum. This behavior is due to an interplay between the decrease of $1/\Delta G_V^2$ and the increase of the exponential term. This minimum is located at low undercoolings. Since, in the case of glass-forming silicate melts, detectable internal homogeneous nucleation rates are observed only at very high undercoolings, $\Delta T/T_m \geq 0.4$ [33], only an increase of the time-lag is usually observed with diminishing temperature.

Figure 4.6 illustrates this trend for lithium disilicate glass. The circles refer to the experimental data. The solid line is determined according to Eq. (4.8) with $\sigma_{cm} = 0.2$ J m^{-2} assuming that the activation free energy ΔG_D is close to that for viscous flow, ΔG_η. For very high undercoolings, typically needed to observe homogeneous nucleation, the validity of this assumption has been a subject of controversial discussion. However, this supposition is commonly assumed to be valid for relatively low undercoolings ($T > 1.2\, T_g$) (see, e.g., [35]).

4.4.3 Transient Nucleation at Preexisting Nucleus Size Distributions

In Sects. 4.2 and 4.4, we discussed nonsteady state nucleation assuming the absence of an appreciable number of preexisting nuclei. This assumption is quite reasonable for interpreting such time-lag phenomena for glasses obtained via fast quenching of the melt. In contrast, preliminary annealing of a glass at some temperature T_1 for a sufficiently long time $t \geq \tau(T_1)$ results in the formation of a cluster distribution that may act as an initial distribution at the temperature T_2. Then this distribution evolves toward a steady-state distribution corresponding to the temperature T_2, complicating the time dependence of the nucleation rate. For example,

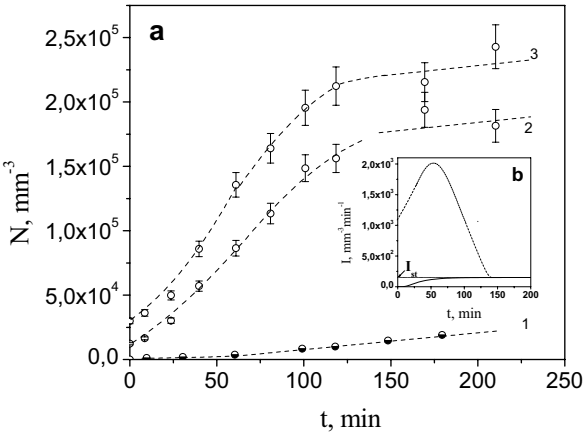

Figure 4.7: (a) Number density of $Li_2O \cdot 2SiO_2$ crystals obtained via the "development" method ($T_d = 626$ °C) versus time of nucleation at $T_n = 465$ °C. Curve (1) refers to quenched glass. Curves (2) and (3) refer to glasses subjected to preliminary treatment at $T = 430$ °C for 65 h (2) and 89 h (3) [36]. (b) Nucleation rate versus time. Solid and dashed lines correspond to curves (1) and (3) from Fig. 4.7(a), respectively

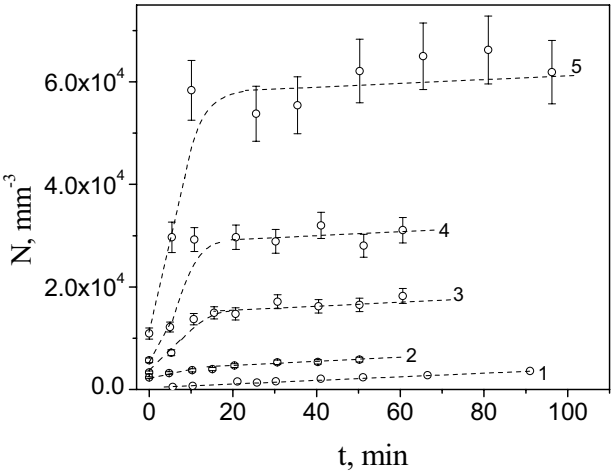

Figure 4.8: Number density of $Li_2O \cdot 2SiO_2$ crystals obtained via the "development" method ($T_d = 626$ °C) versus time of nucleation at $T_n = 485$ °C. Curve (1) quenched glass, curves (2)–(5) glass subjected to preliminary treatment at $T = 473$ (2), 451 (3), 440 (4), and 430 °C (5) for the following times: $t = 0.75$ (2), 4.5 (3), 18 (4), and 65 h (5) [36]

in the case of lithium disilicate glass annealed at T_1, the transient nucleation rate at $T_2 > T_1$ passes through a well-expressed maximum before reaching the steady-state value.

Figure 4.7 shows the respective $N(t)$ curves at $T_2 = 465$ °C for a fast quenched parent glass (1) and for glasses that had been preliminarily annealed at $T_1 = 430$ °C (2) and (3). All curves were obtained by the "development" method, with $T_d = 626$ °C. Curves (2) and (3) demonstrate, as compared with curve (1), a strong increase in the number of crystals, and only for times higher than about 120 min the nucleation rate achieves the steady-state value, corresponding to the temperature T_2. The evolution of the nucleation rate corresponding to curve (3) is shown in Fig. 4.7(b). Such unusual behavior of the nucleation kinetics is caused mostly by the nuclei formed at T_1 – with sizes between $r_*(T_2)$ and $r_*(T_d)$ – and partly by subcritical nuclei – with sizes less than $r_*(T_2)$. Since the number of nuclei with sizes $r \geq r_*(T)$ increases with decreasing temperature, down to $T = T_m/3$, the effect of the preliminary heat treatment becomes stronger when T_1 is diminished (see Fig. 4.8). The data presented in Fig. 4.8 are well described by simulations performed in the framework of the kinetic model of the classical theory of nucleation [37, 38]. Thus, the nucleation kinetics is governed by the evolution of the nucleus distribution.

4.4.4 Steady-State Nucleation

Temperature Dependence of Steady-State Nucleation Rates

Some examples of steady-state nucleation rates, I_{st}, measured from the slope of the linear part of the $N(t)$ plots, such as those shown in Fig. 4.3, are presented in Fig. 4.9 as a function of reduced temperature. The values of $I_{st}(T)$ pass through a maximum at a temperature T_{max}. The magnitudes of $I_{st}(T_{max}) = I_{max}$ vary from 5×10^{13} to 3×10^{2} m^{-3} s^{-1} and cover practically all available measurements of nucleation rates in silicate glasses of stoichiometric composition up to the present time.

The reason for the existence of the nucleation rate maximum follows from a simple analysis of Eq. (4.1). Since the preexponential term, I_0, depends only weakly on temperature, the temperature dependence of the nucleation rate is determined mainly by the thermodynamic and kinetic barriers for nucleation. A temperature decrease produces two effects: a decrease of the thermodynamic barrier, due to an increase in the thermodynamic driving force for crystallization, leading to a higher nucleation rate, and an increase of the kinetic barrier leading to a lower nucleation rate (the kinetic barrier is, as mentioned earlier, often replaced by the activation free energy for viscous flow). As a result of these two opposite tendencies, one finds a maximum of the steady-state nucleation rate at a temperature T_{max}, which is well-below T_m. Equation (4.4) for the thermodynamic barrier can be rewritten as

$$\frac{W_*}{k_B T} = C_1 \frac{1}{T_r\,(1 - T_r)^2}\,, \quad C_1 \equiv \frac{16\pi}{3}\frac{\alpha_{ST}^3\,\Delta H_m}{R T_m}\,, \quad T_r \equiv \frac{T}{T_m}\,, \tag{4.28}$$

using the Turnbull approximation for the thermodynamic driving force, Eq. (4.6), and the following semi-empirical equation proposed by Scapski and Turnbull for the specific surface energy of the nucleus/melt interface [41]

$$\sigma_{cm} = \alpha_{ST}\frac{\Delta H_m}{V_m^{2/3} N_A^{1/3}}\,, \tag{4.29}$$

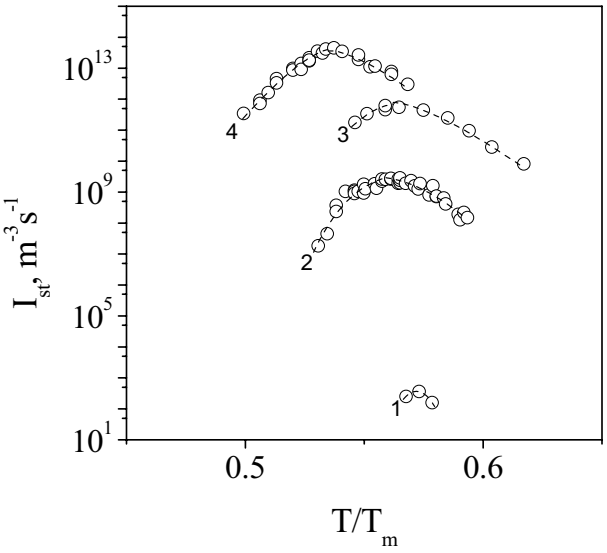

Figure 4.9: Steady-state nucleation rate versus reduced temperature for some stoichiometric glasses: (1): $3MgO \cdot Al_2O_3 \cdot 3SiO_2$ [39], (2): $Li_2O \cdot 2SiO_2$ [30], (3): $Na_2O \cdot 2CaO \cdot 3SiO_2$ [40], (4): $2Na_2O \cdot 1CaO \cdot 3SiO_2$ [31]

where ΔH_m is the melting enthalpy per mole, V_m is the molar volume, N_A is Avagadro's number, and α_{ST} is an empirical dimensionless coefficient. Assuming that ΔG_D is of the same order of magnitude as the activation free energy of viscous flow, ΔG_η, one can write the kinetic barrier also as

$$\frac{\Delta G_D}{k_B T} = \frac{C_2}{T_r - T_{0r}} \; , \; C_2 \equiv \frac{2.30B}{T_m} \cong 30(T_{gr} - T_{0r}) \; , \; T_{0r} = \frac{T_0}{T_m} \; , \; T_{gr} = \frac{T_g}{T_m} \; , \quad (4.30)$$

where T_0 and B are empirical coefficients of the Vogel–Fulcher–Tammann (VFT) equation and T_g is the glass transition temperature. The application of the VFT-relation implies the assumption of a temperature-dependent activation free energy ΔG_η. In the definition of C_2 we took into account the fact that $\Delta G_\eta/(k_B T) \cong 30$ at $T = T_g$.

Figure 4.10 shows $I_{st}(T_r)$ curves calculated with Eqs. (4.1), (4.28), and (4.30) and reasonable values of the preexponential term and values of the parameters C_1 and C_2, as indicated in the figure caption. One can see that the decrease in the kinetic barrier, caused by a decrease in C_2 at fixed values of C_1, results in a shift of the nucleation rate maximum to lower temperatures (cf. curves (1)–(4)). The reduced temperature $T_r \equiv T/T_m = 1/3$ is a lower limit to $T_r^{max} \equiv T_{max}/T_m$ obtained when the kinetic barrier tends to zero (cf. curve (5)). This shift is accompanied by a strong increase in the magnitude of $I(T_{max}) \equiv I_{max}$. When the thermodynamic barrier is diminished at fixed values of C_2, by decreasing the parameter C_1 (which is proportional to α_{ST} and the reduced melting enthalpy $\Delta H_m^r = \Delta H_m/RT_m$), the value of I_{max} also increases (curves (1), (6)–(8)), but the value of T_{max} shifts to higher temperatures.

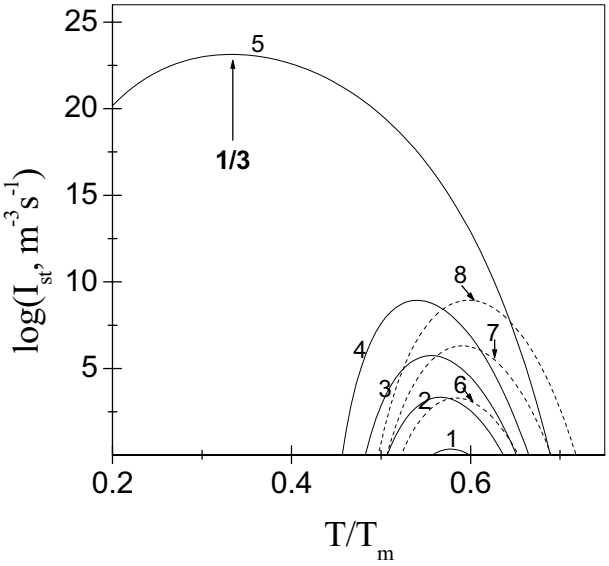

Figure 4.10: Temperature dependence of the homogeneous nucleation rate. The curves are calculated with Eqs. (4.1), (4.28), and (4.30) with a preexponential term $I_0 = 10^{42}$ m^{-3} s^{-1} and the following values of the parameters characterizing the temperature independent parts of the thermodynamic (C_1) and kinetic (C_2) barriers: $C_1 = 6.5$ (1)–(5), 5.8 (6), 5.1 (7), 4.5 (8); $C_2 = 6$ (1), (6), (7), (8), 4.8 (2), 3.9 (3), 2.8 (4), 0 (5)

The effect of the variation of the kinetic barrier on the nucleation rate can be qualitatively illustrated for lithium disilicate [42] and sodium calcium metasilicate [43] glasses with different contents of H_2O (few percent of water result in a significant decrease of viscosity) as shown in Fig. 4.11. A decrease in the thermodynamic barrier can be also caused by a decrease in the crystal/melt interfacial energy as in the case of heterogeneous nucleation. As a result, as will be shown in Sect. 4.6, the temperature T_{max} for heterogeneous nucleation is displaced to higher values as compared with homogeneous nucleation.

4.4.5 Correlation between Nucleation Rate and Glass Transition Temperature

The methods discussed in Sect. 4.3 to measure nucleation kinetics are both difficult and time consuming. Also, owing to several restrictions they cannot always be employed. Hence, the knowledge of any correlation between nucleation rate and easily measurable properties of glasses is highly desirable. As one example, well before the development of nucleation theory for condensed systems, Tammann called attention to the following tendency: the higher the melt viscosity at the melting temperature, the lower its crystallizability [44].

Almost 80 years after Tammann, James [45] and Zanotto [46], based on numerous experimental nucleation rate data for several silicate glasses, concluded that *glasses having a reduced glass transition temperature,* $T_{gr} \equiv T_g/T_m$, *higher than* $\sim$ 0.58–0.60*, display only*

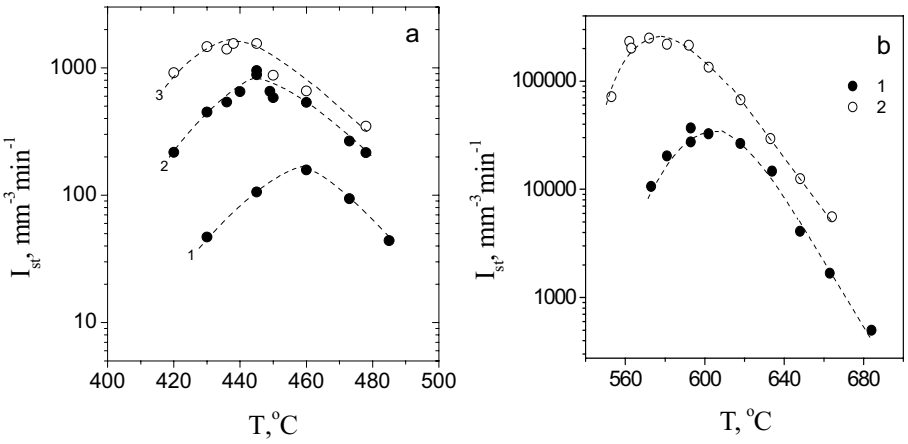

Figure 4.11: Temperature dependences of steady-state nucleation rates in $Li_2O \cdot 2SiO_2$ [42] (a) and $Na_2O \cdot 2CaO \cdot 3SiO_2$ [43] (b) glasses containing different amounts of H_2O: (a) 0.05 (1), 0.12 (2) and 0.20 (3) mol%; (b) 0.01 (1), 0.02 (2) mol%

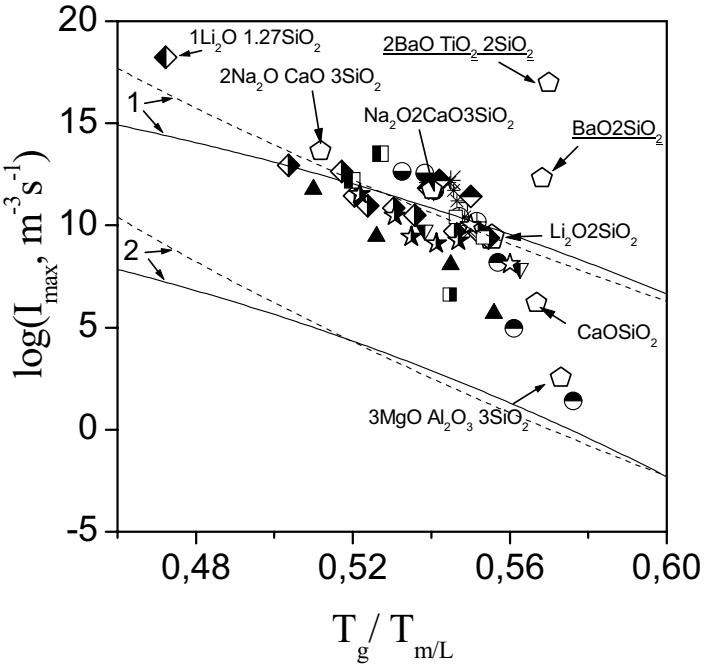

Figure 4.12: Maximum nucleation rates as a function of reduced glass transition temperature for 55 silicate glasses. The lines are calculated from CNT with $C_1 = 4.5$ (1) and 6.5 (2). Solid lines refer to $C_2 = 4.5$ and $T_{or} = T_{gr} - C_2/30$; dashed lines to $T_{or} = 0.4$ [48]

surface (mostly heterogeneous) crystallization; while glasses showing volume (homogeneous) nucleation have values $T_{gr} < 0.58$–0.60. However, since at temperatures $T < T_m$ the nucleation rate is always positive, the absence of volume nucleation for glasses having $T_{gr} > 0.60$ merely indicates undetectable nucleation on laboratory time/size scales. Hence, an increase in the nucleation rate with decreasing T_{gr} could be expected. Indeed, a drastic increase of the magnitude of I_{max} with decreasing T_{gr} was demonstrated recently by Deubener [47].

Figure 4.12 presents a plot of the $I_{max}(T_{gr})$ dependence, which has been extended in Ref. [48] and in the present work. Using data for 55 glasses of stoichiometric and nonstoichiometric compositions belonging to eight silicate systems, in a relatively narrow range of T_{gr} (ranging from 0.47 to 0.58) the *nucleation rates drops by about 17 orders of magnitude!* When T_{gr} increases, the kinetic inhibition of nucleation proceeds at higher temperatures and, thus, at higher values of the thermodynamic barrier (at lower values of the thermodynamic driving force). As a consequence, nucleation becomes practically undetectable at $T_{gr} > 0.58$. This result confirms the findings of James [45] and Zanotto [46]. The lines in Fig. 4.12 are calculated from CNT (Eqs. (4.1), (4.28), and (4.30)) with reasonable values of the parameters C_1 and C_2 indicated in the figure. Remember that C_1 and C_2 characterize the temperature independent parts of the thermodynamic and kinetic barriers for nucleation, respectively.

Since Eq. (4.30) contains two independent parameters C_2 and T_{or}, the viscosity and, correspondingly, T_{gr} was varied in two different ways, by keeping either C_2 (solid lines) or T_{or} (dashed lines) fixed. In the most interesting temperature range ($0.5 < T_r < 0.6$) these different ways of varying T_{gr} lead to similar results. The lines bound the experimental points and reflect the correct trend. However, the experimentally observed trend must be analyzed within some limits, since a substantial variation of the thermodynamic barrier can result in a considerable variation of I_{max} for glasses having similar values of T_{gr}. For instance, fresnoite ($2BaO \cdot TiO_2 \cdot 2SiO_2$) and wollastonite ($CaO \cdot SiO_2$) glasses have T_{gr} about 0.57, while the values of the parameter α_{ST} are 0.4 and 0.6, respectively. The latter fact leads to a strong difference in the values of the thermodynamic barriers and correspondingly to a strong difference in I_{max}. Also nucleation of metastable phases, such as $BaO{\cdot}2SiO_2$, is possible as shown in Ref. [49].

Computations of $I_{st}(T)$ temperature dependences similar to those published in Ref. [48] and presented here were performed by Turnbull in the 60s (see, e.g., Ref. [50]). However, at that time, with the exception of the measurements of Tammann [51] and Mikhnevich, Browko [52] for organic liquids, nucleation rate data were not available for wide temperature ranges including T_{max}. In order to verify the existence of the correlation between I_{max} and T_{gr}, as proposed here, an abundance of experimental points should be available. This is now the case (cf. Fig. 4.12).

4.5 Nucleation Rate Data and CNT: Some Serious Problems

4.5.1 Different Approaches to the Interpretation of Experimental Data by CNT

As shown in the previous sections, in its original form CNT provides a good *qualitative* description of nucleation rate data. However, serious problems arise when one tries to employ it for a quantitative interpretation of experimental data. Using the Stokes–Einstein equation to connect the kinetic barrier of nucleation with the glass viscosity one can rewrite Eq. (4.1) for the steady-state nucleation rate as

$$I_{\mathrm{st}} = K_\eta \frac{1}{\eta} \exp\left(-\frac{W_*}{k_{\mathrm{B}}T}\right), \quad K_\eta = I_0 \frac{h}{4l^3}\ , \tag{4.31}$$

where the size parameter l has a value of the order of the Si–O bond length. The application of the Stokes–Einstein equation in Eq. (4.31) can be avoided if one estimates the kinetic barrier from the time-lag in nucleation. In this case, Eq. (4.1) takes the following form:

$$I_{\mathrm{st}} = K_\tau \frac{1}{\Delta G^2 t_{\mathrm{ind}}} \exp\left(-\frac{W_*}{k_{\mathrm{B}}T}\right), \quad K_\tau = I_0 \frac{8h\sigma_{\mathrm{cm}}}{3a^4}\ . \tag{4.32}$$

In the analysis of experiments on crystallization in glass-forming systems, it is commonly accepted – in accordance with CNT and Gibbs' classical description of heterogeneous systems – to use the properties of the newly evolving macrophase as reference states for the description of the bulk properties of the critical nucleus. Additionally, one has to properly specify the values of the specific interfacial energy. Since measurements of the specific interfacial energy of the crystals in their own melt, σ_{cm}, are confronted with serious difficulties, one usually employs the easily measurable thermodynamic driving force for crystallization of the macrophase for the determination of the work of critical cluster formation. Thus, σ_{cm} is commonly taken as a fit parameter and is treated, to a first approximation, as a size-independent (capillarity approximation) and temperature-independent quantity. The respective values of σ_{cm} are denoted in Tables 4.1 and 4.2 as σ^*_{cm}. These approximations allow one to estimate both the magnitude of the preexponential term, I_0, in Eq. (4.1) and the value of the crystal-melt surface energy, σ_{cm}, from a fit of the experimental data (I_{st}, η, or t_{ind}).

Indeed, according to Eqs. (4.31), (4.32), and (4.4) the plots of the dependences $\ln(I_{\mathrm{st}}\eta)$ and $\ln(I_{\mathrm{st}} t_{\mathrm{ind}} \Delta G_{\mathrm{V}}^2)$ versus $1/(T\,\Delta G_{\mathrm{V}}^2)$ should yield straight lines. Their intercepts and slopes can be employed to evaluate I_0 and σ_{cm}, respectively. However, these approximations lead to the following problems:

(i) The application of both Eqs. (4.31) [45,53] and (4.32) [54] leads to drastic discrepancies between the experimental, I_0^{exp}, and theoretical, I_0^{theo}, values of the preexponential factor I_0. This discrepancy was first observed for crystal nucleation in undercooled Ga [55] and Hg [56]. In order to illustrate this conclusion, in Table 4.1 the $(I_0^{\mathrm{exp}}/I_0^{\mathrm{theo}})$-ratio and the surface energy values for some stoichiometric silicate glasses calculated from the plots $\ln(I_{\mathrm{st}} t_{\mathrm{ind}} \Delta G_{\mathrm{V}}^2)$ versus $1/T\,\Delta G_{\mathrm{V}}^2$ are presented for temperatures above the glass

Table 4.1: Ratio of experimental and theoretical preexponential and surface energy values calculated by CNT for different glasses [33]. The specific interfacial energy is given in J m^{-2}

Glass	$\Delta C_p = 0$		$\Delta C_p = f(T)$	
	$\log\left(\frac{I_0^{exp}}{I_0^{theo}}\right)$	σ^*_{cm}	$\log\left(\frac{I_0^{exp}}{I_0^{theo}}\right)$	σ^*_{cm}
$Li_2O{\cdot}2SiO_2$	15	0.19	19	0.20
$Na_2O{\cdot}2CaO{\cdot}3SiO_2$	18	0.17	72	0.19
$2Na_2O{\cdot}CaO{\cdot}3SiO_2$	27	0.15	139	0.17

transition temperature. To trace these plots, both the Turnbull approximation (4.6) and the experimental values for the thermodynamic driving force (4.5) for crystallization of the macro-phases were used. The discrepancy between theory and experiment is strongly affected by the choice of ΔG_V. The experimental values of ΔG_V are close to Turnbull's approximation in the case of $Li_2O \cdot 2SiO_2$ glass and to Hoffman's approximation in the case of $2Na_2O \cdot 1CaO \cdot 3SiO_2$ glass. It is easy to show that the ratio (I_0^{exp}/I_0^{theo}) increases as one passes from Turnbull's to Hoffman's approximation. These equations bound the experimental values of ΔG_V [13]. However, independent of particular choice of expression for the thermodynamic driving force, i.e., with any reasonable approximation or with reasonable experimental values of ΔG_V, the mentioned discrepancy remains quite large.

(ii) The values of the surface energy σ_{cm}, calculated as described above, are lower than the melt–vapor surface energy, σ_{mv}, which can be measured directly [57, 58], by a factor of about 0.5–0.6. These values must be corrected since σ_{cm} refers to nuclei of critical size r_*, while σ_{mv} refers to planar melt/vapor interfaces. In the case of lithium disilicate glass, for instance, corrections made with the Tolman equation (4.33) increase this factor to 0.8 [59]. Such high values of σ_{cm}, as compared with σ_{mv}, seem to strongly overestimate its real magnitude. Indeed, according to Stefan's rule [60], one would expect that the ratio σ_{cm}/σ_{mv} is of the same order of magnitude as $\sigma_{cm}/\sigma_{mv} \cong \Delta H_{cm}/\Delta H_{mv} \ll 1$. Here $\Delta H_{cm} \equiv \Delta H_m$ and ΔH_{mv} are the melting enthalpy of the crystalline phase and the enthalpy of evaporation, respectively.

In the following sections, possible reasons for the failure of CNT regarding its application to the quantitative description of nucleation experiments will be analyzed.

4.5.2 Temperature and Size-Dependence of the Nucleus/Liquid Specific Surface Energy

The discrepancy between experimental and theoretical values of I_0 can be removed if one calculates σ_{cm} from nucleation data (I_{st} and t_{ind} or η) employing the theoretical expression for I_0. This procedure does not change significantly the values of σ_{cm}, but leads to a slight increase of σ_{cm} with increasing temperature [61] ($d\sigma/dT \sim (0.06 - 0.16) \times 10^{-3}$ J/m^2K) regardless of the method of estimating the kinetic barrier. However, most (but not all) authors

express the opinion that, from a thermodynamic point of view, a decrease of σ_{cm}, measured for planar interfaces (σ_∞), with increasing temperature should be generally expected [50, 62–64].

The latter contradiction between experimental results and theoretical expectations can be partly removed by taking into account a possible curvature (or nucleus size) dependence of the surface tension. Recall that the specific surface energy, estimated from nucleation rate data, refers to nuclei of critical size. Curvature corrections can be expected to lead to a reduction in the effective value of the surface energy. When the critical nucleus size increases with increasing temperature, the effect of curvature corrections decreases (see Eq. (4.33)), leading to higher effective values of the surface energy.

To decouple these size and temperature effects, to a first approximation Tolman's equation (that was originally derived for a liquid drop being in equilibrium with its vapor) can be used. The Tolman equation reads

$$\sigma(r_*) = \frac{\sigma_\infty}{\left(1 + \frac{2\delta}{r_*}\right)}, \tag{4.33}$$

where δ, the Tolman parameter, is a measure of the (unknown) width of the interfacial region between the coexisting phases. Employing this relation, the work of formation of a spherical critical nucleus may be written as

$$W_* = \frac{16\pi}{3} \frac{\sigma_\infty^3}{\left(1 + \frac{2\delta}{r_*}\right)^3 \Delta G_V^2}, \tag{4.34}$$

where

$$r_* = \frac{2\sigma_\infty}{\Delta G_V} - 2\delta \tag{4.35}$$

holds.

Figure 4.13 shows the average values of $(d\sigma_\infty/dT)$ at $T \geq T_g$ versus the Tolman parameter. The fits of σ_∞ to experimental nucleation data for $Li_2O{\cdot}2SiO_2$ glass were performed for different values of δ. For this purpose Eq. (4.32) was employed. As δ increases, $(d\sigma_\infty/dT)$ progressively decreases becoming negative for $\delta > 2.4 \times 10^{-10}$ m. Thus, reasonable values of the Tolman parameter may be chosen such that σ_∞ decreases with increasing temperature in line with the theoretical predictions given in Refs. [62, 63]. However, the values of surface energy remain too high as compared with the respective melt-vapor values.

4.5.3 Estimation of Crystal/Liquid Surface Energies via Dissolution of Subcritical Nuclei

Essentially all existing methods to determine the nucleus–melt surface energy are based on nucleation experiments involving certain additional assumptions. However, in order to test the classical nucleation theory or to make predictions in their framework, independent estimates of the specific surface energy are required. Such an independent method of estimating σ_{cm} of clusters of near-critical sizes has been developed recently [59]. The results are summarized below.

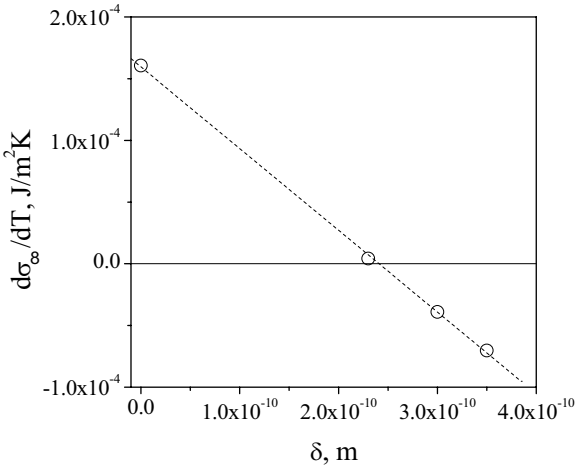

Figure 4.13: $(\mathrm{d}\sigma_\infty/\,\mathrm{d}T)$ versus the Tolman parameter for $Li_2O \cdot 2SiO_2$ crystals in a glass of the same composition. The kinetic barrier for nucleation was estimated from the nucleation time-lag

Table 4.2: Liquid–crystal surface energies (in J m^{-2}) calculated from nucleation and growth data [59]

Glass	σ_{cm}	σ^*_{cm}	σ^{**}_{cm}	K	σ^r_{cm}
$Li_2O{\cdot}2SiO_2$	1.4	0.20	0.152–0.156 450 °C $< T <$ 485 °C	0.19–0.23	0.050–0.060
$Na_2O{\cdot}2CaO{\cdot}3SiO_2$	1.5	0.18	0.099–0.110 580 °C $< T <$ 685 °C	0.13	0.026

The method is based on the dissolution phenomenon (discussed in Sects. 4.3 and 4.4) of subcritical nuclei with an increase in temperature. As already shown, the $N(T_n, r_*(T_n), t)$ plot coincides widely with the $N(T_n, r_*(T_\mathrm{d}), t)$ plot with the only difference that the latter is shifted along the time-axis by a time t_0 (Eq. (4.25)). Then, the kinetic curves $N(T_n, t)$ obtained with different development temperatures T_{d1} and $T_{d2} > T_{d1}$ should be shifted with respect to each other by a time $\Delta t_0 = t_{02} - t_{01}$. Figure 4.4 presents an example of such kinetic curves. The following equation was derived in Ref. [32] to estimate this shift:

$$\begin{aligned}\Delta t_0 &= \int_{r_*(T_{d1})}^{r_*(T_{d2})} \frac{\mathrm{d}r}{U(T_n, r)} \\ &= \frac{1}{U(T_n, \infty)} \left[r_*(T_{d2}) - r_*(T_{d1}) + r_*(T_n) \ln \left(\frac{r_*(T_{d2}) - r_*(T_n)}{r_*(T_{d1}) - r_*(T_n)} \right) \right] .\end{aligned} \tag{4.36}$$

In the derivation of Eq. (4.36) a size-dependent crystal growth velocity [65] was utilized of the form

$$U(T, r) = U(T, \infty) \left[1 - \frac{r_*(T)}{r} \right] . \tag{4.37}$$

Employing Eq. (4.3) for the critical nucleus size and assuming that σ_{cm} depends only slightly on temperature, Eq. (4.36) can be rewritten as

$$\sigma_{\mathrm{cm}} = \frac{1}{2} \frac{\Delta t_0 \, U(T_n, \infty)}{\left\{ \dfrac{1}{\Delta G(T_{d2})} - \dfrac{1}{\Delta G(T_{d1})} + \dfrac{1}{\Delta G(T_n)} \ln \left[\dfrac{\dfrac{1}{\Delta G(T_{d2})} - \dfrac{1}{\Delta G(T_n)}}{\dfrac{1}{\Delta G(T_{d1})} - \dfrac{1}{\Delta G(T_n)}} \right] \right\}} \, . \tag{4.38}$$

Hence, it is possible to calculate the average value of σ_{cm} in the temperature range T_n–T_{d2} from experimental values of Δt_0, $U(T_n, \infty)$, and ΔG_{V}. Note that in doing so neither nucleation rate nor time-lag data are required. The values of σ_{cm}, calculated by this method for $Li_2O \cdot 2SiO_2$ and $Na_2O \cdot 2CaO \cdot 3SiO_2$ glasses, are presented in Table 4.2. Also, here the values are estimated with the assumption of a size- and temperature-independent specific surface energy, σ^*_{cm} (see also Table 4.1) and $\sigma^{**}_{\mathrm{cm}}$ employing the theoretical values of I_0. The values of σ_{cm} calculated via Eq. (4.38) strongly exceed the corresponding values calculated from a fit of nucleation rate data to CNT (σ^*_{cm}, $\sigma^{**}_{\mathrm{cm}}$). *Such high values of σ_{cm} have to lead – according to CNT – to vanishing nucleation rates.* However, nucleation processes do occur.

In order to find out the origin of this discrepancy it should be realized that the methods discussed above do not provide the surface energy directly, but only its combination with the thermodynamic driving force. In particular, σ_{cm} is calculated from the measured values of Δt_0 and $U(T_n, \infty)$ via (see Eq. (4.38))

$$\Delta t_0 = 2\sigma_{\mathrm{cm}} f \left(\frac{1}{\Delta G_{\mathrm{V}}} \right) U \tag{4.39}$$

and $\sigma^{**}_{\mathrm{cm}}$ (as well as σ^*_{cm}) from the thermodynamic barrier for nucleation

$$W_* \propto \frac{(\sigma^{**}_{\mathrm{cm}})^3}{\Delta G_{\mathrm{V}}^2} \, . \tag{4.40}$$

One should recall that, in line with Gibbs's thermodynamic description of heterogeneous systems, the thermodynamic driving force for the crystallization of macro-crystals was applied to critical and near-critical nuclei to estimate their surface energy. However, the bulk properties of near-critical crystallites may deviate significantly from the properties of the newly evolving macroscopic phase. In order to arrive at the correct values of the work of critical cluster formation in nucleation, the value of the surface tension has to be chosen appropriately to obtain the correct results. However, in such approach, the surface energy plays the role (in the above-presented methods) of a fit parameter. Hence, the discrepancy discussed above may result from the difference between the values of ΔG_{V} employed and the correct driving force of cluster growth, which is determined by the real physical state of the critical and near-critical clusters.

It follows as a consequence that, from a general theoretical point of view, both surface energy and the thermodynamic driving force have to be considered as unknown quantities. Let us then introduce a coefficient $K(r)$ that connects the (supposed) real thermodynamic driving force, ΔG_{V}, with the respective value for the macrophase, ΔG_∞, as

$$\Delta G_{\mathrm{V}} = K(r) \Delta G_\infty \, . \tag{4.41}$$

The coefficient $K(r)$ reflects the fact that the thermodynamic driving force for critical nuclei may differ from that of the corresponding macrophase. If one denotes by σ_{cm}^{r} the true value of the surface energy estimated with account of Eq. (4.41) and takes into consideration that $U \sim \Delta G_V$, the following equations connecting σ_{cm}^{r} with σ_{cm} and σ_{cm}^{**} are obtained from Eqs. (4.39) and (4.40):

$$\sigma_{cm}^{r} = K(r)^2 \sigma_{cm} , \quad \sigma_{cm}^{r} = K(r)^{2/3} \sigma_{cm}^{**} . \tag{4.42}$$

Equations (4.42) yield immediately

$$K = \left(\frac{\sigma_{cm}^{**}}{\sigma_{cm}} \right)^{2/3} . \tag{4.43}$$

Thus, both methods provide the same value of crystal/melt surface energy if the reduced thermodynamic driving force, $\Delta G_V = K(r) \Delta G_\infty$, is employed in the description.

The values of K presented in Table 4.2 show a considerable reduction in the thermodynamic driving force for nucleation and growth of critical and near-critical nuclei as compared with that for macrocrystal growth ($K < 1$). The following reasons could lead to a reduction in thermodynamic driving force: (a) It is reasonable to assume that near-critical nuclei are less ordered than the material in the corresponding bulk phase. It is possible to show that in this case $\Delta G_V < \Delta G_\infty$ holds [59]. (b) According to the model of ideal associated solutions [66, 67], a glass-forming melt can be considered as a solution of oxide components and salt-like products. Then, critical cluster formation should be represented as a segregation process in a multicomponent solution. As shown in Ref. [68], in this case the driving force may be smaller than that for the macroscopic phase. (c) The deviation of the critical nuclei composition from that of the evolving macrophase (e.g., owing to the formation of metastable phases or solid solutions) also leads to a reduction in the thermodynamic driving force as compared to that for the stable macrophase. This effect, i.e., the deviation of the critical nuclei composition from that of both the evolving macrophase and the parent stoichiometric glass, was recently observed experimentally. The results are presented in the following section.

It should be emphasized that the value of σ_{cm}^{r} (see Table 4.2) is smaller than that of σ_{cm}^{*} and σ_{cm}^{**}. This way, the decrease of the thermodynamic driving force results in values of the interfacial energy that are significantly more reasonable (taking Stefan's rule into account).

4.5.4 Compositional Changes of the Crystal Nuclei in the Course of Their Formation and Growth

Within certain limits, an addition, removal or replacement of different components can continuously change the composition of a given crystallographic system. Hence, generally speaking, compositional variations of critical nuclei of a new phase and, consequently, variations of its properties as compared with those of the corresponding macrophase could be expected. Indeed such deviations were observed in both stoichiometric $Na_2O \cdot 2CaO \cdot 3SiO_2$ glass and glasses belonging to the solid solution (s/s) region between $Na_2O \cdot 2CaO \cdot 3SiO_2$ ($N_1C_2S_3$) and $Na_2O \cdot CaO \cdot 2SiO_2$ ($N_1C_1S_2$) [72]. It was shown that the formation of stoichiometric crystals occurs via nucleation of s/s nuclei enriched in sodium as compared with both the parent glass and the evolving macrocrystals. During crystallization, the composition of s/s

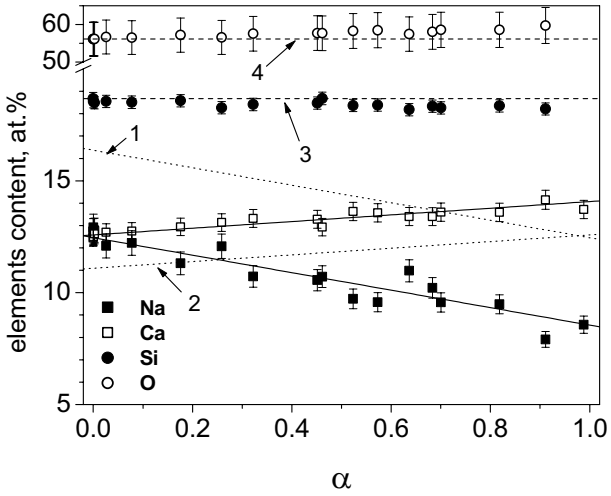

Figure 4.14: Composition of the glassy matrix, measured by EDS (points), and of crystals calculated from the parent glass composition, $N_1C_2S_3$, (dotted lines (1) and (2) – Na and Ca, respectively) versus volume fraction crystallized at $T = 650$ °C. Solid lines fit the experimental data. Dashed lines (3) (Si) and (4) (O) correspond to the parent glass composition [72]

continuously approaches the stoichiometric one. Figures 4.14 and 4.15 show the evolution of crystal and glassy matrix compositions and the corresponding change of the lattice parameter, respectively. An extrapolation of the change of crystal composition to zero time (or zero volume fraction, $\alpha = 0$, of the crystallized phase) gives a strong indication that the critical clusters are also enriched in sodium.

The exhaustion of sodium in the glassy matrix during crystallization leads to an inhibition of nucleation and crystal growth. According to an analysis of overall crystallization kinetics using crystal growth data, the nucleation process is terminated if about 20% of the volume is crystallized. Figures 4.16(a) and (b) present the volume fraction of crystals and the size of the largest crystals as a function of the heat treatment time at $T = 650$ °C for a glass of stoichiometric composition $N_1C_2S_3$. Nucleation takes place up to $t \sim 150$ min($\ln(t) = 5$): $n \cong 4$, $m \cong 1$, $k = n - m \cong 1$ ($n = 1 + 3m$) (see Eq. (4.22)). This conclusion is confirmed by $N(t)$ plots obtained by the "development" method (see Fig. 4.16(c)). But at $\ln(t) > 5$, the crystallization kinetics proceeds only by crystal growth with $n \cong 1$, $m \cong 0.33$, $k \cong 0$ (n=3m).

Diffusion fields around growing crystals, depleted in sodium, can be visualized by a second heat treatment at a temperature corresponding to reasonable values of nucleation and growth rates. A comparison of the sample subjected to single-stage (cf. Fig. 4.17(a)) and double-stage (cf. Fig. 4.17(b)) heat treatments reveals that preexisting crystals (formed in first heat treatment) diminish the number of crystals nucleated in the subsequent treatment. In Ref. [40] it was shown that the nucleation rate decreases with decreasing sodium content in the glass. Hence, it becomes apparent that the areas observed around the large crystals are diffusion fields. A similar transformation path was observed for glasses of compositions be-

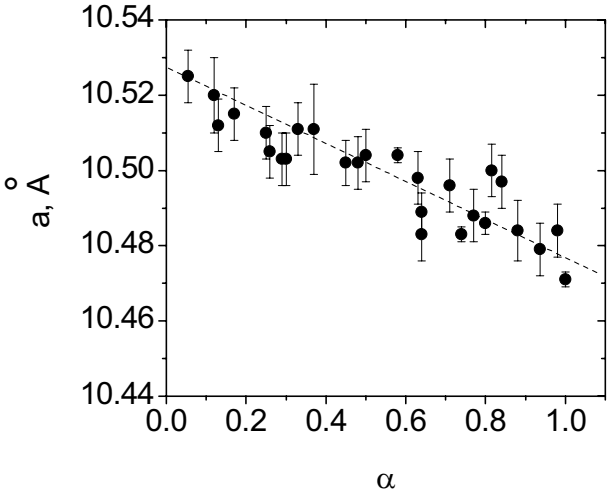

Figure 4.15: Parameter of the hexagonal crystal cell of the solid solutions versus volume fraction of the crystallized phase in stoichiometric $N_1C_2S_3$ glass heat-treated at 650 °C [72]

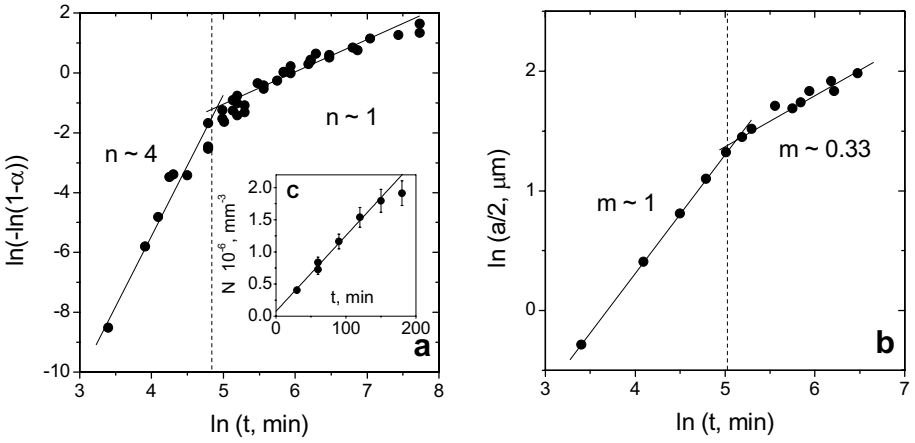

Figure 4.16: Volume fraction of crystals (a), size of largest crystals (b), and number of crystals (c) as a function of heat treatment time at $T = 650$ °C for stoichiometric glass $N_1C_2S_3$ [72]

tween $N_1C_2S_3$ and $N_1C_1S_2$, with the only difference that fully crystallized glasses are s/s with compositions of the parent glasses.

According to the results presented in Fig. 4.18, the difference between the composition of the critical nuclei and the parent glass diminishes as the latter approaches the boundary of s/s formation. The deviation of the nuclei composition from the stoichiometric one (glass $N_1C_2S_3$) or the initial glass compositions (glasses from s/s region) diminishes the thermodynamic driving force for crystallization, ΔG_V, and increases the thermodynamic barrier for

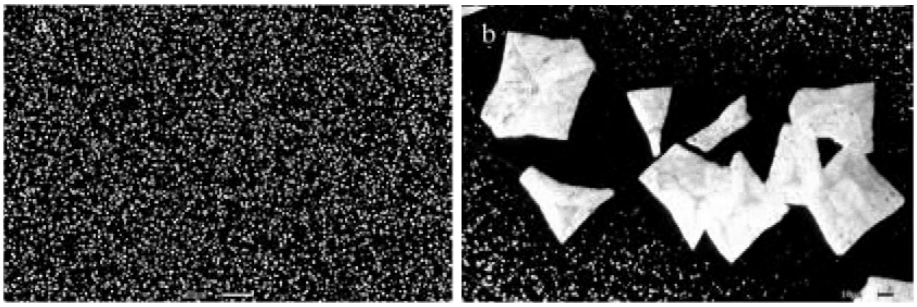

Figure 4.17: SEM micrographs of $N_1C_2S_3$-glass subjected to single (a) and double (b) stage heat treatments: (a) $T = 590$ °C, $t = 1560$ min; (b) $T_1 = 720$ °C, $t_1 = 20$ min and $T = 590$ °C, $t = 1560$ min. The bars have a length of (a) 20 and (b) 10 μm

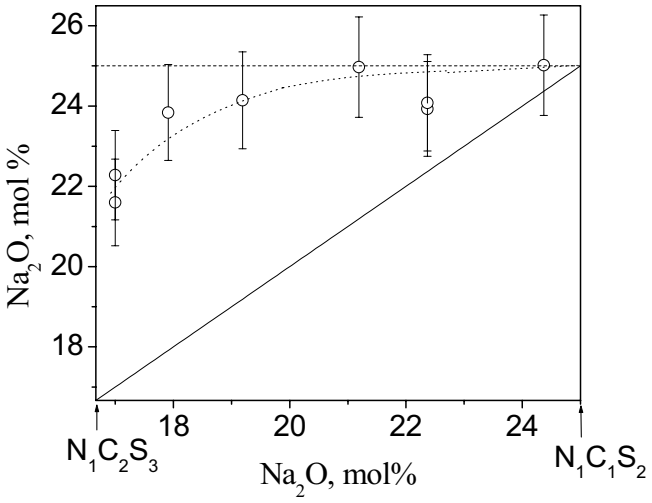

Figure 4.18: Sodium oxide content in the critical nuclei versus composition of the parent glass. The solid line represents the case when the compositions of the critical nuclei and the parent glasses are the same. The upper dotted line shows the sodium oxide content in $N_1C_1S_2$ crystals

nucleation. Moreover, this deviation also leads to an increase in the kinetic barrier. Nevertheless, nucleation of crystals with shifted compositions (as compared with that of the parent glasses) takes place as well. Hence, the decrease in ΔG_V must be compensated by a decrease in surface energy in Eq. (4.4). However, the determination of the variation in surface energy with composition is not a trivial problem and needs further study.

The above interpretation of the shifts in the composition of the critical nuclei is consistent with Ostwald's rule of stages, generalized in Ref. [68] to nucleation as "Those classes of critical clusters determine the process of the transformation, which correspond to a minimum work of critical cluster formation (as compared with all other possible alternative struc-

tures and compositions, which may be formed at the given thermodynamic constraints)." This concept was employed then to develop a new approach to the determination of the work of critical cluster formation based on a generalization of Gibbs' classical approach (cf. Chapters 11 and 12). Recently, this theory was further extended [69–71] to allow one to describe both nucleation and growth processes taking into account changes in the state parameters of the clusters depending on supersaturation and cluster size. Hereby, a criterion was advanced allowing one to determine the changes in the bulk properties of the cluster phase in the course of its growth. The theory has been developed, in detail, so far in application to segregation in regular solutions, condensation and boiling processes. In the future, this theory will be extended to allow application to the description of crystallization processes. Thus, in a correct theoretical treatment not only deviations of the composition of the critical nuclei from the values of the respective macrocopic phases have and can be accounted for then, but also the variations in the composition of the sub- and supercritical crystals.

Since the formation of s/s is a common phenomenon in silicate systems, it is important to keep in mind that the composition of the critical nuclei and, correspondingly, their thermodynamic properties may differ considerably from those of the final macroscopic phase. We expect that, by taking into account such effects, the deviations between experimental results and theoretical predictions concerning nucleation rates and growth processes in these systems will considerably diminish.

4.5.5 On the Possible Role of Metastable Phases in Nucleation

As mentioned in Sect. 4.5.3, the precipitation of metastable phases in the early stages of nucleation may be one of the reasons for the deviation of the critical nuclei composition from that of the evolving (stable) macrophase. Employing the Scapski–Turnbull equation Eq. (4.29) to estimate the crystal/liquid interfacial energy in the thermodynamic barrier for nucleation, one can show that the latter is proportional to the melting enthalpy. Hence, higher nucleation rates of metastable phases than those of the stable phase could be expected due to a lower melting enthalpy and correspondingly a lower thermodynamic barrier. Once crystallites of the metastable phase are formed, they may favor the evolution of crystallites of the stable phase. Thus, metastable phase crystals can catalyze, in principle, nucleation processes of the stable phase. Some authors suggested that such a crystallization path occurs in $Li_2O \cdot 2SiO_2$ (LS_2) glass, which has been used for many years as a model system to study homogeneous nucleation. Indirect evidence favoring this assumption was obtained in Ref. [73], based on a comparative analysis of the nucleation time-lag (obtained by the "development" method) and the induction time for crystal growth. According to these results, the latter considerably exceeds the former.

This interesting observation may result, however, not from processes of formation of metastable phases but from possible differences in the compositions of the near-critical nuclei and macrocrystals (to which experimental measurements of the crystal growth rates refer). In Ref. [74] it was shown that, at a relatively high temperature ($500\,^{\circ}C > T_{max} = 455\,^{\circ}C$), the effect reported in Ref. [73] is not observed if one applies single-stage treatments to measure the nucleation rate. However, the problem posed in Ref. [73] remains open for low temperatures, close to the glass transition interval.

Reference [73] and the papers cited therein stimulated an intensive search for metastable phase formation in LS_2-glass [74–77], mainly by transmission electron microscopy (TEM)

and X-ray diffraction (XRD) methods. In addition to stable lithium disilicate and metastable metasilicate crystals, other, so far unknown, phases were found. However, the observations of different authors were often in contradiction with each other. As it turned out, in general, the probability of observing such new phases increases with a decrease in time and temperature of heat treatment [78]. Due to low nucleation rates and correspondingly low crystal number densities, the statistics of TEM measurements are quite poor. Moreover, the electron beam can degrade the crystals under study in a short time. As an example, however, the results of Ref. [79] show that at $T = 454$ °C (close to the nucleation rate maximum), only $Li_2O \cdot 2SiO_2$ (LS_2) and $Li_2O \cdot SiO_2$ (LS) crystals were detected in the early stages of crystallization (less that 1% crystallized fraction), but LS crystals were not detected in the most advanced stages (5–10% crystallized fraction).

It should be emphasized that, according to the data collected in a time interval 0–100 h at 454 °C, the LS crystal sizes practically do not change, while the LS_2 crystals significantly grow. This result agrees with calculations according to which the thermodynamic driving force for LS crystallization in lithium disilicate glass is lower than that for LS_2 crystals [80], because a higher thermodynamic driving force results in higher growth rates. Since there was no evidence of heterogeneous nucleation of lithium disilicate on lithium metasilicate crystals, it was concluded that LS nucleates concurrently with the stable phase LS_2 and disappears with time. Lithium disilicate has a wide range of solid solution (s/s) formation [81]; hence, one can suppose that the critical nuclei are also (s/s). This assumption does not contradict the results presented above, but allows one to consider changes in composition of the evolving nuclei with size, such as those demonstrated in Sect. 4.5.4 for soda–lime–silica glasses. Thus, in some cases, it is possible that the assumed role of metastable phases in nucleation could simply be a continuous variation of nuclei composition and properties during the phase transformation. However, there also exists another factor which is not normally taken into consideration, but may be of considerable influence, this is the effect of elastic stress on nucleation in glass-forming melts. The possible influence of elastic stress on phase formation will be analyzed in the next section.

4.5.6 Effect of Elastic Stresses on the Thermodynamic Barrier for Nucleation

As follows from Sect. 4.5, the thermodynamic barrier for nucleation, W_*, can be calculated in the framework of CNT by a fit of experimental I_{st} and t_{ind} data employing Eq. (4.32). For such computations, apart from the validity of CNT, no additional assumptions are needed. In addition, one has to make some choice concerning the value of the surface energy in the preexponential term. However, the choice of the surface energy affects the final result only weakly.

According to Eq. (4.4), the work of critical cluster formation W_* monotonically decreases with decreasing temperature. Nevertheless, the value of $W_*(T/T_m)$, calculated from nucleation data for lithium disilicate glass shows, at temperatures close to T_g, an anomalous increase with decreasing temperature (cf. Fig. 4.19).

A similar behavior of W_* was observed also in different other systems, e.g., for wollastonite glass [82]. The above-mentioned deviations of the $W_*(T)$ dependence from the expected

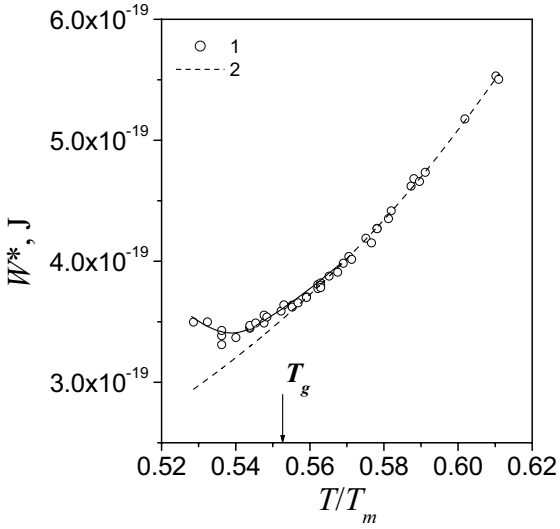

Figure 4.19: Thermodynamic barrier for nucleation in $Li_2O_2SiO_2$ glass (1) estimated from a fit of experimental I_{st} and t_{ind} temperature dependences to Eq. (4.32), and (2) calculated with Eq. (4.4) [87]

(according to CNT) one may be caused by elastic stresses. Since, in most cases of interest, the crystal densities differ from those of the corresponding glasses, glass crystallization is accompanied by volume changes. Such changes may result in stress development which, in turn, diminishes the thermodynamic driving force for phase transformation by a term connected with the elastic strain energy. This energy can partly or even fully [14] suppress the nucleation-growth process. This effect may be the origin not only of the anomalous behavior of the work of critical cluster formation $W_*(T)$, but also of a number of well-known additional experimental facts, e.g., the preference of surface to volume nucleation [12], or the existence of a correlation according to which glasses having densities much lower than those of the corresponding crystals usually reveal only surface crystallization [83].

A theory of nucleation in viscoelastic bodies has been recently developed [84, 85] that takes into account both stress development and relaxation in phase formation in glass-forming melts. It was concluded that the effect of elastic stresses on nucleation can be remarkable if the time of stress development (estimated as the time-lag for nucleation) is smaller than the characteristic time of stress relaxation governed by viscous flow. Such a situation is possible at temperatures lower than the so-called decoupling temperature $T_d \sim 1.2\ T_g$, when the Stokes–Einstein equation may no longer be valid, i.e., when the nucleation kinetics is not governed by viscous flow. A detailed analysis, performed for lithium disilicate glass, shows that elastic stresses may decrease the steady-state nucleation rate by up to two orders of magnitude [86]. In this analysis, the work of critical cluster formation in the absence of elastic stresses was determined following the classical nucleation theory.

Recently an attempt was made directly to estimate the elastic stress energy using the deviation of the $W_*(T)$ curves from the theoretical one [87] for the same glass (lithium disilicate).

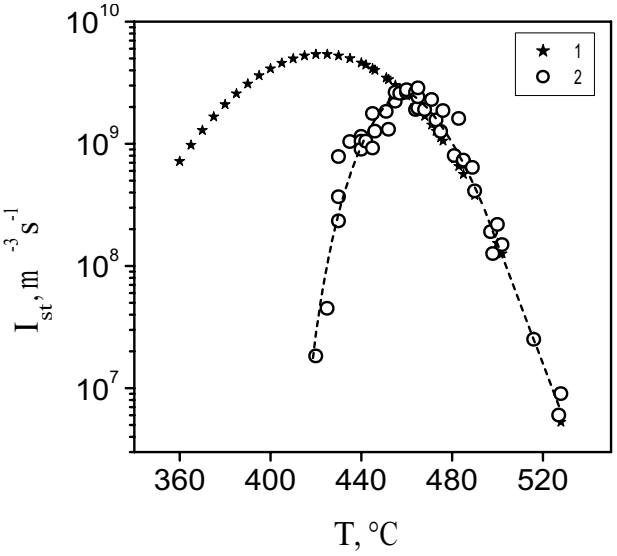

Figure 4.20: Temperature dependence of the steady-state nucleation rate in lithium disilicate glass [87]. (1) I_{st} calculated with Eq. (4.32) for the case when elastic stresses do not play any role; (2) experimental values of I_{st}. The dashed line is placed to guide the eyes

The obtained values of the elastic strain energy were comparable in magnitude with those calculated using the elastic constants of glass and crystals. It should be noted that in the extrapolation of the $W_*(T)$ dependence from relatively high temperatures, at which the elastic stress effect can be neglected, to low temperatures, where the minimum of experimental W_*-values is observed, both the thermodynamic driving force and the crystal/melt surface energy were considered as fit parameters to be determined. Thus, this analysis was performed here without the application of the basic assumptions of CNT. The fitting procedure produced, in accordance with the conclusions made in Sect. 4.5.2, values of the effective surface energy that decrease with decreasing temperature. Moreover, the value of the thermodynamic driving force turned out to be considerably less as compared to that for the respective macroscopic phase.

In Fig. 4.20 experimental data for steady-state nucleation rates versus temperature are shown together with the theoretical ones calculated by neglecting elastic stresses and employing values for the driving force and surface tension obtained via the above-discussed fitting procedure. At low temperatures, the calculated I_{st}-values considerably exceed the experimental data giving an indirect evidence of the essential role of elastic stresses in nucleation.

4.6 Crystal Nucleation on Glass Surfaces

4.6.1 Introductory Remarks

As already mentioned, surface crystallization is much more widespread than homogeneous volume crystallization. As shown in Ref. [12], about 90% of the silicate glasses have a value of the reduced glass transition temperature $T_{gr} > 0.60$ and, hence, only reveal surface crystallization on laboratory time scales (see Sect. 4.4). This particular form of glass crystallization is of great practical importance [33, 88–92].

In Ref. [93], the hypothesis was developed that the effect of elastic stresses, discussed in Sect. 4.5, may be a possible cause for the preferential surface crystallization. According to the results of Ref. [94], close to or at interfaces the decrease in the thermodynamic driving force for crystallization due to elastic stresses may be less effective than for the case of nucleus formation in the bulk of the material. By this reason, a reduction in the thermodynamic barrier for surface nucleation can be expected as compared with homogeneous nucleation in the bulk of the glass.

Surfaces can be generated and modified in a number of different ways, moreover, glass surfaces are exposed to various, often hard to control, factors. This variety in the possible states and properties of glass surfaces is the main reason why attempts to study the kinetics of surface crystallization, especially the nucleation stage, are faced with serious difficulties. Therefore, analyses dealing with crystal nucleation on glass surfaces are mainly of qualitative character or supply us merely with a limited amount of data about the number density of crystals evolving on the different kinds of glass surfaces. A comprehensive analysis of different kinds of defects on various types of glass surfaces in connection with crystal nucleation can be found in Ref. [92]. Here we focus on a few papers that present data on the *nucleation kinetics* on glass surfaces.

Theoretically it is possible to imagine the existence of homogeneous nucleation on flawless glass surfaces [95]. This statement means that nucleation can be supposed to have the same probability to occur on any given surface site. However, so far there does not exist any reliable information that such kind of surface nucleation really occurs. Most authors believe and experiments give strong evidence that surface nucleation is a particular process of heterogeneous nucleation occurring on surface defects, such as scratches, tips, microcracks, compositional inhomogeneities, solid particles, etc. The number of such nucleation sites restricts the total number of crystals that may form. Fast nucleation and fast exhaustion of such active sites are the main reasons why only a constant number density of crystals, N, is (typically) observed experimentally in most glasses and most types of heat treatment.

Existing experience shows that it is indeed quite difficult to study, in detail, the surface nucleation kinetics. The values of N determined experimentally can strongly depend on the type of the surface and can vary by many orders of magnitude for difference samples even of the same material but prepared differently, e.g., for a fractured glass surface and a surface of a powdered glass (cf. Refs. [92, 96, 97]). Strnad and Douglas [98] were among the first to report nucleation rates on glass surfaces. The presented nucleation rates for three soda-lime-silica glasses increase with decreasing temperature (Fig. 4.21). Unfortunately neither the method used nor the primary kinetic $N(t)$ curves are given in their paper Ref. [98]. In addition, any

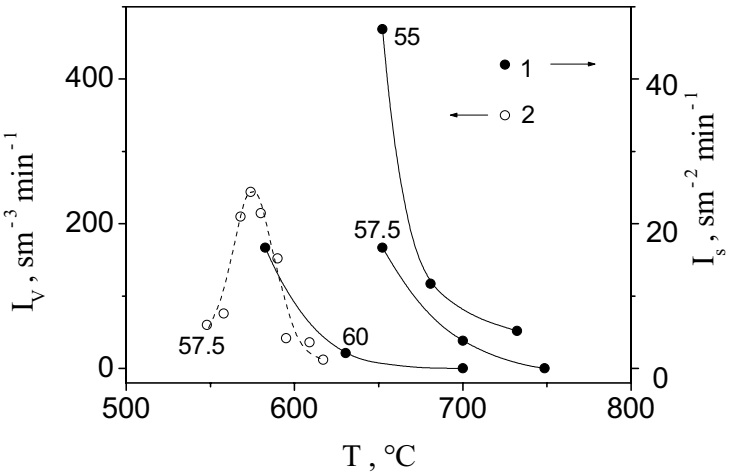

Figure 4.21: Temperature dependences of the nucleation rate of $Na_2O \cdot 2CaO \cdot 3SiO_2$ crystals in the volume (I_V) and at the surface (I_s) for glasses of compositions $xNa_2O \cdot xCaO \cdot (1 - 2x)SiO_2$ [98]. The numbers near the curves show the content of SiO_2 in mol%

information about the type of surface is absent. All these facts complicate the analysis of the data reported by them.

In 1986, employing the "development" method, Kalinina et al. [99] obtained kinetic $N(t)$ curves for polished surfaces of cordierite glass, which not only show an increase in the crystal number density, but also provided evidence for nonsteady state surface nucleation.

Nucleation of cristobalite crystals at the atmospheric side of float glass was studied in detail by Deubener et al. [100] by the single-stage treatment method. They have shown that at relatively low temperatures (665–730 °C) the induction period is followed by a linear increase in the crystal number density, while at high temperatures (850–900 °C) such period is absent, and the $N(t)$ curves show saturation. The nucleation rates calculated from the slope of the linear parts of the $N(t)$ curves are presented in Fig. 4.22. The authors interpreted nucleation as being heterogeneous on surface sites associated with impurity particles, but did not comment on the difference in the temperature dependences of nucleation rates at low (1) and high (2) temperatures.

4.6.2 Crystal Nucleation on Cordierite Glass Surfaces

Considerable progress in understanding surface nucleation was achieved by a cooperative program (1990 to 2000) of the Technical Committee 7 of the International Commission on Glass [101]. Cordierite glass ($2MgO \cdot 2Al_2O_3 \cdot 5SiO_2$) was chosen as a model system owing to its high chemical durability, polymorphic course of crystallization, and absence of volume nucleation. Two easily distinguishable crystal morphologies were observed on glass surfaces polished by cerium oxide after heat treatments at 800–910 °C (see Fig. 4.23) [99, 102, 103]. One of these morphologies refers to the well-known metastable high-quartz solid solution crystals ("μ-cordierite"), while the other refers to the so-called X-phase (the latter one has so

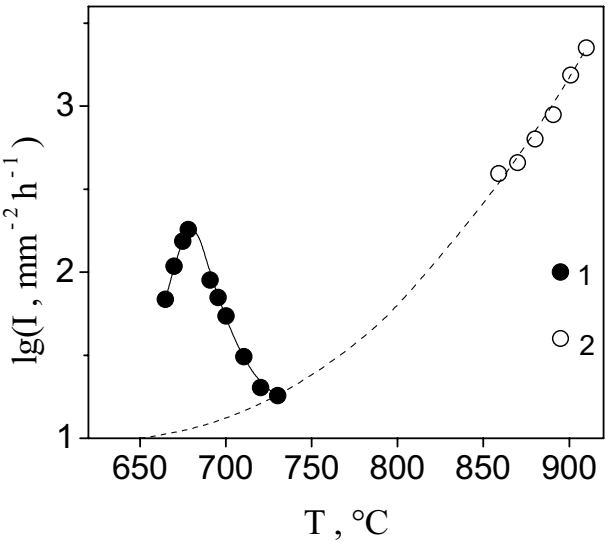

Figure 4.22: Temperature dependence of the surface nucleation rate of cristobalite crystals at the atmospheric side of float glass ((1) and (2) – see text) [100]

far not been identified due to the insufficient volume fraction crystallized and as a result only very poor X-ray diffraction spectra are obtained). These two types of crystals exhibit quite different nucleation and growth kinetics, the first will be discussed in the following analysis.

It will be shown that nucleation occurs on some (yet unknown) surface defects that act as active centers for heterogeneous nucleation. To diminish scattering in the crystal number density (caused by difficulties in reproducing the surface quality), the following precautions were undertaken in Ref. [102]: (i) 5–6-mm-wide, 40–70-mm-long, 1-mm-thick glass plates with polished sides were prepared. Then, notches were made across one side. For each heat-treatment time at a given temperature, a sample was broken off from the same plate at the cross-cut notches.

Thus, similar qualities of polished surfaces could be expected, at least, for a given temperature. (ii) All heat treatments were performed in a vertical silica–glass tube closed by a lid, which was set in an electric furnace. A sample was placed directly into a small silica–glass crucible in such a way as to avoid any contact of the polished glass sides with its wall. These precautions were undertaken against possible contaminations during heat treatment.

4.6.3 Nucleation Kinetics Measured by the "Development" Method

Figure 4.24 shows typical plots of number densities, N_μ and N_X, for μ-cordierite and X-phase crystals, respectively, versus time of nucleation obtained by the "development" method [102]. The number of μ-cordierite crystals, N_μ, does not vary within the limits of experimental scatter, while the values of N_X clearly increase with increasing nucleation time, revealing a saturation, N_S^X, at times larger than about 1000 h. The saturation of the $N_X(t)$ curves indicates

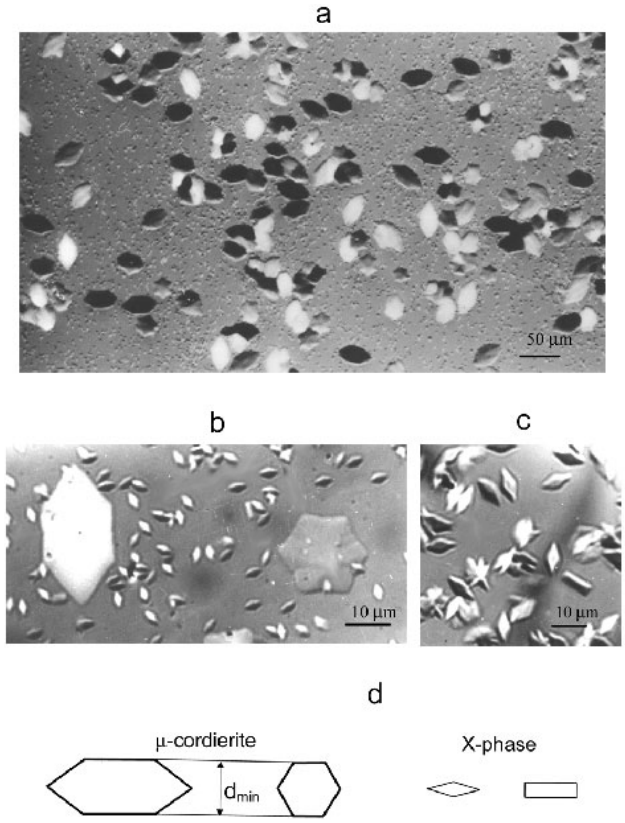

Figure 4.23: Photographs of the X-phase and μ-cordierite crystals on a polished cordierite glass heat treated at $T = 825$ (a,b) and 850 °C (c) for 72 (a), 43 (b), and 94 h (c). The development time is (a,b) 1 and (c) 2.5 h at $T_d = 933$ °C. (d) Characteristic shapes of the two phases. Data are taken from Ref. [102]

heterogeneous nucleation governed by exhaustion of nucleation sites. The sigmoidal shape of the $N_X(t)$ curves results from nonsteady state nucleation [104]. The absence of an initial period of increase in the number of μ-cordierite crystals (as observed for the X-phase crystals) is caused by the combination of a small number of nucleation sites and their high activity, which leads to a saturation $N_\mu = N_S^\mu$ before the development temperature is reached. The considerable difference between N_S^X and N_S^μ ($N_S^X / N_S^\mu \cong 50$) indicates that the formation of the X-phase and μ-cordierite are induced by different kinds of nucleation sites.

Similar findings were observed for devitrite, diopside, and tridymite crystals on as-received surfaces of float glass [89], which demonstrate quite different levels of saturation, N_S. These findings resemble different kinds of surface defects of float glass that are responsible for nucleation at low and high temperatures (presented in Fig. 4.22). The strong differences in the temperature dependences of the saturation levels, N_S, for the X-phase and μ-cordierite

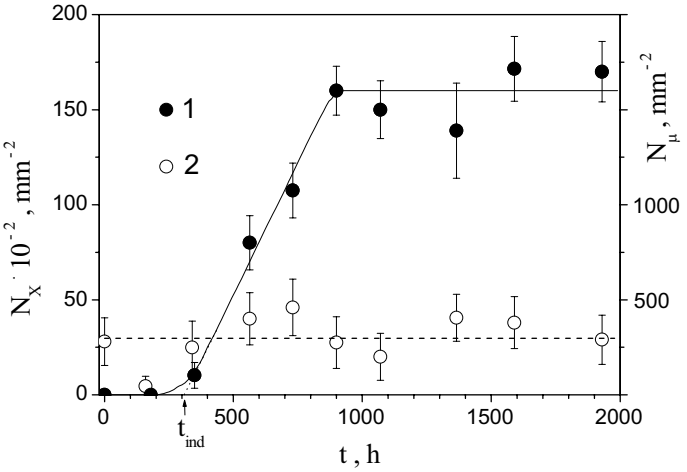

Figure 4.24: Crystal number density of the X-phase (1) and μ-cordierite (2) crystals on a polished surface of a cordierite glass versus time of treatment at $T = 800$ °C ($T_d = 933$ °C for 0.5–1.5 h). Data are taken from Ref. [102]

(Fig. 4.25) support the conclusion about the different nature of the nucleation sites. The drastic drop of N_S^X with increasing temperature allows one to conclude that some of the potential nucleation sites for the X-phase existing on the parent glass surface can disappear during heat treatment, thus causing no nucleation.

Kinetic $N_X(t)$ curves, similar to those shown in Fig. 4.24, were obtained for the temperature range 800–910 °C [102]. Since different polished plates were used for different temperatures, some scattering in the N_S^X numbers for a given temperature was observed. As will be shown below, N_S^X is proportional to the number, N_0, of nucleation sites on the parent surface. Hence the curves $N_X(t, T)$ can be normalized by $N_{Sr}^X(T)$, which was obtained for one polished plate used as a surface quality reference

$$N_{X,r}(t, T) = N_X(t, T)\frac{N_{Sr}^X(T)}{N_S^X(T)} \,. \tag{4.44}$$

Normalized curves $N_{X,r}(t)$ were used to determine the maximum nucleation rates, I_{max}^X, as the highest value of the derivative $(dN_{X,r}/dt)_{max}$ (see Table 4.3). The results are plotted as a function of temperature in Fig. 4.26. Table 4.3 includes also $N_{Sr}^X(T)$, the induction period, t_{ind}, and some parameters of nucleation sites that will be introduced later. The values of t_{ind} were determined from the intercept of the time-axis with the line having a slope equal to I_{max}^X that crosses the $N_{X,r}(t)$-curve at a moment of time corresponding to $(dN_{X,r}/dt)_{max}$ (see Fig. 4.24). The temperature dependence of $I_{max}^X(T)$ reveals a maximum at $T_{max} = 890$ °C, which is about 70 °C higher than the glass transition temperature, $T_g = 820$ °C.

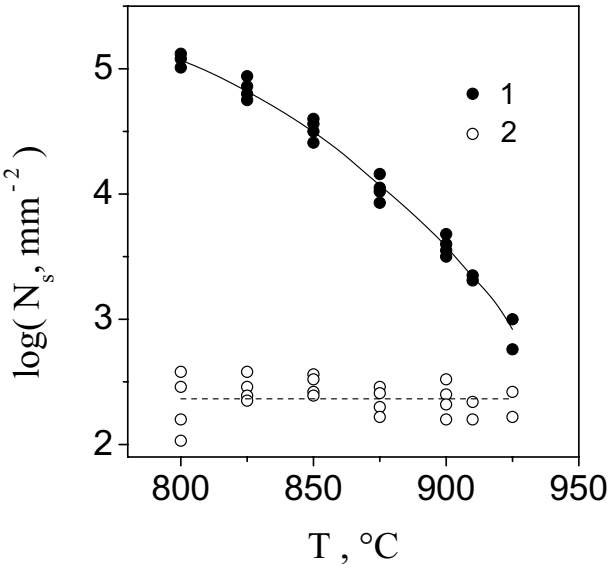

Figure 4.25: Crystal number density saturation level plotted against the temperature of nucleation for the X-phase (1) and μ-cordierite (2) on a polished surface of cordierite glass. Data are taken from [102]

Table 4.3: Parameters of the $N_{Xr}(t,T)$ curves and nucleation rates [103]

T	t_{ind}	$N^X_{Sr} \times 10^{-3}$	$I^X_{\max}$	$(\alpha_X + \beta_D)\times 10^4$	$\alpha_X \times 10^4$
°C	h	mm^{-2}	$\text{mm}^{-2} \cdot \text{min}^{-1}$	min^{-1}	min^{-1}
800	310	114.8	3.2	0.28	0.054
825	41	66.1	23.2	3.51	0.550
850	17	31.6	33.0	10.40	0.954
870	6.5	14.5	54.9	37.90	2.410
890	4.0	6.0	59.3	98.30	6.270
900	2.2	4.0	57.1	143.00	3.780
910	1.5	2.2	32.5	145.00	1.200

4.6.4 Nucleation on Active Sites of Variable Number

In general, the number of potential nucleation sites can vary during heat-treatment for reasons that are not connected with nucleation itself. In Refs. [105, 106] a formal theoretical scheme for the nucleation kinetics was developed for the cases of increasing and decreasing number density of active sites. The latter version corresponds to the case of X-phase nucleation. A brief theoretical description of nucleation kinetics allowing to account for a deactivation of active sites is presented below [103]. As will be shown, such mechanism is an alternative realistic possibility in surface nucleation.

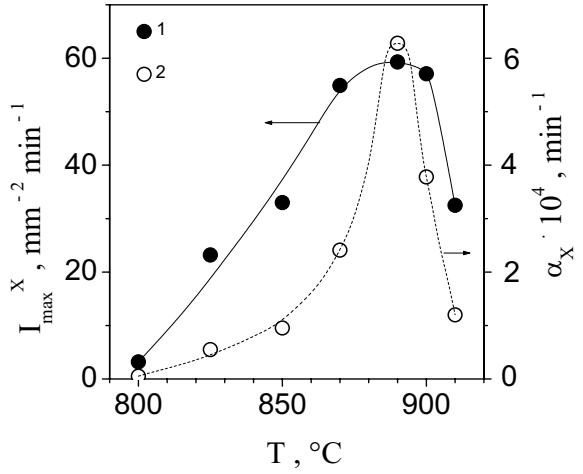

Figure 4.26: Effective nucleation rate $I^X_{\max}$ and probability of crystal nucleation on active sites per unit time, α_X, for X-phase crystals on polished surfaces of cordierite glass versus temperature [102]

The number of crystals, $N(t, T)$, randomly nucleating at an unit area of the surface in time t, and the number of randomly deactivated active sites per unit area, $N_{\rm D}(t, T)$, can be described by a system of differential equations of the form

$$\mathrm{d}N = (N_0 - N - N_{\rm D})\alpha \, \mathrm{d}t \ , \tag{4.45}$$

$$\mathrm{d}N_{\rm D} = (N_0 - N - N_{\rm D})\beta_{\rm D} \, \mathrm{d}t \ , \tag{4.46}$$

where N_0 is the initial number density of active sites, $(N_0 - N - N_{\rm D})$ is the number density of active sites at time t, α is the probability of crystal nucleation on any active site per unit time, and $\beta_{\rm D}$ is the probability of active site deactivation per unit time. In the general case, α and $\beta_{\rm D}$ are functions of time t. Combining Eqs. (4.45) and (4.46), we get

$$\mathrm{d}(N + N_{\rm D}) = (N_0 - N - N_{\rm D})(\alpha + \beta_{\rm D}) \ \mathrm{d}t \ , \tag{4.47}$$

$$N + N_{\rm D} = N_0 \left\{ 1 - \exp\left[- \int_0^t (\alpha + \beta_{\rm D}) \ \mathrm{d}t' \right] \right\} \ . \tag{4.48}$$

A substitution of Eq. (4.48) into Eqs. (4.45) and (4.46) yields

$$N(t, T) = N_0 \int_0^t \alpha \exp\left[- \int_0^{t'} (\alpha + \beta_{\rm D}) \, \mathrm{d}t'' \right] \mathrm{d}t' \ , \tag{4.49}$$

$$N_{\rm D}(t, T) = N_0 \int_0^t \beta_{\rm D} \exp\left[- \int_0^{t'} (\alpha + \beta_{\rm D}) \, \mathrm{d}t'' \right] \mathrm{d}t' \ . \tag{4.50}$$

As can be seen from Eq. (4.49), N is proportional to N_0. Hence the normalization procedure via Eq. (4.44) is correct.

Let us consider in more detail one of the simplest cases. Suppose that $\alpha = 0$ holds for $0 \leq t < t_{\text{ind}}$, α is constant (different from zero) for $t \geq t_{\text{ind}}$, and β is constant for $t \geq 0$. Then from Eq. (4.49) (see [103]) we get

$$\begin{aligned} N(t) &= 0 \quad \text{for} \quad t < t_{\text{ind}} \,, \\ N(t) &= N_0' \frac{\alpha}{\alpha + \beta_{\text{D}}} \{1 - \exp[-(\alpha + \beta_{\text{D}})(t - t_{\text{ind}})]\} \quad \text{for} \quad t > t_{\text{ind}} \,, \\ N_0' &= N_0 \exp(-\beta_{\text{D}} t_{\text{ind}}) \,. \end{aligned} \tag{4.51}$$

For $t \to \infty$, Eq. (4.51) yields

$$N(t \to \infty) = N_0' \frac{\alpha}{\alpha + \beta_{\text{D}}} \,. \tag{4.52}$$

Obviously, $N(\infty)$ can be identified with the level of saturation N_{S}.

The surface nucleation rate $I(t, T)$ is equal, by definition, to the derivative $\mathrm{d}N/\mathrm{d}t$. Then we have from Eq. (4.51)

$$I = N_0' \alpha \exp[-(\alpha + \beta_{\text{D}})(t - t_{\text{ind}})] \,. \tag{4.53}$$

The nucleation rate has its maximum $I_{\max}$ at $t = t_{\text{ind}}$

$$I_{\max} = N_0' \alpha \,. \tag{4.54}$$

Dividing Eq. (4.54) by Eq. (4.52) yields

$$\frac{I_{\max}(T)}{N(\infty)} \equiv \frac{I_{\max}(T)}{N_S(T)} = \alpha + \beta_{\text{D}} \,. \tag{4.55}$$

Employing the $I_{\max}$ and N_{S}-values for the X-phase, we find via Eq. (4.55) the values of $\alpha_X + \beta_{\text{D}}$ (see Table 4.3). According to the experimental data given in Table 4.3 the term $\exp[-(\alpha_X + \beta_{\text{D}})t_{\text{ind}}]$ varies insignificantly with temperature. Hence, the value of N_0' (see Eq. (4.52)) also depends only weakly on temperature. On the other hand, N_{S}^X is a strong function of temperature (Fig. 4.25). Such result can be found only then if $\alpha/(\alpha + \beta_{\text{D}})$ in Eq. (4.52) is a strong function of temperature. It means that the relations

$$\beta_{\text{D}} \gg \alpha \,, \quad \alpha + \beta_{\text{D}} \cong \beta_{\text{D}} \tag{4.56}$$

have to be fulfilled. Thus, one can suppose that a considerable fraction of the active sites loose their activity causing no nucleation.

Accounting for Eqs. (4.55) and (4.56), the parameter β_{D} can be approximately estimated as

$$\beta_{\text{D}} \cong \frac{I_{\max}^X}{N_{\text{S}}^X} \,. \tag{4.57}$$

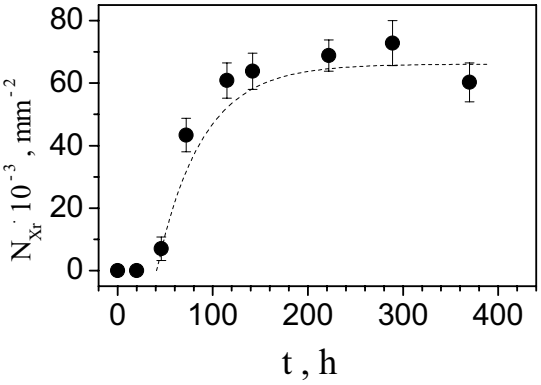

Figure 4.27: Number density of X-phase crystals versus time of nucleation at $T = 825$ °C. Points are normalized with Eq. (4.44). The dashed line was calculated by Eq. (4.51) [102, 103]

The values of β_D, calculated in this way, are presented in Table 4.3.

The quantity α can be evaluated, combining Eqs. (4.54) and (4.51), as

$$\alpha = \frac{I_{max}}{N_0' \exp(-\beta_D t_{ind})} . \tag{4.58}$$

In order to apply Eq. (4.58), one has to know the value of N_0'. Obviously, N_S cannot be greater than the initial number density of active sites N_0 and N_0'. The maximum value for N_S^X, that is equal to 1.15×10^5 mm^{-2}, was obtained for a temperature $T = 800$ °C (see Table 4.3). Let us suppose a value of N_0' equal to $N_0' = 10^6$ mm^{-2}. The values of α_X, calculated from Eq. (4.58) with $N_0' = 10^6$ mm^{-2}, are shown in Table 4.3. The maximum of α_X is located in the same temperature range as for the $I_{max}^X(T)$ curve (see Fig. 4.26, Table 4.3).

Using the value of $\alpha_X + \beta_D$, t_{ind} and I_{max}^X and Eqs. (4.51) and (4.54), one can plot the $N_{X,r}(t)$ curves. An example of such calculation is presented in Fig. 4.27 together with the experimental values of N_{Xr}. The agreement between calculated and experimental data could be improved taking into account that α_X and β_D can be time-dependent functions.

4.6.5 Analysis of Nucleation Kinetics by Köster's Method

As shown earlier the "development" method cannot be employed to measure nucleation rates of μ-cordierite crystals due to the high activity, α, and the small number density, N_0, of active sites. Nevertheless, crystal size distributions from single-stage heat treatments give evidence that nucleation takes place in the temperature range 850–1010 °C (see e.g. Fig. 4.28(a)) [107, 108]. Hence, Köster's method can be used. According to this method, the average "birth-date" for crystals belonging to a given size group with a mean size D can be written as

$$t_D = t_T - \frac{D}{2U(T)} , \tag{4.59}$$

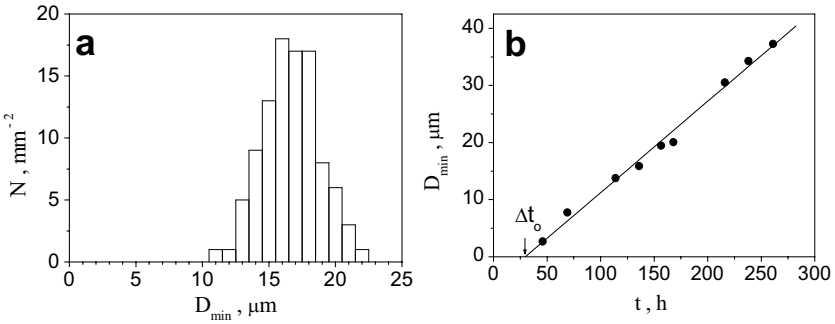

Figure 4.28: (a) Size distribution of μ-cordierite crystals on the surface of cordierite glass polished by cerium oxide after heat treatment at $T = 850$ °C for 168 h [108]. (b) Minimum diameter of the largest μ-cordierite crystals versus time of treatment at $T = 850$ °C [108]

where t_T is heat treatment time at temperature T and U is the crystal growth rate. Knowing t_D and the number of crystals of a given size group one can plot the complete kinetic curve, $N(t)$.

The crystal growth rate of μ-cordierite was calculated from the dependences of the largest crystal sizes on heat treatment time like that presented in Fig. 4.28(b). No crystals were observed during a time Δt_0, which decreased with increasing temperature. Δt_0 may be imagined as a sum of the induction time t_n, due to nucleation kinetics, and of the time t_g, during which the growth rate is strongly affected by crystal size. Therefore, two limiting cases can be considered, $\Delta t_0 = t_n$ and $\Delta t_0 = t_g$. The first case corresponds to Eq. (4.59). In the second case, Eq. (4.59) has to be transformed to

$$t_D = t_T - \Delta t_0 - \frac{D}{2U(T)} \ . \tag{4.60}$$

Thus, two kinetic curves $N(t)$ can be obtained from one crystal size distribution. The true one can be expected to be located between them (Fig. 4.29).

The sigmoidal shape and the strong saturation of the kinetic curves $N(t)$ are typical of nonsteady state heterogeneous nucleation that is restricted by the number of active sites [12]. Unlikely nucleation of the X-phase, the level of saturation, N_S^μ, does not vary with temperature. Hence it is equal to the number density of active sites, N_0, on the parent glass surface. Such kinetics can be described by the following equation derived in [109]

$$\frac{N(t)}{N_0} = 1 - \exp\left\{-\alpha_{st} t \left[\exp\left(-\frac{\tau}{t}\right) + \left(\frac{\tau}{t}\right) \mathrm{Ei}\left(-\frac{\tau}{t}\right)\right]\right\} \ , \tag{4.61}$$

where α_{st} is the stationary value of the crystal nucleation probability $\alpha(t) = \alpha_{st} \exp(-\tau/t)$ on a single active site per unit time, τ is the time-lag of nucleation and Ei is the exponential integral function.

The values of $\alpha_{\mu,st}$ and τ, calculated by fitting $N(t)/N_0$ measurements to Eq. (4.61), are plotted in Fig. 4.30 as functions of temperature together with the crystal growth rate, U. The probability of nucleation on single active sites increases with increasing temperature, at

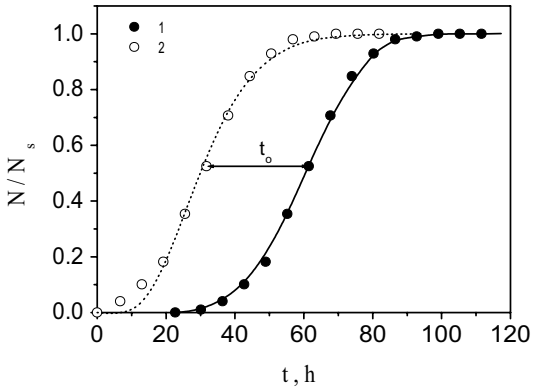

Figure 4.29: Kinetic $N(t)$ curves of μ-cordierite crystal nucleation on surfaces of cordierite glass polished by cerium oxide and heat treated at $T = 850$ °C. Points (1) and (2) are calculated from the crystal size distribution using Eqs. (4.59) and (4.60), respectively. The level of saturation, N_S, is equal to 100 mm^{-2}. The lines are plotted by utilizing Eq. (4.61) with the fit parameters τ and $\alpha_{\mu,st}$ (data are taken from [108])

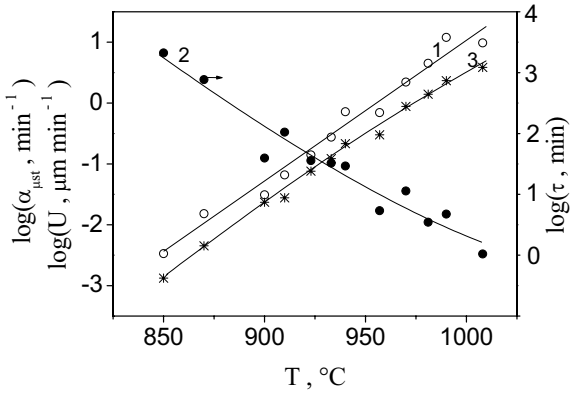

Figure 4.30: Temperature dependences of the stationary probability, $\alpha_{\mu,st}$, of μ-cordierite nucleation on single active sites per unit time: (1) time-lag of nucleation, τ, on single active sites, (2) crystal growth rate, U, (3) $\alpha_{\mu,st}$ and τ refer to kinetic curves plotted with Eq. (4.61) (data are taken from Ref. [108])

least, up to 1010 °C, along with the crystal growth rate. It should be noted that, by the time the $N(t)$ curve saturates, the coefficient α_μ does not reach its stationary value $\alpha_{\mu,st}$ and the inequalities $0.1 < \alpha_\mu(t_s)/\alpha_{\mu,st} < 0.7$ hold in the temperature range 850–1008 °C.

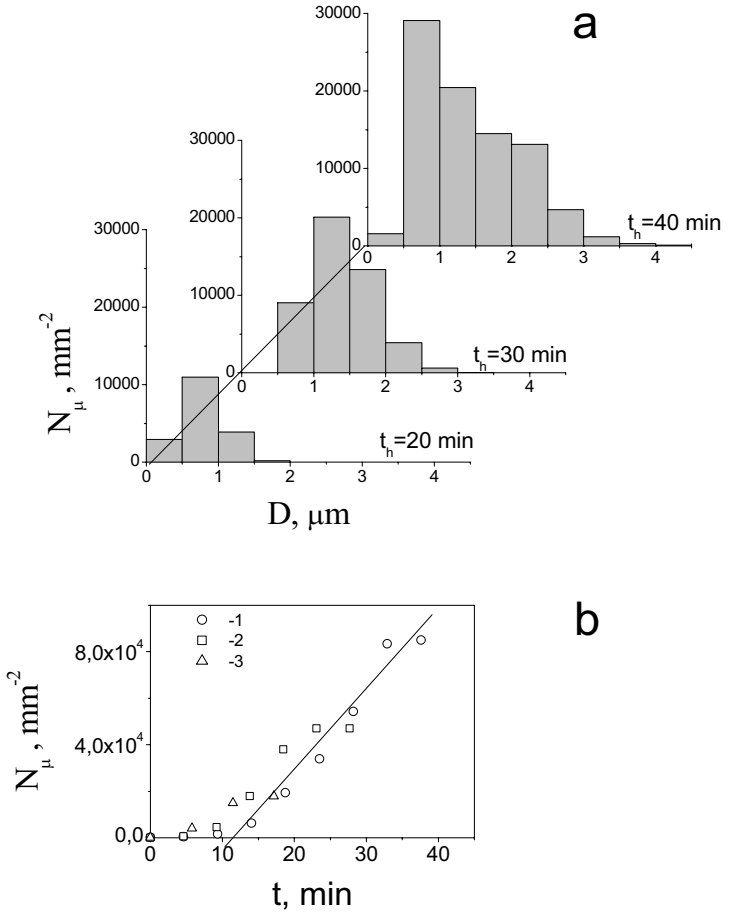

Figure 4.31: (a) Size distributions of μ-cordierite crystals on diamond polished surfaces of cordierite glass (containing 8.14 wt% TiO_2) after treatment at 850 °C for 20, 30 and 40 min. (b) Calculated time dependence $N(t)$ for these treatments ((1) 40, (2) 30, (3) 20 min) [110]

4.6.6 Comparison of Surface and Volume Nucleation

As far as we know, internal and surface nucleation rates in the same glass have been measured simultaneously only for a cordierite glass containing 8.1 wt% TiO_2 (which serves as a nucleation catalyst) [110]. Nucleation rates of μ-cordierite crystals at diamond-polished surfaces were estimated by Köster's method from size distributions such as those presented in Fig. 4.31. The internal nucleation rates of the same crystal phase were measured by the "development" method. The temperature dependences of both surface (apparent rate $I_s = dN/dt$) and steady-state bulk nucleation rates, I_V, are shown in Fig. 4.32. These plots demonstrate clearly that the maximum surface nucleation rate occurs at a temperature considerably higher than that of the maximum volume nucleation rate.

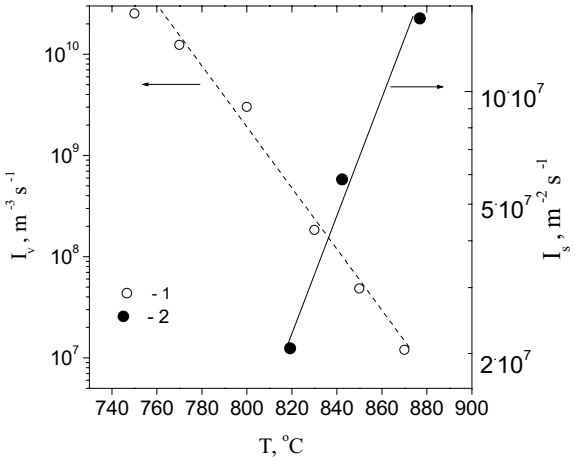

Figure 4.32: Steady-state bulk nucleation rate, I_V (1), and apparent surface nucleation rate, I_S (2), versus temperature in a cordierite glass with 8.14 wt% TiO_2 (data are taken from Ref. [110])

Table 4.4: Values of $\Delta T = T_{max} - T_g$ for different glasses and types of surfaces (here $^{(*)}$ refers to cristobalite-crystal nucleation at two different types of active sites on the atmosphere side of float glass.)

Glass	Surface	Crystal	$\Delta T = T_{max} - T_g$	Ref.
Cordierite	Mechanically polished with cerium oxide	X-Phase	70	[103]
		μ-cordierite	> 190	[108]
	Fractured	μ-cordierite	> 235	[114]
Cordierite with 8.1 wt % TiO_2	Mechanically diamond-polished	μ-cordierite	> 110	[110]
Float	Fire-polished	Cristobalite	130*	[100]
		Cristobalite	> 300*	[100]

As we have shown in Sect. 4.4 (see Fig. 4.10, curves (1), (6)–(8)), a decrease in the thermodynamic barrier results in an increase of both T_{max} and $I(T_{max})$. Hence the difference in the temperature dependences of I_s and I_V can be interpreted as the result of a decrease in the thermodynamic barrier for nucleation (decrease of Φ in Eq. (4.13)), when one passes from volume heterogeneous nucleation to surface heterogeneous nucleation. The maximum of volume homogeneous nucleation is found, as a rule, in the vicinity of the glass transition temperature [33, 95]. According to Table 4.4, for the case of heterogeneous surface nucleation the values of T_{max} considerably exceed the glass transition temperature. This fact agrees with the theoretical analysis performed in Sect. 4.4 according to which T_{max} increases with decreasing thermodynamic barrier for nucleation.

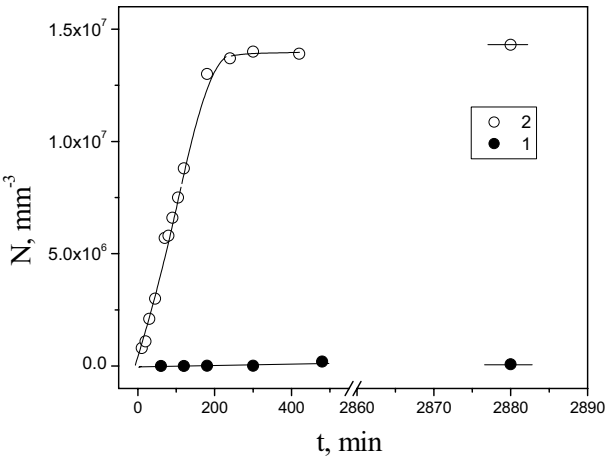

Figure 4.33: Dependences of the number of $Li_2O \cdot 2SiO_2$ crystals on nucleation time at $T = 480$ °C for 23.4 $Li_2O \cdot 76.6\,SiO_2$ (mol%) glass free from additives (1) and with 0.03 wt% Ag exposed to X-ray radiation (2) (data are taken from Ref. [111])

Heterogeneous bulk nucleation can occur independently and simultaneously with homogeneous nucleation [111]. Figure 4.33 illustrates such case. Curves (1) and (2) represent the number density of $Li_2O \cdot 2SiO_2$ crystals versus time of nucleation in lithium disilicate glass free from additives and with 0.03 wt% Ag, respectively. Curve (1) refers to homogeneous nucleation while curve (2) corresponds to nucleation on Ag-crystals. The rate of heterogeneous nucleation substantially exceeds that of homogeneous nucleation as long as there free Ag-crystals exist at which lithium disilicate crystals nucleate ($t < 200$ min). After exhaustion of Ag ($t > 200$ min), only homogeneous nucleation takes place.

4.7 Concluding Remarks

It follows from the present review that the main problem regarding the application of the classical nucleation theory (CNT) to a quantitative description of nucleation kinetics in glass-forming liquids consists in the adequate description of the properties of critical nuclei. Direct experimental methods usually employed to study micron-size or larger crystals cannot be used for nuclei of critical sizes, which are only a few nanometers in size in the temperature range of interest. Therefore, one typically follows Gibbs' description of heterogeneous systems and assigns the thermodynamic properties (particularly the thermodynamic driving force for crystallization) of proper macrophases to the critical nuclei, thus assuming that critical nuclei and evolving stable macrophase can be characterized by widely similar bulk state parameters. However, since the thermodynamic barrier for nucleation includes together with the thermodynamic driving force the nucleus-melt surface energy, a maximum thermodynamic driving force (corresponding to the stable phase) is not a necessary condition to attain the lowest value of the thermodynamic barrier and, correspondingly, the highest value of the nucleation rate.

Moreover, the thermodynamic properties of critical nuclei can be affected by elastic stresses arising from differences between the densities of the nucleus and the melt. Hence, one can suppose that in some cases the deviation of the composition of the nuclei from those of the stable phase may be accompanied by the approach of the nuclei density to that of the melt. In such cases, the effect of elastic stresses is reduced and, correspondingly, a decrease in the thermodynamic barrier for formation of such nuclei (as compared with the respective value for the stable phase) could be expected. Thus, elastic stress effects can considerable complicate the thermodynamic aspects of nucleation and extend the variety of possible structures and compositions of the critical nuclei.

Since, with rare exceptions, direct measurements of the characteristic properties of critical nuclei are inaccessible, it is difficult or impossible to attribute the measured nucleation rates to definite crystal phases. It seems that such situation will not change in the near future. Nevertheless, there are indirect evidences (partly presented in this review) for the existence of considerable differences between the properties of near-critical nuclei and those of the respective stable macroscopic phases. Glasses of stoichiometric compositions have been used as model systems in a variety of studies of crystal nucleation. Such choice was made in the hope that it should be possible to treat such systems similarly to one-component ones. However, it became clear now that a stoichiometric glass composition does not guarantee that the nuclei have the same stoichiometric composition as well. Moreover, the assumption that stoichiometric liquids consist only of stoichiometric species is a very rough one. Therefore, systematic investigations of nucleation rates versus glass compositions are of great interest for understanding the true nature of the nucleation processes. The great value of such analyses will be reinforced if simultaneously the crystal growth rates are measured. In this way, additional informations can be accumulated allowing to specify the mechanisms of nucleation and growth for the systems under study.

On the other hand, the further development of the classical theory of nucleation and growth – aimed to describe not only critical nuclei formation but also its subsequent growth including the possible evolution of its composition – may allow a more adequate description of the phase transformation kinetics, in general. Different theories and modifications of the CNT do indeed exist (see e.g. [112,113]). However the description of the critical nuclei properties remains the main problem of the application of any nucleation theory regardless of the approaches used to estimate the thermodynamic barrier for nucleation.

Acknowledgements

The authors would like to express their gratitude to the State of Sao Paulo Research Foundation FAPESP (Grants 03/12617-0; 2003/03575-2; 99/00871-2), CNPq, and Pronex (Brazil) for financial support.

References

[1] J.W.P. Schmelzer, *Introductory Remarks*, In: J.W.P. Schmelzer, G. Röpke, and V.B. Priezzhev, *Nucleation Theory and Applications* (Joint Institute for Nuclear Research Publishers, Dubna, 1999).

[2] J.M.F. Navarro, *El Vidrio* (CSIC, Spain, 1991).

[3] W. Höland and G. Beall, *Glass-Ceramic Technology* (American Ceramic Society, Washington, DC, 2002).

[4] J.W. Gibbs, The collected works, *Thermodynamics* (Longmans Green, New York, 1928), Vol. 1.

[5] R. Kaischew and I.N. Stranski, Z. Phys. Chem. B **26**, 317 (1934).

[6] M. Volmer and A. Weber, Z. Phys. Chem. B **119**, 277 (1926).

[7] R. Becker and W. Döring, Ann. Phys. B **24**, 712 (1935).

[8] M. Volmer, *Kinetik der Phasenbildung* (Steinkopff, Dresden, 1939).

[9] J. Frenkel, *Kinetic Theory of Liquids* (Clarendon, Oxford, 1946).

[10] D. Turnbull and J.C. Fisher, J. Chem. Phys. **17**, 71 (1949).

[11] H. Reiss, J. Chem. Phys. **18**, 840 (1950).

[12] I. Gutzow and J. Schmelzer, *The Vitreous State: Thermodynamics, Structure, Rheology, and Crystallization* (Springer, Berlin, 1995).

[13] K.F. Kelton, Solid State Phys. **45**, 75 (1991).

[14] J.W. Christian, *Transformations in Metals and Alloys. Part I* (Pergamon, Oxford, 1981).

[15] F.C. Collins, Z. Electrochem. B **59**, 404 (1955).

[16] D. Kashchiev, Surf. Sci., **14** 209 (1969).

[17] G. Tammann, Z. Phys. Chem. B **25**, 441 (1898).

[18] M. Ito, T. Sakaino, and T. Moriya, Bull. Tokyo Inst. Technol. **88**, 127 (1968).

[19] V.N. Filipovich and A.M. Kalinina, Izv. Akad. Nauk SSR, Neorg. Mater. **4**, 1532 (1968) (in Russian).

[20] I. Gutzow, Contemp. Phys. **21**, 121, 243 (1980).

[21] U. Köster, Mater. Sci. Eng. **97**, 183 (1988).

[22] E.D. Zanotto and P.F. James, J. Non-Cryst. Solids **124**, 86 (1990).

[23] E.D. Zanotto, J. Mater. Res. **13**, 2045 (1998).

[24] A.N. Kolmogorov, Izv. Akad. Nauk. SSR **3**, 355 (1937).

[25] W.A. Johnson and R.F. Mehl, Trans. AIME. **135**, 416 (1939).

[26] M. Avrami, J. Chem. Phys. **7**, 1103 (1939).

[27] V.N. Filipovich, A.M. Kalinina, V.M. Fokin, E.K. Shischkina, and D.D. Dmitriev, Fiz. Khim. Stekla **9**, 58 (1983).

[28] E.D. Zanotto and A.C. Galhardi, J. Non-Cryst. Solids **103**, 73 (1982).

[29] A.A. Cabral, V.M. Fokin, and E.D. Zanotto, J. Non-Cryst. Solids **330**, 174 (2003).

[30] V.M. Fokin, A.M. Kalinina, and V.N. Filipovich, J. Cryst. Growth **52**, 115 (1980).

[31] A.M. Kalinina, V.M. Fokin, and V.N. Filipovich, J. Non-Cryst. Solids **38**/**39**, 723 (1980).

[32] A.M. Kalinina, V.M. Fokin, and V.N. Filipovich, Fiz. Khim. Stekla **2**, 298 (1976).

[33] E.D. Zanotto and V.M. Fokin, Philos. Trans. R. Soc. Lond. A **361**, 591 (2002).
[34] V.M. Fokin, A.M. Kalinina, and V.N. Filipovich, Fiz. Khim. Stekla **3**, 122 (1977).
[35] S.C. Glotzer, J. Non-Cryst. Solids **274**, 342 (2000).
[36] V.M. Fokin, A.M. Kalinina, and V.N. Filipovich, Fiz. Khim. Stekla **3**, 129 (1977).
[37] Z. Kozisek, Cryst. Res. Technol. **23**, 1315 (1988).
[38] K.F. Kelton and A.L. Greer, Phys. Rev. B **38**, 10089 (1988).
[39] J. Deubener, in *Proceedings of the XIXth International Congress on Glass* (Extended Abstracts, Society Glass Technology, Edinburgh, 2001), Vol. 2, p. 66.
[40] O.V. Potapov, V.M. Fokin, V.L. Ugolkov, L.Y. Suslova, and V.N. Filipovich, Glass Phys. Chem. **26**, 39 (2000).
[41] D. Turnbull, J. Chem. Phys. **18**, 769 (1950).
[42] A.M. Kalinina, V.N. Filipovich, V.M. Fokin, and G.A. Sycheva, in *Proceedings of the XIVth International Congress on Glass* (New Delhi, 1986), Vol. 1, p. 366.
[43] O.V. Potapov, V.M. Fokin, and V.N. Filipovich, J. Non-Cryst. Solids **247**, 74 (1999).
[44] G. Tammann, Z. Elektrochemie **10**, 532 (1904).
[45] P.F. James, Volume nucleation in silicate glasses, in *Glasses and Glass-Ceramics*, edited by M.H. Lewis, (Chapman and Hall, London, 1989).
[46] E.D. Zanotto, J. Non-Cryst. Solids **89**, 361 (1987).
[47] J. Deubener, J. Non-Cryst. Solids **274**, 195 (2000).
[48] V.M. Fokin, E.D. Zanotto, and J.W.P. Schmelzer, J. Non-Cryst. Solids **321**, 52 (2003).
[49] M.H. Lewis, J. Metacalf-Johanson, and P.S. Bell, J. Am. Ceram. Soc. **62**, 278 (1979).
[50] D. Turnbull, Thermodynamics and kinetics of formation of the glassy state and initial devitrification, in *Physics of Non-Crystalline Solids* (North-Holland, Amsterdam, 1964).
[51] G. Tammann, *Der Glaszustand* (Leopold Voss Verlag, Leipzig, 1933).
[52] G.L. Mikhnevich and J.F. Browko, Phys. Sowjetunion **13**, 113 (1938).
[53] P.F. James, Nucleation in glass-forming systems, in *Advances in Ceramics*, edited by J.H. Simmons, D.R. Uhlmann, and G.H. Beall (Am. Ceram. Soc., Columbus, 1982).
[54] M.C. Weinberg and E.D. Zanotto, J. Non-Cryst. Solids **108**, 99 (1989).
[55] Y. Miyazawa and G.M. Pound, J. Cryst. Growth. **23**, 45 (1974).
[56] D. Turnbull, J. Chem. Phys. **20**, 411 (1952).
[57] L. Shartsis and S. Spinner, J. Res. Natl. Bur. Stand. **46**, 385 (1951).
[58] A.A. Appen, K.A. Schishov, and S.S. Kaylova, Silicattechnik **4**, 104 (1953).
[59] V.M. Fokin, E.D. Zanotto, and J.W.P. Schmelzer, J. Non-Cryst. Solids **278**, 24 (2000).
[60] J. Stefan, Ann. Phys. **29**, 655 (1886).
[61] V.M. Fokin and E.D. Zanotto, J. Non-Cryst. Solids **265**, 105 (2000).
[62] I. Gutzow, D. Kashchiev, and I. Avramov, J. Non-Cryst. Solids **73**, 477 (1985).
[63] A.I. Rusanov, *Phasengleichgewichte und Grenzflächenerscheinungen* (Akademie-Verlag, Berlin, 1978).
[64] V.P. Skripov and M.Z. Faizullin, *Solid–Liquid and Liquid–Vapor Phase Transitions: Similarities and Differences*, In: J.W.P. Schmelzer (Ed.) Nucleation Theory and Applications (Wiley-VCH, Berlin, 2005), pp. 4–38.

[65] V.N. Filipovich and T.A. Jukovskaiy, Fiz. Khim. Stekla **14**, 300 (1988).
[66] B.A. Shakmatkin and N.M. Vedisheva, J. Non-Cryst. Solids **171**, 1 (1994).
[67] B.A. Shakmatkin, N.M. Vedisheva, M.M. Shultz, and A.C. Wright, J. Non-Cryst. Solids **177**, 249 (1994).
[68] J.W.P. Schmelzer, J. Schmelzer, Jr., and I.S. Gutzow, J. Chem. Phys. **112**, 3820 (2000).
[69] J.W.P. Schmelzer, Phys. Chem. Glasses **45** (2), 116 (2004).
[70] J.W.P. Schmelzer, A.R. Gokhman, and V.M. Fokin, J. Colloid Interface Sci. **272**, 109 (2004).
[71] J.W.P. Schmelzer, A.S. Abyzov, and J. Möller, J. Chem. Phys. **121**, 6900 (2004).
[72] V.M. Fokin, O.V. Potapov, E.D. Zanotto, F.M. Spiandorello, V.L. Ugolkov, and B.Z. Pevzner, J. Non-Cryst. Solids **331**, 240 (2003).
[73] J. Deubener, R. Brückner, and M. Strernizke, J. Non-Cryst. Solids **163**, 1 (1993).
[74] E.D. Zanotto, and M.L.G. Leite, J. Non-Cryst. Solids **202**, 145 (1996).
[75] P.C. Soares Jr., *Initial Stages of Crystallization in Lithium Disilicate Glass Revisited*. M.D. thesis, Universidade Federal de São Carlos, Brazil, 1997.
[76] Y. Iqbal, W.E. Lee, D. Holland, and P.F. James, J. Non-Cryst. Solids **224**, 1 (1998).
[77] L.I. Burger, P. Lucas, M.C. Weinberg, P.C. Soares Jr., and E.D. Zanotto, J. Non-Cryst. Solids **274**, 188 (2000).
[78] J. Deubener, *Homogene Volumenkeimbildung in Silicatschmelzen: Theorie und Experiment* (Habilitationsschrift, Berlin, 2001).
[79] P.C. Soares Jr., E.D. Zanotto, V.M. Fokin, and H.J. Jain, J. Non-Cryst. Solids **331**, 217 (2003).
[80] B.A. Shakhmatkin and N.M. Vedishcheva, personal communication (2001).
[81] I. Hasdemir, R. Brückner, and J. Deubener, Phys. Chem. Glasses **39**, 253 (1998).
[82] L. Granasy, T. Pusztai, and P.F. James, J. Chem. Phys. **117**, 6157 (2002).
[83] E.D. Zanotto and E.J. Müller, J. Non-Cryst. Solids **130**, 220 (1991).
[84] J.W.P. Schmelzer, R. Müller, J. Möller, and I.S. Gutzow, Phys. Chem. Glasses **43C**, 291 (2002).
[85] J.W.P. Schmelzer, R. Müller, J. Möller, and I.S. Gutzow, J. Non-Cryst. Solids **315**, 144 (2003).
[86] J.W.P. Schmelzer, O.V. Potapov, V.M. Fokin, R. Müller, and S. Reinsch, J. Non-Cryst. Solids **333**, 150 (2004).
[87] V.M. Fokin, E.D. Zanotto, J.W.P. Schmelzer, and O.V. Potapov, J. Non-Cryst. Solids, in press.
[88] G. Partridge, Glass Technol. **28**, 9 (1987).
[89] E.D. Zanotto, J. Non-Cryst. Solids **129**, 183 (1991).
[90] E.D. Zanotto, Ceram. Trans. **30**, 65 (1993).
[91] V.N. Filipovich, A.M. Kalinina, V.M. Fokin, N.S. Yuritsyn, and G.A. Sycheva, Glass Phys. Chem. **25**, 246 (1999).
[92] R. Müller, E.D. Zanotto, and V.M. Fokin, J. Non-Cryst. Solids **274**, 208 (2000).
[93] J. Schmelzer, R. Pascova, J. Möller, and I. Gutzow, J. Non-Cryst. Solids **162**, 26 (1993).

[94] J. Schmelzer, J. Möller, R. Pascova, I. Gutzow, R. Müller, and W. Pannhorst, J. Non-Cryst. Solids **183**, 215 (1995).

[95] V.N. Filipovich, V.M. Fokin, N.S. Yuritsyn, and A.M. Kalinina, Thermochimica Acta **280**/**281**, 205 (1996).

[96] R. Müller, J. Non-Cryst. Solids **219**, 110 (1997).

[97] S. Reinsch and R. Müller, Nucleation at silicate glass surfaces, in *Analysis of the Composition and Structure of Glass and Glass Ceramics*, edited by H. Bach and D. Krause (Springer, Berlin, 1999), p. 379.

[98] Z. Strnad and R.W. Douglas, Phys. Chem. Glasses **14**, 33 (1973).

[99] A.M. Kalinina, N.S. Yuritsyn, V.M. Fokin, and V.N. Filipovich, *Crystal Nucleation and Growth on the Surface of Glass of the Composition* $2MgO \cdot 2Al_2O_3 \cdot 5SiO_2$. in: VIII. Vses. Soveshch. po Stekloobraznomu Sostoyaniyu (VIIIth All-Union Conf. on the Vitreous State), Leningrad, Nauka, 1986, p. 235 (in Russian).

[100] J. Deubener, R. Brückner, and H. Hessenkemper, Glastech. Ber. B **65**, 256 (1992).

[101] *Surface Nucleation*. (Collection of selected papers published by the members of TC 7 during their 10 years long attempt to understand the nature of the active sites in surface nucleation). Published by the Intern. Commission on Glass, 2000.

[102] N.S. Yuritsyn, V.M. Fokin, A.M. Kalinina, and V.N. Filipovich, Glass Phys. Chem. **20**, 116 (1994).

[103] N.S Yuritsyn, V.M. Fokin, A.M. Kalinina, and V.N. Filipovich, Glass Phys. Chem. **20**, 125 (1994).

[104] I. Gutzow and S. Toschev, The kinetics of nucleation and the formation of glass-ceramic materials, in *Advances in Nucleation and Crystallization in Glasses* (American Ceramic Society, Columbus, 1971), p. 10.

[105] A. Milchev, Electrochim. Acta **30**, 125 (1985).

[106] A. Milchev, Electrochim. Acta **31**, 977 (1986).

[107] V.M. Fokin, N.S. Yuritsin, A.M. Kalinina, V.N. Filipovich, and D.N. Filippova, *The Temperature Dependence of the μ-cordierite Crystals Nucleation Rate on the Polished Surface of Cordierite Glass*, in Proceedings of the 5th International Otto Schott Colloquium. Glastech. Ber. Glass Sci. Technol. **67C**, 392 (1994).

[108] V.M. Fokin, N.S. Yuritsyn, V.N. Filipovich, and A.M. Kalinina, J. Non-Cryst. Solids **219**, 37 (1997).

[109] S. Toschev and I. Gutzow, Krist. Tech. **B7**, 43 (1972).

[110] V.M. Fokin and E.D. Zanotto, J. Non-Cryst. Solids **246**, 115 (1999).

[111] V.N. Filipovich, G.A. Sycheva, and A.M. Kalinina, Fiz. Khim. Stekla **11**, 123 (1985) (in Russian).

[112] D.W. Oxtoby, Acc. Chem. Res. **31**, 91 (1998).

[113] L. Granasy and P.F. James, J. Chem. Phys. **113**, 9810 (2000).

[114] R. Müller, S. Reinsch, and W. Pannhorst, Glastech. Ber. Glass Sci. Technol. **69**, 12 (1996).

5 Boiling-Up Kinetics of Solutions of Cryogenic Liquids

Vladimir G. Baidakov

Seeking no profits whatsever, Inspired solely in his flight,
Chopin transforms – alone as ever – The probable into the right
Boris Pasternak

A kinetic theory of the process of boiling-up of superheated binary solutions is developed. In the framework of the Kramers–Zeldovich method, describing nucleation as a process of Brownian motion of the nucleus in the field of thermodynamic forces, an equation for the steady-state nucleation rate is derived. In the analysis of this kinetic problem, the whole spectrum of possible factors is included, which may limit the growth of the nucleus: the volatility of the solution, viscosity and inertia effects in the motion of the liquid, diffusion, and thermal conduction effects at the phase boundaries. For the determination of the work of critical cluster formation, the van der Waals theory of capillarity is utilized. This theory allows an account of the dependence of the properties of critical clusters on cluster size. The results of experiments on nucleation (the determination of the mean lifetimes of the solutions and the steady-state nucleation rates) in metastable solutions with full (Ar–Kr) and partial (He–O_2) solubility are given in dependence on temperature, pressure, and composition of the solutions. The results of the experiments are compared with the theoretical predictions. It is shown that a good agreement between experimental and theoretical results is reached when the curvature corrections to the surface tension, calculated via the van der Waals approach, are taken into account.

5.1 Introduction

A first-order phase transition presupposes the existence of metastable states. It proceeds frequently via the formation and subsequent growth of critical nuclei of a new phase. In *pure* systems, in the absence of external factors initiating a phase transition, nuclei form via spontaneous fluctuations (homogeneous nucleation). The emergence of a new-phase fragment in a homogeneous metastable system is connected with the formation of a phase boundary and accompanied by an increase in the excess free energy $\Delta\Phi$. The competition of the surface and volume terms, entering the expression for the free energy with opposite signs, results in the existence of a finite maximum $\Delta\Phi = W_*$. The fragments corresponding to the maximum of $\Delta\Phi$ are called critical nuclei, and the quantity W_* is the work of their formation. At each moment of time, the overwhelming majority of fragments has precritical sizes $R < R_*$. Their existence is unfavorable from a thermodynamic point of view and they dissolve as a rule. However, due to fluctuations some of the fragments may grow up to sizes exceeding the critical one and then their further growth is thermodynamically irreversible.

The discussed concepts form the basis of the classical nucleation theory formulated among others by Volmer [1], Döring [2], Zeldovich [3], and Frenkel [4]. For one-component systems,

Nucleation Theory and Applications. edited by J. W. P. Schmelzer

ISBN: 3-527-40469-4

the theory defines the nucleation rate J, i.e., the number of viable fragments of a new phase forming per unit volume in a unit time, as

$$J = \rho B \exp\left(-\frac{W_*}{k_B T}\right) . \tag{5.1}$$

Here ρ is the number of molecules per unit volume of the metastable phase, B is a kinetic coefficient which determines the rate of the transition of fragments through the critical size, k_B is the Boltzmann constant, and T is the absolute temperature.

In the papers by Volmer [1], Zeldovich [3], and Frenkel [4], the kinetic theory of nucleation was formulated and applied to one-component systems. Equation (5.1) was employed for the first time by Flood [5], Neumann and Döring [6] in a more general context with the aim to interpret experimental data on the condensation of supersaturated vapors in a binary system. These authors [5, 6] took the coefficient B equal to its value for pure components in the solution.

In contrast to one-component systems, in order to characterize new-phase fragments in a binary system, it is necessary to introduce into the description at least two parameters: the radius of a new-phase fragment, R, and its composition, c'', or the number of molecules of the first, n_1'', and the second, n_2'', components in the fragment. Binary gas nucleation, as the process of fluctuational overcoming the activation barrier in terms of the variables n_1'' and n_2'', was first considered in detail by Reiss [7], Nesis and Frenkel [8]. In Ref. [7] it was assumed that the direction of the two-dimensional vector of the flow of nuclei in phase space in the vicinity of the activation-barrier passes the saddle point and is determined only by the local relief of the surface $\Delta\Phi(n_1'', n_2'')$. The later papers by Stauffer [9], Shi and Seinfeld [10], and Melikhov et al. [11] took into account the dependence of the direction of the fastest descent from the saddle point on all the physical parameters of the problem.

All the mentioned approaches postulate the existence of a Boltzmann distribution for subcritical fragments. The possibility of an abnormal binary nucleation regime, when the equilibrium of subcritical fragments is violated, and the flow of nuclei by-passes the saddle point, was discussed, for example, in [10, 12, 13]. This nucleation regime is observed if the rate of change of the number of one of the components of the solution in the nucleus is much smaller than that of the other. Thus, nucleation in a binary system may proceed not necessarily via the saddle point of the free energy.

While losing stability for finite disturbances connected with the formation of a new phase, a metastable system retains a stabilizing reaction to infinitesimal continuous changes in the state parameters. As soon as the relation

$$\left(\frac{\partial \Delta\mu}{\partial c}\right)_{p,T} = 0 \tag{5.2}$$

is fulfilled, the system becomes unstable with respect to such infinitesimal changes. This way, Eq. (5.2) determines the boundary where the homogeneous phase becomes essentially unstable. The respective curve is denoted as the (diffusion) spinodal of the solution. Here $\Delta\mu = \mu_1 - \mu_2$ is the chemical potential difference.

A superheated liquid is a particular case of a metastable state and a most convenient object for verification of the homogeneous nucleation theory [14]. Of special interest are investigations of nucleation in liquefied inert gases. The good wettability of solid materials by liquefied

gases, the low content of dissolved gases and solid particles in them makes it possible to realize the homogeneous nucleation mechanism at comparatively low rates of intrusion into the metastable region. Being phenomenological, the homogeneous nucleation theory does not supply rigorous expressions for the parameters B and W_* in Eq. (5.1). The simplicity of the molecular structure of liquefied inert gases makes it possible to determine these quantities by using the methods of statistical mechanics.

Fewer papers [15, 16] are devoted to the study of the boiling-up of superheated liquid solutions with complete solubility of the components as compared with investigations of condensation in mixtures of supersaturated vapors [17, 18]. Both for the analysis of the boiling-up of binary solutions and condensation of binary vapors a variety of experiments have been performed on sufficiently complex molecular systems and in a comparatively narrow range of nucleation rates. The first papers investigating nucleation in superheated solutions are published by Baidakov et al. [19, 20].

A supersaturated solution of a gas in a liquid is an example of a two-component metastable system, in which nonequilibrium is caused by the excess of the concentration of a dissolved component over its value in the saturated state. The removal of supersaturation takes place as a result of separation of the gas phase in the form of numerous bubbles ("the effect of champagne"). This phenomenon manifests itself in the Caisson's disease, it is used as a means for degassing liquids, foaming of polymeric materials and in other technological processes. If at a given temperature and pressure of a supersaturated solution a pure solvent (liquid) and a dissolved substance (gas) are in the stable state, the solvent in the solution is characterized by low volatility, and the dissolved gas by low solubility. New-phase nuclei in such solutions practically fully consist of molecules of the dissolved substance. The theory of boiling-up of such supersaturated nonvolatile liquids was developed by Deryagin and Prokhorov [21] and Kuni et al. [22]. The first experimental investigations of nucleation in nonvolatile liquid solutions were made by Hemmingsen [23], Finkelstein and Tamir [24] and Bowers et al. [25]. Supersaturation was created by an abrupt release of pressure on the liquid (water), which was saturated with a gas at pressures equal to several hundreds of atmospheres. The concentration of a dissolved gas, c', was determined in this case by the value of the saturation pressure, p_s, and the depth of penetration into the metastable region – by the pressure difference $p_n(c', T) = p_s - p_n$, where $p_n(c', T)$ is the pressure where an intensive gas emission is observed.

An approach to the investigation of nucleation in gas-supersaturated water solutions, different from that used in Ref. [23], was suggested by Rubin and Noyes [26]. In a solution, kept in a vessel of a fixed volume at controlled values of temperature and pressure, supersaturation was initiated by a chemical reaction. If the rate of gas production during a chemical reaction in a solvent exceeds considerably the rate of its removal through a free interface, considerable supersaturations can be achieved in the volume of a liquid solvent. A decay of the metastable state was accompanied by an abrupt (explosive) gas release. The concentration of the dissolved gas in the supersaturated solution was determined by the data for the volumes of the solution, gas and liquid phases in a measuring cell and the pressure increase in the system during the initiation of gas release, e.g., by stirring the solution. In this case, the value of supersaturation is characterized by the value of $\Delta c'_n(p, T) = c'_n - c_s$. According to the data given in Ref. [26], the concentration, c'_n, of nitrogen dissolved in water before the formation

of bubbles was approximately 20–40 times larger than its equilibrium concentration, c_s, at atmospheric pressure.

A comparison of experimental data, obtained by two different methods of creating supersaturation in a liquid solution, with the predictions of homogeneous nucleation theory has shown that the degrees of metastability obtained by experiment are considerably lower than their theoretical values. Thus, in the system oxygen – water the limiting values of concentration c'_n, calculated from the homogeneous nucleation theory, at atmospheric pressure and a nucleation rate $J = 10^7$ s^{-1} m^{-3} have been proven to be 15 times larger than those achieved by experiment [27]. In this system at the limiting values of supersaturation registered in experiment, the critical bubble is characterized by a radius $R_* = 15$ nm, and the pressure $p''_* = 9.5$ MPa. The Gibbs number $G_* = W_*/k_B T$, i.e., the ratio between the work of formation of a critical nucleus and the energy of thermal motion of molecules $k_B T$, is about $\simeq 1.56 \times 10^4$ in this case [28]. Overcoming such a high potential barrier via homogeneous nucleation of the gas phase in characteristic times of an experiment is an unlikely event. In the case of spontaneous boiling-up of superheated pure liquids, the value of G_* is about $\simeq 72$ [29].

To remove such contradictions between theory and experiment, a number of authors have suggested models of nucleation in gas-supersaturated solutions different from that of the classical thermodynamic model [28,30]. It has been postulated, for example, that the formation of gas bubbles in the solution proceeds in two stages. In the first stage, according to Kwak and Panton [30], the molecules of a dissolved gas form a cluster, which has no distinct interface and, consequently, no surface energy. In the paper by Bowers et al. [28], the spatial region of increased gas concentration in the solution is called a "blob." The small difference of gas concentrations in a "blob" and the surrounding liquid ensures, in the author's opinion [28], a small surface contribution to its excess free energy. The latter proves to be much lower than in a bubble of the same size. Both the "clusters" of Kwak and Panton [30] and the "blobs" of Bowers et al. [28], after achieving a certain size exceeding the size of a critical nucleus, are transformed into a supercritical gas bubble. The models, described in Refs. [28, 30], make it possible, for limiting supersaturations observed by experiment [23, 26], to decrease the height of the nucleation barrier to $\sim 10^2 k_B T$.

A peculiar situation for bubble formation in a liquid solution is observed at temperatures close to the critical point of the solvent. Here a two-component system may prove to be "doubly" metastable. At a given temperature, T, and concentration of the dissolved component, c', a solution under a pressure p lower than the saturation pressure p_s is supersaturated and characterized by the degree of metastability $\Delta p(T, c') = p_s - p$, a pure solvent is superheated by the value of $\Delta T(p) = T - T_s(c' = 0)$, where $T_s(c' = 0)$ is the saturation temperature of a pure solvent at a given pressure. In the vicinity of the critical point one can no longer neglect the volatility of the solvent, viscous and inertial forces and heat exchange at the interface begin to play an important role in the bubble-growth dynamics. The theory of boiling-up of such solutions has been developed by Baidakov [31].

Experimental investigations of limiting superheats $\Delta T(p, c') = T_n - T_s$ for solutions of carbon dioxide and nitrogen in organic liquids were conducted by Mori et al. [32] and Forest and Ward [33]. In their papers, they used the method of emerging droplets. At nucleation rates $J = 10^{24}$–10^{26} s^{-1} m^{-3}, liquid solutions of high-temperature liquids were investigated by the method of pulse heating of a wire probe [34]. Gas-filling of a liquid resulted in a shift of the spontaneous boiling-up boundary toward lower temperatures. The authors of the papers [32–

34] state satisfactory agreement between homogeneous nucleation theory and experiment, at least, with respect to the value of the limiting superheat of the solutions.

The present paper is devoted to the development of a kinetic theory of boiling-up of binary solutions taking into account all the main factors determining the growth of a vapor bubble (Sect. 5.2). The final result of the theory consists in an expression for the steady-state homogeneous nucleation rate. The main quantity, determining the nucleation rate, is the work of formation of a critical nucleus, W_*. To find W_*, the van der Waals capillarity theory is utilized. This theory allows to determine, in addition, the distribution of the densities of the different components in a critical bubble and the dependence of the bubble surface tension on its characteristic size (Sect. 5.3).

To investigate by experiment the kinetics of spontaneous boiling-up of binary solutions (Sect. 5.4), a method of measuring the lifetime of a metastable liquid is used, which is approximately an order of magnitude more accurate in determining the temperature of the degree of superheating of the solution than the methods employed in papers [32–34]. By experiment, temperature, baric and concentration dependences of the nucleation rate are determined. The objects of investigation are solutions with complete solubility of the components and gas-supersaturated solutions. Gas-supersaturated solutions of cryogenic liquids belong to the class of weak solutions. At pressures of 5 MPa, the solubility of helium in oxygen does not exceed 2–3 mol% [35]. Considerable differences between the parameters of the potential of the intermolecular interaction of a solvent and a dissolved substance result in a well-expressed nonideality of a two-component system with helium behaving as a surface-active substance decreasing the excess free energy of the liquid–vapor interface [36]. Solutions of argon dissolved in krypton have been chosen as a system with complete solubility (Sect. 5.3). The simplicity of the molecular structure of these solutions makes it possible to employ the van der Waals capillarity theory for taking into account both the adsorption and size effects in nucleation.

The results of the experimental and theoretical investigations are compared in Sect. 5.5 of the present contribution. A summary of the results and discussion (Sect. 5.6) completes the chapter.

5.2 Nucleation Kinetics

5.2.1 Introduction

The problem of the boiling-up of multicomponent solutions is a multiparameter problem of the kinetics of phase transitions. Already in the case of a binary liquid mixture, the state of a new-phase nucleus is given at least by three variables, for example, volume v, pressure p'' and concentration c'' [29]. The number of significant variables is reduced to two if the new phase is incompressible, or if one of the solution components is nonvolatile. The approximation of incompressibility of the new phase may be valid in describing condensation of supersaturated gas mixtures far from the critical point [7, 10, 11], the assumption of nonvolatility – during the boiling-up of liquid solutions [21]. The multiparameter version of the nucleation theory is developed as an extended version of the classical Kramers–Zeldovich approach [3] to systems, where the state of the nucleus is determined by several variables. It has been repeatedly dis-

cussed in the literature [37–39]. The main difficulty in applying this approach to the boiling-up of superheated binary solutions is connected with the fact that the dynamics of evolution of the nucleus in binary solutions is governed by the hydrodynamic equations of motion of a viscous liquid in combination with the diffusion equation.

The kinetic nucleation theory treats the growth of a nucleus as a diffusion process in the space of its significant variables in the field of appropriate thermodynamic forces. As the main thermodynamic parameters of a vapor bubble in a binary liquid mixture it is convenient to choose its volume v and the partial pressures of the components p_1'' and p_2''. The growth of a vapor bubble in a superheated liquid is accompanied by irreversible losses in energy connected with the inertial motion of the liquid, viscosity, and thermal conductivity. The inertial forces produce an additional pressure at the bubble surface, and the work performed by vapor against this pressure is spent in transferring the kinetic energy to the liquid. Therefore, when taking into account inertia effects one should include into the significant variables of a new-phase nucleus the rate of change of the volume $dv/dt = \dot{v}$ of the vapor bubble. The effect of viscosity manifests itself through the force of viscous friction acting on the bubble surface. As the friction force is proportional to the rate of change of the bubble radius (volume), its account does not require the introduction of an additional nucleus variable, besides those that have already been considered. The expansion (compression) of a bubble results in the evaporation of the liquid (vapor condensation), and as a consequence the temperature on its interface becomes lower (higher) than the temperature of the liquid. Thus, in the vicinity of the bubble surface a temperature gradient develops, and its evolution will be largely determined by the process of heat supply (removal) to the bubble from the surrounding liquid. Since this process concerns the values of all the chosen variables of the problem under consideration, we shall take it into account through corrections to the values of the variables v, p_1'', p_2'', and $\dot{v}$.

The development in time t of the distribution of nuclei of a newly evolving phase $n(\mathbf{q}, t)$ will obey in this case the Kramers–Zeldovich four-dimensional continuity equation for the density of the fluxes of nuclei $\mathbf{j}$

$$\frac{\partial n}{\partial t} = -\frac{\partial}{\partial \mathbf{q}}\mathbf{j}\,, \quad \mathbf{j} = -n_e \mathbf{D}\frac{\partial}{\partial \mathbf{q}}\frac{n}{n_e}\,. \tag{5.3}$$

Here $\mathbf{D}$ is the tensor of generalized diffusion in the space of variables $\mathbf{q} \in \{v, p_1'', p_2'', \dot{v}\}$; $n_e(\mathbf{q})$ is the equilibrium distribution function of boiling-up nuclei connected with some well-defined potential function $\Psi(\mathbf{q})$ by the relation

$$n_e(\mathbf{q}) \sim \exp\left[-\frac{\Psi(\mathbf{q})}{k_B T}\right]\,. \tag{5.4}$$

The problem of determination of the nucleation rate, the main kinetic characteristic of the nucleation process, is reduced in this case to the determination of the shape of this potential in the space of nucleus variables, in the computation of the coefficient of the generalized diffusion of the nucleus in this space and the solution of the kinetic equation governing the nucleation process.

The analysis as carried out below includes the following simplifications. The flux of nuclei via the saddle or the ridge of the potential barrier $\Psi(\mathbf{q})$, separating in the space of variables v, p_1'', p_2'', $\dot{v}$ the region of heterophase states from two-phase ones, is assumed to be independent of time, i.e., the nucleation process is assumed to proceed under steady-state conditions.

The analysis is restricted to systems with weak metastability, when the height of the nucleation barrier obeys the inequality $\Psi_* \gg k_B T$. This condition makes it possible to use a macroscopic approximation for the description of the critical nuclei, treating them as spherical vapor bubbles. It is assumed further that the liquid solutions are viscous and incompressible, and that the vapor mixture in a bubble can be treated as a mixture of perfect gases.

5.2.2 Analysis of the Potential Surface in the Space of Nucleus Variables

The phase space of a nucleus in a binary system is given by the thermodynamic variables v, p_1'', p_2'' and a dynamic variable, the rate of change of the bubble volume, $\dot{v}$. In the space of these variables, the potential surface $\Psi(v, p_1'', p_2'', \dot{v})$, separating the region of heterophase fluctuations from the two-phase region, is determined by the expression

$$\Psi(v, p_1'', p_2'', \dot{v}) = \frac{\Delta\Phi(v, p_1'', p_2'')}{k_B T} + \frac{M_v}{2k_B T}\dot{v} \ . \tag{5.5}$$

Here $\Delta\Phi(v, p_1'', p_2'')$ is the thermodynamic potential difference corresponding to the minimum work of formation of a bubble of volume v with partial pressures of the components p_1'', p_2'', and a temperature T. The second term in Eq. (5.5) is the kinetic energy of a growing bubble with an "effective" mass M_v in variables p_1'', p_2'', v, and $\dot{v}$. The potential surface $\Psi(v, p_1'', p_2'', \dot{v})$ has the form of Eq. (5.5) only for $t \gg \tau_{\text{rel}}$ (τ_{rel} is Maxwell's relaxation time), i.e., with the establishment of an equilibrium growth-rate distribution of the bubbles.

In a binary system, the thermodynamic work of formation of a vapor bubble of volume v with N_1'' molecules of the first component and N_2'' molecules of the second component is equal to the increase in the Gibbs potential and determined via the relation [40]

$$\Delta\Phi = \left(p' - p_1'' - p_2''\right) v + \sigma A + \left(\mu_1'' - \mu_1'\right) N_1'' + \left(\mu_2'' - \mu_2'\right) N_2'' \ . \tag{5.6}$$

Here p' is the pressure in a liquid solution, σ is the surface tension, A is the area of the bubble surface, and μ_i are the chemical potentials of the different components of the mixture ($i = 1, 2$). It is assumed that the state of the phase surrounding the bubble does not change in the process of its growth.

The function $\Delta\Phi(v, p_1'', p_2'')$ has in the metastable region an extremum characterized by the parameters v_*, p_{1*}'', and p_{2*}''. Going over to dimensionless variables x, y, and z and the reduced rate of growth of the bubbles, $\dot{x}$, via

$$x = \frac{v - v_*}{v_*}, \quad y = \frac{p_1'' - p_{1*}''}{p_{1*}''}, \quad z = \frac{p_2'' - p_{2*}''}{p_{2*}''}, \quad \dot{x} = \frac{\dot{v}}{v_*} \ , \tag{5.7}$$

the dimensionless potential surface $\Psi(x, y, z, \dot{x})$ in the space of the variables x, y, and z, $\dot{x}$ can be written as

$$\Psi(x, y, z, \dot{x}) = \frac{\Delta\Phi(x, y, z)}{k_B T} + \frac{M_{\dot{x}}}{2k_B T}\dot{x}^2 = G + \frac{M_{\dot{x}}}{2k_B T}\dot{x}^2 \ . \tag{5.8}$$

Using Eqs. (5.6) and (5.8) and the assumption of ideality of the gas mixture in a bubble we have

$$\begin{aligned}\Psi(x,y,z,\dot{x}) = {} & \frac{p''v_*(x+1)}{k_BT} - \frac{p''_{1*}v_*(x+1)(y+1)}{k_BT} - \frac{p''_{2*}v_*(x+1)(z+1)}{k_BT} \\ & + \frac{p''_{1*}v_*(x+1)(y+1)\ln(y+1)}{k_BT} + \frac{p''_{2*}v_*(x+1)(z+1)\ln(z+1)}{k_BT} \\ & + \frac{3^{2/3}(4\pi)^{1/3}\sigma v_*^{2/3}(x+1)^{2/3}}{k_BT} + \frac{M_{\dot{x}}}{2k_BT}\dot{x}^2 \,. \end{aligned} \tag{5.9}$$

After expansion of $\Psi(x,y,z,\dot{x})$ in the vicinity of the extremum into a series in terms of powers $x, y, z, \dot{x}$ up to second order terms, we obtain

$$\Psi(x,y,z,\dot{x}) = G_*\left(1 - \frac{1}{3}x^2 + \frac{1}{b_1}y^2 + \frac{1}{b_2}z^2\right) + \frac{M_{\dot{x}}}{2k_BT}\dot{x}^2 \,, \tag{5.10}$$

where $G_* = \Delta\Phi_*/k_BT$ is the Gibbs number, $b_i = 2\sigma/R_*p''_{i*}$ is a dimensionless parameter characterizing the degree of superheating of the solution, R_* is the radius of the critical bubble, and $M_{\dot{x}} = M_v v_*^2$.

According to Eq. (5.10), in the vicinity of the extremum point, the function $\Psi(x,y,z,\dot{x})$ shows a quadratic dependence on the relevant variables without any mixed terms. The coefficients at the squares of the variables x, y, z, v determine the curvature of the potential surface. The difference in the sign of one of the radii of curvature ($R_x = -(3/2)G_*^{-1}$) from the three others ($R_y = (b_1/2)G_*^{-1}$, $R_z = (b_2/2)G_*^{-1}$, $R_{\dot{x}} = k_BT/M_{\dot{x}}$) implies that the $\Psi(x,y,z,\dot{x})$ surface is a hyperbolic paraboloid in the vicinity of the origin of the system of coordinates, and the extremum is a saddle point. In the variables $x, y, z, \dot{x}$ the relations $y = 0$, $z = 0$, $\dot{x} = 0$ determine the ridge line of the activation barrier. The minus sign of the variable x in Eq. (5.10) shows that this variable is unstable, while the variables $y, z, \dot{x}$ are stable.

By separating "stable" and "unstable" variables in the thermodynamic potential, Eq. (5.8), the equilibrium distribution function of nuclei in $x, y, z, \dot{x}$ is obtained in the form

$$\begin{aligned} n_e(x,y,z,\dot{x})n_{ex}n_{ey}n_{ez}n_{e\dot{x}} = {} & C_x \exp\left(-G_* + \frac{1}{3}G_*x^2\right) \\ & \times C_y \exp\left(-\frac{1}{b_1}G_*y^2\right) C_z \exp\left(-\frac{1}{b_2}G_*z^2\right) C_{\dot{x}} \exp\left(-\frac{M_{\dot{x}}}{2k_BT}\dot{x}^2\right) \,, \end{aligned} \tag{5.11}$$

where C_x, C_y, C_z, and $C_{\dot{x}}$ are the normalization constants. The function n_{ex}, which describes the distribution of bubbles along the path of evolution, is similar to the equilibrium distribution function in a one-dimensional problem of nucleation. Kagan [41], in considering the boiling-up of a pure liquid, assumes that the normalization constant is proportional to the number of particles in a unit volume of the metastable phase. Then in a binary system $C_x = \rho' = \rho'_1 + \rho'_2$ holds, where ρ'_1 and ρ'_2 are the number densities of the solvent and the substance dissolved in the liquid phase, respectively. According to Ref. [42], $C_x = v_*\rho'^2$ holds.

The functions n_{ey} and n_{ez} determine the equilibrium distributions of bubbles in terms of partial pressures ("stable variables") and are normalized as

$$\int_{-\infty}^{+\infty} n_{ey}\,\mathrm{d}y = 1, \quad \int_{-\infty}^{+\infty} n_{ez}\,\mathrm{d}z = 1\ . \tag{5.12}$$

The value of $C_{\dot{x}} = [M_{\dot{x}}/(2\pi k_{\mathrm{B}}T)]^{1/2}$ follows from

$$\int_{-\infty}^{+\infty} n_{e\dot{x}}\,\mathrm{d}\dot{x} = 1\ . \tag{5.13}$$

5.2.3 The Diffusion Tensor of Nuclei

The determination of the tensor of generalized diffusion is reduced to the specification of the forces that act on a nucleus and the rates of change of its parameters under the action of these forces. In the respective computations, we assume that the interaction of a bubble with a liquid is the result of a hydrodynamic interaction caused by the pressure of the liquid, the Laplace force, the viscous and the inertial forces; the emission–absorption interaction, connected with the exchange of molecules of the components of the solution between the bubble and the liquid, and the diffusion interaction caused by the presence of a depletion zone around the bubble owing to the finite rate of supply of one of the components of the solution to it.

The bubble radius at each moment of time is determined by a relation which follows from the Navier–Stokes equation if the latter is integrated with respect to r from R to ∞. For an incompressible Newtonian liquid in the absence of mass forces, when the speed of motion of the bubble surface, R, coincides with the speed of motion of molecules of the solvent and the dissolved substance adjoined to this surface, we have

$$\rho_{\mathrm{l}} R\ddot{R} + \frac{3}{2}\rho_{\mathrm{l}}\dot{R}^2 = p'' - p' - \frac{2\sigma}{R} - 4\eta\frac{\dot{R}}{R}\ , \tag{5.14}$$

where ρ_{l} is the mass density of a liquid, η is its viscosity. By neglecting, in the vicinity of the saddle point, the term containing $\dot{R}^2$ as a small term of second order as compared with the term proportional to $\dot{R}$, we obtain

$$\rho_{\mathrm{l}} R\ddot{R} = p'' - p' - \frac{2\sigma}{R} - 4\eta\frac{\dot{R}}{R}\ . \tag{5.15}$$

Equation (5.15) determines the hydrodynamic interaction of a bubble with the liquid.

Let us go over in Eq. (5.15) to dimensionless variables defined via Eq. (5.5). Then for the acceleration of the nucleus "drift" we have

$$\ddot{x} = \frac{bp''_*}{\rho_{\mathrm{l}}R_*^2}x + \frac{3bp''_*}{\rho_{\mathrm{l}}R_*^2}\frac{1}{b_1}y + \frac{3bp''_*}{\rho_{\mathrm{l}}R_*^2}\frac{1}{b_2}z - \frac{4\eta}{\rho_{\mathrm{l}}R_*^2}\dot{x}\ . \tag{5.16}$$

The effective mass $M_{\dot{x}}$ of a bubble will be found by bringing Eq. (5.16) to the form of the equation of motion for a particle of mass $M_{\dot{x}}$ under the action of external forces F_x, F_y, F_z in a medium with a friction proportional to the velocity

$$\ddot{x} = \frac{F_x}{M_x} + \frac{F_y}{M_y} + \frac{F_z}{M_z} - \gamma\,\dot{x}\ . \tag{5.17}$$

Projections of the forces acting parallel to the axes x, y, z, $\dot{x}$ are determined by the following expressions:

$$\begin{aligned} F_x &= -\frac{\partial\Psi}{\partial x} = \frac{2}{3}G_* x\ , \qquad F_y = -\frac{\partial\Psi}{\partial y} = -\frac{2}{b_1}G_* y\ , \\ F_z &= -\frac{\partial\Psi}{\partial z} = -\frac{2}{b_2}G_* z\ , \quad F_{\dot{x}} = -\frac{\partial\Psi}{\partial\dot{x}} = \frac{M_{\dot{x}}}{k_{\mathrm{B}}T}\ . \end{aligned} \tag{5.18}$$

From Eqs. (5.16)–(5.18) it follows that

$$M_{\dot{x}} = M_x = M_y = M_z = \frac{M_l R_*^2}{3}\ , \quad \gamma = \frac{4\eta}{\rho_{\mathrm{l}} R_*^2}\ , \tag{5.19}$$

where $M_l = \frac{4}{3}\pi R_*^3 \rho_{\mathrm{l}}$ is the mass of the liquid in the volume of a critical nucleus.

We introduce further a dimensionless parameter

$$\varphi = \frac{3bp_*'' M_l}{64\eta^2 R_*}\ , \tag{5.20}$$

characterizing the inertial nature of a liquid and rewrite Eq. (5.16) in the form

$$\ddot{x} = \frac{3b^2 p_*''^2}{16\eta^2}\frac{1}{\varphi}\left[\frac{1}{3}x + \frac{1}{b_1}y + \frac{1}{b_2}z - \frac{4\eta}{3bp_*''}\dot{x}\right]\ . \tag{5.21}$$

For the potential barrier in the vicinity of the saddle point, we have, according to Eqs. (5.10), (5.19), and (5.20), the following result:

$$\Psi(x, y, z, \dot{x}) = G_*\left(1 - \frac{1}{3}x^2 + \frac{1}{b_1}y^2 + \frac{1}{b_2}z^2 + \frac{16\eta^2}{3b^2 p_*''^2}\varphi\dot{x}^2\right)\ . \tag{5.22}$$

The rates of change of the number of molecules for each of the components in a bubble as a result of molecular exchange are

$$\dot{N}_{i,m}'' = \frac{\pi\beta_i \upsilon_{ti} R^2}{k_{\mathrm{B}}T}\left(p_{Ri}'' - p_i''\right)\ , \tag{5.23}$$

where $\upsilon_{ti} = (8k_{\mathrm{B}}T/\pi m_i)^{1/2}$ represents the mean energetic velocities of molecular motion of the components of the mixture, β_i is the condensation coefficient, m_i is the mass of a molecule, and p_{Ri}'' is the equilibrium partial pressure in a bubble of a given radius of curvature.

Let us assume that a bubble grows at a rate defined by the diffusion of the different components through the liquid to the bubble surface. The concentration field around the bubble is determined by solving the diffusion equation

$$\frac{\partial c'}{\partial t} = D_g \frac{1}{r} \frac{\partial^2}{\partial r^2} r c'(r) \,, \tag{5.24}$$

where D_g is the diffusion coefficient. The characteristic time of diffusion in the vicinity of the bubble is R^2/D_g. The time of bubble growth is proportional to $R/\dot{R}$. In the vicinity of the saddle point the rate $\dot{R}$ is small and $R\dot{R} \ll D_g$. This difference makes it possible to omit in Eq. (5.24) the derivative of concentration with respect to time. Then in the vicinity of the saddle point of the potential barrier, Eq. (5.24), determining the concentration profile around a nucleus of radius R, is reduced to

$$D_g \frac{1}{r} \frac{\partial^2}{\partial r^2} r c'(r) = 0 \,. \tag{5.25}$$

The solution of this equation with the boundary conditions

$$c'(\infty) = c'_\infty, \quad c'(R) = c'_R \tag{5.26}$$

is

$$c'(r) = c'_\infty + (c'_R - c'_\infty)\frac{R}{r} \,. \tag{5.27}$$

Hence the diffusion flux into the direction of the nucleus is

$$\dot{N}''_{i,g} = -4\pi R^2 D_g \frac{\mathrm{d}\rho_i}{\mathrm{d}r} = -4\pi R^2 D_g \rho' (c'_R - c'_\infty) \,. \tag{5.28}$$

The total rate of change of the number of molecules of each of the components in a bubble due to molecular exchange and diffusional supply of substance is given by

$$\dot{N}''_i = \left[\left(\dot{N}''_{i,m}\right)^{-1} + \left(\dot{N}''_{i,g}\right)^{-1} \right]^{-1} \,. \tag{5.29}$$

In order to take into account changes in temperature at the boundary of a growing bubble, Eqs. (5.15) and (5.29) should be supplemented by the heat conduction equation. In the stationary regime, the temperature field around a bubble is determined by the solution of the equation

$$\frac{\partial^2}{\partial r^2} T'(r) = 0 \tag{5.30}$$

with the boundary conditions

$$T'(\infty) = T'_\infty \,, \quad \left(\frac{\partial T'}{\partial r}\right)_{r=R} = \frac{\dot{N}'' l}{4\pi \lambda R^2} \,, \tag{5.31}$$

where λ is the thermal conductivity factor, $\dot{N}'' = \dot{N}_1'' + \dot{N}_2''$ is the rate of change of the number of molecules in a bubble, and l is the latent heat of evaporation. In a binary mixture

$$l = l_1(1 - c'') + l_2 c'' - L \tag{5.32}$$

holds, where l_1, l_2 are the latent heats of evaporation of the components of the solutions, and L is the heat of mixing.

From Eqs. (5.30) and (5.31), we have for the temperature of the liquid at the bubble boundary

$$T_R' = T_\infty' - \frac{l}{4\pi\lambda}\frac{\dot{N}''}{R} \,. \tag{5.33}$$

A small change in temperature around a growing bubble will affect considerably only the value of the equilibrium pressure of the components of the vapor in the bubble p_{Ri}''. By expanding p_{Ri}'' into a series in the vicinity of $T' = T_\infty'$ and restricting ourselves to the first terms of the expansion, we obtain

$$p_{Ri}''(T') = p_{i*}''(T_\infty') + \left(\frac{\partial p_i''}{\partial T}\right)(T_R' - T_\infty') \,. \tag{5.34}$$

Substitution of Eq. (5.33) into Eq. (5.34) yields

$$p_{Ri}''(T') = p_{i*}''(T_\infty') - \frac{l\,\mathrm{d}_{Ti}}{4\pi\lambda}\frac{\dot{N}''}{R_*} \,, \tag{5.35}$$

where $\mathrm{d}_{Ti} = (\partial p_i''/\partial T)$. Thus, an account of the thermal effects on bubble growth will be reflected only on the molecular and the diffusional interaction of a bubble with the liquid surrounding it. From Eqs. (5.23) and (5.35) we have

$$\dot{N}_{i,m}'' = \frac{\pi\beta_i v_{ti} R^2}{k_\mathrm{B} T}\left(p_{i*}'' - p_i'' - \frac{l\,\mathrm{d}_{Ti}}{4\pi\lambda}\frac{\dot{N}''}{R_*}\right) \,. \tag{5.36}$$

For weak solutions, Eq. (5.28) may be written as

$$\dot{N}_{i,g}'' = 4\pi R\rho' D_g H(p_{Ri}'' - p_i'') \,, \tag{5.37}$$

where H is the Henry constant. After substitution of Eq. (5.35) into Eq. (5.37) we have

$$\dot{N}_{i,g}'' = 4\pi R\rho' D_g H\left(p_{i*}'' - p_i'' - \frac{l\,\mathrm{d}_{Ti}}{4\pi\lambda}\frac{\dot{N}''}{R_*}\right) \,. \tag{5.38}$$

Let us go over now in Eq. (5.38) to dimensionless variables (cf. Eq. (5.5)). By expanding the right-hand side of the expressions in the vicinity of the saddle point as power series in y, z, $\dot{x}$ and restricting ourselves, due to the smallness of the rates $\dot{N}_1''$ and $\dot{N}_2''$ to linear terms, we arrive at

$$\dot{y} = \frac{1+\delta_2}{1+\delta_1+\delta_2}\frac{\nu_1}{\nu_1 b_1\omega_1 + 1}\frac{3bp_*''}{4\eta}y + \frac{\delta_1}{1+\delta_1+\delta_2}\frac{\nu_2}{\nu_2 b_2\omega_2 + 1}\frac{3bp_*''}{4\eta}z - \dot{x} \,, \tag{5.39}$$

$$\dot{z} = \frac{\delta_2}{1+\delta_1+\delta_2}\frac{\nu_1}{\nu_1 b_1\omega_1+1}y + \frac{1+\delta_1}{1+\delta_1+\delta_2}\frac{\nu_2}{\nu_2 b_2\omega_2+1}\frac{3bp''_*}{4\eta}z - \dot{x}, \tag{5.40}$$

where

$$\omega_i = \frac{p''_{i*}R_*}{\beta_i v_{ti}\eta}\ ,\ \nu_i = \frac{2D_g H\rho'\eta kT}{\sigma R_*}\ ,\ \delta'_i = \frac{l\beta_i v_{ti}R_* d_{Ti}}{4\lambda k_B T}\ ,\ \delta_i = \frac{\nu_i b_i\omega_i}{1+\nu_i b_i\omega_i}\delta'_i\ . \tag{5.41}$$

The components of the tensor of generalized diffusion in the space of x, y, z, $\dot{x}$ can be found from the system of equations

$$\begin{aligned} D_{xx}F_x &+ D_{xy}F_y &+ D_{xz}F_z &+ D_{x\dot{x}}F_v &= \dot{x}\ ,\\ D_{yx}F_x &+ D_{yy}F_y &+ D_{yz}F_z &+ D_{y\dot{x}}F_v &= \dot{y}\ ,\\ D_{zx}F_x &+ D_{zy}F_y &+ D_{zz}F_z &+ D_{z\dot{x}}F_v &= \dot{z}\ ,\\ D_{\dot{x}x}F_x &+ D_{\dot{x}y}F_y &+ D_{\dot{x}z}F_z &+ D_{\dot{x}\dot{x}}F_v &= \ddot{x}\ . \end{aligned} \tag{5.42}$$

By writing Eq. (5.42), taking into account Eqs. (5.20), (5.22), (5.39), (5.40) and the fact that $\dot{x} = v/v_*$, after setting equal the terms on the left- and right-hand sides at x, y, z, $\dot{x}$, we have

$$\begin{aligned} &D_{xx} = D_{xy} = D_{xz} = D_{yx} = D_{zx} = 0\ ,\\ &D_{x\dot{x}} = -D_{\dot{x}x} = D_{y\dot{x}} = -D_{\dot{x}y} = D_{z\dot{x}} = -D_{\dot{x}z} = \frac{3b^2 p''^2_*}{32\eta^2\varphi G_*}\ ,\\ &D_{zy} = D_{yz} = \frac{\delta_2}{1+\delta_1+\delta_2}\frac{\nu_1 b_1}{\nu_1 b_1\omega_1+1}\frac{3bp''_*}{8\eta G_*}\ ,\\ &D_{yy} = \frac{1+\delta_2}{1+\delta_1+\delta_2}\frac{\nu_1}{\nu_1 b_1\omega_1+1}\frac{3bp''_*}{8\eta G_*}\ ,\\ &D_{zz} = \frac{1+\delta_1}{1+\delta_1+\delta_2}\frac{\nu_2}{\nu_2 b_2\omega_2+1}\frac{3bp''_*}{8\eta G_*}\ ,\quad D_{\dot{x}\dot{x}} = \frac{3b^3 p''^3_*}{128\eta^3 G^2_*\varphi}\ . \end{aligned} \tag{5.43}$$

The tensor obtained is symmetrical, which is in agreement with the general principles of the linear thermodynamics of irreversible processes.

5.2.4 The Nucleation Rate

The presence of nonzero cross-terms in the tensor of generalized diffusion equation (5.43) implies that the variables of a nucleus $\mathbf{q}$ are not separated in the kinetic equation (5.3). As shown in [37–39], such a separation of variables without the loss of diagonality of the matrix of the second-order derivatives for the potential surface Ψ can be achieved by transition to a system of coordinates $\{x', y', z', \dot{x}'\}$, which is the system of the main axes of the tensor $\mathbf{D}\Psi$. In the new system of coordinates, the diagonal components $(\mathbf{D}\Psi)' \equiv \mathbf{diag}\{\chi_0, \chi_1, \chi_2, \chi_3\}$ of the tensor are determined as the roots of the characteristic equation

$$\det(\mathbf{D}\Psi - \chi\mathbf{I}) = \mathbf{0}\ , \tag{5.44}$$

where $\mathbf{I}$ is a unit tensor. Owing to the presence of one negative term in the matrix Ψ, among the eigenvalues of χ one value χ_0 is negative and the other three χ_1, χ_2 and χ_3 possess a positive real part.

After going over in Eq. (5.3) to new variables and integrating the obtained equation with respect to y', z', $\dot{x}'$, we have a one-dimensional kinetic equation with respect to the variable χ', whose stationary solution under the boundary conditions

$$\frac{n_{sx'}}{n_{ex'}} \to \begin{cases} 1 & x' \to -\infty \\ 0 & x' \to +\infty \end{cases} \tag{5.45}$$

may be presented in the form [37]

$$J \equiv j'_{x'} = |\chi_0| \left(\frac{1}{2\pi |\Psi_{x'x'}|} \right)^{1/2} n_{ex'}|_{x'=0} \, . \tag{5.46}$$

In Ref. [38], one can find evidence for the fact that the form of Eq. (5.46) is invariant with respect to the choice of the unstable variable x'. By returning to the initial variable x (the dimensionless volume of a bubble) and going over to dimensional quantities we obtain

$$J = C_v |\chi_0| \left(\frac{4}{3} \pi G_* \right)^{1/2} \exp(-G_*) = C_v |\chi_0| \frac{R_*^2}{v_*} \left(\frac{k_B T}{\sigma} \right)^{1/2} \exp(-G_*) \, . \tag{5.47}$$

Equation (5.47) is the final result of the steady-state multiparameter nucleation theory.

The specific character of the metastable system is mainly taken here into account by the decrement of increase of the unstable variable χ_0. A substitution of Eqs. (5.10) and (5.43) into Eq. (5.44) yields a fourth-order equation for the determination of χ_0. We have (with $\tilde{\chi} = \chi(4\eta/3bp''_*)$)

$$\begin{aligned}
&\tilde{\chi}^4 - \tilde{\chi}^3 \left[\frac{1+\delta_2}{1+\delta_1+\delta_2} \frac{\nu_1}{\nu_1 b_1 \omega_1 + 1} + \frac{1+\delta_1}{1+\delta_1+\delta_2} \frac{\nu_2}{\nu_2 b_2 \omega_2 + 1} + \frac{1}{3\varphi} \right] \\
&+ \tilde{\chi}^2 \left[\frac{(1+\delta_1)(1+\delta_2)}{(1+\delta_1+\delta_2)^2} \frac{\nu_1}{\nu_1 b_1 \omega_1 + 1} \frac{\nu_2}{\nu_2 b_2 \omega_2 + 1} + \frac{1+\delta_2}{1+\delta_1+\delta_2} \frac{\nu_1}{\nu_1 b_1 \omega_1 + 1} \frac{1}{3\varphi} \right. \\
&+ \frac{1+\delta_1}{1+\delta_1+\delta_2} \frac{\nu_2}{\nu_2 b_2 \omega_2 + 1} \frac{1}{3\varphi} - \frac{\delta_1 \delta_2}{(1+\delta_1+\delta_2)^2} \frac{\nu_1}{\nu_1 b_1 \omega_1 + 1} \frac{\nu_2}{\nu_2 b_2 \omega_2 + 1} \\
&\left. + \left(\frac{1}{3b_1} + \frac{1}{3b_2} - \frac{1}{9} \right) \frac{1}{\varphi} \right] - \tilde{\chi} \left[\frac{(1+\delta_1)(1+\delta_2)}{(1+\delta_1+\delta_2)^2} \frac{\nu_1}{\nu_1 b_1 \omega_1 + 1} \frac{\nu_2}{\nu_2 b_2 \omega_2 + 1} \frac{1}{3\varphi} \right. \\
&+ \frac{1+\delta_2}{1+\delta_1+\delta_2} \frac{\nu_1}{\nu_1 b_1 \omega_1 + 1} \frac{1}{3b_2\varphi} + \frac{1+\delta_1}{1+\delta_1+\delta_2} \frac{\nu_2}{\nu_2 b_2 \omega_2 + 1} \frac{1}{3b_1\varphi} \\
&- \frac{\delta_1 \delta_2}{(1+\delta_1+\delta_2)^2} \frac{\nu_1}{\nu_1 b_1 \omega_1 + 1} \frac{\nu_2}{\nu_2 b_2 \omega_2 + 1} \frac{1}{3\varphi} - \frac{1+\delta_2}{1+\delta_1+\delta_2} \frac{\nu_1}{\nu_1 b_1 \omega_1 + 1} \frac{1}{9\varphi} \\
&- \frac{1+\delta_1}{1+\delta_1+\delta_2} \frac{\nu_2}{\nu_2 b_2 \omega_2 + 1} \frac{1}{9\varphi} - \frac{\delta_1 \delta_2}{(1+\delta_1+\delta_2)^2} \frac{\nu_1}{\nu_1 b_1 \omega_1 + 1} \frac{\nu_2}{\nu_2 b_2 \omega_2 + 1} \frac{1}{3\varphi} \\
&\left. + \frac{\delta_1}{1+\delta_1+\delta_2} \frac{1}{b_1} \frac{\nu_2}{\nu_2 b_2 \omega_2 + 1} \frac{1}{3\varphi} + \frac{\delta_2}{1+\delta_1+\delta_2} \frac{1}{b_2} \frac{\nu_1}{\nu_1 b_1 \omega_1 + 1} \frac{1}{3\varphi} \right]
\end{aligned}$$

$$- \frac{(1+\delta_1)(1+\delta_2)}{(1+\delta_1+\delta_2)^2} \frac{\nu_1}{\nu_1 b_1 \omega_1 + 1} \frac{\nu_2}{\nu_2 b_2 \omega_2 + 1} \frac{1}{9\varphi} + \frac{\delta_1 \delta_2}{(1+\delta_1+\delta_2)^2} \frac{\nu_1}{\nu_1 b_1 \omega_1 + 1} \frac{\nu_2}{\nu_2 b_2 \omega_2 + 1} \frac{1}{9\varphi} = 0 \,. \quad (5.48)$$

5.2.5 Discussion of the Results

We will examine, now, some limiting regimes of nucleation in a binary solution. If the characteristic time of heat supply to a bubble is much shorter than all other time scales of the problem, the temperature of the solution is constant up to the bubble surface. In this case $\delta_1 \ll 1$, $\delta_2 \ll 1$, and Eq. (5.48) is reduced to

$$\tilde{\chi}^4 - \tilde{\chi}^3 \left[\frac{\nu_1}{\nu_1 b_1 \omega_1 + 1} + \frac{\nu_2}{\nu_2 b_2 \omega_2 + 1} + \frac{1}{3\varphi} \right] + \tilde{\chi}^2 \left[\frac{\nu_1}{\nu_1 b_1 \omega_1 + 1} \frac{\nu_2}{\nu_2 b_2 \omega_2 + 1} + \frac{\nu_1}{\nu_1 b_1 \omega_1 + 1} \frac{1}{3\varphi} + \frac{\nu_2}{\nu_2 b_2 \omega_2 + 1} \frac{1}{3\varphi} + \left(\frac{1}{3b_1} + \frac{1}{3b_2} - \frac{1}{9} \right) \frac{1}{\varphi} \right] - \tilde{\chi} \left[\frac{\nu_1}{\nu_1 b_1 \omega_1 + 1} \times \frac{\nu_2}{\nu_2 b_2 \omega_2 + 1} \frac{1}{3\varphi} + \frac{\nu_1}{\nu_1 b_1 \omega_1 + 1} \frac{1}{3b_2 \varphi} + \frac{\nu_2}{\nu_2 b_2 \omega_2 + 1} \frac{1}{3b_1 \varphi} - \frac{\nu_1}{\nu_1 b_1 \omega_1 + 1} \frac{1}{9\varphi} - \frac{\nu_2}{\nu_2 b_2 \omega_2 + 1} \frac{1}{9\varphi} \right] - \frac{\nu_1}{\nu_1 b_1 \omega_1 + 1} \frac{\nu_2}{\nu_2 b_2 \omega_2 + 1} \frac{1}{9\varphi} = 0 \,. \quad (5.49)$$

Equation (5.49) describes the dynamics of isothermal growth for a vapor bubble of near-critical size in a superheated binary solution for any arbitrary dependence among viscosity, inertia effects, rate of evaporation of molecules of a solvent and a dissolved substance into a bubble, and the diffusional supply of a substance to a growing nucleus.

At a high viscosity of the solution and high supersaturations, inertia effects of the liquid may be neglected. The number of significant variables is reduced in this case to three. The condition of neglect of inertia effects can be written as

$$\varphi \ll 1 \,. \quad (5.50)$$

Equations (5.48) and (5.49) reduce in this situation to cubic equations. In the isothermal case we get from Eqs. (5.49) and (5.50) the result

$$\tilde{\chi}^3 - \tilde{\chi}^2 \left[\frac{3-b}{3b} + \frac{\nu_1}{\nu_1 b_1 \omega_1 + 1} + \frac{\nu_2}{\nu_2 b_2 \omega_2 + 1} \right] + \tilde{\chi} \frac{1}{b_1 b_2} \left[\frac{\nu_1 b_1}{\nu_1 b_1 \omega_1 + 1} \frac{\nu_2 b_2}{\nu_2 b_2 \omega_2 + 1} + \frac{3-b_1}{3} \frac{\nu_2 b_2}{\nu_2 b_2 \omega_2 + 1} + \frac{3-b_2}{3} \frac{\nu_1 b_1}{\nu_1 b_1 \omega_1 + 1} \right] + \frac{1}{3} \frac{\nu_1}{\nu_1 b_1 \omega_1 + 1} \frac{\nu_2}{\nu_2 b_2 \omega_2 + 1} = 0 \,. \quad (5.51)$$

Substitution of the negative root of Eq. (5.51) into Eq. (5.47) gives an expression for the nucleation rate in a viscous volatile solution, in which the diffusional supply of the components

of the mixture to a growing bubble is of great importance. If the diffusional mechanism is characteristic only for one (the first) of the components of the solution ($\nu_2 \gg 1$), Eq. (5.51) yields

$$\tilde{\chi}^3 - \tilde{\chi}^2\left[\frac{3-b}{b} + \frac{\nu_1}{\nu_1 b_1\omega_1 + 1} + \frac{1}{b_2\omega_2}\right] + \tilde{\chi}\frac{1}{b_1 b_2}\left[\frac{\nu_1 b_1}{\nu_1 b_1\omega_1 + 1}\frac{1}{\omega_2} + \frac{3-b_1}{3\omega_2} + \frac{3-b_2}{3}\frac{\nu_1 b_1}{\nu_1 b_1\omega_1 + 1}\right] + \frac{1}{3b_2\omega_2}\frac{\nu_1}{\nu_1 b_1\omega_1 + 1} = 0\,. \quad (5.52)$$

In such a form the equation for the description of the bubble nucleation kinetics in supersaturated liquid solutions is given in Ref. [43]. Baidakov [31, 44] was the first to examine the boiling-up kinetics of binary liquid solutions accounting for both the molecular and the diffusional mechanism of transport of matter to the growing bubble at arbitrary values of the viscosity of the solution and volatility of both dissolved substance and solvent.

In Refs. [31, 44], Eq. (5.52) has a somewhat different form. This difference is connected with the fact that in these papers the diffusional flux to a bubble was not taken into account independently of the molecular exchange, but as a certain additional term to the molecular exchange. Numerical calculations show that the results of these two approaches agree within the errors of the thermophysical parameters entering the equations. As distinct from Eq. (5.52), to which the diagonal tensor of generalized diffusion corresponds, in Refs. [31, 44] the diffusion tensor is nondiagonal.

The diffusional flux to a bubble may be neglected if the characteristic time of diffusion is much shorter than the other time scales connected with the pressure changes in the bubble. In this case, the concentration in the solution is uniform up to the bubble surface, $\nu_i \to \infty$, and Eq. (5.51) is transformed to

$$\tilde{\chi}^3 - \tilde{\chi}^2\left(\frac{3-b}{3b} + \frac{1}{b_1\omega_1} + \frac{1}{b_2\omega_2}\right) + \tilde{\chi}\frac{1}{b_1 b_2}\left(\frac{3-b_2}{3\omega_1} + \frac{3-b_1}{3\omega_2} + \frac{1}{\omega_1\omega_2}\right) + \frac{1}{3b_1 b_2\omega_1\omega_2} = 0\,. \quad (5.53)$$

Substitution of the negative root of Eq. (5.53) into Eq. (5.47) gives an expression for the nucleation rate in a viscous and volatile solution with a sufficiently high diffusion coefficient which ensures the absence of a depletion zone around the bubble.

With $p''_{1*} \to 0$, $\beta_1 \to 0$, $c' \neq 0$ and $p''_{2*} \to 0$, $\beta_2 \to 0$, $c' \to 0$, Eqs. (5.51) and (5.47) describe the boiling-up of a solution with a nonvolatile component and a pure volatile liquid, respectively. In this case, the number of essential variables of the bubble reduces to two: the volume and the gas pressure in the bubble (nonvolatile solvent), the volume and the vapor pressure in the bubble (one-component liquid). The cubic equation (5.51) reduces then to a quadratic one: if the solvent is nonvolatile, we have

$$\tilde{\chi}^2 - \tilde{\chi}\left(\frac{3-b_2}{3b_2} + \frac{\nu_2}{\nu_2 b_2\omega_2 + 1}\right) - \frac{\nu_2}{\nu_2 b_2\omega_2 + 1} = 0\,, \quad (5.54)$$

if the system is one-component, one gets

$$\tilde{\chi}^2 - \tilde{\chi}\left(\frac{3-b_1}{3b_1} + \frac{1}{b_1\omega_1}\right) - \frac{1}{3b_1\omega_1} = 0\,. \quad (5.55)$$

With appropriately chosen definitions of the parameters, Eq. (5.55) coincides with Eq. (29) from Ref. [42], and Eq. (5.54) at $D_g \to \infty$ transforms to Eq. (39) from Ref. [21].

The limiting case $\omega_1 \to \infty$, $\omega_2 \to \infty$ is realized if $\eta \to 0$ and it is responsible for the boiling-up of a nonviscous volatile solution. At a low viscosity, liquid inertia effects may prove to be essential. The range of superheatings, where the effect of the viscosity is small, and at the same time the liquid inertia effects does not affect the process yet, is determined by the following inequalities:

$$\varphi \ll 1 \ll \begin{cases} \omega_1 , \\ \omega_2 . \end{cases} \tag{5.56}$$

Here at

$$\frac{3-b}{3} + b\nu_1 + b\nu_2 < 0 \tag{5.57}$$

it follows from Eq. (5.51) that

$$\chi_0 = \frac{3}{4}\frac{p''_*}{\eta}\left(\frac{3-b}{3} + b\nu_1 + b\nu_2\right) . \tag{5.58}$$

If the supply of a substance to a growing bubble proceeds much faster than it is expanded by the pressure variation in the nucleus, and this occurs when

$$D_g \gg \frac{3R_*^2 p''_* \rho''(\beta_1 v_{t1}\, \mathrm{d}_{T1} + \beta_2 v_{t2}\, \mathrm{d}_{T2})}{4p''_*\rho' |2\sigma - 3p''_* R_*|} \tag{5.59}$$

holds, then the last terms in Eq. (5.58) may be neglected and we obtain

$$\chi_0 = \frac{1}{4}\frac{p''_*}{\eta}(3-b) . \tag{5.60}$$

Equations (5.47) and (5.60) describe the boiling-up of a weakly viscous solution with volatile components at tensile stresses exceeding $2p''_*$. At a finite value of p''_{2*}, the parameters η and σ in Eq. (5.60) refer to a solution each of the components of which is volatile. If

$$\frac{3-b}{3} + b\nu_1 + b\nu_2 > 0 , \tag{5.61}$$

the cubic equation (5.51) reduces to a quadratic one

$$\tilde{\chi}^2\left(\frac{3-b}{3b} + \nu_1 + \nu_2\right) - \tilde{\chi}\frac{1}{b_1 b_2}\left[\frac{3-b_1}{3}\frac{\nu_2 b_2}{\nu_2 b_2 \omega_2 + 1} + \frac{3-b_2}{3}\frac{\nu_1 b_1}{\nu_1 b_1 \omega_1 + 1} + \frac{\nu_1 b_1}{\nu_1 b_1 \omega_1 + 1}\frac{\nu_2 b_2}{\nu_2 b_2 \omega_2 + 1}\right] - \frac{1}{3}\frac{\nu_1}{\nu_1 b_1 \omega_1 + 1}\frac{\nu_2}{\nu_2 b_2 \omega_2 + 1} = 0 . \tag{5.62}$$

For the negative root of Eq. (5.62), we are interested in, we have

$$\chi_0 = \frac{3bp''_*}{8\eta}\left(\frac{3-b}{3b}+\nu_1+\nu_2\right)^{-1}\left\{\frac{1}{b_1b_2}\left(\frac{3-b_1}{3}\frac{\nu_2b_2}{\nu_2b_2\omega_2+1}\right.\right.$$
$$+\frac{3-b_2}{3}\frac{\nu_1b_1}{\nu_1b_1\omega_1+1}+\frac{\nu_1b_1}{\nu_1b_1\omega_1+1}\frac{\nu_2b_2}{\nu_2b_2\omega_2+1}\Bigg)-\Bigg[\frac{1}{b_1^2b_2^2}\Bigg(\frac{3-b_1}{3}\frac{\nu_2b_2}{\nu_2b_2\omega_2+1}$$
$$+\frac{3-b_2}{3}\frac{\nu_1b_1}{\nu_1b_1\omega_1+1}+\frac{\nu_1b_1}{\nu_1b_1\omega_1+1}\frac{\nu_2b_2}{\nu_2b_2\omega_2+1}\Bigg)^2$$
$$\left.\left.+\frac{4}{3}\frac{\nu_1}{\nu_1b_1\omega_1+1}\frac{\nu_2}{\nu_2b_2\omega_2+1}\left(\frac{3-b}{3b}+\nu_1+\nu_2\right)\Bigg]^{1/2}\right\}. \quad (5.63)$$

Equations (5.47) and (5.63) describe the nucleation rate in a superheated nonviscous solution with volatile components at positive as well as small negative pressures and diffusional gas supply to a bubble. If diffusion processes may be neglected, then

$$\chi_0 = \frac{3bp''_*}{8\eta}\left(\frac{3-b}{3b}\right)^{-1}\left\{\frac{1}{b_1b_2}\left(\frac{3-b_2}{3\omega_1}+\frac{3-b_1}{3\omega_2}\right)-\left[\frac{1}{b_1^2b_2^2}\left(\frac{3-b_2}{3\omega_1}+\frac{3-b_1}{3\omega_2}\right)^2\right.\right.$$
$$\left.\left.+\frac{4}{3b_1b_2\omega_1\omega_2}\left(\frac{3-b}{3b}\right)\Bigg]^{1/2}\right\}. \quad (5.64)$$

At $p''_{2*} \to 0$, $1 \ll \omega_2 \ll b_2\omega_2$, we consider the boiling-up of a nonviscous liquid solution with one volatile component. In this case, from Eq. (5.64) we have for the decrement χ_0 the result

$$\chi_0 = \frac{\beta_1 v_{t1}\sigma}{2p''_{1*}R_*^2}\left(\frac{b_1}{3}-1\right)^{-1}. \quad (5.65)$$

Here the parameters β_1, v_{t1}, p''_{1*} characterize the volatile component, and σ, R_* the solution as a whole. By substituting Eq. (5.65) into Eq. (5.47), we obtain an expression for the nucleation rate, which coincides in its form with Eq. (39) from Ref. [42] and differs from Eq. (36) from Ref. [41]. The latter, with neglect of the temperature effects at the bubble surface, differs from the obtained expression by the factor ρ'/ρ'' connected with a different choice of the constant of normalization of the equilibrium distribution function in Refs. [41, 42].

At $p''_{1*} \to 0$, $p''_{2*} \to 0$, a bubble is characterized by only one variable, its volume, and the problem becomes an one-parametric one. From Eq. (5.51) we obtain then

$$\chi_0 = -\frac{\sigma}{2\eta R_*}. \quad (5.66)$$

Substituting Eq. (5.66) into Eq. (5.47) gives for the nucleation rate an expression which coincides with Eqs. (36) and (51) of Refs. [21, 42], and also, accurate up to the normalization constant, with Eq. (34) in Ref. [41]. The difference is due to the fact that, if the parameters η and σ in Eq. (5.66) characterize a mixture of two nonvolatile liquids, in Eqs. (34) and (36) of Refs. [41, 42] these are properties of a pure liquid. At high negative pressures, when $b \gg 3$, Eq. (5.65) is converted into Eq. (5.66).

It should be mentioned that Eq. (5.47) is valid after completion of a certain incubation time τ_l, after which nuclei, irrespective of their initial distribution, appear at a regular rate J. The time τ_l may be defined as the time of diffusional transition of nuclei of a new phase over the critical region with respect to the unstable variable x [29], i.e.

$$\tau_l = \tau_x \cong \frac{R_x}{\dot{R}_x} \cong \frac{1}{|\chi_0|} \; . \tag{5.67}$$

Such an approach is in agreement with other evaluations of the nonsteady-state time [14] and a nonsteady-state solution [38] of the nucleation problem for the multiparameter case.

5.3 Nucleation Thermodynamics

5.3.1 The Gibbs Method

We examine, now, the process of homogeneous formation of a new phase at conditions of constant pressure and temperature. A vapor bubble is in equilibrium with a superheated binary solution if the following conditions are fulfilled

$$p_*'' = p' + \frac{2\sigma}{R_*} \; , \tag{5.68}$$

$$\mu_i''(p_*'', c_*'') = \mu_i'(p', c'), \quad i = 1, 2 \; . \tag{5.69}$$

Substituting Eqs. (5.68) and (5.69) into Eq. (5.6) gives an extremum value for the change of the thermodynamic potential $\Delta\Phi$, corresponding to the work of formation of a vapor bubble which is in equilibrium with the medium [45]

$$\Delta\Phi_* = W_* = \tfrac{1}{3}\sigma A_* = \tfrac{4}{3}\pi R_*^2 \sigma \; . \tag{5.70}$$

At a given temperature T, pressure p', and concentration c', Eqs. (5.68) and (5.69) determine unambiguously the pressure p_*'', the size R_* and the composition c_*'' of an equilibrium nucleus, which we will denote in the subsequent discussion as a critical one. The calculation, by Eqs. (5.68) and (5.70), of p_*'', R_*, c_*'', and W_* requires knowledge of the equation of state for a binary solution and of the nucleus surface tension as a function of its size, temperature and concentration. In order to obtain approximative expressions, making it possible to calculate p_*'', c_*'', R_* by a limited amount of data, we will express the composition c_*'' and the pressure p_*'' inside a critical bubble in terms of their values at a flat interface, c_s', p_s and the parameters of the initial phase, c' and p'.

The chemical (or diffusion) equilibrium at a flat interface is determined by the following conditions:

$$\mu_i''(p_s, c_s'') = \mu_i'(p_s, c_s') \; . \tag{5.71}$$

By subtracting Eq. (5.71) from Eq. (5.69), we obtain

$$\mu_i''(p'', c'') - \mu_i''(p_s, c_s'') = \mu_i'(p', c') - \mu_i'(p_s, c_s') \; . \tag{5.72}$$

This relation may be rewritten as

$$\int_{p_s}^{p''} \mathrm{d}\mu_i''(p'', c'') = \int_{p_s}^{p'} \mathrm{d}\mu_i'(p', c') \,. \tag{5.73}$$

Considering the vapor mixture in a bubble to be an ideal gas, and the liquid to be incompressible, after integrating Eq. (5.73) we have [46]

$$c_{i*}'' = c_{si}'' \frac{p_s}{p_*''} \exp\left(-\frac{p_s - p'}{p_s} \frac{v_i'}{v''}\right) \,, \tag{5.74}$$

where v_i is the ideal partial volume of the ith component, v'' is the specific volume of the gas mixture in equilibrium with the solution. From Eq. (5.74) the total pressure in a critical bubble is obtained as

$$p_*'' = p_*'' c_*'' + p_*''(1 - c_*'') = p_s \left[c_s'' \exp\left(-\frac{p_s - p'}{p_s} \frac{v_1'}{v''}\right) + (1 - c_s'') \exp\left(-\frac{p_s - p'}{p_s} \frac{v_2'}{v''}\right)\right] \,. \tag{5.75}$$

Substituting Eq. (5.75) into Eq. (5.74) gives

$$c_*'' = c_s'' \left\{ c_s'' + (1 - c_s'') \exp\left[\frac{(p_s - p')}{p_s} \frac{(v_1' - v_2')}{v''}\right]\right\}^{-1} \,. \tag{5.76}$$

When the supersaturations are not too high, the exponents of the exponential functions in Eqs. (5.75) and (5.76) are small. By expanding the exponential function into a series and limiting ourselves to the first terms, we obtain for equilibrium values of p_*'' and c_*'' the estimates

$$c_*'' = c_s'' \left[1 + (1 - c_s'') \frac{(p_s - p')}{p_s} \frac{(v_1' - v_2')}{v''}\right]^{-1} \,, \tag{5.77}$$

$$p_*'' = p_s \left[1 - \frac{p_s - p'}{p_s} \frac{v_2'}{v''} - c_s'' \frac{(p_s - p')}{p_s} \frac{(v_1' - v_2')}{v''}\right] \,. \tag{5.78}$$

Using the conditions of mechanical equilibrium for a critical bubble Eq. (5.68), we have

$$R_* = \frac{2\sigma}{(p_s - p')\left[1 - \frac{v_2'}{v''} - c_s'' \frac{(v_1' - v_2')}{v''}\right]} \,. \tag{5.79}$$

Substitution of Eq. (5.79) into Eq. (5.70) gives

$$W_* = \frac{16\pi}{3} \left\{ \frac{\sigma^3}{(p_s - p')^2 \left[1 - \frac{v_2'}{v''} - c_s'' \frac{(v_1' - v_2)}{v''}\right]^2} \right\} \,. \tag{5.80}$$

Equations (5.77)–(5.80) make it possible to calculate all the main parameters of a new-phase nucleus in a superheated binary solution by employing data on the phase equilibrium. The last expression is similar to the formula for the work of formation of a critical bubble in a one-component system [14] and goes over into it at $c_s'' = 0$.

At some distance from the critical point of the solvent, and at superheatings that are not too high, solutions of cryogenic liquids may be regarded as weak solutions. In this case, the parameters of a critical nucleus may be expressed in terms of the phase-equilibrium parameters of a pure solvent [47]. For the chemical potentials of a solvent and a dissolved substance in the phase surrounding the bubble, we have [48]

$$\mu_1' = \mu_{01}(p') - k_B T c' \,, \tag{5.81}$$

$$\mu_2' = \mu_2(p', c_s') + k_B T \ln\left(\frac{c'}{c_s'}\right) \,, \tag{5.82}$$

where the subscript 0 refers to a pure component. Since $c' \ll 1$, the concentration c', defined as the mole fraction of a dissolved substance, may be taken, in a first approximation, equal to the ratio of the number of molecules of a gas component in the solution to the number of molecules of a solvent. In an ideal gas approximation for the chemical potentials of vapor and gas in a bubble one can write [49]

$$\mu_1'' = \mu_{01}(p_{0s}) + k_B T \ln\frac{p_*''}{p_{0s}} + k_B T \ln(1 - c_*'') \,, \tag{5.83}$$

$$\mu_2'' = \mu_2(p', c_s'') + k_B T \ln\frac{p_*''}{p'} + k_B T \ln\frac{c_*''}{c_s''} \,. \tag{5.84}$$

Assuming the liquid solvent to be incompressible, we may present Eq. (5.81) as follows

$$\mu_1' = \mu_{01}(p_{0s}) + v_{01}'(p' - p_{0s}) - k_B T c' \,, \tag{5.85}$$

where v_{01}' is the specific volume of a pure solvent. From Eqs. (5.83), (5.85), and the condition of chemical equilibrium equation (5.69), we have

$$p_{1*}'' = p_*''(1 - c_*'') = p_{0s} \exp\left[\frac{v_{01}'}{k_B T}(p' - p_{0s}) - c'\right] \,. \tag{5.86}$$

At some sufficient distance from the critical point of the solvent, the exponent of the exponential function in Eq. (5.86) is much less than one. By expanding the exponential function into a series we obtain

$$p_{1*}'' = p_{0s}\left(1 - \frac{v_{01}'}{v_{01}''}\frac{p_{0s} - p'}{p_{0s}} - c'\right) \,. \tag{5.87}$$

Similarly from Eqs. (5.82), (5.84), and (5.69) for the partial gas pressure in a critical bubble, we find

$$p_{2*}'' = p_*'' c_*'' = p' c' \frac{c_s''}{c_s'} \,. \tag{5.88}$$

For the total pressure in a critical bubble we have

$$p''_* = (p_{0s} - p') \left(1 - \frac{v'_{01}}{v''_{01}}\right) + p' \left[1 - c' \left(1 - \frac{c''_s}{c'_s}\right)\right] . \tag{5.89}$$

Substitution of Eq. (5.89) into Eq. (5.68) gives a formula for determining the radius of a critical bubble, and substitution of Eqs. (5.89) and (5.68) into Eq. (5.70) yields the expression for the work of formation of a critical bubble in a liquid solution.

As it has been mentioned already, Eqs. (5.77), (5.78), and (5.89) have been applied here in the region of weak metastability. In approaching the spinodal curve, the assumptions of incompressibility of the liquid phase and the ideal character of a vapor–gas mixture in a bubble, used in the derivation, are violated. Another problem of Eqs. (5.68), (5.79), and (5.80) is connected with the absence of information on the size dependence of the surface tension σ. Usually, in calculating the properties of nuclei of a new phase, a macroscopic approximation is utilized, i.e., the nucleus surface tension is considered to be equal to its value at a flat interface. This gap can be removed utilizing the van der Waals method of description of heterogeneous systems, which we are going to discuss in application to the problem considered in the subsequent section.

5.3.2 The van der Waals Method

Another approach that may be used in describing the properties of new-phase nuclei is based on the van der Waals capillarity theory [50]. This method does not require the introduction of the notion of a dividing surface. Cahn and Hilliard were the first to apply it to the problem of nucleation [51].

The change in the grand thermodynamic potential due to the formation of a spherical inhomogeneity in a binary solution is given in van der Waals' approach by

$$\Delta\Omega\{\rho_1, \rho_2\} = 4\pi \int_0^\infty \left(\Delta\omega + \sum_{i,j=1}^{2} \kappa_{ij} \frac{\mathrm{d}\rho_i}{\mathrm{d}r} \frac{\mathrm{d}\rho_j}{\mathrm{d}r} \right) r^2 \, \mathrm{d}r \tag{5.90}$$

with

$$\Delta\omega = p' - p + \sum_{i=1}^{2} [\mu_i(\rho_1, \rho_2) - \mu'_i]\rho_i = f(\rho_1, \rho_2) - f' - \sum_{i=1}^{2} (\rho_i - \rho'_i)\mu'_i . \tag{5.91}$$

Here f is the density of the free energy of a homogeneous system, κ_{ij} is the matrix of the influence coefficients. One prime, as before, refers to the initial value of a parameter in the liquid phase, a parameter without primes shows the current local value. From the conditions of stability of a two-phase two-component system it follows that the inequalities

$$\kappa_{11}\kappa_{22} - \kappa_{12}^2 > 0 , \quad \kappa_{11} > 0 , \quad \kappa_{22} > 0 \tag{5.92}$$

have to be fulfilled. If we take, for the cross coefficient κ_{12}, the relations [52]

$$\kappa_{12} = (\kappa_{11}\kappa_{22})^{1/2} , \tag{5.93}$$

the first of the inequalities (5.92) transforms to an equality, which corresponds to an indifferent equilibrium of the system with respect to density gradients opposite in sign and determines the limiting value of the coefficient κ_{12}. With Eq. (5.93), Eq. (5.91) gets the simpler form

$$\Omega\{\rho_1, \rho_2\} = 4\pi \int_0^\infty \left[\Delta\omega + \kappa_{22} \left(\frac{\mathrm{d}\rho_\beta}{\mathrm{d}r} \right)^2 \right] r^2 \, \mathrm{d}r \ . \tag{5.94}$$

Here $\rho_\beta = (\kappa_{11}/\kappa_{22})^{1/2}\rho_1 + \rho_2$.

The distributions of the densities, ρ_i $(i = \beta, 1, 2)$, in a critical bubble can be found from the solution of the Euler system of equations for the functional equation (5.94), which includes one differential equation

$$\frac{\mathrm{d}^2\rho_\beta}{\mathrm{d}r^2} + \frac{2}{r}\frac{\mathrm{d}\rho_\beta}{\mathrm{d}r} = \frac{\mu_2 - \mu_2'}{2\kappa_{22}} \tag{5.95}$$

with the boundary conditions $\rho_\beta \to \rho_\beta'$ at $r \to \infty$, $\mathrm{d}\rho_\beta/\mathrm{d}r \to 0$ at $r \to 0$ and $r \to \infty$ and one algebraic equation

$$\mu_1 - \mu_1' = (\kappa_{11}/\kappa_{22})^{1/2}(\mu_2 - \mu_2') \ . \tag{5.96}$$

In this case, the work of formation of a critical bubble is given by

$$W_* = \min \max \Delta\Omega\{\rho_1, \rho_2\} \ . \tag{5.97}$$

Equation (5.97) gives an alternative to Eq. (5.70) for calculating W_* and together with Eqs. (5.68)–(5.70) makes it possible to determine the dependence $\sigma(R_*)$. The solution to this problem presupposes a knowledge of the equation of state for a binary solution and the influence coefficients κ_{ij}. The coefficients κ_{ij} are functions of temperature and have a weak dependence on density [52, 53]. Neglecting the dependence of κ_{ij} on ρ_i, the value of κ_{22} for a pure solvent may be determined by data on the surface tension at a flat interface via

$$\sigma_\infty = 2\kappa_{22}^{1/2} \int_{p_s'}^{p_s''} (\Delta\omega)^{1/2} \, \mathrm{d}\rho \ . \tag{5.98}$$

The distribution of density ρ_β in a transition layer is found in this case by solving the equation

$$\kappa_{22} \left(\frac{\mathrm{d}\rho_\beta}{\mathrm{d}z} \right)^2 = \Delta\omega \tag{5.99}$$

with the known boundary conditions.

5.3.3 On the Size Dependence of the Surface Tension of New-Phase Nuclei

According to Gibbs' method of dividing surfaces [45], the formation of a nucleus of radius R in a metastable system results in a change of the thermodynamic potential given by

Eq. (5.6). For bubbles, which are in equilibrium with the phase surrounding them ($R = R_*$), from Eqs. (5.6) and (5.70) we have

$$W_* = 4\pi R_*^2 \sigma + (p' - p'')\frac{4\pi R_*^3}{3} . \tag{5.100}$$

In further derivations, we will omit the subscript $*$ in the specification of the parameters of the critical nucleus in all cases, when such omission is possible without causing confusion.

By solving the system of equations (5.94), (5.97), and (5.100) with respect to the surface tension, we obtain

$$\sigma = \int_0^R (p'' - p)\frac{r^2}{R^2}\,\mathrm{d}r + \int_R^\infty (p' - p)\frac{r^2}{R^2}\,\mathrm{d}r + \int_0^\infty \left[\rho_\beta(\mu_1 - \mu_1') + \kappa_{11}\left(\frac{\mathrm{d}\rho_\beta}{\mathrm{d}r}\right)^2\right]\frac{r^2}{R^2}\,\mathrm{d}r . \tag{5.101}$$

Equations (5.101), (5.95), and (5.96) determine (in the approximation of Eq. (5.93)) the value of the surface tension for a binary solution at a curved interface.

At small curvatures of the separating surface, the surface tension σ may be presented as a series in terms of $1/R$, in which the first term in the expansion is the surface tension at a flat interface. Restricting ourselves to terms squared in curvature, we have

$$\sigma = \sigma_\infty + \frac{\sigma_1}{R} + \frac{\sigma_2}{R^2} . \tag{5.102}$$

Going over to a new variable $z = r - R$ and expanding the quantities in Eqs. (5.95), (5.96), and (5.101) into the Taylor series, we obtain [54]

$$\sigma_0 = 2\kappa_{22}\int_{-\infty}^{+\infty}\left(\frac{\mathrm{d}\rho_{0,0}}{\mathrm{d}z}\right)^2 \mathrm{d}z , \quad \sigma_1 = \sum_{i=1}^{2}\mu_{i,1}'\Delta\rho_{i,\infty}\delta_{i,\infty} , \tag{5.103}$$

$$\sigma_2 = I_1 + 2I_2 + I_3 - I_4 + \sigma_\infty z_*^2 + \frac{1}{2}\sum_{i=1}^{2}\mu_{i,2}'\Delta\rho_{i,\infty}\delta_{i,\infty} , \tag{5.104}$$

where $\Delta\rho_{i,\infty} = \rho_{i,\infty}' - \rho_{i,\infty}''$ is the difference of the densities of the components at a flat interface, $\delta_{i,\infty} = z_{i,e} - z_*$ is the distance between the equimolecular dividing surfaces and the tension surface in a flat interfacial layer,

$$z_* = \frac{2\kappa_{22}}{\sigma_\infty}\int_{-\infty}^{+\infty}\left(\frac{\mathrm{d}\rho_{0,0}}{\mathrm{d}z}\right)^2 z\,\mathrm{d}z , \quad z_{i,e} = \frac{1}{\Delta\rho_{i,\infty}}\int_{-\infty}^{+\infty}\frac{\mathrm{d}\rho_{i,0}}{\mathrm{d}z}z\,\mathrm{d}z , \tag{5.105}$$

$$I_1 = 2\kappa_{22}\int_{-\infty}^{+\infty}\left(\frac{\mathrm{d}\rho_{0,0}}{\mathrm{d}z}\right)^2 (z - z_*)^2\,\mathrm{d}z , \quad I_2 = \sum_{i=1}^{2}\frac{\mu_{i,1}'}{2}\int_{-\infty}^{+\infty}\frac{\mathrm{d}\rho_{i,0}}{\mathrm{d}z}(z - z_*)^2\,\mathrm{d}z , \tag{5.106}$$

$$I_3 = \sum_{i=1}^{2} \frac{\mu'_{i,1}}{2} \int_{-\infty}^{+\infty} \frac{\mathrm{d}\rho_{i,1}}{\mathrm{d}z}(z - z_*)^2 \, \mathrm{d}z \, , \quad I_4 = 2\kappa_{22} \int_{-\infty}^{+\infty} \frac{\mathrm{d}\rho_{0,0}}{\mathrm{d}z}\rho_{0,1} \, \mathrm{d}z \, . \tag{5.107}$$

Equations (5.103)–(5.107) express the parameters of Eq. (5.102) only in terms of the characteristics of a flat interface. This method of calculating the functions $\rho_{i,1}(z)$ is described in detail in Ref. [54].

The values of the coefficients of decomposition for the chemical potentials $\mu'_{i,1}$ and $\mu'_{i,2}$ depend on the way how metastability is generated. At constant temperature, the penetration of a binary solution into a metastable region may be realized in different ways. The particular way of penetration is determined by a trajectory in the space of two independent variables, whose role can be played by the densities ρ_1 and ρ_2, chemical potentials μ_1 and μ_2, etc. We shall examine two ways of penetration: along the line determined by the condition

$$c' = \frac{\rho'_2}{(\rho'_1 + \rho'_2)} = \text{const} \tag{5.108}$$

(c-penetration) and along the line

$$(\mu'_1 - \mu'_{1,0}) = (\kappa_{11}/\kappa_{22})^{1/2}(\mu'_2 - \mu'_{2,0}) \tag{5.109}$$

(β-penetration). The first of the mentioned ways is the traditional one for experimental investigations of nucleation in creating phase metastability in a binary system [29, 43]. The second possibility is interesting as it allows to establish some isomorphism in the behavior of the surface tension of nuclei in a binary and a one-component system.

In fulfilling the condition of Eq. (5.108) we obtain

$$\rho'_{2,1} = \rho'_{1,1}c'/(1 - c') \, , \quad \rho'_{2,2} = \rho'_{1,2}c'/(1 - c') \, . \tag{5.110}$$

Then for the decomposition coefficients of the chemical potential we can write [54]

$$\mu'_{1,1} = \mu'_{2,1}\zeta \, , \quad \mu'_{1,2} = \mu'_{2,2}\zeta + \rho_1'^2\xi \, , \quad \mu'_{2,1} = \frac{-2\sigma_0}{\Delta\rho_{1,0}\zeta + \Delta\rho_{2,0}} \, , \tag{5.111}$$

$$\mu'_{2,2} = \frac{\rho_1'^2\Delta\rho_{1,0}\xi + \sum_{i=1}^{2} \Delta\rho_{i,1}\mu'_{i,1} + 4\sum_{i=1}^{2} \Delta\rho_{i,0}\mu'_{i,1}\delta_{i,0}}{\Delta\rho_{1,0}\zeta + \Delta\rho_{2,0}} \, , \tag{5.112}$$

$$\zeta = \left(\frac{\partial\mu_{1,0}}{\partial\rho}\right)_{c=c'} \Big/ \left(\frac{\partial\mu_{2,0}}{\partial\rho}\right)_{c=c'} \, , \tag{5.113}$$

$$\xi = \left(\frac{\partial^2\mu_{1,0}}{\partial\rho^2}\right)_{c=c'} - \left(\frac{\partial^2\mu_{2,0}}{\partial\rho^2}\right)_{c=c'} \zeta \, , \quad \rho = \rho_1 + \rho_2 \, , \quad \rho_1 = \rho_{1,1} + \rho_{2,1} \, . \tag{5.114}$$

At β-penetration, we have

$$\mu'_{1,1} = \left(\frac{\kappa_{11}}{\kappa_{22}}\right)^{1/2} \mu'_{2,1} \, , \quad \mu'_{1,2} = \left(\frac{\kappa_{11}}{\kappa_{22}}\right)^{1/2} \mu'_{2,1} \, . \tag{5.115}$$

As a result of isomorphism, the coefficients in Eq. (5.102), and also the quantities determining them, prove to be similar to the respective parameters for a one-component system [55]

$$\sigma_1 = -2\sigma_\infty\delta_{0,0}\,, \quad \sigma_2 = I_1+2I_2+I_3-I_4+\sigma_\infty\frac{\Delta\rho_{0,1}}{\Delta\rho_{0,0}}\delta_{0,0}+3\sigma_0\delta_{0,0}^2+\sigma_0 z_{0,e}^2\,, \tag{5.116}$$

where

$$\Delta\rho_{0,0}\mu'_{1,1} = -2\sigma_\infty\,, \quad \Delta\rho_{0,0}\mu'_{1,2} = -\Delta\rho_{0,1}\mu'_{1,1}-4\mu'_{1,1}\Delta\rho_{0,0}z_{0,e}-4\sigma_\infty z_*\,, \tag{5.117}$$

$$I_2 = \frac{\mu'_{1,1}}{2}\int\limits_{-\infty}^{+\infty}\left(\frac{\mathrm{d}\rho_{0,0}}{\mathrm{d}z}\right)z^2\,\mathrm{d}z\,, \quad I_3 = \frac{\mu'_{1,1}}{2}\int\limits_{-\infty}^{+\infty}\left(\frac{\mathrm{d}\rho_{0,1}}{\mathrm{d}z}\right)z\,\mathrm{d}z\,. \tag{5.118}$$

In the Gibbs method of dividing surfaces, the differential equation determining the size dependence of the surface tension takes the form [52]

$$\frac{1}{\sigma}\frac{\mathrm{d}\sigma}{\mathrm{d}(1/R)} = -\frac{2\psi}{1+2\psi/R}\,, \tag{5.119}$$

where

$$\psi = \left(\Gamma_1\frac{\mathrm{d}\mu'_1}{\mathrm{d}(1/R)}+\Gamma_2\frac{\mathrm{d}\mu'_2}{\mathrm{d}(1/R)}\right)\Big/\left(\Delta\rho_1\frac{\mathrm{d}\mu'_1}{\mathrm{d}(1/R)}+\Delta\rho_2\frac{\mathrm{d}\mu'_2}{\mathrm{d}(1/R)}\right)\,. \tag{5.120}$$

Here Γ_i is the absolute adsorption of the ith component. At a small curvature of the dividing surface, the function $\psi(R)$ may be represented as follows:

$$\psi = \psi_\infty + \frac{\psi_1}{R}\,, \tag{5.121}$$

where ψ_1 is a parameter depending on temperature and concentration. Substitution of (5.121) into (5.119) gives (5.102), where

$$\sigma_1 = -2\psi_\infty\,, \quad \sigma_2 = 4\psi_\infty^2 - \psi_1\,. \tag{5.122}$$

If $\psi_\infty < 0$ and $\psi_1 \gg 4\psi_\infty^2$, then Eq. (5.109) gives a nonmonotonic dependence of $\sigma(R)$ in R with a maximum

$$\frac{\sigma_{\max}}{\sigma_\infty} = 1+\frac{\psi_\infty^2}{\psi_1}\,, \quad R_{\max} = \frac{\psi_1}{(-\psi_\infty)}\,. \tag{5.123}$$

In pure substances, the maximum manifests itself only in liquid droplets [56]. In a binary system, the presence or the absence of a maximum on the dependence $\sigma(R)$ at $T = \text{const}$ will depend on the method of creating metastability, that is on the trajectory of motion in space of unfixed variables. Thus, if in the process of penetration of a liquid into the region of metastable states a constant concentration is maintained, then for the solution of equimolecular composition a maximum is observed in the dependence $\sigma(R)$ of vapor bubbles [52]. On the line

$c' = \text{const}$, vapor bubbles and liquid droplets are characterized by two different parameters ψ. For the β-line, this is the parameter

$$\psi = \psi_\beta = \frac{\Gamma_\rho}{\rho''_\rho - \rho'_\rho} , \tag{5.124}$$

where $\Gamma_\rho = \Gamma_1 + (\kappa_{11}/\kappa_{22})^{1/2}\Gamma_2$ is the absolute adsorption determined by the density ρ_β. As distinct from the parameter ψ_∞ on the line $c' = \text{const}$, the parameter ψ_∞ on the β-line does not change its sign in passing from pure substances to mixtures, and the character of the dependence $\sigma(R)$ in a binary solution on the β-line is similar to the dependence $\sigma(R)$ in a one-component system in the whole range of state variables from the binodal to the spinodal.

5.4 Experiment

5.4.1 Superheat of Liquid Mixtures

The equilibrium state of a liquid mixture is characterized by three parameters: temperature, pressure, and composition. Penetration of a mixture into the metastable region may be realized by changing any one of these parameters while retaining the values of the other two. Figure 5.1

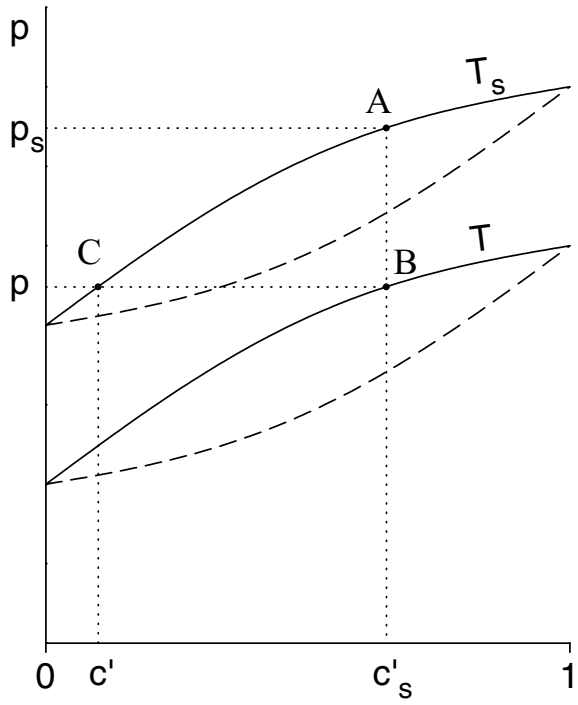

Figure 5.1: (p, c) projection of the phase diagram of a binary mixture

shows the (p, c) diagram of liquid (upper curve) – vapor (lower curve) phase equilibrium for a binary mixture at a constant temperature $T = T_s$. It is assumed that the components in both phases are mixed in arbitrary proportions. If at constant temperature, T_s, and concentration in the liquid phase, c'_s, the pressure in the mixture is increased to the value p', the solution will be transferred into a supercompressed state, and the formation of the vapor phase will be impossible. As a result of a rapid pressure decrease, a liquid mixture may be transferred to the point B, where it has the same composition, c'_s, temperature, T_s, but pressure $p < p_s$. An equilibrium isotherm, corresponding to a certain temperature T, goes through this point. The liquid state at the point B is superheated as the actual temperature T_s of the mixture is higher than the equilibrium value for this composition c'_s and pressure p. The state at the point B may also be regarded as supersaturated in the sense that the actual concentration c'_s is higher than the equilibrium concentration c' for the temperature T_s and pressure p (point C).

5.4.2 Apparatus and Methods of Measurements

The nucleation rate in superheated liquid argon–krypton solutions was determined by the lifetime measuring method [14, 29, 57, 58]. The solution under investigation was filled into a glass tube (3) and into metallic bellows (7) (Fig. 5.2). In the experiment, a part of the liquid solution with the volume $V \simeq 70$ mm^3, thermostated (± 0.002 K) in a copper block (1) was superheated. The temperature in the block was measured with a platinum resistance thermometer (2). The error in determining the temperature of the solution under investigation taking into account the inhomogeneity of the temperature field in the block was ± 0.02 K. The pressure was created with compressed helium and transferred to the solution through bellows (7). The bellows chamber and low-temperature valve (6) were thermostated (± 0.05 K) in block (8) at a temperature close to the normal boiling point of the solution. The measuring device was placed into vacuum jacket (4) fixed in a Dewar vessel (5). Cooling was realized with liquid nitrogen.

An experiment began with the preparation of the gas mixture of the required concentration. The purity of the initial components was 99.993% and 99.997% (Kr). The mixture was condensed into the measuring device. Differences in the temperatures of blocks (1) and (8) resulted in the evolution of a concentration gradient throughout the height of the measuring device. To define the solution concentration in a superheated volume before the beginning and after completion of an experiment, the saturation pressure of the solution was measured. For this purpose, at temperature T of the experiment (the temperature in block (1)), the pressure in the solution was decreased below the saturation pressure. The liquid solution in the upper part of tube (3) was transferred then into a gaseous state. Then the pressure was gradually increased and with the help of a system of detection of changes in the volume of the solution under investigation the pressure was recorded at the moment of the transition of the solution from a gaseous into a liquid state (the saturation pressure $p_s(T)$). The system for detection of changes in the volume consists of the rod (9) attached to the bellows (7) and ending with a core (10) made of a ferromagnetic material. The displacement of the core results in a change in the inductive reactance of the coil (11) connected in the bridge circuit. The error in determining the saturation pressure was ± 0.01 MPa. In calculating the concentration, use was made of the data on phase equilibrium. The error in determining the concentration is $\pm 0.5\%$.

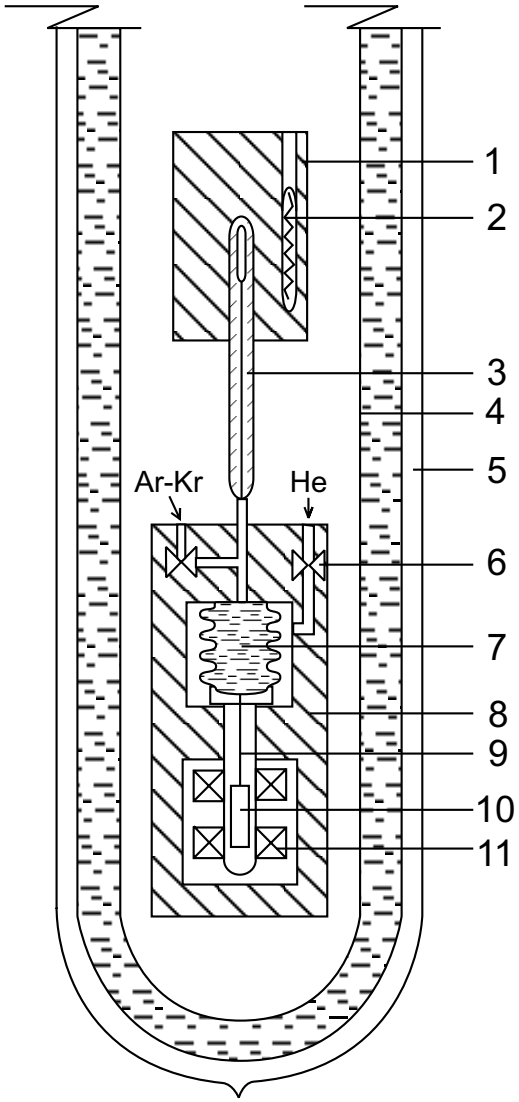

Figure 5.2: Schema of experimental apparatus

After preparing a solution of the required concentration c', the initial pressure $p_1 > p_s(T, c')$ was created in the measuring system. The penetration into the metastable region was realized by an abrupt pressure decrease below the saturation pressure. To reduce both the effect of cooling a liquid solution and the hydraulic oscillations in the measuring system, the liquid was brought to a metastable state in two stages. First the pressure was decreased to the value p_2, which is 0.3–0.5 MPa less than the saturation pressure $p_s(T, c')$. The probability of boiling-up of a solution at pressure p_2 is sufficiently small. The solution was kept at this

pressure p_2 for approximately 20 s, after which its final release to the value p' was realized. The error of maintenance of the pressure p' was ± 0.005 MPa. At the moment of the final pressure release a chronometer was started. It recorded the time τ of the stay of the solution in the given metastable state before its boiling-up (the lifetime of a superheated solution). The moment of boiling-up was recorded by a water hammer in the measuring system. After the boiling-up of a solution, the initial pressure p_1 was created in the bellows chamber and the measurement process was repeated. Up to $N = 100$ values of τ were measured at every given p' and c', and the mean lifetime $\bar{\tau} = \sum_i \tau_i / N$ was determined. In processing the results of the experiments, corrections for cooling of the liquid in the process of pressure release were made and the delay time τ_0, caused by the inertia effects of the pressure-release system, was subtracted from the measured value of $\bar{\tau}$. For our setup, τ_0 is equal to 0.5 s.

The time τ measured in the experiment was determined by the time τ_n of waiting for a viable nucleus in the system and the time of its growth τ_g ($\tau = \tau_n + \tau_g$). In the investigated range of state parameters, we have $\tau_g \simeq 10^{-3}$ s. The characteristic times τ in our experiments were larger than 0.1 s. The relationship $\tau \gg \tau_g$ makes it possible to assume $\tau \simeq \tau_n$ and to determine the nucleation rate J from the equation

$$J = \frac{1}{(\bar{\tau} V)} \,. \tag{5.125}$$

The temperature, corresponding to a fixed nucleation rate value, was denoted as the temperature of attainable superheating T_n. The error in the determination of T_n is equal to ± 0.2 K.

5.4.3 Statistical Laws of Nucleation

The classical homogeneous nucleation theory treats the evolution of aggregates of a new phase as a continuous Markovian process described by a Fokker–Planck equation. As for the emergence of a spontaneous nucleus in the metastable phase, it is a random event of discrete type and represents a discontinuous Markovian process. The probability $P(R, R_0, \tau)$ that the size of an aggregate of a new phase at the moment τ will be equal to R, if at $\tau = 0$ it was equal to R_0, in the region $R_0 < R < R_*$ obeys a one-dimensional Fokker–Planck equation [59]

$$\frac{\partial P}{\partial \tau} = \frac{\partial^2 P}{\partial R^2} - \frac{\partial P}{\partial R} \,. \tag{5.126}$$

A solution of this equation can be represented in the form

$$P(R, R_0, \tau) = \sum_i a_i w_i(\tau) P_i(R) \,, \tag{5.127}$$

where the coefficients a_i are determined by the initial distribution $P(0, R_0, 0)$ and $P_i(R)$ is an eigenfunction of the equation

$$\frac{\mathrm{d}}{\mathrm{d}R}\left(P_i - \frac{\mathrm{d}P_i}{\mathrm{d}R}\right) = \varepsilon_i P_i \tag{5.128}$$

with the eigenvalue ε_i. For the function $w_i(\tau)$ we have

$$\frac{\mathrm{d}w_i}{\mathrm{d}\tau} = -\varepsilon_i w_i \,. \tag{5.129}$$

In the region of weak metastability, where the probability of emergence of a critical nucleus is small, the equilibrium distribution of fragments in size is established rapidly. This statement means that in equation (5.127) the term with $i = 0$ is dominant and for all $i > 0$ the eigenvalues obey the inequality $\varepsilon_i > \varepsilon_0$. Then from Eqs. (5.127)–(5.129), we obtain

$$P(R, R_0, \tau) \simeq \exp(-\varepsilon_0 \tau) P_0(R) \; . \tag{5.130}$$

We are interested in the probability of formation of a critical nucleus (boiling-up of the liquid solution) in the time interval $\tau, \tau + \Delta\tau$. This probability is found by the multiplication of two other probabilities: the probability $w_0(\tau)$ and the probability $1 - w_0(\Delta\tau)$ of emergence of a critical nucleus during the succeeding small time interval $\Delta\tau$. As a first approximation for $w_0(\tau)$ we have

$$w_0(\tau) = \exp(-\varepsilon_0 \tau) \int_0^R P_0(R) \; \mathrm{d}R \simeq \exp(-\varepsilon_0 \tau) \; . \tag{5.131}$$

Expanding Eq. (5.131) into a series and restricting ourselves to the first term of the expansion, we get $1 - w_0(\Delta\tau) = \varepsilon_0 \Delta\tau$. Thus, for the average number of events of boiling-up of the liquid solution in the interval $\tau, \tau + \Delta\tau$ in a series of N experiments one can write

$$n = N \varepsilon_0 \Delta\tau \exp(-\varepsilon_0 \tau) \; . \tag{5.132}$$

Equation (5.132) describes a Poissonian process. According to Eq. (5.132) the mean waiting time for a critical nucleus is $\bar{\tau} = \varepsilon_0^{-1}$. The dispersion of the random quantity τ in this case coincides with its average value, i.e., $\sigma_\tau = \bar{\tau}$. In experiments with solutions, as well as with pure liquids [14, 29], in the whole range of p', T, c'-values investigated, one observes commonly similar values of the quantities $\bar{\tau}$ and σ_τ verifying the Poissonian character of the process. The Poisson character of the boiling-up of a superheated solution is also reconfirmed by the histograms of experiments (Fig. 5.3), which are in good agreement with the distribution equation (5.132).

5.4.4 Results

The System Argon–Krypton

The dependence of the mean lifetime of superheated liquid Ar–Kr solutions on temperature and concentration has been investigated in experiments at two pressures $p' = 1.0$ and 1.6 MPa. The range of investigated values of the mean lifetime changes from 0.1 to 1000 s, which corresponds to a variation in nucleation rate from 10^4 to 10^8 $\mathrm{m}^{-3}\ \mathrm{s}^{-1}$.

Figure 5.4 shows in a semi-logarithmic scale the temperature dependences of the mean lifetimes for several values of concentration [57]. The vertical size of the bars in the figure corresponds to the statistical error of determination of $\bar{\tau}$.

The character of the temperature dependence of $\bar{\tau}$ in the solution is similar to the respective dependence for pure liquids [19, 60]. On all the lines of constant concentration, after a certain value of the temperature (the boundary of spontaneous boiling) is reached, one can observe sections of an abrupt decrease in $\bar{\tau}$. We associate these sections of the curves with

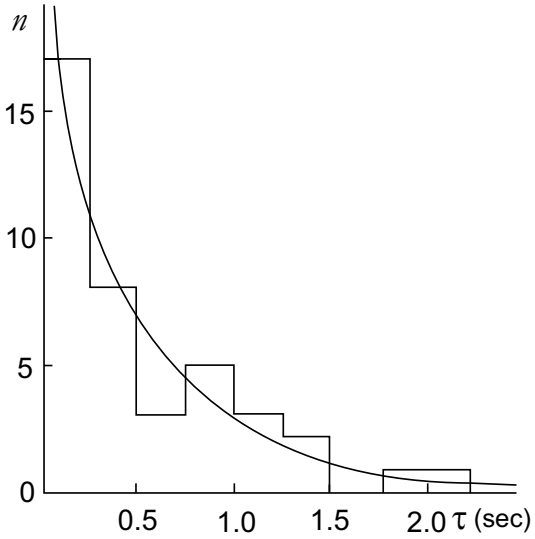

Figure 5.3: Histogram of experimental data. The parameter values are $c' = 0.428$; $p' = 1.6$ MPa; $T = 154.47$ K; $N = 40$, $\bar{\tau} = 0.52$ s. The smooth curve has been calculated from Eq. (5.132)

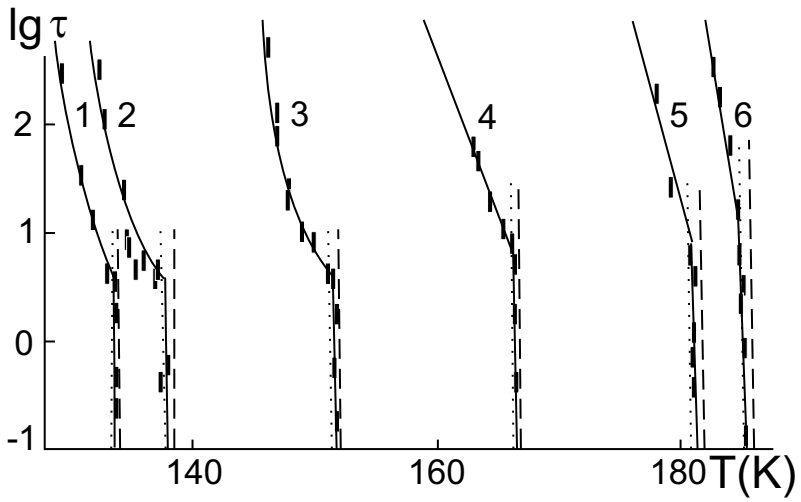

Figure 5.4: Temperature dependences of the mean lifetime of argon–krypton solutions at $p' = 1.0$ MPa for different concentrations: (1) $c' = 0$; (2) 0.109; (3) 0.428; (4) 0.708; (5) 0.938; (6) 1. Dashed lines represent calculations using Eqs. (5.47), (5.70), and $\sigma = \sigma_\infty$; dotted lines employ Eqs. (5.47) and (5.97)

homogeneous nucleation. Here with an increase of temperature by 0.1 K the value of $\log \bar{\tau}$ decreases by 0.6–1.2.

The bend of the experimental curves at $\bar{\tau} \simeq 8$–10 s is caused by heterogeneous nucleation and ionizing radiation nucleation. The authors of Ref. [61] connect the bend in the dependence $\bar{\tau}(T)$ with only one factor, the influence of ionizing radiation. The source of such radiation in experiments are cosmic rays and the natural radiation background. Heat peaks, which appear during the slowing-down of secondary electrons (δ-electrons) in superheated liquids, are the centers of its boiling-up. A convincing argument in favor of the ionization hypothesis to explain the bends of experimental curves is the result of experiments of measuring the lifetime of a superheated liquid in the field of γ-radiation (for argon the results of such experiments are presented in Ref. [19]). The increase of intensity of ionizing radiation results in a shift of the gently sloping sections of the curves into a region of smaller values of $\bar{\tau}$ without violating the character of the dependence $\bar{\tau}(T)$. The effect of initiation in the series of condensed inert gases correlates with the radiation-stability and scintillation properties of a substance, which increases with increasing atomic number of the respective element [62].

The greatest resistance to ionizing radiation, which is determined by well-expressed scintillation properties, is exhibited by liquid xenon. As a result, a part of the energy of ionizing radiation is not transformed into thermal energy, but fluoresces. The bend in experimental curves for xenon manifests itself at a value of the nucleation rate $J_{\mathrm{m}} = (\bar{\tau}v)^{-1} = 2.2 \times 10^4\ \mathrm{m}^{-3}\ \mathrm{s}^{-1}$ [21]. The bend of the experimental curves in the case of krypton is found at a rate $J_{\mathrm{m}} \simeq 1.5 \times 10^6\ \mathrm{m}^{-3}\ \mathrm{s}^{-1}$, and in argon at $J_{\mathrm{m}} \simeq (2-3) \times 10^6\ \mathrm{m}^{-3}\ \mathrm{s}^{-1}$. The increase of the krypton concentration in argon results in a monotonic decrease in J_{m} (Fig. 5.5). As distinct from krypton, where at all pressures one can observe a linear dependence of $\lg J$ on T, in argon at low pressures ($p' < 0.3$ MPa, see [19]) a section of approximately constant radiation sensitivity is revealed, which is adjacent to the boundary of liquid spontaneous boiling-up. The presence of such a section may be connected with the fact that the work of formation of a critical nucleus is here much smaller than the average energy of a thermal spike, and the probability of boiling-up on every thermal spike is close to unity [63]. The details of the process of transformation of the ionizing radiation into thermal energy and the detailed mechanism, the work of nucleation is affected, are not finally established to allow to calculate the probability of nucleation initiation by radiation in dependence on the molecular characteristics of a substance. In addition, at present one cannot be absolutely sure that the action of ionizing particles is the only reason for bends of experimental curves at large times of waiting for boiling-up. The similarity of the temperature and pressure dependences of $\bar{\tau}$ obtained in natural conditions and in the presence of a γ-source is merely a possible indication of the close link between these phenomena. As shown in Ref. [64], the value of J_{m} changes in passing from glassy to metallic measuring cells. The character of the dependence $\bar{\tau}(T)$ at $J < J_{\mathrm{m}}$ is affected by easily activated boiling centers [29, 65], and ultrasonic fields [66].

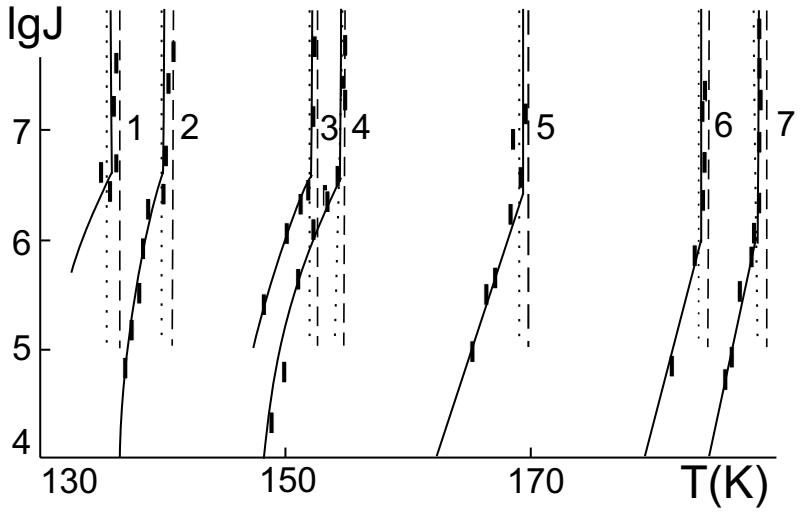

Figure 5.5: Nucleation rate in superheated argon–krypton solutions at $p' = 1.6$ MPa for the following concentrations: (1) $c' = 0$; (2) 0.109; (3) 0.382; (4) 0.428; (5) 0.708; (6) 0.938; (7) 1. Dashed and dotted lines are determined in the same way as explained in the caption to Fig. 5.4

The System Helium–Oxygen

In the temperature range where oxygen forms a liquid phase, the He–O_2 system is a gas-supersaturated solution. Experiments on nucleation in helium–oxygen solutions have been performed at two values of pressure $p' = 1.171$ and 1.667 MPa and several values of helium concentration in the solution. The purity of the substances under investigation is 99.99% (He) and 99.92% (O_2). Under fixed external conditions (T, p', $c' = \text{const}$) the appearance of the first viable nucleus in a metastable liquid is a stochastic event of the Poisson type. This statement has been confirmed by experiments on one-component liquids [14]. In these experiments, the time of "hold-up" of a liquid under pressure was ≈ 3 min, and it was sufficient for complete decompression of the vapor phase and the relaxation of thermal inhomogeneities in the measuring system. In experiments on gas-supersaturated liquids it has been discovered that at times of "hold-up" of ≈ 3 min one can often observe boiling-up with expectation times that are "anomalously" small for the given values of T, p', and c'. "Anomalously" small values of τ may appear and disappear in the course of experiments, or may be retained during the whole period of measurements. Such behavior of a gas-supersaturated system is similar to that of a one-component system, when in the latter there are easily activated nucleation centers [29, 64]. The law of distribution of "anomalously" low times of boiling-up expectation is also close to the Poisson one (Fig. 5.6, smooth curves). With an increase in the "hold-up" time between measurements up to 30–40 min (i.e., by an order of magnitude) premature liquid boiling-ups did not manifest themselves. In the course of treatment of the experimental data "anomalously" low values of τ were excluded from consideration.

Figures 5.7 and 5.8 show in a semi-logarithmic scale the results of determination of the mean lifetime and the nucleation rate in helium–oxygen solutions at two values of pres-

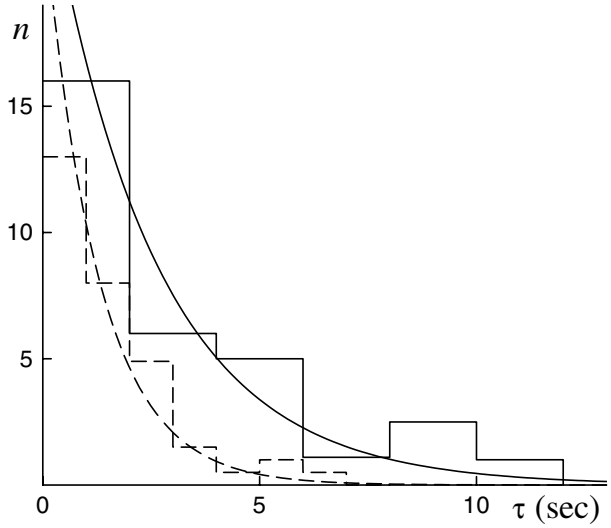

Figure 5.6: Distribution of the number of boiling-up events n that fall within the interval τ, $\tau + \Delta\tau$: $c' = 0.14$ mol%; $p' = 1.171$ MPa; $T = 166.66$ K; $N = 31$. Solid lines: $\bar{\tau} = 2.66$ s at a "holding" time of 40 min, dashed lines: $\bar{\tau} = 1.34$ s at a "holding" time of 3 min

sure [67]. As in the case of one-component liquids, on the curves $\bar{\tau}(T)$ and $J(T)$ one can distinguish two sections with different characters of the temperature dependences $\bar{\tau}$ and J. At low degrees of superheating experimental isobars have characteristic gently sloping sections, which with increasing temperature go over to sections with an abrupt change in the time of expectation of boiling-up of the solutions. The first section is connected with initiated, and the second with spontaneous nucleation. Dissolution of 0.1 mol% of helium in liquid oxygen decreases the limiting superheat $\Delta T = T_n - T_s$ by approximately 10%. In this case, in the region of initiated nucleation the mean lifetime of a solution decreases by three or four times. It is important that most noticeably gas saturation manifests itself here at very low helium concentrations.

In the parts of an abrupt decrease in τ (increase of J) the value of the derivative $\mathrm{d}\ln J/\mathrm{d}T$ does not depend within the experimental error on concentration. At a pressure of 1.171 MPa it is about 18, at $p' = 1.667$ MPa it is equal to 21. This value corresponds to an increase in the nucleation rate by approximately 8 or 9 orders of magnitude with an increase in temperature of 1 K.

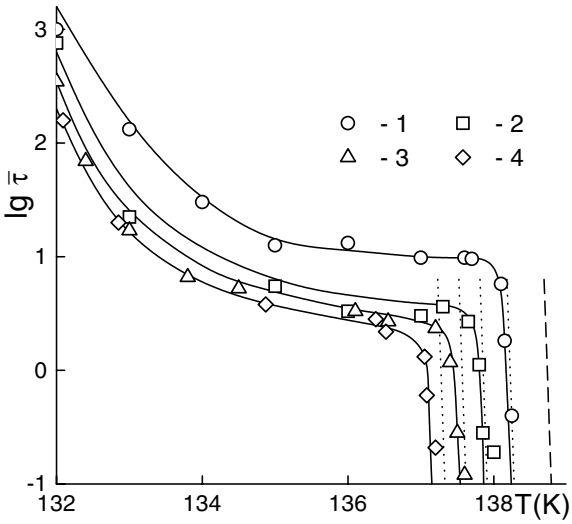

Figure 5.7: Temperature dependence of the mean lifetime of a metastable mixture at a pressure $p' = 1.171$ MPa and the following concentrations: (1) $c' = 0$ mol%, (2) 0.08, (3) 0.14, and (4) 0.20. Dashed lines shows results of the calculations for a one-component system by homogeneous nucleation theory with $\sigma = \sigma_\infty$; Dotted lines show calculations by the homogeneous nucleation theory with $\sigma = \sigma(R_*)$

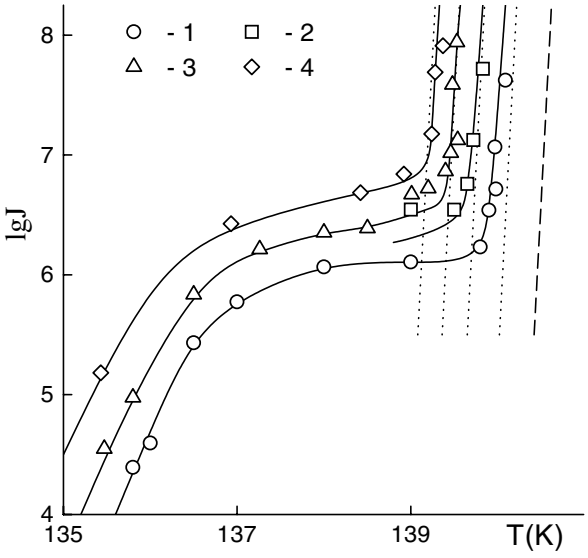

Figure 5.8: Temperature dependence of the nucleation rate at a pressure $p' = 1.667$ MPa and the following concentrations: (1) $c' = 0$ mol%, (2) 0.08, (3) 0.14, and (4) 0.20. For the way of determination of the dashed and the dotted lines see caption to Fig. 5.7

5.5 Comparison between Theory and Experiment

5.5.1 Equation of State and Boundaries of Thermodynamic Stability of Solutions

For describing the properties of new-phase nuclei and the determination of the boundary of stability for homogeneous solutions with respect to constantly changing state variables (the spinodal curve), it is necessary to have an equation of state which describes both stable and metastable states. Such an equation of state for argon–krypton and helium–oxygen systems has been obtained in the framework of a one-liquid solution model on the basis of experimental data on thermodynamic properties of pure components and phase equilibria in solutions. In order to arrive at these basic equations, equations of state for argon [68] and oxygen [69] were used which are of the same form both for the liquid and the vapor phase. These equations have, in the region of liquid–gas phase transition, isotherms of the van der Waals type and satisfy the Maxwell rule. The general form of the equation of state for the solution is given by

$$\frac{p}{\rho RT} = 1 + \eta \sum_{i,j} b_{ij} \frac{\tilde{\rho}^i}{\tilde{T}^j} \,. \tag{5.133}$$

Here $\tilde{\rho} = \rho/\rho_c$, $\tilde{T} = T/T_c$ holds, ρ_c and T_c are the density and the temperature at the critical point, respectively. Both parameters, as well as the individual parameter η, are functions of concentration. The coefficients b_{ij} are determined by experimental data on the thermodynamic parameters of the less volatile component of the solution (argon, oxygen) and are given in the papers [68, 69].

The three individual parameters of Eq. (5.133) (T_c, $\rho_c = 1/v_c$, η) have been approximated by the expressions

$$T_c(c) = T_{c,1}c^2 + 2\alpha_T T_{c,12}c(1-c) + T_{c,2}(1-c)^2 \,, \tag{5.134}$$

$$v_c(c) = v_{c,1}c^2 + 2\alpha_v v_{c,12}c(1-c) + v_{c,2}(1-c)^2 \,, \tag{5.135}$$

$$\eta(x) = \eta_1 c^2 + 2\alpha_\eta \eta_{12}c(1-c) + (1-c)^2 \,, \tag{5.136}$$

where the cross terms $T_{c,12}$, $v_{c,12}$, and η_{12} satisfy the combination rules

$$T_{c,12} = \delta_T (T_{c,1}T_{c,2})^{1/2} \,, \tag{5.137}$$

$$v_{c,12} = \delta_v \frac{\left(v_{c,1}^{1/3} + v_{c,2}^{1/3}\right)^3}{8} \,, \tag{5.138}$$

$$\eta_{12} = \frac{(1+\eta_1)}{2} \,. \tag{5.139}$$

$T_{c,i}$ and $\rho_{c,i}$ are the density and the temperature, respectively, at the critical point of any of the pure components.

In developing an equation of state for an argon–krypton solution, we started from the fact that for these substances the law of corresponding states is fulfilled with an error close to

the experimental one [70]. It means that, in reduced coordinates, the (p, ρ, T) properties of argon and krypton may be described by one equation of state of the form of Eq. (5.133) with coefficients b_{ij} determined, for example, by the properties of argon, $\eta = 1$. The coefficients $\delta_T = 1.0012$ and $\delta_v = 1.017$ have been found by minimizing the mean-square deviations of experimental data concerning the pressure of saturated vapors [71] and the density of the liquid phase [72] for Ar–Kr solutions calculated from Eqs. (5.133)–(5.135), (5.137), and (5.138). Since the region of stable existence of the oxygen liquid phase is located considerably above the helium critical temperature, helium may be regarded here as a gas close to a perfect one. This circumstance makes it possible to use for describing helium the equation of state for oxygen having introduced into the latter the correction factor η. In pure oxygen $\eta = 1$, at $\eta = 0.431$ the equation of state, Eq. (5.133), with coefficients b_{ij} of oxygen describes in an optimum way the (p, ρ, T) properties of helium in the range of reduced densities $0 < \tilde{\rho} < 1$ and temperatures $0.6 < \tilde{T} < 1$.

The free parameters α_T, α_v and α_η of the equation of state may be determined by the pressure of saturated vapor and the composition of the liquid and the vapor phase of the solution. However, the available data [73] on p_s, c' and c'' have been proven to be insufficient for a reliable representation of the phase diagram in the range of temperatures adjoining the critical point of the solvent. In the absence of information about the (p, ρ, T, c) properties of a helium–oxygen system, we used, as additional information, data about the surface tension [36]. The incorporation of the information about the properties of a liquid–vapor interface into the considerations made it possible not only to increase the reliability of the description of the (p, ρ, T, c) properties of the solution by the equation of state, Eq. (5.133), but also to determine the influence parameter of pure helium, κ_{11}. Calculations were made using Eqs. (5.133)–(5.139) and (5.98)–(5.99). The solvent influence parameter was determined from Eq. (5.98) by data on the surface tension of pure oxygen [74]. The results of such calculations may be presented in the following form

$$\frac{\kappa_{22}\rho_{c,2}^{8/3}}{p_{c,2}} = 0.5552 + 12.6638\varepsilon - 187.164\varepsilon^2 + 1468.46\varepsilon^3 - 6583.0\varepsilon^4 + 16993\varepsilon^5 - 23465\varepsilon^6 + 13500\varepsilon^7 , \quad (5.140)$$

where $\varepsilon = 1 - T/T_{c,2}$ holds. The temperature dependences of the free parameters in Eqs. (5.134)–(5.136), and also the coefficient κ_{11} have been approximated by the following expressions

$$\begin{aligned} \alpha_T &= 3, \quad \alpha_v = 2.88 - 16.8\varepsilon + 54.0\varepsilon^2 - 50.0\varepsilon^3 , \\ \alpha_\eta &= -0.238 + 14.95\varepsilon - 61.1\varepsilon^2 + 103.0\varepsilon^3 - 61.0\varepsilon^4 , \\ \frac{\kappa_{11}\rho_{c,2}^{8/3}}{p_{c,2}} &= 7.93 - 176.5\varepsilon + 1530\varepsilon^2 - 6248\varepsilon^3 + 12100\varepsilon^4 - 8900\varepsilon^5 . \end{aligned} \quad (5.141)$$

The coefficient κ_{12} was found according to Eq. (5.93).

The phase diagram of a helium–oxygen system, calculated by the equation of state equation (5.133), is shown in Fig. 5.9. The lines of phase equilibrium separate the regions of stable

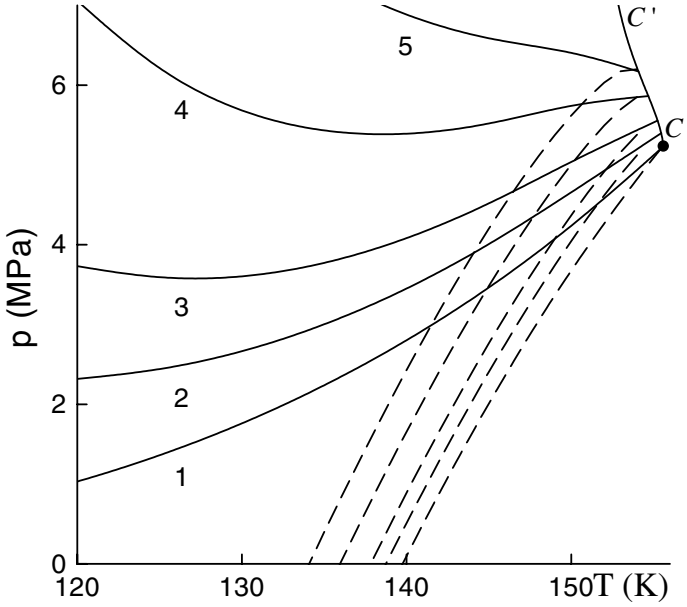

Figure 5.9: (p, T)-projection of the phase diagram of He–O_2 mixtures. Solid lines show the curves of phase equilibrium, dashed lines the diffusion spinodals. (1) $c' = 0$ mol%; (2) 0.5; (3) 1; (4) 2; (5) 3. CC' is the critical line

and metastable phases on the thermodynamic surface of the homogeneous states. The metastable phase of a two-component system retains the restoring reaction to infinitesimal changes in state variables up to the diffusive spinodal determined by the condition

$$\left(\frac{\partial \Delta\mu}{\partial c}\right)_{p,T} = 0\,, \tag{5.142}$$

where $\Delta\mu = \mu_1 - \mu_2$. In a one-component system, the stability of the metastable phase is disturbed, if

$$\left(\frac{\partial p}{\partial \rho}\right)_T = 0 \tag{5.143}$$

holds. In pure oxygen at a temperature $T = 140$ K a stretch of the liquid by $\Delta p_{\rm sp}(T) = p_{\rm s} - p_{\rm sp} = 2.65$ MPa corresponds to the spinodal. Dissolution in oxygen of 1 mol% helium results in a rise of the limiting value of the tensile stress up to $\Delta p_{\rm sp}(T, c) = p_{\rm s} - p_{\rm sp} \simeq 3.17$ MPa. Thus, with increasing concentration of a dissolved gas, the width of the metastable region increases. It should be mentioned that at high gas concentrations ($c' > 3$ mol%) penetration into the metastable region at a fixed external pressure is already connected with decreasing rather than increasing temperature (see Fig. 5.9).

5.5.2 Surface Tension and other Properties of Vapor-Phase Nuclei

For describing the properties of new-phase nuclei in the framework of the van der Waals capillarity theory Eq. (5.90), in addition to the equation of state for a homogeneous solution, it is necessary to know the matrix of the influence coefficients κ_{ij}. By using the combination rule

$$\kappa_{ij} = \delta_\kappa (\kappa_{ii}\kappa_{jj})^{1/2} \tag{5.144}$$

and the formula for the surface tension at a flat interface

$$\sigma_\infty = 2 \int_{-\infty}^{+\infty} \sum_{i,j} \kappa_{ij} \left(\frac{\mathrm{d}\rho_i}{\mathrm{d}z}\right)\left(\frac{\mathrm{d}\rho_j}{\mathrm{d}z}\right) \mathrm{d}z \,, \tag{5.145}$$

we have determined the values of $\kappa_{11}(T)$ and $\kappa_{22}(T)$ for argon and krypton by the data on the surface tension taken from Refs. [75,76], and also the coefficient δ_k by the results of measuring σ_∞ for argon–krypton solutions [77]. Numerical calculations have resulted in $\delta_k \cong 1$, which, according to Eqs. (5.92) and (5.93), corresponds to the state of an indifferent equilibrium ($\det \kappa_{ij} = 0$). Thus, the properties of the nuclei in an argon–krypton system can be described with good accuracy by Eqs. (5.94)–(5.96).

The results of the numerical solution of the system of Eqs. (5.94)–(5.96) for states close to the boundary of spontaneous boiling-up of a liquid and the spinodal are presented in Fig. 5.10. At small supersaturations, one can distinguish in a nucleus a homogeneous core and a transition layer, the thickness of which is small as compared with the bubble size. With further penetration into a metastable region the homogeneity core becomes smaller, and the functions $\rho_1(r)$ and $\rho_2(r)$ get a bell-like shape. A shift in the distribution of $\rho_1(r)$ with respect to $\rho_2(r)$ results in an excess adsorption of the first component on the surface layer of a nucleus. By solving the system of Eqs. (5.68)–(5.70) and (5.97) with respect to σ and R, one can determine the dependence of the surface tension on the radius of curvature of the surface of tension. The results of such a calculation at a fixed temperature and several values of the concentration in the solution are given in Fig. 5.10. In contrast to a one-component system, where σ is a monotonically increasing function of R [53,56], for a solution with $c' \simeq 0.5$ the dependence $\sigma(R)$ has a characteristic maximum [57]. The value of $\sigma_{\max}$ exceeds that of σ_∞ only by (0.5–0.7)%, which is close to the error of experimental determinations of σ_∞.

The results of the numerical calculations of the dependence $\sigma(R)$ may be described in a wide range of nucleus radii by Eq. (5.102), where the parameters σ_1 and σ_2 are determined by Eq. (5.122). Bubbles, responsible for the spontaneous boiling-up of a liquid up to nucleation rates $J = 10^{15}$ s^{-1} m^{-3}, fall within the area of applicability of Eq. (5.102). The results of the calculation of the properties of such bubbles in an argon–krypton system are given in Table 5.1.

Distributions of the densities of the components in a critical bubble of a helium–oxygen solution are presented in Fig. 5.11. Distinct from solutions with complete solubility of the components, the density of the first (gas) component in a bubble is higher than in the solvent. The presence of a weak maximum in the density profile on the side of the gas phase indicates an excess adsorption of the first component on the surface layer of the critical nucleus. The

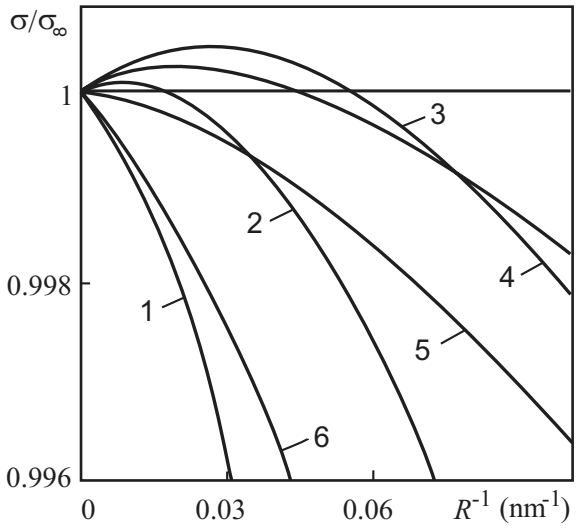

Figure 5.10: The dependence of the reduced surface tension of critical bubbles on curvature of the interface for boiling in an argon–krypton solution at $T = 145$ K for the following concentrations of krypton: (1) $c' = 0$; (2) 0.1; (3) 0.3; (4) 0.5; (5) 0.7; (6) 1

Table 5.1: Characteristic parameters of critical bubbles in an argon–krypton solution at a pressure of 1.0 MPa

Parameter	c'		
	0	0.5	1.0
T (K)	134	155	186
p_s (MPa)	2.440	2.906	2.738
W_*/k_BT, Eq. (5.70)	78.0	82.9	71.1
W_*/k_BT, Eq. (5.97)	64.1	76.7	57.9
$\lg J$, Eqs. (5.47), (5.70)	5.5	4.1	8.3
$\lg J$, Eqs. (5.47), (5.97)	11.5	6.8	14.0
σ_∞ (mN/m)	2.402	3.065	2.952
δ_∞ (nm)	0.035	−0.023	0.036
$\delta_{1,\infty}$ (nm)	0.035	−0.210	–
$\delta_{2,\infty}$ (nm)	–	0.182	0.036
$\sigma(R_*)$ (mN/m)	2.249	2.987	2.758
R_* (nm)	3.55	3.62	3.59
n''_*	319	330	265
n''_{2*}	0	75	265
δ (nm)	0.207	0.095	0.219
δ_1 (nm)	0.207	−0.067	–
δ_2 (nm)	–	0.329	0.219

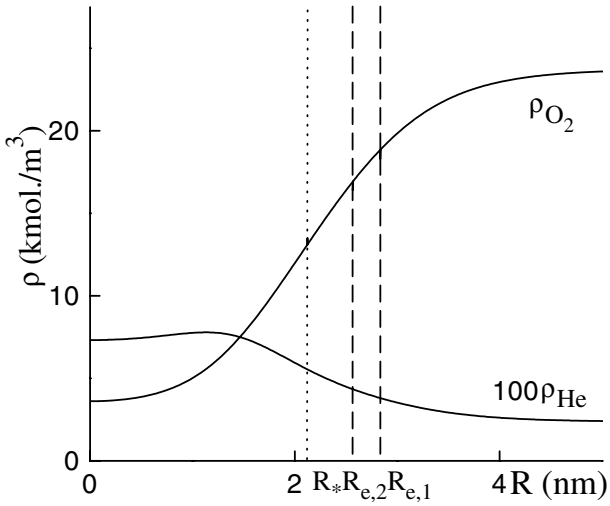

Figure 5.11: Density distributions of the components of the solution in a critical bubble at the following values of the parameters: $T = 140$ K, $c' = 0.1$ mol%, $p' = 1.0$ MPa. Here R_* is the radius of the surface of tension and $R_{e,i}$ are the equimolecular dividing surfaces for the respective components

Tolman parameters of the components of a binary solution ($\delta_i = R_{e,i} - R_*$, $i = 1, 2$) behave similar to the Tolman parameter δ of pure substances, i.e., they increase monotonically with increasing curvature (in the region of weak metastability, the dependence $\delta_i(1/R_*)$ is linear). At small radii of the bubble, the Tolman parameters diverge proportionally to $R_*^{-1/3}$. As distinct from σ_1 and σ_2, the value of $\delta_{1(2)} = \delta_1 - \delta_2 = R_{e,1} - R_{e,2}$ shows a weak dependence on both the curvature of the separating surface and on concentration.

Figure 5.12 shows the surface tension of critical bubbles of He–O_2 solutions as a function of the curvature of the surface of tension at constant temperature for several compositions of the ambient phase. Small additions of helium in liquid oxygen do not change the character of the size dependence of the surface tension, evenly shifting the whole dependence toward smaller values of δ. The account of the dependence $\delta(R_*)$ in the work of formation of a critical nucleus leads to a decrease in the height of the activation barrier from $G_* = W_*/k_B T = 85$ to 70 and facilitates the boiling-up of a gas-supersaturated solution.

The characteristic parameters of critical bubbles corresponding to the Gibbs number $G_* = 70$ are given in Table 5.2. It follows from the data given in the table that, at $T = 138$ K and $p' = 1.171$ MPa, the radius of a critical bubble R_* in superheated pure oxygen equals 3.732 nm, and the number of molecules in it equals $n''_* \cong 457$. Dissolution in oxygen of 0.2 mol% helium decreases the size of a critical bubble to $R_* = 3.615$ nm. This decrease is balanced by increasing $\sigma(R_*)$-values from 2.288 to 2.422 mN m^{-1}. The helium concentration in a bubble is, in this case, equal to $c''_* \cong 6$ mol%, the number of molecules $n''_* \cong 428$ and the bubble is practically free of atoms of helium ($n''_{1*} \cong 31$). Before the formation of a bubble, its volume was occupied by $n'_2 \cong 3575$ oxygen molecules and $n'_1 \cong 9$ helium atoms. The supply

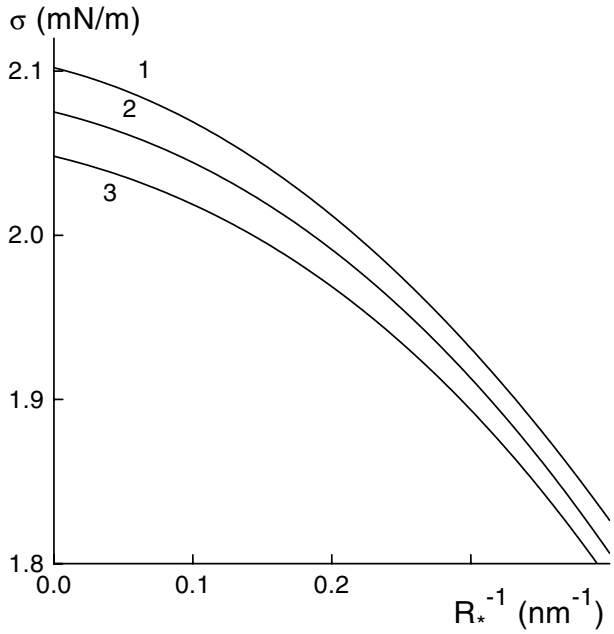

Figure 5.12: Surface tension of the critical bubbles in the He–O_2 solution along the line $c' =$ const (c' is the concentration of helium) at $T = 140$ K: (1) $c' = 0$ mol%, (2) 0.1, (3) 0.2

to a growing bubble of $\cong 22$ atoms of a dissolved gas does not require evidently a diffusion process and may be performed by molecular exchange. Thus, the process of nucleation in a gas-supersaturated solution at temperatures close to the temperature of the attainable superheating of the solvent differs only slightly from the process of nucleation in a superheated pure liquid. The decrease in the temperature of superheating of a liquid, observed as a gas component is dissolved in it, is first of all connected with a shift of the line of equilibrium coexistence of the liquid and vapor phases and, to a less degree, with the change in the value of the surface tension. All these properties make a gas-supersaturated solution in the vicinity of the solvent critical point different from a gas-supersaturated liquid at low temperatures.

5.5.3 Classical Nucleation Theory and Experiment

In this section, experimental data on the boiling-up kinetics of argon–krypton and helium–oxygen solutions are analyzed in the framework of the homogeneous nucleation theory employing the expression for the steady-state nucleation rate. An evaluation of the time τ_l of establishing a stationary flux of critical nuclei in solutions is given in the paper [47]. In the region of state variables, where the experiments have been conducted, the time τ_l does not exceed 10^{-8} s, which justifies the neglect of nonsteady state effects.

In the expression for steady-state nucleation rate, the exponential term is dominant. The value of the kinetic factor B depends only slightly on temperature, pressure and concentration. A very strong dependence of the nucleation rate on the exponent in the exponential term

Table 5.2: Characteristic parameters of critical bubbles of pure oxygen and helium–oxygen mixtures at pressure $p' = 1.171$ MPa and the Gibbs number $G_* = 70$

Parameter	c' (mol%)		
	0	0.1	0.2
T (K)	138.149	137.650	137.150
p_s (MPa)	2.567	2.665	2.754
B, 10^8 s^{-1}	1.969	0.855	0.556
log J, Eqs. (5.47) (5.70)	6.09	5.72	5.60
σ_∞ (mN/m)	2.44	2.51	2.58
$\delta_{1,\infty}$ (nm)	–	0.301	0.297
$\delta_{2,\infty}$ (nm)	0.036 3	0.036 7	0.037 1
R_* (nm)	3.732	3.673	3.615
$\sigma(R_*)$ (mN/m)	2.288	2.354	2.422
n''_*	457	442	428
n''_{1*}	–	16	31
δ_1 (nm)	–	0.463	0.458
δ_2 (nm)	0.215	0.213	0.210
c''_* (mol%)	0	3.03	6.02
n'_1	0	5	9
n'_2	3 894	3 731	3 575

makes differences in evaluations of the factor B insignificant. Thus, an uncertainty in the value of B of 1–2 orders of magnitude results in an uncertainty in the temperature of the attainable superheat of the liquid equal to 0.1–0.2 K. This uncertainty does not exceed the error of determination of this value by experiment. Another fundamental issue, connected with the use of Eq. (5.11), is the value of the normalization constant for the equilibrium function of the volume distribution of nuclei C_v. Usually it is assumed that a nucleus can form on any molecule of the system, so $C_v = \rho' = \rho'_1 + \rho'_2$ holds, where ρ'_1 and ρ'_2 are the number densities of a solvent and a dissolved substance in the liquid phase. Another approach to the determination of C_v is proposed by Deryagin [42]. According to [42], $C_v = \upsilon_* \rho'^2$ holds. A change from the normalization constant $C_v = \rho'$ to $C_v = \upsilon_* \rho'^2$ decreases the temperature of attainable superheating for helium–oxygen solutions by approximately 0.2–0.3 K. In comparing theory and experiment, we use $C_v = \rho'$ as the normalization constant for the distribution function.

In Table 5.3 and Fig. 5.13, experimental data on the temperature of attainable superheat for Ar–Kr solutions are compared with the results of their calculation by the homogeneous nucleation theory in a macroscopic approximation and with incorporation of the dependence $\sigma = \sigma(R_*)$. In the macroscopic approximation, the discrepancies in theory and experiment in T_n do not exceed 0.6 K. They have the largest values for pure substances and the lowest ones for solutions of equimolecular composition. Taking into account the dependence $\sigma(R_*)$ in the work of formation of a critical bubble improves the agreement between theory and experiment for pure substances and weak solutions. The nonmonotonic character of the dependence $\sigma(R_*)$ in a solution in the vicinity of equimolar composition leads to the convergence of the values

Table 5.3: The attainable temperature of superheating in Ar–Kr solutions for $J = 10^7$ m^{-3} s^{-1}

	c'	T_s	p_s	T_n (K)		
		K	MPa	Experiment	Theory[a]	Theory[b]
$p' = 1.0$MPa						
	0.0	116.55	2.431	133.9	134.12	133.65
	0.109	118.60	2.559	138.1	138.29	137.88
	0.428	125.86	2.887	151.8	151.81	151.50
	0.708	136.38	2.973	166.5	166.73	166.30
	0.938	152.72	2.784	181.1	181.42	180.81
	1.0	159.13	2.673	185.3	185.84	185.17
$p' = 1.6$ MPa						
	0.0	125.18	2.698	136.2	136.41	136.05
	0.109	127.63	2.823	140.5	140.63	140.33
	0.382	134.76	3.098	152.1	152.19	151.97
	0.428	136.21	3.151	154.4	154.37	154.14
	0.708	148.09	3.224	169.2	169.42	169.10
	0.938	164.71	3.034	183.8	184.21	183.72
	1.0	170.70	2.934	188.1	188.63	188.10

[a] Calculations with $\sigma = \sigma_\infty$, data from Ref. [76]

[b] Calculations with $\sigma = \sigma(R_*)$, data from this work

of σ for critical bubbles and σ_∞. This property manifests itself in decreasing disagreement between experiment and the theoretical values of the temperature of attainable superheat calculated in a macroscopic approximation.

Temperature dependences of the nucleation rate are also close to theoretical predictions (Fig. 5.5). A shift in the temperature of 1 K results in a change of J by 6–12 orders of magnitude. The derivative $\mathrm{d}\ln J/\mathrm{d}T$ increases with increasing pressure. The theory gives a qualitatively correct representation of the concentration dependence of the temperature of attainable superheat observed by experiment (Fig. 5.13). At a pressure $p' = 1.0$ MPa and concentration $c' = 0.5$, the attainable superheating, achieved in experiment, was given by $\Delta T = T_n - T_s = 27.2$ K. At the same conditions, the superheating $\Delta T_{sp} = 36.2$ K corresponds to the diffusional spinodal. The spinodal has been calculated from Eq. (5.133) according to its definition Eq. (5.142).

Table 5.4 provides data on the temperature of attainable superheating for helium-oxygen solutions corresponding to a nucleation rate $J = 10^7$ s^{-1} m^{-3}. The results of the experiments are compared with calculations of T_n by the homogeneous nucleation theory in a macroscopic approximation ($\sigma = \sigma_\infty$) taking into account the dependence of the bubble surface tension on the curvature of its separating surface $\sigma = \sigma(R_*)$. The kinetic factor B was determined from Eqs. (5.47) and (5.48). In addition, Table 5.4 shows the values of the saturation temperature T_s at a given pressure p and the values of pressure p_s corresponding to the experimental temperature of attainable superheating T_n. In Figs. 5.7 and 5.8, one can see the temperature dependences of $\bar{\tau}$ and J, calculated by Eq. (5.12), taking into account the dependence $\sigma(R_*)$,

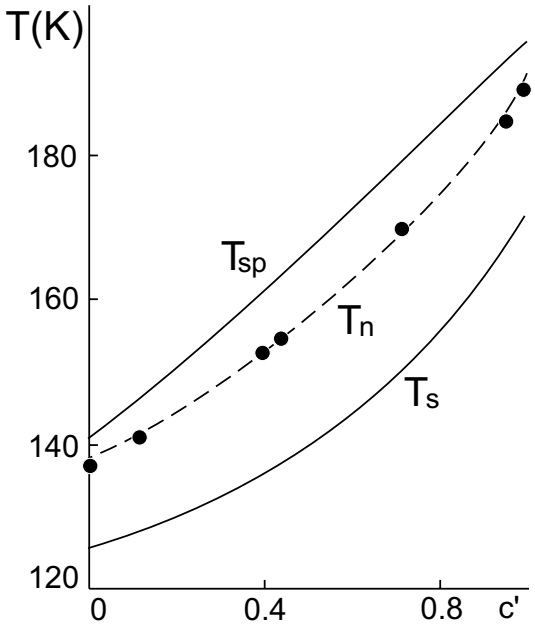

Figure 5.13: Temperature of attainable superheating of an argon–krypton solution at $p' = 1.6$ MPa. Circles are experimental data. T_n has been calculated using Eqs. (5.47), (5.70) and $\sigma = \sigma_\infty$, $J = 10^7$ m^{-3} s^{-1}. $T_{\rm sp}$ specifies the spinodal curve, $T_{\rm s}$ the binodal curve of the liquid

and also the results of calculation of the functions $\bar{\tau}(T)$ and $J(T)$ for pure oxygen in a macroscopic approximation. The data from Table 5.4 and Figs. 5.7 and 5.8 show good agreement between experiment and the classical homogeneous nucleation theory, when the latter takes into account the size dependence of the properties of critical nuclei. The disagreement between theoretical and experimental values of the temperature of attainable superheating does not exceed the limits of experimental error and the accuracy of determining the thermophysical parameters in Eqs. (5.47) and (5.48). The experimental data do not reveal any peculiarities in nucleation kinetics in the vicinity of $c' = 0$ and $c' = 1$, where the fluxes of nuclei can develop by-passing the saddle point. This result confirms the assumption of the equilibrium character of composition in a critical bubble used in the theory of binary nucleation.

Figure 5.14 shows the line of attainable superheating and the spinodal in a He–O_2 system at two investigated pressure values. The dissolution of helium in oxygen decreases both the temperature of superheating and the temperature of loss of stability of the system to infinitely small perturbations of concentration. At a helium concentration in oxygen of 0.3 mol%, the temperature of spontaneous boiling-up of the solution is approximately 1.2–1.5 K lower than that of oxygen. At a concentration of 0.1 mol% and a pressure of 1.171 MPa the superheating is $\Delta T \cong 20$ K, and the loss of stability of the homogeneous solution takes place at $\Delta T_{\rm sp} \cong 25$ K.

Table 5.4: Temperature of attainable superheating of helium–oxygen mixtures for nucleation rates $J = 10^7$ s^{-1} m^{-3}

	c'	T_s	p_s	T_n (K)		
	mol%	K	MPa	Experiment	Theory[a]	Theory[b]
$p' = 1.171$ MPa						
	0	122.40	2.570	138.17	138.73	138.22
	0.08	118.96	2.640	137.79	138.38	137.85
	0.14	114.55	2.686	137.43	138.11	137.56
	0.20	–	2.732	137.06	137.85	137.27
$p' = 1.667$ MPa						
	0	129.05	2.786	140.00	140.53	140.13
	0.08	127.12	2.860	139.72	140.18	139.76
	0.14	125.34	2.910	139.46	139.91	139.47
	0.20	123.04	2.963	139.23	139.64	139.19

[a] $\sigma = \sigma_\infty$, σ_∞ taken from Ref. [16]
[b] $\sigma = \sigma(R_*)$, results of this work

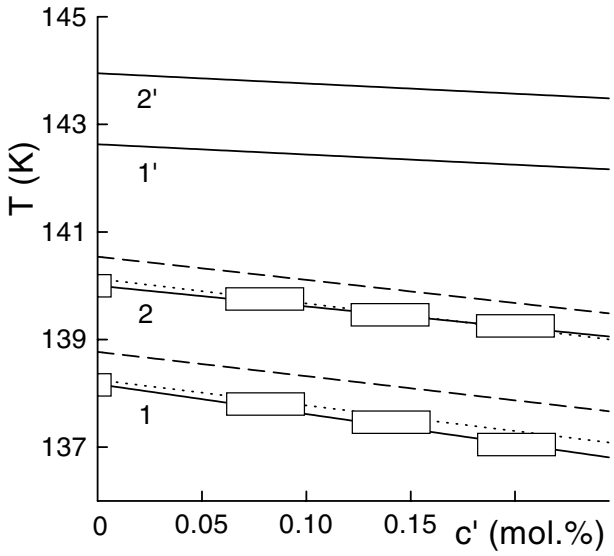

Figure 5.14: Temperature of attainable superheating (1, 2; $J = 10^7$ s^{-1} m^{-3}) and spinodal (1′, 2′) at pressures $p' = 1.171$ (1, 1′) and 1.667 MPa (2, 2′). The dashed line shows the results of the calculation by the homogeneous nucleation theory in a macroscopic approximation $\sigma = \sigma_\infty$, the dotted line accounts for the dependence $\sigma(R_*)$. The width and length of the rectangles illustrate the errors in the determination of temperature and concentration

5.6 Conclusions

The general picture of nucleation in liquid mixtures remains the same as in a pure liquid. The time, required for a bubble of radius R to form in a pure liquid, is connected with the time of heat dissipation and by the order of magnitude equal to [46]

$$\tau_h \approx \frac{R^2}{4a_T} , \tag{5.146}$$

where a_T is the thermal diffusivity. Thermodynamic parameters of solutions of simple liquids have the same order of magnitudes as thermodynamic parameters of pure liquids. Therefore, the time of formation of a bubble in a mixture, calculated by Eq. (5.146), is close to the time of formation of a bubble in a pure liquid. Assuming $R \approx R_* = 5$ nm and $a_T = 5 \times 10^{-8}$ m^2 s^{-1}, we obtain $\tau_n \approx 10^{-10}$ s.

The composition of the equilibrium vapor differs from that of a liquid mixture by a large content of an easily volatile component. Therefore, during the formation of a vapor bubble with a vapor composition equilibrium for the liquid composition a certain additional quantity of an easily volatile component should be supplied to the bubble boundary from the bulk of the liquid. The characteristic time of diffusion to the surface of a spherical bubble of radius R is equal to

$$\tau_D \approx \frac{R^2}{4D_g} . \tag{5.147}$$

The diffusion coefficient in a simple mixture is of the order $\sim 5 \times 10^{-10}$ m^2 s^{-1}. Thus, the characteristic time of diffusion proves to be two orders of magnitude larger than the time of formation of a bubble, and the equilibrium conditions for a rapidly formed bubble will differ from those examined in Sect. 5.3 for a bubble staying in a liquid for an infinitely long time.

Under rapid evaporation, the vapor composition in a bubble will be close to the initial composition of the liquid. The liquid layer, directly adjacent to the bubble surface, is depleted by an easily volatile component to the composition equilibrium for the composition of the vapor. As the change in the liquid composition at the boundary proceeds very slowly, the bubble is in the state of temporary equilibrium with the liquid at the surface having the composition $c < c'$ and the temperature T. The equilibrium radius of such a bubble is determined by Eq. (5.79), in which the equilibrium pressure p'_s for the temperature T and the liquid equilibrium composition c' far from the bubble should be replaced by the equilibrium pressure p''_s for the same temperature T and the vapor composition $c'' = c'$. Since $p''_s < p'_s$, the vapor bubble radius, determined from the pressure p''_s, exceeds the radius given by Eq. (5.79).

The experiments conducted and the results of their analysis in the framework of the classical homogeneous nucleation theory demonstrate good agreement between theory and experiment. At temperatures close to the temperature of the critical point of the solvent, the homogeneous nucleation theory gives not only a qualitatively, but also a quantitatively correct representation of the temperature of attainable superheat for liquid mixtures, and, what is even more significant, gives a correct representation of the temperature and pressure dependences of the nucleation rate. The disagreement between theory and experiment does not exceed the experimental error in the temperature of superheat if the theory takes into account the size

dependence of surface tension for a critical bubble. Such agreement is an indirect evidence of the correctness of the assumption of an equilibrium composition of a vapor–gas mixture in a critical nucleus used in the theory. As is shown in Sect. 5.5, close to the temperature of spontaneous boiling-up of a pure solvent ($T > 0.9T_c$) a critical bubble of a gas-supersaturated solution contains a number of molecules of a dissolved substance about an order of magnitude less than that of a solvent. If we assume that an easily volatile component, to be dissolved, is distributed uniformly in a solvent, then, in the process of nucleation, the solvent molecules predominantly leave the volume where a critical bubble forms. To obtain an equilibrium composition of a dissolved component in a bubble, diffusion may not be required as the inflow of the lacking number of gas molecules may take place at the expense of the thermal motion of molecules.

The situation in a gas-supersaturated solution changes cardinally if nucleation proceeds at temperatures much lower than the solvent critical temperature. Thus in a helium–oxygen solution at a temperature of 100 K, a pressure of 1.171 MPa, when the helium concentration c' equals 3 mol% and the solution is supersaturated (the Gibbs number equals $G_* \cong 80$), the radius of a critical nucleus will be $\cong$ 1.7 nm, the number of helium molecules in a bubble $n''_{1*} \cong 176$, and the number of oxygen molecules $n''_{2*} \cong 3$. Before the formation of a nucleus in the volume of critical size, about $\cong$ 12 helium atoms were contained in it. To provide an equilibrium concentration in a bubble, helium atoms should diffuse via distances approximately 2.5 times greater than the bubble radius. The characteristic times of diffusion in this case are $\tau_D \cong 2 \times 10^{-8}$ s, which is comparable with the time of establishment of a stationary size distribution of the nuclei.

In constructing a theory of boiling-up for binary solutions, it was assumed that in the process of formation of a critical nucleus there was always enough time for the establishment of thermal, mechanical and diffusion equilibria, and the trajectory of the fluctuative motion of a bubble in the space of its significant variables passes through the saddle point of the potential barrier. This assumption is justified if the stable variables of a nucleus relax to their equilibrium values more rapidly than the unstable variable. When this condition is violated, then, as has been shown by Trinkaus [12], the trajectory of the nuclei flow may by-pass the saddle point of the free energy surface. The nucleation regime with by-passing the saddle point may be considered in the framework of the multidimensional nucleation theory presented in Sect. 5.2. However, such a consideration is limited in its applicability to small deviations from equilibrium owing to the fact that the Kramers–Zeldovich method is valid only in the critical region of the potential barrier, i.e., in the interval $W_* \pm k_B T$.

At low temperatures one may observe a stronger size dependence of the surface tension of critical bubbles [78]. The character of the dependence $\sigma(R_*)$ may differ not only quantitatively, but even qualitatively from that revealed at elevated temperatures. At temperatures $T = 0.6T_c$ the radius of a critical bubble is 2–2.5 times smaller than at $T = 0.9T_c$. This fact implies a stronger sensitivity of supersaturated solutions at low temperatures to inhomogeneities and accidental inclusions in a system and on the walls of the vessel surrounding it.

An increase in the number of regions, where a viable bubble is easily activated, hinders the realization in experiment of the homogeneous nucleation mechanism. However, even with existing boiling centers and free liquid surfaces, the temperature of intensive fluctuation nucleation in a supersaturated solution can be achieved in nonstatic processes with a rapid in-

troduction of heat into the system or an abrupt removal of the external pressure [14, 63]. For this purpose, it is necessary that the rate of penetration into a metastable region should satisfy a certain criterion, which would ensure superheating of the liquid under an intensive heat flow into existing centers of evaporation. At low temperatures the conditions of realization of such a shock liquid boiling-up regime prove to be more rigid than at temperatures close to the critical point. Practically all experiments on the investigation of nucleation in gas-supersaturated solutions at low temperatures were made with quasi-static methods [23–28] with a sufficiently slow transfer of the system into a metastable state. As in the case of cavitation [29], the achievement of conditions of homogeneous nucleation requires here, evidently, the use of nonstatic (pulse) methods.

Acknowledgements

The author is grateful to G.Sh. Boltachev and A.M. Kaverin, who participated in obtaining some of the results presented here, and also to E.V. Urakova for translating the paper into English. The work was performed with financial support of the Russian Foundation of Fundamental Investigations (project 01-02-04014) and of the Deutsche Forschungsgemeinschaft (DFG, Grant 436 RUS 113/605/0-1).

References

[1] M. Volmer, *Kinetik der Phasenbildung* (Edwards Brothers, Inc., Ann Arbor, 1945).
[2] W. Döring, Z. Phys. Chem. **36**, 376 (1937).
[3] Ya.B. Zeldovich, Zh. Eksp. Teor. Fiz. **12**, 525 (1942).
[4] Ya.I. Frenkel, *Kinetic Theory of Liquids* (Oxford University Press, Oxford, 1946).
[5] H. Flood, Z. Phys. Chem. A **170**, 286 (1934).
[6] K. Neumann and W. Döring, Z. Phys. Chem. **186**, 203 (1940).
[7] H. Reiss, J. Chem. Phys. **18**, 840 (1950).
[8] Ye.I. Nesis and Ya.I. Frenkel, Zh. Tekh. Fiz. **22**, 1500 (1952).
[9] D. Stauffer, J. Aerosol Sci. **7**, 319 (1976).
[10] G. Shi and J.H. Seinfeld, J. Chem. Phys. **93**, 9033 (1990).
[11] A.A. Melikhov, V.B. Kurasov, Yu.Sh. Djikaev, and F.M. Kuni, Zh. Tekh. Fiz. **61**, 27 (1991).
[12] H. Trinkaus, Phys. Rev. **12**, 7372 (1983).
[13] V.Y. Zitserman and L.M. Berezhkovski, Zh. Fiz. Khim. **64**, 1975 (1990).
[14] V.P. Skripov, *Metastable Liquids* (Wiley, New York, 1974).
[15] M. Blander, D. Hengstenberg, and J.L. Katz, J. Phys. Chem. **75**, 3613 (1971).
[16] C.T. Avedisian, J. Phys. Chem. Ref. Data. **14**, 695 (1985).
[17] H. Reiss, D.I. Margolese, and J. Schelling, J. Colloid Interface Sci. **56**, 511 (1976).
[18] B.E. Wyslouzil, J.H. Seinfeld, R.C. Glagan, and K. Okuyama, J. Chem. Phys. **94**, 6827 (1991).
[19] V.G. Baidakov, V.P. Skripov, and A.M. Kaverin, Zh. Eksp. Teor. Fiz. **38**, 557 (1974).

[20] V.P. Skripov, V.G. Baidakov, and A.M. Kaverin, Physica A **95**, 169 (1979).
[21] B.V. Deryagin and A.V. Prokhorov, Kolloidn. Zh. **44**, 847 (1982).
[22] F.M. Kuni, V.M. Ochenko, L.N. Ganiuk, and L.G. Grechko, Kolloidn. Zh. **55**, 28 (1993).
[23] E.A. Hemmingsen, Science **167**, 1493 (1970); Gerth, W.A., Hemmingsen, E.A., Z. Naturforsch. A **31**, 1711 (1976).
[24] Y. Finkelstein and A. Tamir, AIChE J. **31**, 1409 (1985).
[25] P.G. Bowers, C. Hofstetter, H.L. Ngo, and R.T. Toomey, J. Colloid Interface Sci. **215**, 441 (1999).
[26] M.B. Rubin and R.M. Noyes, J. Phys. Chem. **91**, 4193 (1987).
[27] P.G. Bowers, C. Hofstetter, C.R. Letter, and R.T. Toomey, J. Phys. Chem. **99**, 9632 (1995).
[28] P.G. Bowers, K. Bar-Eli, and R.M. Noyes, J. Chem. Soc., Faraday Trans. **92**, 2843 (1996).
[29] V.G. Baidakov, *Superheat of Cryogenic Liquids* (Ural Branch of Russian Academy of Sciences Publishers, Ekaterinburg, 1995).
[30] H. Kwak and R.L. Panton, J. Chem. Phys. **78**, 5795 (1983).
[31] V.G. Baidakov, J. Chem. Phys. **110**, 3955 (1999).
[32] Y. Mori, K. Hijikata, and T. Nagatani, Int. J. Heat Mass Transf. **19**, 1153 (1976).
[33] T.W. Forest and C.A. Ward, J. Chem. Phys. **69**, 2221 (1978).
[34] P.A. Pavlov and P.V. Skripov, Teplofiz. Vys. Temp. **23**, 70 (1985).
[35] R.N. Herring and P.L. Barrick, Int. Adv. Cryogenic Eng. **10**, 151 (1965).
[36] V.G. Baidakov and I.I. Sulla, Int. J. Thermophys. **16**, 909 (1995).
[37] J.S. Langer, Ann. Phys. **41**, 108 (1967).
[38] F.M. Kuni, A.A. Melikhov, T.Yu. Novozhilova, and I.A. Terent'ev, Teor. Mat. Fiz. **83**, 274 (1990).
[39] E.A. Brener, V.I. Marchenko, and S.V. Meshkov, Zh. Eksp. Teor. Fiz. **85**, 2107 (1983).
[40] A.I. Rusanov, *Phase Equilibria and Surface Phenomena* (Leningrad, Khimiya, 1967).
[41] Yu. Kagan, Zh. Fiz. Khim. **34**, 92 (1960).
[42] B.V. Deryagin, A.V. Prokhorov, and N.N. Tunitskii, Zh. Eksp. Teor. Fiz. **73**, 1831 (1977).
[43] V.G. Baidakov, A.M. Kaverin, and G.Sh. Boltachev, J. Phys. Chem. **106**, 167 (2002).
[44] V.G. Baidakov, High Temp. **37**, 565 (1999).
[45] J.W. Gibbs, *Collected Works* (Yale University Press, New Haven, CT, 1948).
[46] Yu.A. Aleksandrov, G.S. Voronov, V.M. Gorbunkov, N.B. Delone, and Yu.I. Nechaev, *Puzyr'kovye kamery* (Gosatomizdat, Moskva, 1963).
[47] V.G. Baidakov, Kinetika zarodysheobrazovanija v peregretyh rastvorah gaza v zhidkosti, in *Metastabilnye Sostojanija i Fazovye Perekhody*, (Ural Branch of Russian Academy of Sciences, Ekaterinburg, 1998), pp. 12–38.
[48] L.D. Landau and E.M. Lifshitz, *Statisticheskaja Fizika* (Nauka, Moskva, 1976).
[49] I. Prigogine and R. Defay, *Chemical Thermodynamics* (Longmans Green, London, New York, Toronto, 1954).
[50] J.D. van der Waals and Ph. Kohnstamm, *Lehrbuch der Thermodynamik* (Maas and Van Suchtelen, Leipzig, 1908).

[51] J.W. Cahn and J.E. Hilliard, J. Chem. Phys. **31**, 688 (1959).

[52] V.G. Baidakov and G.Sh. Boltachev, Zh. Fiz. Khim. **71**, 1965 (1997).

[53] V.G. Baidakov, *Mezhfaznaya Granitsa Prostykh Klassicheskikh i Kvantovykh Zhydkostei* (Nauka, Ekaterinburg, 1994).

[54] G.Sh. Boltachev and V.G. Baidakov, Kolloidn. Zh. **62**, 1 (2000).

[55] V.G. Baidakov and G.Sh. Boltachev, Phys. Rev. E. **59**, 469 (1999).

[56] V.G. Baidakov and G.Sh. Boltachev, Zh. Fiz. Khim. **69**, 515 (1995).

[57] V.G. Baidakov, A.M. Kaverin, and G.Sh. Boltachev, J. Chem. Phys. **106**, 5648 (1997).

[58] V.G. Baidakov and A.M. Kaverin, High Temp. **38**, 852 (2000).

[59] A.T. Bharucha-Reid, *Elements of the Theory of Markov Processes and Their Applications* (McGraw-Hill, New York, Toronto, London, 1960).

[60] A.M. Kaverin, V.G. Baidakov, and V.P. Skripov, Inzh.-Fiz. Zh. **38**, 680 (1980).

[61] N.N. Danilov, E.N. Sinitsyn, and V.P. Skripov, Kinetika vskipanija peregretyh binarnykh rastvorov, in *Teplofizika Metastabilnykh Sistem* (Ural Division of Academy of Sciences of the USSR, Sverdlovsk, 1977), pp. 28–42.

[62] M.N. Medvedev, *Stsintillyatsionnye Detektory* (Atomizdat, Moskva, 1977).

[63] V.P. Skripov, E.N. Sinitsyn, P.A. Pavlov, G.V. Ermakov, G.N. Muratov, N.V. Bulanov, and V.G. Baidakov, *Thermophysical Properties of Liquids in the Metastable (Superheated) State* (Gordon and Breach, New York, 1988).

[64] A.M. Kaverin, V.G. Baidakov, V.P. Skripov, and A.N. Kat'yanov, Zh. Tekhn. Fiz. **55**, 1220 (1985).

[65] V.G. Baidakov and A.M. Kaverin, Teplofiz. Vys. Temp. **28**, 90 (1990).

[66] V.G. Baidakov, A.M. Kaverin, and V.P. Skripov, Akust. Zh. **27**, 697 (1981).

[67] V.G. Baidakov, A.M. Kaverin, and G.Sh. Boltachev, J. Phys. Chem. B **106**, 167 (2002).

[68] A.A. Vasserman and A.Ya. Kreyzerova, Teplofiz. Vys. Temp. **16**, 1185 (1978).

[69] V.V. Sychev, A.A. Vasserman, A.D. Koslov, G.A. Spiridonov, and V.A. Tsimarnii, *Thermodynamical Properties of Oxygen* (Izdat. Standartov, Moskva, 1981).

[70] V.G. Baidakov, Sov. Tech. Rev. B. Therm. Phys. **5**, 1 (1994).

[71] J.A. Schouten, A. Deerenberg, and N.J. Trappeniers, Physica A **81**, 151 (1975).

[72] S.F. Barreiros, J.C.G. Calado, P. Clancy, M.N. da Ponte, and W.B. Streett, J. Phys. Chem. **86**, 1722 (1982).

[73] R.N. Herring and P.L. Barrick, Int. Adv. Cryogenic Eng. **10**, 151 (1965).

[74] V.G. Baidakov, K.V. Hvostov, and G.N. Muratov, Zh. Fiz. Khim. **56**, 814 (1982).

[75] V.G. Baidakov and V.P. Skripov, Kolloidn. Zh. **44**, 409 (1982).

[76] V.G. Baidakov, Ukr. Fiz. Zh. **27**, 1332 (1982).

[77] C.D. Holcomb and J.A. Zollweg, J. Phys. Chem. **97**, 4797 (1993).

[78] V.G. Baidakov and G.Sh. Boltachev, Zh. Fiz. Khim. **75**, 33 (2001).

6 Correlated Nucleation and Self-Organized Kinetics of Ferroelectric Domains

Vladimir Ya. Shur

If we were in equilibrium we would not only be dead –
we would be homogeneous!
Sidney Nagel

In the present chapter, we present a review of the most interesting aspects of the kinetics of nonequilibrium domain structure evolution in ferroelectrics and discuss the problem in the framework of a unified approach. The basic idea is to consider the domain structure evolution during polarization reversal as an example of a phase transformation in a first-order phase transition. Thus it can be described in terms of the elementary nucleation processes. Within such approach all different forms of the domain kinetics can be explained as the result of elementary processes associated with the formation of nuclei with the preferred orientation of spontaneous polarization. The nucleation rate is determined by the local value of the electric field. It has been proposed that all existing static domain patterns in any ferroelectric, being metastable and far from equilibrium, are formed in the course of the discussed domain kinetics scenario and are fastened by the bulk screening processes. Original scenarios of domain structure evolution were revealed experimentally and discussed accounting for the decisive role of the retardation of the screening process. The domain evolution during decay of the highly nonequilibrium states represents a self-organizing process, in which the screening of polarization reversal plays the role of the feedback mechanism. It has been shown both experimentally and by computer simulation that the correlation length of quasi-periodic self-assembled nanodomain structures is determined by the thickness of the intrinsic or artificial surface dielectric layer. The discussed results of these fundamental investigations are of great interest as a physical basis for a modern field of technology denoted as "domain engineering."

6.1 Introduction

The polarization reversal phenomenon, being an attribute of ferroelectric materials, was at the center of attention of scientists for years. Nevertheless, the recent direct systematic study of the domain structure evolution using in situ observation with high time and spatial resolution reveals unexpected scenarios of domain evolution through formation of quasi-regular nanoscale domain structures [1]. Moreover, the accumulated experimental data on the domain images obtained in different ferroelectric materials demonstrate an essential dependence on the experimental conditions and are waiting for a systematic explanation based on a universal approach.

It is evident that the understanding of the domain kinetics is very important for various significant applications of ferroelectric materials on the basis of polarization reversal, such as, for example, the widely used modern ferroelectric thin film memory devices. Moreover, the artificial creating of tailored periodic domain structures with proper geometry and sizes denoted as

Nucleation Theory and Applications. edited by J. W. P. Schmelzer

ISBN: 3-527-40469-4

"domain engineering" is rapidly developing nowadays as a new branch of ferroelectric science and technology. Fabrication of the precisely governed regular domain patterns with periods of about several microns is a key problem on the way of improvement of the characteristics of electrooptical and nonlinear optical devices [2]. Engineerable (periodically poled) nonlinear optical materials are widely used for the development of various tunable coherent light sources based on quasi-phase matching [3–7].

In this publication, we discuss the role of the correlated nucleation occurring during electric field induced domain growth in ferroelectrics. We show that even the simplest variant of the domain kinetics representing itself as the motion of the domain wall can be a very complicated self-assembled process. Along with a detailed discussion of the classical approach we demonstrate several unusual domain wall motion scenarios including the "discrete switching" through formation and self-terminated propagation of self-assembled nanoscale domain structures. In this case the propagation of the boundary of the enlarging complicated domain ensemble replaces the usual domain wall motion. We proposed and clearly demonstrated that the discrete switching was caused by the retardation of the bulk screening of the depolarization field. In the framework of such approach the interchange of the domain wall (boundary) propagation scenarios induced by the experimental conditions is a result of the competition between screening and switching processes.

We present a systematic explanation of the experimental investigations of the domain kinetics in a wide range of domain growth velocities in various uniaxial ferroelectrics with optically distinguished domains, such as lead germanate ($Pb_5Ge_3O_{11}$) (PGO), lithium tantalate ($LiTaO_3$) (LT), and lithium niobate ($LiNbO_3$) (LN). We investigate, in detail, the domain evolution using in situ optical observation of the instantaneous domain patterns under application of an electric field. "Slow", "fast", and "superfast" domain boundary motion regimes have been revealed and investigated in details. It is claimed that the main parameter for the proposed classification is the ratio, R, of the switching rate $(1/t_s)$ to the bulk screening rate $(1/\tau_{scr})$, where t_s is the switching time and τ_{scr} is the screening time constant. The crucial role of the intrinsic or artificial dielectric surface layer is clearly exhibited as well. Computer simulation has been used for the verification of the proposed models.

According to the classical theoretical approach, the static domain structure configuration of a ferroelectric corresponds to an equilibrium domain state, which is obtained by minimizing the total free energy of the sample including the depolarization energy induced by bound charges in the finite sample and the domain wall energy [8]. This approach coincides with the one usually used in ferromagnetism. Two limiting types of equilibrium domain states have been predicted by this approach depending on either neglecting the screening processes or taking them into account. The first so-called ferromagnetic case exactly coincides with the experimentally observed behavior of ferromagnetic domains and predicts the periodical laminar or maze domain structure with neutral domain walls. The domain period corresponding to the minimum of the free energy is determined unambiguously by the values of spontaneous polarization, dielectric permittivity, density of the domain wall energy, and sample thickness. In such a case the equilibrium domain structure must be necessarily periodic with an average value of the spontaneous polarization over the sample equal to zero. Moreover, for a proper material the period has to be strictly governed by the temperature and the sample sizes [8, 9]. The situation qualitatively changes if one considers the compensation of the depolarization field by screening processes, which is the fundamental property defining the distinction in the

kind of domain behavior in ferroelectrics and ferromagnets. The complete screening of the depolarization field favors the single-domain equilibrium state without any domain walls, in other words the equilibrium state is characterized by the absence of any domain structure.

It is well-known that the both limiting predictions of the classical approach contradict the domain structure configurations observed in real ferroelectrics. The great variety of the domain patterns formed are metastable but nevertheless persist for a very long time (about months and years). Thus these structures are stable enough to be considered as static ones from experimental and applied points of view. In the following, we present experimental evidence and theoretical considerations which reveal the kinetic nature of the observed domain configurations. In other words, the real domain configurations are determined by the domain kinetics prehistory. We demonstrate the crucial role of the bulk screening processes in the stabilization of the metastable domain structures [10–12]. This approach allows one to choose the proper experimental conditions for fastening almost any domain patterns evolution.

6.2 Domain Structure Evolution during Polarization Reversal

Most of the classical experimental investigations of the domain dynamics during polarization reversal (switching) have been made on $BaTiO_3$ by in situ optical methods [13–16]. Later the systematical study of the domain structure evolution has been carried out in several uniaxial ferroelectric single PGO-crystals [17, 18], molybdate gadolinium $Gd_2(MoO_4)_3$ [19–21], LN [22, 23], and LT [24, 25] with optically distinguished domains, which can be considered as model systems. The commonly observed scenario of domain evolution is as follows. After application of the external electric field oriented in the direction opposite to the existing orientation of the spontaneous polarization of the single-domain sample, new domains appear, mainly at the surface, and then grow through the sample thickness. After having grown through the sample they begin to expand sideways. The formation of new domains continues to take place while the first ones progress in their sideways expansion. Later they begin to merge/coalesce until the entire unswitched region is completely overrun by them [9]. Based on usually obtained experimental data it is common to separate the whole process of domain evolution during polarization reversal for complete switching from the single domain state to another one with opposite direction of the spontaneous polarization into four main stages (Fig. 6.1).

The first stage, "nucleation of new domains" (Fig. 6.1(a)), is the most mysterious process. A wide gap (several orders of magnitude) between the value of the threshold field, measured experimentally and predicted theoretically, still exists [26]. There are several approaches to a qualitative explanation of this contradiction. It can be attributed to the lack of perfection existing in any real crystal, which is confirmed by the experimentally observed nucleation sites defined by natural or artificial surface and bulk defects. The special properties of the surface layer in any ferroelectric capacitor representing the intrinsic dielectric gap (see Sect. 6.3) provoke the incomplete compensation of the depolarization field near the surface, thus facilitating nucleation in the vicinity of the electrodes [27]. Finally, it is a matter of discussion whether the initial domain state could be completely single-domain or it contains a large quantity of

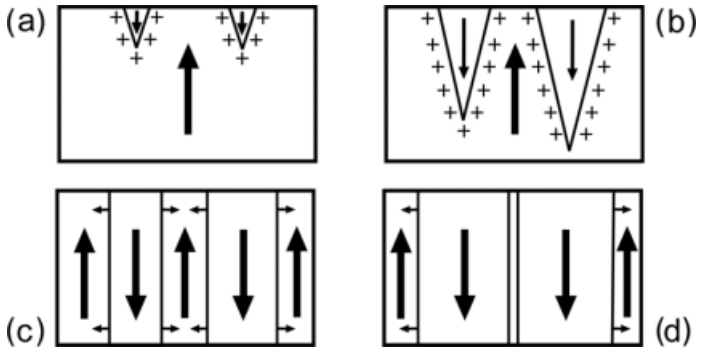

Figure 6.1: The main stages of the polarization reversal in ferroelectrics

nanoscale irremovable residual domains [12]. In the latter case the nucleation stage represents a transition of the invisible residual nanodomains into visible ones as a result of the field induced domain growth. The second stage, denoted as "forward growth," represents an expansion of the formed "nuclei" in polar direction through the sample (Fig. 6.1(b)). It is clear that all domains at this stage possess charged domain walls. This is the reason why this process is an unbeloved child for theoreticians. The additional energy produced by such unusual walls is enormously high because the fast external screening mechanisms are unable to compensate effectively the depolarization field produced by the bound charges existing at the boundary of encountered domains in the bulk. Formation of needle-like domains with high aspect ratio is the way to reduce this energy. For example, in LN at room temperature the ratio of the longitudinal to transversal domain sizes reaches 100 (see Section 6.9) [28]. Moreover, the strong interaction between the individual growing domains due to long-range electrostatic fields plays an essential role thus determining the kinetic properties of the domain ensemble and the final configuration of the formed static structure. This effect is brightly demonstrated during formation and expansion of the quasi-regular cogged "charged domain wall" occupying the large area in the bulk of LN-crystals under switching using continuous metal electrodes [29]. The third stage, "sideways domain growth," is achieved through the domain wall motion in the direction transversal to the polar one (Fig. 6.1(c)). It is the experimentally best studied stage because the regions in the vicinity of the domain walls in many ferroelectrics demonstrate the remarkable optical contrast which allows to apply the direct in situ methods of domain observation with high time resolution. It must be pointed out that usually an essential anisotropy of the sideways domain wall motion is observed. It results in the formation of the regular shaped polygon individual domains with sides strictly oriented along the preferred crystallographic directions. Nevertheless, the wall orientation is determined by competition between the generation of the steps at the wall and their subsequent growth along the wall. The most impressive experimental evidence of this competition is the possibility to vary the wall orientation and corresponding domain shape by varying the strength of external field and experimental conditions (see Section 6.6) [30–32]. The fourth stage, "coalescence of residual domains," is observed at the completion of the switching process (Fig. 6.1(d)). At this stage the sideways wall motion decelerates due to the essential electrostatic and mechan-

ical interactions between approaching walls. Thus the walls halt and after some definite rest time the residual region between the walls disappears very rapidly. This process is one of the well-known mechanisms which causes the jump-like switching behavior and is displayed as a noise component of the switching current, the so-called Barkhausen noise [8, 33, 34].

Recent research has shown that the alternative scenario of domain structure evolution through "discrete switching" can be realized as well [1, 35–37]. In this case the usual domain growth mechanism, through wall motion as a whole, is essentially suppressed. The domain kinetics during switching is achieved through development of a quasiregular structure consisting of isolated needle-like submicron- or nanoscale domains. The superfast expansion of the "switched area" covered by this domain ensemble is due to self-maintained generation of the domain chains/arrays in the vicinity of its boundary.

6.3 General Considerations

The possibility to change the direction of the spontaneous polarization under the action of an electric field is the main feature, which singles out the ferroelectrics among other materials. It is quite natural that the investigation of the polarization reversal is always in fashion. The amount of experimental data obtained for various ferroelectrics is enormous. Complete and direct information about the domain kinetics is received through a real-time recording of the sequence of the momentary domain configurations. It has been shown that the actual evolution of the domain structure is a multivariable irreproducible process not only for different ferroelectrics but even for different samples of the same material. These features hinder the understanding of the common laws governing the dynamics of the ferroelectric domains.

In this publication, we will consider all these complicated phenomena from a unified point of view. According to this approach, the domains with different orientations of the spontaneous polarization coexisting in the same sample are not one but different phases, while the domain walls represent the phase boundaries. It must be stressed that, in contrast to the ferromagnetic domain wall, the width of ferroelectric ones is about one unit cell size. This experimental fact is an indication in favor of consideration of the domain kinetics as a discrete process. Thus, the domain structure evolution during switching is an example of a first-order phase transformation. It is well-known that such transformation is achieved through nucleation. All the above-mentioned stages of the domain kinetics can be attributed to the elementary processes of evolution of thermally activated nuclei with a preferred orientation of the spontaneous polarization. It is worth to mention that the nucleation probability is defined by the activation energy. It is clear that during the switching process it is always spatially heterogeneous, as it is determined by the local value of the electric field originating from different sources.

The nucleation process The domain kinetics, similarly to any first-order phase transformation, is achieved through competitive formation of nuclei of three different dimensionalities (Fig. 6.2). Each nucleus represents the minimum domain with preferential orientation of the spontaneous polarization determined by the direction of the local electric field. The appearance of new domains is due to the formation of $(3D)$-nuclei. The domain growth by motion of the domain walls is a result of $(1D)$- and $(2D)$-nucleation at the already existing walls. The nucleation probability in a multidomain state is essentially inhomogeneous due to the

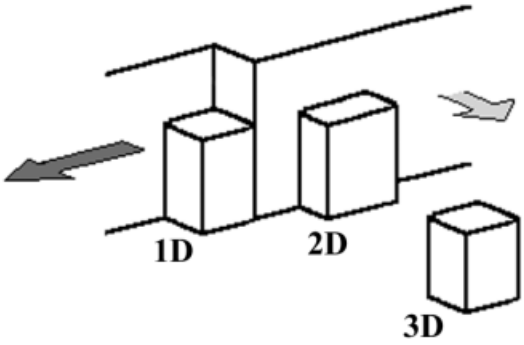

Figure 6.2: Nucleation processes of various dimensionalities

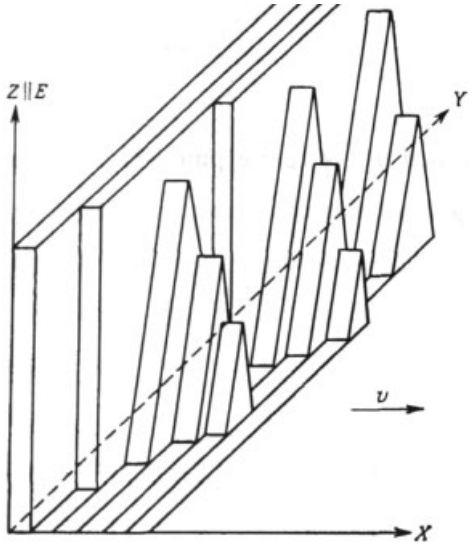

Figure 6.3: Classical scheme of the domain wall motion [39]

spatial variation of the local electric field. Moreover, the imperfections of the real material and the finite size of the samples influence the position of the nucleation sites. It is shown experimentally that nucleation starts at the sample surface and in the vicinity of defects.

Shape of the nuclei The triangular shape of the nuclei shown in Fig. 6.3 is due to the remarkable role of the surface depolarization energy. The same effect leads to the formation of the new domains elongated in polar direction, which are usually observed at the first and second stages of the polarization reversal. It has been shown by Miller and Weinreich [38] that the triangular shape of $2D$-nuclei forming at the wall essentially diminishes its electrostatic energy arising as a result of a jump-like change of the sign of the spontaneous polarization at the "tail to tail" or "head to head" wall. Thus, such nuclei shape facilitates the formation of the

charged domain walls in the bulk, which always appear during the switching [39]. It is necessary to stress that this approach does not take into account the role of any screening effect. The nucleation probability is determined by the value of the electric field averaged over the volume of the order of the nucleus sizes ("local field"). This field plays the role of the driving force of all nucleation processes during polarization reversal in ferroelectrics [12].

Local value of electric field During switching, the internal electric field is essentially spatially inhomogeneous. The local field value E_{loc} in a ferroelectric capacitor is determined by the sum of (1) the external field produced by the potential difference between the electrodes, (2) the depolarization field produced by bound charges developing as a result of the spatial inhomogeneity of the spontaneous polarization, (3) the external screening field originating from the redistribution of the charges at the electrodes, and (4) the bulk screening field governed by bulk screening processes.

The external field strongly depends on the shape of the electrode and demonstrates the singularities in the surface layer at the electrode edges due to the fringe effect. This is the reason why the switching process starts through formation of the first nuclei at the electrode boundary. It is clear that due to this fact the real value of the local field corresponding to the beginning of the switching process in single-domain states can be essentially higher than the averaged value of the applied field calculated as the potential difference divided by sample thickness. The fringe effect leading to the field concentration is most pronounced in the vicinity of the ends and corners of the stripe electrodes.

The depolarization field is produced by bound charges existing at the polar surfaces of the sample and at the charged walls of the domains encountering in the bulk ("head to head" or "tail to tail"). The surface charge density for the ferroelectric plate cut perpendicular to the polar axis is equal to spontaneous polarization. For typical ferroelectrics the depolarization field strength in a single-domain plate can reach the value of $10^8\ \mathrm{V\,m^{-1}}$. This enormous field is essentially reduced for narrow strip domains and especially for the needle-like ones. This is the reason why the triangular and needle-like nuclei shapes are the most favorable ones. The averaged value of the depolarization field sufficiently decreases in multidomain states, when it is determined by the shape and average size of domains. It has been shown that the depolarization field in the vicinity of the domain walls is strongly spatially inhomogeneous [40]. This field decreases the nucleation probability at the wall, which leads to hampering of the switching by the external electric field. Such approach is usually employed for the explanation of the kinetics of ferromagnetic domains, but the screening of the electric field in ferroelectrics changes essentially the role of the depolarization field during domain kinetics. For slow switching, when the screening of the depolarization field is almost total, one can obtain a complete switching in a comparatively low electric field. Whereas for fast switching rates, when the screening retards, the commonly used value of the applied external field leads only to a small shift of the existing domain walls. After the external field is switched off the recovering of the initial domain state ("spontaneous backswitching") is observed for incomplete screening. It is common to divide all the screening processes into two groups: external and bulk screening.

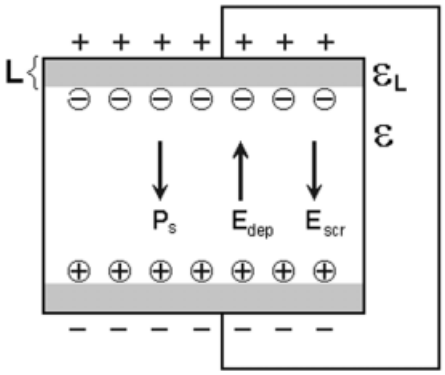

Figure 6.4: Scheme of the real ferroelectric with the intrinsic dielectric surface layer

External screening in a ferroelectric capacitor (a ferroelectric platelet with polar facets completely coated by electrodes) is a result of external current and it depends upon the characteristic time of the external circuit τ_{ex} determined by the product of resistance and capacity of the circuit. This time constant usually ranges from a few nanoseconds to microseconds. The external screening effectively compensates the depolarization field thus allowing the long-distance-shift of the domain wall and drastically diminishes the value of the field, which is necessary for the complete switching. It must be understood that the experimentally observed switching time, t_s, is limited by the value of τ_{ex}. This dependence is due to the fact that complete switching at comparatively low fields can be obtained only if the depolarization field is sufficiently compensated. Nevertheless, the fast external screening never compensates the depolarization field completely due to existence of the intrinsic dielectric surface layer ("dielectric gap" or "dead layer"), in which spontaneous polarization is absent (Fig. 6.4) [12, 41]. This is the reason why the role of the comparatively slow bulk screening processes must be accounted for as well.

Bulk screening by bulk processes is the only way to compensate the residual depolarization field existing in the bulk of the ferroelectric capacitor after completion of the external screening. Three different groups of bulk screening mechanisms are considered usually: (1) redistribution of the bulk charges [12,41], (2) reorientation of the defect dipoles [42], and (3) injection of carriers from the electrode through the dielectric gap [43]. All considered bulk screening mechanisms are very slow as compared to the external ones with time constants τ_b ranging from milliseconds up to days and even months. While the residual depolarization field is several orders of magnitude less than the depolarization one, nevertheless it is of the order of the experimentally observed threshold fields. This is why bulk screening, which becomes apparent in various memory effects, plays an essential role in the evolution of the domain structure.

The systematic investigation of the polarization reversal in various ferroelectric single crystals reveals a great variety of domain kinetics scenarios. The main problem in their classification is that it is absolutely impossible to attribute a given scenario to a definite range of applied fields and switching rates. The critical values of the fields and rates corresponding to a replacement of one domain kinetics scenario by another one differ drastically for different

materials and experimental conditions. We have proposed and confirmed both experimentally and by computer simulation that the ratio R between switching rate $(1/t_s)$ and bulk screening rate $(1/\tau_{scr})$ can be used as the crucial parameter determining the selection of the particular scenario of the domain kinetics including the exotic ones. Our approach to field induced domain kinetics is based on the consistent account of the key role of the bulk screening effects [10, 11]. It is well known that the polarization reversal from the single domain state is achieved by nucleation of the new domains and their subsequent growth [9,12]. Both processes are governed by elementary nucleation (1) at the domain wall for domain growth and (2) far from the wall for formation of new domains. The electric field being the driving force of all nucleation processes is spatially inhomogeneous and time dependent.

The local value of the electric field at the given point and at the given moment of time $E_{loc}(r, t)$ is the sum of the external field $E_{ex}(r)$, the depolarization field $E_{dep}(r, t)$ produced by bound charges, and two types of screening fields caused by (1) the charge redistribution at the electrodes – the external screening field $E_{scr}(r, t)$ – and (2) bulk processes – the bulk screening field $E_b(r, t)$ [10–12] – , i.e.,

$$E_{loc}(r, t) = E_{ex}(r) + E_{dep}(r, t) + E_{scr}(r, t) + E_b(r, t) \; . \tag{6.1}$$

For a ferroelectric capacitor of thickness d the bulk residual depolarization field E_{rd} remains in the area freshly switched from one single-domain state to another one even after complete external screening due to existence of the intrinsic surface dielectric layer of thickness L [12, 41]. We have

$$E_{rd} = E_{dep} - E_{scr} = \frac{2L}{d}\frac{P_S}{\varepsilon_L \varepsilon_0} \; , \tag{6.2}$$

where P_S is the spontaneous polarization and ε_L is the dielectric permittivity of the surface dielectric gap. Due to this the application of the short field pulse, for which the bulk screening of the new state lags behind, is absolutely ineffective for creation of a modified domain pattern. The cooperative action of the residual depolarization field and the bulk screening field, remaining after the external field is switched off, leads to the spontaneous backswitching process. This effect could be observed in the areas, where the local value of $E_{loc}(r, t)$ exceeds the threshold field for the switching process E_{th}, i.e.,

$$E_{loc}(r, t) = -[E_{dep}(r, t) - E_{scr}(r, t) + E_b(r, t)] = [E_{rd}(r, t) + E_b(r, t)] > E_{th} \; . \tag{6.3}$$

The initial domain state can be even completely reconstructed for ineffective screening of the modified depolarization field produced by domain pattern formed at the end of the electric field pulse. The conservation of the new domain configuration can be realized only when the duration of the external field pulse is long enough for effective bulk screening. Thus, it is clear that for an appropriate duration of application of the field it is possible to conserve almost any domain pattern.

We consider three ranges for R, distinguished between the different values of the bulk screening effectiveness: (1) $R \ll 1$ – "complete screening," (2) $R > 1$ – "incomplete screening," and (3) $R \gg 1$ – "ineffective screening." The following sections are devoted to a detailed discussion of the special features of domain kinetics in all the three switching regimes defined by the value of R.

6.4 Materials and Experimental Conditions

Three different ferroelectric crystals: lead germanate $Pb_5Ge_3O_{11}$ (PGO), lithium niobate ($LiNbO_3$), and lithium tantalate ($LiTaO_3$) have been chosen by us for the main investigations of the domain kinetics. All these crystals are uniaxial thus possessing a comparatively simple domain structure with 180° domain walls only. Moreover, the domain shape in all of them is very similar due to C_3 symmetry in the ferroelectric phase. Finally, in all crystals the domains are optically distinguishable, this is why the most effective optical methods can be used for in situ observation of the field induced domain kinetics.

PGO can be considered as a model crystal. The 180° domains are easily observed with high optical contrast in a polarized microscope due to the different sign of the optical activity in the domains with opposite sign of the spontaneous polarization. The low value of the coercive field (about 3–5 kV/cm) favors PGO as one of the ferroelectric materials with a thoroughly investigated static and dynamic domain structure [18]. LN and LT are the favorite objects of the domain engineering. At the same time the coercive fields in the most popular congruent compositions of LN and LT are enormously high (about 210 kV/cm in both). For many years both materials were classified as "frozen ferroelectrics" as long as the attainment of the necessary threshold field value was coupled with great experimental difficulty. The tasks of the domain engineering forced a recent solution of the experimental problems [4] and stimulate the experimental study of the domain switching in LN and LT under application of the external electric fields. Moreover, the trend to create tailored periodical domain structures leads to a necessity of studying the domain kinetics in LN and LT under the action of the inhomogeneous electric field produced by lithographically prepared electrode patterns. The direct study of the domain kinetics becomes easier due to the pronounced electro-optical effects existing in both crystals. Easy optical visualization of the domain structure is due to an essential change of the refractive index in the vicinity of the domain walls induced by the above discussed incompletely compensated depolarization field.

Recently a new LN and LT family of crystals, which are closer to stoichiometric composition, have become available for research [44–47]. It has been shown that stoichiometric LN and LT demonstrate essentially lower values of the coercive field and a very different domain behavior as compared with congruent ones [45, 46]. LN and LT single crystals of congruent composition, such as PGO crystals of high optical quality, were grown from the melt by the Czochralski method. The double-crucible modification of the Czochralski method and top-seeded solution growth method were used for growth of stoichiometric LN and LT [45–47]. Switching experiments were held in optical-grade single-domain wafers cut perpendicular to the polar axis. The typical thickness for PGO samples ranges from 0.15 to 2 mm, for CLN and CLT – from 0.2 to 0.5 mm, and for SLN and CLT – from 1 to 2 mm. The polar surfaces of all investigated plate-like samples were carefully polished.

An electric field has been applied to PGO-samples using ITO-electrodes, which completely cover the polar surfaces. Visualization of the domain structure evolution was performed by polarizing optical microscope in transmitted light. The reproducible domain kinetics during periodical poling allows us to use the stroboscopic lighting for observation of the series of instantaneous domain patterns with high time resolution of about 10 ns while using the dye pulse laser pumped by nitrogen laser [35, 36]. Comparison of the switching currents recorded

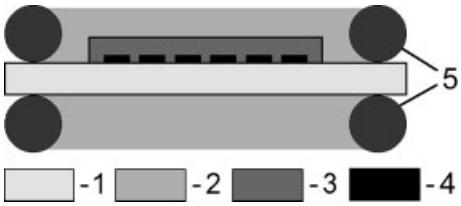

Figure 6.5: Experimental setup used for periodical poling. (1) wafer, (2) liquid electrolyte, (3) insulating layer, (4) periodic electrodes, (5) (O)-rings

during switching with pulse illumination and in the dark allows us to reveal that the used light intensity does not influence the polarization reversal process.

For the in situ investigation of the domain kinetics in a uniform electric field in LN and LT, we prepared 1-mm-diameter circular transparent electrodes of two types: (1) liquid electrolyte (water solution of LiCl) in a special fixture and (2) In_2O_3:Sn (ITO) films deposited by the magnetron sputtering. We carried out direct observations of the domain evolution using a polarizing microscope with simultaneous TV-recording and subsequent processing of the image series.

LN and LT-wafers, used for the periodical poling, were lithographically patterned with periodic stripe NiCr electrodes deposited on the Z^+-surface only and oriented along one of the Y-directions. The patterned surface was covered by a photoresist layer about one micron thick. A high voltage pulse producing an electric field greater than the coercive one ($E_c = 210$ kV/cm) was applied to the structure through the fixture containing a saturated water solution of LiCl (Fig. 6.5). For the observation of the domain patterns after partial poling both Z-surfaces were etched by pure hydrofluoric acid (HF) for 5 to 20 min at room temperature. The obtained surface relief was visualized by optical microscopy, scanning electron microscopy (SEM), and various modes of atomic force microscopy (AFM).

The motion of the domain walls has been also studied in improper ferroelectric–ferroelastic gadolinium molybdate ($Gd_2(MoO_4)_3$) (GMO), which allows us to realize easily the simplest model scenario of the field induced switching by motion of the single plane domain wall. The used GMO-single crystals were grown by the Czochralski technique [48]. Rectangular GMO-plates were cut perpendicular to the polar axis. All faces of the plates were carefully polished. Sample thickness has been chosen equal to 0.39 mm for optimal optical domain contrast. Polar surfaces were covered by transparent ITO-electrodes. A single planar domain wall oriented parallel to a shorter side of the sample was formed by mechanical stress. The special shape of electrodes limits the domain wall shift, thus allowing to prevent the wall disappearance during cyclic switching [49].

6.5 Slow Classical Domain Growth

Slow domain growth is obtained for complete bulk screening ($R \ll 1$). In this case the switching process in PGO, SLT, CLN, and SLN is achieved through the sideways motion of the strictly oriented walls of a few domains (Fig. 6.6). The predominant switching mecha-

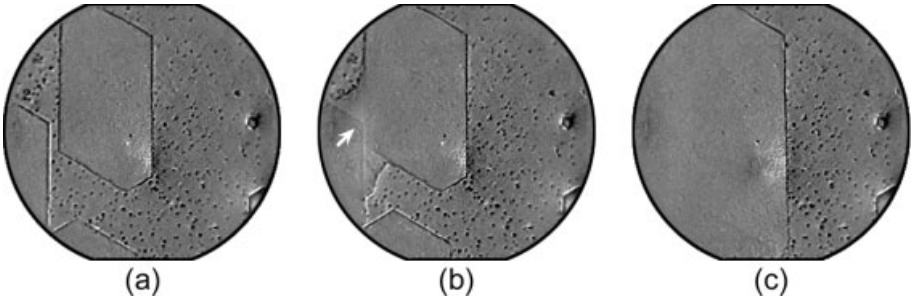

Figure 6.6: In situ optical visualization of the domain kinetics during switching by rectangular field pulse in CLN. Time intervals from the field switch-on are: (a) 1.5 s, (b) 2.3 s, and (c) 3.3 s. The arrow indicates the domain wall print. 1-mm-diameter liquid electrodes. $E_{ex} = 220\,\mathrm{kV/cm}$

nism is $2D$-step nucleation at the existing walls with subsequent step growth along the wall by $1D$-nucleation. The domain walls orientation parallel to the crystal facets remained during the whole switching process. In situ observation of the domain kinetics in congruent LN allowed us to study in detail the domain structure evolution during switching (Fig. 6.6). It has been shown that the switching process always starts with nucleation at the electrode edges and at the artificially produced surface defects in the center of the electrode area [28, 50, 51]. Isolated domains grow conserving the strict orientation of the domain walls along the Y-directions (Fig. 6.6). The domain wall motion usually proceeds via the propagation of optically distinguished microscale domain steps (bunches of the elementary nanoscale steps) along the wall (Fig. 6.7). The preferential wall orientation is clearly demonstrated from the beginning to the end of the switching process recovered after each act of domain merging (Fig. 6.6(b)) [28, 50, 51]. Irregular wall propagation due to merging of the growing individual domains formed at the artificial defect in the middle of the switched area is observed (Fig. 6.8(b)). It is seen that any local deviation from the allowed crystallographic directions disappears rapidly (Fig. 6.8(c)). It must be pointed out that each domain merging with formation of a concave shape domain leads to rapid transformation to the ordinary convex shape (Fig. 6.8(c)). The domain merging leads to an effective generation of an enormously large number of steps at the place of merging. The simultaneous rapid propagation of these steps along the existing walls drastically accelerates the domain growth [28,50,51]. The abnormally fast domain growth process ("domain gulping") obtained after merging of two large domains (Fig. 6.8) allows to visualize clearly the memory effect caused by retardation of the bulk screening. "Domain wall prints" remain for some time at the places, where the walls stay for a comparatively long time before jumping to a new position (Fig. 6.6(b)) and 6.8(b) and (c).

A similar behavior has been obtained by Gopalan and Mitchell during wall motion in CLT [24]. Such effect can be easily explained by retardation of the bulk screening process and represents a clear confirmation of the electrooptical nature of the observed domain contrast. The anomaly of the bulk distribution of the electric field near the staying domain wall evolves while the bulk screening process changes slowly in accordance with the new spatial distribution of the depolarization field after the wall shift. It is clear that the variation of the refractive

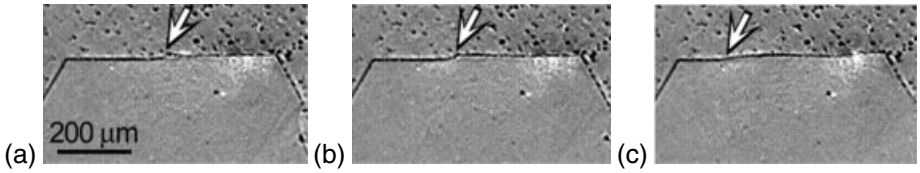

Figure 6.7: In situ optical visualization of the layer-by-layer domain growth by step propagation along the wall during poling from an initial single-domain state in CLN. Time intervals from field switch-on: (a) 1.20 s, (b) 1.28 s, and (c) 1.36 s. Liquid electrodes. $E_{ex} = 220\,\text{kV/cm}$

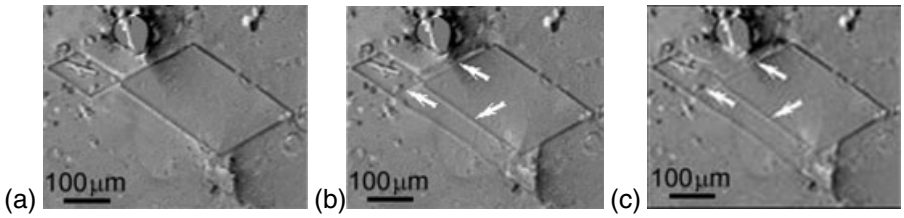

Figure 6.8: In situ optical visualization of "domain gulping" during reversal poling to initial state in uniform field in CLN. Arrows indicate the domain wall prints. Time interval between the subsequent frames 0.04 s. Liquid electrodes. $E_{ex} = 153\,\text{kV/cm}$

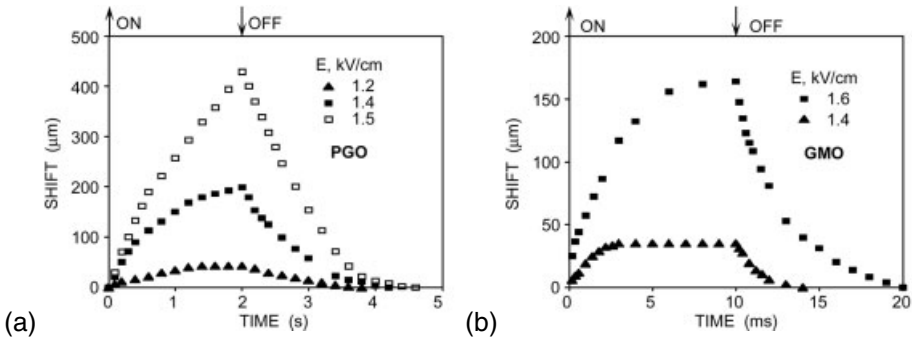

Figure 6.9: Time dependence of the planar domain wall shift from the initial position under application of rectangular electric field pulses. Deceleration effect for shifting wall and its spontaneous return to the initial position after field switch off in (a) PGO and (b) GMO

index induced by this field anomaly leads to the obtained domain wall print, which erases as a result of bulk screening. The erasing rate is defined by the bulk screening time constant.

It has been shown experimentally (Fig. 6.9) that the motion of the planar domain wall slows down during shifting from the initial state [40, 52]. This effect can be attributed to a reduction of the switching field E_{loc} at the moving wall by a residual depolarization field produced by bound charges in the freshly switched area behind it. Such deceleration is amplified by additional action of the bulk screening field still remaining in this area and coinciding in sign with the depolarization one [10–12]. The wall motion terminates if the effect is strong

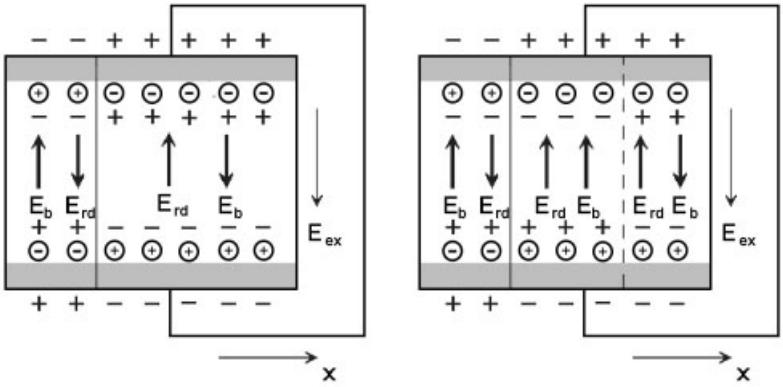

Figure 6.10: Scheme of the spatial distribution of the electric fields and charges for wall shift from the initial state with accomplished bulk screening. (a) Wall in the initial state and (b) wall shifted from the initial state

enough and the value of E_{loc} is lower than the threshold field value. In this case the growth of the individual domains by the classical mechanism is terminated.

Let us consider in detail the deceleration effect in the ferroelectric capacitor for the simplest experimental situation: The switching by a shift of the single plane neutral domain wall from the state with the accomplished bulk screening process. In the initial state the residual depolarization field is completely compensated by the bulk screening one. Let the bulk screening be so slow that the spatial distribution of the bulk screening field remains fixed during field induced wall shift. As a result, the field distribution becomes asymmetric relatively to the wall shifted on the distance Δx from the initial state (Fig. 6.10). Moreover, the bulk screening field is of the same direction as the residual depolarization field in the whole region passed by the wall. It is easy to show [40, 52] that the value of the decelerating field at the wall, averaged over the sample thickness, ΔE_{loc} can be approximated by a field produced by a stripe capacitor with the width equal to the wall shift Δx and the surface charge determined by the doubled bulk screening charge density $2\sigma_{\mathrm{b}}$. The dependence of ΔE_{loc} on the wall shift is given by the following expression:

$$\Delta E_{\mathrm{loc}}(\Delta x) = \frac{2\sigma_{\mathrm{b}}}{\varepsilon\varepsilon_0} F\left(\frac{\Delta x}{d}\right) , \tag{6.4}$$

$$\sigma_{\mathrm{b}} = 2P_{\mathrm{S}}\left(\frac{\varepsilon}{\varepsilon_L}\right)\frac{L}{d} , \tag{6.5}$$

$$F\left(\frac{\Delta x}{d}\right) = \frac{1}{\pi}\left[2\arctan\left(\frac{\Delta x}{d}\right) + \left(\frac{\Delta x}{d}\right)\ln\left(1 + \frac{d^2}{\Delta x^2}\right)\right] . \tag{6.6}$$

The wall motion velocity diminishes with the shift as the decelerating field at the wall increases with Δx. For low enough local fields the wall can even stop at the proper distance $\Delta x_{\max}$ from the initial state, as it has been discussed above. Moreover, after the external field switch-off the sum of the residual depolarization field and the remaining bulk screening field

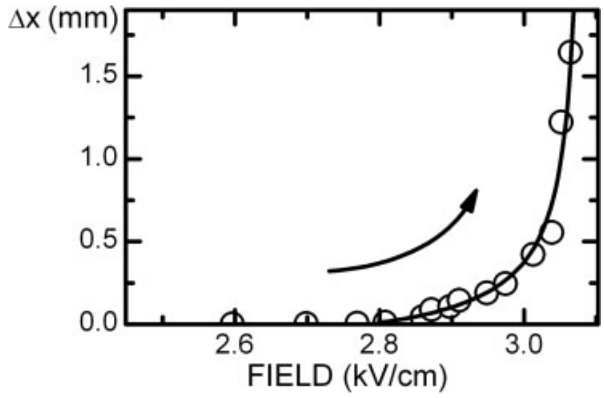

Figure 6.11: Field dependence of the wall shift for step-by-step increasing of the external field amplitude in GMO. Experimental points are fitted by Eq. (6.4)

return the domain wall to the initial state (the so-called "complete backswitching" effect). This effect is very pronounced for the sideways domain wall motion during the switching from the multidomain state. A complete spontaneous backswitching is usually experimentally observed in this case for the motion of the single plane domain wall in PGO and GMO (Fig. 6.9). The experimentally obtained field dependence of the wall shift measured during step-by-step increasing of the external field amplitude is fairly well described by Eq. (6.4) (Fig. 6.11). A similar decelerating effect must be taken into account also for any moving domain wall due to retardation of the external screening. In this case the trail of the uncompensated depolarization field follows the moving wall, decreasing the switching field and slowing down the wall motion [12]. The effective width of this trail is of the order of the product of the domain wall velocity and the time constant of the external circuit τ_{ex}.

6.6 Growth of Isolated Domains

It has been shown experimentally for PGO, LN, and LT that the regular shapes of isolated domains growing in a uniform electric field essentially depend on the switching field, although it is commonly accepted that the domain shapes are strictly defined by the crystallographic symmetry [30–32, 54]. Let us consider the main types of shapes of isolated domains formed as a result of switching in different experimental conditions.

A hexagonal shape is formed for switching under complete screening ($R < 1$), as it was discussed in the previous section. This situation is the most pronounced in any LN (Fig. 6.12(a)) and SLT (Fig. 6.12(b)), where the domains are perfect hexagons with sides strictly oriented along the Y-directions and with 120° angles. In PGO, the hexagons are distinctly rounded (Fig. 6.12(c)). For incomplete screening ($R > 1$) the residual depolarization field suppresses the slow regular domain growth. Step propagation along the walls is decelerated, thus leading to an essential deviation from the hexagonal shape. In LN the domain shapes essentially

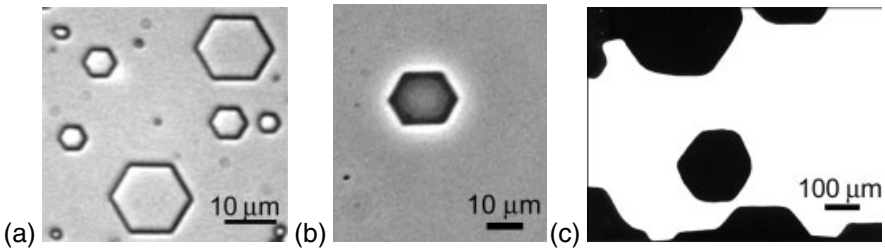

Figure 6.12: Domains of hexagonal shape in (a) CLN, (b) SLT, and (c) PGO. *(a)* Optical observation in reflected light, domains revealed by etching, (b) phase contrast microscopy, and (c) polarized microscopy, without etching

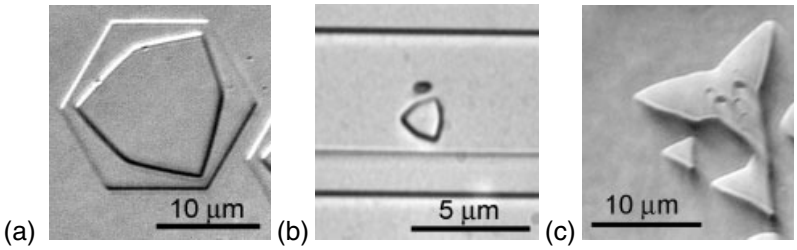

Figure 6.13: Exotic nonequiangular hexagon domains arising under switching in CLN covered by an artificial dielectric layer. (a) and (b) are convex hexagons, and (c) hexagon with concave angles ("Mercedes star") and regular triangle. Optical observation. Domains revealed by etching. (a) Sample was switched by two pulses and the Z^--surface was etched after each pulse

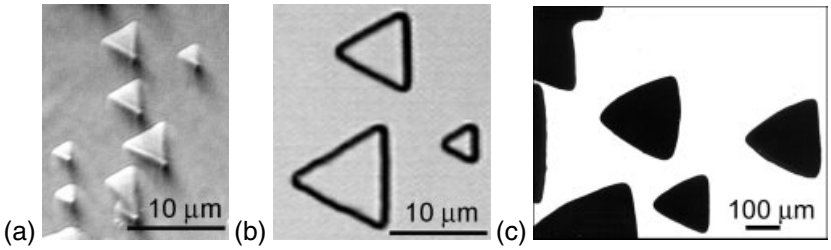

Figure 6.14: Triangular shaped domains in (a) CLN, (b) CLT, and (c) PGO. (a) and (b) optical observation in reflected light, domains revealed by etching. (c) Polarized microscopy in transmitted light, without etching

deviate from equiangular hexagons and can be produced during very fast switching or in the sample covered by an artificial dielectric surface layer (Fig. 6.13(a)). It must be pointed out that for optical visualization such shape of the small domains can be misinterpreted as rounded triangles (Fig. 6.13(b)).

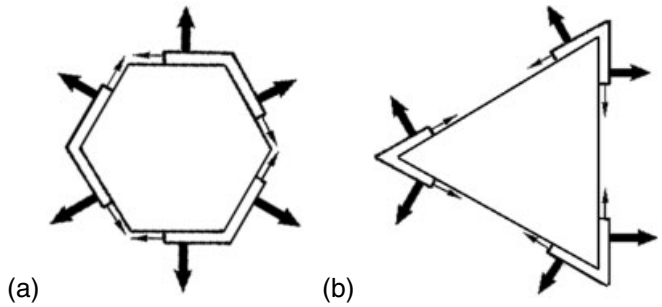

Figure 6.15: Scheme of domain growth: (a) hexagons, and (b) triangles

Triangular shape The formation of triangular-shape individual domains with the sides strictly oriented along the X-directions was observed in CLN, CLT, and PGO (Fig. 6.14). In CLT, the regular triangular domains were always obtained for switching at room temperature at any switching conditions (Fig. 6.14(b)), whereas creation of the triangular domains in CLN and PGO requires special switching conditions. In CLN, the triangular domains appear only for switching with an artificial dielectric layer or as a result of fast spontaneous backswitching (Fig. 6.14(a)). In PGO, we have produced the rounded triangles for switching by series of short pulses of the high electric field in the samples with fine mechanical treatment (Fig. 6.14(c)) [18, 31]. The observed quantitative difference between domain shapes in CLT (triangles) and SLT or any LN (hexagons) for switching in ordinary conditions can be attributed to the large difference of the screening time. It has been shown by direct measurements that the screening process in CLT is essentially slower ($\tau_{\mathrm{scr}} \sim 1$ s) as compared with LN and SLT ($\tau_{\mathrm{scr}} \sim 50$–$100$ ms). The evolution from hexagons to triangles in the same material is a clear proof that the domain shape is governed not only by crystal symmetry, but also by the specific kinetics of domain growth for different values of R.

We have investigated and verified by computer simulation the kinetic nature of domain shape selection. The model is based on several experimentally revealed features of domain growth. First, it has been found by in situ experimental observation using the polarizing optical microscopy that the generation of new steps ($2D$-nucleation) is obtained at three vertices of the regular hexagonal isolated domain, which corresponds to the Y^{-}-crystallographic directions (see schemes of domain growth in Fig. 6.15). Second, the arising steps grow along the existing domain walls along the Y^{-}-directions as a result of $1D$-nucleation. It is clear that the observed wall orientation would be determined by the step concentration. A similar effect is observed for vicinal faces during crystal growth. For very low step concentration caused by much faster step growth as compared with the step generation the classical hexagons have to be observed (Fig. 6.12).

The above discussed retardation of bulk screening leads to the existence of a trail of uncompensated field, which follows the moving step. The deceleration of the step growth induced by the trail field leads to an increase of the step concentration along the wall. This effect leads to a change of the wall orientation and allows to create the nonequiangular polygons with sides oriented in arbitrary directions (Fig. 6.16).

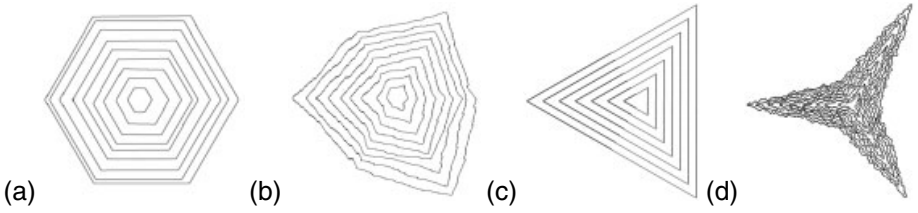

Figure 6.16: Isolated domain shapes obtained by computer simulation of the domain growth. The ratio between probabilities of step generation by $2D$-nucleation and step growth by $1D$-nucleation increases from (a) to (d)

We have simulated the growth of the isolated domain for various probabilities of step generation by $2D$-nucleation at all three vertices and step growth by $1D$-nucleation at the end of the step (Fig. 6.15). The best confirmation of the validity of our approach is the prediction of polygons with concave angles (Fig. 6.16(d)), which have been experimentally observed later during switching in CLN covered by an artificial dielectric layer. It must be pointed out that in the same experimental conditions both perfect triangular-shaped domains and unusual domain shapes similar to a "Mercedes star" are observed (Fig. 6.13(c)).

6.7 Loss of Domain Wall Shape Stability

6.7.1 Basic Mechanisms

When the classical step-by-step wall motion is completely suppressed due to the ineffective screening of the depolarization field ($R > 1$), the alternative mechanism of ongoing switching can be realized caused by any perturbation of the planar wall shape. This mechanism leads to a loss of the domain wall shape stability and to the formation of the self-assembled domain structure with submicron fingers (Fig. 6.17). The fluctuation of the domain wall shape is induced by a local electric field inhomogeneity, which can be produced (1) by the maximum of the external field due to electrode shape irregularity or (2) by the bulk defects decreasing the local value of the threshold field. In any case the fluctuation of the domain wall shape evolves leading to the formation of a ledge at the domain wall (the so-called "finger") oriented along the proper crystallographic direction (Fig. 6.18(a)). The peculiarities of the local field spatial distribution, which are discussed in connection with the correlated nucleation effect (see Section 6.9), result in the generation of the neighboring fingers. This effect is observed as a propagation of the finger structure along the wall (Fig. 6.18(b)). Finally, the structure with a correlated distance between fingers forms along the whole wall (Fig. 6.18(c)).

The subsequent growth of the front of the finger structure is caused by the field maximum existing at the tips of the fingers. The origin of this peculiarity is the same as discussed in Section 6.9. This field maximum increases the probability of $2D$-nucleation at the tips of the fingers and the front of the finger structure propagates parallel to the wall (Fig. 6.18(d)). During periodical domain poling this mechanism provides the abnormally large shift of the domain wall from the electrode edge, in other words abnormally strong "domain broaden-

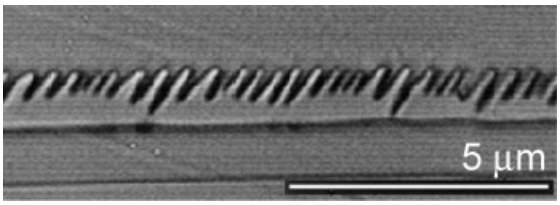

Figure 6.17: Instabilities of the domain wall shape leading to self-maintained formation of submicron fingers. Switching in CLN in the area covered by an artificial dielectric layer

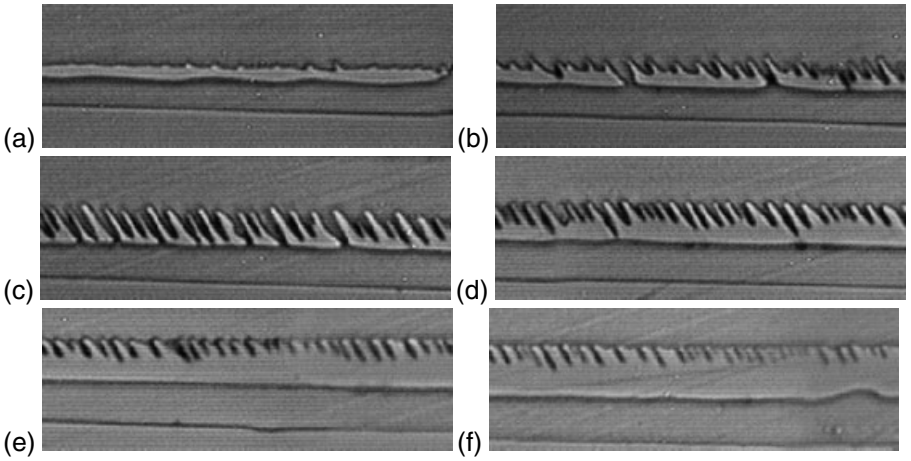

Figure 6.18: Loss of the wall shape stability through the formation of the finger structure during switching in CLN in the area covered by an artificial dielectric layer. Different stages of the structure evolution. Optical observation of domains revealed by etching

ing," which is extremely undesirable, because it leads to domain merging, thus destroying the periodicity of the domain pattern (see Sect.6.10) [3, 54, 55].

6.7.2 Dendrite Structures

The back switched poling allows to create domain structures consisting of stripelike units covering large areas of about several square millimeters during the poling in uniform electric field produced by continuous electrodes. The geometry of the arising domain ensemble differs essentially from above discussed finger structure. This structure demonstrates irregularity while comparing the orientation of the neighboring structure units.

The observed structures resemble in its appearance dendrites. The orientation of each array as a whole along the crystallographic directions is lost while the local symmetry is still preserved (Fig. 6.19). This effect can be attributed to a loss of long-range order, because this kinetic process develops under highly nonequilibrium conditions induced by the super-strong backswitching fields.

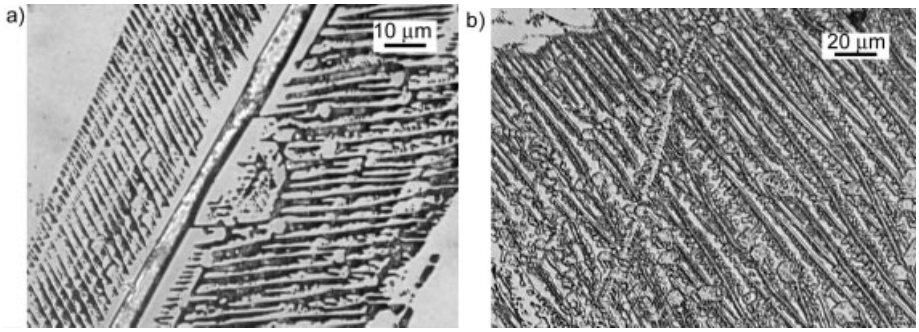

Figure 6.19: Dendrite domain structures formed during backswitching under an artificial dielectric layer in MgO:LN. Optical observation of the domains revealed by etching

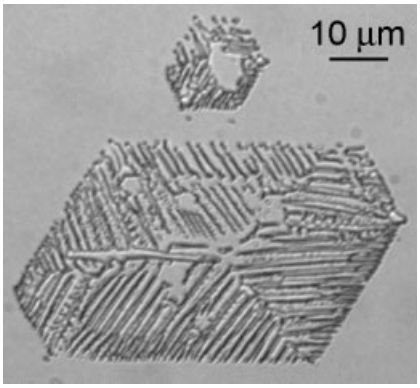

Figure 6.20: Dendrite domain structure evolving into a hexagonal shape. The structure is formed under an artificial dielectric layer in MgO:LN. Optical observation of the domains revealed by etching

Enlarging of the dendrite structure during switching leads in some cases to the propagation of a strictly oriented front (Fig. 6.20). For growth from the center it corresponds to the formation of the hexagonal shape structure filled by irregularly-shaped dendrite domains. During the spontaneous backswitching after fast removal of the external field the dendrite structure starts to grow from the boundaries of the hexagonal domains, which were formed during the slow switching in the same place by the classical mechanism of domain growth (Fig. 6.21). It is noted that the fingers choose the growth direction along one of the three equivalent crystallographic directions. It is clear that the dendrite structure consists of the nonthrough domains with charged domain walls.

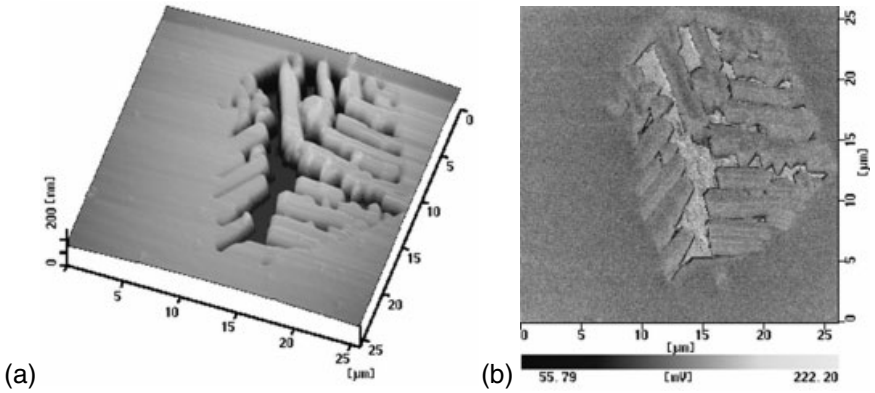

Figure 6.21: Backswitching after external field switch-off in CLN: Illustration of the quantitative difference between switching by classical wall motion leading to the formation of the hexagonal domain and spontaneous backswitching through formation of fingers. Domains revealed by etching and visualized by SFM (a) topographic mode and (b) piezoresponse imaging mode

6.8 Fast Domain Growth

Fast domain growth prevails for incomplete screening ($R > 1$), as far as the residual depolarization field suppresses the classical mechanism of the domain wall motion through generation and growth of the individual nanoscale steps. Although the step generation probability becomes negligible, the applied field is strong enough for the step growth. It is clear that domain merging can be considered as an alternative mechanism of step generation. Thus, the switching can be realized for multidomain initial states with high concentration of small isolated domains. In such a case the simultaneous appearance and subsequent growth of a large quantity of steps organized in micro-scale bunches is obtained after each act of the domain merging. The switching rate and completeness for "step generation by merging only" mechanism of domain wall motion is determined by only one parameter – the concentration of the individual domains in the initial state. The process can provide the complete switching if the initial domain concentration exceeds the critical value and only partial switching is observed for lower concentrations. It is clear that for high enough domain concentration the domain walls move much faster than for the classical wall motion mechanism. The discussed switching scenario prevails for the first switching from the single-domain state in CLT (Fig. 6.22). The switching process in CLT [32, 56] starts with an immediate formation of a great number of submicron-diameter domains with a density achieving 1000 mm^{-2} (Fig. 6.22(a)).

Two domain growth mechanisms were clearly distinguished by an analysis of the series of instantaneous domain configuration images: (1) very slow classical growth of isolated domains (wall velocity v_s) and (2) anisotropic wall motion after domain merging (Figs. 6.22 and 6.23). The fast wall motion velocity v_{f1} in Y^+-directions is a result of step generation by merging of the moving wall with small isolated domains and step growth along the wall. Super-mobile "zig-zag" domain walls with high step concentration form after merging of the

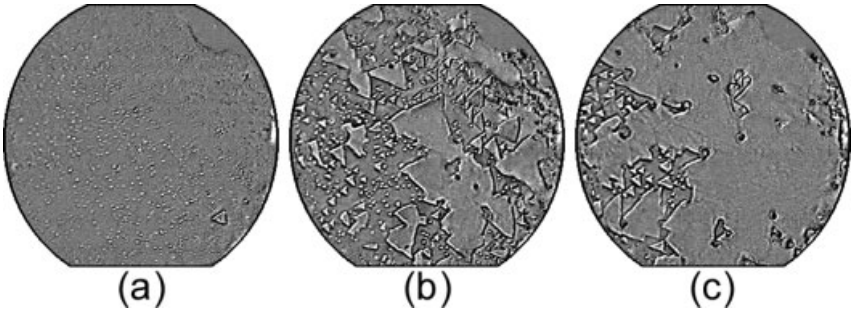

Figure 6.22: In situ optical visualization of the domain kinetics during switching by a rectangular field pulse in CLT. Time intervals from the field switch-on are: (a) 0.3 s, (b) 0.9 s, and (c) 1.5 s. 1-mm-diameter liquid electrodes. $E_{ex} = 190\,\text{kV/cm}$

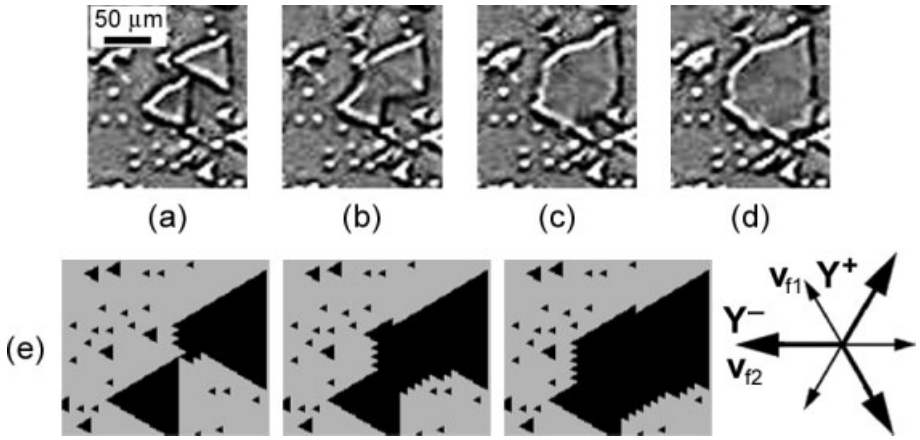

Figure 6.23: Fast wall motion in Y^+-directions and formation of super-mobile "zig-zag" domain walls moving in Y^--directions in CLT. In situ optical visualization of the domain kinetics in a rectangular field pulse. Time interval from field switch-on: (a) 0.7 s, (b) 0.8 s, (c) 0.9 s, and (d) 1.0 s. $E_{ex} = 190$ kV/cm. (e) Simulated stages of the domain kinetics

large domains leading to the fastest wall motion in Y^--directions (v_{f2}). The averaged wall motion velocities extracted from the experimental data by statistical image processing are essentially different: $v_s \sim 1$ µ/s, $v_{f1} \sim 20$–60 µm/s, and $v_{f2} \sim 130$ µm/s ($E_{ex} = 190$ kV/cm). It is shown that a high enough concentration of individual domains leads to an acceleration of the domain growth by more than two orders of magnitude. The computer simulation of the domain kinetics defined only by the step generation by merging confirms the proposed mechanism (Fig. 6.23(e)). It has been revealed by simulation of the domain growth at a triangular lattice and finite sizes of the switched area that the critical value of the domain concentration in the initial state necessary for complete switching is about 0.02.

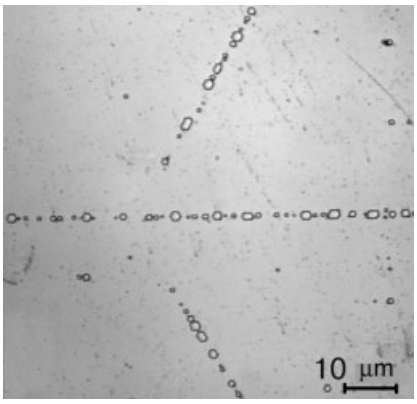

Figure 6.24: Domain arrays oriented along the *Y*-axis. Switching under uniform electrode in CLN. Optical observation of the domains revealed by etching

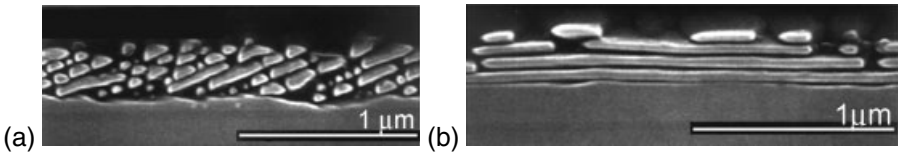

Figure 6.25: SEM images of (a) nanodomain arrays and (b) a quasi-periodic stripe nanodomain structure. Domain patterns form as a result of backswitching near the edge of the stripe electrode under an artificial dielectric layer in CLN. Domains revealed by etching

6.9 Superfast Domain Growth

Incomplete screening of the depolarization field hinders the classical domain growth. For single-domain initial states and uniform spatial distribution of the switching field along the wall both the above discussed alternative mechanisms of domain wall motion are impossible. Nevertheless, the switching process can take place even when the screening becomes absolutely ineffective ($R \gg 1$), demonstrating several qualitatively new scenarios of domain structure evolution and various exotic discrete mechanisms of domain growth.

It has been shown experimentally that several types of self-organized structures develop, such as long domain arrays strictly oriented along the crystallographic directions (Fig. 6.24) and nanoscale domain arrays (Fig. 6.25), form and expand during "superfast switching" in PGO [35, 36], LN, and LT crystals with an artificial dielectric surface layer and during the spontaneous backswitching after abrupt removing of the external switching field [1, 7, 57]. The special features of the obtained variety of quasi-regular domain patterns can be explained when taking into account the correlated nucleation effect and the key role of the intrinsic or artificial surface dielectric layer.

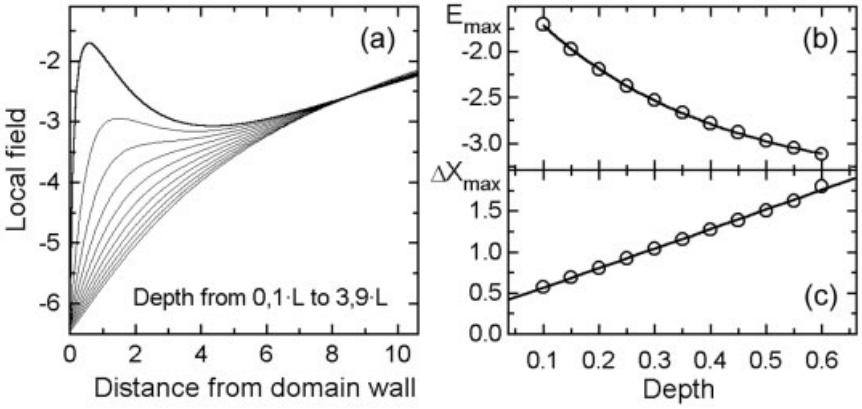

Figure 6.26: (a) Simulated local field distribution near the stripe non-through domain at different depth from the dielectric surface layer. (b) Local field maximum $E_{\max}$ and (c) distance from the wall to the position of field maximum $\Delta x_{\max}$ versus the depth h. The distance from the wall and the depth are divided by the thickness of the surface dielectric layer L

6.9.1 Correlated Nucleation

We consider all types of obtained self-assembled structures as various manifestations of the correlated nucleation effect in the vicinity of the moving domain wall or the propagating boundary of the enlarging complicated domain structure. This effect has its origin in the influence of the trail of the uncompensated depolarization field behind the domain wall on the nucleation probability. It has been shown by computer simulation that the spatial distribution of the local electric field in the vicinity of the domain wall with the trail demonstrates a pronounced maximum in the ferroelectric media at the boundary with the surface dielectric gap at some distance from the wall (Fig. 6.26). This distance is nearly equal to the thickness of the above discussed dielectric gap (surface dielectric layer) L.

While the field maximum diminishes with the depth, nevertheless this field singularity drastically changes the scenario of the domain kinetics. It is clear that the existence of the trail on one hand suppresses nucleation at the wall, thus terminating the classical wall motion. On the other hand it induces the field maximum, which essentially increases the $3D$-nucleation probability at a definite distance in front of the moving wall. This effect leads to an appearance of new isolated domains along the wall. Any arising isolated domain cannot spread out due to the same effect of the uncompensated depolarization field. The arising domains repel each other by this long-range field. The decrease of the local electric field in the vicinity of each isolated domain initiates the formation of new domains at some distance from each other. As a result, the quasi-regular domain chain aligns along the wall. It consists of needle-like domains with micro- or nanoscale transversal sizes and charged walls (Figs. 6.27 and 6.28).

It has been shown by simulation that the new field maximum appears at approximately the same distance from the formed domain chain thus initiating formation of the second one. The process can be reproduced infinitely. Thus, self-maintained enlarging of the quasi-regular

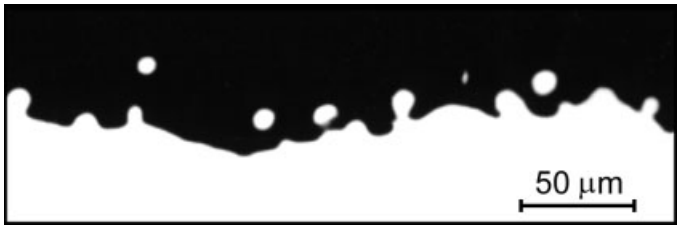

Figure 6.27: Formation of micro-scale domains in the vicinity of the moving domain wall in PGO during "superfast switching". Observation by polarized microscopy

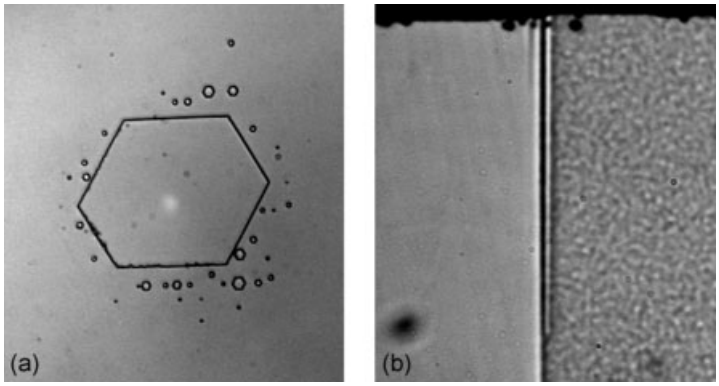

Figure 6.28: Nucleation in the vicinity of the moving wall in CLN. (a) Z^+-view and (b) *Y*-view

domain structure is observed. It has been shown experimentally that the fast growing self-assembled structures can cover areas of about square millimeters.

There are two ways to intensify the role of the correlated nucleation process. One of them has been discussed above and is realized by increasing the ratio R, by amplification of the switching field or by hindering the screening processes. The alternative possibility is the deposition of an artificial surface dielectric layer, thus increasing the residual depolarization field. The period of the quasi-regular structure increases accordingly in this case. It has been revealed experimentally that the velocity of such process exceeds by orders of magnitude the usual wall motion velocity. Due to this the process can be named as "*superfast domain growth*."

6.9.2 Switching with Artificial Surface Dielectric Layer

The crucial role of the dielectric surface layer has been brightly displayed during formation of the structure consisting of isolated domains with given density in a ferroelectric capacitor with artificial dielectric gaps of given thickness (Fig. 6.29). It is noted that this discrete correlated structure appears under the application of a uniform electric field. We have switched a 2-mm-thick SLT sample covered by an artificial dielectric layer (2-μm-thick photoresist) using liquid electrodes. The switching process starts as the formation of a hexagon domain around

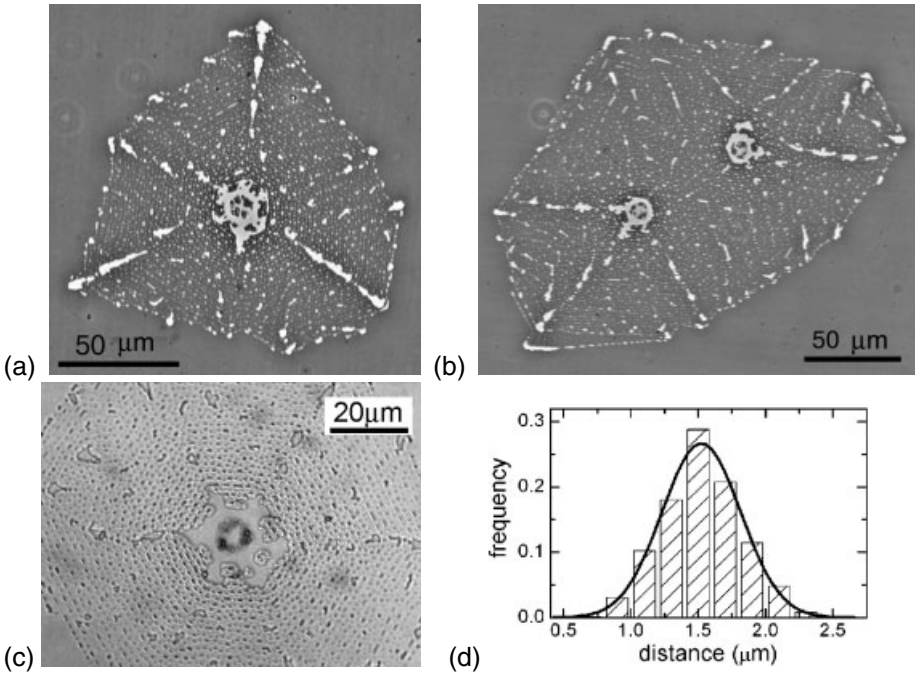

Figure 6.29: Self-assembled domain structures formed around the pinholes in the dielectric layer in 2-mm-thick SLT with Z^+-surface covered by 2-μm-thick photoresist. (a), (b), and (c) optically visualized domains revealed by etching. (d) Distribution function of the distances between the neighboring domains

the pin-hole in the dielectric layer. The subsequent growth is achieved through the propagation of the quasi-regular ensemble of micro-scale isolated domains. The spreading of this structure follows the same mechanisms as the continuous growth of the isolated domain. In the case of discrete switching the boundary of the area covered by isolated switched domains plays the role of the domain wall. One can observe the formation of the steps and their propagation along the boundary of the structure, which plays the role of the domain wall (Figs. 6.29(a) and (b)). The shape of the switched area is the same regular polygon as in the case of growth of isolated domains (see Section 6.6). The boundaries are oriented in strict crystallographic directions. Even for the more complicated switching process starting from two pin-holes separated by a short distance the growth of the quasi-regular structure is very similar to that for usual domains (Fig. 6.29(b)). The merging of the individual growing ensembles leads to an immediate formation of a structure with a shape of convex polygons. The average distance between the nuclei obtained by statistical analysis of the experimental data (Fig. 6.29(c)) is very close to the thickness of the artificial dielectric gap (Fig. 6.29(d)). It opens a possibility to evaluate the effective depth of the intrinsic dielectric gap for any material and any experimental condition by measuring the average period of the quasi-regular structure appearing during "superfast" switching.

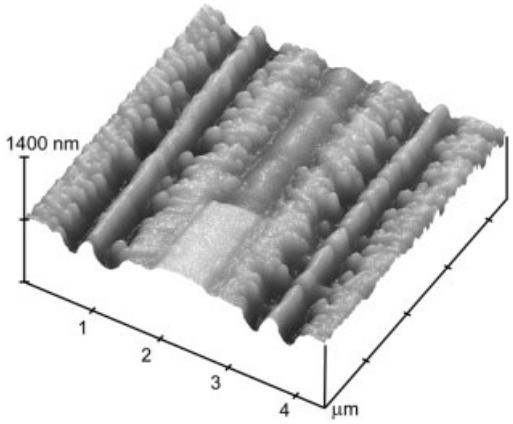

Figure 6.30: SFM image of nanodomain arrays in LN oriented along the *Y*-directions (at 60° to the electrode edges) with the fragment of the electrode. Z^+-view. Domains revealed by etching

6.9.3 Nanoscale Domain Arrays

Correlated nucleation plays the most important role during backswitching in CLN after an abrupt removal of the external field. This effect can be easily explained when the record-breaking value of spontaneous polarization in CLN, leading to an abnormally high value of the bulk screening field, is taken into account. After external field is switched off the local field changes the sign for incomplete screening (see Eq. 6.3) leading to a spontaneous backward switching. The backswitching process is very fast in CLN as it occurs under the action of extremely high fields.

It is easy to show experimentally that the backward motion of the domain wall is achieved in this case through propagation of the boundary of the ensemble of isolated nanoscale domains (Fig. 6.30). It is important to point out that under these experimental conditions the forward and backward wall motions differ qualitatively. The forward motion occurs, when the applied field slightly exceeds the abnormally high bulk screening field. Thus, even when the applied field value exceeds the coercive value ($E_c = 210$ kV/cm), the switching field is comparatively low. In this case the classical low field wall motion scenario is realized. Contrary, the backward motion is governed by the abnormally high bulk screening field itself. It is clear that such cyclic switching process is absolutely irreproducible.

Recently, we have discovered the effect of self-maintained spontaneous decay of the stripe domain structure in CLN through arising and growth of the oriented nanoscale domain arrays [1, 7, 37, 54, 57]. The domain patterns, revealed by etching and visualized by SFM (Fig. 6.30) and SEM (Fig. 6.31), demonstrate the array-assisted reversal motion of the existing domain walls through propagation of the highly organized quasi-periodical structure of domain arrays strictly oriented along the crystallographic directions (Fig. 6.31). Each quasi-regular array is comprised of nanodomains with a diameter 30–100 nm and an average linear density exceeding 10^4 mm^{-1}. Such domain evolution scenario was observed during switching using periodical stripe electrodes oriented along the *Y*-direction deposited on the Z^+-surface.

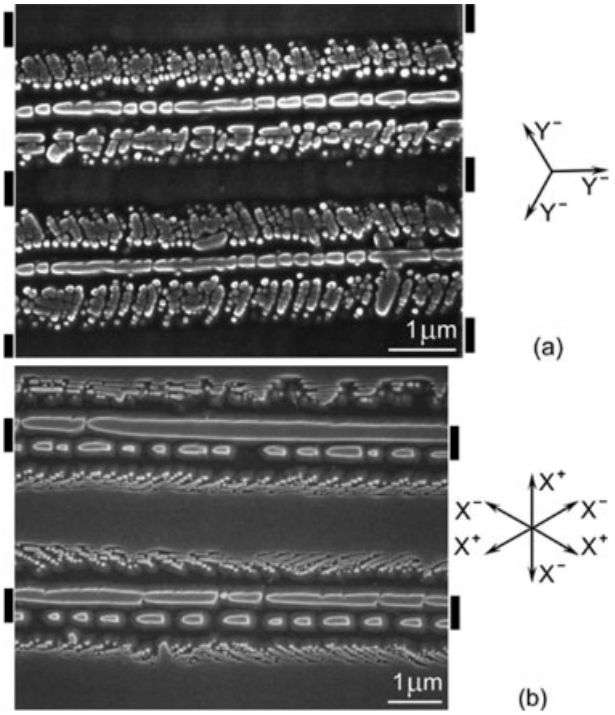

Figure 6.31: Nanodomain arrays oriented along (a) Y^--directions and (b) X-directions evolving during backswitched periodical poling of CLN. Domain patterns revealed by etching and visualized by SEM. Black rectangles – electrode position

It has been shown that, for a sufficient domain spreading out of the electrodes, short switching pulse duration $\Delta t_{sp} \sim 5$ ms and a small field-diminishing amplitude $\Delta E \sim 2$ kV/mm, the backswitched domain evolution represents self-maintained self-organized growth of oriented nanoscale domain arrays.

Two variants of array orientation are obtained. In the usual case, all nanodomain arrays are strictly oriented along the Y^--direction at 60° to the electrode edges (Fig. 6.31(a)). A similar oriented nucleation has been observed during polarization reversal in strong homogeneous fields (Fig. 6.24). In some cases the domain arrays are strictly oriented along the X^-- or X^+-directions (Fig. 6.31(b)), and individual nanodomains have a triangular shape. There are four equal X-directions oriented at 30° to the electrode edges. So, domain patterns consisting of regular 30° array fragments with different array orientations are obtained along one domain wall (Fig. 6.31(b)). The array patterns, which are growing along the X-directions at 90° to the electrodes, differ as the fast growth of nanodomains along electrodes leads to the formation of a periodic set of nanoscale stripe domains (Fig. 6.32(a)) with a period of about 100 nm (Fig. 6.32(b)).

All effects observed during backswitching can be explained by the nonuniform distribution of the local backswitching field near the electrode edges and domain walls due to spatially

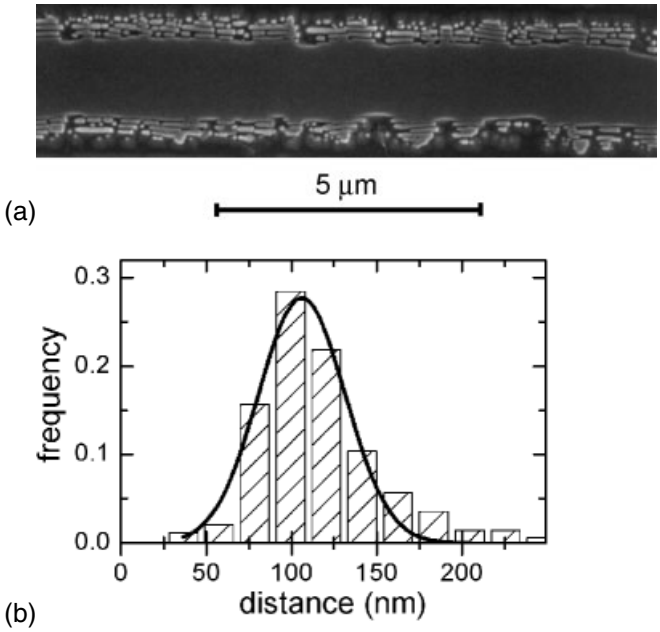

Figure 6.32: Formation of a quasi-periodic nanoscale stripe domain structure in the vicinity of the electrode during backswitching in CLN. (a) Optical visualization of the domains revealed by etching. (b) Distribution function of the distances between the neighboring stripe domains

nonuniform screening of the external and depolarization fields. Our estimations reveal the field maximum at a distance of about the thickness of the insulating layer from the domain wall or nanodomain array. An array aggregate existing at a given moment generates the new maximum of the backswitching field at a fixed distance in front of its boundary and triggers the formation of the new array. The developing correlated nucleation leads to the self-maintained generation of the parallel arrays. The array-assisted propagation of the correlated domain structure is similar to the formation of the "wide domain boundary" discovered in PGO during switching in "super-strong" fields [35, 36].

6.10 Domain Engineering

Domain engineering – a new branch of science and technology directed to the creation of periodic and quasi-periodic domain structures with desired parameters in commercially available ferroelectrics – is rapidly developing nowadays. Domain engineering in ferroelectric crystals such as LN and LT has revolutionized their use in nonlinear optical applications [2, 5]. It has been shown that LN and LT with periodical 1D [5, 58] and 2D [59] domain structures open up a wide range of possibilities for bulk and waveguide nonlinear optical interactions. During ten years after the first electrical poling of bulk LN samples [4], research on periodically poled LN and LT is in the center of interest around the world resulting in the production

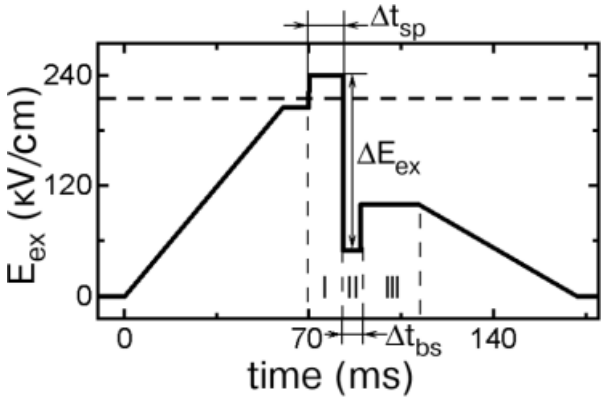

Figure 6.33: Backswitched poling voltage waveform. (I) switching stage in "high field", (II) backswitching stage in "low field", (III) stabilization stage in "stabilization field"

of photonic devices. Breaking the micron-period barrier for periodical domain patterning in LN and LT is highly desirable for several new electrooptical applications such as tunable cavity mirrors, which need a periodicity of about 350 nm. The most efficient exploitation of engineered submicron domain gratings in LN and LT for photonic devices is related with the waveguide fabrication.

For advanced electrooptical and acoustical applications the submicron domain patterns are of great importance, but nevertheless the micron limit has not been experimentally overcome yet. Two different branches of domain engineering have been developed recently: (1) predetermined domain patterning and (2) domain patterning by self-organization. In the first case, the periodicity of the domain patterns is determined by the spatial distribution of the external electric field usually produced by the lithographic electrode structure. In the second case, the formation of quasi-regular domain patterns is the result of self-maintained evolution of the domain structure. In this section, we demonstrate recent achievements in application of both approaches to LN and LT single crystals based on the above discussed scenarios of the domain kinetics.

The understanding of field induced domain kinetics in LN and LT allowed us to propose recently an original poling method for creation of short-pitch periodical domain structures, the so-called backswitched poling [1, 7, 60]. Let us consider the main advantages of this method. Periodic domain structures were obtained in standard optical-grade single-domain 0.5-mm-thick CLN wafers of congruent composition cut perpendicular to the polar axis. The wafers were photolithographically patterned with a periodic stripe metal-electrode structure (NiCr) deposited on a Z^+-surface and oriented along the Y-axis. The patterned surface was covered by a thin (about 1-μm-thick) insulating layer (photoresist) (Fig. 6.5). A high voltage pulse producing an electric field greater than the coercive field ($E_c = 210\,\mathrm{kV/cm}$) was applied to the structure through a fixture containing liquid electrolyte (LiCl–water solution).

The commonly used electric field poling technology, based on the application of a high voltage pulse through lithographically defined electrodes, cannot be straightforwardly applied to the fabrication of submicron gratings. Thus, for nanoscale domain engineering such alterna-

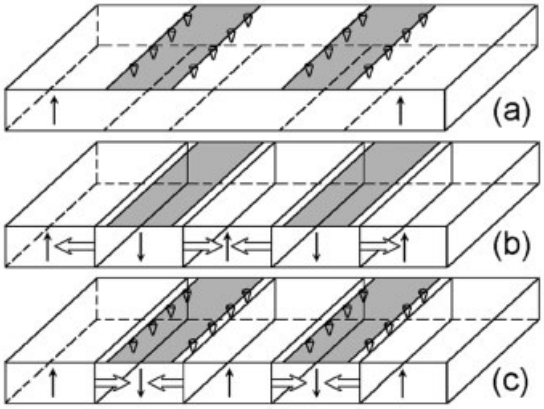

Figure 6.34: Main stages of the domain evolution during backswitched poling: (a) nucleation, (b) domain broadening, (c) backswitching after external field switch-off. White arrows show the directions of the domain wall motion

tive technique as "self-organized domain patterning," due to self-maintained evolution of domain structure, is under consideration [1,57]. The waveform for backswitched poling consists of three levels of external field: "high field," "low field," and "stabilization field" (Fig. 6.33). Such waveform allows one to control the different stages of domain evolution during poling. Moreover, we exploit the unique abilities of the backswitching process. It must be pointed out that this process is always considered as an undesirable one, because it destroys the tailored structure.

During backswitched poling, several distinguishable stages of domain evolution can be revealed (Fig. 6.34). The process starts with nucleation (formation of new domains) at the Z^+-polar surface along the electrode edges. The position of the nuclei arrays is due to field singularities caused by the fringe effect (Fig. 6.34(a)). The real value of the local field along the electrode edge alters profoundly with small deviations of its shape, thus introducing field fluctuations. During the second stage, the formed domains grow and propagate through the wafer. As a result of merging, laminar domains with planar walls are formed. The main problem of the periodical poling is an essential domain broadening out of the electroded area, which is always observed (Fig. 6.34(b)). This effect leads to an essential difference between the lithographically defined electrode patterns and the produced periodical domain structure. For short periods domain broadening results in domain merging, thus limiting the production of the short-pitch domain patterns. During broadening, the domain wall moves in the regions with the artificial surface dielectric layer, thus the above-discussed exotic scenarios of domain wall motion can be realized (see Sections 6.7 and 6.9). The formation of the domain fingers and arrays leads to abnormally high domain broadening, which is extremely undesirable for periodical poling.

After rapid decreasing of the poling field, the backswitching starts through shrinkage of the laminar domains by the backward wall motion and nucleation of the domains with the initial orientation of spontaneous polarization along the electrode edges (Fig. 6.34(c)). As it was discussed above, the backswitching occurs under the action of an abnormally high field.

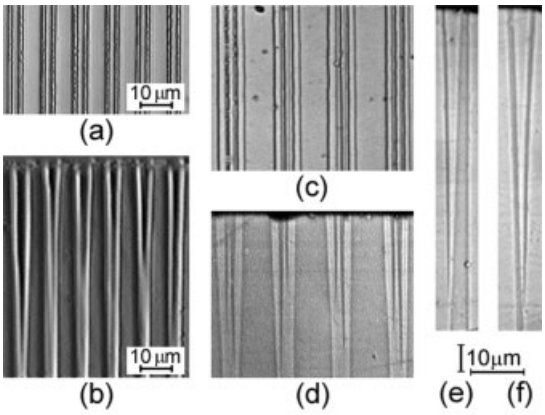

Figure 6.35: Backswitched domain frequency multiplication in CLN. (a) and (b) "frequency doubling," (c) and (d) "frequency tripling," (e) "erasing," (f) "splitting." (a) and (c) Z^+-view, and (b), (d), (e), and (f) Y-cross-sections. Optical visualization of the domains revealed by etching

This is the reason why various regular self-assembled nanodomain structures can be produced by backswitched poling by presetting the voltage waveform parameters. The types of domain patterns also depend on the value of the domain wall shift out of the electrodes. The switching from the single-domain state takes place at the "high field" and the backswitching occurs at the "low field." The crucial parameters for backswitching kinetics are the duration of the "high field" stage Δt_{sp} and the field-diminishing amplitude ΔE (Fig. 6.33). The application of this improved poling method to LN and LT single crystals demonstrates the spatial frequency multiplication of the domain patterns as compared to the spatial frequency of the electrodes and self-maintained formation of the oriented domain arrays consisting of individual nanoscale domains with diameters down to 30 nm and average linear density exceeding 10^4 mm^{-1} [1,57].

Domain frequency multiplication For a small domain-wall shift out of the electrodes a multiplication of the domain pattern spatial frequency as compared to the spatial frequency of the electrode pattern was obtained. The mechanism of this process is based on nucleation along the electrode edges during backswitching, when the wall motion is suppressed. For "frequency tripling" (Fig. 6.35(c)), the subsequent growth and merging of the nucleated domains lead to the formation of a couple of strictly oriented submicron-width domain stripes under each electrode. Their depth is about 20–50 μm (Fig. 6.35(d)). It is clear that this structure can be produced only by using wide enough electrodes. For narrow electrodes these stripes immediately merge and "frequency doubling" can be obtained (Fig. 6.35(a)). The depth of the backswitched domain stripes is in this case about 50–100 μm (Fig. 6.35(b)). The backswitched domain cross sections reveal two distinct variants of domain evolution during frequency multiplication: "erasing" and "splitting." During "erasing" the backswitched domains are formed in the earlier switched area without any disturbance of the external shape of the switched laminar domains (Fig. 6.35(e)). During "splitting" the backswitched domain cuts the

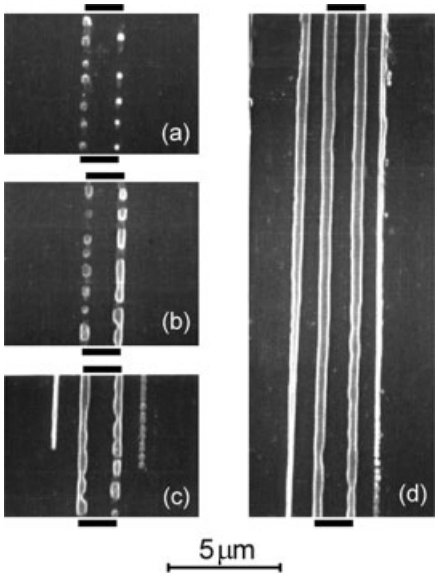

Figure 6.36: SEM patterns demonstrating the stages of formation of periodic stripe domains along the electrode edges in CLN. Electrodes covered the area between the black rectangles. Electrodes are oriented along the Y-direction. Domains revealed by etching. Z^+-view

switched one conserving its volume and varying the shape (Fig. 6.35(f)). The most complicated process of frequency multiplication (the so-called "pentaplication") is demonstrated for sufficient domain spreading out of the stripe electrodes during switching. For a long switching pulse $\Delta t_{sp} \sim 15$ ms and large field-diminishing amplitude $\Delta E \sim 20$ kV/mm (Fig. 6.33) the backswitching starts as usual with the formation of a couple of nanodomain arrays under the electrode edges (Fig. 6.36(a)). Then the arrays turn into a pair of stripe domains through growth and merging of the individual domains (Fig. 6.36(b)).

The above discussed effect of correlated nucleation results in the fact that after complete merging the secondary couple of arrays appears in the nonelectroded area parallel to the initial ones (Fig. 6.36(c)). This self-maintained process leads to the formation of periodic stripe domains oriented along the electrodes (Fig. 6.36(d)). The experimentally observed distance between secondary and initial stripes is close to the thickness of the insulating layer in accordance with our theoretical considerations.

6.11 Conclusions

In the present chapter, we have discussed the nonequilibrium domain structure kinetics in ferroelectrics. For the description of the various experimental data we used a simple and clear approach based on the nucleation mechanism of the polarization reversal. The specific features of ferroelectrics consist in the fact that the nucleation rate is determined by the local electric field. This field is time-dependent due to an essential retardation of the screening subsystems

redistribution. As a result, the kinetics of the ferroelectric domain structure depends on the ratio of the switching rate and the rate constants of the screening processes. These parameters depend on many factors: value of spontaneous polarization, bulk and surface layer conductivity, dielectric permittivity, and time constant of external circuit. The variation of these factors makes it possible to control the ferroelectric domain structure and its behavior in the electric field. Original scenarios of domain structure evolution were revealed experimentally and discussed within a unified approach accounting for the decisive role of the retardation of the screening process. The evolution of the domain structure in ferroelectrics during decay of the highly nonequilibrium state represents a selforganizing process, in which the screening of depolarization field plays the role of feedback. It has been shown both experimentally and by computer simulation that the correlation length of quasi-periodic self-assembled nanodomain structures is determined by the thickness of the intrinsic or artificial surface dielectric layer (dielectric gap). It has been proposed that all the existing static domain patterns in any ferroelectric being metastable and far from equilibrium are formed in the course of the given domain kinetic scenario and are fastened by the bulk screening processes. The results of the fundamental investigations discussed here are of great interest as a physical basis for a modern field of technology denoted as "domain engineering." We have proposed and realized several new techniques, which allows one to produce the short-pitch regular domain patterns with record periods and nanoscale quasi-regular domain structures in lithium niobate and lithium tantalate single crystals. The crystals possessing such regular structures demonstrate new nonlinear optical properties required for modern coherent light frequency conversion devices.

Acknowledgements

This work was supported in part by INTAS (Grant 03-51-6562), by RFBR-DFG (Grant 02-02-04006), by RFBR-NNSF (Grant 03-02-39004), by Ministry of Education RF (Grants E02-3.4-395 and by program "Basic Research in Russian Universities" Grant YP.06.01.028), and by Award No. EK-005-X1 of CRDF and Ministry of Education of the Russian Federation. It is a pleasure to acknowledge the many helpful stimulating discussions with A. Alexandrovski, A. Bratkovski, R.L. Byer, L.E. Cross, M.M. Fejer, J. Fousek, V.M. Fridkin, K. Kitamura, A.L. Korzhenevskii, A.P. Levanyuk, D. Lupascu, A.L. Roytbourd, E.L. Rumyantsev, J.F. Scott, and L.A. Shuvalov in the course of preparation of this publication.

References

[1] V.Ya. Shur, E.L. Rumyantsev, E.V. Nikolaeva, E.I. Shishkin, D.V. Fursov, R.G. Batchko, L.A. Eyres, M.M. Fejer, and R.L. Byer, Appl. Phys. Lett. **76**, 143 (2000).

[2] R.L. Byer, J. Nonlinear Opt. Phys. Mater. **6**, 549 (1997).

[3] G. Rosenman, A. Skliar, and A. Arie, Ferroelectr. Rev. **1**, 263 (1999).

[4] M. Yamada, N. Nada, M. Saitoh, and K. Watanabe, Appl. Phys. Lett. **62**, 435 (1993).

[5] L.E. Myers, R.C. Eckhardt, M.M. Fejer, R.L. Byer, W.R. Bosenberg, and J.W. Pierce, J. Opt. Soc. Am. **B 12**, 2102 (1995).

[6] G.D. Miller, R.G. Batchko, M.M. Fejer, and R.L. Byer, *Visible quasi-phasematched harmonic generation by electric-field-poled lithium niobate* in SPIE Proc. on Solid State Lasers and Non-linear Crystals **2700**, 34 (1996).
[7] R.G. Batchko, V.Ya. Shur, M.M. Fejer, and R.L. Byer, Appl. Phys. Lett. **75**, 1873 (1999).
[8] M.E. Lines and A.M. Glass, *Principles and Application of Ferroelectrics and Related Materials* (Clarendon, Oxford, 1977).
[9] E. Fatuzzo and W.J. Merz, *Ferroelectricity* (North-Holland, Amsterdam, 1967).
[10] V.Ya. Shur and E.L. Rumyantsev, Ferroelectrics **191**, 319 (1997).
[11] V.Ya. Shur, Phase Transit. **65**, 49 (1998).
[12] V.Ya. Shur, Fast polarization reversal process: evolution of ferroelectric domain structure in thin films, in *Ferroelectric Thin Films: Synthesis and Basic Properties*, edited by C.A. Paz de Araujo, J.F. Scott, G.W. Taylor (Gordon and Breach, New York, 1996) Vol. 10, pp. 153–192.
[13] E.A. Little, Phys. Rev. **98**, 978 (1955).
[14] W.J. Merz, Phys. Rev. **95**, 690 (1954).
[15] R.C. Miller and A. Savage, Phys. Rev. Lett. **2**, 294 (1959).
[16] D.P. Cameron, *Domain orientation in barium titanate single crystals*, IBM J. Res. Dev. **1**, 2 (1957).
[17] R.E. Newnham and L.E. Cross, Endeavour **33**, 18 (1974).
[18] V.Ya. Shur, A.L. Gruverman, V.V. Letuchev, E.L. Rumyantsev, and A.L. Subbotin, Ferroelectrics **98**, 29 (1989).
[19] A. Kumada, Phys. Lett. **30A**, 186 (1969).
[20] R.B. Flippen, J. Appl. Phys. **46**, 1068 (1975).
[21] V.Ya. Shur, A.L. Gruverman, V.P. Kuminov, and N.A. Tonkachyova, Ferroelectrics **111**, 197 (1990).
[22] V.Ya. Shur, E.L. Rumyantsev, R.G. Batchko, G.D. Miller, M.M. Fejer, and R.L. Byer, Phys. Solid State **41**, 1681 (1999).
[23] V. Gopalan, Q. Jia, and T. Mitchell, Appl. Phys. Lett. **75**, 2482 (1999).
[24] V. Gopalan and T. Mitchell, J. Appl. Phys. **85**, 2304 (1999).
[25] V. Gopalan and T. Mitchell, J. Appl. Phys. **83**, 941 (1998).
[26] R. Landauer, J. Appl. Phys. **28**, 227 (1957).
[27] V. Janovec, Czechosl. J. Phys. **9**, 468 (1959).
[28] V.Ya. Shur, E.L. Rumyantsev, E.V. Nikolaeva, E.I. Shishkin, R.G. Batchko, G.D. Miller, M.M. Fejer, and R.L. Byer, Ferroelectrics **236**, 129 (2000).
[29] V.Ya. Shur, E.L. Rumyantsev, E.V. Nikolaeva, and E.I. Shishkin, Appl. Phys. Lett. **77**, 3636 (2000).
[30] V.Ya. Shur, V.V. Letuchev, and E.L. Rumyantsev, Sov. Phys.-Solid State **26**, 1521 (1984).
[31] V.Ya. Shur, V.V. Letuchev, E.L. Rumyantsev, and I.V. Ovechkina, Sov. Phys.-Solid State **27**, 959 (1985).
[32] V.Ya. Shur, E.V. Nikolaeva, E.I. Shishkin, A.P. Chernykh, K. Terabe, K. Kitamura, H. Ito, and K. Nakamura, Ferroelectrics **269**, 195 (2002).
[33] R.C. Miller, J. Phys. Chem. Solids **17**, 93 (1960).

[34] V.Ya. Shur, E.L. Rumyantsev, D.V. Pelegov, V.L. Kozhevnikov, E.V. Nikolaeva, E.I. Shishkin, A.P. Chernykh, and R.K. Ivanov, Ferroelectrics **267**, 347 (2002).

[35] V.Ya. Shur, A.L. Gruverman, N.Yu. Ponomarev, and N.A. Tonkachyova, Ferroelectrics **126**, 371 (1992).

[36] V.Ya. Shur, A.L. Gruverman, N.Yu. Ponomarev, E.L. Rumyantsev, and N.A. Tonkachyova, Integr. Ferroelectr. **2**, 51 (1992).

[37] V.Ya. Shur, E.V. Nikolaeva, and E.I. Shishkin, Physics of Low-Dimensional Structures **3–4**, 139 (2003).

[38] R.C. Miller, and G. Weinreich, Phys. Rev. **117**, 1460 (1960).

[39] M. Hayashi, J. Phys. Soc. Jpn. **33**, 616 (1972).

[40] M.E. Drougard, R. Landauer, J. Appl. Phys. **30**, 1663 (1959).

[41] V.M. Fridkin, *Ferroelectrics Semiconductors* (Consult. Bureau, New York, London, 1980).

[42] P.V. Lambeck and G.H. Jonker, J. Phys. Chem. Solids **47**, 453 (1986).

[43] A.K. Tagantsev, I. Stolichnov, E.L. Colla, and N. Setter, J. Appl. Phys. **90**, 1387 (2001).

[44] Y. Furukawa, K. Kitamura, S. Takekawa, K. Niwa, and H. Hatano, Opt. Lett. **23**, 1892 (1998).

[45] K. Kitamura, Y. Furukawa, K. Niwa, V. Gopalan, and T. Mitchell, Appl. Phys. Lett. **73**, 3073 (1998).

[46] K. Niwa, Y. Furukawa, S. Takekawa, and K. Kitamura, J. Cryst. Growth **208**, 493 (2000).

[47] L. Huang, D. Hui, D.J. Bamford, S.J. Field, I. Mnushkina, L.E. Myers, and J.V. Kayser, Appl. Phys. **B 72**, 301 (2001).

[48] V.Ya. Shur, A.L. Gruverman, V.P. Kuminov, and N.A. Tonkachyova, Ferroelectrics **130**, 341 (1992).

[49] V.Ya. Shur, E.V. Nikolaeva, E.L. Rumyantsev, E.I. Shishkin, A.L. Subbotin, and V.L. Kozhevnikov, Ferroelectrics **222**, 323 (1999).

[50] V.Ya. Shur, E.L. Rumyantsev, E.V. Nikolaeva, E.I. Shishkin, R.G. Batchko, M.M. Fejer, R.L. Byer, and I. Mnushkina, Ferroelectrics **269**, 189 (2002).

[51] V.Ya. Shur, E.L. Rumyantsev, E.V. Nikolaeva, E.I. Shishkin, R.G. Batchko, M.M. Fejer, and R.L. Byer, Ferroelectrics **257**, 191 (2001).

[52] V.Ya. Shur, E.L. Rumyantsev, V.P. Kuminov, A.L. Subbotin, and E.V. Nikolaeva, Phys. Solid State **41**, 112 (1999).

[53] J. Hatano, F. Suda, and H. Futama, J. Phys. Soc. Jpn. **45**, 244 (1978).

[54] V.Ya. Shur, E. Rumyantsev, E. Nikolaeva, E. Shishkin, R.G. Batchko, G.D. Miller, M.M. Fejer, and R.L. Byer, *Micro- and nanoscale domain engineering in lithium niobate and lithium tantalate*, in SPIE Proc. on Smart Structures and Materials **3992**, 143 (2000).

[55] V.Ya. Shur, E. Rumyantsev, R. Batchko, G. Miller, M. Fejer, and R. Byer, Ferroelectrics **221**, 157 (1999).

[56] V.Ya. Shur, E.V. Nikolaeva, E.I. Shishkin, V.L. Kozhevnikov, A.P. Chernykh, K. Terabe, and K. Kitamura, Appl. Phys. Lett. **79**, 3146 (2001).

[57] V.Ya. Shur, E.L. Rumyantsev, E.V. Nikolaeva, E.I. Shishkin, D.V. Fursov, R.G. Batchko, L.A. Eyres, M.M. Fejer, R.L. Byer, and J. Sindel, Ferroelectrics **253**, 105 (2001).

[58] G.W. Ross, M. Pollnau, P.G.R. Smith, W.A. Clarkson, P.E. Britton, and D.C. Hanna, Opt. Lett. **23**, 171 (1998).

[59] N.G.R. Broderick, G.W. Ross, H.L. Offerhaus, D.J. Richardson, and D.C. Hanna, Phys. Rev. Lett. **84**, 4345 (2000).

[60] R. Batchko, G. Miller, R. Byer, V. Shur, and M. Fejer, Backswitch poling method for domain patterning of ferroelectric materials, United States Patent No. 6,542,285 B1, April 1, 2003.

7 Nucleation and Growth Kinetics of Nanofilms

Sergey A. Kukushkin and Andrey V. Osipov

It follows that it cannot be our task to find an absolutely correct theory, but rather a picture that is as simple as possible while representing the phenomenon as well as possible.
Ludwig Boltzmann

The present chapter gives an outline of basic results concerning the theoretical description of processes of formation and growth of nanofilms in one- and multicomponent cases. Hereby the attention is directed to the analysis of both nucleation and further evolution of nanoparticle ensembles on substrates in metastable and unstable regions of the thermodynamic phase space. Models for nanofilm growth from vapor and liquid solutions are analyzed. They include the description of nanoisland size distributions, coalescence, orientation, morphological stability, etc. Processes of formation and further development of different instabilities, the formation of nonlinear density waves and oriented growth of nanoislands are studied as well. Condensation kinetics of nanofilms in dependence on possible chemical reactions of the components is analyzed. The technique of calculation of phase coexistence diagrams is outlined. The influence of various factors affecting nucleation of nanoparticles – such as wetting effects, electromagnetic radiation, and acidity of the medium – is studied.

7.1 Introduction

Electronic devices based on nanostructures are widely used in many fields of human activity. At present, a great interest is found directed to an application of nanostructures, especially double heterostructures, in semiconductor physics, optics, and microelectronics [1–5]. Nanostructures can be prepared by a variety of different methods [1–10]. Here, we examine in detail processes of formation of nanoparticles on the surface of solid substrates. Particles of sizes, which are not larger than 100 nm, are considered hereby as nanoparticles. As for crystals of such sizes, they do not contain, in general, dislocations or some other linear defects. Films composed of such particles have a well-developed surface. This feature leads to the formation of unique properties of the nanosystems, which are not observed in ordinary materials.

On the surface of solid substrates, nanoparticles can be prepared by deposition from liquid or solid phases [1–7]. In addition, they can be obtained by using the sol–gel technology or electrodeposition [9, 10]. Processes of nanocrystal formation represent typical first-order phase transitions. While the nanocrystals formed on the surface of substrates are not elastically stressed, processes of their formation by nucleation can be described by means of the classical nucleation theory. In the case, where nanocrystals are elastically stressed and they are formed on crystal substrates, the main approaches and methods of description of their nucleation remain unchanged; however, the mechanism of formation and growth of nanoparticles is of another physical nature. Therefore, we start with the analysis of nucleation of unstressed nanostructures and then, in the next section, we present new approaches to the description and

Nucleation Theory and Applications. edited by J. W. P. Schmelzer

ISBN: 3-527-40469-4

examination of growth of coherent nanostructures under stress. In the literature, it is common to denote the new phase nuclei as islands, whereas the island ensembles are denoted as island films. Here and further, we will follow the above notations.

During the growth of films containing islands of nanosizes, experimentators and engineers are forced to control a large number of parameters, specifying the material and structure of the substrate, such as the temperature of the substrate, composition of vapor, and intensity of its inflow. To obtain the island sizes and composition needed, the values of the parameters are selected, as a rule, empirically. In this case, it is necessary to establish a time parameter at which the growth process has to be terminated in order that the size of the islands does not reach values above the nanosize limits.

It is already clear now that the further development of nanostructure technology will not be possible without a theoretical analysis of the complicated physical and chemical phenomena that take place in the nucleation process [9–16]. The study of these phenomena began in the mid of the 1950s. Principal attention was paid first to new phase nucleation on solid surfaces. Initially, the majority of theoretical analyses of new phase nucleation were carried out in the framework of the classical nucleation theory [17–20], disregarding the variation of supersaturation during condensation and, even more, disregarding a possible change of the growth mechanisms of the different individual islands. Hence, the comparison of experimental results on new phase nucleation on surfaces with the classical nucleation theory revealed a substantial deviation between them. This result led the researchers to the erroneous conclusion that it is impossible to employ the concepts of the classical theory of phase transitions to the analysis of surface processes and the necessity of rejecting classical methods. In particular, it was assumed that such quantity, as the specific interphase energy, cannot be used at all in the description of the early stages of thin-film nucleation. This is the reason why, in the early 1960s, the so-called discrete models appeared that described the new phase nucleation employing the methods of equilibrium statistical mechanics [18].

It should be noted that these theories could not describe the nucleation of strongly metastable and unstable systems similar to the rejected classical model since these first approaches ignored the most important effect, namely, the increase of long-wavelength density fluctuations in the spinodal region [17, 21]. To establish a correspondence between theory and experiment, it was actually sufficient to allow for the variation of the supersaturation in time and the related possibility of changing of the growth mechanisms of individual islands [6, 7, 22]. Furthermore, most of the models were constructed for single-component films only, while a wide variety of experiments were carried out with multicomponent systems. Simultaneously, a number of fundamental studies on the kinetics of first-order phase transitions were conducted in the same period. It has been shown, that the kinetics of first-order phase transitions is a complicated multistage process accompanied by various nonlinear phenomena [6, 13, 14, 22–26]. Such stages typically include nucleation, the separate growth of new phase nuclei, coalescence, and the late stage, i.e., Ostwald ripening (OR), where the growth of the larger islands proceeds at the expense of dissolution of the smaller ones.

The above-mentioned processes have widely different time scales. The most rapid stage is nucleation, then the system goes over into a stage of growth, and so on. This time hierarchy means that the fast processes have time to "keep up" with the slow ones [23]. The solution of the equations for fast processes provides, in fact, the initial conditions for the equations of slower processes. It turned out that the solution, obtained in the framework of the classical

theory, was valid at the nucleation stage only. At later stages, it is necessary to take into account the equations of conservation of matter in a system and to solve the corresponding nonlinear problems.

The extension of these ideas and methods to nucleation processes of islands, as well as the development of a consistent field-theoretical approach [27] providing an unified standpoint for the description of condensation under any arbitrarily high supersaturations, offered quite a new view on the problems of the formation of nanofilms. The supersaturation levels were found, for which it was appropriate to employ the classical nucleation theory for the description of the nucleation of islands, and also the levels, for which it was necessary to use the field-theoretical approach [54]. These developments made it possible to apply a unified approach to the description of condensation of multicomponent nanofilms, irrespective of the type of the initial phase (vapor, gas, liquid, etc.) and condensation conditions. It was shown that the surface leads to an appreciable diversity in the phase transformation kinetics, although the basic stages stay unchanged.

7.2 Thermodynamics of Adsorbed Layers

An important specific feature of new phase nucleation on substrate surfaces, as compared to homogeneous nucleation in the bulk, is the presence of various defects on the substrate. Defects are typically divided into point and linear ones; the latter include steps, surface dislocations, and scratches. No rigorous theory of heterogeneous new phase nucleation on a surface has been developed so far. The existing theories of new phase nucleation on solid surfaces proceed either from the classical nucleation theory [11], modified for the two-dimensional case and allowing for the possible role of defects in nucleation, or from the atomistic model [18].

The surfaces of solids can be both crystalline [28] and amorphous [29]. Modern concepts [28] distinguish between atomically "smooth" and atomically "rough" surfaces. The former usually include singular and vicinal facets, while the latter include nonsingular ones. Singular surfaces are characterized by a local minimum in the surface tension σ and a discontinuity in the angular derivative $\partial\sigma/\partial\theta$ (here θ is the angle in polar plot [28]). Such peculiar features of σ and $\partial\sigma/\partial\theta$ behavior are typical for all directions described by rational Miller indices, the minima being sharpest and deepest in the directions normal to the close-packed planes (with minimum values of the Miller indices).

Vicinal planes have a small deviation from the alignment of close-packed facets [28]. To describe the atomic structure of vicinal facets, the TLK (terrace, ledge, kink) model [28] is most frequently used, which allows one to obtain the binding energy of atoms that are in different positions. In terms of the TLK model, one can calculate both the number of ledges and the spacing between them and can also determine the concentration of atoms in each position, i.e., in atomically smooth regions of the surface, on a step, in a ledge, etc. [28]. Thus, even ideal crystal surfaces having a slight deviation from a close-packed orientation are step-like; at $T > 0$, the steps are covered with ledges; the surfaces of real crystals are rough, contain surface vacancies, surface dislocations, inter-grain boundaries, and other defects [13, 28]. All these defects essentially affect the parameters of the condensation process and may serve as orienting centers for nucleation of nanoislands.

Crystal surfaces of substrates for nanostructures can be exposed to thermal or chemical treatment [13, 14, 30–32]. As a result of such a modification, crystal surfaces change their properties. The orientation and the number of free chemical bonds change in the process of the respective modification. Surface tension changes as well. So, the treatment of substrate surfaces allows for a control of nucleation of nanoislands.

Processes of adsorption, desorption, and diffusion of atoms on the surface of a substrate have been rather well investigated [28, 33]. Adsorption is typically thought of as the first stage of film condensation [20]. In condensation from a single-component vapor, monomolecular and dissociative adsorptions are most frequently distinguished that, for small substrate occupation numbers, lead to a uniform formation of adatoms over the entire nonoccupied substrate surface with a constant rate, J, given by

$$J = \frac{C_g P}{(2\pi M k_B T_v)^{1/2}} , \tag{7.1}$$

where P is the vapor pressure, T_v is the vapor temperature, M is the mass of one deposited molecule, k_B is the Boltzmann constant, and C_g is a geometric shape factor. The adsorbed atoms can either desorb back into vapor or diffuse to one of the neighboring sites.

In the single-component case, the rate of desorption is described by the following equation:

$$\frac{dn_1}{dt} = -\frac{n_1}{\tau_r} , \quad \tau_r = \frac{1}{\nu} \exp\left(\frac{E_a}{k_B T}\right) , \tag{7.2}$$

where n_1 is the surface adatom density, t is the time, dn_1/dt is the desorption rate, τ_r is the characteristic time of monomolecular desorption (re-evaporation time), E_a is the desorption activation energy, and ν is the frequency of tangential oscillations of an atom on the substrate surface [28]. After establishing equilibrium between the surface and the surrounding initial phase, a two-dimensional "gas" of adatoms with surface density n_1 is formed on the surface of solids [13, 14]. In the case of monomolecular desorption, this process proceeds approximately within a time τ_r. The process of associative desorption is analyzed in Ref. [34]. A large number of papers are devoted to the study of the thermodynamic and kinetic characteristics of such an adsorbed "gas" [35, 36]. The most interesting and important for us properties are thermodynamic stability, instability and metastability of those systems, because these characteristics are directly connected with the possibility of phase transformations in adsorbed layers.

An expression for the state of an adsorbed gas on a substrate surface was derived in Ref. [27]. The equation is of the form

$$\frac{P}{k_B T_c} = \frac{T}{T_c} \ln\left(\frac{1}{1-n}\right) - 2n^2 , \tag{7.3}$$

where n is the density of atoms adsorbed on the surface and T_c is the critical temperature. For $T < T_c$, $P < P_c = (\ln 2 - 1/2) k_B T_c$, the $P(V)$ isotherms exhibit a characteristic van der Waals loop testifying to a first-order phase transition of the gas–liquid type (the pressure here has the dimensions of energy since the volume is given as $V = 1/n$ in dimensionless units). In real systems, such a transition occurs only in the interval $T_t < T < T_c$ between the triple and the critical points. The given model (similar to other models of this type) describes only phase

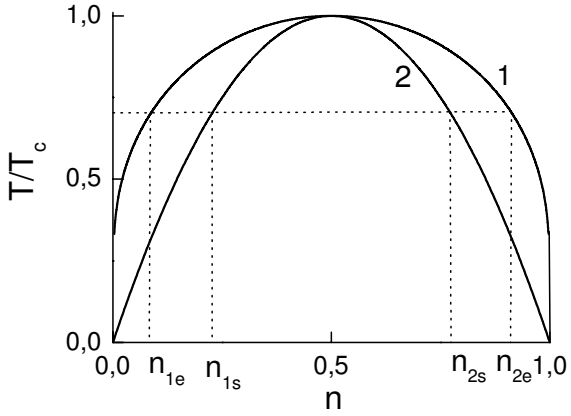

Figure 7.1: Phase equilibrium (binodal) curve (1) and spinodal curve (2). The values of n_{1e}, n_{1s}, n_{2s}, and n_{2e} are shown for a value of the reduced temperature equal to $T/T_c = 0.7$

transitions of the gas–liquid type (amorphous state), i.e., amorphous film condensation and the first stage of crystalline film condensation, which proceeds via the vapor–liquid–crystal mechanism. Despite the simplifications made, this continuum's model satisfactorily describes many principal features of the behavior of the adatom system.

The phase equilibrium and spinodal curves can be obtained from Eq. (7.3). Such curves are plotted in Fig. 7.1. Here n_{1e} and n_{2e} are the equilibrium densities of the adsorbed gas and amorphous phase, respectively; n_{1s} and n_{2s} are the concentrations corresponding to the spinodal range. The region of metastable states, $n_{1e} < n < n_{1s}$, corresponds to a supersaturated vapor $\xi = (n/n_{1e}) - 1$, and the region $n_{2s} < n < n_{2e}$ to a superheated liquid. It is precisely in the range $n_{1e} < n < n_{1s}$ that the film condensation proceeds via nucleation, and for $n = n_{1s}$ the critical nucleus consists of only one particle. The quantity $\xi_{\max} = (n_{1s}/n_{1e}) - 1$ implies maximum possible supersaturation. For supersaturations exceeding $\xi_{\max}$, the adatom population becomes unstable and spinodal decomposition determines its evolution [17,21,27].

7.3 Growth Modes of Nanofilms

The thin-film growth regimes are typically divided into layer-by-layer, island, and intermediate (Stranski–Krastanov) modes of growth [20]. Similarly the same regimes are realized during the growth of nanofilms. The layer-by-layer or the Frank–van der Merwe regime is realized in the case when the deposited atoms are bound by the substrate more strongly than with each other. Monoatomic layers in this regime are occupied in turn, i.e., two-dimensional nuclei (one monolayer thick) of a subsequent layer are formed on the upper part of the nuclei of the preceding layer after the latter is occupied. The equilibrium form of the nuclei is found by the Wulff theorem [28]. The theoretical description of the layer-by-layer growth is customarily given in the framework of the Kashchiev model [11] or its modifications [37, 38].

The island or the Volmer–Weber regime is realized in the opposite case, i.e., for the atoms of a deposited substance bound with each other more strongly than with the substrate. Island growth can only be realized under the condition [39]

$$\sigma_{\mathrm{s}} < \sigma_{\mathrm{d}} + \sigma_{\mathrm{s-d}} - \mathrm{const} \times k_{\mathrm{B}} T \ln(\xi + 1) \,, \tag{7.4}$$

where σ_{s} is the free energy of a unit substrate surface, σ_{d} is the free energy of a unit adsorbate surface, and $\sigma_{\mathrm{s-d}}$ is the free energy of a unit substrate-adsorbate interface. Otherwise, the layer-by-layer regime holds. In the island regime, small nuclei are formed straight on the substrate surface and then grow transforming into large islands of the condensed phase [39]. Thereupon, these islands merge to form a continuous film after the channels between them are filled [39]. In the intermediate, or the Stranski–Krastanov regime, the first to be realized is a layer-by-layer growth and then, after one or two layers are occupied, island growth begins. There may be several reasons for the change of the growth mechanisms [39]. The principal cause is that the lattice parameter cannot remain unchanged upon occupation of an intermediate layer. Its variation entails a strong increase of the adsorbate–intermediate layer interface energy, which fulfills the island regime criterion Eq. (7.4).

A large number of examples illustrating all three thin-film growth conditions and experimental methods of their investigation are presented in Ref. [20]. It was shown in Ref. [40] that under certain conditions the faceting of cap-shaped clusters at the (OR) stage may lead to a replacement of the island mechanism by the layer-by-layer one. In this regime, condition (7.4) holds first and then a change in the condensate symmetry causes its violation. Thus, the kind of substrate and the type of its surface determine the film growth regime.

At present, investigators pay peculiar attention to the growth of films via the Stranski–Krastanov mechanism [1, 2, 41, 42]. First of all, this fact is connected with requirements of optoelectronics in semiconductor structures based on quantum dots. During the growth of quantum dots, an elastic energy arises along the substrate–wetting layer interface that turns out to be of great importance. The elastic energy is responsible for a substantial difference in the kinetics of nanostructure nucleation. Nevertheless, the basic equations describing the nucleation processes of nanoparticles coherently conjugated with a substrate and, accordingly, the methods for their solution are, from a mathematical point of view, in most cases similar to the equations describing the growth of unstrained structures. Therefore, we start to analyze the nucleation of nanoislands without taking into account the elastic energy, i.e., the islands forming and growing by the Volmer–Weber mechanism, and afterwards in Section 7.9, we investigate the growth of coherent nanoparticles.

7.4 Nucleation of Relaxed Nanoislands on a Substrate

The most widely employed approximation in the description of nucleation is the so-called capillary model [11, 12, 18] first formulated by Volmer and Weber, Becker and Döring, and Zel'dovich. According to this model, positive free-energy fluctuations that lead to overcoming the activation barrier are necessary for the condensation of a new phase from a supersaturated vapor in the metastable state (i.e., over the region $n_{1e} < n_1 < n_{1s}$) [27]. The presence of such a barrier is associated with the fact that the free energy of nucleation from a supersaturated vapor has a maximum at a certain critical size. Nuclei on a substrate may have various shapes [28] but

theoretically they are most frequently assumed to look like a disk or a hemisphere according to the film growth mechanism, because many films grow by the vapor–liquid–crystal mechanism.

The free energy F (expressed in units $k_{\mathrm{B}}T$) of formation of disc-shaped clusters on an ideal substrate can be written in the form [7]

$$F(i) = 2\sqrt{ai} - i\ln(\xi + 1) - \ln\left(\frac{n_0}{n_1}\right), \quad a = \left(\frac{\sigma_{\mathrm{eff}}}{k_{\mathrm{B}}T}\right)^2 \frac{\pi w}{h}. \tag{7.5}$$

Here i is the number of particles in a nucleus, σ_{eff} is the effective interphase energy per unit length of the disk boundary, h is the disc height, w is the volume occupied by one particle in the nucleus, n_0 is the number of adsorption sites on the substrate surface; $n_0 \sim 1/B^2$, where B is the substrate lattice constant. The first term in Eq. (7.5) is the free energy term connected with surface tension effects, the second one is the chemical potential difference between the new and the old phases, and the third is a statistical correction term due to the distribution of n_1 atoms over n_0 lattice sites [15, 17]. The maximum of the free energy (see Eq. (7.5)) is found at

$$i_c = \frac{a}{\ln^2(\xi + 1)}, \tag{7.6}$$

and equal to

$$F(i_c) = \frac{a}{\ln(\xi + 1)} - \ln\left(\frac{n_0}{n_1}\right). \tag{7.7}$$

The nucleus has to overcome just such a potential barrier of height $H(\xi) = F(i_c)$ owing to heterophase fluctuations in order that it might grow further regularly. According to the capillary model, an elementary act changing the nucleus size is either an attachment to it or, in contrast, a loss of one molecule (processes of merging of nuclei are ignored). For sufficiently large nuclei containing $i \gg 1$ particles, this change is small, and, therefore, the evolution of large nuclei can be described by the Fokker–Planck equation [6, 7]

$$\frac{\partial g}{\partial t} = -\frac{\partial I}{\partial i}, \quad I = -W(i)\left[\frac{\partial g}{\partial i} + g\frac{\mathrm{d}F(i)}{\mathrm{d}i}\right], \tag{7.8}$$

where $g(i, t)$ is the distribution function of nuclei with respect to the number of particles i they contain, I is the nucleation rate (it vanishes for an equilibrium distribution $g = \text{const} \times \exp(-F(i))$) and $W(i)$ is the diffusion coefficient in cluster size space, which is equal to the number of molecules incorporated into the nucleus from the ensemble of adatoms per unit time. The stationary solution $g_s(i)$ of Eq. (7.8) has the form [7]

$$g_s(i) = I\exp[-F(i)]\int_i^\infty \frac{\exp(F(i'))}{W(i')}\,\mathrm{d}i' \tag{7.9}$$

(the standard boundary condition: $g_s\exp(F(i)) \to 0$ as $i \to \infty$ was taken into account here).

The probability of fluctuations, described by the second-order derivative of g with respect to i increases rapidly with decreasing size. Hence, the distribution of subcritical nuclei may

be regarded as supplemented so rapidly owing to the fluctuations that their number remains in equilibrium in spite of the permanent outflow of the flux I. Consequently, the boundary condition to Eq. (7.8) takes the form $g_s(i) \to n_1 \exp[-F(i)]$ as $i \to 0$ and therefore from Eq. (7.9) we find

$$I = n_1 \left[\int_0^\infty W^{-1}(i') \exp(F(i'))\, \mathrm{d}i' \right]^{-1} . \tag{7.10}$$

The integrand in Eq. (7.10) has a sharp maximum at the position $i = i_c$, which allows us to calculate the integral, using the Laplace method, as

$$I = n_1 \sqrt{\frac{-F''(i_c)}{2\pi}} W(i_c) \exp[-F(i_c)] . \tag{7.11}$$

The square root in Eq. (7.11) is sometimes called the nonequilibrium Zel'dovich factor.

Let us now estimate the quantity $W(i_c)$, which is the frequency at which adatoms are attached to a critical nucleus. To this end, we shall use the lattice model. Let R_c be the radius of the critical nucleus linear boundary, l_0 the length of diffusive jumps of adatoms, ν the desorption frequency, and E_d the activation energy of surface diffusion. Then we have

$$W(i_c) = 2\pi R_c n_1 \ell_0 \left(\frac{\nu_d}{4}\right) \exp\left(-\frac{E_d}{k_\mathrm{B}T}\right) = 2\pi R_c n_1 \frac{D_\mathrm{a}}{\ell_0} , \tag{7.12}$$

where $D_\mathrm{a} = (\ell_0^2 \nu/4) \exp(-E_d/k_\mathrm{B}T)$ is the diffusion coefficient of adatoms. From this, for disk-shaped nuclei we arrive at [7]

$$I(\xi) = C_1 n_{1e} n_0 D_\mathrm{a} (\xi + 1) \ln^{1/2}(\xi + 1) \exp\left[-\frac{a}{\ln(\xi + 1)}\right] . \tag{7.13}$$

Similarly, for nuclei with the shape of a hemisphere we have

$$I(\xi) = C_2 n_{1e} n_0 D_\mathrm{a} (\xi + 1) \ln(\xi + 1) \exp\left[-\frac{b}{\ln^2(\xi + 1)}\right] . \tag{7.14}$$

Here the notations

$$\begin{aligned} C_1 &= \sqrt{\frac{2\omega}{h\ell_0^2}} , \quad C_2 = \frac{2\sin\theta}{b^{1/2}} \left[\sqrt{\frac{3}{2\pi}} \ell_0^3 (1 - \cos\theta)^2 \frac{(2 + \cos\theta)}{\omega} \right]^{-1/3} , \\ b &= \frac{4\pi}{3} \left(\frac{\sigma}{k_\mathrm{B}T}\right)^3 \omega^3 (2 + \cos\theta)(1 - \cos\theta)^2 \end{aligned} \tag{7.15}$$

are employed. In addition, σ is the interphase energy per unit area, and θ is the contact angle.

The time t_s of establishment of a stationary nucleation rate has been repeatedly evaluated by various authors with similar in the order of magnitude values [43–45]. The mean value is

$$t_\mathrm{s} = \frac{1}{-F''(i_c) W(i_c)} . \tag{7.16}$$

In thin-film condensation, this time interval is usually very short and of the order ($10^{-4} - 10^{-8}$ s) both for disk- and cap-shaped nuclei, and therefore, in practice it is sufficient to calculate the stationary flow of nuclei, I, only. Methods accounting for nonstationary effects (necessary for the description of very fast processes), were proposed, for example, in Refs. [43–45].

We now analyze nucleation processes of multicomponent nanofilms. Multicomponent systems may be divided into two groups. One of them includes systems with islands that can be considered as solid solutions, and the other involves systems with islands consisting of stoichiometric compounds. We first discuss nucleation of multicomponent stoichiometric islands and then examine nucleation processes in islands of solid solutions. According to Ref. [7], islands of stoichiometric compounds can be formed in the following ways: (i) The rate of the chemical reaction is much higher than the rate at which a new phase forms. In this case, molecules of the chemical compound are formed first, and then nucleation of the islands takes place. (ii) The nucleation rate of the islands is much higher than the rate of formation of a chemical compound on the substrate. In this case, islands of a mixture of chemical elements are formed due to heterogeneous fluctuations, and the chemical reactions take place afterwards in the islands producing a stoichiometric compound. (iii) The rates of chemical reactions and formation of islands are of comparable magnitude; the rate of the chemical reaction is nonlinear and the reaction product behaves as a catalyst of the reaction. In this case, self-induced oscillations in the number of new phase nuclei and their self-organization are possible. (iv) Growth of the islands proceeds as a result of chemical reactions at their surface [16].

According to the results obtained in [46], the stationary flow of multicomponent stoichiometric disk-shaped islands of height h nucleating on the substrate surface is given by

$$I'_s(\xi) = \alpha'_s(\xi+1)\ln^{1/2}(\xi+1)\exp\left[-\frac{a^s}{\ln(\xi+1)}\right]. \tag{7.17}$$

The flow of cap-shaped nuclei can be expressed by

$$I''_s(\xi) = \alpha''_s(\xi+1)\ln(\xi+1)\exp\left[-\frac{b^s}{\ln^2(\xi+1)}\right]. \tag{7.18}$$

In Eqs. (7.17) and (7.18), the notation

$$\begin{aligned}
&\alpha'_s = A_{1s}n_0^2 D_s^0\,, \quad \alpha''_s = A_{2s}n_0^2 D_s^0\,, \quad A_{1s} = \left(\frac{\omega_m^s}{h}\right)^{1/2}\\
&A_{2s} = \frac{2\sin\theta}{(b^s)^{1/2}}\left[\sqrt{\frac{3}{2\pi}}(1-\cos\theta)^2\frac{(2+\cos\theta)}{\omega_m^s}\right]^{-1/3},\\
&b^s = \frac{4\pi}{3}\left(\frac{\sigma}{k_{\mathrm{B}}T}\right)^3(\omega_m^s)^3(2+\cos\theta)(1-\cos\theta)^2\,,\\
&a^s = \left(\frac{\sigma_{st}}{k_{\mathrm{B}}T}\right)^2\frac{\pi\,\omega_m^s}{h}\,, \quad \omega_m^s = \sum_{i=1}^{n^{\mathrm{s}}}\nu_i\omega_i \quad n_{1e}^{\mathrm{s}} = n_0\prod_{i=1}^{n^{\mathrm{s}}}\rho_{i0}^{\nu_i}
\end{aligned} \tag{7.19}$$

are employed. Here ω_m^s is the volume of a molecule of the chemical compound; ω_i is the volume of an atom of the ith component of the chemical compound; ν_i is the stoichiometric

coefficient of the ith component; n^{s}_{1e} is the equilibrium density of molecules of the chemical compound on the substrate; D^0_s, given by

$$D^0_s = \left[\sum_{i=1}^{n^{\mathrm{s}}} \frac{p_i^2 l_i}{D_{ai}\rho_{i0}} \right]^{-1} , \quad p_i = \frac{\nu_i}{\sum_{i=1}^{n^{\mathrm{s}}} \nu_i} , \tag{7.20}$$

is the generalized diffusion coefficient; ρ_{i0} is the equilibrium concentration; p_i are the reduced stoichiometric coefficients; D_{ai} is the diffusion coefficient of the ith component; l_i is the length of diffusive jumps of an ith adatom. The supersaturation ξ is given, in the case of phase formation in multicomponent systems, by

$$\xi = \frac{\prod_{i=1}^{n^{\mathrm{s}}} \bar{\rho}_i^{\nu_i} - K^s_\infty}{K^s_\infty} , \quad K^s_\infty = \prod_{i=1}^{n^{\mathrm{s}}} \rho_{i0}^{\nu_i} , \tag{7.21}$$

where K^s_∞ is the equilibrium constant of the chemical reaction yielding the chemical compound of composition s, and $\bar{\rho}_i$ is the concentration on the surface of the ith component of the multicomponent system. It follows from Eqs. (7.17) and (7.18) that the formal expression for the nucleation rates in multicomponent stoichiometric systems is similar to that of single-component ones. However, the kinetic coefficients in the equations depend on the kinetic coefficients for each of the components.

In the case of nucleation of multicomponent films of solid solutions, the free energy of a nucleus depends on the number of particles of each component. Its calculation is a separate fairly complicated problem [47]. Let us consider here a nucleus of the new phase to be a mixture of different components. The mixture is assumed to be a regular solid solution. Further, let us denote by m the number of vapor phase components, and $i_1, i_2, \ldots, i_m$ are the number of particles of each component in a nucleus. Then, the free energy F of formation of a nucleus, expressed in thermal units $k_{\mathrm{B}}T$, is equal to [47]

$$F(i_1, \ldots, i_m) = \sigma(i_1, \ldots, i_m)S - \sum_{j=1}^{m} i_j \ln\left(\frac{n_j}{n_{je}(i_1, \ldots, i_m)}\right) - \ln\left[n_0 \Big/ \sum_{j=1}^{m} n_j \right] , \tag{7.22}$$

Here σ is the specific interphase energy, S is the area of the nucleus phase boundary, n_j is the surface concentration of the component j, n_{je} is the vapor concentration of the component j, which is in equilibrium with the nucleus of this particular composition, and n_0 is the concentration of the lattice sites on which atoms are adsorbed. The composition of the nucleus is determined by the set of molar concentrations $\{\nu_k\}$ of each component

$$\nu_k = \frac{i_k}{\sum_{j=1}^{m} i_j} , \quad \sum_{j=1}^{m} \nu_j = 1 . \tag{7.23}$$

The dependence of σ and n_{je} on ν_k for a regular solid solution with a given heat of mixing of components can be calculated within the thermodynamic theory of solutions [7, 47]. In particular, if a nucleus can be considered as an ideal solution, then we get

$$\sigma = \sum_{j=1}^{m} \sigma_j \nu_j \ , \quad n_{je} = n_{je}^0 \nu_j \ , \tag{7.24}$$

where σ_j and n_{je}^0 are the interphase energies and densities of a saturated vapor of pure components. By employing these dependences and solving the system of equations ($\partial F/\partial i_j = 0$), one obtains the number of particles of each component i_{jc} in the critical nucleus. In the next step, one can readily calculate the height of the activation barrier $H = F(i_{1c}, \ldots, i_{mc})$. The equation $H^{-1}(n_1, \ldots, n_m) = 0$ specifies the surface that separates the regions of concentrations with and without nucleation. In the simplest case of an ideal solution with equal values of σ_j, this equation gets the form [47]

$$\sum_{j=1}^{m} \left(\frac{n_j}{n_{je}^0} \right) = 1 \ . \tag{7.25}$$

Along with nuclei containing all m components, nuclei involving a smaller number of components can be formed on the substrate as well. Therefore, the whole range of concentration variation is divided into different phase regions by $2^m - 1$ interfaces of the types $H^{-1}(n_j) = 0$, $H^{-1}(n_j, n_k) = 0$, etc. In particular, for $m = 2$, three dividing lines $H^{-1}(n_1) = 0$ ($n_1 = n_{1e}^0$), $H^{-1}(n_2) = 0$ ($n_2 = n_{2e}^0$), and $H^{-1}(n_1, n_2) = 0$ specify five regions in the thermodynamic phase space, which are shown in Fig. 7.2. In region (a) no new phase formation is observed, in region (b) only two-component islands nucleate, in region (c) two-component islands and those of the atoms of the second component can develop, in region (d) two-component islands and those of the atoms of the first component may evolve, and in region (e) two-component islands and islands of the atoms of each component (the nucleation rate for islands of a mixture is, as a rule, much higher than that for the single-component islands).

In the newly formed islands of a new phase a reaction begins among the components or (if the components cannot make up a chemical compound) an eutectic decay. Alternatively, the formation of a solid solution may take place. The behavior of the system is determined by the type of the corresponding phase diagram for a solid mixture. In particular, for a binary system there exist five main types of phase diagrams for a solid mixture [7, 47]. All possible cases of condensation are accordingly divided into 25 groups. All of them are considered in detail in Ref. [47]. Systems with three or more components are analyzed similarly. But here a significantly larger number of different types of behavior are found. The analysis of the behavior of an ensemble of adsorbed particles shows that all the forms of multicomponent film condensation make up a set of processes, each proceeding at a certain stage. Below we summarize those processes that play the key role: (i) Chemical reaction in an adsorbed multicomponent gas with a simultaneous nucleation of the final product of the reaction; (ii) formation of nuclei representing a mixture of components; (iii) chemical reaction in such nuclei; (iv) growth of islands of a new phase from a supersaturated adsorbed vapor; (v) separation of an eutectic mixture; (vi) evaporation of nuclei. The methods of description of processes (i)–(vi) are presented in Ref. [7].

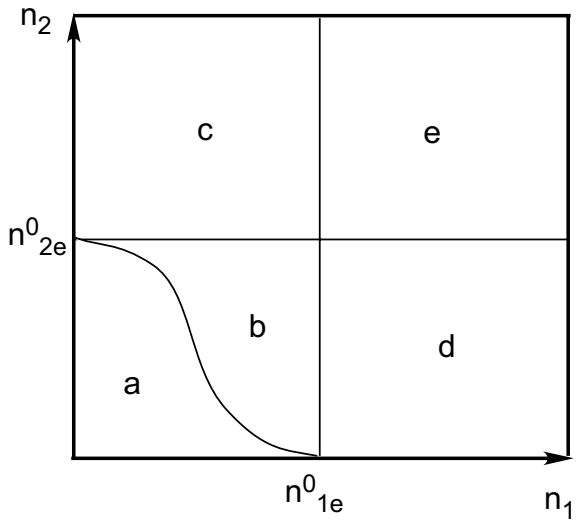

Figure 7.2: Phase diagram of a binary system

In the case of nucleation of islands from a solid solution, the Fokker–Planck equation becomes multidimensional, and accordingly the boundary condition at the zero point becomes more complicated. The method of its solution is based on the simultaneous diagonalization of both the equation and the boundary condition by a linear change of variables [23]. Then, it turns out that the nucleation rate I can be estimated as

$$I = n_0 \left(\sum_{k=1}^{m} d_k \right) \exp(-H_0) \,, \quad H_0 = H + \ln \left(\frac{n_0}{\sum_{k=1}^{m} n_{1k}} \right) \,, \tag{7.26}$$

where d_k are the diffusion coefficients for each of the m components in the dimension space for $i = i_c$ and H_0 is the nucleation barrier height without the entropy correction.

It has been assumed here that nucleation takes place on an ideal substrate, namely, in a homogeneous way. However, various substrate defects often initiate nucleation by reducing the activation barrier, H. In particular, the work of heterogeneous nucleation at the step of a substrate was determined by Hirth and Pound more than 40 years ago. They showed that steps may substantially increase the nucleation rate [18]. This result is confirmed by numerous experimental data [18–20]. The activation barrier of nucleation on a step can be so small ($\sim k_B T$) that a nucleus consisting of two particles will already be supercritical, i.e. $F(2) < F(1)$ (or $n_1 > n_{1s}$). In this case, as has already been mentioned, a new phase will be formed not through conventional nucleation, but through a spinodal decomposition process, namely, by an amplification of the different modes of density fluctuations of substance concentration [17,21]. At the same time, the size distribution of new phase islands on the step and their spatial distribution will already be different.

Numerous modifications of the classical capillary model of nucleation on a substrate exist. Several corrections to the height of the activation barrier are introduced, namely, the correction due to internal degrees of freedom of a cluster [18], the correction due to free energy variation

on separation of a group of i molecules from a large ensemble [11], the correction due to cluster boundary smearing, corrections due to cluster faceting [28], nonisothermal effects [48], and so on. These corrections are, as a rule, relatively small and, moreover, have different signs. The most significant one is obviously the correction due to the influence of the nucleus surface curvature on the interphase energy [49]. It leads to a $10^2 \pm 10^6$-fold increase in the nucleation rate. We recall that the capillary model, described above, is only applicable for $i_c \gg 1$, because it is only in this case that the attachment and detachment of particles to and from critical nuclei can be described by the continuous Fokker–Planck equation (7.8). An alternative to this model for $i_c < 10$ is the atomistic Walton model [18] exploiting the methods of equilibrium statistical mechanics. It allows I to be expressed in terms of i_c, but does not give the dependence of i_c on ξ. Moreover, it is invalid for $i_c = 1$ and $i_c = 2$, when the increase of long-wave density fluctuations is of importance.

7.5 Formation and Growth of Space-Separated Nanoislands

7.5.1 Growth Mechanisms

After the formation of nuclei of a new phase on the substrate surface they start growing and interacting with atoms of the old phase out of which they were formed. The latter mentioned phase may be a single- or multicomponent vapor, a single- or multicomponent liquid solution, and an amorphous phase or a solid solution. Accordingly, the island growth mechanisms may vary substantially as well. In any case, the diffusion flux of atoms of the old phase toward the surface of the nuclei is responsible for their growth from vapor. Both the removal of the latent heat of the phase transformation and the diffusion of atoms of the old phase are responsible for the island growth from liquid solutions and from an amorphous ambient phase. If the film growth is due to decomposition of a supersaturated solid solution, the islands will grow via a diffusion flux of atoms of the old phase. In the case, when the film growth proceeds in the course of another type of phase transformation, for instance, a film decay caused by elastic strains [41, 50, 51] occurring at the film–substrate interface, the islands grow owing to the diffusion flux of atoms induced by elastic strains.

The surface introduces an appreciable diversity into the nucleus-growth mechanisms as compared to the growth in the bulk of solids. According to contemporary concepts [52], the following basic ways of atomic migration and energy transfer, in particular, heat transfer over the surface, are distinguished: (i) three-dimensional or volume diffusion of atoms and three-dimensional heat removal; (ii) two-dimensional atomic diffusion over the substrate surface and two-dimensional heat removal; (iii) one-dimensional atomic diffusion along substrate steps, surface dislocations, and other linear defects. Islands may also grow due to an immediate arrival of atoms from a vapor onto their surface. The ultimate goal of the study of island growth mechanisms is the determination of the islands growth rate as a function of their radius and the degree of supersaturation. For this purpose, the corresponding heat and mass transfer equations have to be formulated and solved [13]. Such problems have been widely examined for three-dimensional systems [53], in particular, for crystal growth from single-component and binary melts. The structure of the diffusion fields in the bulk of a vapor phase, on a

substrate surface, and with linear defects has been investigated in detail and the expressions for the island growth rate υ_R were found in Refs. [13,53]. Islands usually grow simultaneously through several atomic diffusion mechanisms. The main mechanisms of nanoisland growth are shown in Fig. 7.3.

It is convenient to consider each mechanism of island growth separately. According to Refs. [13, 53], the expression for the new phase island growth rate υ_R can be written in the following general form for each of the mass transfer mechanisms:

$$\upsilon_R = -M^{2-d'} w \frac{J_{DR}\Psi(\theta)}{R^{3-d'}} \ . \tag{7.27}$$

Here w is the volume per atom in the islands of a new phase; d' is the dimension of the space in which the diffusion fluxes propagate: $d' = 3$ for mass transfer in the bulk of a phase, $d' = 2$ for mass transfer over the surface, and $d' = 1$ for one-dimensional atomic diffusion along substrate steps or other linear defects (in this formula the difference $2 - d'$ is assumed to take only nonnegative values); J_{DR} is the diffusion flux of atoms onto the island surface, which is found from the corresponding diffusion equations, and $\Psi(\theta)$ is a function taking into account the island geometry. For cap-like islands we have $\Psi(\theta) = 2(2 - 3\cos\theta + \cos^3\theta)^{-1}(1 - \cos\theta))$ when the diffusion of atoms proceeds in the bulk of a gas phase, $\Psi(\theta) = 2\sin\theta/(2 - 3\cos\theta + \cos^3\theta)$ for the diffusion of atoms over the substrate surface, and $\Psi(\theta) = [2\pi(2 - 3\cos\theta + \cos^3\theta)]^{-1}$ for the one-dimensional atomic diffusion. Finally, M is the number of linear defects that are crossed by an island during its growth.

To find the atomic diffusion flux of atoms J_{DR} to a nucleus, one has to solve the corresponding diffusion equations. The form of these equations, their boundary conditions, and the methods of their solution can be found in Refs. [7, 13]. The general expression for the new phase island growth rate has the form

$$\upsilon_R = \frac{K_p}{R^{p-1}} \left(\frac{R}{R_c} - 1 \right) \ . \tag{7.28}$$

Here K_p is a constant determined by the values of the parameters that characterize the material of the island and the kinetic parameters of its growth (values of K_p for different special cases can be found in Ref. [13]), and the number p may have the values 2, 3, 4 depending on the mass transfer mechanism. For our further purposes, it is convenient to express the number p in terms of the island dimension d (being equal to 2 or 3) and the growth index m, which may have the values 1, 3/2, 2, and 3 depending on the island shape and the type of the limiting stage: $p = d/m + 1$.

At the initial stages of phase transformation in the stage of independent growth, the island radius R is much larger than R_c, and therefore the number one in the right-hand side of Eq. (7.28) is commonly ignored being negligibly small as compared with R/R_c. Furthermore, it is convenient to write this equation not in terms of the growth rate referred to the radius but via the change of the number of atoms in the nucleus. Then, Eq. (7.28) can be rewritten in the form [7]

$$\frac{\mathrm{d}i}{\mathrm{d}t} = m \frac{\xi}{t_0} i^{\frac{m-1}{m}} \ , \tag{7.29}$$

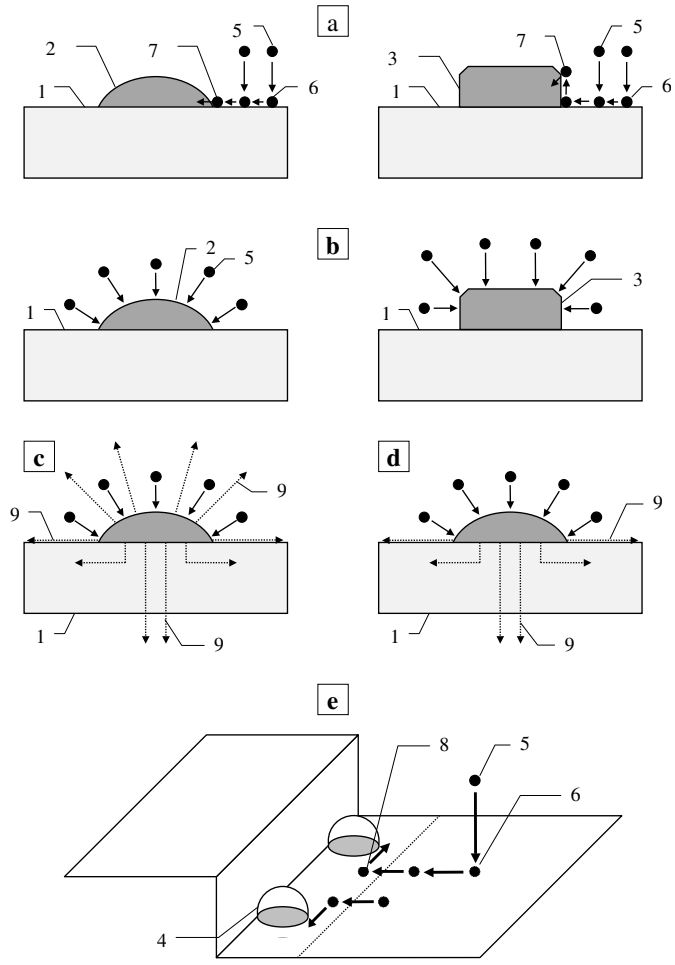

Figure 7.3: Schematic sketch of the fundamental mechanisms of nanoisland growth: (a) growth of edged and nonedged islands, when the limiting stage is surface diffusion of adatoms; (b) the limiting process is diffusion of atoms in the vapor phase (evaporation–condensation), (c) growth of nonedged islands, when the process is controlled by the entry of atoms from the vapor phase, but heat removal occurs over all their surfaces; (d) the same, but with heat removal through the substrate only; (e) growth of islands through linear diffusion along the steps of the substrate: (1) substrate; (2) nonedged island; (3) edged island, to the surface of which atoms join only in specific places; (4) the island at a substrate step; (5)–(8) the atom in the vapor phase, on the substrate surface, on an island surface, and at a substrate step, respectively; (9) heat flow angle

where ξ is the supersaturation, and t_0 is a constant having the dimension of time and denotes the characteristic time of the island growth. This parameter can be expressed via the constant K_p and the constants relating supersaturation to the critical radius.

It has been shown theoretically and experimentally that the new phase island growth is determined by two principal processes, namely, substance transfer to the island, i.e., diffusion properties, and the passage of atoms through the old–new phase interface, i.e., the boundary kinetics. After passing through the interface, an atom joins the island surface. The island surface, similarly as the surface of any crystal, can be atomically rough, atomically smooth, or vicinal. The ways in which the atoms join the island surface are different and depend on the type of the surface. So, interfaces, rough at the atomic level, grow by the normal mechanism of growth. Atomically smooth surfaces grow by two-dimensional nucleation on their facets. Vicinal surfaces grow either through the motion of already existing steps or utilizing screw dislocations appearing on their surfaces. Island growth by two-dimensional nucleation, as well as the evolution of an ensemble of such islands, is described in Ref. [54]. The next stage represents the process of incorporation of adatoms into a new phase island. The growth rate equation (7.28), namely the constant K_p and the index p, is significantly influenced by the condition determining which of the processes is limiting the growth. The particular form of the constant K_p for each type of mass transfer mechanism can be found in Ref. [13].

In the course of formation of multicomponent nanofilms, atoms arrive at the substrate surface and may initiate islands of various chemical compounds. Many of the islands of these compounds represent an intermediate phase in the course of growth of other phases. Islands of a chemical compound will further be referred to as phase s. As in single-component systems, the growth of multicomponent islands is due to the same mass transfer mechanisms. However, there is one important difference in that the chemical components, of which an island of phase s is formed, may diffuse toward it in different ways. One of the components may arrive at the island surface through surface diffusion, and another one through gas diffusion. In this situation one usually has to find the component limiting the rate and by this component determine the main flow of the substance toward the island.

The growth rate of a multicomponent island of an arbitrary phase s will be described as before by Eq. (7.27). However, in this equation, the product of the atomic flux J_{DR} and the volume w has to be replaced by the sum of the products of the atomic fluxes from each component by their volume w_i, i.e., $\sum_{i=1}^{n^s} w_i^s J_{iR}^s$, where the subscript i stands for the corresponding components. Since the islands have a given stoichiometric composition, it follows that, on their surfaces, the stoichiometry condition $J_{iRr}^s/\nu_i^s = J_{i'Rr}^s/\nu_{i'}^s$ holds. This condition allows us to express the quantity $\sum_{i=1}^{n^s} w_i^s J_{iR}^s$ in terms of the product of the flux of one of the components i by the volume w_m^s of a molecule of the chemical compound of phase s, i.e., $J_{iR}^s w_m^s/p_i^s$, where $w_m^s = \sum_{i=1}^{n^s} p_i^s w_i^s$ is the volume per molecule of phase s and $p_i^s = \nu_i^s / \sum_{i=1}^{n^s} \nu_i^s$. Thus, to calculate the growth rate of a multicomponent island, it is sufficient to find the flux J_{iR}^s of only one arbitrarily chosen component.

In Refs. [13, 55], all possible mechanisms of substance transport in multicomponent systems were investigated and analytical expressions for any type of fluxes J_{iR}^s were found. Their substitution into an equation for the growth rate of the type of Eq. (7.27) leads to an equation of motion for an island of phase s, which has the form of Eq. (7.28), where the constant K_p is replaced by a generalized constant containing kinetic and some other coefficients of each component entering the phase s. Hereby the critical radius R_c in Eq. (7.28) is replaced by the critical radius R_c^s for a given phase. The exact calculation of the growth rate of solid solution islands is much more sophisticated than that for stoichiometric compounds. If the diffusion

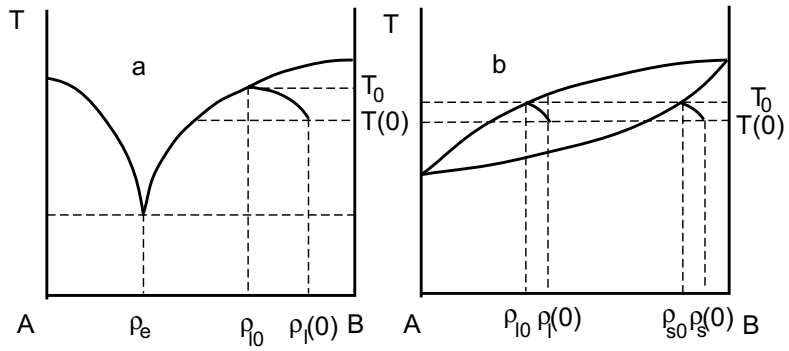

Figure 7.4: Phase diagrams of binary systems: (a) a system with an eutectic point; (b) a system with an infinite solubility of the components in the solid phase; ρ_s and ρ_l are the equilibrium concentrations in the solid and liquid phases, respectively; T_0 is the equilibrium temperature, $T(0)$ and $\rho(0)$ are respectively the temperature and the composition at the onset of island growth

processes inside the islands are slowed down as compared to the same processes outside the islands, the island composition along their radii will be inhomogeneous. Only when the diffusion rate inside the islands appreciably exceeds the rate of variation of their radii, the island composition may be thought of as homogeneous. To determine the island growth rate, it is necessary to know in what proportion the components are incorporated into an island. This question can only be answered after the mixing entropy of the components is calculated [56].

The solution of this problem can be approached differently. One may use here the phase diagram relating the composition of the old and new phases. Solid solution islands are formed as a rule from the vapor phase and melts. Any phase diagrams of substances in which there are no chemical interactions, can be represented in the form of one or the other modification of the two simplest phase diagrams, namely, the diagram describing melting and crystallization of substances insoluble in each other when in solid state (in Fig. 7.4(a) the diagram with an eutectic point) and the diagram describing melting–crystallization (evaporation–condensation) of substances that form a continuous solid-solution series (Fig. 7.4(b)) [57]. Islands produced from systems of the first type are single-component substances of composition A or B, respectively. At an eutectic point (see Fig. 7.4(b)), islands of both A and B compositions appear simultaneously. In Ref. [57] it is shown that whenever the volume diffusion in the island matrix is fast enough, the expression for the growth rate remains similar to Eq. (7.27), but the flux J_{DR} already consists of the difference of atomic fluxes of components A and B. The average composition of islands changes during their growth by a definite law.

The examination of island growth from single-component melts has shown that the principal mechanisms of island growth are as follows: three-dimensional heat removal into the melt, three-dimensional heat removal into the substrate, and two-dimensional heat removal from the nucleus along the substrate. The limiting stages in this process are the thermal conductivity and the mechanism of atomic incorporation into an island, which depends on the crystalline structure of its surface. The general expression for the island growth rate for each heat transfer

mechanism takes the form

$$v_R = w \frac{J_{TR}\Psi(\theta)}{q R^{3-d'}} , \tag{7.30}$$

where q is the latent heat of phase transition per atom. Concrete expressions for the heat fluxes and the island growth rates can be found in Refs. [13, 58]. Thus, the mechanism of island growth defines its growth rate v_R which enters the basic equations of film condensation kinetics and hence ultimately determines the structure and composition of the growing nanofilm. In more detail, this connection will be analyzed below.

7.5.2 Domain Structure of Nanofilms

In the case of multicomponent systems, more than one phase can be in equilibrium with the original vapor phase. In such cases, some domain structure may arise. For example, in the case of a two-component system with an eutectic point the gas phase may be in equilibrium with two crystalline phases with different compositions. Nucleation processes from the gas phase lead then to a new crystalline phase with some complicated domain structure. In other words, the new phase consists of two equilibrium phases of different compositions. The nucleation process for such systems was described in Ref. [59]. For a description, we introduce the local density of the system, ρ, and the local composition x defined as

$$\rho = \frac{N_1 + N_2}{V} , \quad x = \frac{N_1 - N_2}{N_1 + N_2} , \tag{7.31}$$

where V is the volume of the system, N_1 is the number of atoms of the first type, and N_2 is the number of atoms of the second type. The free energy of such a system with an eutectic point was calculated in Ref. [59]. Employing this result, we can describe the evolution of this system.

For example, in the simplest symmetric case, when the eutectic composition x_e is equal to zero, nucleation and growth of the new phase (characterized by domain structure) is described by the following system of equations:

$$\frac{\partial \rho}{\partial t} = \Delta\rho - \left(\mu_\rho - \mu_{\rho e}\right) + \varepsilon , \quad \mu_\rho = \mu_1 + \mu_2 , \tag{7.32}$$

$$\frac{\partial x}{\partial t} = \Delta x - \vec{v} \times \nabla x - (\mu_x - \mu_{xe}) , \quad \mu_x = \frac{1}{\rho} \left[\mu_1 - \mu_2 - x\,(\mu_1 + \mu_2)\right] . \tag{7.33}$$

Here, $\vec{v}$ is the rate of the "composition flux"

$$\vec{v} = \frac{2}{\rho} \nabla\rho . \tag{7.34}$$

In above equations, μ_ρ is the chemical potential "in density," and μ_x is the chemical potential "in composition." Here $\mu_{\rho e}$, μ_{xe} are the equilibrium values of the chemical potentials, correspondingly. Figure 7.5 shows the dependence of $\mu_x - \mu_{xe}$ on composition in the symmetric case.

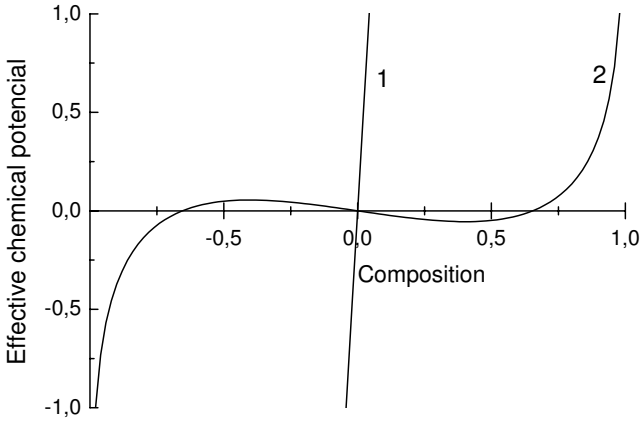

Figure 7.5: The dependence of the "effective" chemical potential $\mu_x - \mu_{xe}$ (cf. Eq. (7.33)) on composition in the eutectic point: (1) is the vapor phase, and (2) is the crystalline phase

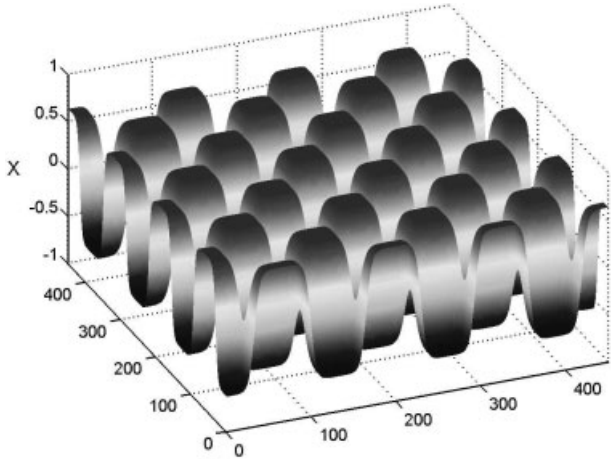

Figure 7.6: Domain structure for a two-component eutectic symmetrical system obtained from Eq. (7.33)

It is evident that for the original gas phase $x = 0$ is the only solution. Therefore, the gas phase cannot possess a domain structure. But for the crystalline phase, the solution $x = 0$ is absolutely unstable. The hydrodynamic force $\vec{v}\nabla x$ results in a heterogeneous decomposition of this phase into two phases with different compositions x_{cr} and $-x_{\text{cr}}$. The final domain structure of the new phase is shown in Fig. 7.6 [59].

7.5.3 Morphological Stability of Nanoisland Shapes

The main problem in the analysis of the morphological stability is to find out whether a given particular form of a vapor-, solution-, or melt-grown island is stable under small perturbations. The analysis of stability is carried out by the following scheme: one assumes the shape of an island or a crystal to be slightly distorted, and then finds out whether this distortion increases or disappears with time. The necessity of examining stability stems from the fact that crystals often grow in the form of dendrites. Dendrites, or tree-like crystals, consist of a central trunk and primary, secondary, etc. branches. They are often observed in nature and in laboratory conditions in melt crystallization. A quantitative analysis of the stability of the shape of the growing crystal was first carried out in the classical paper by Mullins and Sekerka [60]. Numerous experiments on film growth show that the form of nuclei on the surface changes as they grow. They either become edged or, in contrast, unstable or dendrite-like [61]. This fact significantly influences both nucleation and structure of nanofilms.

The growth of islands on the surface from vapor medium differs noticeably from the melt growth of three-dimensional crystals. This difference is first of all associated with the fact that deposited atoms are permanently supplied to the substrate surface and, having a finite lifetime, leave the surface by evaporation. This mechanism introduces essential changes and has thus a crucial effect on the physics of the process. The morphological stability of nanoparticles, growing on the surface of solid substrates, is examined in Ref. [61]. The stability of the shape for a flat disk-shaped island of a height H and a radius R is analyzed there. It is assumed that the island grows due to diffusion of adatoms. A change in the island shape is induced by two factors. On one hand, a ledge on the island surface appears to be in the region of higher concentration gradients of adatoms and must, therefore, increase in size. On the other hand, a ledge increases the curvature and thus increases the saturation vapor density at this point, which in turn slows down the growth rate of the ledge as compared to the neighboring points of the nucleus boundary.

The analysis of the corresponding diffusion equation [61] has shown that the shape of nanoislands becomes unstable in the case, when the island radius R_0 is located within the range $R_1(\nu) < R_0 < R_2(\nu)$, where $R_1(\nu) = R_c$ for $R_c/\sqrt{D_a\tau_r} \ll 1$, R_c is the critical radius of a nanoparticle, and $R_2(\nu) = \left[(\nu^2 - 1)/2\right]\sqrt{D_a\tau_r}$, ν are integers corresponding to the order of modes arising in the course of an island shape change. Note that the conditions that have to be fulfilled for an evolution of an instability of the islands are substantially different from the conditions leading to the formation of dendrites in the course of crystal growth from melts. The shape of the islands is more stable with respect to minor fluctuations as compared to the corresponding shape of three-dimensional crystals.

7.5.4 Structure of the Nanoisland–Vapor Interface

As it was noted before, the physical properties of nanoislands differ significantly from the properties of the respective bulk materials. The reason for this difference consists in the influence of the surface of the particles on their properties. The problem of the development of a rigorous model for the determination of the structure of the interphase between a nanoisland and the surrounding vapor and the influence of surface active substances on the structure have been attracting attention of researchers for a long time (see, for example, [12–14, 62–64]).

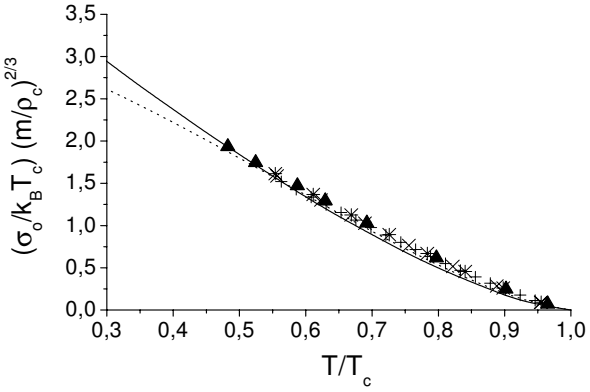

Figure 7.7: Temperature dependence of the surface tension at a planar interface for the van der Waals gas (solid line) and the 2D-lattice gas (dashed line). Experimental data are taken from [64]: ▲ for CH_4; + for Ne; × for Ar; ∗ for Kr

A rigorous perturbation theory of the evolution of a small-sized cluster was developed in the framework of the density functional method in Ref. [64]. In this analysis, for the first time, the size dependence of the surface tension for a cluster on a substrate is defined and the structure of the nanocluster–vapor phase interface is determined analytically. In the case of bubbles (gas nuclei in a liquid), the correction to the surface tension $\sigma(R)$ with respect to the curvature is shown to be of the form

$$\sigma(R) = \sigma_0 \frac{R + (d-1)\delta}{R} + O\left(\frac{1}{R^2}\right) , \tag{7.35}$$

where R is the nanocluster radius, d is the space dimension ($d = 3$ for a drop and $d = 2$ for a disk-shaped island in the growth of nanofilms), σ_0 is the surface tension of a solid material, which is calculated by an approach as outlined in Ref. [64]. The Tolman parameter δ determines here the magnitude of the correction to the surface tension due to the curvature. The value of δ is strictly estimated within the framework of perturbation theory [64]. The $O\left(1/R^2\right)$ term denotes higher corrections within the framework of perturbation theory.

The temperature dependence of the surface tension, as calculated in Ref. [64] for the three-dimensional van der Waals gas and the two-dimensional lattice gas, is displayed in Fig. 7.7. This figure also shows experimental values of the surface tension for four gases, namely, methane, neon, argon, and krypton [64]. As is clearly seen, the theoretical results obtained above for the surface tension of the van der Waals gases are in excellent agreement with experimental data. Figure 7.8 shows the temperature dependence of the Tolman parameter for the van der Waals gas. It can be shown easily that in the temperature range $0.5 < T/T_c < 1$, where T_c is the critical temperature, the Tolman parameter is of the order of $\delta \sim 0.1\sqrt[3]{\rho_c/m} \sim 0.5 \times 10^{-10}$ m. This value is sufficiently large to allow a pronounced effect on nucleation.

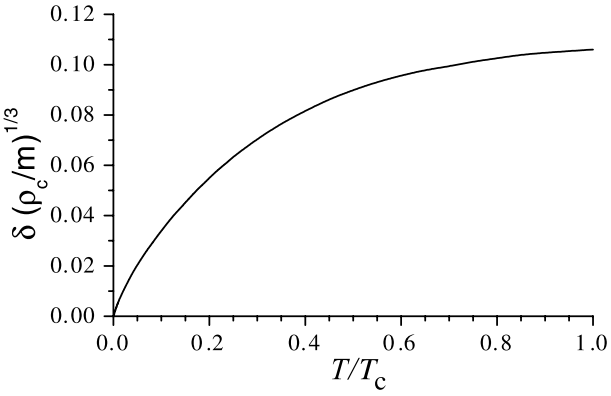

Figure 7.8: Temperature dependence of the Tolman parameter for the three-dimensional van der Waals gas

7.5.5 The Surface Migration of Islands

Numerous experimental studies demonstrate that, at the initial stages of crystal nanofilm condensation on foreign crystalline substrates, the nuclei of a new phase can rather rapidly move over the substrate surface [64–66]. This process serves as an important link in nanofilm structure formation. Such migrations proceed under the action of various external forces: collisions with fast particles of the flow, temperature gradients, electric and magnetic fields, the interaction with moving steps, etc.

As far as the mechanism of island migration is concerned, only two basic models describing the island transfer have been used up to now [67]. The first case is when particle diffusion proceeds only across the island surface, and particles attached to the boundary surface remain immobile about it. Second, an island is assumed to slide over the substrate surface. Many specific mechanisms of the morphological change of the island and of the sliding process have been proposed, but all of them yield relatively low values for the migration velocity and the diffusion coefficient as compared to those actually observed in some cases [18]. In the models of the first type this result is associated with the low values of the coefficients of selfdiffusion of adatoms that cannot provide sufficiently fast island migration. In models of the second type this is caused by the high values of the sliding friction forces between the island and the substrate (i.e., the high activation energy of slide) particularly during epitaxial growth.

We have recently proposed [67] an essentially different model of transfer of growing islands oriented over a foreign substrate. As is well known, under certain conditions mismatch dislocations are generated on the island-substrate interface. If the Burgers vector is located in the slip plane, the motion of the island can be provided by the motion of these dislocations (solitons) [67]. Such mechanism looks preferable as compared to the usual sliding because during the motion of the dislocations at every moment of time almost all atoms of the island remain immobile with respect to the substrate, and it is only a very small group of atoms that move. The passage of a dislocation (compression or rarefaction waves) from one end of an island to the other is equivalent to island displacement by one lattice constant of the sub-

strate [67]. If the dislocation (soliton) velocity is much smaller than the velocity of sound in the material of the film, then the energy losses during its motion are very small, i.e., in such displacement of an island there is almost no friction against the substrate.

The estimate of the "effective" mass of an island migrating over a substrate owing to soliton motion takes the form [67]

$$M_{\text{eff}} = 4cM \ln \frac{1}{\varepsilon - \varepsilon_{\text{c}}} , \tag{7.36}$$

where M is the island mass, c is the ratio of forces acting on an atom from the side of other atoms of the island to those from the side of the substrate, ε is the parameter of lattice mismatch between the film and the substrate, and ε_{c} is the critical lattice mismatch parameter corresponding to the onset of generating mismatch dislocations.

7.6 Kinetics of Nanofilm Condensation

The description of the kinetics of new phase nucleation and the coverage of a condensation surface by the nuclei is one of the most important problems of the theory of first-order surface phase transitions. A large number of papers of both classical and nonclassical character have been devoted to this issue (see, for example, reviews [6,11,13,18–20,68]). The corner stone of any such theory is the correct account of the nonlinear feedback between supersaturation and the size distribution function of new-phase islands. Indeed, growing islands absorb adatoms and thus diminish the supersaturation that is responsible for the nucleation rate and the growth rate of the islands, i.e., ultimately for the distribution function [55].

Earlier theoretical approaches, such as the Zinsmeister model, the Kikuchi model, the Binder model, and the Walton–Rhodin model, were discussed in our review [7]. The kinetic theory [22] yields analytical expressions for all of the basic characteristics of film condensation at the initial stage using especially developed methods for an approximate account of the nonlinear feedback mentioned above. The continuum's model [27] represents thin-film condensation as an order-parameter field relaxation, the surface adatom density being the order parameter in this case. This approach is apparently the most general because it allows a description of film deposition both in terms of nucleation and spinodal decomposition, and for low supersaturations it becomes a standard kinetic model. Furthermore, there is an opinion that it is precisely this approach that will allow us to describe the appearance of the crystalline order during film growth from a vapor or melt.

7.6.1 Perturbation Theory

The variety of approaches to the description of thin-film growth are largely due to the impossibility of an exact analytical solution of the main system of equations of film formation in the ripening stage, i.e., the system consisting of the equation of conservation of matter on the substrate and the kinetic equation for the size distribution function of nuclei (this system is

derived using the division of the whole size axis into three portions: subcritical, critical, and supercritical [27]). The set of equations is of the form [27, 69]

$$\frac{\xi_0}{\xi(t)} - 1 = \frac{(k+1)\tau_r}{n_{1e}t_0} \int_0^\infty \rho^k g(\rho, t)\, \mathrm{d}\rho \ , \tag{7.37}$$

$$\frac{\partial g}{\partial t} + \frac{\xi(t)}{t_0}\frac{\partial g}{\partial \rho} = 0 \ , \tag{7.38}$$

$$g(0, t) = \frac{I(\xi(t))t_0}{\xi(t)} \ , \quad g(\rho, 0) = 0 \ . \tag{7.39}$$

Equation (7.37) describes the law of conservation of matter on the substrate, Eq. (7.38) is the kinetic equation describing the evolution of the size distribution function for nanoparticles, and Eq. (7.39) includes the initial and boundary conditions, where t_0 is the characteristic cluster growth time involved in the law of growth of stable islands (Eq. (7.29)), $g(\rho, t)$ is the size distribution function of stable clusters ρ ($\rho = i^{1/(k+1)}$), $I(\xi)$ is the nucleation rate, ξ_0 is the initial value of supersaturation, and $k = m + 1$.

Practically, all the above-mentioned model approaches employ approximate methods for the solution of this system of equations, which are based on the existence of some small parameter of the theory. From a physical point of view, the "principal" small parameter is the inverse number of particles in a critical nucleus (at the moment of the highest supersaturation). It is just this parameter that is found in the denominator of the nucleation rate exponent. Expanding all the quantities in power series of this small parameter directly, one obtains a series that diverges for sufficiently large times, i.e., it is a not uniformly valid series. In order to provide convergence of the series, it is necessary to use a rigorous perturbation theory [69]. It should be noted that the presence of a small parameter does not always allow one to represent the solution of the mathematical problem in the form of convergent series, i.e., it is not always possible to provide a uniform validity of the series in some particular renormalization procedure [70]. Therefore, it should be especially emphasized that the system of equations governing the kinetics of first-order phase transitions in general and of thin-film condensation in particular admits an analytical solution in the form of a power series with respect to the small parameter. The uniform convergence of this series is provided by the time renormalization procedure that was proposed in Ref. [69].

In the capillary nucleation model, the nucleation rate $I(\xi)$, entering Eq. (7.39), has the form (see Eqs. (7.14) and (7.16))

$$I(\xi) = P(\xi)\mathrm{e}^{-H(\xi)} \ , \tag{7.40}$$

where H is the height of the nucleation barrier and P is the preexponential factor depending on supersaturation. The most important parameter Γ of the phenomenological theory is connected with the function H as follows [27, 69]:

$$\Gamma = -\left.\xi_0 \frac{\mathrm{d}H}{\mathrm{d}\xi}\right|_{\xi=\xi_0} \ . \tag{7.41}$$

For films growing from vapor with high values of ξ_0, we have $\Gamma \sim i_c \gg 1$, where i_c is the number of particles in a critical nucleus at $\xi = \xi_0$. Consequently, the quantity $\varepsilon = 1/\Gamma$ is the small parameter of the given problem.

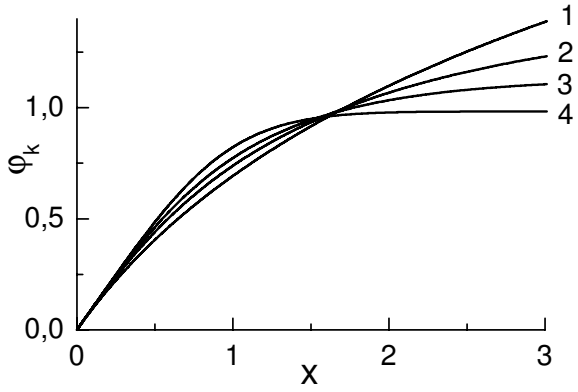

Figure 7.9: Dependence of the function $\varphi_k(x)$ on x: (1): $k = 0$; (2): $k = 1/2$; (3): $k = 1$; (4): $k = 2$

As a result of the analysis performed in Ref. [69], it has been proven that all unknown functions may be expressed here in terms of the function $\varphi_k(x)$ determined by the equation

$$\frac{\mathrm{d}\varphi_k}{\mathrm{d}x} = \exp(-x^k\varphi_k) \ , \quad \varphi_k(0) = 0 \ . \tag{7.42}$$

The dependence of these functions φ_k on x is plotted in Fig. 7.9. We present here only the net result of the first approximation in powers of ε [69] determined via

$$\xi(t) = \frac{\xi_0}{1 + \left(\frac{1}{\Gamma}\right) T^k(t)\, \varphi_k(T(t))} \ , \tag{7.43}$$

$$I(t) = I(\xi_0)\frac{\exp\left[-T^k(t)\varphi_k(T(t))\right]}{1 + \left(\frac{1}{\Gamma}\right) T^k(t)\varphi_k(T(t))} \ , \tag{7.44}$$

$$N(t) = I(\xi_0)t_k\varphi_k(T(t)) \ , \tag{7.45}$$

$$g(\rho,t) = \begin{cases} \frac{I(\xi_0)t_0}{\xi_0}\exp\left[-\left(T(t) - \frac{t_0\rho}{t_k\xi_0}\right)^k \varphi_k\left(T(t) - \frac{t_0\rho}{t_k\xi_0}\right)\right] & \text{for} \quad \rho \le \xi_0\frac{t_k}{t_0}T(t) \ , \\ 0 & \text{for} \quad \rho > \xi_0\frac{t_k}{t_0}T(t) \ . \end{cases} \tag{7.46}$$

$$T = \frac{t}{t_k} - \frac{1}{\Gamma}\int\limits_0^T x^k\varphi_k(x)\ \mathrm{d}x \ , \quad t_k = \frac{t_0}{\xi_0}\left[\frac{n_{1e}\,\xi_0}{(k+1)\Gamma I(\xi_0)\tau}\right]^{1/(k+1)} \ . \tag{7.47}$$

The time dependences of the nucleation rate and the size distribution function of new phase islands are illustrated in Figs. 7.10 and 7.11.

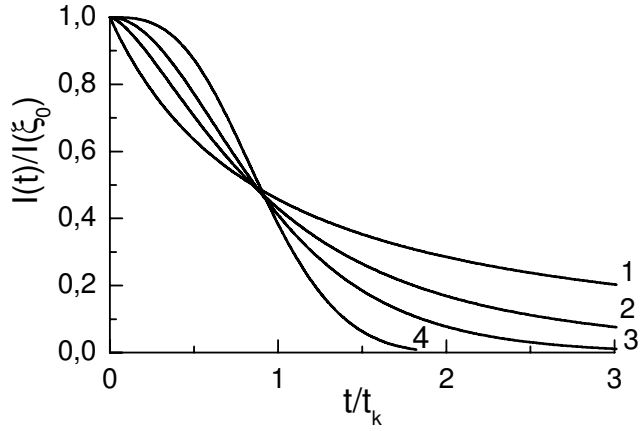

Figure 7.10: Time dependence of the nucleation rate for $\Gamma = 10$: (1): $k = 0$; (2) $k = 1/2$; (3): $k = 1$; (4): $k = 2$

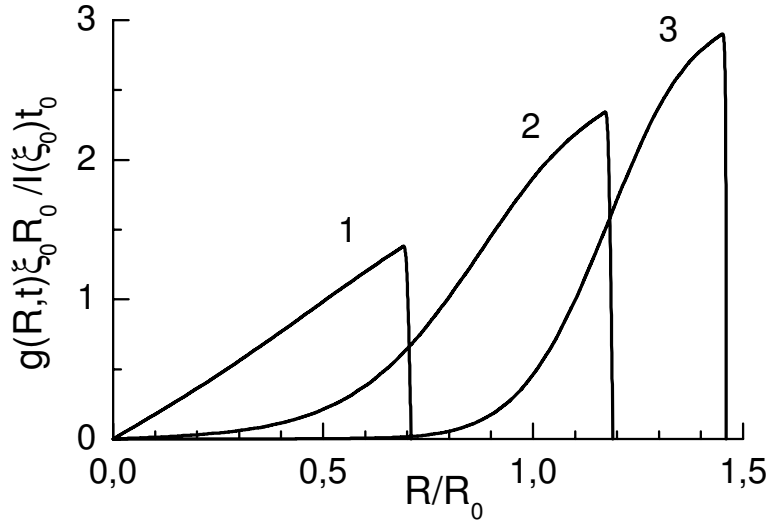

Figure 7.11: Size distribution function of new phase islands for $\Gamma = 10$, $k = 2$: (1) $t = 0.54t_k$; (2) $t = 1.7t_k$; (3) $t = 4.4t_k$

The perturbation theory technique, developed in Ref. [69], turned out to be rather effective. The application of the approach allows us to describe the kinetics of phase transitions proceeding in various systems. Thus, for instance, in Ref. [71] processes of nucleation of nanofilms from solutions or melts are described. Phase transitions in ferroelectrics are investigated in Ref. [71]. The shortcomings of the small parameter technique consist in the impossibility of describing a phase transition for arbitrary τ_r, Γ, and t_0, which can only be done numerically by solving the equations of condensation kinetics.

7.6.2 Nanofilm Condensation at High Supersaturation

If the external source of deposited particles has a large power such that a one-particle nucleus is energetically more advantageous than a two-particle nucleus, i.e., $F(2) > F(1)$, then in the ensemble of adatoms spinodal decomposition starts [17, 21]. In this case, any thermodynamic fluctuations increase in time, the long-wave fluctuations increasing faster.

A theory of spinodal decomposition in a system of adatoms was formulated in Ref. [27]. If the external source of deposited particles has such a power that in a metastable system it creates a supersaturation ξ close to $\xi_{\max}$, which corresponds to approximately $i_c = 2 - 4$, then the character of the nucleation process radically changes. Firstly, the correlation radius in the system may exceed the average cluster size (for $i_c = 1$ the correlation radius is equal to infinity). Secondly, the distribution of subcritical nuclei may differ from the equilibrium distribution, and, thirdly, for small i_c the structure of critical nuclei and, therefore, the character of the interphase energy significantly change. Hence, strongly metastable systems should be considered separately. It is appropriate to describe them in the framework of the continuum's theory [27], which represents a phase transition as a relaxation of the order parameter field. The nucleation rate in this case depends on the supersaturation as

$$I(\xi) = I(\xi_{\max}) \exp\left[-\text{const}(\xi_{\max} - \xi)^2\right] . \tag{7.48}$$

Thus, there exist three ways of relaxation of a supersaturated adatom population. The first is realized in weakly metastable systems where the supersaturation ξ is much lower than $\xi_{\max} = (n_{1s}/n_{1e}) - 1$. In this case, the critical nucleus is so large ($i_c \gg 1$) that its fluctuations lead to a change of the coordinate of its boundary, only, although it has a considerable thickness. The structure of the nucleus itself will remain unchanged. In this case, it is convenient to apply the capillary model, in particular, Eq. (7.14). The second way of relaxation takes place for $\xi \leq \xi_{\max}$. Here the critical nucleus contains only a few particles and is so small that its fluctuations affect not only the boundary, but the whole nucleus. In other words, the internal structure of the critical nucleus itself changes during fluctuations. And, finally, the third way of relaxation is the process via spinodal decomposition. It is realized for $\xi \geq \xi_{\max}$. In this case the system is unstable, $i_c = 1$, and thermal fluctuations generally destroy the structure of the critical nuclei and lead to an increase of periodic fluctuations of substance concentration. This periodicity is a consequence of the fact that near a growing new phase island no other islands are produced, and the whole ensemble of islands is strongly interacting [27].

7.7 Coarsening of Nanofilms

The late stage of nanofilm growth is characterized by the property that the new phase islands, generated earlier, begin to interact. There exist three main types of cluster interactions. The first is cluster merging due to their migration over the surface (the migration mechanisms were briefly discussed in Section 7.5). The second is cluster merging due to their lateral growth. The third is the growth of larger clusters at the expense of the evaporation of smaller ones (Ostwald ripening). The latter type of interaction is realized through generalized diffusion or temperature fields.

As a rule, cluster coalescence, according to the first two types, proceeds in a rather fast way. When merging, the islands are increased in their size. This process can transfer the size of the islands outside the range of nanodimensions. However, the investigation of this problem is outside the scope of this paper, and we do not discuss it here in detail. Readers interested in this phenomenon are referred to the original paper [72] or the reviews Refs. [6, 7], where the problem is discussed more thoroughly. We only note that in preparation of nanostructures, it is necessary to avoid this process of coalescence.

The Ostwald ripening (OR) is a slow process. When changing such parameters as the substrate temperature, and the feed rate of the components of the substrate, one can effectively control the size and composition of nanoparticles. We shall discuss this process in more detail below.

7.7.1 The Ostwald Ripening Stage

The OR stage is the late stage of the phase transition. It starts only when the sources of evaporated adatoms are sufficiently weak and the supersaturation ξ on the substrate tends to zero. No new islands are formed in this situation. The estimate of the starting point of this stage can be found in Refs. [7, 13].

The physical meaning of OR is as follows. At a late stage of evolution of an ensemble of islands they begin to interact in a peculiar manner. This interaction is realized through a generalized self-consistent diffusion field. On a substrate, this field can be established by adatoms with a concentration $\bar{\rho}_a$, vapor atoms with a density $\bar{\rho}_r$ or, if the substrate surface contains linear defects, by adatoms ($\bar{\rho}_l$) adsorbed at the steps. This field depends on the size distribution function, $f(R, t)$, of islands and is in equilibrium with islands of critical size R_c. Islands of size $R < R_c$ are dissolved in the diffusion field because near them the equilibrium concentration ρ_R of atoms exceeds the mean field concentration: $\rho_R > \bar{\rho}_a$, $\rho_R > \bar{\rho}_l$, or $\rho_R > \bar{\rho}_l$. Islands of size $R > R_c$ grow because for them $\rho_R < \bar{\rho}_a$, $\rho_R < \bar{\rho}_l$. The critical size R_c itself continues to increase because the islands absorb the substance from the substrate thus lowering the supersaturation. For this interaction and, therefore, the OR stage to take place, it is necessary that the two-dimensional island density satisfies the inequalities

$$\left[\pi(\bar{R} + \lambda_i)^2\right]^{-1} < N_s < (\pi \bar{R}^2)^{-1} , \tag{7.49}$$

where N_s is the two-dimensional island density, $\bar{R}$ is the mean island radius, $\lambda_i = \lambda_s$ for mass transfer over the substrate surface, and $\lambda_i = \lambda_l$ for mass transfer along the steps, λ_s and λ_l being the mean free path along the substrate surface and along the steps, respectively. Otherwise, if $N_s \geq (\pi R^2)^{-1}$, the islands will "collide" and for $N_s \leq [\pi(R + \lambda_i)]^{-1}$ the adatoms on the substrate will evaporate and will not participate in the OR process provided that $\lambda_i = \lambda_s$. When $\lambda_i = \lambda_l$, the adatoms can leave the step and will not participate in ripening of the ensemble of islands located at the step.

OR of an ensemble of islands in thin films was first investigated by Chakraverty [73]. He examined the evolution of an ensemble of single-component islands with the shape of a spherical segment and located on solid substrates in the regime of complete condensation and also in the presence of atoms sputtered onto the substrate. Chakraverty [73] believed that mass transfer between islands is realized only through a surface diffusion of adatoms and

that the island growth rate can be controlled by both surface diffusion (heterodiffusion) of adatoms and the rate of consumption and emission of atoms by the islands, i.e. by boundary kinetics. He assumed that emission and absorption (building-in) of atoms are realized not by the island contour, but by its whole surface. Such an assumption corresponds to the fact that self-diffusion flows along a free island surface must exceed the heterodiffusion flows on the substrate surface. This statement should have been additionally founded.

The above-mentioned problem was solved more exactly by Geguzin and Kaganovski [74]. They studied the evolution of an ensemble of islands growing by the following mechanisms: surface diffusion of atoms, gas diffusion of atoms, evaporation-condensation of atoms, one-dimensional atomic diffusion along steps, and surface dislocations on a substrate with allowance for a possible island growth control by boundary kinetics. Later, the OR stage of an ensemble of single-component islands with allowance for all possible growth mechanisms and in the presence of atoms sputtered on the substrate was investigated by various authors (see reviews [7, 13]). The authors of these papers found the laws of variation of the critical radius, its height (if the islands had the shape of a flat disk), the island density in time, and island size distribution in a zeroth approximation. The analysis has shown that these characteristics depend substantially on the island growth mechanism and the intensity of atomic supply onto the substrate. According to Refs. [7–13], if a flux of atoms coming onto a substrate has a power-law asymptotics: $g(t) \to ng_0 t^{n-1}$, where $n \geq 0$ and g_0 is a constant, then there exist only two types of sources, namely, weak with $n < (d/p)$ and strong ones with $(d/p) \leq n$.

The main ideas of the OR analysis of such systems have been developed in the pioneering paper by Lifshitz and Slezov [75]. These authors showed that any disperse systems containing new-phase nuclei and old-phase atoms possesses a whole number of common properties inherent only in disperse systems and appearing in the course of their evolutionary growth. From a thermodynamic point of view, this common property of disperse systems is their deviation from equilibrium state simultaneously in many parameters.

One of the main signs showing that a disperse system resides in a nonequilibrium state is the presence of a fairly extended phase interface associated with an excess free energy. At higher temperatures, when an appropriate diffusion mechanism becomes valid, some processes proceed in disperse systems that lead to a relaxation of the excess energy. These processes must be accompanied by a diffusive mass transfer that is responsible for the emergence of OR. This process was named after the German scientist W. Ostwald who, at the beginning of the last century, examined this phenomenon experimentally during precipitation ripening. The basic system of equations describing this process has been presented in numerous works generalized in reviews and monographs [7, 13].

The basis for the analysis of the OR process is the Fokker–Planck equation (7.8) in which the term with the second-order derivative of the distribution function is omitted. When describing the nonisothermal ripening below, we propose a more general system of equations, a particular case of which is the one given. The general OR theory at nonisothermal conditions was constructed in Refs. [76, 77]. The OR processes in multicomponent systems are richer and more diverse than similar processes in single-component systems. In multicomponent systems, substance redistribution is a consequence not only of the Gibbs–Thomson effect but also of the chemically nonequilibrium state. Islands of a chemical substance (phase s) may be stable from the point of view of the Gibbs–Thomson effect but unstable from the point of view of the thermodynamics of chemical reactions.

At the OR stage in multicomponent systems, when the component concentration is $\rho_j(0) \ll 1$ (here $\rho_j(0)$ is the concentration of the component j by the onset of OR), new islands are not formed and all the islands of the ensemble interact with each other through their generalized diffusion field. Islands of phase s with a radius R smaller than the critical radius R_c^s are dissolved in the diffusion field, while islands with a radius exceeding the critical one grow. In a multi-phase system, not only islands of the same phase but also those of different phases will interact, and of all the stable phases only those for which the solution is supersaturated will be stable.

For moderate concentrations of the components, when the law of mass action can be applied to the proceeding chemical reactions, this law can be written in the form

$$\sum_j \nu_j^s \mu_j^s = \ln\left\{\frac{\prod_{s^j}(\rho_j(0))^{\nu_j^s}}{K_\infty^s}\right\} \geq 0\,. \tag{7.50}$$

Here K_∞^s is the equilibrium constant of the sth chemical reaction, s^j is the number of the phase containing the jth component, μ_j^s is the chemical potential of the jth component. If the islands generated in the system do not contain common components, Eq. (7.50) is necessary and sufficient since they will grow independently. Providing the islands contain common components, during their growth substance redistribution among the islands is possible and, although the solution was at first supersaturated in separate components, it may further appear to be unsaturated. In this case Eq. (7.50) is only necessary for a selection of islands capable of further competitive growth.

In multicomponent systems, in the course of OR heat may be released in chemical reactions, which affects the reaction constants. The thermal fields induced due to the heat release in chemical reactions affect the size distribution of islands in a nonlinear manner. The equilibrium concentration of the dissolved substance is not constant, but increases with temperature. The supersaturation will then tend to zero faster than in the isothermal case; however, the substance concentration gradient decreases in the process, which leads in turn to a decrease of the island growth rate. The amount of heat released in the course of the phase transformation therewith decreases (if the system is conservative), which brings about stabilization of the equilibrium concentration, i.e., the diffusion and thermal fields become self-consistent. Thus, the increase of the temperature of the system may lead to a decay of some phases.

The complete system of equations governing the evolution of an ensemble of multicomponent and multiphase islands at the OR stage is given by

$$\frac{\partial f^s(R,t)}{\partial t} + \frac{\partial}{\partial R}\left(f^s(R,t)\,v_R^s\right) = 0\,, \tag{7.51}$$

$$\chi^s \sum_{s^j} \int_0^\infty f^s(R,t) R^{3-d} h^{3-d} J_{DR}^s \,\mathrm{d}R = n_1 |g_{D_j}| t^{n_1-1}\,, \tag{7.52}$$

$$\prod_{j=1}^{n^s} \left(\rho_{jR}^s\right)^{\nu_j^s} = K_R^s(T_R)\,, \quad \frac{J_{jr}^s}{\nu_j^s} = \frac{J_{j'R}^s}{\nu_{j'}^s}\,, \tag{7.53}$$

$$\sum_{s=1}^{k} \chi^s q^s \int_0^\infty f^s(R,t) R^{d-1} h^{3-d} J^s_{T,R}\, \mathrm{d}R = n_2 |g_T| t^{n_2-1} \ , \tag{7.54}$$

$$q^s \sum_{j=1}^{n^s} \nu_j^s J^s_{jR} = J^s_{TR} \ , \quad K^s_R = \varphi(T^s_R) \ . \tag{7.55}$$

Here $f^s(R,t)$ is the size distribution function of islands of phase s, J^s_{jR} is the flux of atoms of the jth component onto an island of phase s, J^s_{TR} is the heat flux released during the growth of phase s, ρ_j is the mean concentration of the jth component on the substrate (or in a vapor), χ^s is a coefficient depending on the island shape, q^s is the chemical reaction heat released during the growth of islands of phase s per molecule of phase s, $|g_{D_j}|$ and $|g_T|$ are the intensities of the fluxes of the jth component and heat, respectively, and, finally, n_1 and n_2 are damping exponents.

A method for the solution of this type of system was developed in Ref. [78]. This method allows the reduction of the system of Eqs. (7.51)–(7.55) to the respective dependences for a single-component system. Then, this set of equations can be solved by the Lifshitz and Slezov approach [75]. However, not long ago, a rigorous asymptotic theory of OR was developed in Ref. [79]. According to the rigorous results obtained there, the asymptotic laws of variation of the critical radius, the height and the density of islands coincide with those of Ref. [79], whereas the asymptotic size distribution function differs from the functions obtained in the zeroth approximation. In accordance with the results obtained in Ref. [79], derived from the asymptotic solution of the set of equations (7.51)–(7.55) for sources with $n < (d/p)$, we get

$$\bar{R}(t) = \text{const}\ R^s_{\mathrm{c}}(t) \ , \quad R^s_{\mathrm{c}}(t) = \text{const}\ (A^s_{pd} t)^{1/p} \ , \tag{7.56}$$

$$h(t) = \text{const}\ (A^s_{pd} t)^{1/p} \ , \quad N(t) = \text{const}\ t^{n-d/p} \ , \tag{7.57}$$

$$f(R,t) = \frac{N(t)}{R_{\mathrm{c}}(t)} P_p\left(\frac{R}{R_{\mathrm{c}}(t)}\right) \ , \tag{7.58}$$

$$P_p(u) = \frac{u^p}{u^{p+1} - (p+1)u + p} \exp\left[\frac{d - n(p+1)}{2} \int_u^{u_p} \frac{x^p\, \mathrm{d}x}{x^{p+1} - (p+1)x + p}\right] . \tag{7.59}$$

Here $P_p(u)$ is the distribution function, normalized to unity, so that $\int_0^\infty P_p(u)\, \mathrm{d}u = 1$, and

$$v_p(u) = \frac{p^p (p-1)^{-(p-1)} (u-1) - u^p}{p\, u^{p-1}} \ . \tag{7.60}$$

Here $u = (p-1)R/pR_{\mathrm{c}}$ and u_p are constants in Eqs. (7.57)–(7.60) determined from the normalization condition $\int P_p\, \mathrm{d}u = 1$, $N(t)$ is the density of the islands of phase s, A^s_{pd} is the kinetic coefficient of phase s depending on mass- or heat-transfer coefficients and on other constants of the deposited material.

The values of these constants are given in Ref. [13] for all the cases of heat and mass transfer that can be realized in the course of evolution of an ensemble of islands. As an example, here we present only the value for the case where the principal mechanism is the surface

diffusion of adatoms and the heat is transferred over the substrate surface. In this case, one gets

$$A^s_{pd} = \frac{27 D^{os} \sigma^s n_0 K_{sb} l T^s_0 (w^s_0)^2 \psi_1(\theta)}{32 \left[D^{os}_s n_0 (q^s)^2 \ln\left(\frac{H}{R^s_1}\right) + K_{sb} \lambda_{\text{eff}} k_{\text{B}} (T^s_0)^2 \right]}, \tag{7.61}$$

where

$$D^{os} = \left(\sum_{j=1}^{n^s} \frac{(p_j)^2 \ln(\lambda_j / R^s_1)}{D_{aj} \rho^s_{j\infty}} \right)^{-1} \tag{7.62}$$

is a generalized surface diffusion coefficient for $\lambda_{sj} \gg R^s_1$; D_{aj} is the coefficient of Brownian motion of adatoms of the jth component, $\psi_1(\theta) = 2(2-3\cos\theta+\cos^3\theta)^{-1}$, with θ being the contact angle, and the other designations were presented above. In the case of atomic sources with $d/p \le n < d/(p-1)$, for both cap-shaped and disk-shaped islands the critical radius is also specified by Eq. (7.56) and the distribution function can be calculated within the kinetic nucleation model (see Eq. (7.46)). The solution also showed [78] that at the OR stage

$$N_{a,n} \sum_{s=1}^{K} q^s |g^s_D| = |g_T| \tag{7.63}$$

and $n_1 = n_2$ hold, i.e., the powers of sources (sinks) of all the phases and heat are related to one another and vary in time by one and the same law. Otherwise, the ripening process is impaired. The equations, allowing the determination of regions in the concentration and temperature space that demonstrate the coexistence of phases, were obtained in Ref. [77]. In Section 7.8, an example of the construction of the phase diagram, i.e., the coexistence of phases for the system of GaN nanoislands, is considered.

Thus, in multicomponent systems the conditions of quasi-thermodynamic equilibrium are favorable to the distribution of the substance of components in a most advantageous way over phases and to the establishment of the regions of phase coexistence, while the action of the surface tension leads to an universal size distribution of islands of the existing phases. Note that such a distribution is only possible for low-component concentrations, when the law of mass action can be applied to the chemical reactions proceeding in the system.

7.7.2 Evolution of the Composition of Nanofilms

It is a well-known fact that the properties of films are mainly determined by their composition. It is precisely the composition that determines the majority of electrophysical, optical, strength, and other properties. To gain an insight into the evolution of film composition, such as to be able to control this composition during film growth, is one of the most important problems of thin-film physics. It was shown in Ref. [80] that at the OR stage, the radius of solid solution islands and their composition are in a one-to-one correspondence. Later, a rigorous theory describing the evolution of phase composition of ensembles of such islands at

the OR stage was formulated in Ref. [80]. In particular, the composition distribution function of islands $\varphi(1/\chi_R, t)$ in the presence of substance sources with $0 \le n < (d/p)$ has the form

$$\varphi\left(\frac{1}{\chi_R}, t\right) = N(t)\Delta(t)P_p(u)\ . \tag{7.64}$$

The average film composition changes according to the law

$$\bar{\chi}(t) = \frac{2\sigma w\rho_{L0}(1+\gamma)}{k_{\mathrm{B}}T(A_p^0 t)^{-1/p}}\ . \tag{7.65}$$

Here σ is the specific interphase energy of the island–vapor boundary; ρ_{L0} is the equilibrium concentration of one of the components, for example, A (Fig. 7.4(b)) in the liquidus line, i.e., in the liquid or vapor phase; γ is the slope of the straight line joining the liquidus and solidus lines (Fig. 7.4(b)).

7.8 Nucleation and Growth of GaN Nanofilms

Processes of nucleation of GaN nanoislands prepared by the molecular beam epitaxy (MBE) and metallorganic chemical vapor deposition (MOCVD) methods are intensively investigated because of their importance in numerous applications in optics, optoelectronics, and microelectronics. The GaN is a stoichiometric compound; therefore, the analysis of nucleation processes is performed [81, 82] in the framework of the theory of island growth of stoichiometric compounds (see Eqs. (7.17)–(7.19)). The analysis shows that at the temperature of the substrate (sapphire covered with a layer of AlN), $T = 480$°C, the probability of nucleation of liquid Ga islands is higher than that of nucleation of islands of GaN compounds. GaN particles are formed after nucleation of islands of liquid Ga as a result of chemical reactions between gallium and nitrogen. At 750 °C $> T \ge$ 600 °C, only GaN is nucleated. The physical origin for such behavior is the following.

Diffusion coefficients, lengths of diffusion jumps, and equilibrium concentrations of Ga and N, determining the generalized coefficient of diffusion, are highly dependent on the substrate temperature. At low temperature, Ga atoms make a main contribution to diffusion mobility; therefore, the probability of nucleation of liquid GaN islands (at $T = 480$ °C gallium is present in a liquid phase) determined by Eq. (7.14) is higher than that of nucleation for islands of GaN compound estimated by Eq. (7.18). At higher temperatures, the mobility of N atoms, the equilibrium concentration of Ga, and the rate of chemical reaction between gallium and nitrogen are increased. It leads to the result that the probability of nucleation for islands of the GaN compound becomes higher as compared to that of Ga.

Mechanisms of growth of islands of GaN in the temperature range $T > 480$ °C and temperature conditions for a change in nanoisland growth mechanisms are described in the papers cited above. Dependences of the nucleation rate and size distribution functions of nanoislands, estimated via Eqs. (7.18) and Eqs. (7.41)–(7.45) for the substrate temperature $T = 650$ °C, are given in Figs. 7.12 and 7.13. The OR of an ensemble of GaN nanoislands is examined in Ref. [81]. The analysis proved that at the substrate temperature $T > 650$ °C, the process of OR of the ensembles is fairly subjected to the laws described by Eqs. (7.56)–(7.59) with a parameter $p = 3$. In Ref. [81] the kinetic phase diagram is plotted as well.

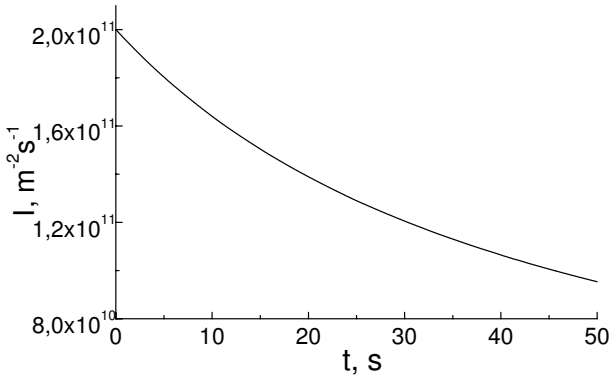

Figure 7.12: Time dependence of the nucleation rate $I(t)$ of GaN on the substrate surface at a temperature $T = 650$ °C

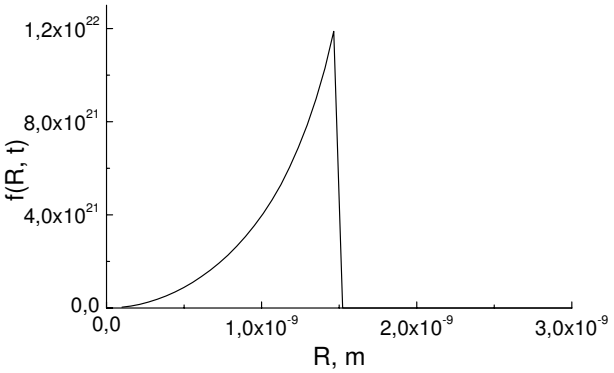

Figure 7.13: Time dependence of the size distribution function, $f(R, t)$, where R is the radius of islands of GaN nuclei on the substrate surface at the nucleation stage at a temperature $T = 650$ °C

The set of equations describing the phase diagram for GaN is of the form

$$Q_{0\mathrm{Ga}} = \rho_{0\mathrm{Ga}} + M^{\mathrm{Ga}} + M^{\mathrm{GaN}}\,, \quad Q_{0\mathrm{N}} = \rho_{0\mathrm{N}} + M^{\mathrm{GaN}}\,, \quad \rho_{0\mathrm{Ga}} = k^{\mathrm{Ga}}\,,$$
$$\left(1 - \frac{1}{Q_{0\mathrm{N}}} M^{\mathrm{GaN}}\right)\left(1 - \frac{1}{Q_{0\mathrm{Ga}}} M^{\mathrm{GaN}} - \frac{1}{Q_{0\mathrm{Ga}}} M^{\mathrm{Ga}}\right) = \frac{K_{\infty}^{s}}{Q_{0\mathrm{N}} Q_{0\mathrm{Ga}}}\,, \quad (7.66)$$

where $Q_{0\mathrm{N}}$ and $Q_{0\mathrm{Ga}}$ are the relative initial amounts of nitrogen and gallium on the substrate and in the new phase nuclei at the beginning of the ripening stage; M^{Ga} and M^{GaN} are the total masses of the nuclei of liquid Ga and GaN at the end of the ripening stage; K_{∞}^{s} is the constant of GaN dissociation on the substrate surface; $\rho_{0\mathrm{Ga}}$ and $\rho_{0\mathrm{N}}$ are the equilibrium concentrations of Ga and N on the substrate; k^{Ga} is a quantity equivalent to the chemical reaction constant for single-component substances. The GaN phase diagram calculated by equations from Eq. (7.66) for three different temperatures is given in Fig. 7.14.

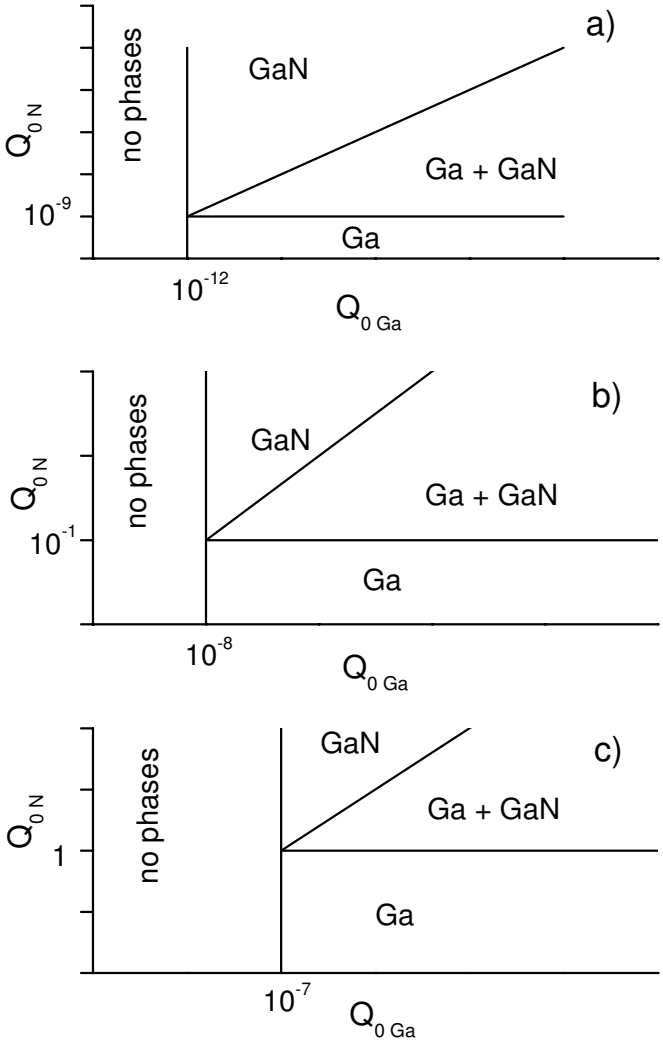

Figure 7.14: Phase diagrams of island GaN films at different temperatures: (1): $T = 480$ °C, (2): $T = 850$ °C, (3): $T = 1000$ °C

7.9 Nucleation of Coherent Nanoislands

At present, the Stranski–Krastanov growth of coherent semiconductor islands, which do not contain lattice mismatch defects, is actively used for obtaining ordered structures with nano-dimensional quantum dots (QDs) [1–4]. The great interest in such structures is due to the prospects of their practical implementation in optoelectronics in application to the localization of charge carriers in the vicinity of QDs [3]. In order to control the physical properties of QDs during the island growth, it is necessary to determine the driving force of nucleation. We note

that two principal mechanisms of nanofilm growth exist. According to the first mechanism, the growth of nanoislands is due to a high density of adsorbed atoms on the wetting layer surface. The islands grow in such cases as a rule by the Volmer–Weber mechanism. In the case when there is a close interaction between a substrate and the film material, the islands ought to grow due to the Stranski–Krastanov mechanism. Thus, in this case, the free energy of an island decreases due to the difference in chemical potentials of the atoms in the two-dimensional adsorbate gas and in the island itself, whereas in the second case, the free energy decreases due to the difference between chemical potentials of the atoms in the wetting layer and in the island. Here, the chemical potential is determined by the difference between the elastic energy and the wetting energy. The island growth by the first mechanism occurs on the wetting layer of constant thickness. In the second case, the thickness of the wetting layer should decrease during nucleation. The reason is that some of the atoms of the wetting layer transfer to islands primarily to decrease the elastic energy [51].

A theory of growth of coherent nanoislands via the Stranski–Krastanov mechanism is outlined in Refs. [42, 51]. There, calculations and estimations are made taking the growth of Ge on (100) and (111) Si surfaces as an example. Experimental investigations to verify the extended theory are described in Ref. [42]. The Ge films were deposited by chemical vapor deposition in a vacuum chamber equipped with a spectroscopy ellipsometer and a mass spectrometer. Digermane Ge_2H_6, which was diluted with pure He, was used as the precursor in the pressure range from 4 mbar. A picture of coherent Ge islands on a (100) surface of Si is given in Fig. 7.15. The following mechanism of the formation of coherent islands, which is based on the experimental data on the growth of Ge on Si(100) [41,42], was considered in Ref. [51]. Initially, the layer-by-layer growth of the Ge film on the Si substrate takes place, since the Si surface energy is noticeably higher than the Ge surface energy, and wetting is favorable. However, Ge and Si have different lattice parameters, and the elastic energy increases with film growth (the elastic energy per atom is constant). The wetting energy per atom continuously decreases, since the Ge atoms are removed farther and farther apart from the substrate. At the moment when the elastic energy per atom is equal to the wetting energy per atom for the upper atoms of the wetting layer, the layer itself is in equilibrium. However, the wetting layer continues to grow and becomes metastable, allowing the elastic energy to relax. One of the possible ways of relaxation is nuclei formation on the wetting layer surface, since the higher clusters have a higher elastic energy compared to the lower clusters. This process starts when the nucleation barrier becomes low enough. Due to this fact, the nuclei formed start to grow and reduce the elastic energy of the film, and the wetting layer becomes thinner thus supplying the growing islands with atoms. After some time, the nucleation process will be completed, since a decrease in the wetting layer thickness will lead to a heightening of the nucleation barrier.

As a result of the studies, the expression for the free energy is derived. The free energy of the formation of the coherent island from the wetting layer is represented by three terms

$$F = \Delta F_{\text{surf}} - (\Delta F_{\text{elas}} - \Delta F_{\text{att}}) \ . \tag{7.67}$$

Here, ΔF_{surf} is the increase in the surface energy due to the formation of an additional surface of film material, ΔF_{elas} is the decrease in the free energy due to the elastic energy relaxation within the island, and ΔF_{att} is the increase in the free energy due to weakening of the attraction

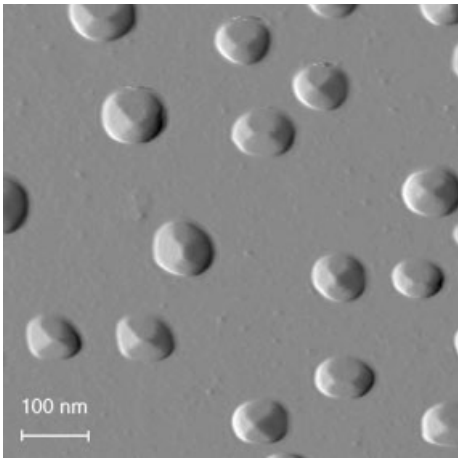

Figure 7.15: SFM picture of Ge coherent islands on Si (100) at $T = 500$ °C and the average deposition rate of 2 monolayers per minute

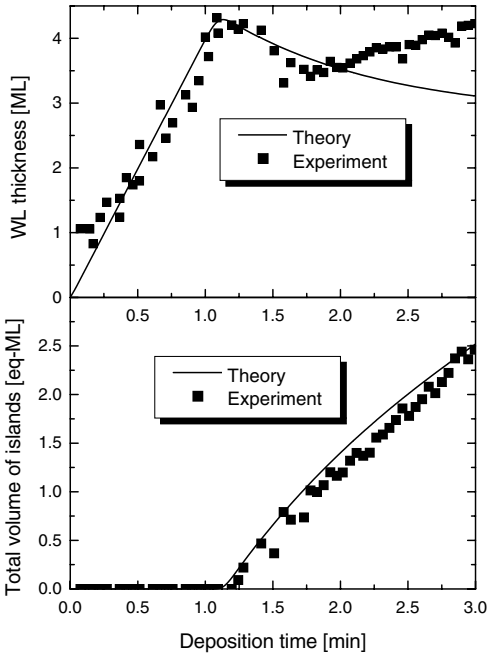

Figure 7.16: Theoretical and experimental dependences of the wetting layer thickness and the total Ge amount in the islands measured in monolayer units versus the deposition time for Si (100)

(wetting) of the island atoms to the substrate. It is evident that the free energy as given by Eq. (7.67) is the only driving force of this nucleation process. Each of the three quantities in Eq. (7.67) depends not only on the number of atoms in the island but also on its shape. This property is the distinction of this model from the theory of nucleation of incoherent islands. To calculate ΔF_{surf}, ΔF_{elas} and ΔF_{att}, the simplest island configuration is used. Specifically, we assume that a cuboid-shaped island with a square base L and height H is located on the wetting strained layer with a height h. For such an island configuration with two parameters L and H, all results are obtained in an analytical form. Calculations given in Ref. [82] show that the free energy Eq. (7.67) can be expressed in this case as follows

$$\frac{F(i,\beta,\xi)}{k_{\text{B}}T} = ai^{2/3}\beta^{1/3} + b\frac{i}{\beta} - c\xi i \ . \tag{7.68}$$

Here k_{B} is the Boltzmann constant, and T is the temperature,

$$a = \frac{4\sigma_f (h_0 l_0^2)^{2/3}}{k_{\text{B}}T} \ , \quad b = \frac{\varkappa}{6\pi}\frac{h_0}{l_0} \ , \quad \varkappa = \frac{\lambda\varepsilon_0^2 h_0 l_0^2}{k_{\text{B}}T} \ . \tag{7.69}$$

Here $\varkappa$ is the elastic-to-thermal energy ratio, $c = \varkappa\gamma$ and $\gamma = \ln(\Phi_\infty/\lambda\varepsilon_0^2 h_0)$ is the constant characterizing the wetting-to-elastic force ratio (the lattice mismatch between the film and a substrate), h_0 is the height of the monolayer film, l_0 is the average interatomic distance in the same layer, d_{f} is the lattice parameter for the film, d_{s} is the lattice parameter for the substrate, λ is the elastic modulus, $\Phi_\infty = \sigma_{\text{s}} - \sigma_{\text{f}} - \sigma_{\text{s–f}}$, where latter σ-parameters are the surface tensions of the substrate, film, and interface between them.

The expression derived for the free energy of a coherent nanoisland allows one to describe the whole process of nucleation of the islands. Thus, the equations for nucleation rate, elastic energy relaxation rate, time–density relations for the islands and evolution laws of the thickness of a wetting layer in dependence on time were obtained. Theoretical and experimental dependences for the wetting layer thickness and the total Ge amount in the islands measured in monolayer units in dependence on the deposition time are given in Fig. 7.16. A model of self-limiting growth of coherent islands is developed in Ref. [8]. It is shown there that in the case when there is a barrier for addition of atoms on the boundary of an island and the barrier is dependent on the island size, the process of secondary nucleation is probable there. Accordingly, the size distribution function of nuclei becomes bimodal. This kind of behavior is substantially different from the size distribution function of incoherent nanoislands, which has only one maximum in all cases. Dependencies of the nucleation rate and size distribution functions of coherent Ge islands on (100) surfaces of Si with the barrier for addition of atoms on the island boundary can be found in Ref. [8].

7.10 Conclusions

In the present chapter, we have presented the basic results of the modern theoretical concepts describing both nucleation and the further evolution of nanoparticles on surfaces. Our presentation was based on the general theory of first-order phase transitions. This theory provides the general approaches allowing one to formulate an unified standpoint in the investigation

of processes proceeding on the substrate surface and in the surrounding volume in the course of nanofilm deposition from gaseous, liquid, amorphous, and solid phases. Employing such generalized approach, we could investigate the influence of various factors on processes of nucleation of nanoparticles. In this chapter, we considered, in particular, the effects of the free energy, arising between substrates and nanoparticles, of the composition of the environment, temperature, electromagnetic radiation, and acidity of a medium on the processes of nanoparticle nucleation. It was shown that the application of the field-theoretical approach to the investigation of nucleation of nanoparticles allows us to calculate the structure of the interface and the dependence of the surface tension on the size of the nanoparticles.

In this chapter, from time to time a comparison of theoretical and experimental results has been given for illustration purposes. A detailed analysis of the huge amount of experimental studies of these phenomena is out of scope of this chapter. A huge amount of literature exists, where experimental devices and techniques for preparation of nanostructures are described. For details, the readers are referred to the respective literature.

Acknowledgements

This work was sponsored by the Russian Foundation for Basic Research (Grant No. 03-03-32503, and 03-01-00574), State Contract No. NFM-1/03, and Complex Program 19 of the Prezidium of the Russian Academy of Sciences.

References

[1] V.A. Shchukin and D. Bimberg, Rev. Mod. Phys. **71**, 1125 (1999).

[2] O.P. Pchelyakov, Yu.B. Bolkhovityanov, A.V. Dvurechenskii, A.I. Nikiforov, A.I. Yakimov, and B. Voigtlander, Thin Solid Films **367**, 75 (2000).

[3] Zh.I. Alferov, Semiconductors **32**, 1 (1998).

[4] Yu.B. Bolkhovityanov, O.P. Pchelyakov, and S.I. Chikichev, Phys.-Usp. **171**, 689 (2001).

[5] M. Roco, R. Williams, and P. Alivisatos (Eds.), *Nanotechnology Research Directions* (Kluwer, Dordrecht, 2000).

[6] S.A. Kukushkin and A.V. Osipov, Usp. Fiz. Nauk **168**, 1083 (1998) (Phys.-Usp. **41**, 983 (1998)).

[7] S.A. Kukushkin and A.V. Osipov, Prog. Surf. Sci. **56**, 1 (1996).

[8] A.V. Osipov, F. Schmitt, S.A. Kukushkin, and P. Hess, Phys. Rev. B **64**, 205421 (2001).

[9] L.K. Kurihana, in *Nanostructured Films and Coatings*, edited by G.M. Chow, I.A. Ovid'ko, and T. Tsakalakos (Kluwer, Dordrecht, 1999), Vol. 78, p. 55.

[10] G.M. Chow, J. Ding, J. Zhang, K. Lee, and D. Surani, Appl. Phys. **83**, 7818 (1998).

[11] D. Kashchiev, *Nucleation: Basic Theory with Applications* (Butterworth-Heinemann, Oxford, 2000).

[12] J.W.P. Schmelzer, J. Colloid Interface. Sci. **242**, 354 (2001).

[13] S.A. Kukushkin and V.V. Slezov, *Disperse Systems on Solid Surfaces* (Nauka, St. Petersburg, 1996) (in Russian).

[14] J.W.P. Schmelzer, G. Röpke, and V.B. Priezzhev (Eds.), *Nucleation Theory and Applications* (Joint Institute for Nuclear Research Publishing House, Dubna, Russia, 2002).

[15] R.S. Berry and B.M. Smirnov, J. Chem. Phys. **114**, 6816 (2001).

[16] V.P. Koverda and V.N. Skokov, Physica A **262**, 376 (1999).

[17] K. Binder and D. Stauffer, Adv. Phys. **25**, 343 (1976).

[18] B. Lewis and J.C. Anderson, *Nucleation and Growth of Thin Films* (Academic Press, New York, 1978).

[19] R. Kern, G. Le Lay, and J.J. Metois, Curr. Top. Mater. Sci. **3**, 139 (1979).

[20] A. Venables, G.D.T. Spiller, and M. Hanbucken, Rep. Prog. Phys. **47**, 399 (1984).

[21] J.S. Langer, Ann. Phys. **65**, 53 (1971).

[22] A.V. Osipov, Thin Solid Films **227**, 111 (1993).

[23] F.M. Kuni, A.K. Shchekin, and A.P. Grinin, Phys.-Usp. **171**, 331 (2001).

[24] V.A. Shneidman and M.C. Weinberg, J. Chem. Phys. **95**, 9148 (1991).

[25] Zd. Kozisek and P. Demo, J. Cryst. Growth **147**, 491 (1995).

[26] A.I. Rusanov, F.M. Kuni, and A.K. Shchekin, Adv. Colloid Interface Sci. A **7**, 122 (1997).

[27] A.V. Osipov, J. Phys. D.: Appl. Phys. **28**, 1670 (1995).

[28] A.A. Chernov, in *Modern Crystallography*, edited by B.K. Vanshtein, A.A. Chernov, and L.A. Shuvalov (Springer, Berlin, 1980), Vol. 3, p. 1.

[29] I. Gutzow and J. Schmelzer, *The Vitreous State: Thermodynamics, Structure, Rheology, and Crystallization* (Springer, Berlin, 1995).

[30] Z.H. Ma, I.K. Sou, K.S. Wong, Z. Yang, and G.K.L. Wong, J. Cryst. Growth **201**, 1218 (1999).

[31] S.H. Cheung, L.X. Zheng, M.H. Xie, S.Y. Tong, and N. Ohtani, Phys. Rev. B **62**, 033304 (2000).

[32] M. Barth and P. Hess, Appl. Phys. Lett. **69**, 1740 (1996).

[33] H.J. Kreuzer, Surf. Sci. **231**, 213 (1990).

[34] A.V. Kandakov, G. Mamedov, and A.V. Osipov, Inorg. Mater. **35**, 710 (1999).

[35] V.P. Zhdanov and B. Kasemo, Surf. Sci. Rep. **20**, 111 (1994).

[36] M.A. Mittsev, N.D. Potekhina, and A.Y. Potekhin, Surf. Sci. **318**, 217 (1994).

[37] J.A. Nieminen and K. Kaski, Phys. Rev. A **40**, 2096 (1989).

[38] M.C. Bartelt and J.W. Evans, J. Phys. A, Math. Gen. **26**, 2743 (1993).

[39] P. Müller and R. Kern, Appl. Surf. Sci. **102**, 6 (1996).

[40] S.A. Kukushkin and T.V. Sakalo, Acta Metall. **41**, 1237 (1993).

[41] V.A. Shchukin, N.N. Ledentsov, P.S. Kop'ev, and D. Bimberg, Phys. Rev. Lett. **75**, 2968 (1995).

[42] S.A. Kukushkin, A.V. Osipov, F. Schmitt, and P. Hess, Semiconductors **36**, 1097 (2002).

[43] G. Shi, J.H. Seinfeld, and K. Okuyama, Phys. Rev. A **41**, 2101 (1990).

[44] V.A. Shneidman, Phys. Rev. A **44**, 2609 (1991).

[45] P. Demo and Zd. Kozisek, Philos. Mag. B **70**, 49 (1994).

[46] S.A. Kukushkin, V.N. Bessolov, A.V. Osipov, and A.V. Luk'yanov, Phys. Solid State **43**, 2229 (2001).
[47] S.A. Kukushkin and A.V. Osipov, J. Phys. Chem. Solids **56**, 831 (1995).
[48] S.A. Kukushkin and A.V. Osipov, J. Phys. Chem. Solids **56**, 211 (1995).
[49] P.V. Gordon, S.A. Kukushkin, and A.V. Osipov, Phys. Solid State **44**, 2175 (2002).
[50] F. Schmitt, A.V. Osipov, and P. Hess, Appl. Surf. Sci. **188**, 103 (2002).
[51] A.V. Osipov, F. Schmitt, S.A. Kukushkin, and P. Hess, Appl. Surf. Sci. **188**, 156 (2002).
[52] Yu.S. Kaganovkii and L.M. Paritskay, Interface Sci. **6**, 165 (1998).
[53] R.W. Cahn and P. Haasen (Eds.), *Physical Metallurgy* (North-Holland, Amsterdam, 1983).
[54] P. Wynblatt and N.A. Gjostein, Acta Metall. **24**, 1165 (1976).
[55] S.A. Kukushkin, Phys. Solid State **35**, 797 (1993).
[56] S.A. Kukushkin and A.V. Osipov, J. Phys. Chem. Solids **56**, 831 (1995).
[57] S.A. Kukushkin and D.A. Grigoriev, Mater. Phys. Mech. **1**, 111 (2000).
[58] S.A. Kukushkin, J. Phys. Chem. Solids **55**, 779 (1994).
[59] S.A. Kukushkin and A.V. Osipov, Russ. J. Phys. Chem. **77**, 1645 (2003).
[60] W.W. Mullins and R.F. Sekerka, J. Appl. Phys. **34**, 323 (1963).
[61] S.A. Kukushkin and A.V. Osipov, Phys. Rev. E **53**, 4964 (1996).
[62] A.K. Shchekin, T.M. Yakovenko, A.I. Rusanov, and F.M. Kuni, Colloid J. **64**, 499 (2002).
[63] A.I. Rusanov, F.M. Kuni, A.P. Grinin, and A.K. Shchekin, Colloid J. **64**, 605 (2002).
[64] P.V. Gordon, S.A. Kukushkin, and A.V. Osipov, Phys. Solid State **44**, 2175 (2002).
[65] R. Kern, G. Le Lay, and J.J. Metois, Curr. Top. Mater. Sci. **3**, 139 (1979).
[66] V.P. Rubets and S.A. Kukushkin, Thin Solid Films **221**, 267 (1992).
[67] S.A. Kukushkin and A.V. Osipov, Surf. Sci. **329**, 135 (1995).
[68] R. Kern, G. Le Lay, and J.J. Metois, Curr. Top. Mater. Sci. **3**, 139 (1979).
[69] S.A. Kukushkin and A.V. Osipov, J. Chem. Phys. **107**, 3247 (1997).
[70] A.H. Nayfeh, *Perturbation Methods* (Wiley, New York, 1973).
[71] S.A. Kukushkin and A.V. Osipov, Phys. Rev. B **65**, 174101 (2002).
[72] A.V. Osipov, Thin Solid Films **231**, 173 (1995).
[73] B.K. Chakraverty, J. Phys. Chem. Solids **28**, 2413 (1967).
[74] Ya.E. Geguzin and Yu.S. Kaganovski, Sov. Phys.-Usp. **21**, 611 (1978).
[75] I.M. Lifshitz and V.V. Slezov, Sov. Phys.-JETP **35**, 331 (1958).
[76] S.A. Kukushkin and V.V. Slezov, Phys. Solid State **29**, 2092 (1987).
[77] S.A. Kukushkin, Phys. Solid State **35**, 804 (1993).
[78] V.V. Slezov, Phys. Rep. **17**, 1 (1995).
[79] S.A. Kukushkin and A.V. Osipov, JETP **113**, 1201 (1998).
[80] S.A. Kukushkin and A.V. Osipov, J. Appl. Phys. **86**, 1370 (2002).
[81] S.A. Kukushkin, V.N. Bessolov, A.V. Osipov, and A.V. Luk'yanov, Phys. Solid State **43**, 2229 (2001).
[82] S.A. Kukushkin, V.N. Bessolov, A.V. Osipov, and A.V. Luk'yanov, Phys. Solid State **44**, 1399 (2002).

8 Diamonds by Transport Reactions with Vitreous Carbon and from the Plasma Torch: New and Old Methods of Metastable Diamond Synthesis and Growth

Ivan Gutzow, Snejana Todorova, Lyubomir Kostadinov, Emil Stoyanov, Victoria Guencheva, Günther Völksch, Helga Dunken, and Christian Rüssel

Everything is vague to a degree you do not realize
till you have tried to make it precise.
Bertrand Russell

The aim of the present chapter is to summarize existing and newly developed theoretical ideas on the physical and chemical nature of the processes of nucleation and growth of diamond at metastable conditions. At these conditions the thermodynamically stable modification of carbon–graphite should be expected to form, but as it turns out, diamond can also be obtained and even exclusively formed. Using the classical capillary theory of nucleation, Ostwald's rule of stages is accommodated in a first theoretical approach to explain diamond nucleation, accounting for the peculiarities of diamond structure and growth. In a second theoretical scenario, the possibilities are analyzed that in some cases (e.g., on a substrate, heavily bombarded by incoming vapor phase molecules) the 2D pressure in the condensate may be so high that nucleation takes place in a pseudo-metastable manner: at pressures, corresponding to the range of thermodynamic stability of diamonds. A third new possibility for diamond formation is also considered connected with the size dependence of stability of liquid carbon droplets of graphite and of diamond for nanosized clusters. Thus the possibility of another theoretical model of evolution (vapor $\rightarrow$ liquid carbon $\rightarrow$ diamond) is analyzed as well. Accounting for the phase diagram of carbon, this possibility seems mostly reserved to processes of binodal or spinodal nucleation at extreme vapor pressures and temperatures, e.g., in interstellar space. Particular attention is given also on the effect of known or even hypothetical carbonaceous compounds in diamond growth and nucleation, on the influence of atomic hydrogen on carbon incorporation into diamond lattices, and on the design of optimal C(hemical)V(apor)D(eposition)-gaseous transport reaction schemes for diamond growth and nucleation. Results are given on two different experimental realizations of diamond synthesis, including nucleation and growth. A comparison with own experimental results and existing experimental evidence demonstrates both the possible applications and the limits of physical and chemical approaches explaining essential features in metastable diamond synthesis.

8.1 Introduction

In the present chapter, an effort is made to describe the possibilities and present first results obtained by the application of two new and several more or less known, even classical, variants of metastable diamond synthesis. According to one of these methods, as a precursor carbon source, guaranteeing a constant thermodynamic driving force of the process, vitreous carbon

Nucleation Theory and Applications. edited by J. W. P. Schmelzer

ISBN: 3-527-40469-4

and other carbon materials with frozen-in disorder or dispersity and thus with an increased thermodynamic potential, may be employed. In this way, diamond seeds can be grown at constant temperature in a closed volume of simple reaction vessels. The first experimentally obtained results indicate that this method may, when compared with other techniques of diamond synthesis and growth at metastable conditions, promise several technological advantages. More important advantage, according to the opinion of the present authors, is, however, that this method seems to give an example of the possibilities, a release of kinetically frozen-in disorder and configurational energy, accumulated in solids with an increased thermodynamic potential, can offer. According to the second method of metastable diamond synthesis, results of which are also summarized in the framework of the present investigation, diamond microcrystals are directly formed and then grown up in conditions of a new variant of plasma-assisted chemical vapor deposition (CVD) methods. The particularly significant point in this second approach is that diamond is thus not only grown, but also nucleated at metastable conditions, at which graphite is the thermodynamically stable crystalline modification of carbon. Of significance is the possibility of uniting both above-mentioned methods of metastable diamond synthesis by first forming a glass-like carbon microdroplet in the plasma torch and then a diamond microcrystal. After that the diamond microcrystal can be grown up by a process of isothermal glass → crystal plasma sustained vacuum distillation.

In the first group of our experiments, the kinetic barrier, arresting the disordered solid in a state of increased thermodynamic potential and reactivity, is reduced or removed, thus enabling the reaction **carbon glass → diamond** to take place. This reduction is most conveniently performed with gaseous transport reactions in a closed reaction volume at normal (or even reduced) pressure and at temperatures in the vicinity of 1300 K. Other possibilities, which have also been tested by us, are to facilitate this reaction in appropriate solvents of carbon (in silicate melts or in molten alloys). This second way of experimental realization brought, however, no distinct results so far. Thermodynamic calculations and kinetic estimates show, nevertheless, that this second possibility could also result in a realization of the above given reaction path. It corresponds, in some respect, both to diamond synthesis on geological scales (e.g., in olivine-type silicate melts, leading to South Africa's kimberlite diamond deposits) or to the direct high-pressure synthesis of technical diamond in Ni alloys at diamond stable conditions. Latter possibility was in fact realized experimentally years ago [1]. From a thermodynamic point of view at normal pressure the above reaction is a change from the state of nonequilibrium (the carbon glass) to a metastable phase (the diamond). This is the case since graphite and not diamond is the allotropic form of carbon, stable at normal pressure and temperatures we employ.

The larger part of the experimental results and some of the theoretical considerations, on which this chapter is based, have been reported by the present authors and their colleagues in several preceding publications, which are listed below. Here things are theoretically reconsidered, and new problems, possibilities, and solutions for a further development are outlined and discussed, taking into account newly obtained theoretical and experimental findings. These reconsiderations and developments, although based mostly on results procured by a large group of authors working both in Sofia and in Jena, were done primarily by the first three authors of the present chapter. These authors thus took the responsibility not only for the way of outlining most of the new developments reported here, but also for any possible miscalculations and misunderstandings that may eventually arise.

8.2 Some History

In the present-day artificial diamond synthesis, two main possibilities are employed. The first one is diamond formation and growth at high pressures and temperatures in the region of the carbon phase diagram, where diamond is the stable phase. The second method is metastable diamond synthesis and growth at relatively low temperatures and normal (or even reduced) pressure in the range of the phase diagram, where graphite is the stable modification. The realization of this second path of diamond synthesis can be interpreted as being based on the predictions of Ostwald's rule of stages and its kinetic interpretation in the framework of the classical nucleation theory. Here this possibility is discussed in several variants taking into consideration the thermodynamic peculiarities of the graphite to diamond transition. Presently, the technical applications of metastable diamond synthesis are mostly realized in different variants of CVD processes, taking place either at constant temperature or in temperature gradients and usually in the $C/H_2/H^*$ system [2, 3].

Efforts to synthesize artificially diamonds have a long and exciting history. First attempts in this direction were reported as early as 1870 and an account of the various techniques employed may be traced in the older chemistry textbooks [4] and in the subsequent reference literature (see [5] and especially [6]). Besides several of these efforts, which can be termed as obvious failures or even as falsifications, usually the experiments of the famous French chemist Henri Moissan (who first obtained elemental fluorine) have to be mentioned. In his investigations, Moissan subjected the highly dispersed graphite (or carbon in metallic solutions) in several ingenious ways (see [6, 7]) to short pulses of relatively high pressures and to temperature rises (up to 1500–1800 K) and received in fact hard, translucent microcrystals. These crystals were, however, identified later on as metal carbides. Considering the thermodynamic data on different carbon modifications and the mentioned phase diagram of carbon available now, it is evident that Moissan could not succeed at these conditions in the direct synthesis of diamond, i.e., in the **graphite** $\rightarrow$ **diamond** transition in the field of stability of diamond. Both temperatures and pressures he had at his disposal were too low. In fact, neither of the early experiments on diamond synthesis claims, performed before 1955, has been successfully repeated.

In 1955, in the laboratories of the General Electric Company (Schenectady, NY) the first direct diamond synthesis was performed at pressures of 70 000 bar and temperatures 2000 K. At nearly the same time, similar successful experiments were made in Sweden [5, 7, 8], and then in the Soviet Union, in South Africa, and later on in the laboratories of every industrialized nation. Thus, all over the world the direct synthesis of diamond was introduced in technological scales [9, 10]. This development was based, on one hand, on the thermodynamic predictions of several authors (Simon [11], Leipounskii [12], Berman and Simon [13]). They determined the equilibrium $P(T)$ curve, separating the range of stable existence of diamond and graphite in the phase diagram of carbon (the famous Simon–Leipounskii line). On the other hand, it was based on the results of the experiments of P. W. Bridgman, who conducted prolonged studies on the changes in various materials subjected to high pressures. These experiments gave the clue for the development of the means of producing high-pressure, high-temperature equipment (e.g., the Belt apparatus, see the literature summarized in Refs. [9, 10]). Usually in this way in a volume of several cubic centimeters diamond microcrystals (for technical uses mostly) are produced in experimental times of minutes.

However, in recent developments [14, 15], which became possible with the construction of new high-temperature–high-pressure synthesizing equipment, even single-crystal diamonds up to one or two carats have been synthesized, using the direct, "stable" way of synthesis, via appropriate metallic solutions and durations of growth up to 24 h (1 metric carat = 200 mg). As a particularly interesting development in this line, experiments on the "explosive" synthesis of diamonds have to be mentioned, performed beginning from the 1960s [16]. In these experiments (resembling some features of Moissan's ingenious investigations), in steel cameras by the ignition of appropriate explosives combined pressure and temperature shock waves are produced (reaching up to 300 000 bar) with millisecond duration. By this method, populations of micro- or nano-diamonds are formed (see [16, 17]). Explosive synthesis is thus also a variant of diamond formation at "stable" conditions. The story of the realization of the first metastable diamond synthesis may be followed in more detail in several review articles [2, 3, 18, 19].

According to the first classical variants of this method, diamond seeds (usually fine ground diamond powders) are brought into contact with supersaturated carbonaceous gases (methane CH_4 [2, 3], alcohol–water solutions [20, 21]) or with gaseous mixtures, in which the Bouduard reaction ($CO_2 + C \Leftrightarrow 2CO$) can take place at normal pressures and at 1000–1300 K. The results of the last 50 years have shown that in most cases of metastable gaseous diamond synthesis, a very high energy of the growth sustaining vapor mixtures is required (plasma-assisted growth or hot filaments, at 3000 K) guaranteeing the dissociation of hydrogen and thus the presence of atomar hydrogen H^* (or oxygen O^*). Consequently, the first essential factor in metastable diamond growth experiments seems to be the nature and activity of the precursor carbon gas. The second significant factor, the kinetic factor to be accounted for, is determined by the mechanism of incorporation of ambient phase molecules into the growing diamond face. This process depends mainly on the chemical transport reaction employed. Because of the enormous strength of the C–C bonding, the direct incorporation of vapor phase C atoms at the desired relatively low temperatures (1000–1400 K) into the diamond lattice is very improbable.

Detailed investigations of the system $C/H_2/H^*$ show that most probably at plasma conditions hydrogen atoms (H^*) are adsorbed on the diamond surface, occupying active growth sites $C^{\#}$. As the next step, the incorporation of new carbon atoms into the diamond lattice is realized via the reaction [22, 23] $C(H^*) + H^* \rightarrow C^* + H_2 \uparrow$, thus forming "dangling bond" diamond lattice sites and molecular hydrogen [24]. At temperatures about 1400 K this process proceeds much easier than the direct incorporation of C atoms into the diamond face. It is claimed that the incorporation of carbon atoms into the diamond lattice at relatively low temperatures (below 500 K, see [25, 26]) can be additionally enhanced in H/CH_4 gaseous mixtures by the presence of halogen atoms. Via the reaction $H_2 + Cl^* \rightarrow H^* + HCl$, they catalyze the formation of atomic hydrogen at the diamond face at lower temperatures. Metastable growth only via the halogen reaction $CI_4 \Leftrightarrow C + I_4$ has also been reported [27]. Of great significance for the following discussion is also that in some plasma-assisted CVD condensation techniques not only diamond growth but also diamond nucleation was achieved at metastable (or, at least, at seemingly metastable) conditions [3, 20, 21, 28]. Here both hydrogen plasma-assisted CVD processes, taking place at relatively cold anodes at high condensation rates, and evaporation–condensation methods (eventually via intermediate formation of carbon clusters at 3000–4000 K) from pure carbon vapors have to be mentioned. These and similar nucleation

experiments, also performed by the present authors, are discussed in detail in Sect. 8.4.4. Of particular interest for the present discussion are also the results when the reaction **carbon glass → diamond** or other possible changes of the type **active carbon materials → diamond** are used to grow diamond by employing the appropriate gas transport reactions [29, 30]. The results thus obtained with the so-called vitreous carbon are described in both its thermodynamic premises and kinetic limitations in several of the subsequent sections.

Glasses and defect solid states of matter are, from a thermodynamic point of view, non-equilibrium frozen-in systems. In such systems not only a structure with increased disorder, but also a state with increased thermodynamic potential is arrested [31]. This feature determines higher vapor pressure and solubility and increased reactivity of vitreous and vitreous-like solids [32, 33]. In any glass, the possibility is thus accumulated to be the source of an increased thermodynamic driving force (i.e., of increased supersaturation) in processes of both phase segregation and crystallization. This possibility can be realized, as mentioned above, provided the kinetic restrictions, arresting the increased disorder and the higher thermodynamic potential of glasses, are reduced or even removed. This can be achieved by the dissolution of the vitreous solid in an appropriate solvent [32]. There is a well-known classical experiment in this respect: The dissolution of SiO_2 as two forms, once as a glass and then as a quartz, in hydrofluoric acid gives in the calorimeter a considerable enthalpy difference. In Refs. [31, 33], results are summarized for several glass-forming systems, where, taking into account the difference in solubility of the glass and of the crystal, the respective Gibbs potential difference between the glass and the crystal, ΔG, is calculated and compared with the results of the corresponding calorimetric measurements.

The use of glass as a source of constant supersaturation in crystallization processes was proposed for the first time by Nacken [34] for isothermal growth of quartz crystals from alkaline aqueous solutions of quartz glass at temperatures higher than the critical temperature, T_c, of water. These experiments failed, because (as becomes evident, now [29, 31]) the supersaturation in Nacken's experiments was too high: So instead of the expected growth of the introduced quartz seed crystals, new quartz microcrystals were formed. At lower supersaturations, as they were realized in experiments performed by Grantscharova and Gutzow [33, 35] with a simple model glass and its crystal (phenolphthaleine, growing from aqueous solution), smooth growth of the introduced seed crystals was in fact experimentally observed. These experiments and results on solution growth of selenium single crystals, sustained by vitreous selenium [36], gave the impetus for our experiments with diamond and vitreous carbon.

Before going into the details we would like, however, to return to one of the classical experiments on diamond synthesis performed at the end of the 19th century. This experiment, sometimes believed to be the only example of successful diamond synthesis in the 19th century, displays features of both diamond nucleation and growth at conditions where diamond is metastable. It was reported in 1880 in a paper submitted to the Royal Society in London by the Scottish chemist James Ballantyne Hannay [37]. In this paper, Hannay claims that he has synthesized small diamond crystals by heating in sealed massive wrought-iron tubes for 15 h at "red heat" (i.e., probably at $\sim$ 1100 K), a mixture of "paraffin oil" (i.e., of naphta), "bone oil" (i.e., the pyrrole and pyridine containing product of the dry distillation of animal bones: of organic constituents, rich in organically bond nitrogen), and alkali metals (usually lithium). Lithium in elemental form produces with the paraffins nascent hydrogen (i.e., H^*) and elemental carbon. As a necessary ingredient to this mixture, "lamp sooth" (i.e., finely dis-

persed, almost amorphous carbon in a very reaction-active form) was also always added. Thus, according to the present-day considerations (see [5, 7]) in Hannay's reaction tubes a very active reaction mixture of active hydrogen and carbon existed at the mentioned temperature at approximately 1000 bar. At these conditions the transport reaction $HCN + H_2 \rightarrow NH_3 + C$ could have taken place (as argued in [5]) leading to diamond growth. Hannay mentions in fact about the typical deadly smell of hydrocyanic acid when he opened his reaction vessels. Eleven of the crystals he synthesized were officially deposited by him with the curator of the British Museum, London. Many years later (1935), a well-known crystallographer, Dame Kathlean Lonsdale [7], gave an X-ray proof (not known at Hannay's times) that 10 of the 11 deposited crystals are in fact diamonds, and (and this is essential!) that their optical luminescence does not correspond to any of natural diamonds, known at this time. So, has in fact Hannay succeeded in diamond synthesis? Is it really possible to obtain diamonds at his conditions? Despite several attempts neither of his experiments could be successfully repeated. Moreover, in later times it was claimed [7] that very rare natural diamonds exist having a luminescence similar to Hannay's diamond samples. Could he had possessed in 1880 such rare natural diamonds? These are serious, still unanswered questions and this is why there have been also opinions expressed in the literature that Hannay may have been an imposter, or that he has been the victim of some strange (wanted or unwanted) perfectly done falsification.

In our present analysis, we make an effort to use the existing experimental and theoretical results and our own experience in explaining essential features in several types of diamond synthesis, occurring in nature at geological and at cosmic conditions. Can our experience also be of help in solving the mystery with Hannay's diamonds? In Sect. 8.3.5, considerations are given, supporting the possibility that in Hannay's iron tubes diamond growth and even diamond nucleation may have in fact taken place.

This analysis as well as the whole discussion of the experimental and technical possibilities of any method of metastable diamond synthesis requires first the construction of the complete phase diagram of carbon for its equilibrium vapor, liquid, and crystalline phases. Moreover, the introduction of the properties of thermodynamically nonstable, active carbon materials (such as the mentioned vitreous carbons, carbon blacks and sooth, even of fullerenes, etc.) into these diagrams is necessary. A first attempt toward the construction of the *thermodynamic* phase diagram of carbon, outlining the possibilities of phase transformations and growth, was made in two of our previous contributions [30, 38]. In the following two sections 8.3.1 and 8.3.2, they are introduced together with an enlarged classical phase diagram of carbon. These diagrams, we hope, not only outline possible ways of metastable synthesis from the vapor phase, by using different CVD procedures or reactions, but also indicate unexpected possibilities of diamond synthesis in nature and especially of cosmic diamond synthesis. The synthesis of cosmic diamond, as it seems, may explain both processes taking place in catastrophic supernovae explosions in the universe and in the quiet of industrial laboratories, where thin diamond films and diamond gems are synthesized.

8.3 Basic Theoretical and Empirical Considerations

8.3.1 The Phase Diagram of Carbon and Diamond and Graphite Formation

In Fig. 8.1, the phase diagram of elementary carbon is given as constructed by Bundy (see [5]). It not only illustrates the possible areas of stability of graphite, diamond, and liquid carbon, but also shows a schematical prolongation to the carbon vapor phase. At very high pressures, the possible existences of a third still hypothetical phase ("metallic" carbon) is indicated in analogy with the extrapolated phase diagrams of Si, Ge, and Sn [39]. By solid lines, the experimentally and thermodynamically more or less confirmed course of the coexistence curves is drawn between the corresponding equilibrium phases of carbon. By dashed lines, the extrap-

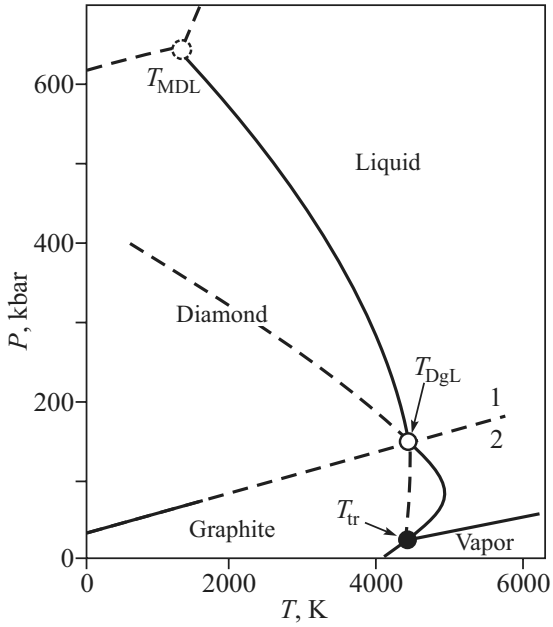

Figure 8.1: The phase diagram of carbon in p vs. T coordinates according to Bundy (see Ref. [5] and the literature cited there). The thermodynamic stability fields of graphite, diamond, and liquid carbon are separated by solid lines, prolonged into the metastable regions as dashed lines. Also with a dashed line, the Simon–Leipounskii line (Eq. (8.1)) is indicated in its extrapolation for temperatures above 1700 K (where no thermodynamic data for diamond are available). Additionally introduced as a solid line is the vapor/liquid equilibrium course (more clearly seen in Fig. 8.2). With T_{MDL}, T_{DgL}, and T_{tr}, the three triple points (metallic carbon/diamond/liquid, diamond/graphite/liquid, and graphite/liquid/vapor) are specified. Metallic carbon is introduced as a hypothetical possibility in line with similar metallic phases for Pb, Sn, Si, and Ge. With (1) and (2) the hypothetical areas of diamond-like and graphite-like liquid carbon are indicated

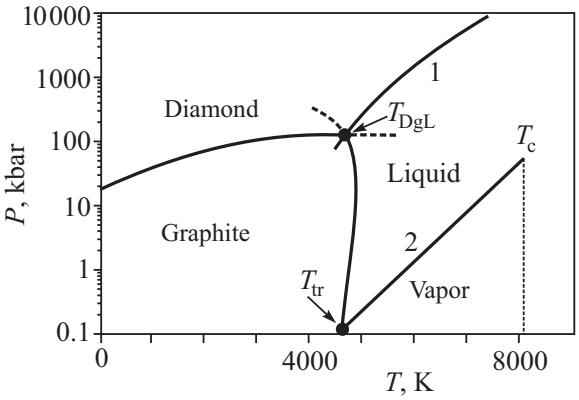

Figure 8.2: The phase diagram of carbon in logarithmic representation according to Bundy et al. (see [5]). The different triple points as in Fig. 8.1 are indicated. With T_c the critical point of carbon is denoted estimated in Eq. (8.2)

olated coexistence lines of the same phases in the respective metastable regions are shown: They illustrate schematically *possible* changes.

Of greatest significance for the direct synthesis of diamond is the already mentioned Simon–Leipounskii–Berman line separating diamond from graphite. It can be approximated by a straight line

$$p = A_0 + B_0 T \ , \tag{8.1}$$

Its knowledge enabled the first technical "direct" synthesis of diamond. The carbon vapor–liquid coexistence line in Fig. 8.1 is introduced in the form as proposed by Wentorf (see again [5]). This line is of great significance in analyzing the condensation processes in the metastable synthesis of diamond to be discussed below. The vapor–liquid–graphite fields in the vicinity of the triple point T_{tr} of graphite–liquid–vapor become more evident in Bundy's logarithmic representation (Fig. 8.2), also used by Wentorf [5]. For the melting point of graphite usually $T_m = 4000$ K is given as an estimate.

From Figs. 8.1 and 8.2, the possible three triple points in the discussed phase diagram are evident as well: metallic carbon–diamond–melt T_{MDL}; diamond–graphite–melt T_{DgL}; and the already mentioned vapor coexistence temperature T_{tr}. In Figs. 8.1 and 8.2, we have also introduced the critical point T_c of carbon. It is estimated in older literature (see [5]) from less convincing vapor pressure data in $\log p$ vs. T constructions in the limits from $T_c \cong$ 7000 K to $T_c \cong 8000$ K at $p_c \cong 1500$ bar. More recent estimates, made in the framework of Lennard–Jones model theories of liquid carbon [40], give also $T_c \cong 7000$ K. In Table 8.1, we have summarized the temperatures and pressures corresponding to the mentioned coexistence points. We introduce the following estimates as the values of the critical parameters T_c, V_c, and p_c of carbon: We employ the empirical rule Eq. (8.2) as a simplest estimate of the critical temperature, T_c, of carbon [41]:

$$T_c = \tfrac{5}{2} T_m \tag{8.2}$$

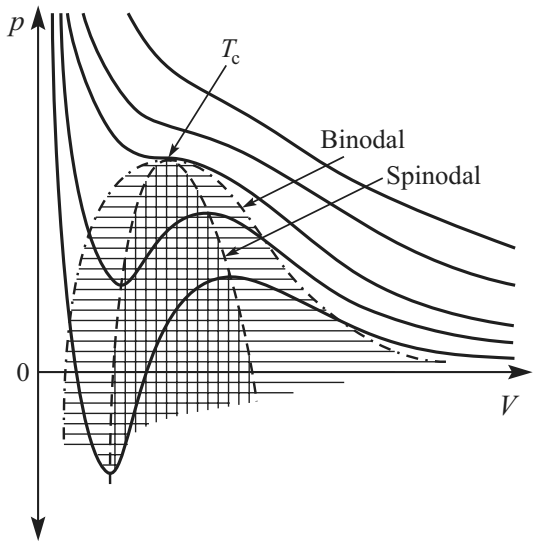

Figure 8.3: The pV diagram of vapor–liquid phase coexistence in terms of the van der Waals equation of state. The binodal and spinodal curves are both terminating at the critical point T_c

resulting in $T_c \cong 10^4$ K. Utilizing, as a first approximation, the van der Waals equation of state and taking the constants a_*, b_* from this equation, the critical pressure p_c and volume V_c are given by

$$p_c = \frac{a_*}{27b_*^2}\,, \quad V_c = 3b_*\,, \quad T_c = \frac{8a_*}{27b_*^2 R}\,, \quad \frac{p_c V_c}{RT_c} = 0.375\,. \tag{8.3}$$

The critical volume of carbonaceous compounds is usually calculated via the respective parachor value, Π, which for carbon is given as $\Pi = 9$. Thus, with the empirical rule [42]

$$V_c \cong (0.4\Pi + 11)^{1.25} \tag{8.4}$$

the value $V_c \cong 15\ \mathrm{cm}^3/\ \mathrm{mol}$ is obtained. With Eqs. (8.3) it follows

$$p_c \cong \frac{21T_c}{V_c - 8} \tag{8.5}$$

and with Eq. (8.2) and the mentioned value of T_m (as given in Table 8.1) we obtain values well above older estimates $p_c \cong 3.5 \times 10^4$ bar. From vapor pressure measurements usually the boiling point, T_b, of liquid carbon (at $p = 1$ atm) is estimated, in earlier literature, to be 3800 K (i.e., well below its melting point, T_m).

Summarizing the foregoing evidence it has also to be mentioned that according to the above calculations, C_1 was considered as the only possible form of carbon vapor. Other forms of aggregation (e.g., C_2, C_3, ..., C_n [43]) with different degrees of molecular polymerization were disregarded. Below the critical temperature, T_c, condensation of liquid carbon should

be possible and (considering what is known from the van der Waals equation of state for any substance) a population of liquid droplets can be formed either via nucleation and growth (between binodal and spinodal) or via a spinodal decomposition process (below the spinodal, see Fig. 8.3). As typical for spinodal decomposition (since the value of the surface energy vapor/liquid, σ, tends to zero), the form and size of spinodal droplets are not determined by interface effects (requiring spherical clusters at the initial stages with Gibbs–Thomson dimensions).

In Figs. 8.1 and 8.2, the two main crystalline polymorphs of carbon (graphite and diamond), the hypothetical metallic carbon field, and the liquid carbon area are shown. In addition, in the literature [39] also the possible existence of two liquid polymorphic carbon modifications is discussed (in analogy with the case of liquid silicon) as a special case of polyamorphism [44]: a graphite-like and a diamond-like liquid ((1) and (2) in Fig. 8.2). The possible existence of the still hypothetical glassy carbon should also be taken into account. It could be obtained by the vitrification of any of the two above-mentioned liquid carbon polyamorphs (1) and (2). Thus two different glasses with diamond-like and graphite-like structure could also be expected. It is even possible that such glass-like forms with graphite- or diamond-like structure have already been obtained as thin extra-hard carbon films formed under various conditions of vacuum condensation. The possible formation of such glass-like carbon structures in processes of plasma condensation we have previously discussed in Ref. [30]. A thorough discussion of these and similar condensates and other amorphous solid forms of carbon requires the knowledge of the thermodynamics of carbon modifications, which will be established in Sect. 8.3.2. Here we only have to mention that the so-called vitreous carbons, synthesized as the result of high-temperature pyrolysis of carbon-rich resins, are in their thermodynamic properties far from the expected properties of the above anticipated diamond- and graphite-like glasses.

In the phase diagrams shown in Figs. 8.1 and 8.2, new carbon modifications (fullerenes, carbon tubes, and carbin), the synthesis of which is based on particular structural principles, are not introduced. They are characterized by very interesting particular and striking structural principles, but too little is known at present about the thermodynamics of these carbon polyamorphs. Their possible significance as precursor materials in diamond synthesis has already been examined [45], however, with little promising results.

8.3.2 The Thermodynamic Phase Diagram of Carbon

The temperature dependence of the thermodynamic functions of the two crystalline modifications of carbon, graphite, and diamond can be found in the reference literature [46] and are represented in their essential part, as the Gibbs potential course $G\,(T)$, in Fig. 8.4 (at a pressure 25 kbar). In addition, the $G\,(T)$ function of carbon vapors is given (treated as a single atomic gas [46]). These $G\,(T)$ functions are constructed employing both the corresponding specific heat measurements, $C_{\mathrm{p}}\,(T)$, the heats of transformation, ΔH_{tr}, diamond/graphite, the heat of melting, ΔH_{m}, of carbon (ΔH_{m} is determined usually as an extrapolation of the known values for Sn, Ge, Si (see [46, 47] and Fig. 8.5) and vapor pressure measurements (for ΔH_{evap} [43, 46]). The heat of transition diamond/graphite $\Delta H_{\mathrm{d/gr}}$ (at $T = 293$ K) is calculated from direct caloric measurements (as heats of combustion in the calorimetric bomb [47]). In Table 8.1, the most reliable respective caloric data for carbon employed in the present study are given.

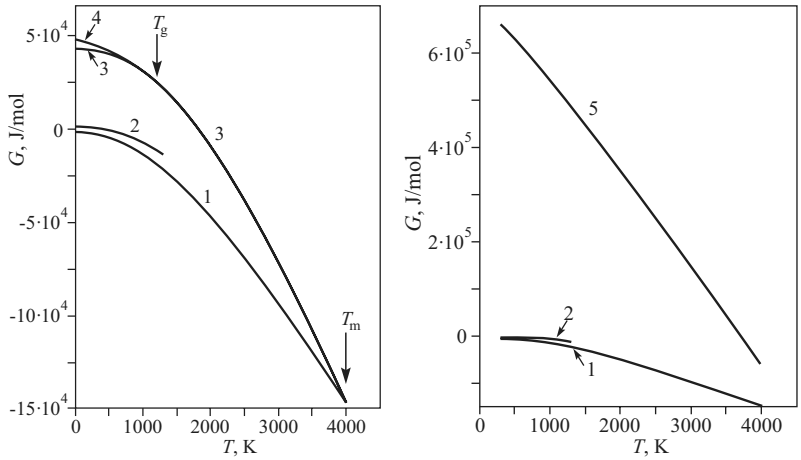

Figure 8.4: The thermodynamic properties of the different forms of carbon in terms of Gibbs' thermodynamic potential. The left figure shows the temperature course of the thermodynamic potential $G_{\mathrm{gr}}(T)$ of graphite (1), $G_{\mathrm{d}}(T)$ of diamond (2), of the undercooled carbon melt (3), and of the hypothetical glass (4), formed from the undercooled melt at an imaginary glass transition temperature $T_{\mathrm{g}} = (1/3)\,T_{\mathrm{m}}$, where T_{m} is the melting temperature of graphite. The right figure shows the temperature dependence (5) of the thermodynamic potential $G_{\mathrm{v}}(T)$ of carbon C_1 vapors. Note that the values of the differences $\Delta G_{\mathrm{v/gr}}(T) = G_{\mathrm{v}}(T) - G_{\mathrm{gr}}(T)$ and of $\Delta G_{\mathrm{v/d}}(T) = G_{\mathrm{v}}(T) - G_{\mathrm{d}}(T)$ are nearly equal in this representation

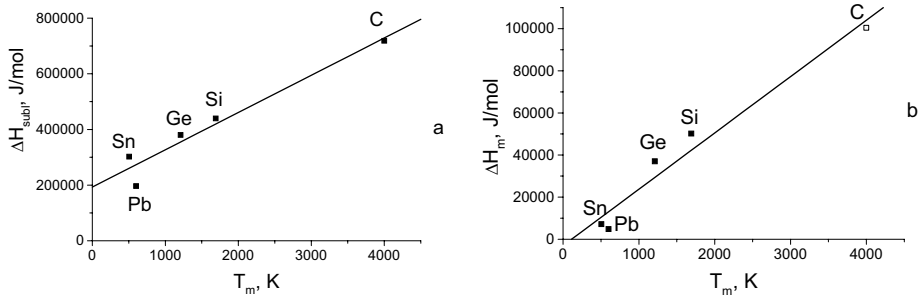

Figure 8.5: The thermodynamic potential of the fourth group of elements in dependence on their melting temperature, T_{m}: (a) heat of sublimation ΔH_{subl}; (b) enthalpy of melting ΔH_{m}. Note the way ΔH_{m} for carbon is estimated

In Fig. 8.4, the $G(T)$ course of liquid carbon is shown as well (again calculated at $p =$ 25 kbar). It has been first constructed in our paper [38] taking into account the following considerations [48]: (i) According to the second law of thermodynamics (and the resulting stability conditions following from it for the metastable and the stable phases) the inequality

$$\Delta C_{\mathrm{p}}(T) = C_{\mathrm{p}}(T)_{\mathrm{carbonmelt}} - C_{\mathrm{p}}(T)_{\mathrm{graphite}} > 0 \tag{8.6}$$

Table 8.1: Characteristic transition temperatures ([5, 46] and the newest reference data) and thermodynamic properties of carbon in its basic equilibrium [5, 38, 46] and vitreous [38, 54] modifications. The exceptionally high values of T_m, T_b, T_{tr}, etc. of carbon determine a scatter of temperatures of about ±500 K in reference literature and differences up to 25–30% in the caloric data reported. We use here only the latest and seemingly most reliable data

Temperatures in phase diagram	Temperature, T K	At pressure, p kbar
Melting point, T_m (graphite)	4300	25
Boiling point, T_b	4500	10^{-3}
Triple point, T_{tr}	4700	10^{-1}
Critical point, T_c	8000	35
Triple point, T_{DgL}	4200	120
Triple point, T_{MDL}	1800	640
Melting enthalpy of graphite, $\Delta H_{gr/l}$ (at 25 kbar)		100 kJ/mol
Melting entropy, $\Delta S_{gr/l}$, of graphite (at 25 kbar)		24 J/(mol · K)
Sublimation enthalpy, ΔH_{subl}, of graphite (at 10^{-3} kbar)		700 kJ/mol
Enthalpy difference, $\Delta H_{gr/d}$, graphite/diamond (at 293 K and 10^{-3} kbar)		1.8 kJ/mol
Hypoth. carbon-glass transition temperature, T_g (at 25 kbar) [38]		1700 K
Hypoth. carbon glass: frozen-in enthalpy, ΔH_g [38]		40 kJ/mol
Hypoth. carbon glass: frozen-in entropy, ΔS_g [38]		3.5 J/(mol · K)
Real vitreous carbon: frozen-in enthalpy [38, 54]		5.4 kJ/mol
Real vitreous carbon: frozen-in entropy [38, 54]		≅ 0
Real vitreous carbon: enthalpy (according to [55])		3 kJ/mol
Real vitreous carbon: entropy (according to [55])		0.77 J/mol · K

has to be fulfilled and with

$$\frac{d\Delta S}{dT} = \frac{\Delta C_p(T)}{T}\,, \quad \frac{d\Delta H}{dT} = \Delta C_p(T)\,, \quad \Delta G(T) = \Delta H(T) - T\,\Delta S(T) \tag{8.7}$$

we get

$$\frac{d\Delta G(T)}{dT} = -\Delta S(T) < 0\,. \tag{8.8}$$

(ii) The third law of thermodynamics implies, moreover, that for any (stable or metastable) *thermodynamic* phase we have to write for temperatures, approaching zero, the relations

$$\Delta C_p\,(T)\big|_{T\to 0} = 0\,, \quad \Delta S_p\,(T)\big|_{T\to 0} = 0\,, \tag{8.9}$$

$$\left.\frac{\mathrm{d}\Delta G(T)}{\mathrm{d}T}\right|_{T\to 0} = \left.\frac{\mathrm{d}\Delta H(T)}{\mathrm{d}T}\right|_{T\to 0} = 0\,, \quad \Delta G(T)\,|_{T\to 0} = \Delta H(T)\,|_{T\to 0}\ . \tag{8.10}$$

In the above well-known thermodynamic relations the Δ-sign refers both to the melt/graphite and to the diamond/graphite difference. (iii) The thermodynamic conditions for first-order phase transitions (here at the melting point, T_m, of graphite) are [31]

$$\Delta G(T)|_{T=T_\mathrm{m}} = 0\,, \quad \Delta S(T)|_{T=T_\mathrm{m}} = \Delta S_\mathrm{m} > 0\,, \tag{8.11}$$

$$\Delta H(T)|_{T=T_\mathrm{m}} = \Delta H_\mathrm{m} > 0\,. \tag{8.12}$$

(iv) In order to specify the particular temperature course of the thermodynamic potential difference in the vicinity of the melting point, T_m, of graphite, we expand $\Delta G(T)$ as a truncated Taylor series at $T \to T_\mathrm{m}$. With Eqs. (8.7) and (8.8), we obtain

$$\Delta G(T) \cong \Delta S_\mathrm{m} T_\mathrm{m} (1-x)\left[1 - a_0\,(1-x)/2\right]\,. \tag{8.13}$$

Here x denotes the reduced temperature, $x = T/T_\mathrm{m}$, and the so-called thermodynamic structural parameter, $a_0 = (\Delta C_\mathrm{p}\,(T_\mathrm{m}))/\Delta S_\mathrm{m}$, is introduced, which we discussed for the first time in Ref. [49] (see also [31]). It determines the "fragility" of the temperature course of the thermodynamic functions of the undercooled melts. For this parameter, values ranging from $a_0 = 1$ (metallic behavior) to $a_0 = 2$ (complex polymer melts) have been predicted and found [31, 49]. Knowing the good electric conductivity of carbon melts (as determined by experiments performed in the electric arc at pressures $p > 10$ kbar), where, according to the phase diagram, only the existence of liquid carbon is possible (see Fig. 8.1), $a_0 = 1$ has to be assumed for liquid carbon [38]. With this value of a_0, Eq. (8.13) gives for the melt/graphite potential difference (i.e., for the thermodynamic driving force of graphite melt crystallization)

$$\Delta G(T) \cong \Delta S_\mathrm{m} T_\mathrm{m} \left(1 - x^2\right)/2\,. \tag{8.14}$$

This result was used in constructing the $\Delta G(T)$ course of undercooled carbon melts as is given in Figs. 8.4–8.6. The thermodynamic potential difference, $\Delta G\,(T,\,p)$, between graphite and diamond is determined by the relation

$$\Delta G_T\,(T,\,p) = \Delta G_{p=0}\,(T) + \int_{p_0}^{p} \Delta V_T\ \mathrm{d}p \tag{8.15}$$

and can be approximately expressed, as first found by Simon [11] in 1926, as

$$\Delta G_\mathrm{p}\,(T) \cong 60 + 1.0\,T\,. \tag{8.16}$$

This dependence is given in Fig. 8.4 above the $G(T)$ course of graphite and separately shown in Fig. 8.6 in ΔG vs. T coordinates as a straight line. To this $\Delta G_\mathrm{p}(T)$ line, in the $(p,\,T)$ phase diagram the already introduced coexistence line corresponds (also first determined by Simon [11]) given with Eq. (8.1). It divides the area of stable diamond existence from the graphite stability field. Simon calculated the constants in Eq. (8.1) as $A_0 = 1500$ and $B_0 = 22$, when p is expressed in bar. Leipounskii [12, 50] found $A_0 = 7000$ and $B_0 = 27$. In the present-day

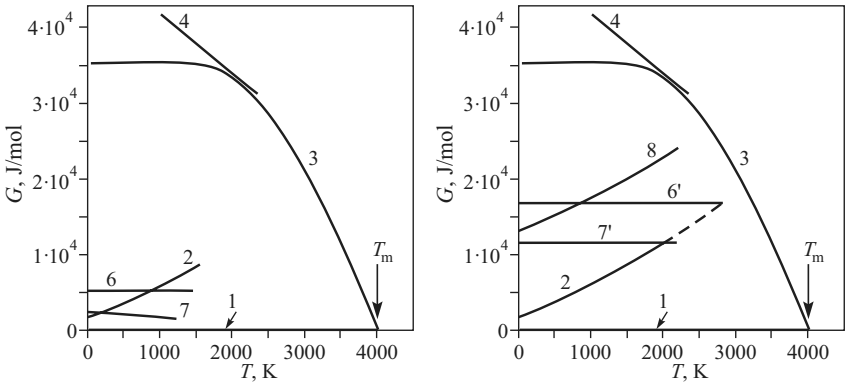

Figure 8.6: Left: Thermodynamic potential of the same forms of carbon as in Fig. 8.4 in terms of the differences of the thermodynamic potential $G(T)$ vs. $G_{gr}(T)$, given now as the ordinate line (1). Thus, curves (3) and (2) indicate here the potential difference melt/graphite and diamond/graphite. With curves (6) and (7) the thermodynamic potential differences of two vitreous carbon materials are introduced, one we synthesized from furfuryl resins, and a commercial product, respectively. Here, as in Fig. 8.4, both $G(T)$ and $\Delta G(T)$ refer to bulk materials. Note the considerable values of $\Delta G_{v/gr}(T)$ and $\Delta G_{v/d}(T)$ and of $\Delta G(T)_{gr/melt}$ when compared with the difference $\Delta G_{d/gr}(T) = G_d(T) - G_{gr}(T)$ given with curve (2). Right: Gibbs' potential differences as in the left part: Here curves (6′) and (7′) refer to vitreous carbon glasses brought to nanosize dimensions. The potential difference $\Delta G(T)$ for nanosized diamond vs. bulk graphite is introduced with curve (8). Note the change of the interception point of the two curves: Simon's $\Delta G(T)$ line (curve (2) for bulk material) and the curves for nanosized materials (curves (6′), (7′) and (8)). The straight line (4) has the same meaning as in Fig. 8.4

reference literature [46], for the first constant in Eq. (8.16) the value 453 cal/mol is used and for the second constant a value very close to the first finding by Simon (0.80 cal/(grad mol)) is employed.

In Figs. 8.4 and 8.6, besides the thermodynamic properties of the two main thermodynamic solid phases of carbon (its allotropic crystalline modifications diamond and graphite), also the thermodynamic potential course of the still hypothetical carbon glass and (in Fig. 8.5) of several representatives of the so-called vitreous carbon materials are introduced. The way of determination (or, at least, estimation) of the thermodynamic properties of these vitreous carbon materials is discussed in Ref. [38] and in the next section. Unfortunately, there are no thermodynamic data known to the present authors on such carbon modifications as the already mentioned fullerenes [51, 52] or of carbonaceous structures, such as hydrogen- or fluorine–graphite adducts, graphitic acids, etc. discussed in Refs. [5, 53]. Such aducts may be of significance in processes of graphite–diamond transitions and thus in metastable diamond synthesis. In Fig. 8.6, for the discussed carbon materials also the $\Delta G(T)$ course for fine-dispersed samples is drawn.

8.3.3 The Thermodynamic Properties of Glassy Carbon Materials

The only previous analysis of the thermodynamic functions of so-called vitreous carbon materials, known to us, may be found in a paper by Vereshchagin [54]. It is based on $C_p(T)$ measurements of several vitreous carbon materials. His $\Delta G(T)$ construction is unfortunately performed without taking into account the most substantial thermodynamic characteristics of a frozen-in system: the increased zero-point entropy, ΔS_g, of glasses. The significance of zero-point entropies in characterizing and defining glassy systems is discussed in detail in Ref. [31]. The first proof of the expected increased zero-point entropy of vitreous carbons was given in a paper by Mahadevan and Weisweiler [55] based on solubility measurements of vitreous carbon materials in molten nickel. A similar proof, with several vitrified carbonaceous resins, was also given years ago by Das and Hucke [56] based on direct determinations of the EMF of galvanic cells, in which carbon oxidation was performed in a graphite/vitreous carbon arrangement.

In our paper [38], we established the $G(T)$ course of several so-called vitreous carbon materials (either synthesized in our laboratory or commercial samples) taking into account both our own measurements and literature data: (i) from caloric measurements (enthalpy difference determinations in the bomb calorimeter, giving ΔH_g, see Table 8.1); (ii) solubility determinations (giving additionally the frozen-in entropy, ΔS_g). In this way, the temperature dependence of the Gibbs potential difference between vitreous carbon and graphite was established as

$$\Delta G_g(T) = \Delta H_g - T\,\Delta S_g \tag{8.17}$$

for several commercial glasses and for our own vitreous carbon samples (synthesized from furfuryl-alcohol resins at 1500 °C). The results from solubility measurements for typical cases of carbon materials are shown in Figs. 8.7 and 8.8 [38, 55, 57].

The general phenomenological theory of the glass transition defines glasses in such a way [31] that (i) the frozen-in system, the glass, displays increased $\Delta G(T)$ values. This property

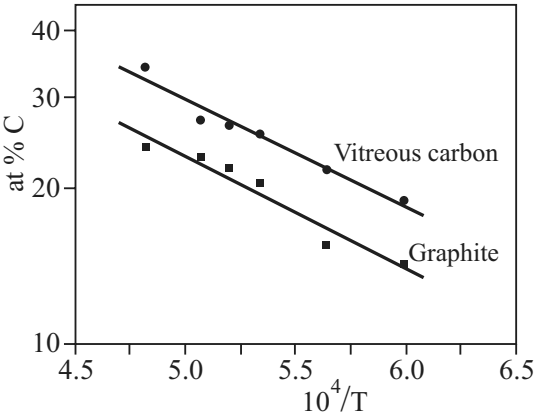

Figure 8.7: Solubility of graphite and the so-called vitreous carbon material in pure Ni melts according to data reported by Weisweiler and Mahadevan [55]

should be manifested in increased vapor pressures and solubilities of glasses and, as seen from Fig. 8.7, is typically fulfilled with vitreous carbons. (ii) ΔH_g and ΔS_g have positive constant values, as is also demonstrated for vitreous carbon in Ref. [38] and Figs. 8.7 and 8.8. (iii) The $\Delta G_g(T)$ course of a glass has to be (in a first approximation) a tangent to the $\Delta G(T)$ course of the corresponding metastable melt (in our case: to undercooled liquid carbon). This requirement, established by Gutzow [32, 33] and by Gupta and Moynihan [58], is, however, not fulfilled for any of the so-called vitreous carbon glasses, analyzed up to the now in their thermodynamic behavior (Figs. 8.6). This property implies [38] that none of the so-called vitreous carbons analyzed corresponds in its structure and thermodynamic properties to the hypothetical carbon melt as it is depicted in Figs. 8.4 and 8.6 with a straight line. There is no wonder in this finding. In fact, all so-called vitreous carbon materials are the product not of liquid carbon quenching but of high-temperature pyrolysis of carbonaceous resins. In these amorphous carbon materials the structure is thus frozen-in and the properties of the precursor organic materials are reflected. From the results of Das and Hucke [56] it is seen that both ΔH_g and ΔS_g in vitreous carbon materials (i.e., the disorder and energy, frozen-in in them) depend strongly on the chemical properties of the precursor resin used and the thermal prehistory of the amorphous materials obtained.

From Fig. 8.8 and especially from our previous discussion in Ref. [38] it is obvious that in general the vitreous carbons analyzed are relatively highly ordered frozen-in systems (with $(\Delta S_g/\Delta S_m) \approx 0.1$ and, for some samples, with ΔS_g approaching even zero). For typical silicate and metallic alloy glasses for the same ratio the estimate $(\Delta S_g/\Delta S_m) \approx 1/3$ is found [31] indicating a much higher degree of frozen-in disorder. These thermodynamic results are confirmed by structural investigations. They show that "vitreous carbon" materials have in general

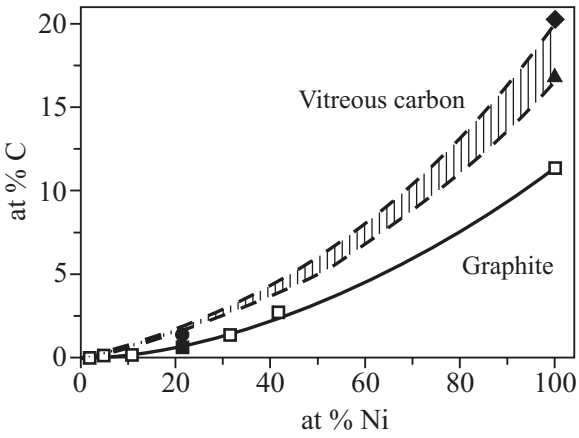

Figure 8.8: Summary of solubility for graphite and amorphous vitreous carbon materials in Ni–Cu alloys as compiled in Ref. [38]. (□): solubility of graphite (data by Strong [57]); (■): solubility of graphite (own results [38]); (▲): solubility of graphite (Weisweiler and Mahadevan [55]); (●): solubility of vitreous carbon materials [38]; (♦): solubility for vitreous carbon materials [55]

a typical graphite-like sp^2-bonded structure with a high percentage of graphite-like crystallites with a mean size approaching 8–10 nm. The direct crystallization of such vitreous carbon materials, at high temperatures and at normal pressures, leads, as shown in Fig. 8.8 from the results obtained in our laboratory, only to graphite [59]. Results, reported in the literature [1, 54], show moreover that even under extremal pressures and high temperatures (corresponding to the stability field of diamond), such vitreous carbon materials give in experiments on the direct synthesis of diamond relatively poor results. It seems that these vitreous materials have to be first crystallized into graphite, which forms then diamond crystals [54].

Similar amorphous, glass-like but hydrogen-rich carbonaceous structures are also obtained in employing various techniques of carbon vapor deposition [60, 61]. It is claimed that in these cases amorphous, frozen-in structures are obtained, corresponding more or less to diamond-like glassy carbon with dominantly sp^3-bonding (*i*-diamond or *a*-diamond). However, no thermodynamic data are reported for these glass-like structures, usually obtained as ultrahard thin solid carbon films at the conditions of hydrogen plasma-assisted H^*-condensation. There are also indications that interstellar cosmic dust may be to a high percentage constituted of similar H-enriched (up to 5–6% H) condensates [53]. To what extent these amorphous structures can be treated as a case of vitreous-like carbon polyamorphism is not clear at present. Also of interest for the experiments reported below is the possible formation of intercolation H-graphite aduct structures in thin graphitic films, subjected to activated atomic hydrogen (H^*) influence in both the vacuum chamber and at cosmic conditions [53]. Such structures may have an increased frozen-in thermodynamic potential and could also be eventually responsible for the observed graphite–diamond transitions in vacuum CVD deposits. No enthalpy or $\Delta G(T)$ measurements are known, however, also for these structures, which may have close resemblance with other already mentioned better studied intercalation structures of graphite.

In assuming a metal-like thermodynamic behavior of the still hypothetical graphite-like melt it could be expected that a real carbon glass could be formed from it (e.g., at ultrahigh splat-cooling rates under increased pressures). Such a glass should have a T_g-value of approximately $T_g = T_m/2$ (as corresponding to metallic glasses) or even $T_g = T_m/3$, where T_m denotes again the mentioned melting point of graphite. Thus, with $\left(\Delta S_g/\Delta S_m\right) = 1/3$, as discussed in Ref. [38], such a "true" but still hypothetical carbon–glass should have a $\Delta G(T)$ course as indicated in Figs. 8.4 and 8.6. Some of the glasses, we have synthesized as small droplets in our vacuum apparatus, may in fact correspond to the above outlined structures (see Fig. 8.4 and the discussion in Ref. [30]).

8.3.4 Activated Carbon Materials: Size Effects and Mechanochemical Pretreatment

The simplest way of increasing the activity of solid materials is their disintegration. Applying the well-known Gibbs–Thomson formula

$$\Delta G_r^* = \frac{2\sigma V_m}{r}\,, \tag{8.18}$$

giving the increase of the thermodynamic potential, ΔG^*, of a solid cluster of radius, r, with an interface energy, σ, as compared to the surrounding phase, a vertical shift of the $\Delta G(T)$ curves to higher potential values is to be expected (see Fig. 8.6). Introducing $r = 10$ nm

Table 8.2: Density (ρ), specific energy (σ), and thermodynamic driving force ($\Delta\mu$) determining the processes of vapor condensation and melt segregation of diamond and graphite. The σ-values, calculated by Eq. (8.19), are specified by the superscript $^{(*)}$. For comparison, data by Novikov et al. [50] $^{(\#)}$ and by Deryaguin [27] $^{(\bullet)}$ are included as well

	Vapor phase condensation		Melt segregation	
	Diamond	Graphite	Diamond	Graphite
ρ (g/cm^3)	3.51	2.26	3.51	2.26
σ (J/m^2)	$19^{(*)}$	$14^{(*)}$	$1.3^{(*)}$	$1^{(*)}$
	$10–18^{(\#)}$		$2.4–4.7^{(\bullet)}$	$1.2–3.4^{(\bullet)}$
$\Delta\mu$ (J/mol)	714 800	716 700	36 300	42 600
$\left(\sigma_{gr}/\sigma_d\right)^3 \left(V_m^{gr}/V_m^d\right)^2$	1.00		1.1	
$\left(\Delta\mu_{gr}/\Delta\mu_d\right)^2$	1.00		1.4	

and applying reasonable values for σ and for the molar volume V_m (see Table 8.2) for the corresponding carbon phases, we constructed the $\Delta G(T)$ curves as given in Fig. 8.6. Thus the interception points of the $\Delta G(T)$ curve for vitreous carbon with the $\Delta G(T)$ curve for diamond appear at considerably higher temperatures. Curve (8) in Fig. 8.6 gives the thermodynamic potential of nanodispersed diamond dust.

The values of σ corresponding to different diamond crystal faces and found in literature are based on calculations of the surface and volume energy constituents of the diamond lattice. A simple, but reliable approximation to determine σ for any interface (crystal/vapor, crystal/melt, crystal/solution, etc.) is the Stefan–Scapski–Turnbull rule [31], according to which

$$\sigma = \gamma_0 \frac{\Delta H_0(T)}{N_A^{1/3} V_m^{2/3}} \tag{8.19}$$

holds. Here ΔH_0 indicates the enthalpy difference at the respective interface. Thus, ΔH_0 is the heat of sublimation of diamond or graphite, when σ is calculated with respect to the vapor phase. ΔH_0 is determined by the enthalpy of melting, ΔH_m, of graphite, when the graphite/molten carbon interface is considered. In Eq. (8.19), N_A is Avogadro's number and V_m indicates the molar volume of the corresponding solid (see Table 8.2). The value of the dimensionless factor, γ_0, changes from face to face (and from interface to interface [31]) but, according to Turnbull's experimental finding [31], $\gamma_0 = 0.4–0.6$ gives sufficiently correct results for low-indexed faces or when a mean σ-value, corresponding to the whole crystal, is considered. In the present analysis, we have adopted the compromise value, $\gamma_0 = 0.5$.

In phase transitions in one-component systems, the thermodynamic potential difference, ΔG, determines directly the thermodynamic driving force, $\Delta\mu$, of the phase transition. Introducing the equilibrium vapor pressures p_r and p_∞ of small droplets and at planar surfaces, the relative supersaturation, χ, determined by Eq. (8.18), is given as

$$\chi_s = \frac{p_\infty - p_r}{p_\infty} \approx \frac{\Delta\mu^*}{RT} \equiv \frac{\Delta G_r(T)}{RT} \,. \tag{8.20}$$

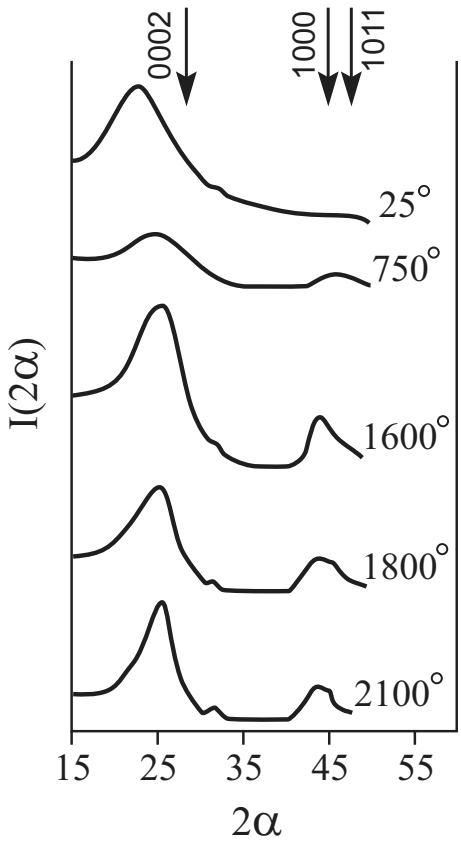

Figure 8.9: Crystallization of vitreous carbon (synthesized in our laboratory from furfuryl–alcohol resins) at different temperatures, indicated at the respective curves (according to the results summarized in Refs. [38, 59]). Time of thermal treatment to each curve is 1 h at the indicated temperature. The X-ray peaks, indicated with an arrow, correspond to graphite

According to Eqs. (8.19) and (8.20), the increase of the relative supersaturation, when the precursor graphite phase is dispersed into clusters containing n building units, is determined by Eq. (8.18) as

$$\chi_s \approx 2\gamma_0 \frac{\lambda_{subl}}{RT} \frac{1}{n^{1/3}} , \tag{8.21}$$

when $r \approx n^{1/3} d_0$ is assumed. According to Fig. 8.9, λ_{subl} is given both for graphite and diamond by $\lambda_{subl} \cong 25 RT_m$ (see [38]). It follows that in diamond synthesis (e.g., at temperatures $T \approx T_m/2$) a relative supersaturation $\chi_s \approx 10^2 \gamma_0 / n^{1/3}$ can be additionally produced by disintegration of the precursor carbon materials. In considering the effect of disintegration procedures (e.g., of various forms of milling) it has also to be taken into account that additional increases in the thermodynamic potential have to be accounted for stemming from the incor-

poration of defects and strains into the solids subjected to mechano-chemical pretreatment. It is usually assumed that the mechano-chemical treatment causes, besides disintegration of the sample and an increase of its surface, also bulk strains due to the defects created. Suppose the defects introduced by the treatment have changed the molar volume of the samples by $(\Delta V/V_\mathrm{m})$, e.g., by inclusion of ν point defects (holes) per mole, so that $\Delta V = \nu V_0$ holds. The additional elastic energy, thus accumulated in the sample by the introduced voids, can be estimated to be (if the corresponding configurational entropy increase is assumed to be $\Delta S_\mathrm{c} \cong 0$) equal to

$$\chi_E = \frac{\Delta G}{RT} = \frac{E}{3\,(1-\mu)} \frac{\Delta V^2}{V_\mathrm{m}} \frac{1}{RT} \,. \tag{8.22}$$

Here E is the Young's modulus of elasticity of the sample (in our case the carbonaceous material) and μ the respective Poisson ratio ($\mu \approx 0.3$). With the formula of Born and Lande, connecting the modulus of elasticity with the heat of sublimation of the respective solid as

$$E \approx \frac{MN}{9V_\mathrm{m}} \Delta H_\mathrm{subl} \,, \tag{8.23}$$

it becomes evident (with Mie's coefficients $M = N = 1$) that the relative change of ΔG_E is given by

$$\chi_E \approx \frac{\Delta H_\mathrm{subl}}{20RT} \left(\frac{\Delta V}{V_\mathrm{m}} \right)^2 \,. \tag{8.24}$$

With the mentioned estimate for ΔH_subl it follows (again for $T \approx T_\mathrm{m}/2$) that measurable χ-changes are to be expected only for solids subjected to various forms of mechano-chemical pretreatment, guaranteeing at least a volume increase of $\Delta V/V_\mathrm{m} = 0.01$. Our experience has shown that mechano-chemical pretreatment of diamond and even of vitreous carbon by means of milling in standard milling apparatus may be sometimes quite dangerous. Even with customary super-hard wolfram-carbide milling equipment a considerable amount of undesired contamination is introduced in this way up to several % W as witnessed by microprobe X-ray measurements. Nevertheless, Eqs. (8.21) and (8.24) indicate a promising way of diamond growth via the route **finely dispersed diamond → bulk diamond**, if contamination by milling can be avoided.

8.3.5 Phase Transitions in Carbon Clusters, Diamond, and Graphite Crystallization in Small Droplets

Let us first consider the fate of a small droplet of molten carbon, formed from a carbon vapor phase in a process of either binodal or spinodal condensation. The van der Waals (p, V, T) diagram for the case of carbon vapor–liquid transition is schematically shown in Fig. 8.3 in p vs. V coordinates. A similar construction can be also anticipated in the case when the precursor carbon or carbonaceus phase is enriched with a second (e.g., hydrogen) or even with a third and fourth constituent (e.g., CH_4 and H_2). The thermodynamics and kinetics of similar processes of new phase formation is considered in Sect. 8.3.5 for the 2D case. Suppose first

that in the binodal region small liquid nuclei, resembling liquid droplets, have been formed in a nanoscale dimension range. Considering the phase diagram of carbon (Figs. 8.1 and 8.2), it becomes evident that liquid carbon phase formation is only possible at increased pressures ($>10^3$ bar). Because of the well-known pressure increase, Δp, in liquid droplets, as predicted by Laplace's equation [62]

$$\Delta p = \frac{2\sigma}{r} \,, \tag{8.25}$$

the pressure in droplets of radius r is increased to the value p_r, so that $\Delta p = p_r - p_\infty$. Here p_∞ indicates the equilibrium pressure for phase coexistence at a planar liquid–gas interface (i.e., at $r \to \infty$). Employing the Stefan formula (8.19), above dependence can also be written as

$$\Delta p = \frac{\Delta H_{\mathrm{ev}}}{C_0 V_{\mathrm{m}}^{2/3} r} \,. \tag{8.26}$$

In this relation, ΔH_{ev} is the heat of evaporation of molten carbon. Its value can be estimated from the known value of the heat of sublimation, ΔH_{subl}, and the melting enthalpy, ΔH_{m}, of graphite as $\Delta H_{\mathrm{ev}} = \Delta H_{\mathrm{subl}} - \Delta H_{\mathrm{m}}$ (see Table 8.1). When ΔH_{ev} is expressed in J/mol, V_{m} in $\mathrm{cm}^3/\mathrm{mol}$, r in cm, and Δp in bar, the constant C_0 in the above equation has the value $C_0 = 2.2 \times 10^7\ \mathrm{cm/mol}^{2/3}$. Thus, it turns out that a liquid carbon droplet of dimension $r = 1$ nm is subjected to an additional Laplace pressure $\Delta p = 10^5$ bar (assuming $V_{\mathrm{m}} = 0.95\ \mathrm{cm}^3/\mathrm{mol}$). At 5 nm, the Laplace pressure in a liquid carbon droplet will be 5×10^4 bar, rapidly falling to only $\Delta p = 10^2$ bar and $\Delta p = 10$ bar, when diamond droplets of respectively 1 μm or 10 μm are considered.

The above estimates show that the crystallization of initially formed nanometric carbon droplets should correspond (at a temperature below 4000 K) to conditions leading to the direct formation of diamond. In contrast, these estimates also show that micron-sized carbon droplets should crystallize under the same conditions to graphite. Thus, in processes leading to the formation of a population of nanosized carbon clusters of radius r, their subsequent crystallization to diamond becomes a necessity, provided their temperature is below the corresponding melting temperature, $T_{\mathrm{m}}(r)$. In this context it has to be recalled that according to one of the well-known forms of the Gibbs–Thomson equation given initially by Hanssen (see [31, 63, 64]), the melting point of any small crystal is a function of its size, e.g., of its mean radius r. The proper handling of this problem requires the analysis of the equilibrium of a crystalline and a liquid cluster of equal masses, embedded in the same vapor volume. In the case of carbon also the mentioned stability areas of the liquid have to be accounted for. According to these calculations [31, 64], the melting point of a small crystalline cluster of radius, r, is given by

$$\left(\frac{T_{\mathrm{m}}(r)}{T_{\mathrm{m}\infty}}\right) = 1 - \frac{2\sigma_{\mathrm{cv}} V_{\mathrm{mc}}}{\lambda_{\mathrm{m}}} \frac{1}{r} \left[1 - \frac{\sigma_{\mathrm{fV}}}{\sigma_{\mathrm{cv}}} \left(\frac{V_{\mathrm{f}}}{V_{\mathrm{c}}}\right)^{2/3}\right] \,. \tag{8.27}$$

It is seen that $T_{\mathrm{m}}(r)$ also depends on the ratio of the molar volumes of solid (c) and liquid (f) clusters. In a similar way, the transition temperature $T_{\mathrm{g/d}}(r)$ of graphite–diamond

(as any transition temperature between small, differently structured clusters) should also be size-dependent. The size dependence of the graphite–diamond transition temperature of small graphite clusters was calculated by Fedoseev [65] in 1983. He derived this dependence in a similar way as Eq. (8.27). It reads

$$T_{\mathrm{TR}} \cong \frac{2\sigma_{\mathrm{gr}} V_{\mathrm{md}}}{r_{\mathrm{gr}} B_0} \left[1 - \frac{\sigma_{\mathrm{gr}}}{\sigma_{\mathrm{d}}} \left(\frac{V_{\mathrm{mgr}}}{V_{\mathrm{md}}} \right)^{2/3} \right] - A_0 \, . \tag{8.28}$$

Here B_0 and A_0 are the constants from the Simon–Leipounskii–Berman line (Eq. (8.2)).

The melting point depression of small crystals, given with Eq. (8.27), has been subjected to several experimental verifications, mostly by determining the melting points $T_{\mathrm{m}}(r)$ of differently sized clusters in vacuum deposited metals. Equation (8.27) also gives an elegant way of determining the corresponding interfacial energy σ between melt and crystal. The applicability of Fedoseev's formula (8.28) to graphite–diamond transition thermodynamics has been confirmed in brilliant experiments performed by Fedoseev et al. [66] and other authors [67]. In these experiments, a strain of micro- to nanosized sooth or graphite particles, sedimenting in vacuum or in air under normal pressure, is subjected to short-time heating by a high-intensity laser beam. In the laser-treated sediment, a high percentage of nanosized diamond crystallites is found as proven by direct electron microscopy, electron-spot diffraction, and X-ray analysis. In the precursor nanosized carbon samples, used in these experiments, only graphite and amorphous carbon were found. The melting point depression experiments in thin metallic condensates and the above-discussed size-dependent graphite–diamond transition give the most direct proofs of small cluster thermodynamics, known to the present authors. The effects connected with the Fedoseev relation, Eq. (8.28), explain several aspects of unexpected diamond formation at metastable conditions. In particular, it may be possible that in Hannay's 19th-century experiments (mentioned in Sect. 8.2), a population of nanosized graphite clusters (coming from the sooth initially introduced, or formed as nascent carbon upon the Li-paraffin reaction) had a chance to be subsequently transformed into diamond at the elevated temperatures employed. The relatively high pressure, existing in Hannay's reaction tubes, guaranteed an even better fulfillment of the premises of Fedoseev's formula, as in the above-mentioned laser-beam experiments.

With Stefan's formula, Eq. (8.19), Eqs. (8.27) and (8.28) can be written in analogy with Eq. (8.21) in the form

$$T_{\mathrm{m}}(r) \cong T_{\mathrm{m}}(\infty) \left[1 - \frac{2\gamma_0}{n^{1/3}} \right] , \quad T_{TR} \cong T_x(\infty) \left[1 + \frac{2\gamma_0}{n^{1/3}} \frac{\lambda_{\mathrm{subl/gr}}}{A_0} \right] , \tag{8.29}$$

when, again, $r \cong (V_{\mathrm{m}}/N_{\mathrm{A}})^{1/3}$ is assumed and simple connections, such as $\lambda_{\mathrm{subl/gr}} = \lambda_{\mathrm{evap/gr}} + \lambda_{\mathrm{m/gr}}$ and $T_x = -A_*^0/B_*^0$, are introduced via Eq. (8.1). The relative supersaturation, χ_{d}, guaranteed, e.g., in a vapor gas transition reaction by a population of graphite clusters (containing n carbon atoms) to a growing diamond cluster can be calculated by a combination of Simon's equation, Eq. (8.16), with the respective Gibbs–Thomson dependence, written in the form of Eq. (8.29) as

$$\chi_{\mathrm{d}} = \frac{\Delta G\,(r/d)}{RT} = \left[\frac{\lambda_{\mathrm{subl/gr}}}{A_*} \frac{2\gamma_0}{n^{1/3}} - \left(1 + \frac{B_*^0}{A_*^0} \right) \right] \frac{1}{RT} \, . \tag{8.30}$$

Here A_*^0 and B_*^0 are again the constants appearing in Eq. (8.16). The above relation indicates that a population of graphite clusters, placed around a diamond crystal, could guarantee diamond growth, i.e., $\chi > 0$ (e.g., $\chi = 0.04$, see Sect. 8.3.8) only at nanosizes. Values $\chi > 1$, or even $\chi \gg 2$–3, as necessary for any nucleation process and for diamond nucleation, in particular, cannot be realized in this way. However, additional effects, e.g., H-occlusion into the graphite clusters, could additionally increase their chemical potential and eventually even guarantee values of relative supersaturation, $\chi > 1$, against diamond. This possibility is discussed by several authors from the American School of Metastable Diamond Growth [2, 69, 70] (see also [68]). However, at present there are no calorimetric data that give a sufficiently sound confirmation of such effects. As a most elaborate suggestion in this sense the paper of Badziag et al. [70] can be mentioned, in which computer modeling of H end-stabilized graphite-structured clusters indicates that at a H/C ratio of 0.2–0.3, nanosized hexagonal carbon clusters could be more stable than equally sized carbon clusters with diamond-like structure. It has, however, also to be mentioned that in Ref. [70] and similar publications, Thomson–Gibbs effects are, strangely enough, completely disregarded.

The possibility of graphite–diamond transitions of small clusters, as verified by Fedoseev's experiments [65, 66], is also a demonstration of a newly formulated nucleus growth model scenario (Schmelzer et al. [71]). According to this model, growing subcritical clusters change their structure in dependence on cluster size in order to achieve minimal values of the Gibbs free energy differences to the initial ground state. A first illustration of this model was given by Milev and Gutzow [72] in terms of an enlarged treatment of the Stranski–Totomanov kinetic analysis of Ostwald's rule of stages. The direct graphite–diamond transfer in nanosized graphite clusters, or the liquid–diamond transition scenario, possible by considering the increased pressures in liquid clusters and the structural changes, connected with considerable volume alteration in carbon materials, gives another example of the way, how Ostwald's rule can be fulfilled.

In considering such models and the derivations, based on the thermodynamics of very small clusters constituted of only several building units, n, it has to be recalled that any *quantitative* description of the properties of clusters at $n \to 1$ can be based only on more or less doubtful extrapolations. This is well known since Gibbs' times, and this famous author was also the first to propose corrections, guaranteeing, at least, a qualitatively correct description of the thermodynamic properties of small and even of very small clusters. Beginning with Gibbs, these corrections are at present introduced frequently via the Tolman formula [31], which is one of the possible approximative forms of Gibbs' original relation [73] for size corrections to the value of the specific surface energy, σ. The value of σ, appearing in all the above-cited dependences (the Laplace formula, the Thomson–Gibbs dependences, Eqs. (8.20), (8.27)–(8.30)), determines the whole thermodynamics of nucleation and especially the work, $W(n)$, necessary to form a n-sized cluster. Thus, σ is also the focus of most difficulties involved in all definitions, calculations, and experimental verifications of the present-day nucleation theory. For extremely small clusters atomistic approaches and computer simulations performed at $n \to 1$ give a guarantee that existing ways of classical thermodynamic extrapolations lead to acceptable results. A thorough and general discussion of these problems was given by Mutaftschiev [62] (see also [31]). Its results are schematically illustrated in Fig. 8.10. In this sense all the above derivations, when applied to $n < 10$, have to be considered only as estimates. However, in graphite/diamond transitions, as far as nanosized clusters with $n > 100$

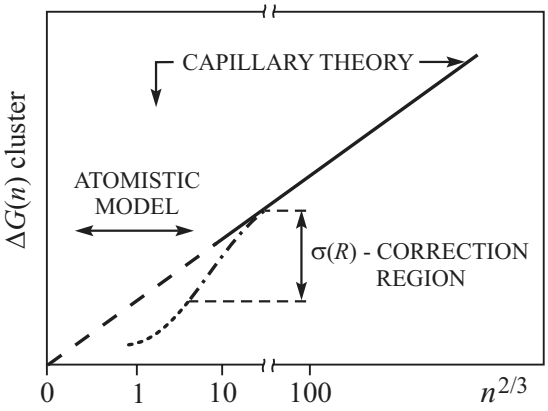

Figure 8.10: The excess free energy of a cluster in dependence on the number, n, of its building units (after Mutaftschiev [62], see also [31]). The course obtained by applying the capillary approximation is indicated by the straight line. The more realistic course, after introduction of the size-dependent corrections of the surface tension of modern nucleation theory (see [31]), shifts the $\Delta G\,(r)$-Thomson–Gibbs line to lower values correlating with atomistic calculations

(for $r \approx 1$ nm) to $n > 1000$ (for $r \approx 5$ nm) are accounted for, even a semiquantitative applicability of the derivations made is guaranteed to a large extent.

8.3.6 Ostwald's Rule of Stages and Metastable Nucleation of Diamond

Let us first consider the general physical aspects of metastable diamond formation in the framework of the classical theory of nucleation, as it is derived and discussed in its present-day formulations in the literature [31, 62]. The formation of metastable phases is usually explained in the framework of this theory in terms of Ostwald's rule of stages. In its present-day kinetic interpretation (as was given by Stranski and Totomanov [74] and as it is summarized by Volmer [75] and by Gutzow and Schmelzer [31]) Ostwald's rule can be formulated in the sense that those phases will be dominantly formed that have the highest rate of nucleation at the given conditions. Thus the prevalent formation of one of two possible modifications (a stable and a metastable one) from a common initial (metastable or unstable) phase is determined by the value, Y_I, of the ratio of steady-state nucleation rates, I, of these two modifications. In our case, I_{d} refers to diamond and I_{gr} to graphite formation, respectively, so that

$$Y_I = \ln\left(\frac{I_{\mathrm{d}}}{I_{\mathrm{gr}}}\right) . \tag{8.31}$$

The formation of diamond will occur preferentially when in the above inequality $Y_I > 0$ holds. Let us suppose, moreover, that the initial phase is either supersaturated carbon vapor or a liquid solution of carbon, e.g., in a molten metallic alloy system. Taking into account

the usually employed expression of the steady-state nucleation rate (see [62, 76, 77] and the respective formalism, developed by Gutzow and Schmelzer [31]), we have

$$I = \text{const} Z Z' \exp\left[\left(-\frac{\Delta W}{k_B T}\right)\Phi\right] , \tag{8.32}$$

and can write the above condition for predominant formation of the metastable diamond phase generally in the form

$$Y_I = \ln\left\{\frac{\text{const}_1 Z_d Z'_d \exp\left[\left(-\frac{\Delta W_d}{k_B T}\right)\Phi_d\right]}{\text{const}_2 Z_{gr} Z'_{gr} \exp\left[\left(-\frac{\Delta W_{gr}}{k_B T}\right)\Phi_{gr}\right]}\right\} > 0 . \tag{8.33}$$

In the above equations, Z is the impingement rate of ambient phase carbon structural units to the growing new phase clusters with either graphite-like (Z_{gr}) or diamond-like (Z_d) structure and Z' is a factor, connected with both steric and reconstructional hindrances in the way of incorporation of ambient phase molecules into the new phase nucleus [31, 38]. The factors Z_d, Z_{gr} in diamond nucleation experiments are also determined by the actual concentration of sp^3 (diamond-like) and sp^2 (graphite-like) structural units in the vapor or liquid phases. In Eqs. (8.32) and (8.33), Φ is the activity of the existing substrates, if heterogeneous nucleation takes place ($0 < \Phi < 1$ [31, 62]). ΔW in Eq. (8.32) is the thermodynamically determined barrier of nucleation (the work of critical cluster formation), given by [31, 62, 77]

$$\Delta W = \left(\frac{16\pi}{3}\frac{\sigma^3 V_m^2}{\Delta\mu^2}\right)\Phi . \tag{8.34}$$

Here σ is the already mentioned interfacial energy of the ambient phase/new phase boundary, V_m is the molar volume of the newly formed phase (either diamond or graphite), and $\Delta\mu$ is the driving force of the nucleation process under consideration (graphite or diamond formation). In the particular case of growth from the vapor phase (v) of diamond (d) and of graphite (gr), we have $\Delta\mu_d = G_v - G_d$ and $\Delta\mu_{gr} = G_v - G_{gr}$, where G denotes the corresponding Gibbs free energy values. With the factor Z' we introduce (for diamond or graphite cluster formation from the same gaseous or liquid ambient phase) the activation energies U_d, U_{gr} via $Z' \approx \exp(-U/k_B T)$ for possible surface reactions when sp^3 or sp^2 units are incorporated into the new phase cluster. In general, the factors Z and Z' (usually neglected in considering simpler nucleation processes), can in fact essentially govern nucleation and subsequent growth. In most of the classical cases of nucleation $Z_d Z'_d = Z_{gr} Z'_{gr}$ can be expected. However, in the case of metastable diamond synthesis in dependence on the presence or absence of sp^3 or sp^2 carbon structural units in the initial vapor phase both cases $Z_d Z'_d \gg Z_{gr} Z'_{gr}$ and $Z_d Z'_d \ll Z_{gr} Z'_{gr}$ are possible. The values of both Z_i and Z'_i can be regulated by extremely high temperatures, by radiation, by the degree of ionization, and thus by the concentration of atomic hydrogen in the vapor phase in CVD processes. In molten metals, the presence of distinct "activators" (e.g., of Ni) can, in terms of the above concepts, essentially determine Z'_d by lowering U_d.

Let us first discuss the particular case when the preexponential factors Z and Z' in Eq. (8.32) can be considered as nearly equal for the processes of formation of both carbon

modifications (i.e., when $Z_d Z'_d = Z_{gr} Z'_{gr}$). Substituting the above given expression for ΔW into Eqs. (8.31) and (8.36), we obtain

$$\left(\frac{\Phi_{gr}}{\Phi_d}\right)\left(\frac{\sigma_{gr}}{\sigma_d}\right)^3\left(\frac{V_m^{gr}}{V_m^d}\right)^2 > \left(\frac{\Delta\mu_{gr}}{\Delta\mu_d}\right)^2 > 1\ . \tag{8.35}$$

This inequality is the general kinetic condition (previously discussed in detail and in several applications in Refs. [77, 78]) to be fulfilled for the predominant formation of a metastable phase (in our case, of diamond). It is determined only by the respective thermodynamic barriers of nucleation ΔW_d and ΔW_{gr}.

As is evident from Fig. 8.4, the thermodynamic driving forces of the process of carbon vapor condensation (i.e., the differences $(G_v - G_d)$ and $(G_v - G_{gr})$) are so close for diamond and for graphite that even at elevated temperatures $\Delta\mu_d \approx \Delta\mu_{gr}$ can be assumed. In the case of melt crystallization (e.g., crystallization from the hypothetical carbon melt we discussed earlier), this assumption cannot be used as also evident from Fig. 8.4. The respective values of $\Delta\mu_d$ and $\Delta\mu_{gr}$ for both carbon vapor condensation and melt segregation of diamond and of graphite are given in Table 8.2. In this table, the σ-values for both diamond and graphite are also given. The above considerations can be applied, strictly speaking, only to the case of normal pressures, since the formation of liquid condensates (or precipitates) is, according to the phase diagram of carbon, excluded at $p < 10$ kbar. At higher pressures, however, also the formation of liquid carbon droplets should be incorporated in the above calculation. Consequently, equations analogous to the foregoing ones have also to be written for $p > 10$ kbar for the nucleation rate I_l of the third phase from the vapor, for nucleation of liquid carbon droplets. As far as for liquids as a rule $\sigma_l < \sigma_{cryst}$ holds and taking into account the possible values of evaporation and sublimation heats of carbon (see Fig. 8.9 and Table 8.1), also $\sigma_l < \sigma_d, \sigma_{gr}$ and (as for any other liquid [31, 77]) $Z_l Z'_l \approx 1$ has to be fulfilled. Thus, the formation of liquid droplets has to be the predominant nucleation process at sufficiently large pressures (if binodal formation of droplets from the vapor is anticipated). In analyzing I_l, I_{gr}, and I_d, moreover, also the influence of pressure on the nucleation rate has to be considered: The values of I_{gr} and I_d will also be changed in accordance with the fulfillment of Ostwald's rule of stages at pressure-dependent nucleation. This problem is discussed in detail in Ref. [79] with the following result: Under pressure, in general, the phase with higher volume change is formed. In an additional complication, the possible crystallization of carbon droplets into both diamond and graphite micro- (or nano-) crystals has to be accounted for as a size-dependent possibility.

In the next section, in considering two-dimensional (2D) nucleation kinetics of condensing carbon vapor these possibilities are discussed in more detail. Two-dimensional nucleation and growth proceed under very particular conditions: at increased two-dimensional pressure, corresponding to more than $p = 10$ kbar. Considering the data in Table 8.2 and Eq. (8.35), it follows that in the process of carbon vapor condensation, direct nucleation of diamond can be expected if $Z_d Z'_d = Z_{gr} Z'_{gr}$ holds. In melt crystallization (e.g., using as a precursor the hypothetical carbon melt) or in carbon segregation from metallic alloys or silicate melts, the chances for diamond nucleation at metastable conditions are considerably lower (see Table 8.2). The presence of diamond seed crystals is also of significance in enabling metastable diamond formation (cf. Eq. (8.35)). Introducing into the precursor system diamond seeds

($\Phi_d = 0$), the left-side term of Eq. (8.35) tends to infinity and the inequality is always fulfilled. For any other (non-diamond, but diamond-like) crystalline seeds, positive growth could be expected if $\Phi_{gr}/\Phi_d > 1.3$ (see also [31, 78]). However, considering the structure of both diamond and graphite crystal faces it is to be expected, in general, that $Z_d Z'_d \ll Z_{gr} Z'_{gr}$. This condition can be reversely fulfilled only in cases when in the precursor vapors a sufficient concentration of sp^3-structured carbon is present.

Very significant is also the influence of the composition of the gaseous precursor phase on the value of $Z_d Z'_d$. Thus, in CH_4/H carbon mixtures the presence of atomic hydrogen increases the incorporation rates of sp^3-carbon units into the H^*-activated diamond structure (see [22, 24, 25, 30]), thus increasing the factor Z'_d. The presence of sp^3-carbon atoms in the vapor phase (as they are present in methane) raises additionally the factor Z'_d. Considering the case when $Z_d Z'_d > Z_{gr} Z'_{gr}$, from Eq. (8.33) we obtain

$$\left(\frac{\Phi_{gr}}{\Phi_d}\right)\left(\frac{\sigma_{gr}}{\sigma_d}\right)^3\left(\frac{V_m^{gr}}{V_m^d}\right) > \left(\frac{\Delta\mu_{gr}}{\Delta\mu_d}\right)^2\left\{1+\left[\ln\left(\frac{Z_{gr}Z'_{gr}}{Z_d Z'_d}\right)\left(\frac{k_B T}{\Delta W_d \Phi_d}\right)\right]\right\} . \quad (8.36)$$

For detectable nucleation to be observed, $\Delta W/k_B T \cong$ 20–30 should hold, i.e., the term $\left[1+\left[\ln\left(Z_{gr}Z'_{gr}/Z_d Z'_d\right)(k_B T/\Delta W_d \Phi_d)\right]\right]$ can be of significance only for differences in $Z_i Z'_i$ of the order of $\ln\left(Z_d Z'_d/Z_{gr}Z'_{gr}\right) > 5$. Thus existing results on the metastable growth of diamond from carbon vapors or carbon-containing gaseous mixtures can be explained, at least, qualitatively in the framework of the above enlarged formulation of Ostwald's rule of stages. In carbonaceous vapor phases, besides possible influences of activated species (atomic hydrogen), the principal factor, guaranteeing the fulfillment of Ostwald's rule in homogeneous vapor condensation is connected with the high (and thus nearly equal) values of the respective thermodynamic driving forces, $\Delta\mu_d$ and $\Delta\mu_{gr}$ (see Fig. 8.4), provided the above condition for Z_d and Z_{gr} is fulfilled. The same approach also indicates that in the case of liquid solutions and melts the fulfillment of inequality Eq. (8.35) is less probable because of considerable difference in $\Delta\mu$-values as can also be seen in Fig. 8.4.

Thus, Ostwald's rule of stages indicates that in processes of condensation (both from the vapor phase or with the more convenient vapor transport reaction scenario), either the direct formation and growth of diamond clusters or their secondary nucleation and growth in initially formed liquid-like clusters is possible even at conditions where graphite is stable. The first process mentioned is stimulated according to Eqs. (8.33) and (8.35) by substrates having a resemblance to diamond (i.e., with $\Phi_d < 0.3$, e.g., of elemental Si, of carbides, formed on the substrate surface, etc.). Condensation on a foreign substrate also gives additional advantages in diamond condensation as discussed in Sect. 8.3.6. They are connected with the specific features of processes of two-dimensional condensation. Here we would like only to mention that there are indications (see Deryaguin and Fedoseev [80]) that Ostwald's rule also essentially determines the formation of diamond at conditions where diamond is stable: in the processes of "direct" diamond synthesis at extreme pressures. According to a hypothetical scenario, proposed by these authors [80], at high pressures initially liquid carbon droplets segregate from the Ni alloys (most probably according to Eq. (8.35)). These liquid carbon droplets are metastable at these conditions. They crystallize in the second stage of the process to the also metastable graphite nanocrystals, which, according to the thermodynamics

indicated with Fedoseev's formula (8.28), are transformed in the third step of the process to diamond. In Ref. [80], several experimental indications are given, confirming this particularly interesting scenario of a two-fold metastable stage phase formation.

8.3.7 Two-Dimensional Condensation of Carbon Vapors and of Carbonaceous Compounds and Metastable Diamond Nucleation

For the first time, Semenov [81, 82] mentioned the possibility that heterogeneous nucleation of vapors can take place via a two-dimensional process of condensation, which can be, at least, qualitatively described in terms of a two-dimensional van der Waals equation. This idea was exploited by Palatnik and Papirov [82] in analyzing the condensation of metallic vapors on solid substrates. Let us try to apply Semenov's proposal to the particular case of diamond nucleation from the gaseous phase. First we recall that as a consequence of the dynamic character of vapor adsorption processes on a solid substrate, there is a critical temperature (the Knudsen temperature, T_{Kn}) above which practically no vapor condensation takes place. This temperature, as is defined by Frenkel [83, 84] (see also [82, 85]), depends on the mean stay-time $\tau_{\mathrm{ad}}(T)$ of adsorbed molecules on the substrate. Suppose a flux, $q_0 \sim p$, of molecules is reaching the substrate and the vapor pressure p can be attributed to the gas volume, which is in contact with the substrate. In such a case, the Knudsen temperature is determined via the corresponding vapor pressure and the adhesion energy between adsorbed molecules and substrate, U_{ad}, as

$$T_{\mathrm{Kn}} = \frac{U_{\mathrm{ad}}}{2.3R}\left[\log\left(\frac{g_0}{p}\right)\right]^{-1} . \tag{8.37}$$

Here g_0 (determined by the reciprocal of the oscillations of the two-dimensional condensate molecules) has values $g_0 \cong 10^{-12}\ \mathrm{s}^{-1}$. Only for temperatures $T < T_{\mathrm{Kn}}$, a surface coverage, N_{d}, is possible (see Fig. 8.11 [84]). Taking into account typical values of g_0, it follows from Eq. (8.37) that for a full surface coverage (i.e., for $\Theta = 1$) we have to expect $T_{\mathrm{Kn}} \approx \gamma_0 T_{\mathrm{m}}/10$.

In considering condensation processes of vapors in contact with their own crystal (e.g., in condensation processes of carbon vapors on a graphite single crystal face), $U_{0\mathrm{ad}} \approx (\lambda_{\mathrm{subl}}/2)$ is expected. On a foreign substrate, U_{ad} can be either larger or smaller than $U_{0\mathrm{ad}}$. The corresponding inequality determines the ratio lateral vs. adsorption forces and thus the character of the processes taking place in the adsorbate. It is also essential to note that T_{Kn} is critically (although on the logarithmic scale) determined by the flux, q_0, of incoming molecules, which especially in the kinetics of plasma-supported condensation processes can determine p-values (corresponding to a static regime of condensation) many times higher than the equilibrium pressure, $p_{\mathrm{eq}}(T)$. Let us now follow the processes on a substrate embedded in a gaseous phase (e.g., constituted of carbon vapors) and let the temperature on the substrate be $T < T_{\mathrm{Kn}}$. The flux, q_0, of condensing molecules (in dynamic conditions, or the vapor pressure p, in "static" condensation experiments) determines a relative adsorption coverage, Θ, of the substrate and the thermodynamic and kinetic behavior of the condensate is determined by a two-dimensional equation of state. In general, the two-dimensional coverage of the substrate with

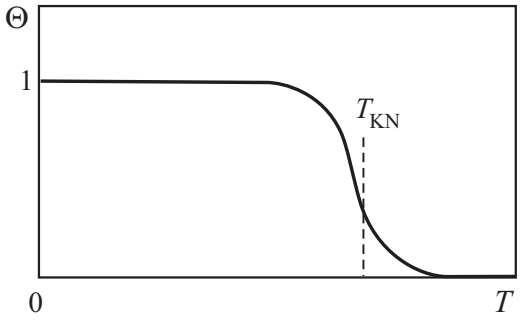

Figure 8.11: The definition of the Knudsen temperature, T_{Kn}, according to Frenkel [84]: It is the temperature at which the relative coverage, Θ, tends to zero values, indicated by the inflection point of the $\Theta(T)$ curve

adsorbed molecules is $\Theta = \alpha q_0$, where α is a constant. In a first approximation, following Semenov's proposal, a van der Waals equation of state

$$\left(F + \frac{a_2}{W^2}\right)(W - b_2) = RT \tag{8.38}$$

can be employed in such cases of adsorption in analogy with the well-known van der Waals equation, describing the behavior of a gas of volume V at pressure p and temperature T. More specific are adsorption isotherms, also based on a mean-field approximation, such as the Frumkin–Fowler equation (see the literature cited in Ref. [86]).

In the above equation, F and W indicate the two-dimensional pressure and the surface area occupied by the two-dimensional gas under consideration, respectively, and a_2 and b_2 are the two-dimensional analogs of the usual van der Waals constants. They determine in the same way as the "tree-dimensional" constants a_*, b_*, introduced with Eq. (8.3), a critical point for the two-dimensional adsorbed gas, where $T = T_{C_2}$, $F = F_{C_2}$, $W = W_{C_2}$. Employing the relations $b_2 = 3b_*/4d_0$ and $a_2 = 3a_*/8d_0$, which exist between a_2, b_2 and a_*, b_* according to simple theoretical considerations [85] (d_0 indicates the mean diameter of the molecules forming the two-dimensional adsorbed gas), a comparison with Eqs. (8.3) gives

$$T_{C_2} \equiv \frac{8a_2}{27Rb_2} = \frac{1}{2}T_{C_3} \tag{8.39}$$

Similar estimates for the ratio T_{C_3}/T_{C_2} are also obtained with other theoretical models of two-dimensional equations of state (see [62, 85]).

Summarizing existing theoretical results, it turns out that (i) the whole $F(T)$ vs. $W(T)$ two-dimensional phase diagram is shifted to considerably lower temperatures when compared with the corresponding "normal three-dimensional" phase diagram. The experimental verification of this seemingly unexpected result, following from Semenov's idea for two-dimensional condensation mechanisms on substrates, was confirmed by Palatnik and Papirov [82] for several metal condensates (in the instructive p vs. T and F vs. T representation). (ii) The critical pressure of the two-dimensional adsorbed gas becomes thus equal to $F_c = (2p_{C_3}/3d_0)$ when

referred to one molecule of area d_0^2. (iii) The critical area, occupied at the critical temperature, becomes $W_c = (V_{C_3}/4d_0)$.

As a general consequence it follows that a two-dimensional nucleation process, e.g., in the binodal area according to the two-dimensional van der Waals like phase diagram, takes place at considerably lower temperatures (with T_{m_2} and T_{b_2} shifted to approximately $T_{C_3}/2$, T_b). The relative areas of occupation or, more significantly, the relative coverages are thus $0.33\Theta_0$ at T_{C_2} and $0.45\Theta_0$ for the formation of a two-dimensional condensate. However, there is also an additional point to be mentioned in connection with possible diamond formation at seemingly metastable conditions of diamond. If adsorbed carbon atoms (eventually in solution with hydrogen, carbonaceous compounds such as CH_4 from the volume of the reaction vessel) are brought by a high flux, q_0, to the substrate (e.g., the anode in plasma-assisted CVD processes), the condensation of carbon droplets could take easily place (at $p > 10$ kbar, transformed from two-dimensional to three-dimensional pressure). Thus, a population of nanosized liquid (or liquid-like) carbon clusters is assumed to exist on the substrate, permitting its enhanced crystallization to diamond according to the mechanism discussed in Sect. 8.3.5. It turns out that condensation and subsequent nucleation in the two-dimensional population of adsorbed carbon films could give an easier way of diamond formation than in the bulk of a supersaturated gaseous volume at a homogeneous condensation process. A first indication of this possibility can be found in Ref. [87].

A number of experiments with a single- or multiple-phase transition in two-dimensional layers on both liquid and solid substrates are described in the literature [62, 85, 86]. As a rule, two-dimensional condensation begins at relative coverage values $\Theta = 0.2$, and at 0.47 only a two-dimensional condensate is present [85]. It has to be kept in mind that even very low two-dimensional pressures (as measured in two-dimensional thin layers) correspond in their physical effect to enormous pressures and pressure changes in the three-dimensional gaseous volume. In general, a two-dimensional pressure F (in dyn/cm) is equivalent to $51F^{3/2}$ bar [85] and thus a two-dimensional pressure of only 50 dyn/cm, measured, e.g., with the Langmuir balance (for a two-dimensional layer on a liquid) corresponds to approximately 1800 bar [85]. Thus phase changes are induced and take place in two dimensions in adsorbed thin layers with greater ease and at lower temperatures than in the three-dimensional case. Remarkable examples in this sense are experimental and theoretical findings summarized by Mutaftschiev in Ref. [62] (see also [86]) on the condensation kinetics and two-dimensional layers of noble gases formed on graphite substrates. For this example, the formation of two-dimensional gaseous, liquid-like, and several crystalline phases was experimentally verified. These transitions take place for the Kr/graphite system at Kr-vapor pressures over the condensate of $p \sim 10^{-2}$ bar, corresponding to pressures in the two-dimensional adsorbed layer, equivalent to about 9×10^2 bar. In this sense, a carbon-vapor flux q_0, reaching a Mo or W substrate and guaranteeing its condensation at $\Theta > 0.2$, can also be equivalent to the effect of pressures as obtained in the Belt chamber by direct synthesis of diamond at "normal" three-dimensional conditions.

In considering these and similar processes of two-dimensional phase transitions, it also has to be kept in mind that the nature of the two-dimensional condensates, their character (localized or freely moving, one-dimensional layers or multilayered, etc.), and the very existence of a layer (see Eq. (8.37), determining the Knudsen temperature) depend on the ratio of the adsorption energy, U_{ad}, to the binding energy, U_0, of the ad-molecules on a given substrate.

Thus, by changing substrates (i.e., U_0) and substrate temperatures, the flux q_0 of molecules, reaching the substrate, and the dependences, describing the processes of two-dimensional condensation and phase transitions, are also changed (described, for example, not in terms of a purely two-dimensional van der Waals equation but with another mean field approximation, e.g., the Frumkin–Fowler adsorption isotherm [86]). These problems are elucidated in detail in the present-day literature (see [62, 86]) including also the case of two-dimensional condensation and two-dimensional mixing of two and more components, which could also be of significance in considering nucleation of carbonaceous gas mixtures, hydrogen, and their reactions in two-dimensional space. The respective temperatures are only a half of T_{C_2} of carbon (~ 1000 K) and at pressures, guaranteed (at the conditions of plasma-assisted processes) to be of the order of 5×10^4 bar [87].

The detailed analysis of two-dimensional condensation of carbon vapors and of carbonaceous compounds could give, according to existing theoretical evidence, a new and relatively simple explanation to the circumstance that nucleation of diamond under seemingly metastable conditions has been as yet observed only on solid substrates (Mo, W, etc.). The foregoing discussion shows that in the condensed two-dimensional state diamond formation could probably take place at "stable" conditions, the vapor pressure over the condensate being a poor indication of the real conditions, existing in the condensate.

Another way of introducing a similar idea of quasi-metastable nucleation into heterogeneous diamond nucleation in plasma-assisted methods at seemingly metastable conditions is to calculate the intrinsic pressure in the thin carbon film formed on the substrate [87] treating the film like a solid, in which new building units are introduced by the flux of condensing molecules. Using a model proposed by Windischmann [88], in Ref. [87] the pressure at which thin carbon films, formed under high-energy sustained condensation, are exposed is estimated to be well over 50 kbar. No direct experiment is known, however, at present, which would allow us to distinguish between real and imaginary metastable conditions in carbon condensation processes on a solid substrate.

8.3.8 Crystal Growth Mechanisms and the Morphology of Diamond Crystals

Present-day concepts on the mechanisms of crystal growth are summarized in several classical or recently published monographs (see, for example, [31, 62, 75, 89]). They are based on three different models of the interface structures between crystal and ambient phase and thus on three possible attachment modes: growth via two-dimensional nucleation (for a perfect, dislocation-free face); continuous (or normal) growth (for atomically rough crystalline faces) and the dislocation mediated crystal growth mechanism, proposed by Frank [31, 89]. The general dependence, determining crystal growth, can be written as

$$g = Z\Omega(T)\left[1 - \exp\left(-\frac{\Delta\mu\,(T,\,p)}{RT}\right)\right], \tag{8.40}$$

where Z is the impingement rate of ambient phase molecules, $\Delta\mu\,(T,\,p)$ is the thermodynamic driving force of crystallization (and thus $\left[\Delta\mu\,(T,\,p)\,/RT\right]$ is the corresponding relative supersaturation), and the factor $\Omega\,(T)$ depends on the considered mode of crystal growth [31].

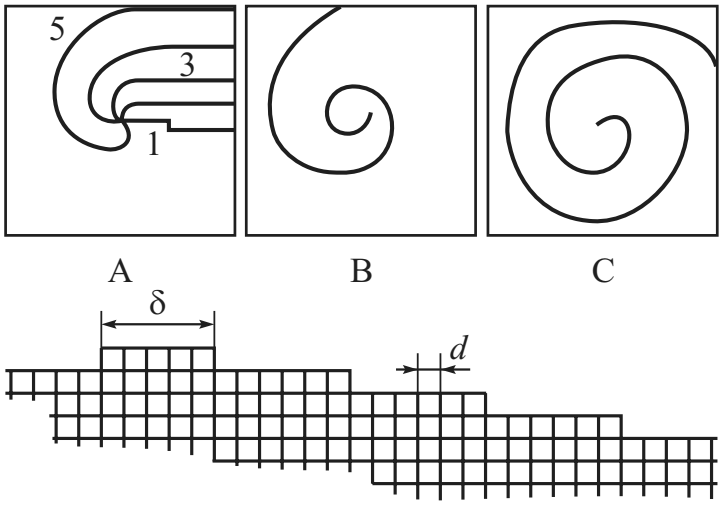

Figure 8.12: Screw dislocations, Archimedean growth spirals, and determination of relative supersaturation from the spiral width (see [31]): (a) Several consecutive stages (A, B, C) of formation of a growth spiral on a crystal face; (b) cross section of the growth spiral: illustration of the determination of the relative number, α_0, of growth sites from the width, δ, of the spiral and mean size, d_0, of crystal building units

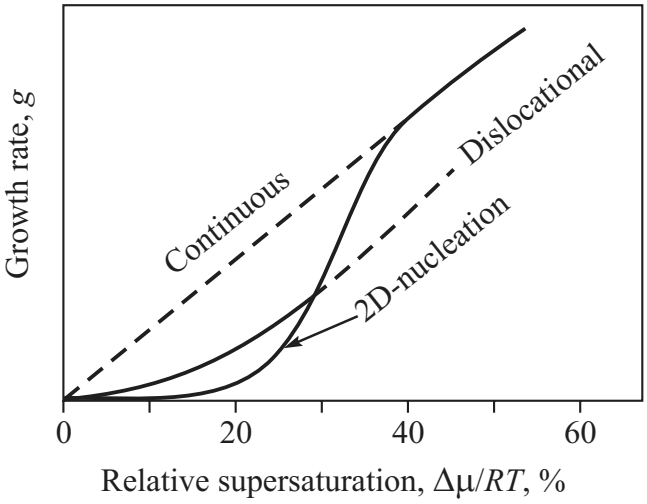

Figure 8.13: The main ranges of relative supersaturation values, $\Delta\mu/RT$, at which continuous, screw-dislocational, and two-dimensional nucleation mediated crystal growth are operable (see [31, 89] and Sunagawa [90])

In melt crystallization, Z is inversely proportional to the bulk viscosity of the melt. In vapor phase crystallization, Z is directly proportional either to the vapor pressure in "static" experimentation or to the flux of crystallizing species (in dynamic experiments, e.g., in CVD or plasma-type diamond growth). In considering growth of diamond, the already introduced dimensionless coefficients Z' (see Sect. 8.3.6) may (and, as proven by many authors) decisively determine the real value of the impingement rates, Z. The expression in the square brackets of Eq. (8.40) gives at $\left[\Delta\mu\,(T,\,p)\,/RT\right] \gg 1$ values practically approaching unity, while at the normally prevailing lower relative supersaturations of growth, we can write

$$\left[1-\exp\left(-\frac{\Delta\mu\,(T,\,p)}{RT}\right)\right] \cong \frac{\Delta\mu\,(T,\,p)}{RT}\,. \tag{8.41}$$

In the continuous growth mechanism, the factor $\Omega\,(T)$ in Eq. (8.40) is given directly by the relative number, α_0, of growth sites ($\Omega(T) \cong \alpha_0$). In typical cases of normal growth, $\alpha_0 \cong 10^{-2}$–10^{-1}. In the case of surface nucleation mediated growth, we have

$$\Omega\,(T) \approx \exp\left[-\frac{\Delta G_{2c}\,(T,\,p)}{RT}\right]\,. \tag{8.42}$$

Here $\Delta G_{2c}\,(T,\,p)$ is the thermodynamic work, which is necessary to form a two-dimensional nucleus on the growing face. For the growth via the screw dislocation mechanism, the theory gives

$$\Omega\,(T) \approx \frac{\Delta\mu\,(T,\,p)}{4\pi\,\sigma\,R}\,. \tag{8.43}$$

The latter relation follows from one of the basic assumptions of dislocational mediated crystal growth: The relative number of growth sites, when this mechanism is operable, is given by $\alpha\,(T) = d_0/\delta_\mathrm{s}$, where

$$\delta_\mathrm{s} = \frac{4\pi\,\sigma\,V_\mathrm{m}}{\Delta\mu} \tag{8.44}$$

is the mean width of the growth spirals (see Fig. 8.12) at the given supersaturation. Thus Eq. (8.44) gives a convenient and simple method of estimating $\Delta\mu\,(T,\,p)$ from the growth morphology. Equation (8.40) indicates that, in general, for continuous modes of growth a linear dependence of g on $\Delta\mu\,(T,\,p)$ is to be expected ($g \approx \alpha_0 Z\Delta\mu/RT$), while for two-dimensional or dislocational growth the corresponding dependences are either parabolic ($g \approx \alpha Z\Delta\mu^2/RT$) or exponential with respect to $\Delta\mu\,(T,\,p)$. In introducing appropriate constants it turns out that continuous growth is operable from lowest relative supersaturations, spiral growth guarantees measurable growth even with several % values of χ (typically for $\chi \cong 1$–5%), and two-dimensional nucleation-mediated growth kinetics can be expected only after a χ-lag higher than 20%. The predominant operation of the various growth mechanisms is illustrated in Fig. 8.13 in a representation due to Sunagawa [90].

The theory of crystal growth specifies distinct dependences of equilibrium and growth forms and morphologies of crystals in dependence of supersaturation. In general, a simplification of growth forms (and of dominant faces) is to be expected at increasing relative supersaturation. The experimentally verified change of diamond crystal morphology at different growth

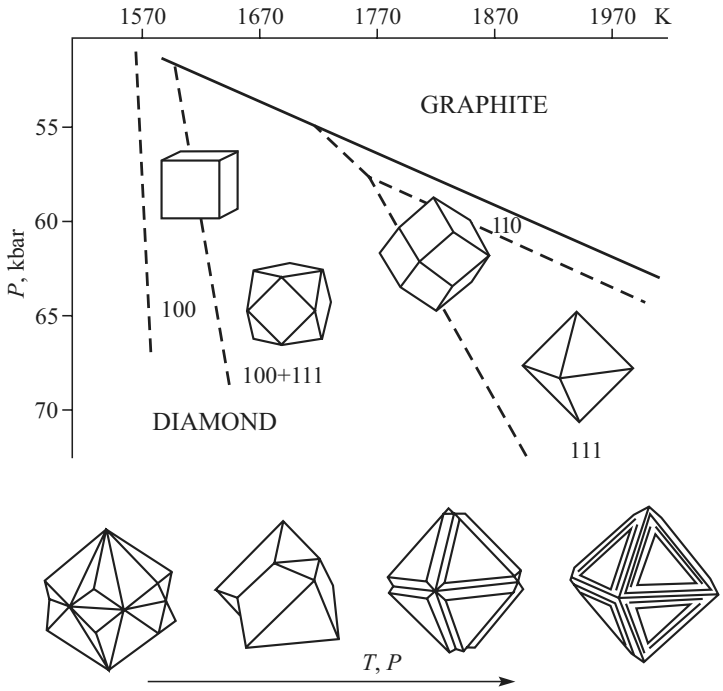

Figure 8.14: Crystal habits of diamond crystals (upper) and way of twining of diamond crystals (lower) synthesized at different temperatures and pressures in the stability field of diamond in the carbon phase diagram ("direct" technical synthesis) according to Kostov and Kostov [91]

conditions both in "direct" (at increased pressure p in the field of stability of diamond) and in metastable growth is given in Figs. 8.14 and 8.15. These results, due to Sunagawa [90] and Kostov and Kostov [91], give a possibility of reconstructing growth conditions of diamond from morphology and general appearance. This possibility is of exceptional significance, especially in cases with geological and cosmic diamond samples. We have to add to the above schema that if diamond microcrystals are formed from liquid carbon, a liquid droplet type appearance should be expected. These considerations are used in the experimental part of the present analysis. It is also to be mentioned here that twin-crystal formation is dependent on supersaturation (see, e.g., [91, 92]). The change of twinning in diamond formation with temperature and pressure is empirically illustrated in Fig. 8.14.

8.3.9 Thermodynamic and Kinetic Conditions of Formation of Crystalline and Glassy Carbon Condensates

In Sects. 8.3.6 and 8.3.7, two possible mechanisms for the formation of diamond condensates at metastable conditions have been discussed in terms of Ostwald's rule of stages, or at quasi-metastable conditions prevailing in a two-dimensional carbon adsorption layer. According to both mechanisms, the formation of graphite-like or diamond-type amorphous condensates has

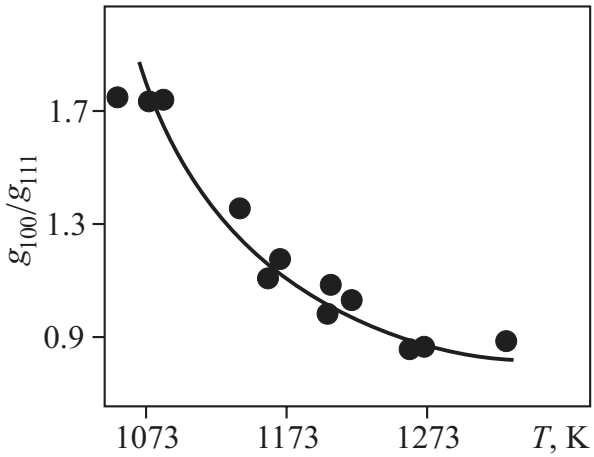

Figure 8.15: Growth morphology of diamond crystals for growth at different substrate temperatures (given on the abscissa) at otherwise equal CVD conditions of metastable synthesis (after Spitzyn [18]). The growth rates, g, in the $\langle 100 \rangle$ and $\langle 111 \rangle$ directions are measured. A continuous change from mainly cubic into mainly octahedric crystal habit is observed with rising substrate temperatures

also to be considered. As shown in section 8.4.3, such condensates were in fact experimentally observed. Let us now transform the final mathematical formulation of Ostwald's rule of stages, Eq. (8.35), into a form that can be easily brought into a graphical representation. For this purpose, we introduce the notation (cf. Eq. (8.35))

$$\left(\frac{\Phi_{\mathrm{gr}}}{\Phi_{\mathrm{d}}}\right)\left(\frac{\sigma_{\mathrm{gr}}}{\sigma_{\mathrm{d}}}\right)^{3}\left(\frac{V_{\mathrm{m}}^{\mathrm{gr}}}{V_{\mathrm{m}}^{\mathrm{d}}}\right)^{2} = F_0 \,. \tag{8.45}$$

Then we have to take into account that in vapor condensation processes

$$\Delta\mu_{\mathrm{gr}} = \Delta\mu_{\mathrm{d}} + \Delta\mu_{\mathrm{gr/d}} \tag{8.46}$$

holds (see Figs. 8.4 and 8.6). Here $\Delta\mu_{\mathrm{gr}}$ and $\Delta\mu_{\mathrm{d}}$ denote the driving force for the vapor/graphite and for the vapor/diamond condensation, and $\Delta\mu_{\mathrm{gr/d}}$ is the thermodynamic driving force for the diamond/graphite transition. The value of $\Delta\mu_{\mathrm{gr/d}}$ is given by Simon's expression (8.16), i.e., $\Delta\mu_{\mathrm{d/gr}} \equiv \Delta G_{\mathrm{p}}(T)$. For the case when condensation takes place at the conditions of a real or imaginary static vacuum deposition experiment between graphite as an evaporator (sustained at $T = T_{\mathrm{evap}}$) and a substrate (held at $T = T_{\mathrm{substr}}$) we have to write (see [33, 93])

$$\Delta\mu_{\mathrm{gr}}(T_{\mathrm{substr}}) = RT_{\mathrm{substr}} \ln\left(\frac{p\left(T_{\mathrm{evap}}\right)}{p\left(T_{\mathrm{substr}}\right)}\right) . \tag{8.47}$$

Thus, the condensation process takes place in such a way that graphite is evaporated at T_{evap} and the carbon vapors are condensed at a temperature $T_{\mathrm{substr}} < T_{\mathrm{evap}}$. For any of these temperatures, we arrive with

$$\ln p \cong -\frac{\Delta H_{\mathrm{subl}}^{\mathrm{gr}}}{RT} + \mathrm{const} \tag{8.48}$$

at another expression of Eq. (8.47), i.e.,

$$\Delta\mu_{\mathrm{gr}}(T) = \frac{\Delta H_{\mathrm{subl}}^{\mathrm{gr}}}{T_{\mathrm{evap}}}\left(T_{\mathrm{evap}} - T_{\mathrm{substr}}\right) . \tag{8.49}$$

In this way, with Eqs. (8.16), (8.45), (8.46), and (8.49) the condition for dominant diamond nucleation, Eq. (8.35), is transformed into

$$Y = 1 - \frac{A_0}{F_0 \Delta H_{\mathrm{subl}}}\left(1 - \frac{B_0 T_{\mathrm{m}}}{A_0} X\right) , \tag{8.50}$$

where we have used the notation $Y = \left(T_{\mathrm{evap}}/T_{\mathrm{m}}\right)$ and $X = (T_{\mathrm{substr}}/T_{\mathrm{m}})$, indicating in both cases with T_{m} the melting point of carbon. Thus, in Y vs. X coordinates, we obtain a straight line

$$Y = 1 - D_0 + D_1 X . \tag{8.51}$$

Here $D_0 = A_0/(F_0 \Delta H_{\mathrm{subl}})$ and $D_1 = (B_0 T_{\mathrm{m}}/A_0)$ are determined by the ratio of Simon's coefficients A_0 to ΔH_{subl} and by the kinetic parameters of the condensation process, given by F_0 (see Eq. (8.45)).

In a similar way and again in Y vs. X coordinates, we have constructed in previous investigations [31, 64, 93] the thermodynamic and kinetic conditions for the formation of liquid or crystalline condensates on a substrate at $T < T_{\mathrm{m}}$, where the crystal is the thermodynamically stable state. In this second case, however, in beginning our calculation in the same way as above with Eq. (8.35), we arrive, with the obvious condition $\Delta\mu_{\mathrm{v/cryst}}(T) = \Delta\mu_{\mathrm{v/liquid}}(T) + \Delta\mu_{\mathrm{liq/cryst}}(T)$, at the more complicated expression

$$\frac{1}{Y} = \frac{1}{X} - \frac{1}{(1 - F_0)}(1 - X) . \tag{8.52}$$

This is so because we have to introduce here (with $a_0 = 2$) the thermodynamic force of crystallization with the expression

$$\Delta\mu_{\mathrm{liq/cryst}} \cong \Delta H_{\mathrm{m}}\left[1 - \frac{T}{T_{\mathrm{m}}}\right]\frac{T}{T_{\mathrm{m}}} , \tag{8.53}$$

where $\Delta H_{\mathrm{m}} = \Delta S_{\mathrm{m}} T_{\mathrm{m}}$ indicates the respective enthalpy of melting. A similar expression, Eq. (8.14), was introduced in Sect. 8.3.2. The value of F_0 in Eq. (8.52) is again given with Eq. (8.45); however, in this second case the indices to σ, Φ, and V_{m} have to be accordingly changed from (gr) and (d) (for graphite to diamond) to (cryst) and (liq) in the liquid/crystal

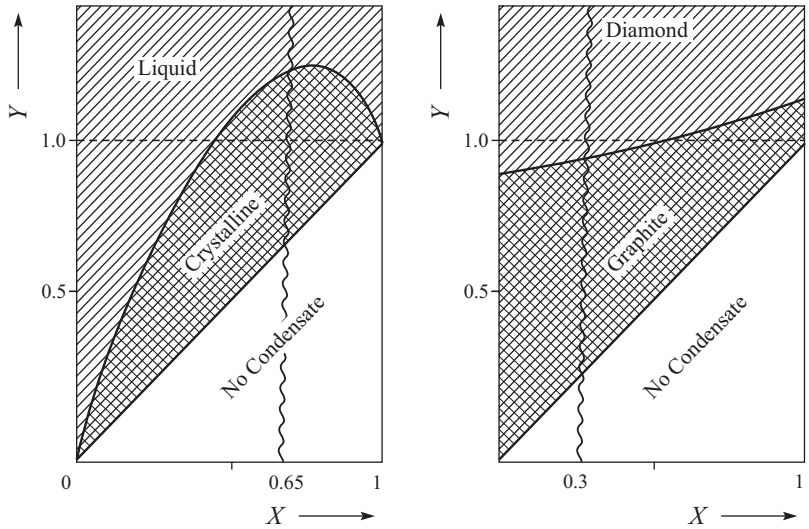

Figure 8.16: The thermodynamic and kinetic boundaries for the formation of metastable and stable condensates and for the glass formation in Y vs. X coordinates in terms of the kinetic formulation of Ostwald's rule of stages: Left: Conditions for the formation of liquid (shaded area) and crystalline condensates (double shaded area) [31, 64, 93], according to Eq. (8.52), for a given F_2-value (at $\Phi_{\text{liq}} \approx \Phi_{\text{cryst}}$). Right: Conditions for the formation of diamond (shaded area) and graphite (double shaded area), according to Eq. (8.50), for typical F_0-values as explained in the text (with $X = (T_{\text{substr}}/T_{\text{m}})$, $Y = (T_{\text{evap}}/T_{\text{m}})$). Note that diamond formation is only possible at relatively high temperatures, T_{substr}, and with a high evaporation temperature

case. The thermodynamic condition for the formation of a condensate on the substrate at our imaginary static condensation experiment is given by $Y \geq X$, i.e., by $T_{\text{evap}} \geq T_{\text{substr}}$.

The thermodynamically stable crystalline condensate, discussed in the second case, is dominantly formed, according to Eqs. (8.53) and $Y \geq X$, in between the straight line and the curve on the left part of Fig. 8.16. For each F_0-value, a corresponding curve can be drawn. At lower values of F_0, the curve reaches higher values and the greater is the double shaded area in this figure, which shows the formation of the stable crystalline condensate. Above this curve, the formation of the metastable liquid condensate becomes possible and is dominantly observed. Experimental evidence in this respect [31, 94] is available (at $T < T_{\text{m}}$) for several cases of formation of liquid and crystalline condensates of various substances.

A similar result follows from Eq. (8.56) for the particular case of the possible formation of diamond condensates at conditions (i.e., normal pressure p) where graphite is stable. The particular form of Simon's equation changes the Y vs. X diagram as shown on the right part of Fig. 8.16. Here again the formation of metastable diamond condensates is to be expected only for conditions corresponding to the area above the straight lines that have to be drawn with various F_0-values. The formation of graphite condensates should be possible in the double shaded area between this curve and the corresponding straight line. In Fig. 8.16, only one of the possible lines corresponding to Eq. (8.5) is given, referring (at $\Phi_{\text{d}} = \Phi_{\text{gr}} = 1$) to the

already mentioned values of σ and V_m for both crystalline modifications of carbon, to the constants A_0, B_0 in Eq. (8.19) and to the high value of ΔV_{subl} for graphite. The expected area of possible diamond formation for $T_{evap} < T_m$ of graphite is relatively small and corresponds to low X-values, where the formation of crystalline condensates is scarcely possible. At these low substrate temperatures, because of the restricted surface mobility, the formation of amorphous glass-like condensates should be expected. Only for conditions where Y is equal to or even higher than 1 (i.e., for temperatures $T_{evap} > 3000$–$4000\,K$) and for relatively high substrate temperatures T_{substr} diamond formation is expected. At these conditions, however, the **vapor→ two-dimensional liquid → diamond mechanism**, already discussed in Sect. 8.3.5, could be more efficient.

At low X-values (e.g., $X < 1/2$), the formation of glass-like amorphous condensates becomes a necessity. This process takes place at vitrification conditions when the time of molecular relaxation, τ_R, of a system becomes larger than the characteristic time of change of external parameters (e.g., temperature variation in cooling processes). In application to vacuum deposition experiments, this condition implies that a vitreous condensate will be formed when the inequality

$$\tau_{R(condensate)} \geq \tau_{(vapor\ deposition)} \tag{8.54}$$

holds. Equation (8.54) is fulfilled when the time of molecular rearrangements of the surface layer of the amorphous condensate becomes equal to or larger than the average time for vapor deposition, $\tau_{(vd)}$, at which a monolayer covers the surface of the condensate, thus burying-in its initial disorder. Defining $\tau_{(vd)}$ through the vapor deposition rate, Z_v (expressed in numbers of monolayers per unit time), as $\tau_{(vapor\,deposition)} = 1/Z_v$, and assuming that $\tau_{R(condensate)}$ may be expressed via a simple Frenkel-type temperature dependence, $\tau \propto \exp(U_0/RT)$, with a constant activation energy U_0, it follows that the critical temperature for vitrification, T_c, of a liquid condensate will be [31, 64, 94]

$$\frac{1}{T_c} \geq \frac{R}{U_0}\left[\ln\left(\frac{1}{\tau_0}\right) - \ln(Z_v)\right]. \tag{8.55}$$

The analogy of the above given expressions with the derivation and the physical meaning of the Bartenev–Ritland equation is obvious. The Bartener–Ritland equation determining the temperature of vitrification T_g of a bulk melt sample, cooled down to room temperature with a rate $\omega_0 = (dT/dt)$, is usually written as $(1/T_g) = [\text{const} - \log(\omega_0)](R/U_0)$ [31]. Defining Z_v in Eq. (8.55) through the (T_{subl}/T_{evap}) ratio, a dependence is obtained in terms of a Y vs. X diagram schematically shown in Fig. 8.16 with a wavy line (at $X \cong 1/3$). In the same way, on the left part of Fig. 8.16 the T_g-value is indicated corresponding to $X = 2/3$ as observed for bulk vitrification of typical glass-forming substances.

From the foregoing analysis it is evident that the set of requirements determining the possibility of formation of vitreous condensates consists of (i) the thermodynamic condition for the possibility of formation of condensed phases, $Y \geq X$, (ii) the kinetic conditions providing the possibility of the initial formation of a liquid condensate, Eq. (8.52), and (iii) the conditions guaranteeing vitrification (i.e., sufficiently low temperatures and/or sufficiently high condensation rates, ω_0), Eqs. (8.54) and (8.55).

In a qualitative way, conditions for the formation of solid amorphous thin films had been already formulated years ago by Hirth and Pound [95] and by Chopra [96]. The mentioned

authors argued that vitreous amorphous films are obtained when the temperature of the substrate is so low that the deposited atoms become immobile. Here we derived Eqs. (8.51) and (8.52) and constructed Fig. 8.16 for a thought experiment in which from an evaporator at a relative temperature Y a vapor pressure $p(T_{\mathrm{evap}})$ is sustained, guaranteeing (for carbon only at $T > T_{\mathrm{m}}$) a deposition rate Z, sufficiently high to form a thin carbon layer.

Only in real experimental conditions several experiments, discussed in Sect. 8.3.3, have been performed up to now, roughly corresponding to these conditions. In most cases, a sufficient impingement rate Z in CVD methods and in similar techniques of carbon thin film deposition, diamond nucleation, and diamond growth, a flux of molecules is produced in complicated chemically reacting vapor systems, which are far above those that can be reached in a one-component carbon system via direct evaporation. Nevertheless, some of the results outlined here as principally possible may be of significance even in systems where chemical reaction equilibrium and stability constants determine the processes taking place on the substrate.

8.3.10 Thermodynamics and Kinetics of Gaseous Transport Reactions with Activated Carbon Materials

The metastable growth of diamond becomes possible at relatively low temperatures (1000–1200 K) only via chemical transport reactions: At these conditions the vapor pressure of any form of carbon is too low to guarantee material transport. Let us first consider the well-known thermodynamics of gaseous reactions with the participation of a solid reagent E, $\alpha^*\mathrm{E} + \beta_i^*\mathrm{A}_i \Leftrightarrow \gamma^*\mathrm{C}$. In our case, E denotes a given form of solid carbon and A_i and C are the corresponding gaseous reactants and reaction products. The equilibrium constant of the above reaction,

$$K = \frac{[\mathrm{C}]^{\gamma}}{\prod\limits_i [\mathrm{A}_i]^{\beta_i}} \,, \tag{8.56}$$

is determined (at $p = \mathrm{const}$) by the respective Gibbs thermodynamic potential change ΔG as

$$\ln K_{\mathrm{p}} = -\frac{\Delta G_{\mathrm{R}}}{RT} \,, \quad \Delta G_{\mathrm{R}}(T) = \gamma^* G_{\mathrm{c}}(T) - \sum_i \beta_i^* G_{\mathrm{A}_i}(T) - \alpha^* G_{\mathrm{E}}(T) \,. \tag{8.57}$$

In the above equation the thermodynamic potential of the solid reagent, $G_{\mathrm{E}}(T)$, has to be referred to the corresponding polymorphic modification of the substance, E (in our case: diamond, graphite, or vitreous carbon), taking part in the reaction. It was shown by Gutzow [31, 32] (see also [33, 35]) that for temperatures sufficiently below the glass transition (i.e., for $T < T_{\mathrm{g}}$) the vapor pressure, p_{gl}, of a vitrified solid can be written as

$$\ln\left(\frac{p_{\mathrm{gl}}}{p_{\mathrm{cryst}}}\right) = \frac{\Delta G_{\mathrm{g}}(T)}{RT} = \frac{\Delta H_{\mathrm{g}}}{RT} - \frac{\Delta S_{\mathrm{g}}}{R} \,, \tag{8.58}$$

where $\Delta G_{\mathrm{g}}(T) = G_{\mathrm{gl}}(T) - G_{\mathrm{cryst}}(T)$ (see Eq. (8.19)). Thus, the vapor pressure (or respective solubilities C_{gl} and C_{cryst}) of the different polymorphic forms of carbon can be calculated using Eq. (8.58). The respective ΔG_{g}-values, following from Figs. 8.7 and 8.8 and in particular,

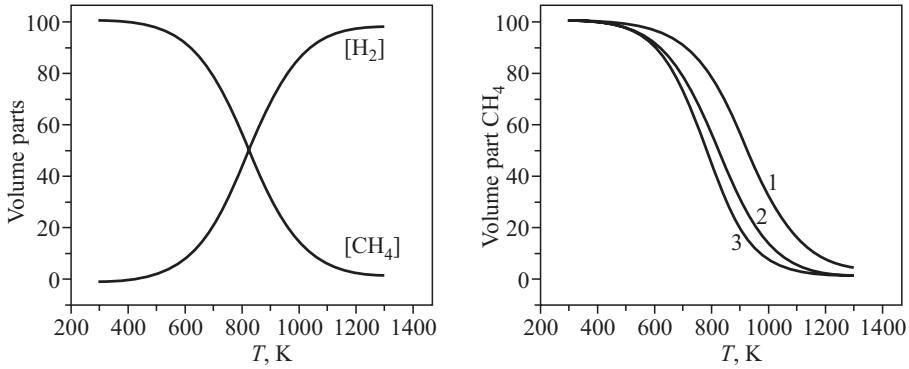

Figure 8.17: Left: Volume parts of hydrogen and CH_4 over graphite at different temperatures for the reaction $C+2H_2 \Leftrightarrow CH_4$ with K_p-values calculated according to Eq. (8.57) (thermodynamic data from Ref. [46]). Right: Comparison of the concentration of CH_4 over different forms of carbon: (1) vitreous carbon, (2) diamond, and (3) graphite, for the reaction $C + 2H_2 \Leftrightarrow CH_4$ according to Eq. (8.59)

the solubilities of different carbon materials indicated there have been calculated and found in satisfactory corroboration with direct calorimetric measurements.

With the connection given above it also follows [33] that the chemical constant of a heterogeneous reaction with the participation of vitrified solids at $T < T_g$ (e.g., vitreous carbon) can be expressed as

$$K_{p_{gl}} = K_{p_{cryst}} \exp\left[\frac{\gamma^* \Delta G_g}{RT}\right] = K_{p_{cryst}} \left(\frac{p_{gl}}{p_{cryst}}\right)^{\gamma^*} . \tag{8.59}$$

Here we refer G_{cryst} to the crystalline modification, stable at the considered conditions (to graphite, according to Figs. 8.4 and 8.6). By exploiting Eqs. (8.20)–(8.22), the additional ΔG_x-values, introduced by foregoing mechano-chemical treatment, can be taken into account in calculating the respective K_p-values. Thus, the whole thermodynamics of possible gaseous transport reactions can be calculated in advance for any of the carbon materials whose $G(T)$-values are given in Figs. 8.4–8.6. This result will be illustrated for one of the most significant gaseous transport reactions in the metastable growth of diamond, namely $C + 2H_2 \Leftrightarrow CH_4$. The corresponding chemical reaction constant is given with

$$K_{p_1}(T) = \frac{[CH_4]}{[H_2]^2} \tag{8.60}$$

and $K_{p_1}(T)_{cryst}$ (for graphite) can be directly calculated using the data for the $G(T)$ curve for graphite (see [46] and Fig. 8.4). With Eq. (8.60) and the obvious condition $[H_2] + [CH_4] = 1$, the equilibrium concentration $[H_2]$ in a closed reaction vessel over graphite is given as

$$[H_2] = \left[\left(1 + 4K_{p_1}\right)^{1/2} - 1\right] \frac{1}{2K_{p_1}} \tag{8.61}$$

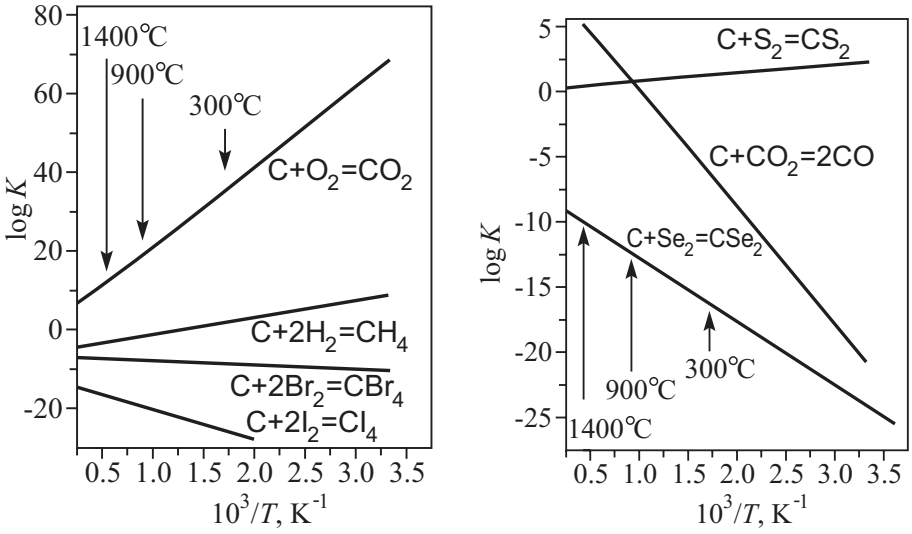

Figure 8.18: Temperature dependence of the chemical constant K_p for (left) halogen/graphite reactions and for oxidation of carbon and (right) for several chalcogen/graphite reactions and for Boudouard's reaction

for graphite, vitreous carbon, diamond, etc., when the corresponding ΔG-values (see Figures 8.4–8.6) are introduced into Eq. (8.60) to calculate the respective K_p-values.

In Fig. 8.17, the results of such calculations are given. The thermodynamic properties of various modifications affect considerably the equilibrium concentrations of the reaction components (here of H_2 and CH_4 over glass, graphite, and diamond). These differences which are usually ignored indicate a natural source of thermodynamic driving force as is illustrated more distinctly on the right part of Fig. 8.17 for various temperatures. The kinetics of incorporation of C-building units into the diamond lattice, as mentioned in Sect. 8.3.5, is determined by the presence of an optimal concentration of free H-atoms (designated here by the symbol H*). Using the chemical constant K_{p_2} of the corresponding reaction ($H_2 \Leftrightarrow 2H$), i.e.,

$$K_{p_2} = \frac{[H^*]^2}{[H_2]} \tag{8.62}$$

and employing again the condition $[H^*] + [H_2] = 1$, we get

$$[H^*] = \left[\left(1 + K_{p_2}^{-1}\right)^{1/2} - 1\right] \frac{K_{p_2}}{2} \,. \tag{8.63}$$

In Figs. 8.18 and 8.19, the temperature dependence of the reaction constants for several simple reactions are given, which are promising as vapor transport reactions for the transition **carbon glass → diamond** in closed silica reaction vessels. A simple requirement, well known from single-crystal growth techniques [93], is that transport reactions can be optimally used

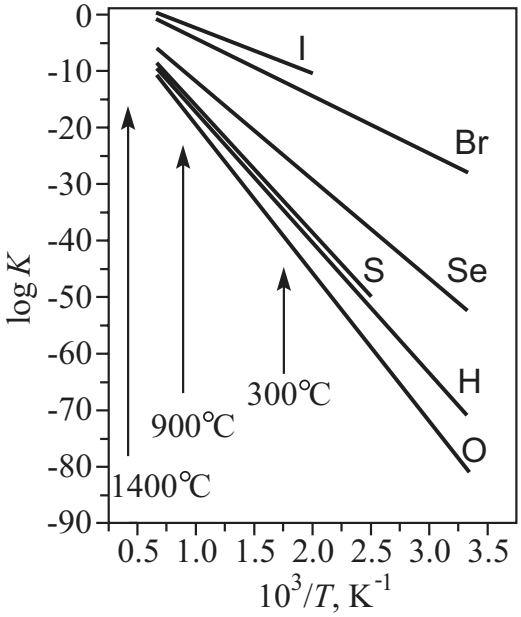

Figure 8.19: The chemical constant, K_p, for the atomization reactions of hydrogen and of several halogen and chalcogene elements (thermodynamic data as in Figs. 8.17 and 8.18 are taken from Ref. [46])

at $\log K_p \approx 1$, where a sufficient concentration of both reactants and reaction products is present. The respective possibilities are obvious from the above mentioned figures, taking into account that in order to guarantee sufficient incorporation rates of carbon into the growing diamond crystal usually temperatures of 1200–1600 K are necessary. These figures also give indications for growth in the presence of either atomic hydrogen or other elements in atomic form (e.g., iodine). These figures, and many others calculated for about 50 additional reactions, indicate possible experimental realizations summarized in the experimental part (Sect. 8.4) of the present investigation. In constructing the respective figures, the $\Delta G\,(T)$ tables of Ref. [46] were used.

Experimental evidence and simple kinetic considerations also show that not only hydrogen but also halogens and chalcogens in atomic form could be essential in gaseous transport mediated metastable growth of diamond. Figure 8.19 and Eqs. (8.62) and (8.63) show that, while for a measurable H-concentration to be obtained in a closed reaction chamber, a temperature of at least 3000 K is necessary (thus the application of hot filament techniques or plasma-assisted growth is required), the formation of I atoms is easily obtainable even at 1000 K. This property explains the good results obtained with the $2I_2 + C \rightarrow CI_4$ reactions [27] as will be shown in Sect. 8.4.5.

8.4 Experimental Part

8.4.1 Introductory Remarks

In this second part of the present chapter, experimental results on the nucleation and growth of diamond and on graphite–diamond transitions, taking place at metastable or, at least, seemingly metastable conditions, are summarized, some of them from our experience, others from the literature. To the opinion of the authors, these results confirm or illustrate most of the derivations and expectations, presented in the foregoing theoretical part. Explicitely mentioned and even discussed in some length are preferentially those experimental findings that in our opinion are indicative from a theoretical point of view. Several outstanding papers giving serious contributions to the solution of problems in technical applications had to be omitted. The reader more or less experienced in the metastable diamond synthesis literature will also miss a thorough discussion of several articles, which brought in the first information on the possibility of metastable synthesis: These results are analyzed in details in the review articles [2, 3, 10, 18, 19, 26, 27, 97]. It is also understandable that predominant significance is given to the results obtained by the present authors during several years of tedious experimentation. Only a small part of these experiments is published at present (see [20, 21, 29, 30, 38]).

Usually in the classical literature on metastable diamond synthesis of the last 20 years it is claimed that this process is possible in gaseous phase transport reactions only in the presence of atomic hydrogen. We begin the present discussion with several confirmed cases of diamond formation and growth at quite different, also metastable conditions, contradicting this claim. First several doubtful, even unsuccessful experiments, are reported. One of them, performed by Hannay [37], was described in some detail in Sect. 8.2. Below more recent results are discussed, demonstrating metastable formation of diamond from vapor phases, as a purely physical process in the absence of reagents such as atomic hydrogen: These are processes of metastable diamond formation in a one-component carbon system. Then a short outline of the results is given on transport chemical reactions in the vapor phase.

8.4.2 Metastable Diamond Growth from Solutions and Melts

In the earlier review literature [19], several attempts are described to grow diamonds at normal pressures either from Mg-silicate melts (carbon has a relatively high solubility in Mg-silicate melts) or in lead or copper (or Ni–Cu) melts. It is claimed that by applying temperature gradients to the mentioned metallic alloy systems (the diamond seed being placed at a lower temperature, graphite, at the higher), diamond growth was observed [19]. No further confirmation of these results is known to the authors. We tried to repeat partly, also without success, these experiments in order to realize in this way the glass/diamond reaction. The simple experimental assembly employed is evident from Fig. 8.20. In both cases, as the source of supersaturation at constant temperature ($\sim$ 1670 K) either crucibles or little combustion boat-like sample holders of vitreous carbon were used. The experiments were performed under argon and the diamond seed crystals were placed in molybdenium cages. In the arrangement given on the right part of Fig. 8.20, the solubility of vitreous carbon and of graphite (with graphite crucibles) was measured in a Ni/Cu alloy, as given in Fig. 8.8 (see also [38]). No distinct growth of the diamond seed crystals was registered either in the Mg/Fe-silicate melt with olivine-like composition

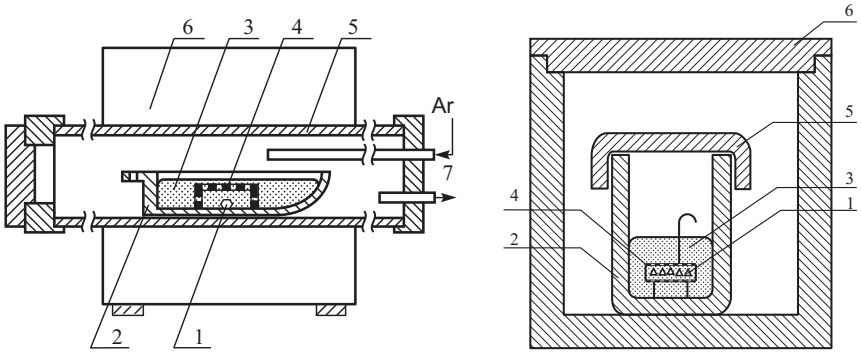

Figure 8.20: Left: Experimental assembly, employed to analyze the possibility of diamond growth in olivine silicate melts: (1) diamond seed crystal; (2) vitreous carbon boat; (3) Mg, Fe-olivine melt; (4) Mo grid, encapsulating the seed crystals; (5) refractory oven tube at 1670 K; (6) electric oven; (7) inlet and outlet of inert Ar gas. Right: Experimental assembly, used to measure the solubility of carbon modifications and diamond growth in $Cu_{30}Ni_{70}$ alloys: (1) diamond seed crystals in Mo grid; (2) vitreous carbon crucible; (3) Ni/Cu alloy melt; (4) Mo grid, encapsulating the seed crystals; (5) vitreous carbon cover lid; (6) graphite crucible and cover lid

(resembling to some extent geologically significant silicate melts, leading to the kimberlite deposits) or in the Ni/Cu alloys after exposure times of more than 6 h. An interesting arrangement for solution growth was more recently reported in [98]. Diamond single crystals grow (or recrystallize after an initial dissolution) in KOH melts at 1100 K in the presence of Ni (claimed to exert catalyzing effects in these processes). The essential point, to be mentioned in this section, is that in coincidence with the predictions in Sect. 8.3.5 and the analysis of Eq. (8.35), no nucleation of diamond from solution or melt was observed.

8.4.3 Metastable Nucleation and Growth of Diamond from Carbon Vapors

Up to now it seems that only in a relatively recent experiment performed by Pavlichenko et al. [99], direct nucleation of diamond from carbon vapors was confirmed. Carbon vapors were produced in vacuum in a Voltaic arc between two graphite electrodes (at $\sim 4000\,\mathrm{K}$) and condensation took place in the dense carbon vapor phase thus formed most probably also at very high temperatures. The thus nucleated diamonds, grown at the mentioned extreme temperatures in the Voltaic arc to micron size, sedimented onto a metallic substrate. To some extent this remarkable experiment corroborates with the conditions, following according to Fig. 8.16 and the predictions of Ostwald's rule of stages for the metastable nucleation of diamond. On the other hand, up to now (in coincidence with Fig. 8.16) any form of physical vapor deposition in its various forms (sputtering of graphite targets or laser abolition of graphite etc. and subsequent condensation at relatively low temperatures $T_{\mathrm{substr}} < T_{\mathrm{m\,carbon}}/3$) resulted only in amorphous graphite or diamond-like (i-diamond, a-diamond [60, 61]) amorphous layers. This result is again in coincidence with our theoretical expectation summarized in Fig. 8.16.

The nanosized diamonds, formed in interstellar space and found in hondride meteorites, may, as a "letter from supernovae explosions" [100], show with their droplet-like appearance clearly a liquid-carbon stage of development as discussed in Sect. 8.3.5. Thus, these nanosized diamond findings have to be categorized as resulting from the secondary crystallization of initially formed carbon droplets. This process implies also pressures of more than 10 bar at the first droplet carbonization stage of their formation when the phase diagram of carbon (Figs. 8.1 and 8.2) is recalled. Here we also have to categorize the already discussed transition of small graphite clusters (see Sect. 8.3.5) and the remarkable experiment performed by Fedoseev et al. [66, 67], giving another example of metastable diamond formation in the absence of catalyzing gases such as elementary hydrogen. The experiments mentioned in this section are of less technical significance but demonstrate the physical side of diamond nucleation and growth, concealed by complicated chemical processes in other methods of metastable diamond formation.

8.4.4 Diamond Nucleation and Growth with Transport Reactions in the Plasma Torch

In the first realization of metastable growth of diamond from the vapor phase, transport reactions of the type as discussed in Sect. 8.3.10 were used. A constant flow of a supersaturated gas mixture CH_4/H_2 was sustained in different experimental arrangements over a population of microsized diamond. After the discovery that atomic hydrogen strongly catalyzes the process, hot filaments, UV radiation and plasma torches were introduced into the reaction volume in hundreds of various arrangements, partly described in several review articles. Thus, out of the pioneering efforts of Eversole [2, 19], Deryaguin, Fedoseev, Ptizyn [9, 18, 27], Angus [2, 22, 23] and many others, real industrial realizations of metastable growth was achieved, leading to thin films, layers and optical windows of diamond, grown out of assemblies of initial seeds [10, 14, 15]. In recent developments, relatively soft, even pliant substrates (e.g., copper) were seeded by a multitude of diamond crystallization centers by a process of ablation with diamond nanopowders, preceding the condensation treatment. Thus, according to Sect. 8.3.6, the condensation process took place on a substrate with an activity $\Phi_d = 0$ and, according to Eq. (8.35), it resulted in continuous diamond growth. Such processes of technical growth of diamond layers are also described in detail in the existing technical and review literature on this subject [14, 15, 28, 98].

Beginning in the 1990s, it was observed that when, in the initial stages of condensation of the plasma-assisted C/H/O process, a more or less prolonged pulse of increased plasma intensity was applied, on the substrate (acting as an anode in the plasma torch) micro-diamonds were nucleated [20, 21, 28, 98]. We used this plasma-initiated diamond nucleation process in a new version described elsewhere [20, 21]. The gaseous mixture was formed in the greater volume of a commercial vacuum deposition apparatus, filled with a gaseous mixture produced by the joint introduction of H_2, H_2O, and CH_3OH (the latter two components as an alcoholic solution [20, 21]). One of the modifications of the apparatus used is seen in Fig. 8.21 (left), in the variant used to grow diamonds from glassy carbon. Thus, our vapor reaction vessel contained (in the plasma torch region) a combination of H_2, O_2, H, O, C, and carbonaceous reactants in a combination governed (as far as equilibrium can be assumed in the plasma torch)

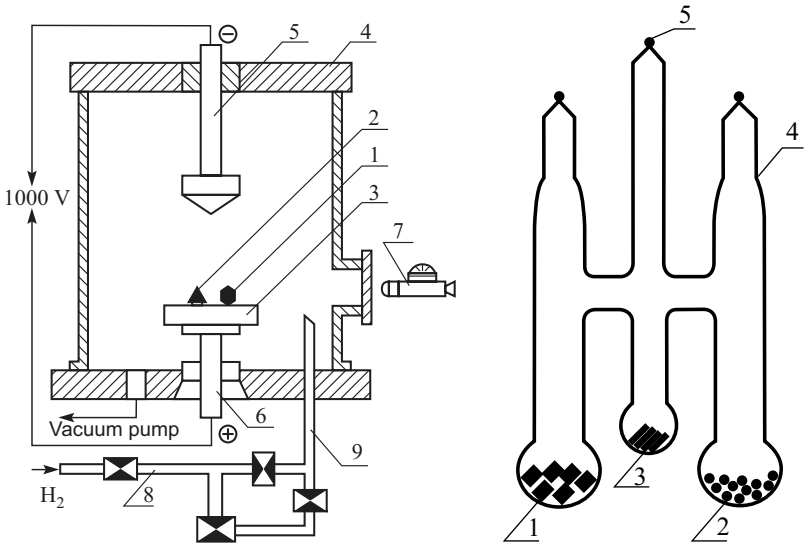

Figure 8.21: Left: Vacuum apparatus (schematically), used to nucleate and grow diamond microcrystals via a H/O/C plasma-supported CVD process, developed by Kostadinov et al. [20, 21]: (1, 2) growing diamond crystals, initially nucleated in an impulse with increased plasma intensity; (3) Mo substrate; (4) vacuum chamber bell; (5) graphite cathode; (6) support and electric connection to Mo anode; (7) optical pyrometer; (8, 9) inlet system for gaseous reaction mixture. Right: Quartz ampoule for the gaseous transport realization of the **vitreous carbon ⇔ diamond transition**: (1) seed diamonds; (2) microsized vitreous carbon; (3) catalysator; (4) transport gas–filled ampoule; (5) sealed ampoule inlet

by the corresponding reaction constants in accordance with the qualitative schema, given in Sect. 8.3.10. Plasma temperatures at similar conditions of experimentation are estimated to be in the range 4000–6000 K [28]. The temperatures on the substrate were usually in the vicinity of 1600 K, as was proven by optical pyrometer measurements. It was also observed that the molybdenum substrates used were transformed at the conditions of the experiment into Mo-carbides (according to our X-ray data into Mo_2C).

It was not possible to decide at the present stage of our investigation that what is the dominant mechanism of this diamond nucleation process. One possibility is that Mo_2C (which however is hexagonal) acts as a diamond nucleant (with $\Phi_d \approx 0$, cf. Eq. (8.35)). Other possibilities are that the increased flux of C- and H-atoms and atoms from the plasma torch forms on the Mo–C substrate a two-dimensional layer of increased pressure, which according to mentioned estimates can reach, in plasma-assisted condensation, values corresponding to 50–60 kbar [87, 88]. Thus, also a quasi-metastable synthesis (at actually increased pressure, corresponding to those in a Belt chamber and to mechanisms discussed in Sect. 8.3.7) cannot be excluded. Possible chemical reactions, increasing the activity of the substrate, also have to be anticipated; the formation of an initial population of graphite clusters (or graphite–H–clatrate clusters) and

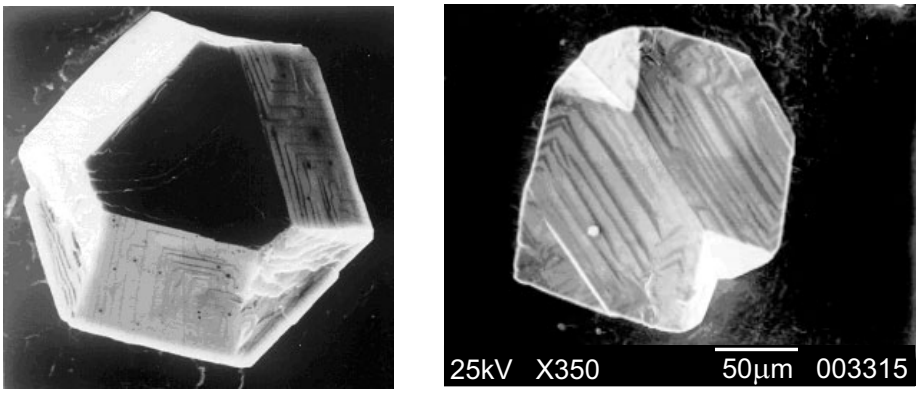

Figure 8.22: Two diamond microcrystals synthesized in the CVD-plasma apparatus shown in Fig. 8.21: (left) single microcrystal; (right) twin microcrystal. The size bar applies to both pictures

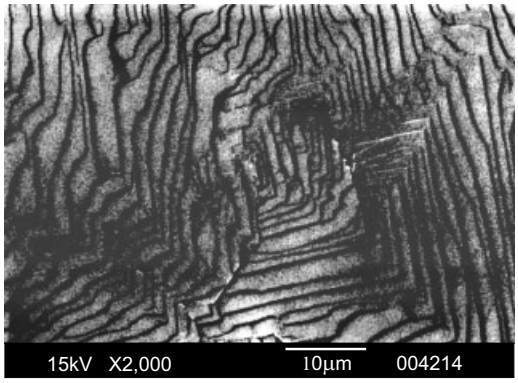

Figure 8.23: Growth spirals on diamond microcrystals of the type shown in Fig. 8.22. This picture was used to determine the effective supersaturation according to Eq. (8.44)

their transformation to graphite can also be a promising way of proposing mechanisms of this process (see Sect. 8.3.2).

After the initial impulse resulting in nuclei formation, the plasma torch was reduced to lower intensity (by reducing the current applied) and growth of the diamonds to dimensions of approximately 1–2 mm could be achieved. In Fig. 8.22, two of these diamonds are represented. The nature of these and similar microcrystals as pure diamond was verified by X-ray, micro-Raman shift spectroscopy and X-ray microprobe analysis (employed as both EDX and WDX). In its morphology, the diamond thus grown corresponded mostly to a combination of 111 and 100 faces (in a similar way as in Spitzyn's CVD-growth diamond seed crystals [18]). Usually twining, corresponding to medium supersaturations (see [91, 92]), was observed. In Fig. 8.23, the typical appearance of one of the faces of such a diamond, nucleated and then grown at the above-described conditions, is also given. The stepwise growth, typical for the

dislocational mechanism (cf. Sect. 8.3.8) and clearly to be seen on this picture, was observed as a rule on both the 100 and 111 faces. With Eq. (8.44) it was found that these steps, having in general a width of 1.5–2.0 μm and a height of 0.2 μm, were grown at a relative supersaturation ($(\Delta\mu/RT) \approx 3$–4). In this calculation, the σ and ρ values, listed in Table 8.2, were used. This result corresponds well to the dislocational mechanism assumed and to Fig. 8.13. There is no possibility, however, of determining directly the supersaturation, acting in the process of diamond nucleation in our case. In general, at homogeneous nucleation $(\Delta\mu/RT) = 2$–4 could be expected as verified for other processes of nucleation (see [31, 62, 76]).

8.4.5 Diamond Growth via Vitreous Carbon Using Chemical Transport Reactions

In a series of experiments, we succeeded to realize the expected **vitreous carbon → diamond** transformation using several gas transport reactions [29, 30]. We performed the first experiments of this series in sealed quartz ampoules with the construction given in Fig. 8.21 (right). In the experiment the seed crystals (natural or synthetic diamonds, 0.01–0.1 mm in size, sometimes in the form of larger polished brilliants), preliminarily weighted on a sensitive microbalance, were placed on the left-hand side of the quartz ampoule. On the right-hand side of the ampoule the precursor carbon material was placed, usually in the form of fine-grained powder (size of grains: usually between 10 and 100 μm). Besides the already mentioned vitreous carbons, some other materials with different degrees of crystallinity, structure, and dispersity were tested as carbon precursor: different blends of soot, medical carbons, and commercial nanodispersed diamond powders. In any of these materials, owing to the amorphous or defect structure and micro- or nanosize dimensions, an increased thermodynamic potential is frozen in (see Sects. 8.3.3 and 8.3.4). The good results obtained with diamond powders may be of principal technical interest, as they demonstrate the possibility of exploiting for diamond growth directly the ΔG_x difference, determined only by size effects via the Thomson–Gibbs dependence (Eq. (8.23)). With these nanosized diamond precursor samples the kinetic problems connected with the $sp^2 \rightarrow sp^3$ transformation are to a great extent reduced and smooth diamond growth was easily achieved.

For the realization of the transformation **graphite → diamond** in the wider limits **precursor carbon material → diamond** in the closed volume of the quartz ampoules several gas-transport reactions were tested. Besides the conventional $CH_4/H_2/H$ system (in which H-atom formation was catalyzed by a heated Pd foil) several other transport reactions were used with greater success, such as $C+2I_2 \rightarrow CI_4$, $C+2Br_2 \rightarrow CBr_4$, $C+S \rightarrow CS_2$, etc., as already discussed in Sect. 8.3.10. The desired gaseous phase was formed by introducing the necessary reagents in solid form (e.g., sulfur, iodine, CBr_4, paraffin, etc.) in small quartz tubes, which cracked upon heating in the initially evacuated quartz ampoules shown in Fig. 8.21 (right). We obtained good results with both sulfur and iodine as transport agents (see [29, 30]). In further developments reaction vessels either of Monel-metal or of vitreous carbon were constructed and used instead of the quartz ampoules.

Another possibility of demonstrating the **vitreous carbon → diamond** transformation consists in using the mentioned vacuum plasma method and apparatus with the construction given in Fig. 8.21 (left). In these experiments, we described in Ref. [30], on the Mo anode

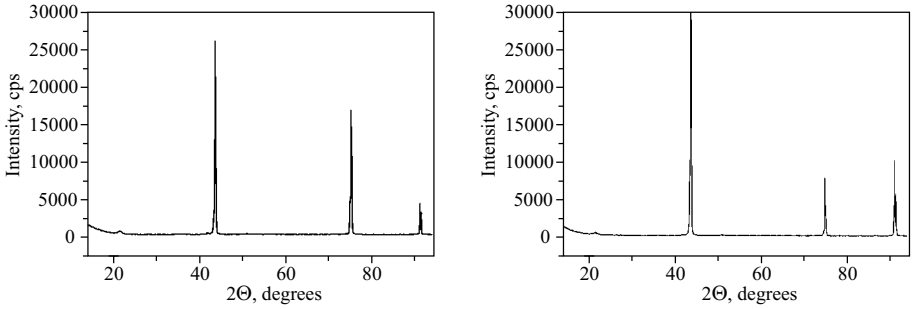

Figure 8.24: X-ray patterns of an assembly of small technical synthetic precursor diamonds (50 μm) used in the experiments before treatment (left) and of the same precursor diamonds after ampoule growth (right). Note that the growth has changed the absolute value of different crystal faces

of the CVD vacuum apparatus at zero supersaturations plasma-synthesized glass-like carbon samples and a diamond single crystal were placed, both having dimensions of approximately 1 mm. In the closed volume of the vacuum chamber, the plasma was triggered (at 1000 V) at a temperature of the substrate 1400 K. In this surrounding, the carbon glassy sample was isothermally transformed into diamond single crystals. The isothermal ampoule growth experiments with vitreous carbons and with the other mentioned precursor carbon materials were performed in the range of 1000–1400 K at approximately 1 bar and with a duration from 12 to 150 h. As a result, diamond growth rates of $\sim 0.5\,\mu m/h$ were achieved, leading (at optimal supersaturations $\gamma = (\Delta G/RT) \approx 0.01$) to the smooth growth of the introduced diamond seed crystals. In the direct plasma-assisted CVD growth, described in Sect. 8.4.4, considerably higher growth rates (up to 100 μm/h) were observed. At higher supersaturations (again determined via Fig. 8.6) besides continuous growth the secondary formation of typical diamond growth pyramids or even of diamond single crystallites was observed on the diamond seeds, thus indicating also the possibility of nucleation processes. As far as we know, the above results are the first proof of the **vitreous carbon → diamond** synthesis at metastable conditions. At further increased supersaturations, the dominant formation of graphite structures even on the diamond seed crystals followed. At lower temperatures (below 1000 K), usually amorphous carbon glass-like condensates were observed (see [30]).

In order to prove diamond growth as a result of the experiments, reported here and in Sect. 8.4.4, several auxiliary methods and techniques were used. The growth of the individual seed crystals was followed by exact weight measurements (with an accuracy of $\pm 2 \times 10^{-6}$ g), by X-ray and electron RHE diffraction (confirming the crystalline nature of the condensate) and by UV-induced luminescent microscopy investigations. With the last method, the overgrowth of luminescenting natural diamonds with the nonluminescent condensate was followed. Figure 8.24 gives the X-ray patterns of an assembly of small technical synthetic precursor diamonds (50 μm mean size) used in the experiments before growth treatment (left part). On the right part of Fig. 8.24, X-ray patterns are shown of the same diamond sample after the described ampoule growth: again the diamond structure is demonstrated, with a somewhat

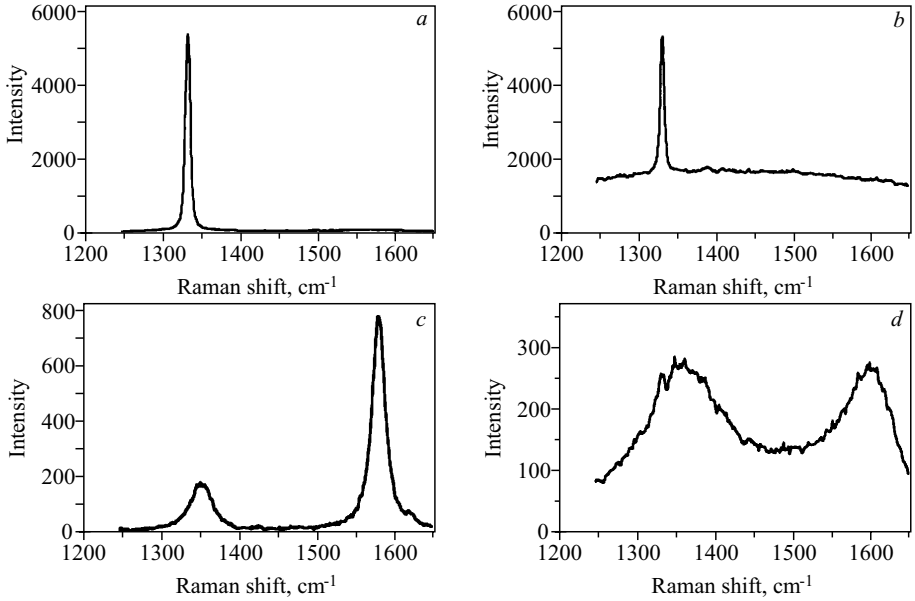

Figure 8.25: Typical Raman spectra of various carbon condensates investigated: (a) diamond obtained in our CVD experiments; (b) diamond ampoule overgrowth on a natural diamond seed crystal. Note the additional luminescent Raman background characteristics of natural diamonds; (c) graphite condensation (right-hand peak) and amorphous material (left-hand peak); (d) vitreous carbon condensate (amorphous microspheres obtained in the CVD apparatus)

changed morphology due to the oriented growth process. Micro-Raman spectrography was used as the most efficient method of analysis and diamond proof (see Fig. 8.25).

Detailed EDX and WDX microanalyses were performed with the X-ray microprobe to verify the chemical composition of the condensates. For the case of the $CI_4/I_2/I$ and $CH_4/H_2/H$ systems only traces of iodine (below 0.01%) were found. However, with sulfur as a carrier gas considerable amount (up to 1–2%) of sulfur was introduced into the growing epitaxial diamond films. As mentioned in Sect. 8.3.4, when microdispersed diamond precursor materials, milled in a W-carbide milling apparatus, were employed, also unwanted W-contaminations were introduced with the transport reactions.

8.4.6 Morphology and Growth Mechanisms of Technical and of Natural Diamonds

In our CVD plasma-assisted growth experiments well-formed microcrystals, which are the known combinations of ⟨100⟩ and ⟨111⟩ faces, were found as also observed by other authors [18, 90]. On them the mentioned relatively thick growth spirals prevailed (see Fig. 8.23). Such growth spirals are also observed on technical diamonds, directly synthesized in the stability field of diamond [101].

Figure 8.26: Typical habit of natural diamond microcrystals from South African kimberlite mining [102, 103]. No dissolution remnants are observed

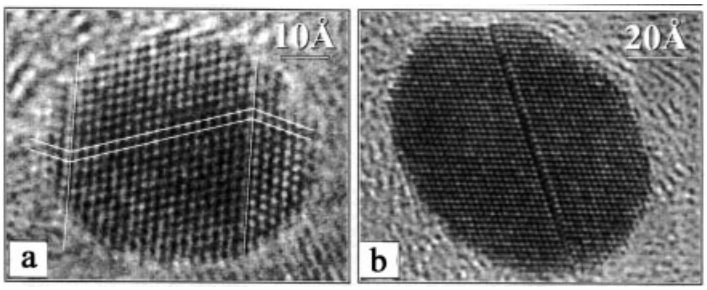

Figure 8.27: Presolar nano-diamonds from interstellar space: high resolution TEM picture from thin slide of carbon material from houndride meteorite (from the Allende and Murchison meteorites in Mexico). Note the typical droplet-like appearance of the two nanosized crystals, formed (according to Xe-isotope dating) 9×10^9 years ago in space [100, 104]

Geological diamonds can also display well-formed faces (Fig. 8.26), but in most cases their appearance is damaged by complicated tectonic processes. These crystals have undergone dissolution and complicated processes of change in their rise from the depths of the earth to its surface (see [102, 103]). Quite different from all these crystalline habits is the appearance of cosmic diamonds found in presolar meteorites (Fig. 8.27) [100, 104–106]. They, it seems, have brought from interstellar space to earth the proof that they have been initially formed as liquid carbon droplets, may be, in the vicinity of supernovae explosions. It is interesting to explore whether the mechanism outlined in Sect. 8.3.5 could be applied to their formation [107].

8.4.7 Formation of Amorphous and Glassy Carbon Condensates at Metastable Conditions

The so-called vitreous carbon materials are synthesized under Ar-atmosphere or in a vacuum furnace by the controlled high-temperature pyrolysis carbon resins. In Sects. 8.3.2 and 8.3.3, we described the properties of both commercial vitreous carbon materials and samples we prepared by the pyrolysis of furfuryl-alcohol resins under Ar at $\sim$ 1750 K. Upon condensation processes in the described plasma-sustained condensation, the formation of amorphous

glass-like structures with the corresponding typical Raman-shift spectrum (Fig. 8.25(d)) was observed at lower substrate temperatures. In our ampoule growth experiments, the formation of amorphous carbon condensates was also found then as a typical process in the form of drop-like structures (with sizes up to 0.1–1 μm).

No distinct connection could be established with these X-ray and Raman-amorphous carbon droplets and isometrical cubic-octahedral isometric diamond crystals also formed in our ampoule experiments. However, these several observations are, nevertheless, worth to be mentioned in connection with the possibilities opened by Eqs. (8.27) and (8.30) and with results [38] and predictions [108] on the thermodynamic nature of the so-called vitreous carbon.

8.5 Conclusions

In the preceding sections, we have tried to apply to the process of metastable nucleation and growth of diamonds some of the basic models and results of the present-day nucleation theory. We used it in its classical, capillary formulation, enlarging it with the results obtained in contemporary two-dimensional condensation models. A general formulation of Ostwald's rule of stages also gives, as shown in the corresponding section, more or less distinct results and opens some new perspectives of possible methods of diamond synthesis.

The processes of diamond nucleation are very complicated, intermixed with chemical and structural problems. Nevertheless, we think that the comparison of existing experimental findings with theory shows some clues, which may be used to open the door for a real quantitative treatment of the process of metastable diamond synthesis. Up to now theoretical thinking in diamond synthesis was concerned only or mostly with the chemical side of the problem. Time has come to understand that this is a primarily physical process. We hope that the present compilation of theoretical models and experimental facts may be of use for further developments.

In our present contribution of greater significance are not so much the technical problems of metastable diamond synthesis, but the possibilities a combination of theory and experiments in metastable diamond nucleation can supply to help in resolving really great problems connected with geological processes or with interstellar physics and the formation of both cosmic diamond and graphite. Thus terrestrial experiments and theoretical models give several interesting indications on processes connected with the development even of cosmic structures.

We opened our analysis with one of the difficult problems in the history of artificial diamond production: with Hannay's experiments. The models we developed show that this unfortunate inventor (who ended his life in dispair [7]) was, may be, on the right track: His results, if they are not a case of falsification, can, at least, be qualitatively explained.

Up to now the theory of metastable diamond synthesis was concerned practically only with the problems of growth. Growth and growth morphology of diamond can be qualitatively and even quantitatively interpreted in the framework of the modern theory of phase transitions. The application of the theory gives the possibility of determining the conditions at which diamond was formed, as attempted also here. Let us hope that a thorough theoretical development could also indicate in the theory of metastable nucleation the direction in which the present-day experimental and technological processes have to change in order to produce technical diamonds and diamond coatings in an easier way.

Acknowledgements

The authors are indebted to many colleagues from both Jena and Sofia for experimental support. They would like to express their particular thanks to Professor Th. Henning and Dr. C. Jäger from the Astronomical Institute of the Friedrich-Schiller University in Jena, who directed their attention to the problems of formation of interstellar nanosized diamonds.

References

[1] Ya. A. Kalashnikov, M.O. Shalimov, and I.B. Nikolskaya, Dokl. Akad. Nauk USSR **219**, 405 (1974).

[2] J.C. Angus and A. Argoitia et al., Chemical vapor deposition of diamond, in *Thin Film Diamond*, edited by A. Lehington and J.W. Steeds (Chapman and Hall, London, New York, 1994), pp. 1–15.

[3] P. Bachmann, Microwave plasma CVD and related techniques for low pressure diamond synthesis, in Ref. [2], pp. 30–51.

[4] D. Mendeleev, *Fundamentals of Chemistry*, edited by P. Frolov (St. Petersburg, 1906), Vol. 1, 12th edition, pp. 544–551 (Moscow & Leningrad, 1947 (in Russian)).

[5] *Gmelins Handbuch der Anorg. Chemie*, 8. Auflage, Syst. Nr. 14 (Kohlenstoff) (Verl. Chemie, Weinheim, 1967), Vol. B-1, pp. 187–247 (in German).

[6] *Mellor's Comprehensive Treatise on Inorganic and Theoretical Chemistry* (Longmans, London, 1960), Vol. 3, pp. 718, 730–737.

[7] D. Elwell, *Man-Made Gemstones* (Wiley, New York, 1980), Chapter 4.

[8] F.P. Bundy, H.M. Strong, and R.H. Wentorf, Jr., *Methods and mechanisms of synthetic diamond growth*, in *Chemistry and Physics of Carbon*, edited by P.L. Walker, Jr. and P.A. Thrower (Dekker, New York, 1973), Vol. 10.

[9] N.B. Novikov and D.B. Fedosseev et al., *Synthetic Diamonds* (Naukova Dumka, Kiev, 1987) (in Russian).

[10] A. Yarnell, Man-made diamonds, Chem. & Engineering News, February 2 (2004), pp. 24–32.

[11] F. Simon, The determination of the free energy, in *Handbuch der Physik*, Thermal Properties of Matter, edited by H. Geiger and K. Scheel (Springer, Berlin, 1926), Vol. 10, pp. 350–404 (in German).

[12] O.I. Leipounskii, Usp. Khim. **8**, 1520 (1939).

[13] R. Berman and F. Simon, Z. Elektrochemie **55**, 333 (1955).

[14] T. Nakahara and N. Fujimori, Mater. Res. Innov. **1**, 38 (1997).

[15] G.M. Swain, J.E. Butler, and J.A. Carlisle, Interface **12**, 8-40 (2003).

[16] P. De Carly and J.C. Jamieson, Science **133**, 367 (1961).

[17] E.P. Smirnov and S.K. Gordeev, *Diamonds: Synthesis, Properties and Applications* (Leningrad University Press, Leningrad, 1984) (in Russian).

[18] B.V. Spitsyn, L.I. Bouilov, and B.V. Deryaguin, J. Cryst. Growth **52**, 219 (1981).

[19] J. Meisel, Wiss. Z. Friedrich-Schiller-Univ. Jena Math.-Nat.wiss. Reihe **20**, 185 (1972).

[20] L. Kostadinov and D. Dobrev, Surf. Coat. Technol. **47**, 623 (1991).
[21] L. Kostadinov, D. Dobrev, and K. Okano et al., Diam. Relat. Mater. **1**, 157 (1992).
[22] R. Sauer, Cryst. Res. Technol. **34**, 227 (1999).
[23] W. Piekarczyk, R. Messier, R. Roy, and C. Endahl, J. Cryst. Growth **106**, 279 (1990).
[24] Y.-Z. Wan and D.W. Zhang et al., Appl. Phys. A **67**, 225 (1998).
[25] R.C. Brown and J.T. Roberts, J. Phys. Chem. **104**, 8420 (2000).
[26] N.J. Kompilin and R.H. Hauge, Other methods for diamond production, in *Low Pressure Synthetic Diamond*, edited by B. Dischler and C. Wild (Springer, Berlin, 1998), pp. 120–37.
[27] B.V. Deryaguin and D.V. Fedoseev, *The Growth of Diamond and of Graphite from the Vapor Phase* (Nauka, Moscow, 1977) (in Russian).
[28] K. Suzuki, A. Sawabe, and T. Inuzuka, Appl. Phys. Lett. **50**, 728 (1988); **53**, 1818 (1988).
[29] V. Guencheva, E. Stoyanov, and I. Gutzow et al., C. R. Bulg. Acad. Sci. **55**, 55 (2002).
[30] I. Gutzow, S. Todorova, and L. Kostadinov et al., J. Mater. Sci. **38**, 3747 (2003).
[31] I. Gutzow and J. Schmelzer, *The Vitreous State: Thermodynamics, Structure, Rheology, and Crystallization* (Springer, Berlin, 1995).
[32] I. Gutzow, Z. Phys. Chem., Neue Folge **81**, 195 (1972).
[33] E. Grantscharova and I. Gutzow, J. Non-Cryst. Solids **81**, 99 (1986).
[34] R. Nacken, FIAT Doc. No. 641 (1945); see A. Smakula, *Einkristalle* (Springer, Berlin, 1962), p. 163.
[35] E. Grantscharova, I. Avramov, and I. Gutzow, Naturwissenschaften **73**, 95 (1986).
[36] E. Kolb, Solubility of selenium, in *Selenium and Tellurium*, *Proc. Int. Symp. Montreal, Oct. 1967*, edited by W.C. Cooper (Plenum, London, 1969), p. 155–9.
[37] J.B. Hannay, Proc. R. Soc. (London) **30**, 450 (1888/89).
[38] V. Guencheva, E. Grantscharova, and I. Gutzow, Cryst. Res. Technol. **36**, 1411 (2001).
[39] F. Bundy, J. Chem. Phys. **38**, 618 (1963); see also [54], pp. 71–5.
[40] M. Chang, R. Ryoo, and M. John, Carbon **13**, 33 (1974).
[41] J.O. Hirschfelder, C.F. Curtiss, and R.B. Bird, *Molecular Theory of Liquids* (Wiley, New York, London, 1954).
[42] *Chemical Handbook*, edited by B.P. Nikolskii et al. (Nauka, Moscow, Leningrad, 1962), Vol. 1, p. 917 (in Russian).
[43] A.H. Nesmeyanov, *Vapor Pressure of the Chemical Elements* (Soviet Academy Sciences Publishers, Moscow 1961), pp. 215–225 (in Russian).
[44] C.A. Angell, Glass formation and the nature of the glass transition, in *Insulating and Semiconducting Glasses*, edited by P. Boolchand (World Scientific, Singapore, London, 2000), pp. 1–52.
[45] D.M. Gruen, Conversion of fullerenes to diamond, US Patent No. 5370855, Dec. 1994.
[46] O. Knacke, O. Kubaschewski, and K. Hasselmann, *Thermodynamical Properties of Inorganic Substances* (Springer, Berlin, 1991).
[47] V. Glushko and L. Gurvich et al., *Thermodynamic Properties of Individual Substances* (Nauka, Moscow, 1979), Vol. 2 (in Russian).

[48] I. Gutzow and A. Dobreva, J. Non-Cryst. Solids **129**, 266 (1991).
[49] I. Gutzow, J. Non-Cryst. Solids **45**, 301 (1981).
[50] N.N. Novikov (Ed.), *The Physical Properties of Diamond* (Naukova Dumka, Kiev, 1987) (in Russian).
[51] R.F. Curl, Rev. Mod. Phys. **69**, 691 (1997).
[52] H.W. Kroto et al., *The Fullerenes* (Pergamon, Oxford, 1993).
[53] A.P. Jones, W.W. Duley, and D.A. Williams, Quart. J. R. Astronom. Soc. **31**, 567 (1990).
[54] L.F. Vereschagin, *Collected Papers on Synthetic Diamond and on Hydroextrusion* (Nauka, Moscow, 1982), pp. 56–63 (in Russian).
[55] W. Weisweiler and V. Mahadevan, High Temp. – High Press. **3**, 111 (1971).
[56] S.K. Das and E.E. Hucke, Carbon **13**, 33 (1974).
[57] H. Strong, J. Chem. Phys. **39**, 2057 (1963).
[58] P.K. Gupta and C.T. Moynihan, J. Chem. Phys. **65**, 4163 (1976).
[59] M. Shkodrov, B. Bogdanov, and I. Gutzow, (in preparation).
[60] T. Neykova and J. Kourtev et al., Bulg. J. Phys. **17**, 52 (1990).
[61] C. Weissmantel, J. Vac. Sci. Technol. A **3**, 2384 (1985).
[62] B. Mutaftschiev, *The Atomistic Nature of Crystal Growth* (Springer, Berlin, 2001).
[63] K. Hanssen, Z. Physik **157**, 523 (1960).
[64] I. Avramov and I. Gutzow, Mater. Chem. **5**, 315 (1980).
[65] D.V. Fedoseev, Kolloidn. J. **40**, 402 (1978) (in Russian).
[66] D.V. Fedoseev and B.V. Deryaguin et al., Carbon **21**, 237 (1983).
[67] M. Alam and R. Roy et al., Carbon **27**, 289 (1989).
[68] A.B. Anderson and L. Kostadinov, J. Appl. Phys. **81**, 264 (1997).
[69] J.E. Butler and R.L. Wood, Thin film growth mechanisms, in Ref. [2], pp. 15–30.
[70] P. Badziag and W.S. Verwoerd et al., Nature **343**, 244 (1990).
[71] J.W.P. Schmelzer, J. Schmelzer, Jr., and I. Gutzow, J. Chem. Phys. **112**, 3820 (2000).
[72] A. Milev and I. Gutzow, Bulg. Chem. Commun. **29**, 597 (1996/97).
[73] J.W.P. Schmelzer, I. Gutzow, and J. Schmelzer, Jr., J. Colloid Interface Sci. **178**, 657 (1996).
[74] I.N. Stranski and D. Totomanov, Z. Phys. Chemie A **163**, 399 (1933).
[75] M. Volmer, *Kinetik der Phasenbildung* (Th. Steinkopff, Dresden, 1939).
[76] D. Kashchiev, *Nucleation: Basic Theory with Applications* (Butterworth-Heinemann, Oxford, 2000).
[77] I. Gutzow, D. Kashchiev, and I. Avramov, J. Non-Cryst. Solids **73**, 477 (1985).
[78] I. Gutzow and I. Avramov, J. Non-Cryst. Solids **16**, 128 (1974).
[79] J. Möller, I. Gutzow, and J. Schmelzer, Z. Phys. Chemie **204**, 171 (1998).
[80] D.V. Fedoseev and B.V. Deryaguin, Kolloidn. J. **26**, 750 (1979) (in Russian).
[81] N.N. Semenov, J. Russ. Phys. Chem. Soc. **62**, 33 (1930) (in Russian).
[82] L.S. Palatnik and I.I. Papirov, *Ordered Crystallization* (Metallurgiya, Moscow, 1964) (in Russian).
[83] Ya.I. Frenkel, Z. Phys. **26**, 117 (1924).

[84] Ya.I. Frenkel, *Statistical Physics* (Soviet Academy of Sciences Publishers, Moscow, Leningrad, 1948) (in Russian).

[85] J.H. de Boer, *The Dynamical Character of Adsorption* (Clarendon, Oxford, 1953).

[86] D. Kashchiev, J. Cryst. Growth **267**, 685 (2004).

[87] D.R. Mackenzie and D. Mueller et al., Properties of amorphous carbon prepared by vacuum deposition, in *Diamond and Diamond-Like Carbon Coatings*, edited by A. Matthews and P.K. Bachmann (Elsevier, Lausanne, New York, 1990), pp. D43–50.

[88] H. Windischmann, J. Appl. Phys. **62**, 1800 (1987).

[89] A.A. Chernov, Formation of crystals, in *Modern Crystallography* (Nauka, Moscow, 1980) (in Russian).

[90] I. Sunagawa, J. Cryst. Growth **99**, 1156 (1990).

[91] I. Kostov and R.I. Kostov, *Crystal Habits of Minerals* (Acad. Publ. House, Sofia, 1999).

[92] N.A. Pangarov, *Rost Kristallov*, edited by N.N. Sheftal (Nauka, Moscow, 1974), Vol. 10 (in Russian).

[93] H. Schaefer, *Chemische Transportreaktionen (Chemical Transport Reactions)* (Verl. Chemie, Weinheim, 1964).

[94] I. Gutzow and I. Avramov, Thin Solid Films **85**, 203 (1981).

[95] J.P. Hirth and G.M. Pound, *Condensation and Evaporation* (Pergamon, London, 1963).

[96] K.L. Chopra, *Thin Film Phenomena* (McGraw Hill, New York, 1962).

[97] K.A. Cherian, Surf. Coat. Technol. **47**, 127 (1991).

[98] D. Satrapa, R. Haubner, and B. Lux, Surf. Coat. Technol. **47**, 59 (1991).

[99] A.V. Pavlichenko and A.M. Jonas et al., Nature **402**, 162 (1999).

[100] U. Ott, Nature **364**, 25 (1993).

[101] G.G. Lemlein, M.O. Klija, and A.A. Chernov, Kristallografia **9**, 231 (1964) (in Russian).

[102] A.E. Fersman, *Kristallography of Diamond* (Soviet Academy Sciences Publishers, Moscow, 1955) (in Russian).

[103] E. Stoyanov, Diploma thesis, Chem. Fac. Kliment Ochridski Univ., Sofia, 2002 (in Bulgarian).

[104] T.L. Daulton and P.P. Eisenhour et al., Geochimica Cosmochimica Acta **60**, 4853 (1996).

[105] H. Mutschke, Th. Henning, and C. Jäger et al., Astrophys. J. **454**, 157 (1995).

[106] Th. Henning, Interstellar dust grains: an overview, in *Molecules in Astrophysics: Probes and Processes*, edited by E.F. van Dishpoeck (IAU, Amsterdam, 1997).

[107] I. Gutzow, S. Todorova, C. Jäger, and Th. Henning, (in preparation).

[108] E. Grantscharova, B. Bogdanov, and I. Gutzow, *Structure and Thermodynamic Properties of Vitreous Carbon*, *Proc. 15th Int. Congress on Glass, "Glass'89", Leningrad* (1989), Vol. 3, pp. 16–19.

9 Nucleation in Micellization Processes

Alexander K. Shchekin, Fedor M. Kuni, Alexander P. Grinin, and Anatoly I. Rusanov

As for our intensive use of calculus . . . ,
we believe it is unnecessary in the present age
to make any apology . . .
For any presentation of this subject
which is to be both concise and comprehensive,
calculus is indispensible . . .
Gilbert Newton Lewis, Merle Randall (1923)

Even though the micelles themselves are not nuclei of a new phase, premicellar molecular aggregates evolve in the course of micellization processes and play the role of critical nuclei (germs) for micelles. This means that nucleation does occur in micellization and the methods of nucleation theory can be, in fact, successfully applied to micellization kinetics. The present review gives an overview of the kinetics and thermodynamics of formation of spherical micelles on the basis of the modern kinetic theory of nucleation. We start with thermodynamic aspects, formulate the kinetic equation of micellization on its basis, consider the characteristic times of aggregation and relaxation processes in surfactant solutions with spherical micelles, and then return back to the thermodynamic modeling of micelles themselves (for the case of nonionic spherical micelles). This approach allows us to find the relaxation times and other kinetic characteristics of micellar solutions in an explicit form.

9.1 Introduction

Nucleation (formation of a new phase within a metastable ambient phase) and micellization (formation of micelles in surfactant solutions) have the common feature to proceed through spontaneous aggregation of molecules or ions. Nevertheless, their kinetic theories have been developed in different pathways. The kinetic theory of nucleation, founded by Volmer, Becker, Döring, Frenkel, and Zeldovich, is based on the phase approach going back to Gibbs' thermodynamics and considering self-forming molecular aggregates as nuclei of a new stable phase [1, 2].

The phase terminology, used in the theory of micellization, has got initially a different meaning. First, the population of micelles as a whole was considered as a macroscopic "pseudo-phase" participating in a first-order phase transition [3]. Second, the entire micellar solution was considered as a macroscopic phase resulting from a second-order phase transition [4]. Third, a single micelle was considered as a specific microscopic phase not having a macroscopic analog [5]. The first two approaches do not have a sound basis [5], although, they can be used for some approximate estimations. The third concept is rigorous and related to the fact that a micelle has a complicated structure resembling a convolute surfactant monolayer [6–12], and cannot be viewed as a nucleus of a real phase. The final state of a surfactant solution at micellization is the state of aggregative equilibrium of micelles and monomers,

Nucleation Theory and Applications. edited by J. W. P. Schmelzer

ISBN: 3-527-40469-4

i.e., the equilibrium state of a disperse system. Increasing the brutto-concentration of a surfactant in a solution above the critical micelle concentration (until other polymorphic forms of micelles become favorable) mostly gives only rise to the equilibrium number of spherical micelles.

Even though micelles are not nuclei of a new phase, premicellar molecular aggregates arise in the course of the micellization process and play the role of critical nuclei (or germs) for micelles themselves. As an indication of this mechanism, one can consider a maximum in the work of formation of such molecular aggregates (aggregation work) that corresponds to a minimum in the curve of the equilibrium distribution of the aggregates in size [5, 13–19]. This maximum precedes the minimum of the work, along the aggregate size axis, associated with micelles. This peculiarity has the consequence that nucleation does occur in micellization, and that the methods of nucleation theory can be in fact successfully applied in micellization kinetics. At the same time, the application of the theory of nucleation to the micellization process, which has features strikingly different from common phase transitions, is of interest for the theory of nucleation itself.

Till recent times, the development of the kinetic theory of micellization was retarded by the fact that, in contrast to the situation with micelles, there is a lack of experimental data on critical premicellar nuclei of micelles. According to the nucleation theory [20, 21], the main parameters of the maximum of the aggregation work are its height and half-width. These parameters enter the equations for the transition rates and specific times and thus allow one to calculate all kinetic characteristics. Even if direct experimental data are not available, these parameters can be found, relying on the analytic properties of the aggregation work, with the aid of data on the aggregation work in other regions of the size of the aggregates [22]. Particularly, in the micellization process, the values of these two parameters have to be consistent with the parameters describing the minimum of the aggregation work that corresponds to the micelles. Therefore, existing experimental data on the equilibrium average micelle size and the dispersion of micelle sizes give an essential additional information about the whole behavior of the aggregation work, including the region of premicellar sizes. This information is needed for solving direct and reverse problems of the micellization kinetics.

The review presents the kinetic and thermodynamic theory of formation of spherical micelles based on the modern kinetic theory of nucleation [18, 19, 22–29]. Just as the theory of nucleation is based, to a significant extent, on thermodynamics, so the kinetic theory of micellization requires data on equilibrium and nonequilibrium states given by the thermodynamics of micellization. This necessity explains the organization of the present review where kinetics and thermodynamics are analyzed hand-in-hand: We will start with the analysis of problems of the thermodynamics of aggregation, formulate the kinetic equation of micellization on this ground, consider the characteristic times of aggregation and relaxation processes in surfactant solutions with spherical micelles, and then return back to the thermodynamic modeling of micelles themselves (for the case of nonionic spherical micelles). This approach allows us to find the relaxation times and other kinetic characteristics of micellar solutions in an explicit form.

9.2 General Aspects of Micellization: the Law of Mass Action and the Work of Aggregation

Let us consider a solution of a single nonionic surfactant capable of forming molecular aggregates. In this case, the role of the solvent is played by a liquid (for example, water) that is passive with respect to aggregation. The solution is assumed to be ideal (infinitely dilute). Considering aggregates to be compact and their temperature equal to that of the solution, the aggregation number, n (the number of monomers in an aggregate), is assumed to be a characteristic parameter of the internal state of the aggregate. The choice of such a discrete characteristic parameter is convenient because it is also applicable to the description of the smallest aggregates beginning from the value $n = 1$ for single surfactant molecules. Let us further denote the chemical potential and concentration (i.e., the number of aggregates per unit volume) of aggregates containing n monomers by μ_n and c_n, respectively. Employing such notation, μ_1 and c_1 represent the chemical potential and concentration of single monomers, respectively. In the considered case of nonionic surfactants, all monomers are identical.

In the analysis of the aggregation processes, it is convenient to introduce the chemical potential, μ_n, of a molecular aggregate in the solution by the relation [18, 23]

$$\mu_n = G_n^0 + k_B T \ln(\Lambda_n^3 c_n f_n) \,, \tag{9.1}$$

where G_n^0 is the Gibbs energy of a single aggregate (consisting of n surfactant molecules) with fixed center of mass in a pure medium (in the absence of other aggregates), k_B is the Boltzmann constant, T is the absolute temperature of the solution, $\Lambda_n = h\,(2\pi m_n k_B T)^{-1/2}$ is the average de Broglie wavelength of a molecular aggregate (h is the Planck constant, m_n is the mass of the molecular aggregate), and f_n is the activity coefficient of the aggregate. Λ_n^{-3} is the partition function for the translational motion of the aggregates, and $k_B T \ln \Lambda_n^3$ is its contribution to the free energy. Similarly, $k_B T \ln f_n$ is the contribution from the interaction of all aggregates with each other.

We may rewrite Eq. (9.1) as

$$\mu_n = G_n + k_B T \ln\left(\frac{c_n}{c_{st}}\right) \,, \tag{9.2}$$

where G_n is the chemical potential (the Gibbs energy) of the molecular aggregate corresponding to a certain arbitrarily chosen standard concentration c_{st}. In the thermodynamics of solutions, c_{st} is usually assumed to be unity (in the corresponding units of measurement) so that only concentration (in fact, a dimensionless number which numerically equals concentration) is retained in the logarithm in Eq. (9.2). Equation (9.2) is valid both in the absence or presence of any interactions between aggregates in the standard state. However, since we assume to consider an ideal system, we suggest that the standard state, corresponding to the concentration c_{st}, is also an ideal one. In other words, we assume that, both in Eqs. (9.1) and (9.2), the relation $f_n = 1$ holds.

We are considering here the situation of fluctuational formation of aggregates consisting of $n = 2, 3, \ldots$ particles in a solution containing originally single-surfactant monomers only.

For this reason, it is convenient to select a standard concentration c_{st} as $c_{st} = c_1$. In this case, Eq. (9.2) is reduced to

$$\mu_n = G_n + k_B T \ln\left(\frac{c_n}{c_1}\right) . \tag{9.3}$$

The convenience of such definition $c_{st} = c_1$ follows from the following considerations: In a solution where monomers are already present with the concentration c_1, the Gibbs energy of a monomer G_1 should coincide with the monomer chemical potential μ_1, i.e., the relation

$$G_1 = \mu_1 \tag{9.4}$$

should be valid. This identity is ensured in fact by Eq. (9.3). Addressing the practically most important case, we consider an aggregating system at constant temperature and pressure and, correspondingly, we shall use the Gibbs energy as the thermodynamic potential (its increase equals the minimal work done on a system to create the same change of its state). If the molecular aggregate is formed at the selected standard concentration, c_1 (both for monomers and aggregates formed), the standard work of molecular aggregate formation (or in short aggregation work), expressed in thermal energy units $k_B T$, is given by the formula [23]

$$W_n = \frac{(G_n - n\mu_1)}{k_B T} . \tag{9.5}$$

The term $n\mu_1$ in Eq. (9.5), which represents the Gibbs energy of the ensemble of n noninteracting monomers, enters this relation because aggregation takes place in a solution originally containing single monomers only. In this case, the work W_n is independent of the concentrations c_n of aggregates with particle numbers $n \geq 2$. However, it depends on the monomer concentration c_1. At the same time, the relation

$$W_1 = 0 , \tag{9.6}$$

which follows from Eqs. (9.4) and (9.5), seems to be natural as well. Indeed, monomers are already present in a solution, and, hence, no work is required for their formation.

The Gibbs energy per unit volume of a solution, G, can be written as $G = \sum_{n\geq 1} \mu_n c_n$. At constant temperature and pressure in the solution, we have

$$\mathrm{d}G = \sum_{n\geq 1} \mu_n \, \mathrm{d}c_n . \tag{9.7}$$

Since the solution is considered as a closed system with respect to particle exchange, the total surfactant concentration, c, in the solution is constant and determined as

$$c = c_1 + \sum_{n\geq 2} n c_n . \tag{9.8}$$

Equation (9.8) yields

$$\mathrm{d}c_1 = -\sum_{n\geq 2} n \, \mathrm{d}c_n . \tag{9.9}$$

Substituting Eq. (9.9) into the right-hand side of Eq. (9.7) results in

$$\mathrm{d}G = \sum_{n\geq 2} (\mu_n - n\mu_1)\,\mathrm{d}c_n \ . \tag{9.10}$$

It follows that the condition $\mathrm{d}G = 0$ of aggregation equilibrium in a solution (with constant total concentration c and at constant temperature and pressure) can be written as

$$\mu_n^{(\mathrm{e})} = n\mu_1 \ , \tag{9.11}$$

where the superscript (e) specifies aggregation equilibrium. With Eqs. (9.3) and (9.5), one can write

$$\mu_n - n\mu_1 = k_\mathrm{B}T \left[W_n + \ln\left(\frac{c_n}{c_1}\right)\right] \ . \tag{9.12}$$

Equations (9.11) and (9.12) yield for the equilibrium aggregate concentration $c_n^{(\mathrm{e})}$

$$c_n^{(\mathrm{e})} = c_1 \exp\left(-W_n\right) \ . \tag{9.13}$$

Equation (9.13) corresponds to the Boltzmann fluctuation principle.

Let us introduce the affinity A_n via

$$A_n \equiv -\left(\mu_n - n\mu_1\right) \ , \quad n = 1, 2, \ldots \ . \tag{9.14}$$

Equations (9.14) and (9.11) show that, at aggregation equilibrium, the relation

$$A_n^{(\mathrm{e})} = 0 \ , \quad n = 1, 2, \ldots \ , \tag{9.15}$$

holds. With Eq. (9.12), we can express the affinity (defined via Eq. (9.14)) as

$$A_n = -k_\mathrm{B}T \left[W_n + \ln\left(\frac{c_n}{c_1}\right)\right] \ . \tag{9.16}$$

According to Eq. (9.16), the lower the work W_n and the c_n/c_1 ratio, the larger the affinity A_n. With Eq. (9.14), Eq. (9.10) can be rewritten as

$$\mathrm{d}G = -\sum_{n\geq 2} A_n\,\mathrm{d}c_n \ . \tag{9.17}$$

Taking into account that the chemical potentials μ_n and μ_1 depend (for the considered ideal solutions) on the concentrations c_n and c_1 via the terms $k_\mathrm{B}T \ln c_n$ and $k_\mathrm{B}T \ln c_1$, the condition of aggregation equilibrium, Eq. (9.11), is transformed into the law of mass action

$$c_n^{(\mathrm{e})} = K_n c_1^n \ . \tag{9.18}$$

Here the coefficient K_n does not depend neither on the concentration c_1 nor on the concentrations c_n with $n \geq 2$, but depends on the aggregation number n. According to Eqs. (9.13) and (9.18), we have

$$W_n = -\ln K_n - (n-1)\ln c_1 \ . \tag{9.19}$$

The term $-(n-1)\ln c_1$ in Eq. (9.19) explicitly determines the dependence of the work W_n on monomer concentration c_1 (the work W_n is independent of the concentrations c_n with $n \geq 2$). Since the work W_n is, by its meaning, not affected by the condition whether the aggregate concentration is in equilibrium or not, Eq. (9.19) is valid at arbitrary aggregate concentrations in an ideal solution. The parameter $-\ln K_n$ is known as the work of micellization, W_n^M, for the case when the standard concentration is expressed by the molarity (1 mol/l). While comparing this work with W_n (then the concentration c_1 should also be expressed in moles), we can see from Eq. (9.19) a significant difference between W_n^M and W_n: If, in an ideal system, the former work is independent of monomer concentration, the latter, in contrast, is dependent on this concentration. This dependence is especially pronounced for micelles with large aggregation numbers.

9.3 General Kinetic Equation of Molecular Aggregation: Irreversible Behavior in Micellar Solutions

According to the basic assumptions of the classical kinetic theory of nucleation [1, 2], the number of molecules in an aggregate varies only as a result of absorption or emission of monomers by the aggregate. This way the kinetics is determined by the sequences

$$\{n\} + \{1\} \rightleftharpoons \{n+1\} \ , \quad n = 1, 2, \ldots \ , \tag{9.20}$$

of direct and reverse transitions of the aggregates occurring during this process. Aggregates containing n monomers are denoted here by $\{n\}$ ($n = 1, 2, \ldots$).

The most important quantity in the classical kinetic theory is the flux of aggregates in the space of cluster sizes according to the mechanism as illustrated in Eq. (9.20), i.e., occurring due to direct and reverse transitions of the aggregates. Denoting this flux by J_n, we have

$$J_n = j_n^+ c_n - j_{n+1}^- c_{n+1} \ , \quad n = 1, 2, \ldots \ , \tag{9.21}$$

where j_n^+ is the number of monomers absorbed by the aggregate $\{n\}$ from the solution per unit time, and j_{n+1}^- is the number of monomers emitted from the aggregate $\{n+1\}$ to the solution per unit time. Evidently, the inequalities $j_n^+ > 0$ and $j_{n+1}^- > 0$ hold. The importance of the flux of aggregates J_n in aggregate size space is that, according to the equation

$$\frac{\partial c_n}{\partial t} = J_{n-1} - J_n \ , \quad n = 2, 3, \ldots \ , \tag{9.22}$$

it determines the variation of aggregate concentration c_n with $n \geq 2$ in time t.

Let us find the relationship between the rates of emission, j_{n+1}^-, and absorption, j_n^+, of monomers by the molecular aggregate. At aggregation equilibrium, i.e., under the condition expressed in Eq. (9.11), a detailed balance of direct and reverse transitions of aggregates on each sequence (9.20) should be established, i.e., the relationship

$$J_n^{(\mathrm{e})} = 0 \ , \quad n = 1, 2, \ldots \ , \tag{9.23}$$

should be fulfilled. Here, $J_n^{(\mathrm{e})}$ is given by Eq. (9.21), where c_n has to be replaced by $c_n = c_n^{(\mathrm{e})}$. Taking into account that at the suggested high density of matter in the aggregates, the

rates j_{n+1}^- are independent of whether the solution is at aggregation equilibrium at a given concentration c_1 or not, we obtain from Eqs. (9.21) and (9.23)

$$j_{n+1}^- = j_n^+ \left(\frac{c_n^{(e)}}{c_{n+1}^{(e)}} \right) , \quad n = 1, 2, \dots . \tag{9.24}$$

Substituting Eq. (9.13) into Eq. (9.24), we arrive at

$$j_{n+1}^- = j_n^+ \exp\left(W_{n+1} - W_n\right) , \quad n = 1, 2, \dots . \tag{9.25}$$

Then, substituting Eqs. (9.25) into (9.21), we obtain

$$J_n = j_n^+ \left[c_n - c_{n+1} \exp\left(W_{n+1} - W_n\right) \right] , \quad n = 1, 2, \dots . \tag{9.26}$$

Finally, substituting Eq. (9.26) into Eq. (9.22) leads to the general kinetic equation of formation of molecular aggregates. It is also called the Becker–Döring step-by-step equation. Using Eq. (9.16), let us represent Eq. (9.26) in the following form:

$$J_n = j_n^+ c_n \left\{ 1 - \exp\left[-\frac{(A_{n+1} - A_n)}{k_B T} \right] \right\} , \quad n = 1, 2, \dots . \tag{9.27}$$

In the case of aggregation equilibrium, when Eq. (9.15) is valid, Eq. (9.27) confirms the relation of detailed balance, Eq. (9.23).

Applying the kinetic theory to the description of a nonequilibrium process in a disperse system, it seems natural to generally refer to the problem of the occurrence of aggregation or disaggregation to a single link in the sequence (9.20) of direct and reverse transitions performed by the aggregates, and, moreover, to refer to this problem to each current moment of process development. Evidently, the occurrence of aggregation or disaggregation on this particular link of the transition sequence depends on whether the inequality $J_n > 0$ or the inequality $J_n < 0$ holds at each moment. In view of the inequality $j_n^+ > 0$, Eq. (9.27) allows us to state that

$$\begin{aligned} &J_n > 0 \ \text{(aggregation)} \quad \text{if } A_{n+1} > 0 \\ &\qquad\qquad\qquad\qquad\qquad\qquad \text{for} \quad n = 1, 2, \dots . \\ &J_n < 0 \ \text{(dissolution)} \quad \text{if } A_{n+1} < 0 \end{aligned} \tag{9.28}$$

Rewriting Eq. (9.16) as

$$A_{n+1} - A_n = -k_B T \left[W_{n+1} - W_n + \ln\left(\frac{c_{n+1}}{c_n} \right) \right] , \quad n = 1, 2, \dots , \tag{9.29}$$

we can see that the sign of the difference $A_{n+1} - A_n$ (important in the conditions given by Eqs. (9.28) for the occurrence of aggregation or disaggregation) depends not only on the value of $W_{n+1} - W_n$, i.e., on the energetic factor, but also on the value $\ln\left(c_{n+1}/c_n\right)$, i.e., on the fluctuation-probability factor. The conditions, as given by Eqs. (9.28) and (9.29), are valid for the whole course of the evolution of the disperse system from arbitrary initial states.

In particular, if only monomers are present in the systems at the initial moment, then, at least at the consecutive moments, the inequalities $c_1 \gg c_2 \gg c_3 \gg c_4 \dots$ are fulfilled with

increasing strength. At the same time (cf. Eq. (9.29)), the inequalities $0 < A_2 - A_1 < A_3 - A_2 < A_4 - A_3 \ldots$ hold. This result is valid despite a possible increase in the work W_n with an increase in n beginning with $n = 1$ where, according to Eq. (9.6), the work W_n is equal to zero. Then, as is seen from Eq. (9.28), at the consecutive moments close to the initial one, aggregation occurs at all levels n of the nonequilibrium process in a disperse system. The aggregation is caused by the probability-fluctuation factor, which can be counteracted (and even noticeably) by the energetic factor.

Let us demonstrate that irrespective of the initial state of a solution the kinetic theory shows a monotonic decrease in the Gibbs energy of a solution with time (total concentration, temperature, and pressure are assumed to be constant, again). Rewriting Eq. (9.17) as

$$\frac{\partial G}{\partial t} = -\sum_{n\geq 2} A_n \frac{\partial c_n}{\partial t} \tag{9.30}$$

and using Eq. (9.22), we obtain (after changing the summation index and taking into account $A_1 = 0$)

$$\frac{\partial G}{\partial t} = -\sum_{n\geq 1} (A_{n+1} - A_n)\, J_n \ . \tag{9.31}$$

According to Eq. (9.28), the sign of the flux J_n coincides with that of the difference $A_{n+1} - A_n$ at all $n \geq 1$. Then it follows from Eq. (9.31) that

$$\frac{\partial G}{\partial t} \leq 0 \ . \tag{9.32}$$

The equality sign in Eq. (9.32) holds only when $J_n = 0$, and, correspondingly, $A_{n+1} - A_n = 0$ at all $n \geq 1$, i.e., when (in agreement with Eqs. (9.23) and (9.27)) the aggregation equilibrium of the solution is established. Thus, irrespective of the initial state of a solution, the kinetic theory indeed shows (according to Eq. (9.32)) a monotonic decrease in the Gibbs energy of a solution with time up to the moment when the Gibbs energy reaches its minimum value at the final state of the aggregation equilibrium of the solution. Since at the assumed conditions of constant total concentration, constant temperature and pressure, a monotonic decrease in the Gibbs energy implies, according to thermodynamic principles, the irreversible tendency of evolution of the system to the state of thermodynamic equilibrium, inequality (9.32) obtained is the kinetic substantiation of the irreversible tendency of a solution to its aggregation equilibrium. As is well known, the statement of the irreversible tendency of a system to thermodynamic equilibrium is one of the most important postulates of thermodynamics. In particular, the derivation of the conditions of thermodynamic stability of a system under thermodynamic equilibrium is based on this postulate. The substantiation of the thermodynamic postulate of the irreversible tendency of a system to thermodynamic equilibrium may be done only by the kinetic theory, for example, by kinetic Boltzmann equation, the Fokker–Planck equations, and the equations of Markovian processes. In our treatment of disperse systems, Eqs. (9.22) and (9.26) constitute precisely such an equation.

In the outline of the results in the present section, we followed widely Ref. [23]. Other aspects of applying the Becker–Döring step-by-step equation to micellization processes as well as the analysis of the general properties of this equation can be found in Refs. [30–33].

9.4 Thermodynamic Characteristics of Micellization Kinetics in the Near-Critical and Micellar Regions of Aggregate Sizes

According to Eq. (9.19) the aggregation work W_n depends on the monomer concentration c_1 via the term $-(n-1)\ln c_1$. The behavior of the work W_n as a function of n at the variable concentration c_1 is shown in Fig. 9.1. Curve 1 corresponds to the case when the surfactant concentration has values below the critical micelle concentration (CMC), i.e., the concentration at which the micelles accumulate the noticeable part of the surfactants in the solution. Curve 2 corresponds to the case when the surfactant concentration is near to the CMC, but from below. Curve 3 corresponds to the practically important case when the surfactant concentration exceeds the CMC, but is lower than the concentration that gives rise to the micelle nonspherical polymorphic transformations in surfactant solutions [5, 9, 12, 34]. It is this curve that will be used in our further analysis.

The positions of the maximum and minimum of the work W_n along the n-axis, i.e., the aggregation numbers of critical and stable molecular aggregates, are denoted by n_c and n_s, respectively. The values of the barrier height and the well depth of the work, W_n, are denoted by $W_c \equiv W_n|_{n=n_c}$ and $W_s \equiv W_n|_{n=n_s}$, respectively. The potential barrier gives rise to the activation barrier of micellization. The half-widths of the potential barrier and potential well of the aggregation work are denoted by Δn_c and Δn_s. They are determined by

$$\Delta n_c = \left[2 \Big/ \left|\partial^2 W_n \Big/ \partial n^2\right|_{n=n_c}\right]^{1/2}, \qquad \Delta n_s = \left[2 \Big/ \left|\partial^2 W_n \Big/ \partial n^2\right|_{n=n_s}\right]^{1/2}. \quad (9.33)$$

The physical meaning of the half-widths Δn_c and Δn_s, introduced in Eq. (9.33), will be discussed below. Figure 9.1 takes into account Eq. (9.6), which implies that the formation of

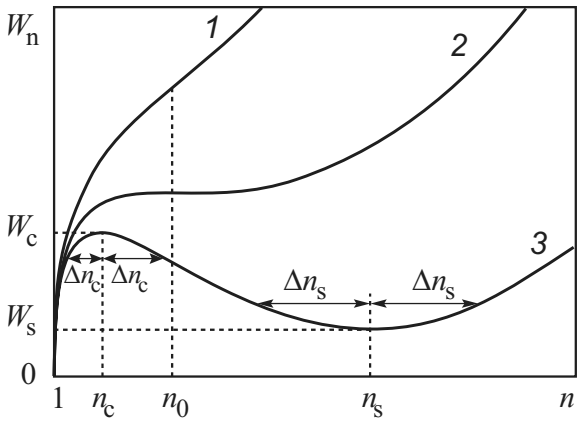

Figure 9.1: Behavior of the work, W_n, of formation of a surfactant molecular aggregate as a function of the aggregation number, n, at a variation of concentration, c_1, of surfactant monomers (see text)

surfactant monomers, present initially in a micellar solution, does not require any work. For definiteness, curve 3 in Fig. 9.1 refers to the case when $W_s > 0$ (when the concentration c_1 is not too high).

The quantities n_c, n_s, W_c, W_s, Δn_c, and Δn_s (as well as the work W_n itself) depend on the monomer concentration, c_1. They represent the thermodynamic characteristics of the micellization kinetics. Furthermore, we assume the conditions

$$\Delta n_c \gg 1 , \qquad \frac{\Delta n_c}{n_c} \ll 1 , \qquad \frac{\Delta n_c}{(n_s - n_c)} \ll 1 , \tag{9.34}$$

$$\Delta n_s \gg 1 , \qquad \frac{\Delta n_s}{(n_s - n_c)} \ll 1 \tag{9.35}$$

to be fulfilled. The first conditions in Eqs. (9.34) and (9.35) allow us to consider the aggregation number n as a continuous variable in the regions of potential barrier and potential well of the work W_n. The remaining conditions in Eqs. (9.34) and (9.35) imply that the potential barrier and potential well of the work W_n are fully exhibited. As is qualitatively shown in Fig. 9.1, they are separated from the initial point $n = 1$ at the n-axis and from each other. This property can also be expressed by the inequalities

$$\exp(W_c) \gg 1 , \qquad \exp(W_c) \gg \exp(W_s) , \tag{9.36}$$

which result from the conditions given in Eqs. (9.34) and (9.35).

Equations (9.34) and (9.35) are fulfilled when the total surfactant concentration sufficiently exceeds the CMC (at this, possibly, the second condition in Eq. (9.34) is valid at its breaking point). In particular, the conditions in Eq. (9.34) and (9.35) imply that the aggregation numbers n_c and n_s are much larger than unity. Equations (9.34) and (9.35) make it possible (employing Eqs. (9.33)) to derive the following quadratic approximations for the work W_n in the regions of its potential barrier and well:

$$W_n = W_c - \left(\frac{n - n_c}{\Delta n_c}\right)^2 \qquad \text{for} \quad n_c - \Delta n_c \lesssim n \lesssim n_c + \Delta n_c , \tag{9.37}$$

$$W_n = W_s + \left(\frac{n - n_s}{\Delta n_s}\right)^2 \qquad \text{for} \quad n_s - \Delta n_s \lesssim n \lesssim n_s + \Delta n_s . \tag{9.38}$$

According to Eq. (9.37), the work W_n decreases by a thermal unit when the variable n deviates from n_c by Δn_c. In accordance with Eq. (9.38), the work W_n increases by a thermal unit when the variable n deviates from n_s by Δn_s. These facts clarify the physical meaning of Δn_c and Δn_s.

The conditions expressed in Eqs. (9.34)–(9.36) allow us to employ a macroscopic description of the micellization kinetics. They generalize the conditions for a macroscopic description revealed previously [20] in the kinetic theory of nucleation. The regions in aggregate size space $n \lesssim n_c - \Delta n_c$, $n_c - \Delta n_c \lesssim n \lesssim n_c + \Delta n_c$ and $n \gtrsim n_c + \Delta n_c$ are called precritical, near-critical, and supercritical regions, respectively. Micelles are accumulated mainly in the region $n_s - \Delta n_s \lesssim n \lesssim n_s + \Delta n_s$. This region is called the micellar region. It is located within the supercritical region. The quantities n_s and Δn_s are the average aggregation number

of micelles and the variance of the aggregation number of micelles around this average value, respectively. As for the regions of potential barrier and potential well of the work W_n, we imply that these regions are the near-critical and micellar regions, respectively.

Molecular aggregates gather mostly in the regions of their sizes, where the work of aggregate formation is minimal. These regions are located to the left- and right-hand sides of the potential barrier of the work, i.e., they are the precritical and supercritical regions. We are not concerned about the part of the supercritical region where $n > n_s + \Delta n_s$, because the concentrations of molecular aggregates in this region are rather low. The large amount of molecular aggregates in the precritical and supercritical regions may be assumed to be varied in their relative proportions so slowly that the aggregate concentrations in each of these separate regions are maintained as quasiequilibrium concentrations irrespective of a permanent decrease or increase in the number of aggregates by their fluxes over the potential barrier of the aggregation work. However, the mutual quasiequilibrium between molecular aggregates in the precritical and supercritical regions is absent due to these fluxes. Mutual quasiequilibrium is only reached as soon as the final equilibrium of a micellar solution is established when the quasiequilibrium concentrations of molecular aggregates in the precritical and supercritical regions as well as the concentrations of molecular aggregates within the entire range of their sizes come to complete equilibrium.

Denoting the quasiequilibrium concentration of molecular aggregates with the aggregation number n by $c_n^{(e)}$ (similar to the equilibrium concentration), we have in the precritical and supercritical regions

$$c_n = c_n^{(e)} \quad \text{for} \quad n \lesssim n_c - \Delta n_c \,, \qquad c_n = c_n^{(e)} \quad \text{for} \quad n \gtrsim n_c + \Delta n_c \,. \tag{9.39}$$

In accordance with Boltzmann's fluctuation principle, similar to Eq. (9.13), we can write

$$c_n^{(e)} = \text{const} \times \exp(-W_n) \,. \tag{9.40}$$

Thus we have in the precritical and supercritical regions

$$c_n^{(e)} = c_1 \exp(-W_n) \qquad \text{for} \quad n \lesssim n_c - \Delta n_c \,, \tag{9.41}$$

$$c_n^{(e)} = c_s \exp[-(W_n - W_s)] \qquad \text{for} \quad n \gtrsim n_c + \Delta n_c \,, \tag{9.42}$$

where $c_s \equiv c_n|_{n=n_s}$ is the concentration of molecular aggregates at the point of minimal work of their formation. The fact that the preexponential factor in Eq. (9.41) is equal to c_1 results from $c_1 \equiv c_n|_{n=1}$ and the equality $W_n|_{n=1} = 0$. The fact that the preexponential factor in Eq. (9.42) is equal to c_s results from the definition of the concentration c_s and the evident equality $(W_n - W_s)|_{n=n_s} = 0$.

Because micelles are accumulated in the micellar region, their total concentration c_M is

$$c_M = \int_{n_s - \Delta n_s}^{n_s + \Delta n_s} c_n \, \mathrm{d}n \,. \tag{9.43}$$

Employing Eq. (9.42) and the quadratic approximation (9.38) and replacing, with a high degree of precision, the integration limits by $-\infty$ and ∞, we get from Eq. (9.43)

$$c_M = \pi^{1/2} c_s \Delta n_s \,. \tag{9.44}$$

Using Eq. (9.44), we may rewrite Eq. (9.42) as [19]

$$c_n^{(e)} = \left(\frac{c_M}{\pi^{1/2}\Delta n_s}\right) \exp\left[-\left(W_n - W_s\right)\right] \qquad \text{for} \quad n \gtrsim n_c + \Delta n_c \,. \tag{9.45}$$

9.5 Kinetic Equation of Aggregation in the Near-Critical and Micellar Regions of Aggregate Sizes

Employing the first conditions in Eqs. (9.34) and (9.35), the aggregation number n may be considered as a continuous variable in the near-critical and micellar regions of the sizes of molecular aggregates. Thus in these regions, Eq. (9.22) may be written as a continuity equation

$$\frac{\partial c_n(t)}{\partial t} = -\frac{\partial J_n(t)}{\partial n} \,. \tag{9.46}$$

Taking into account Eqs. (9.37), (9.38), and $W_{n+1} - W_n = \partial W_n/\partial n$, we obtain

$$W_{n+1} - W_n = -2\frac{(n - n_c)}{(\Delta n_c)^2} \qquad \text{for} \quad n_c - \Delta n_c \lesssim n \lesssim n_c + \Delta n_c \,, \tag{9.47}$$

$$W_{n+1} - W_n = 2\frac{(n - n_s)}{(\Delta n_s)^2} \qquad \text{for} \quad n_s - \Delta n_s \lesssim n \lesssim n_s + \Delta n_s \,. \tag{9.48}$$

Because of the first conditions in Eqs. (9.34) and (9.35), the absolute values of the terms on the right-hand sides of Eqs. (9.47) and (9.48) are much smaller than unity in the near-critical and micellar regions of aggregate sizes. Then, with a high degree of accuracy, we have from Eqs. (9.47) and (9.48) in these regions

$$\exp\left(W_{n+1} - W_n\right) = 1 - 2\frac{(n - n_c)}{(\Delta n_c)^2} \quad \text{for} \quad n_c - \Delta n_c \lesssim n \lesssim n_c + \Delta n_c \,, \tag{9.49}$$

$$\exp\left(W_{n+1} - W_n\right) = 1 + 2\frac{(n - n_s)}{(\Delta n_s)^2} \quad \text{for} \quad n_s - \Delta n_s \lesssim n \lesssim n_s + \Delta n_s \,. \tag{9.50}$$

Using the approximation $c_{n+1} = c_n + \partial c_n/\partial n$ and Eqs. (9.49)–(9.50), and ignoring the products of the small quantities $\partial c_n/\partial n$, $2\,(n - n_c)/(\Delta n_c)^2$, and $2\,(n - n_s)/(\Delta n_s)^2$, we obtain from Eq. (9.26)

$$J_n(t) = j_c^+ \left[2\frac{(n - n_c)}{(\Delta n_c)^2} - \frac{\partial}{\partial n}\right] c_n(t) \qquad \text{for} \quad n_c - \Delta n_c \lesssim n \lesssim n_c + \Delta n_c \,, \tag{9.51}$$

$$J_n(t) = -j_s^+ \left[2\frac{(n - n_s)}{(\Delta n_s)^2} + \frac{\partial}{\partial n}\right] c_n(t) \qquad \text{for} \quad n_s - \Delta n_s \lesssim n \lesssim n_s + \Delta n_s \,, \tag{9.52}$$

where $j_c^+ \equiv j_n^+\big|_{n=n_c}$ and $j_s^+ \equiv j_n^+\big|_{n=n_s}$ are the rates of monomer absorption by critical and stable aggregates, respectively. Equations (9.51), (9.52), and (9.46) result in the differential kinetic equation describing the formation of molecular aggregates in the near-critical and micellar regions of their sizes.

Let us also briefly sketch another way of deriving Eqs. (9.51) and (9.52). The variation of the aggregation number n with respect to time, $\dot{n}$, is given by

$$\dot{n} = j_n^+ - j_n^- \ . \tag{9.53}$$

Assuming n to be a continuous variable, Eq. (9.25) yields approximately

$$j_n^- = j_n^+ \exp\left(\frac{\partial W_n}{\partial n}\right) \ . \tag{9.54}$$

As already mentioned, the derivative $\partial W_n/\partial n$ is small in the near-critical and micellar regions of aggregate sizes. Then, from Eqs. (9.53) and (9.54) we have in these regions with a high degree of accuracy

$$\dot{n} = -j_n^+ \frac{\partial W_n}{\partial n} \ . \tag{9.55}$$

One can also write the flux of molecular aggregates, $J_n\,(t)$, as

$$J_n(t) = \left(\dot{n} + \beta \frac{\partial}{\partial n}\right) c_n(t) \ . \tag{9.56}$$

The term containing $\dot{n}$ describes the regular evolution of a single molecular aggregate. The term including the differential operator $\partial \big/ \partial n$ describes the fluctuation evolution of the ensemble of molecular aggregates. This fluctuational contribution on the evolution is superimposed on the regular one and broadens the regular evolution. Further, we substitute Eq. (9.55) into Eq. (9.56) in the near-critical and micellar regions. Then, determining the unknown coefficient β from the condition of vanishing of the flux of molecular aggregates at their equilibrium concentrations given by Eq. (9.40), we obtain

$$J_n(t) = -j_n^+ \left(\frac{\partial W_n}{\partial n} + \frac{\partial}{\partial n}\right) c_n\,(t) \ . \tag{9.57}$$

Expressing the derivative $\partial W_n \big/ \partial n$ in Eq. (9.57) in the near-critical and micellar regions by means of Eqs. (9.37) and (9.38), we arrive at the previously obtained Eqs. (9.51) and (9.52) again.

9.6 Direct and Reverse Fluxes of Molecular Aggregates over the Activation Barrier of Micellization

As already mentioned above, in contrast to nucleation at micellization we observe, in addition to the direct flux of molecular aggregates overcoming (by fluctuation) the activation barrier of micellization from the side of the precritical region, the reverse flux of molecular aggregates overcoming (by fluctuation) the activation barrier of micellization from the side of the supercritical region. Let us denote the direct and reverse fluxes of molecular aggregates in the region of the potential barrier of the work of their formation, i.e., in the near-critical region, by

$J_n'(t)$ and $J_n''(t)$, respectively. Similarly, the concentrations of molecular aggregates participating in these fluxes in the near-critical region are $c_n'(t)$ and $c_n''(t)$. We have in this case for the total flux $J_n(t)$ of molecular aggregates and their total concentrations $c_n(t)$ in the near-critical region $n_c - \Delta n_c \lesssim n \lesssim n_c + \Delta n_c$

$$J_n(t) = J_n'(t) + J_n''(t) \; , \tag{9.58}$$

$$c_n(t) = c_n'(t) + c_n''(t) \; . \tag{9.59}$$

The approach employed in the previous sections to derive the kinetic equation of micellization can be applied separately for the molecular aggregates transferred (by fluctuations) from the precritical to supercritical regions and for molecular aggregates transferred (by fluctuations) from the supercritical to precritical regions. Therefore, similar to Eqs. (9.46) and (9.51), we have in the near-critical region $n_c - \Delta n_c \lesssim n \lesssim n_c + \Delta n_c$

$$\frac{\partial c_n'(t)}{\partial t} = -\frac{\partial J_n'(t)}{\partial n} \; , \qquad J_n'(t) = j_c^+ \left[2\frac{(n - n_c)}{(\Delta n_c)^2} - \frac{\partial}{\partial n} \right] c_n'(t) \tag{9.60}$$

as well as

$$\frac{\partial c_n''(t)}{\partial t} = -\frac{\partial J_n''(t)}{\partial n} \; , \qquad J_n''(t) = j_c^+ \left[2\frac{(n - n_c)}{(\Delta n_c)^2} - \frac{\partial}{\partial n} \right] c_n''(t) \; . \tag{9.61}$$

Let us formulate the boundary conditions to Eqs. (9.60)–(9.61). Based on the ideas of the kinetic theory of nucleation [21] and taking into account the boundary conditions (9.39), we conclude that the boundary conditions to Eqs. (9.60) for the concentrations $c_n'(t)$ in the near-critical region are [19]

$$\frac{c_n'(t)}{c_n^{(e)}} \cong \begin{cases} 1 & \text{for} \quad n \simeq n_c - \Delta n_c \; , \\ 0 & \text{for} \quad n \simeq n_c + \Delta n_c \; , \end{cases} \tag{9.62}$$

and the boundary conditions to Eqs. (9.61) for the concentrations $c_n''(t)$ in the near-critical region are [19]

$$\frac{c_n''(t)}{c_n^{(e)}} \cong \begin{cases} 0 & \text{for} \quad n \simeq n_c - \Delta n_c \; , \\ 1 & \text{for} \quad n \simeq n_c + \Delta n_c \; . \end{cases} \tag{9.63}$$

The quasiequilibrium concentrations $c_n^{(e)}$ in the boundary conditions (9.62) and (9.63) are determined by Eqs. (9.41) (at $n \simeq n_c - \Delta n_c$) and (9.45) (at $n \simeq n_c + \Delta n_c$). According to Eqs. (9.59), (9.62), and (9.63), the boundary conditions to Eqs. (9.46) and (9.51) for the total concentrations $c_n(t)$ of molecular aggregates in the near-critical region are

$$\frac{c_n(t)}{c_n^{(e)}} \cong 1 \qquad \text{for} \quad n \simeq n_c \mp \Delta n_c \; , \tag{9.64}$$

where the quasiequilibrium concentrations $c_n^{(e)}$ are given by Eqs. (9.41) (at $n \simeq n_c - \Delta n_c$) and (9.45) (at $n \simeq n_c + \Delta n_c$).

At the quasiequilibrium concentrations of molecular aggregates in the precritical and supercritical regions, the concentrations c_n of molecular aggregates in the near-critical region will be quasistationary ones. The prefix "quasi" to the words "equilibrium", "steady", and "stationary" specifies the absence of a significant time dependence of the concentrations c_n within the time intervals, during which the concentrations c_1 and c_M do not vary noticeably in the course of the slow tendency of evolution of the micellar solution to its final state of complete equilibrium. Let us study the quasisteady state of molecular aggregates in the near-critical region. The concentrations $c'_n(t)$, $c''_n(t)$, and $c_n(t)$ of the aggregates are independent of time t in this state, whereas the aggregate fluxes $J'_n(t)$, $J''_n(t)$, and $J_n(t)$ are also independent of the aggregation number n (cf. Eqs. (9.60), (9.61), and (9.46)). We denote the concentrations $c'_n(t)$, $c''_n(t)$, and $c_n(t)$ in a quasisteady state by $c'^{(s)}_n$, $c''^{(s)}_n$, and $c^{(s)}_n$, and the fluxes $J'_n(t)$, $J''_n(t)$, and $J_n(t)$ in this state by J', J'', and J, respectively (for simplicity of the notations, the quasisteady state of the fluxes is specified by the omission of the argument n and t). Then, in the near-critical region, $n_c - \Delta n_c \lesssim n \lesssim n_c + \Delta n_c$, we have

$$c'_n(t) = c'^{(s)}_n, \qquad c''_n(t) = c''^{(s)}_n, \qquad c_n(t) = c^{(s)}_n \tag{9.65}$$

as well as

$$J'_n(t) = J', \qquad J''_n(t) = J'', \qquad J_n(t) = J\ . \tag{9.66}$$

The right-hand sides of the continuity equations (9.60) and (9.61) are equal to zero in the quasisteady state of molecular aggregates. We employ further Eqs. (9.60) and (9.61) for the fluxes of molecular aggregates and the boundary conditions (9.62) and (9.63) (with Eqs. (9.41) and (9.45)). Then, performing the integration, we obtain in the near-critical region $n_c - \Delta n_c \lesssim n \lesssim n_c + \Delta n_c$ [19]

$$c'^{(s)}_n = \frac{c_1 \exp(-W_c)}{\pi^{1/2}\Delta n_c} \exp\left[\left(\frac{n-n_c}{\Delta n_c}\right)^2\right] \int_n^\infty \exp\left[-\left(\frac{n'-n_c}{\Delta n_c}\right)^2\right] dn'\ , \tag{9.67}$$

$$J' = c_1 j_c^+ \exp(-W_c) \Big/ \pi^{1/2}\Delta n_c\ , \tag{9.68}$$

$$\begin{aligned} c''^{(s)}_n \quad &= \quad \frac{c_M \exp[-(W_c - W_s)]}{\pi\,\Delta n_c \Delta n_s} \exp\left[\left(\frac{n-n_c}{\Delta n_c}\right)^2\right] \\ &\times \quad \int_{-\infty}^{n} \exp\left[-\left(\frac{n'-n_c}{\Delta n_c}\right)^2\right] dn'\ , \end{aligned} \tag{9.69}$$

$$J'' = -c_M j_c^+ \exp[-(W_c - W_s)] \big/ \pi\,\Delta n_c \Delta n_s\ . \tag{9.70}$$

For the total concentrations of molecular aggregates and their total flux in the quasisteady state in the near-critical region, we have according to Eqs. (9.59) and (9.58)

$$c^{(s)}_n = c'^{(s)}_n + c''^{(s)}_n\ , \qquad J = J' + J''\ . \tag{9.71}$$

Direct J' and reverse J'' fluxes, given by Eqs. (9.68) and (9.70), are, naturally, positive and negative, respectively. In accordance with Eq. (9.68), higher values of c_1, j_c^+, and lower values of W_c and Δn_c result in larger values of the direct flux J'. According to Eq. (9.70), the higher the c_M, j_c^+ and the lower the $W_c - W_s$, Δn_c, and Δn_s, the larger the absolute value of the reverse flux J''.

9.7 Times of Establishment of Quasiequilibrium Concentrations

9.7.1 Pre- and Supercritical Sizes

Let us consider the initial stages of micellization. At these stages, the quasiequilibrium concentrations of surfactant molecular aggregates in the precritical and supercritical regions of their sizes, as well as the quasisteady concentrations of molecular surfactant aggregates in the near-critical region of their sizes, are established. We will analyze here how this process of establishment of the quasiequilibrium concentrations proceeds with time in the precritical and supercritical regions.

Let us first consider the establishment of the quasiequilibrium state in the micellar region $n_s - \Delta n_s \lesssim n \lesssim n_s + \Delta n_s$. This range of sizes is a part of the supercritical region. The variations in the concentrations c_n of the molecular aggregates with the time t are governed then by the continuity equation (9.46) with fluxes $J_n(t)$ determined by Eq. (9.52). The boundary conditions to the kinetic equation can be written in the form

$$c_n(t) \simeq 0 \qquad \text{for} \quad n \simeq n_s \mp \Delta n_s \, . \tag{9.72}$$

The approximate equality (9.72) should be interpreted as if the concentrations of molecular aggregates at the boundaries $n \simeq n_s \mp \Delta n_s$ of the micellar region are negligible as compared to the concentration at $n = n_s$. For the description of the quasiequilibrium aggregate concentrations, which are established with time in the micellar region, we have Eq. (9.45) at our disposal. Taking into account the approximation for W_n, as given by Eq. (9.38), we can see from Eq. (9.45) that the quasiequilibrium concentrations rather rapidly decrease as n approaches the boundaries $n \simeq n_s \mp \Delta n_s$ of the micellar region. Thus, the boundary conditions (9.72) are fulfilled.

Let us go over in the micellar region from the variable n to the variable

$$u \equiv \frac{(n - n_s)}{\Delta n_s} \qquad \text{for} \quad -1 \lesssim u \lesssim 1 \, . \tag{9.73}$$

Assuming that

$$c\,(u,t) \equiv c_n(t) \, , \qquad c^{(e)}\,(u) \equiv c_n^{(e)} \qquad \text{for} \quad -1 \lesssim u \lesssim 1 \, , \tag{9.74}$$

with Eqs. (9.46) and (9.52) we arrive at the kinetic equation

$$\frac{\partial c\,(u,t)}{\partial t} = \frac{j_s^+}{(\Delta n_s)^2} \frac{\partial}{\partial u} \left(2u + \frac{\partial}{\partial u} \right) c\,(u,t) \qquad \text{for} \quad -1 \lesssim u \lesssim 1 \, . \tag{9.75}$$

In this case, the boundary conditions (9.72) can be rewritten as

$$c\,(u,t) \approx 0 \qquad \text{for} \quad u \approx \mp 1\ . \tag{9.76}$$

According to Eqs. (9.45), (9.73), and (9.74), we also have

$$c^{(\mathrm{e})}(u) = \text{const} \times \exp(-u^2) \qquad \text{for} \quad -1 \lesssim u \lesssim 1\ . \tag{9.77}$$

In order to solve Eq. (9.75), we first recall some properties of the Hermitian polynomials $H_i(\xi)$ $(i = 0, 1, \ldots)$: $H_0(\xi) = 1$, $H_1(\xi) = 2\xi$, $H_2(\xi) = 4\xi^2 - 2, \ldots$. They satisfy the recurrent relations

$$\frac{\partial}{\partial \xi} H_i\,(\xi) = 2i\,H_{i-1}\,(\xi)\ , \qquad \left(2\xi - \frac{\partial}{\partial \xi}\right) H_i\,(\xi) = H_{i+1}\,(\xi)\ , \tag{9.78}$$

and the orthogonality and normalization relations

$$\pi^{-1/2} \int\limits_{-\infty}^{\infty} \exp\left(-\xi^2\right) H_i\,(\xi)\,H_{i'}(\xi)\,\mathrm{d}\xi = i!2^i \delta_{ii'} \qquad \text{for} \quad i, i' = 0, 1, \ldots, \tag{9.79}$$

where $\delta_{ii'}$ is the Kronecker symbol and $0! \equiv 1$.

With Eq. (9.78), we obtain

$$\frac{\partial}{\partial \xi}\left(2\xi + \frac{\partial}{\partial \xi}\right) \exp\left(-\xi^2\right) H_i(\xi) = -2i \exp\left(-\xi^2\right) H_i(\xi) \tag{9.80}$$

for $i = 0, 1, \ldots$. According to Eq. (9.77), the quasiequilibrium concentrations $c^{(\mathrm{e})}\,(u)$ satisfy the kinetic equation (9.75) and the relevant boundary conditions (9.76). It follows that the general solution of Eq. (9.75) with the boundary conditions (9.76) has (in the range $-1 \lesssim u \lesssim 1$) the form

$$c\,(u,t) = c^{(\mathrm{e})}\,(u) + \sum_{i=1}^{\infty} k_i \exp\left[-2i j_s^+ t \Big/ (\Delta n_\mathrm{s})^2\right] \exp\left(-u^2\right) H_i\,(u)\ . \tag{9.81}$$

The coefficients k_i are independent of u and t. They can be expressed with Eq. (9.79) via the initial concentrations $c\,(u,t)|_{t=0}$ in the micellar region. The quasiequilibrium concentrations $c^{(\mathrm{e})}\,(u)$ can be included into Eq. (9.81) in the sum over i, adding the term with $i = 0$ to the sum. This result indicates that the obtained solution (9.81) is indeed the general solution: It represents an expansion in the complete system of functions. Equation (9.81) describes the establishment of the quasiequilibrium concentrations of molecular aggregates in the micellar region. Its analysis shows that the quantities $t_s^{(i)}$ can be determined as

$$t_s^{(i)} = \frac{(\Delta n_\mathrm{s})^2}{2i j_s^+} \qquad \text{for} \quad i = 1, 2, \ldots\ . \tag{9.82}$$

The quantities represent the spectrum of times required to establish these particular concentrations. For the largest of these times and, hence, the characteristic time, t_s, we have

$$t_s = \frac{(\Delta n_\mathrm{s})^2}{2 j_s^+}\ . \tag{9.83}$$

According to Eq. (9.83), the larger the Δn_s and the smaller the j_s^+, the larger is the time t_s.

Now let us find out how the quasiequilibrium concentrations of molecular aggregates are established with time in the precritical region $n \lesssim n_c - \Delta n_c$. We conclude that, since the same precritical region also exists in the case of nucleation, the quasiequilibrium concentrations of molecular aggregates will be established in the precritical region in the same manner as in the course of nucleation. As was shown in [35, 36], it occurs due to the tendency of molecular aggregates with the initial aggregation number equal to unity to overcome (by fluctuations) the potential barrier of the work of their formation. Then, according to Refs. [24, 35, 36], we can estimate the characteristic time, t', required to establish the quasiequilibrium concentrations of molecular aggregates in the precritical region $n \lesssim n_c - \Delta n_c$ as

$$t' \approx n_c \frac{\Delta n_c}{j_c^+} \,. \tag{9.84}$$

According to Eq. (9.84), the larger the n_c and Δn_c and the lower the j_c^+, the larger the time t'.

Finally, it remains to be shown how the quasiequilibrium concentrations of molecular aggregates are established with time in the range $n_c + \Delta n_c \lesssim n \lesssim n_s - \Delta n_s$ of the supercritical region, which is located at the n-axis between the near-critical and micellar regions. Evidently, it occurs due to the tendency of molecular aggregates, which were originally located in the micellar region, to overcome (by fluctuations) the potential barrier of the work of their formation in the backward direction. Hence, there is a complete analogy between the establishment of the quasiequilibrium concentrations of molecular aggregates in the $n_c + \Delta n_c \lesssim n \lesssim n_s - \Delta n_s$ and $n \lesssim n_c - \Delta n_c$ regions. The only difference is that the role of n_c is now played by the difference $n_s - n_c$. Taking these facts into account, we estimate, by analogy with Eq. (9.84), the characteristic time, t'', required for establishment of quasiequilibrium concentrations of molecular aggregates in the range $n_c + \Delta n_c \lesssim n \lesssim n_s - \Delta n_s$ as [24]

$$t'' \approx (n_s - n_c) \frac{\Delta n_c}{j_c^+} \,. \tag{9.85}$$

According to Eq. (9.85), the larger the n_s and Δn_c and the smaller the n_c and j_c^+, the larger the time t''.

9.7.2 Near-Critical Sizes

The assumption of quasisteady concentrations of molecular aggregates in the near-critical region of their sizes is important in the kinetic theory of micellization. Let us consider how the quasisteady state is established with time. The variation in concentrations c_n of molecular aggregates with time in the near-critical region is still determined by the continuity equation (9.46) where, however, the flux $J_n(t)$ of molecular aggregates is determined now by Eq. (9.51). According to Eqs. (9.64) and (9.40), the boundary conditions to the kinetic equations (9.46) and (9.51) can be rewritten in the near-critical region as

$$c_n(t) = c_n^{(e)} = \text{const} \times \exp\left[-(W_n - W_c)\right] \qquad \text{for} \quad n \approx n_c \mp \Delta n_c \,, \tag{9.86}$$

where the factor *const* may be different on the left- and right-hand sides from the near-critical region. Let us analyze the behavior in the near-critical region from the variable n to the variable υ via

$$\upsilon \equiv \frac{(n - n_c)}{\Delta n_c}, \qquad -1 \lesssim \upsilon \lesssim 1 \ . \tag{9.87}$$

Assuming

$$c\,(\upsilon, t) \equiv c_n(t)\ , \qquad c^{(e)}\,(\upsilon) \equiv c_n^{(e)} \qquad \text{for} \quad -1 \lesssim \upsilon \lesssim 1\ , \tag{9.88}$$

we obtain from Eqs. (9.46) and (9.51) the following kinetic equation:

$$\frac{\partial c\,(\upsilon, t)}{\partial t} = \frac{j_c^+}{(\Delta n_c)^2} \frac{\partial}{\partial \upsilon} \left(2\upsilon - \frac{\partial}{\partial \upsilon} \right) c\,(\upsilon, t) \qquad \text{for} \quad -1 \lesssim \upsilon \lesssim 1\ . \tag{9.89}$$

Then, substituting Eq. (9.87) into Eq. (9.86), we arrive at the boundary conditions

$$\frac{c\,(\upsilon, t)}{c^{(e)}\,(\upsilon)} \approx 1 \qquad \text{for} \quad \upsilon \approx \mp 1\ . \tag{9.90}$$

Employing Eq. (9.37) in Eq. (9.86) and using Eq. (9.87), we get

$$c^{(e)}\,(\upsilon) = \text{const} \times \exp(\upsilon^2) \qquad \text{for} \quad -1 \lesssim \upsilon \lesssim 1\ . \tag{9.91}$$

For the determination of the solution of Eq. (9.89) with the boundary condition (9.90), we cannot directly use the results obtained in the previous section. Equation (9.89) and the conditions (9.90) differ from Eqs. (9.75) and (9.76). The quasisteady concentrations of molecular aggregates, $c^{(s)}\,(\upsilon)$, which are established with time in the near-critical region satisfy the kinetic equation (9.89) with the boundary conditions (9.90). From Eq. (9.78), we get further

$$\frac{\partial}{\partial \xi} \left(2\xi - \frac{\partial}{\partial \xi} \right) H_i\,(\xi) = 2\,(i + 1)\, H_i\,(\xi)\ , \qquad i = 0, 1, \ldots\ . \tag{9.92}$$

Then, taking into account that, according to Eq. (9.91), the quasisteady concentrations $c^{(e)}\,(\upsilon)$ increase with $|\upsilon|$ quite rapidly, we can represent the general solution of Eq. (9.89) with the boundary conditions (9.90) as

$$c(\upsilon, t) = c^{(s)}(\upsilon) + \sum_{i=0}^{\infty} p_i \exp\left[\frac{-2\,(i + 1)\, j_c^+ t}{(\Delta n_c)^2} \right] H_i\,(\upsilon) \qquad \text{for} \quad -1 \lesssim \upsilon \lesssim 1\ . \tag{9.93}$$

The coefficients p_i are independent of υ and t. They can be expressed, employing Eq. (9.79), via the initial concentrations $c\,(\upsilon, t)|_{t=0}$ of aggregates in the near-critical region. The solution obtained is indeed the general solution: It represents the expansion of the difference $c\,(\upsilon, t) - c^{(s)}\,(\upsilon)$ in the complete function system of the Hermitian polynomials $H_i(\upsilon)(i = 0, 1, \ldots)$. Note that the rapid increase in the quasiequilibrium concentrations $c^{(e)}\,(\upsilon)$ with $|\upsilon|$ allows us to neglect the contribution from the polynomial sum over i in Eq. (9.93) at the boundaries of the near-critical region, and, hence, provides the fulfillment of the boundary conditions (9.90).

Equation (9.93) describes the establishment of the quasisteady concentrations of molecular aggregates in the near-critical region. As is seen from Eq. (9.93), the quantities $t_c^{(i)}$,

$$t_c^{(i)} = \frac{(\Delta n_c)^2}{2\,(i+1)\,j_c^+} \qquad \text{for} \quad i = 0, 1, \ldots, \tag{9.94}$$

represent the spectrum of times required to establish these concentrations. For the largest of these times and, hence, the characteristic time, t_c, we have [24]

$$t_c = \frac{(\Delta n_c)^2}{2 j_c^+} \, . \tag{9.95}$$

According to Eq. (9.95), the larger the Δn_c and the smaller the j_c^+ , the larger the time t_c.

9.8 Time of Fast Relaxation in Surfactant Solutions

Let us now elucidate the interrelation between the time t_s and the time of fast relaxation of micellar solutions. It is possible to clarify in this way the concept of the fast relaxation of a micellar solution introduced first in Refs. [13–16] and then widely used in the literature [37–40] as the concept corresponding to the process of local rearrangement of micelles without changing their numbers in the micellar region. Besides, we will investigate the validity of the assumption of constancy of the monomer concentration at local rearrangement of the micelle size distribution in the micellar region. The assumption was important for the derivation of the results obtained in the two preceding sections.

We mark the values corresponding to the end of fast relaxation of micellar solutions with superscript zero. We introduce further with

$$\xi_n = \frac{\left(c_n - c_n^{(0)}\right)}{c_n^{(0)}} \tag{9.96}$$

a measure of the relative deviation of the current concentrations c_n of aggregates from the concentrations $c_n^{(0)}$ at the end of the fast relaxation process. Assuming further that fast relaxation is realized only via the emission and absorption of monomers in the micellar region, we take into account in Eq. (9.96) exclusively the aggregates in the micellar region and the monomers at $n = 1$. For a description of the aggregates in the micellar region, we use, together with the aggregation number n, the variable

$$w \equiv \frac{\left(n - n_s^{(0)}\right)}{\Delta n_s^{(0)}} \tag{9.97}$$

varying within the range $-1 \lesssim w \lesssim 1$. Apparently, the variable w is similar to the variable u defined by Eq. (9.73). Taking into account Eqs. (9.45), (9.38), and (9.97), the micelle concentrations $c_n^{(0)}$, reached after completion of fast relaxation, can be written as

$$c_n^{(0)} = \left(\frac{c_M^{(0)}}{\pi^{1/2}\Delta n_s^{(0)}}\right) \exp\left(-w^2\right) \qquad \text{for} \quad -1 \lesssim w \lesssim 1 \, . \tag{9.98}$$

We have already considered the solution of the kinetic equation of aggregation in the micellar region in Section 9.7. There the kinetic equation (9.75) was formulated under the assumption of constancy of the monomer concentration in a surfactant solution. With sufficiently large micelle concentrations in the micellar region, the local rearrangement of the micelle distribution in sizes may be followed by considerable changes in the monomer concentration. Thus we cannot set a priori the monomer concentration as constant in the consideration of fast relaxation. Therefore we need to refine the form of the kinetic equation of aggregation in the micellar region. With Eq. (9.96), we have

$$c_n(t) = c_n^{(0)}(1 + \xi_n(t)) \qquad \text{for} \quad n \geq 1 \,, \qquad j_n^+(t) = j_n^{+(0)}(1 + \xi_1(t)) \,, \tag{9.99}$$

where $j_n^{+(0)} = j_n^+\left(c_1^{(0)}\right)$. As follows from Eq. (9.21), the relations of detailed balance after completion of fast relaxation can be written in the micellar region as

$$j_n^{+(0)} c_n^{(0)} = j_{n+1}^- c_{n+1}^{(0)} \,. \tag{9.100}$$

According to the definition (9.21) and taking into account Eqs. (9.99)–(9.100), the flux J_n of aggregates can be expressed as

$$J_n = j_n^{+(0)} c_n^{(0)} \left(\xi_n - \xi_{n+1}\right) + j_n^{+(0)} c_n^{(0)} \xi_1 + j_n^{+(0)} c_n^{(0)} \xi_1 \xi_n \,. \tag{9.101}$$

Approaching the state of completion of fast relaxation, we have $\xi_n \ll 1$. This inequality allows us to neglect the last term on the right-hand side of Eq. (9.101) and to rewrite Eq. (9.101) at $n \gg 1$ as

$$J_n \simeq -j_n^{+(0)} c_n^{(0)} \frac{\partial \xi_n}{\partial n} + j_n^{+(0)} c_n^{(0)} \xi_1 \,. \tag{9.102}$$

With Eqs. (9.46), (9.96), and (9.102) the desired kinetic equation of fast relaxation can be written as

$$c_n^{(0)} \frac{\partial \xi_n(t)}{\partial t} \simeq \frac{\partial}{\partial n}\left(j_n^{+(0)} c_n^{(0)} \frac{\partial \xi_n(t)}{\partial n}\right) - \xi_1(t) \frac{\partial}{\partial n}\left(j_n^{+(0)} c_n^{(0)}\right) \,. \tag{9.103}$$

As we did before, for a description of the evolution within the micellar region we can set $j_n^{+(0)} \simeq j_s^{+(0)}$ on the right-hand side of Eq. (9.103). One important peculiarity of Eq. (9.103) is the presence of the last term on the right-hand side. The kinetic equation becomes inhomogeneous due to this term. Equation (9.103) transforms at $\xi_1(t) = 0$ into the homogeneous equation (9.75).

In addition to Eq. (9.103), we have to use Eq. (9.8) of mass balance of the surfactant per volume unit of the solution. Substituting the first expression in Eqs. (9.99) into the right-hand side of Eq. (9.8) and recognizing that the total surfactant concentration c remains the same after the completion of the fast relaxation process, we find

$$c_1^{(0)} \zeta_1(t) = -\sum_{n=2}^{\infty} n c_n^{(0)} \zeta_n(t) \,. \tag{9.104}$$

We will search for a solution of Eqs. (9.103) and (9.104) on the basis of the expansion

$$\xi_n(t) = \sum_{i=0}^{\infty} q_i(t) H_i(w) \qquad \text{for} \quad -1 \lesssim w \lesssim 1 \tag{9.105}$$

in the full system of the Hermitian polynomials $H_i(w)$, where $q_i(t)$ are w-independent coefficients of expansion, which are the desired functions of the time t. Substituting Eq. (9.105) into Eq. (9.104) and assuming that the main contribution to the sum on the right-hand side of Eq. (9.104) is given by the micellar region, passing from summation over n to integration over w with Eq. (9.97), taking into account Eq. (9.98) and the orthogonality relations (9.79), we obtain

$$c_1^{(0)} \zeta_1(t) = -c_M^{(0)} \Delta n_s^{(0)} q_1(t) - c_M^{(0)} n_s^{(0)} q_0 \ . \tag{9.106}$$

Substituting further Eqs. (9.105) and (9.106) into Eq. (9.103) and using again Eqs. (9.97) and (9.98), computing the scalar products of both sides of Eq. (9.103) with the Hermitian polynomials H_k, $k = 0, 1, 2, \ldots$, and taking into account Eq. (9.79), we get $(\partial q_0(t)/\partial t) = 0$, i.e., $q_0 = \text{const}$, and

$$\frac{\partial q_1(t)}{\partial t} = \frac{2 j_s^{+(0)}}{\left(\Delta n_s^{(0)}\right)^2} q_1(t) - j_s^{+(0)} \frac{c_M^{(0)}}{c_1^{(0)}} \left(q_1(t) + \frac{n_s^{(0)}}{\Delta n_s^{(0)}} q_0 \right) , \tag{9.107}$$

$$\frac{\partial q_k(t)}{\partial t} = -\frac{2 j_s^{+(0)} k}{\left(\Delta n_s^{(0)}\right)^2} q_k(t) \qquad \text{for} \quad k = 2, 3, \ldots \ . \tag{9.108}$$

We assume here further that

$$q_0(t) = 0 \tag{9.109}$$

holds. Condition (9.109) is required to guarantee that the final concentrations $c_n^{(0)}$ are indeed achieved at the end of fast relaxation of the micellar solution. Equations (9.107)–(9.109) yield

$$q_1(t) = q_1(0) \exp\left(-\frac{t}{t_1}\right) , \qquad q_k(t) = q_k(0) \exp\left(-\frac{kt}{t_s^{(0)}}\right) \tag{9.110}$$

for $k = 2, 3, \ldots$. Here, $q_1(0), q_2(0), \ldots$ are the values of the coefficients $q_1(t), q_2(t), \ldots$ at the initial (for fast relaxation) time $t = 0$. The times t_1 and ${t_s}^{(0)}$ are defined by

$$t_1 = \frac{1}{j_s^{+(0)}} \left[\frac{2}{\left(\Delta n_s^{(0)}\right)^2} + \frac{c_M^{(0)}}{c_1^{(0)}} \right]^{-1} , \qquad t_s^{(0)} = \frac{\left(\Delta n_s^0\right)^2}{2 j_s^{+(0)}} \ . \tag{9.111}$$

Note that the time ${t_s}^{(0)}$ is an analog of the characteristic time t_s given by Eq. (9.83). According to Eqs. (9.106) and (9.110), the relation

$$\xi_1(t) = -\frac{c_M^{(0)} \Delta n_s^{(0)}}{c_1^{(0)}} q_1(0) \mathrm{e}^{-t/t_1} \tag{9.112}$$

holds as well provided that Eq. (9.109) is fulfilled.

Equations (9.43), (9.97), (9.98), (9.99), (9.105), (9.109), and (9.79) result in

$$c_M(t) = c_M^{(0)} \ , \tag{9.113}$$

i.e., the total number of micelles is constant during the fast relaxation process in a micellar solution. According to Eqs. (9.111), we have further

$$t_1 < t_s^{(0)} \ , \quad \text{and} \quad t_1 = t_s^{(0)} \qquad \text{for} \quad \frac{c_M^{(0)}}{c_1^{(0)}} \ll \frac{2}{\left(\Delta n_s^{(0)}\right)^2} \ . \tag{9.114}$$

For the micelles, we get from Eqs. (9.99), (9.105), (9.109)–(9.110), and (9.114) that

$$c_n(t)|_{t \gg t_s{}^{(0)}} = c_n^{(0)} \tag{9.115}$$

holds. For monomers, Eqs. (9.112) and (9.99) lead to

$$c_1(t)|_{t \gg t_1} = c_1^{(0)} \ . \tag{9.116}$$

Equations (9.115) and (9.116) indicate that the time-independent aggregate concentrations $c_n^{(0)}$ in the micellar region and the monomer concentration $c_1^{(0)}$ are actually established with time. If the contributions from the higher terms of the expansion (9.105) with $i = 2, 3, \ldots$ are ignored, then the condition of applicability $t \gg t_s{}^{(0)}$ of Eq. (9.115) can be substituted by a weaker (as compared to Eq. (9.114)) condition $t \gg t_1$. Then, it is evident that the time t_1 defined by the first expression in Eq. (9.111) is the time of fast relaxation of a micellar solution.

Fast relaxation of a micellar solution, as described in Refs. [13–16], is directly observable in experiment [37–39, 41–44] and has been found in numerical modeling [45, 46]. This relaxation can be caused by the instantaneous external disturbance (for example, by temperature or pressure jumps) of the equilibrium micellar solution at the initial moment $t = 0$. The external disturbance of the solution was not considered in the previous sections, where the evolution of the solution was due exclusively to internal processes beginning with the time when only monomers were present in a solution.

According to Eqs. (9.112) and (9.99), the monomer concentration $c_1(t)$ varies in the period of fast relaxation of the solution; it increases at $q_1(0) > 0$ and, on the contrary, decreases at $q_1(0) < 0$. The greater the initial solution disturbance, the greater the variation of the concentration $c_1(t)$.

In contrast, according to Eq. (9.113), the total micelle concentration $c_M(t)$ does not vary in the course of fast relaxation of a micellar solution. However, the micelle concentration varies at the slower (final) stage of micellization as well as at the stage preceding its establishment. This variation is caused by the existence of direct $J'(J' > 0)$ and reverse $J''(J'' < 0)$ fluxes of molecular aggregates over the potential barrier of the aggregation work and will be considered in the next section.

9.9 Time of Slow Relaxation in Surfactant Solutions

Direct J' and reverse J'' fluxes of molecular aggregates over the potential barrier of the aggregation work ($J' + J''$, $J'' < 0$) result in the fluctuational transfer of the total number of

molecular aggregates from the precritical to the micellar regions in a unit volume of a micellar solution per unit time. As a result, we have

$$\frac{\partial c_M}{\partial t} = J' + J'' \,. \tag{9.117}$$

In the case (which is of interest for practice and the forthcoming analysis), where the surfactant concentration exceeds the critical micellization concentration (CMC), the strong inequalities (9.35) are valid. According to the second inequality in Eq. (9.35), the scattering, Δn_s, of the micellar aggregation numbers with respect to their average value, n_s, is quite small. Therefore, the number of surfactant monomers absorbed by micelles in a unit volume of a micellar solution is equal to $n_s c_M$ with a high degree of accuracy. Then, because of the condition $\exp(W_c) \gg 1$ and the resultant steep slope of the potential barrier of the aggregation work (at not too large values of n_c), the inequality $\sum_{n=2}^{n_c+\Delta n_c} n c_n \ll c_1$ is fulfilled. As a result, we have (cf. Eq. (9.8)) the equation of a bimodal approximation for the total concentration of the surfactant in the solution, i.e.,

$$c_1 + n_s c_M = c \,. \tag{9.118}$$

According to Eq. (9.44) the term $n_s c_M$ is of significance in Eq. (9.118) if $\exp(W_s)$ does not exceed $n_s \Delta n_s$ too much. The stronger the inequality $\exp(W_c) \gg \exp(W_s)$, the more noticeable is the role of the term $n_s c_M$.

In the considered case of a closed micellar solution, the total concentration c has a preset value exceeding the CMC. Let us investigate the time evolution of such a solution, assuming that in the initial moment when the surfactant is added to the solvent and mixed throughout its volume, almost the whole amount of dissolved surfactant is present in the system in the form of monomers only. Hence, at the initial moment, the conditions $c_1 = c$, $c_M = 0$, and $J'' = 0$ (only the direct flux J' exists) hold. The concentration c_1 decreases with time (at a given total concentration c), while the micelle concentration c_M becomes different from zero and gradually increases. Correspondingly, the reverse flux, J'', of molecular aggregates develops, which progressively starts to compete with their direct flux, J'. At fairly long times, the reverse flux, J'', begins to fully compensate the direct flux, J'. In this case, the closed micellar solution comes to equilibrium.

With Eq. (9.118) and Eqs. (9.68) and (9.70) for the fluxes J' and J'' at the known dependence of the aggregation work W_n on n and, hence, at the known dependences of n_c, n_s, Δn_c, Δn_s, W_c, W_s, and j_c^+ on the concentration c_1, the relaxation equation (9.117) can be reduced to a nonlinear first-order differential equation with separable variables. The solution of this equation with respect to the monomer concentration $c_1(t)$ can be written in a general form in quadratures over the entire time interval. However, the dependence of W_n on n is known only in some particular cases for specific models of micelles. Therefore, it is of interest to analytically solve the problem of the relaxation of the micellar solution at the final stage of micellization near the state of the complete equilibrium of a solution as well as the problem of the determination of the time of establishment of this final stage, using only the most representative general characteristics of the aggregation work, W_n, instead of the whole dependence of W_n on n. Denoting the values characterizing the equilibrium state of the closed micellar solution by the upper tilde, we have

$$\widetilde{J}' + \widetilde{J}'' = 0 \,. \tag{9.119}$$

Substituting Eqs. (9.68) and (9.70) into Eq. (9.119), we obtain

$$\widetilde{c}_M = \pi^{1/2}\widetilde{c}_1\widetilde{\Delta n_{\rm s}}\,\exp\left(-\widetilde{W}_{\rm s}\right)\ . \tag{9.120}$$

As follows from Eq. (9.120), (9.41), and (9.45) with respect to the concentrations c_n of molecular aggregates in the precritical and supercritical regions of their sizes, the complete equilibrium between all molecular aggregates of a micellar solution is established at the final stage. According to Eqs. (9.120) and (9.45), this state is characterized by the following concentrations of molecular aggregates:

$$\widetilde{c}_n^{\,(\rm e)} = \widetilde{c}_1\exp\left(-\widetilde{W}_n\right). \tag{9.121}$$

Taking into account Eq. (9.120), Eq. (9.118) yields

$$\widetilde{c}_1 + \pi^{1/2}\widetilde{c}_1\widetilde{n}_{\rm s}\widetilde{\Delta n_{\rm s}}\exp\left(-\widetilde{W}_{\rm s}\right) = c\ . \tag{9.122}$$

At a given total concentration c and the known dependences of $\widetilde{n}_{\rm s}$, $\widetilde{\Delta n_{\rm s}}$, and $\widetilde{W}_{\rm s}$ on the monomer concentration $\widetilde{c}_1$, Eq. (9.122) gives an equation for the determination of the equilibrium concentration, $\widetilde{c}_1$. Once the equilibrium concentration $\widetilde{c}_1$ of surfactant monomers is found, the equilibrium concentration $\widetilde{c}_M$ can be determined using the relation

$$\widetilde{c}_M = \frac{(c-\widetilde{c}_1)}{\widetilde{n}_{\rm s}}\ , \tag{9.123}$$

which follows from Eq. (9.118). If the equilibrium concentration $\widetilde{c}_1$ of surfactant monomers is known from the experiment, the total concentration c and the equilibrium concentration $\widetilde{c}_M$ are determined by Eqs. (9.122) and (9.123). If the equilibrium micelle concentration $\widetilde{c}_M$ is known experimentally, the equilibrium concentration $\widetilde{c}_1$ can be calculated by solving Eq. (9.120) with respect to $\widetilde{c}_1$, and the total concentration c can be determined using Eq. (9.123). Hence, for the nonequilibrium micellar solution, two out of three characteristic concentrations, c_1, c_M, and c, are independent parameters (cf. Eq. (9.118)), while for the equilibrium solution, only one concentration will be an independent parameter (due to Eq. (9.119)). It follows from Eq. (9.19) that

$$\frac{\partial W_n}{\partial c_1} = -\frac{(n-1)}{c_1} \tag{9.124}$$

holds. Taking into account the definition $W_{\rm s} \equiv W_n|_{n=n_{\rm s}}$ of the minimum $W_{\rm s}$ of the aggregation work W_n, we have

$$\frac{\partial W_{\rm s}}{\partial c_1} = \left.\frac{\partial W_n}{\partial c_1}\right|_{n=n_{\rm s}} + \left.\frac{\partial W_n}{\partial n}\right|_{n=n_{\rm s}}\frac{\partial n_{\rm s}}{\partial c_1}\ . \tag{9.125}$$

The work W_n is minimal at $n = n_{\rm s}$. Taking into account the necessary extremum condition $\left(\partial W_n/\partial n\right)\big|_{n=n_{\rm s}} = 0$, Eqs. (9.125) and (9.124) yield

$$\frac{\partial W_{\rm s}}{\partial c_1} = -\frac{(n_{\rm s}-1)}{c_1} < 0\ . \tag{9.126}$$

Similar considerations result in

$$\frac{\partial W_{\rm c}}{\partial c_1} = -\frac{(n_{\rm c}-1)}{c_1} < 0 \,. \tag{9.127}$$

According to Eq. (9.35), the inequality $n_{\rm s} \gg 1$ is valid. In this case, the dependence of the second term on the left-hand side of Eq. (9.122) on $\widetilde{c}_1$ is very strong (cf. Eq. (9.126)). As a result, we can make the following conclusion. As the total concentration c exceeds the CMC, the monomer concentration $\widetilde{c}_1$ also begins to exceed gradually (albeit rather slowly) the CMC, but still remains near the CMC. According to Eq. (9.126), the value on the left-hand side of Eq. (9.122) monotonically increases with the concentration $\widetilde{c}_1$. This result indicates that the solution of Eq. (9.122) with respect to the concentration $\widetilde{c}_1$ at a given concentration c is unique. According to Eq. (9.126), the solution of Eq. (9.120) with respect to the concentration $\widetilde{c}_1$ at a given concentration $\widetilde{c}_M$ will also be unique.

The search of the solution of the system of equations (9.117) and (9.118), describing slow relaxation in a micellar solution after the initial addition of surfactant to the solvent and mixing throughout the entire volume, we begin with the times when the concentrations c_1 and c_M are already close to their values $\widetilde{c}_1$ and $\widetilde{c}_M$ at the equilibrium state of a solution and the reverse flux J'' almost completely compensates the direct flux J'. These times correspond to the final stage of micellization. The smallness of the deviations of the solution characteristics from their equilibrium values at the final stage allow us to linearize Eqs. (9.117) and (9.118) at this stage and hereby to significantly simplify the problem. Let us denote the deviations of the parameters from their values at the equilibrium state of a micellar solution by δ. Then, we have

$$c_1 = \widetilde{c}_1 + \delta c_1 \,, \qquad c_M = \widetilde{c}_M + \delta c_M \,. \tag{9.128}$$

Linearizing Eqs. (9.117) and (9.118) with Eqs. (9.128), and taking into account Eqs. (9.68), (9.70), and (9.119) and the constancy of the total concentration c in the closed solution, we obtain

$$\frac{\partial \delta c_M}{\partial t} = \widetilde{J}' \left[(1+\gamma+\eta)\frac{\delta c_1}{\widetilde{c}_1} - \frac{\delta c_M}{\widetilde{c}_M} \right] , \qquad (1+\lambda)\,\delta c_1 + \widetilde{n}_{\rm s}\delta c_M = 0 \,. \tag{9.129}$$

Here γ, η, and λ are the dimensionless parameters defined by

$$\gamma \equiv -\widetilde{c}_1 \left(\frac{\partial W_{\rm s}}{\partial c_1}\right)\bigg|_{c_1=\widetilde{c}_1} , \quad \eta \equiv \widetilde{c}_1 \left(\frac{\partial \ln \Delta n_{\rm s}}{\partial c_1}\right)\bigg|_{c_1=\widetilde{c}_1} , \quad \lambda \equiv \widetilde{c}_M \left(\frac{\partial n_{\rm s}}{\partial c_1}\right)\bigg|_{c_1=\widetilde{c}_1} \tag{9.130}$$

These parameters characterize the influence of the monomer concentration c_1 in the vicinity of its equilibrium value $\widetilde{c}_1$ on the values $W_{\rm s}$, $\Delta n_{\rm s}$, and $n_{\rm s}$. A similar effect of the concentration c_1 on the values j_c^+, $W_{\rm c}$, and $\Delta n_{\rm c}$ in Eqs. (9.68) and (9.70) does not appear in Eq. (9.129) because the dependences on j_c^+, $W_{\rm c}$, and $\Delta n_{\rm c}$ in Eqs. (9.68) and (9.70) are identical. Equations (9.130) and (9.126) yield

$$\gamma = \widetilde{n}_{\rm s} - 1 \,. \tag{9.131}$$

The flux $\widetilde{J}'$ in Eq. (9.129) can be written according to Eq. (9.68) as

$$\widetilde{J}' = \widetilde{c}_1 \widetilde{j}_c^+ \exp\left(-\widetilde{W}_{\rm c}\right) \Big/ \pi^{1/2} \widetilde{\Delta n_{\rm c}} \,. \tag{9.132}$$

According to Eq. (9.119), the reverse flux $\widetilde{J}''$ differs from $\widetilde{J}'$ only in sign. The solution of the system of equations (9.129) results in

$$\delta c_1 = -\widetilde{n}_s \frac{\delta c_M}{(1+\lambda)} , \qquad \delta c_M = \text{const} \cdot \exp\left(-\frac{t}{t_r}\right) , \tag{9.133}$$

where the time t_r is defined by [25]

$$\frac{1}{t_r} = \widetilde{J}' \left[\frac{\widetilde{n}_s (1+\gamma+\eta)}{\widetilde{c}_1 (1+\lambda)} + \frac{1}{\widetilde{c}_M} \right] . \tag{9.134}$$

Let us now perform an estimate of the role of the parameters η and λ in Eq. (9.134). Equations (9.130) and (9.131) result in

$$\frac{\eta}{1+\gamma} = \frac{\widetilde{c}_1}{\widetilde{n}_s} \left(\frac{\partial \ln \Delta n_s}{\partial c_1} \right)\Bigg|_{c_1=\widetilde{c}_1} . \tag{9.135}$$

The value of Δn_s varies quite slowly with the variation of c_1. According to the first inequality in Eq. (9.35), $\ln \Delta n_s$ varies with the concentration c_1 even considerably slowlier than Δn_s. Further, taking into account the inequalities (9.35), the inequality $n_s \gg 1$ is valid. Then it follows from Eq. (9.135) that the inequality $\left|\eta \big/ (1+\gamma)\right| \ll 1$ holds. According to this inequality, the parameter η in Eq. (9.134) can be ignored. Likewise, in view of the weak dependence of the average micelle aggregation number n_s on the concentration c_1, it follows from Eq. (9.130) that the inequality $|\lambda| \ll 1$ holds. It follows that the parameter λ in Eq. (9.134) can also be ignored. Omitting the parameters η and λ in Eq. (9.134), taking into account Eqs. (9.131) and (9.132), we have

$$t_r = \frac{\pi^{1/2} \widetilde{c}_M \widetilde{\Delta n_c} \exp\left(\widetilde{W}_c\right)}{\widetilde{c}_1 \widetilde{j}_c^+} \left(1 + \frac{\widetilde{n}_s^2 \widetilde{c}_M}{\widetilde{c}_1}\right)^{-1} . \tag{9.136}$$

According to Eq. (9.136), the time t_r is positive. Thus, Eqs. (9.133) describe the irreversible tendency of the closed micellar solution to equilibrium. The same expressions indicate that the time t_r, given by Eq. (9.136), is the relaxation time of a solution at the final stage of micellization. According to Eq. (9.136), the relaxation time of the micellar solution does not depend on its volume.

As is seen from Eq. (9.118), the quantity $\widetilde{n}_s \widetilde{c}_M \big/ \widetilde{c}_1$ is the ratio of the amount of substance accumulated by the micelles at the final state of solution equilibrium to that part of the substance, which remains in the form of monomers. In terms of the degree of micellization [5] α,

$$\alpha \equiv \frac{\widetilde{n}_s \widetilde{c}_M}{c} , \tag{9.137}$$

this ratio is equal to $\alpha/(1-\alpha)$. In a typical case, the critical degree of micellization (corresponding to the CMC) has a value of the order of 0.1. Thus, at $\widetilde{n}_s \gg 1$, the strong inequality

$$\frac{\widetilde{n}_s^2 \widetilde{c}_M}{\widetilde{c}_1} \gg 1 \tag{9.138}$$

holds. Since $\widetilde{n}_{\rm s} \gg 1$, this case is surely realized when $\widetilde{n}_{\rm s}\widetilde{c}_M \big/ \widetilde{c}_1 > 1$, i.e., when micelles in the final state of solution equilibrium accumulate noticeable or even the main part of the whole amount of a surfactant is contained in them. With Eq. (9.138), we obtain from Eq. (9.136) that

$$t_{\rm r} = \left(\pi^{1/2}\widetilde{\Delta n_{\rm c}}/\widetilde{n}_{\rm s}^2\widetilde{j}_c^{+}\right)\exp\left(\widetilde{W}_{\rm c}\right) \qquad \text{for} \quad \widetilde{n}_{\rm s}^2\widetilde{c}_M/\widetilde{c}_1 \gg 1\ . \tag{9.139}$$

Let us establish the relation between the time $t_{\rm r}$ and the micelle concentration in the final equilibrium state of the solution at a slow variation of the monomer concentration, when $\widetilde{n}_{\rm s}$, $\widetilde{n}_c$, $\widetilde{\Delta n_{\rm s}}$, and $\widetilde{\Delta n_{\rm c}}$ remain practically constant. We consider two micellar solutions with almost identical monomer concentrations at the final equilibrium states. Specifying the values for these solutions by the superscripts (1) and (2), we then have $\left(\widetilde{c}_1^{(1)}/\widetilde{c}_1^{(2)}\right) \approx 1$, and with Eqs. (9.126) and (9.127), we also have

$$\exp\left(\widetilde{W}_{\rm s}^{(1)}\right)\Big/\exp\left(\widetilde{W}_{\rm s}^{(2)}\right) = \left(\widetilde{c}_1^{(2)}\Big/\widetilde{c}_1^{(1)}\right)^{\widetilde{n}_{\rm s}-1}\ , \tag{9.140}$$

$$\exp\left(\widetilde{W}_{\rm c}^{(1)}\right)\Big/\exp\left(\widetilde{W}_{\rm c}^{(2)}\right) = \left(\widetilde{c}_1^{(2)}\Big/\widetilde{c}_1^{(1)}\right)^{\widetilde{n}_{\rm c}-1}\ . \tag{9.141}$$

Equations (9.120) and (9.140) yield

$$\widetilde{c}_M^{(1)}\Big/\widetilde{c}_M^{(2)} = \left(\widetilde{c}_1^{(1)}\Big/\widetilde{c}_1^{(2)}\right)^{\widetilde{n}_{\rm s}}\ . \tag{9.142}$$

Since $\widetilde{n}_{\rm s} \gg 1$, Eq. (9.142) demonstrates that, at almost identical monomer concentrations in the equilibrium solutions, the micelle concentrations can be quite different. According to Eqs. (9.141) and (9.142), we have

$$\exp\left(\widetilde{W}_{\rm c}^{(1)}\right)\Big/\exp\left(\widetilde{W}_{\rm c}^{(2)}\right) = \left(\widetilde{c}_M^{(2)}\Big/\widetilde{c}_M^{(1)}\right)^{(\widetilde{n}_{\rm c}-1)/\widetilde{n}_{\rm s}}\ . \tag{9.143}$$

Taking into account Eqs. (9.142) and (9.143) and the fact that the rate $\widetilde{j}_c^{+}$ of monomer absorption by the critical molecular aggregate is proportional to the monomer concentration in the solution, with Eq. (9.139) we have

$$t_{\rm r}^{(1)}\Big/t_{\rm r}^{(2)} = \left(\widetilde{c}_M^{(2)}\Big/\widetilde{c}_M^{(1)}\right)^{\widetilde{n}_{\rm c}/\widetilde{n}_{\rm s}} \qquad \text{for} \quad \widetilde{n}_{\rm s}^2\widetilde{c}_M^{(1)}\Big/\widetilde{c}_1^{(1)} \gg 1\ , \qquad \widetilde{n}_{\rm s}^2\widetilde{c}_M^{(2)}\Big/\widetilde{c}_1^{(2)} \gg 1. \tag{9.144}$$

According to Eq. (9.144), the relaxation time $t_{\rm r}$ of a solution to a final equilibrium state decreases with an increase in micelle concentration $\widetilde{c}_M$ inversely proportional to $\widetilde{c}_M^{\widetilde{n}_{\rm c}/\widetilde{n}_{\rm s}}$. The higher the micelle concentration at the final state of solution equilibrium, the higher the total surfactant concentration of this solution. Then we find from Eq. (9.144) that at a rather large degree of micellization at the final state of solution equilibrium, the relaxation time of a solution decreases with an increase in the total surfactant concentration of this solution. This conclusion of the theory is supported by experimental data reported in Refs. [37, 41] and by data of numerical modeling [45, 46].

Analyzing the time $t_{\rm r}$ of slow relaxation, we followed widely Ref. [25]. The concept and a first derivation of this time was introduced by Aniansson and Wall [13].

9.10 Time of Approach of the Final Micellization Stage

Let us now analyze the solution of the system of kinetic equations of aggregation in a micellar solution at the times preceding the final stage of micellization. Assuming the condition $n_s = \widetilde{n}_s$, which will be justified somewhat later, we can rewrite Eqs. (9.118) and (9.117) at a given total concentration c of the solution as

$$c_1 + \widetilde{n}_s c_M = c \ , \qquad \frac{\partial c_1}{\partial t} = -\widetilde{n}_s \left(J' + J'' \right) \ . \tag{9.145}$$

To obtain Eq. (9.129), we used the linearization of $\exp(W_s)$ with respect to the deviation δc_1. Expanding $\exp(W_s)$ in a Taylor series in powers of δc_1 and taking Eq. (9.126) into account, we see that this linearization is valid at

$$\frac{\delta c_1}{\widetilde{c}_1} < \frac{1}{\widetilde{n}_s} \ . \tag{9.146}$$

Equation (9.146) specifies the region on the c_1-axis, where the final stage of micellization occurs. Although this region is quite narrow at $\widetilde{n}_s \gg 1$, the relative variation of the exponent $\exp(W_s)$ can be rather significant as evident from Eq. (9.126).

Assuming the condition $\Delta n_s = \widetilde{\Delta n_s}$, which will be substantiated somewhat later, Equations (9.68), (9.70), and Eq. (9.119) yield

$$\begin{aligned} J' &= \widetilde{J}' \left(\frac{c_1 j_c^+ \widetilde{\Delta n_c}}{\widetilde{c}_1 \widetilde{j}_c^+ \Delta n_c} \right) \exp\left(-W_c + \widetilde{W}_c \right) \ , \\ J'' &= -\widetilde{J}' \left(\frac{c_M j_c^+ \widetilde{\Delta n_c}}{\widetilde{c}_M \widetilde{j}_c^+ \Delta n_c} \right) \exp\left(W_s - \widetilde{W}_s - W_c + \widetilde{W}_c \right) \ . \end{aligned} \tag{9.147}$$

Equations (9.147) result in

$$\frac{J''}{J'} = \left(\frac{c_M}{\widetilde{c}_M} \right) \left(\frac{\widetilde{c}_1}{c_1} \right) \exp\left(W_s - \widetilde{W}_s \right) \ . \tag{9.148}$$

At the assumed equality $n_s = \widetilde{n}_s$, Eq. (9.126) gives

$$\exp\left(W_s - \widetilde{W}_s \right) = \left(\frac{\widetilde{c}_1}{c_1} \right)^{\widetilde{n}_s - 1} \ . \tag{9.149}$$

Employing Eq. (9.149) and the evident inequality $c_M \le \widetilde{c}_M$, we obtain from Eqs. (9.148) and (9.128)

$$\frac{\left| J'' \right|}{J'} \le \exp\left[-\widetilde{n}_s \ln\left(1 + \frac{\delta c_1}{\widetilde{c}_1} \right) \right] \ . \tag{9.150}$$

According to Eq. (9.150), the inequality

$$\left| J'' \right| / J' \ll 1 \tag{9.151}$$

will be actually valid at

$$\delta c_1/\widetilde{c}_1 > 1/\widetilde{n}_\mathrm{s}. \tag{9.152}$$

Taking into account Eq. (9.152), we can transform the second equality in Eqs. (9.145) into

$$\frac{\partial c_1}{\partial t} = -\widetilde{n}_\mathrm{s} J' \qquad \text{for} \quad \frac{\delta c_1}{\widetilde{c}_1} > \frac{1}{\widetilde{n}_\mathrm{s}} \,. \tag{9.153}$$

Let us emphasize the different relative role of the reverse flux J'' compared with the direct flux J' when passing from the concentration range c_1 admitted by Eq. (9.152) to the concentration range c_1 admitted by Eq. (9.146). In the concentration range c_1 admitted by Eq. (9.152), the reverse flux J'' does not play any significant role (cf. Eq. (9.151)). However, the reverse flux J'' is already quite noticeable in the concentration range c_1 admitted by Eq. (9.146) and even determines the condition (9.146) due to the term $\exp(W_\mathrm{s})$ in Eq. (9.70).

We assume the conditions $\Delta n_\mathrm{c} = \widetilde{\Delta n_\mathrm{c}}$ and $n_\mathrm{c} = \widetilde{n}_\mathrm{c}$ which will be substantiated below. Then, from Eqs. (9.68) and (9.127), we have

$$J' = \widetilde{J}' \left(\frac{c_1 j_c^+}{\widetilde{c}_1 \widetilde{j}_c^+} \right) \exp\left(-W_\mathrm{c} + \widetilde{W}_\mathrm{c}\right) \,, \qquad \exp\left(W_\mathrm{c} - \widetilde{W}_\mathrm{c}\right) = \left(\frac{\widetilde{c}_1}{c_1} \right)^{\widetilde{n}_\mathrm{c}-1} \,. \tag{9.154}$$

The number of monomers j_c^+ absorbed by the critical molecular aggregate from a solution per unit time is proportional to the monomer concentration c_1 in the solution. Taking this fact into account, we arrive with Eq. (9.154) at

$$J' = \widetilde{J}' \left(\frac{c_1}{\widetilde{c}_1} \right)^{\widetilde{n}_\mathrm{c}+1} \,. \tag{9.155}$$

Substituting Eq. (9.155) into Eq. (9.153) yields

$$\frac{\partial c_1}{\partial t} = -\widetilde{n}_\mathrm{s} \widetilde{J}' \left(\frac{c_1}{\widetilde{c}_1} \right)^{\widetilde{n}_\mathrm{c}+1} \qquad \text{for} \quad \frac{\delta c_1}{\widetilde{n}_\mathrm{s}} > \frac{1}{\widetilde{n}_\mathrm{s}} \,. \tag{9.156}$$

In order to fit the region specified by Eq. (9.152), the monomer concentration $\left(1 + 1/\widetilde{n}_\mathrm{s}\right) \widetilde{c}_1$ corresponding, according to Eqs. (9.128) and (9.146), to the onset of the final stage of micellization, has to be lower than the monomer concentration $c_1 = c$ corresponding to the onset of the whole process of micellization. Thus, we should have

$$\left(1 + \frac{1}{\widetilde{n}_\mathrm{s}} \right) \frac{\widetilde{c}_1}{c} < 1 \,. \tag{9.157}$$

Otherwise, the condition (9.146) should be valid within the entire concentration range $c \geq c_1 \geq \widetilde{c}_1$ of the micellization process. Then, the final stage would occur from the very beginning of this process, and the relaxation time t_r at this stage would determine the total time of the establishment of the equilibrium in a micellar solution.

We assume hereafter that inequality (9.157) is fulfilled. It is possible only at $\widetilde{n}_\mathrm{s}^2 \widetilde{c}_M / \widetilde{c}_1 > 1$, as is shown by

$$\frac{\left(1 + 1/\widetilde{n}_\mathrm{s}\right) \widetilde{c}_1}{c} = \frac{\widetilde{n}_\mathrm{s} + 1}{\widetilde{n}_\mathrm{s} + \widetilde{n}_\mathrm{s}^2 \widetilde{c}_M / \widetilde{c}_1} \,, \tag{9.158}$$

resulting from Eq. (9.145). Integrating Eq. (9.156) over c_1 from the value $c_1 = \left(1 + 1/\widetilde{n}_s\right)\widetilde{c}_1$ to $c_1 = c$ and taking into account Eq. (9.132), we obtain [25]

$$t_0 = \frac{\pi^{1/2}\widetilde{\Delta n_c}\exp\left(\widetilde{W}_c\right)}{\widetilde{n}_s\widetilde{n}_c\widetilde{j}_c^{+}\left(1 + 1/\widetilde{n}_s\right)^{\widetilde{n}_c}}\left\{1 - \left[\frac{\left(1 + 1/\widetilde{n}_s\right)\widetilde{c}_1}{c}\right]^{\widetilde{n}_c}\right\} \tag{9.159}$$

for

$$\left(1 + \frac{1}{\widetilde{n}_s}\right)\frac{\widetilde{c}_1}{c} < 1\ . \tag{9.160}$$

The time t_0 is the desired time of approach of the final stage of micellization. The accumulation of surfactants in micelles occurs just during the time t_0 (accumulation at the final stage is negligible).

Let us establish the interrelation between the time t_0 and the micelle concentration $\widetilde{c}_M$ at the final state of the solution equilibrium by a small variation in the equilibrium monomer concentration at which $\widetilde{n}_s$, $\widetilde{n}_c$, $\widetilde{\Delta n_s}$, and $\widetilde{\Delta n_c}$ remain practically constant. Ignoring in Eq. (9.159) the small (at $\widetilde{n}_c \gg 1$) value $\left[\left(1 + 1/\widetilde{n}_s\right)\widetilde{c}_1/c\right]^{\widetilde{n}_c}$ (cf. Eq. (9.157)), taking into account Eqs. (9.142) and (9.143) and the fact that $\widetilde{j}_c^{+}$ is proportional to the concentration $\widetilde{c}_1$, we have

$$t_0^{(1)}\Big/t_0^{(2)} = \left(\widetilde{c}_M^{(2)}\Big/\widetilde{c}_M^{(1)}\right)^{\widetilde{n}_c/\widetilde{n}_s} \tag{9.161}$$

for

$$\left(1 + 1/\widetilde{n}_s\right)\widetilde{c}_1^{(1)}\Big/c^{(1)} < 1\ , \qquad \left(1 + 1/\widetilde{n}_s\right)\widetilde{c}_1^{(2)}\Big/c^{(2)} < 1. \tag{9.162}$$

Similar to the behavior of the time t_r, as described by Eq. (9.144), the time t_0 decreases with an increase in the micelle concentration $\widetilde{c}_M$ in inverse proportion to $\widetilde{c}_M^{\widetilde{n}_c/\widetilde{n}_s}$.

Equation (9.156) and $\widetilde{n}_c \gg 1$ lead to the conclusion that the rate of decrease in concentration c_1 with time is relatively high in the region where c_1 exceeds (at least negligibly) $\widetilde{c}_1$, i.e., in the region where $\left(c_1/\widetilde{c}_1\right)^{\widetilde{n}_c} \gg 1$. Consequently, this region does not contribute much in the integration of Eq. (9.156). All discussed above justifies the equalities $n_s = \widetilde{n}_s$, $n_c = \widetilde{n}_c$, $\Delta n_s = \widetilde{\Delta n_s}$, and $\Delta n_c = \widetilde{\Delta n_c}$ advanced above. In view of Eq. (9.154), this result also justifies the suggested practical independence of $\exp(W_c)$ on time.

9.11 The Hierarchy of Micellization Times

Let us consider the hierarchy of the characteristic times of micellization. The existence of such hierarchy proves that the quasiequilibrium concentrations of molecular aggregates in the precritical and supercritical regions of their sizes and the quasisteady concentration of molecular aggregates in the near-critical region of their sizes are actually established. The hierarchy also sets estimates of the relative values of the times of the formation and decomposition of micelles and is a clear indication of the complex multistage process of approaching the final state of equilibrium in a micellar solution.

The average time between two successive acts of emission of a surfactant monomer by a micelle is an important parameter in micellization. We denote this time by τ_1. As follows from Eqs. (9.25) and (9.50) at the condition (cf. Eq. (9.35)) of the applicability of the macroscopic description of the micellization kinetics, the approximate equality

$$j_n^- = j_s^+ \qquad \text{for} \quad n_\mathrm{s} - \Delta n_\mathrm{s} \lesssim n \lesssim n_\mathrm{s} + \Delta n_\mathrm{s} \tag{9.163}$$

is fulfilled in the micellar region with a high degree of accuracy. Thus the average time between two successive acts of emission of a surfactant monomer by the micelle containing n_s molecules is determined by the time

$$\tau_1 = 1 \big/ j_s^+ \, . \tag{9.164}$$

It is evident that, simultaneously, τ_1 is the average time of emission of any of n_s surfactant monomers, contained in a micelle, from a micelle. Because the probability of the emission of some of these monomers from a micelle is larger by n_s times than that of the isolated (labeled) surfactant monomer, the quantity $n_\mathrm{s}\tau_1$ determines the average time for an emission of the labeled surfactant monomer from a micelle, i.e., the average value of the resident time of a surfactant monomer in a micelle.

The average micelle lifetime is also an important parameter of micellization. We found in Section 9.6 the direct flux J' and the reverse flux J'' of molecular aggregates overcoming by fluctuations the potential barrier of the aggregation work. The existence of the reverse flux J'' results in the fluctuational transfer of $-J''$ molecular aggregates from the micellar to the precritical region in a unit volume of the micellar solution per unit time (the outflow of molecular aggregates from the micellar region to the region $n > n_\mathrm{s} + \Delta n_\mathrm{s}$ is not observed at the total surfactant concentrations below the second CMC due to a rather rapid increase in the aggregation work with an increase in n in this region). The fluctuational transfer of molecular aggregates from the micellar to the precritical region results in a "decay" of micelles. This decay proceeds by a multistage mechanism of exchange of surfactant monomers between the molecular aggregates and the micellar solution. During the time τ_M, determined by

$$\tau_M = c_M \big/ \left| J'' \right| \, , \tag{9.165}$$

the micellar region would be left by all micelles due to their fluctuational transfer to the precritical region. Hence, it is the time τ_M that represents the average value of the lifetime of a micelle. Using Eq. (9.70) for the flux J'', we rewrite Eq. (9.165) as

$$\tau_M = \pi \, \Delta n_\mathrm{c} \Delta n_\mathrm{s} \exp(W_\mathrm{c} - W_\mathrm{s}) \big/ j_c^+ \, . \tag{9.166}$$

According to Eq. (9.166), the time τ_M is independent of the volume of the micellar solution.

Let us collect the data on the characteristic kinetic times obtained in this and the previous sections. We are interested in the times t_s and t' required to establish the quasisteady concentrations of molecular aggregates in the micellar and precritical regions, respectively; the time t'' required to establish the quasisteady concentrations of molecular aggregates in the part of the supercritical region located to the left of the micellar region on the n-axis; the time t_c needed to establish the quasisteady concentrations of molecular aggregates in the near-critical region; the time t_1 of fast relaxation; the time t_0 of approaching the final stage of micellization

and the time t_r of relaxation of the micellar solution at the final stage of micellization; the average monomer lifetime τ_1 in a micelle and the average lifetime of a micelle τ_M. While the times t_s, t', t'', and t_c describe the evolution of the ensemble of molecular aggregates within the characteristic ranges of aggregation numbers and the times t_1, t_0 and t_r are related to the relaxation behavior of the whole micellar solution (micelles and monomers), the times τ_1 and τ_M characterize a single micelle. According to Eqs. (9.84), (9.85), and (9.95), we have

$$\frac{t'}{t_c} \approx \frac{2n_c}{\Delta n_c} , \qquad \frac{t''}{t_c} \approx \frac{2(n_s - n_c)}{\Delta n_c} . \tag{9.167}$$

Taking into account Eqs. (9.34) and employing the estimate $n_s - n_c \gtrsim n_c$ (which allows for the equality of the orders of magnitudes for $n_s - n_c$ and n_c), we obtain from Eq. (9.167) the inequalities

$$\frac{t''}{t_c} \gtrsim \frac{t'}{t_c} \gg 1 . \tag{9.168}$$

According to Eqs. (9.83) and (9.95), we have

$$\frac{t_c}{t_s} = \left(\frac{\Delta n_c}{\Delta n_s}\right)^2 \left(\frac{j_s^+}{j_c^+}\right) . \tag{9.169}$$

Analytical models for the aggregation work W_n in surfactant solutions do not result in large differences between the values of Δn_c and Δn_s. Assuming that a large difference in the values of j_c^+ and j_s^+ is also improbable, we can see from Eq. (9.169) that

$$t_c \big/ t_s \sim 1 . \tag{9.170}$$

According to Eqs. (9.83) and (9.164), we have

$$t_s \big/ \tau_1 = (\Delta n_s)^2 \Big/ 2 . \tag{9.171}$$

Substituting the first condition from Eq. (9.35) into Eq. (9.171) yields

$$t_s \big/ \tau_1 \gg 1 . \tag{9.172}$$

Comparing Eq. (9.159) for the time t_0 with Eq. (9.136) for the time t_r and taking into account Eq. (9.158), we obtain

$$\frac{t_0}{t_r} = \frac{\widetilde{n}_s}{\widetilde{n}_c \left(1 + 1/\widetilde{n}_s\right)^{\widetilde{n}_c}} \left[1 - \left(\frac{\widetilde{n}_s + 1}{\widetilde{n}_s + \widetilde{n}_s^2 \widetilde{c}_M \big/ \widetilde{c}_1}\right)^{\widetilde{n}_c}\right] \qquad \text{for} \quad \frac{\widetilde{n}_s^2 \widetilde{c}_M}{\widetilde{c}_1} \gg 1 . \tag{9.173}$$

Let us discuss the results for the realistic estimates $\widetilde{n}_s \sim 10^2$ and $\widetilde{n}_c \sim 30$. At $\widetilde{n}_s^2 \widetilde{c}_M \big/ \widetilde{c}_1 = 3$, when Eq. (9.138) is fulfilled at the breaking point, we have from Eq. (9.173) the result $t_0/t_r \simeq 1.5$. When the ratio $\widetilde{n}_s^2 \widetilde{c}_M \big/ \widetilde{c}_1$ becomes larger than 3, and correspondingly, the inequality Eq. (9.138) becomes stronger, the ratio t_0/t_r slightly increases but still remains smaller than

2.5. Hence, it is clear that the time t_r is an estimate not only of the duration of the very final stage of micellization, but also of the total time $t_0 + t_r$ of the establishment of equilibrium in a micellar solution as well [26].

Hereafter, we will use the estimates for all kinetic times as applied to the final stage of micellization (taken at values of parameters corresponding to the final equilibrium). According to Eqs. (9.139) and (9.85), we have

$$\frac{t_r}{t''} \approx \pi^{1/2} \exp\left(\widetilde{W}_c\right) \Big/ \left[\left(\widetilde{n}_s - \widetilde{n}_c\right) \widetilde{n}_s^2\right] \qquad \text{for} \quad \frac{\widetilde{n}_s^2 \widetilde{c}_M}{\widetilde{c}_1} \gg 1 \,. \tag{9.174}$$

Taking into account that the first inequality in Eq. (9.36) is extremely strong due to its exponential character, we derive from Eq. (9.174) the strong inequality

$$\frac{t_r}{t''} \gg 1 \qquad \text{for} \quad \frac{\widetilde{n}_s^2 \widetilde{c}_M}{\widetilde{c}_1} \gg 1 \,. \tag{9.175}$$

According to Eqs. (9.139) and (9.166) accounting for Eq. (9.120), we have $\tau_M / t_r = \widetilde{n}_s^2 \widetilde{c}_M / \widetilde{c}_1$ and thus

$$\tau_M / t_r \gg 1 \qquad \text{for} \quad \frac{\widetilde{n}_s^2 \widetilde{c}_M}{\widetilde{c}_1} \gg 1 \,. \tag{9.176}$$

Equations (9.83) and (9.111) then yield

$$t_1 \lesssim t_s \qquad \text{for} \quad \frac{\widetilde{n}_s^2 \widetilde{c}_M}{\widetilde{c}_1} \gg 1 \,. \tag{9.177}$$

As a whole, the set of Eqs. (9.168), (9.170), (9.172), (9.173), (9.175), (9.176), and (9.177) discloses the following hierarchy of the times of micellization kinetics [26]:

$$\tau_M \gg t_0 \sim t_r \gg t'' \gtrsim t' \gg t_c \sim t_s \gtrsim t_1 \gg \tau_1 \qquad \text{for} \qquad \frac{\widetilde{n}_s^2 \widetilde{c}_M}{\widetilde{c}_1} \gg 1 \,. \tag{9.178}$$

The last six relations in the hierarchical sequence (9.178) are not related with the limitation as expressed in Eq. (9.138).

According to Eq. (9.178), the times t_s, t', t'', t_c, and t_1 are much shorter than the time t_r. This result proves that the quasisteady concentrations of molecular aggregates in the precritical and supercritical regions and the quasisteady concentrations of molecular aggregates in the near-critical region are actually established. Being the consequence of the proportionality between the time t_r and $\exp\left(\widetilde{W}_c\right)$, the statement of the smallness of the times t_s, t', t'', t_c (compared with time t_r) is valid in the general case, i.e., it is not related to the limitation as given via Eq. (9.138). The time τ_M ranks first and the time τ_1 is the smallest among the characteristic times of the micellization kinetics in the hierarchical sequence (9.178). This result demonstrates that the micelles are stable molecular formations, which are quite capable of renewing the composition of constituting molecules.

The hierarchy of kinetic times established here has recently been confirmed by the numerical solutions of the set of kinetic equations of micellization reported by Grinin and Grebenkov [46]. Some modern results on the experimental investigation of kinetic times in micellization are available in Refs. [41–44]. Results of molecular dynamics simulations can be found in Ref. [47].

9.12 Chemical Potential of a Surfactant Monomer in a Micelle and the Aggregation Work in the Droplet Model of Spherical Micelles

Aggregates of surfactant molecules in micellar solutions, including the relatively stable micelles, are limited by the number of constituent molecules and have such a structure that they cannot be considered as small parts of a new macroscopic phase. This fact complicates the study of the thermodynamics of molecular aggregates as compared with the theory of nucleation and forces one to find a model representation of their structure and the contributions to the work of their formation or the chemical potential of the aggregates [6,7,48–50]. One of the widely recognized models of surfactant molecular aggregates is the droplet model of an aggregate with a liquid-like core formed by the hydrophobic fragments of surfactant molecules. This model was proposed by Tanford [6] and developed later in Refs. [5, 7–11, 17, 27, 28, 51–56]. For definiteness, we shall deal here with a typical case of an aqueous solution of molecules of nonionic or zwitterionic surfactants having dipole hydrophilic parts and hydrophobic fragments in the form of linear hydrocarbon radicals. Let us denote by n_C the number of carbon atoms in a hydrocarbon chain of a surfactant molecule. The end methyl group has the characteristic volume v_0, while the volume of the methylene group is v. According to the published data [6], we have $v_0 \approx 54.3\,\text{Å}^3$ and $v \approx 26.9\,\text{Å}^3$ at an absolute temperature $T = 298\,\text{K}$. Hereafter, we assume that the equality $v_0/v \simeq 2$ holds.

It is accepted in the droplet model of a spherical molecular aggregate that the total number nn_C of hydrocarbon segments of all n surfactant molecules constituting the molecular aggregate are located inside a spherical surface in a compact manner (with no voids). Then, considering volume balance, we have for the radius r of the aggregate surface

$$r = \left(\frac{3v_C}{4\pi}\right)^{1/3} n^{1/3}\,, \tag{9.179}$$

where the approximate equality

$$v_C = v_0 + v\,(n_C - 1) \approx v\,(n_C + 1) \tag{9.180}$$

is taken into account in view of $v_0/v \simeq 2$. At $n_C \gg 1$, Eq. (9.179) remains valid also in the case of a slight deviation of hydrocarbon chains from their complete insertion inside the sphere of radius r.

The inner contents of a sphere of radius r, occupied completely by the hydrocarbon groups of all surfactant molecules in a molecular aggregate, can be considered as a "hydrocarbon core." Let us emphasize that the hydrocarbon core does not include protruding hydrophilic parts of surfactant molecules. According to Eq. (9.179), as the aggregation number n increases, the radius r also increases. Since the hydrophilic parts of surfactant molecules in an aggregate are located outside the sphere of radius r and the droplet model does not suggest the existence of cavities inside the molecular aggregate, the hydrocarbon chains of surfactant molecules in the aggregate become less convolute with an increase in n. Denoting the length of the

completely unfolded hydrocarbon chain of the surfactant molecule by l_C, for which according to [6] we have $l_C = (1.5 + 1.265 n_C)$ Å, we obtain the following packing condition:

$$r \leq l_C \ . \tag{9.181}$$

Rewriting l_C as $l_C = l_1 (n_C + 1)$, where $l_1 \equiv 1.265$ Å is the average length of the hydrocarbon group, using Eq. (9.179), and taking into account the aforementioned equality $\upsilon \approx 26.9$ Å^3, we present Eq. (9.181) in the form of the constraint

$$n < 0.3 (n_C + 1)^2 \ , \tag{9.182}$$

which is imposed from above on the aggregation number n in the droplet model of surfactant spherical molecular aggregates. The stronger the inequality $n_C \gg 1$, the weaker the constraint (9.182). At a sufficiently large value of n_C, the constraint (9.182) is quite comparable with the constraint $n \gg 1$, which is required for the applicability of the asymptotic (with respect to n) thermodynamic and kinetic theories of micellization.

We denote by $\bar{\mu}_{1n}$ and $\bar{\mu}_1$ the dimensionless chemical potential of surfactant molecules in the aggregate and, correspondingly, the dimensionless chemical potential of surfactant monomers in the micellar solution. Both chemical potentials are expressed in thermal energy units $k_B T$. The following general thermodynamic relationship [57]

$$\frac{\partial W_n}{\partial n} = \bar{\mu}_{1n} - \bar{\mu}_1 \tag{9.183}$$

is valid at thermal and mechanical equilibrium between the molecular aggregate and solution. From Eqs. (9.6) and Eq. (9.183), we immediately obtain

$$W_n = \int_1^n (\bar{\mu}_{1n} - \bar{\mu}_1) \, \mathrm{d}n \ . \tag{9.184}$$

We also use the standard expression for the dimensionless chemical potential of a molecule in an arbitrary medium

$$\bar{\mu} = \bar{\mu}^0 + w + \ln\left(c_\upsilon \Lambda^3\right) \ , \tag{9.185}$$

where $\bar{\mu}^0$ is the dimensionless chemical potential of a molecule with a fixed center of mass in vacuum, w is the work of transfer of a molecule from a fixed position in vacuum to a fixed position in a medium with concentration c_υ (the number of molecules per unit volume), and Λ is the de Broglie mean wavelength of a molecule. Equation (9.185) is applicable to both $\bar{\mu}_{1n}$ and $\bar{\mu}_1$, with identical $\bar{\mu}^0$ and Λ in both expressions. The term $\upsilon_1 p$, where p is the pressure and υ_1 is the partial molar volume of a substance in a given phase, is usually separated in the expressions for the chemical potential of a substance in the condensed state. Therefore, for the chemical potential of a surfactant in a solution (let it be the β-phase) with concentration c_1, we can write

$$\bar{\mu_1} = \bar{\mu}^0 + w_1 + \frac{\upsilon_1 p^\beta}{k_B T} + \ln\left(c_1 \Lambda^3\right) \ , \tag{9.186}$$

where the work of transfer w_1 is referred to as zero-value pressure. In view of the low compressibility of condensed media, the partial molar volume of a substance can be considered as constant and coinciding with the molecular volume. The dependence of $\bar{\mu_1}$ on c_1 is given by the $\ln(c_1\Lambda^3)$ term for the dilute solution. Thus, according to Eq. (9.186), w_1 is independent of c_1.

The situation is more complicated when one is dealing with the chemical potential of a surfactant molecule in a molecular aggregate. Let us consider the inner part of a molecular aggregate, the hydrophobic core, as the α-phase. We set a dividing surface between the α- and β-phases and use the concepts of interfacial thermodynamics. In particular, if both phases are considered to be mechanically uniform up to the dividing surface, we should ascribe a certain surface tension γ to the latter. The position of a surfactant molecule in the molecular aggregate is such that the dividing surface splits it into two parts with volumes v^α and v^β,

$$v_1 = v^\alpha + v^\beta \ . \tag{9.187}$$

Moreover, these parts turned out to be at different pressures (p^α and p^β). In addition, the molecule intersects the dividing surface (producing cross section a) and appeared under the action of surface tension γ. Therefore, we arrive at the expression,

$$\bar{\mu}_{1n} = \bar{\mu}^0 + w_{1n} + \frac{\left(v^\alpha p^\alpha + v^\beta p^\beta - \gamma a\right)}{k_\mathrm{B}T} + \ln\left(c_{1n}\Lambda^3\right) \tag{9.188}$$

for the chemical potential $\bar{\mu}_{1n}$ of a surfactant molecule in an aggregate. Here c_{1n} is the concentration of surfactant monomers in the molecular aggregate, the work w_{1n} of the molecular transfer to the aggregate is referred to as zero-valued pressure, and the term $-\gamma a$ is substantiated in the thermodynamics of interfacial phenomena [57]. In view of Eq. (9.187), Eq. (9.186) can be rewritten as

$$\bar{\mu}_1 = \bar{\mu}^0 + w_1 + \frac{\left(v^\alpha p^\beta + v^\beta p^\beta\right)}{k_\mathrm{B}T} + \ln\left(c_1\Lambda^3\right) \ . \tag{9.189}$$

The pressures in the α- and β-phases are interrelated by the condition of mechanical equilibrium (Laplace's equation)

$$p^\alpha - p^\beta = \frac{2\gamma}{r'} \ , \tag{9.190}$$

where r' is the radius of the dividing surface. From Eqs. (9.188)–(9.190), we have

$$\bar{\mu}_{1n} - \bar{\mu}_1 = w_{1n} - w_1 + \frac{2\gamma v^\alpha}{r' k_\mathrm{B}T} - \frac{\gamma a}{k_\mathrm{B}T} + \ln\left(\frac{c_{1n}}{c_1}\right) \ . \tag{9.191}$$

Substitution of Eq. (9.191) into Eq. (9.184) yields

$$W_n = \int_1^n (w_{1n} - w_1)\,\mathrm{d}n + \int_1^n \frac{2\gamma v^\alpha}{r' k_\mathrm{B}T}\,\mathrm{d}n - \int_1^n \frac{\gamma a}{k_\mathrm{B}T}\,\mathrm{d}n + \int_1^n \ln\left(\frac{c_{1n}}{c_1}\right)\mathrm{d}n \ . \tag{9.192}$$

A difficulty arises in the direct calculation of the integrals in Eq. (9.192) if one takes into account the interactions of polar groups. These interactions result in the contribution W_n^{p} to the aggregation work W_n. It is more simple to calculate the contribution of the interactions separately, taking all other integrals in Eq. (9.192) as if the interaction of polar groups is nonexistent. Then, the surface tension γ, the radius of the dividing surface r', and the limiting area a can be referred to as the surface of the hydrocarbon core ($\gamma = \gamma_0$, $r' = r$, $a = (4\pi)^{1/3}(3v)^{2/3}$), and the volume v^α is identified with the volume v_C of the hydrocarbon chain entering the hydrocarbon core. Using such an approach, Eq. (9.192) can be written as

$$W_n = \int_1^n (w_{1n} - w_1)\,\mathrm{d}n + \int_1^n \frac{2\gamma_0 v_C}{r k_{\mathrm{B}} T}\,\mathrm{d}n - \int_1^n \frac{a\gamma_0}{k_{\mathrm{B}} T}\,\mathrm{d}n + \int_1^n \ln\left(\frac{c_{1n}}{c_1}\right)\mathrm{d}n + W_n^{\mathrm{p}}\,. \tag{9.193}$$

Evidently, the difference $w_{1n} - w_1$ is the work of transfer of a surfactant molecule from the solution (the β-phase) to the molecular aggregate in the absence of pressure and surface tension. Considering the hydrocarbon core as the α-phase, we express this work of transfer as $w^{\beta\alpha}$ (the order of indices indicates the direction of transfer). For the dilute solution, the work $w^{\beta\alpha}$ does not depend on the concentration of the solution. This result follows already from the aforementioned absence of the dependence of the work w_1 on c_1 for the dilute solution and also from the fact that the work w_{1n} is generally independent of c_1. If we denote the concentration of the hydrocarbon tails in the β- and α-phases by c^β and c^α, respectively, then it is evident that $c^\beta = c_1$; however, strictly speaking, $c^\alpha \neq c_{1n}$ (the concentration of hydrocarbon chains in the hydrocarbon core is not equal to that of the molecules in the aggregate). However, according to Eq. (9.179), at $n_C \gg 1$ and $n \gg 1$, the radius r is so large that it considerably exceeds the thickness of the hydrophilic layer of an aggregate and the distance from the layer to the surface of the hydrocarbon core. Denoting by R the radius of a spherical molecular aggregate, we then have $R \approx r$, and it follows from $c_{1n} = 3n/4\pi R^3$ and $c^\alpha = 3n/4\pi r^3$ that $c_{1n} \approx c^\alpha$. Since for a dilute solution $c_{1n}/c_1 \sim 10^4$–10^5 and $c^\alpha/c_1 \sim 10^4$–10^5 hold, the equality $\ln(c_{1n}/c_1) \approx \ln(c^\alpha/c_1)$ will be fulfilled with even higher accuracy. Taking into account this equality and $c^\alpha = \text{const}$, we write Eq. (9.193), after calculating the integral in the penultimate term at $n \gg 1$, as

$$W_n = \int_1^n w^{\beta\alpha}\,\mathrm{d}n + \int_1^n \frac{2\gamma_0 v_C}{r k_{\mathrm{B}} T}\,\mathrm{d}n - \int_1^n \frac{a\gamma_0}{k_{\mathrm{B}} T}\,\mathrm{d}n + n\ln\left(\frac{c^\alpha}{c_1}\right) + W_n^{\mathrm{p}}\,. \tag{9.194}$$

In addition to W_n^{p}, there are other contributions to W_n due to the work of transfer. Some of them are already known in the integral form; the others will be calculated by integrating (during the integration, it is admissible to ignore the lower limit, similarly as was done in the penultimate term in Eq. (9.194)).

Let us begin with the hydrophobic contribution W_n^{h} to the work W_n given by the first term on the right-hand side of Eq. (9.194). For the work $w^{\beta\alpha}$ of transfer of the entire hydrophobic part of a single surfactant molecule containing n_C hydrocarbon groups from the surfactant

solution to the hydrocarbon bulk phase through the flat surface, we have the empirical expression

$$w^{\beta\alpha} = -Bn_C \ , \tag{9.195}$$

which is valid at $n_C \gg 1$. Here, B is a positive dimensionless parameter of hydrophobic interaction. Equation (9.195) does not refer to the zero-valued but rather to atmospheric pressure (identical in both phases). However, this difference can be ignored due to the small compressibility of liquids. The positive value of the parameter B reflects the hydrophobicity of the hydrocarbon groups. According to the empirical data, $B \simeq 1.4$ at 20 °C. The difference between the work of transfer of one or two segments of a hydrocarbon chain nearest to the polar group and that of the end methyl group from the work $-B$ does not practically affect the applicability of Eq. (9.195) at $n_C \gg 1$. The fact that in the accepted model of molecular aggregates, the hydrocarbon core is really not the infinite bulk phase but is surrounded by the surface with radius r will be taken into account somewhat later. Equation (9.195) shows that the desired hydrophobic contribution W_n^{h} to the aggregation work W_n is given by

$$W_n^{\mathrm{h}} = -nBn_C \ . \tag{9.196}$$

A negative value of the hydrophobic contribution W_n^{h} to the work W_n facilitates the formation of molecular aggregates in a micellar solution.

The hydrophobic tail of a surfactant molecule is slightly deformed at packing into the spherical hydrocarbon core of the molecular aggregate and its conformation, on average, differs from the conformation in the infinitely large hydrocarbon phase. The difference in conformations generates a positive contribution to the work of the molecular aggregate formation. The corresponding so-called deformation contribution W_n^{d} is described in Refs. [10, 53] and, in the notation employed here, is given by

$$W_n^{\mathrm{d}} = n\frac{3\pi^2}{80}\frac{r^2}{NL^2} \ , \tag{9.197}$$

where N is the number of rigid segments in the hydrophobic part of the surfactant molecule and L is the length of the rigid segment. Evidently, the product NL is equal to the length l_C of the hydrophobic part of a surfactant molecule. According to Ref. [53], the rigid segment contains, on average, 3.6 methylene groups in the case of the hydrophobic part composed of such groups, so that $N = n_C/3.6$. With this relation and Eq. (9.181) we obtain from Eq. (9.197) the estimate

$$W_n^{\mathrm{d}} \leq 0.1nn_C \ . \tag{9.198}$$

Comparing Eqs. (9.196) and (9.198), we see that at $B \simeq 1.4$ the W_n^{d} contribution gives a small correction to the hydrophobic contribution W_n^{h}. Thus, hereafter the contribution W_n^{h} is neglected [27, 28].

As mentioned above, the hydrophobic core is actually not an infinite bulk phase with a flat interface. According to Eq. (9.190), the curvature of latter leads to the appearance of the Laplace pressure, and a contribution W_n^{L} to the work of transfer, which is represented by the

second term on the right-hand side of Eq. (9.194). Using Eqs. (9.179) and (9.180), we rewrite the integrand in the second term on the right-hand side of Eq. (9.194) as

$$\frac{2\gamma_0 \upsilon_C}{r k_B T} = \frac{8\pi\gamma_0}{3k_B T}\left[\frac{3\upsilon\,(n_C+1)}{4\pi}\right]^{2/3}\frac{1}{n^{1/3}}\,. \tag{9.199}$$

Only the dependence of γ_0 on n still remains unspecified in Eq. (9.199) so far. For simplicity, we consider the surface tension γ_0 as constant and equal to its value for the flat surface. The possible dependence of the total surface tension γ on the size of the molecular aggregate is further taken into account through the contribution of polar groups.

Integrating now Eq. (9.199) with respect to the aggregation number n and ignoring the lower limit of integration at $n \gg 1$, we obtain the Laplace contribution W_n^{L} to the aggregation work in the form

$$W_n^{\mathrm{L}} = \frac{4\pi\gamma_0}{k_B T}\left[\frac{3\upsilon\,(n_C+1)}{4\pi}\right]^{2/3} n^{2/3}\,. \tag{9.200}$$

Equations (9.200) and (9.179) indicate that this contribution is equal to the Gibbs surface energy $(4\pi\gamma_0 r^2/k_B T)$ of the hydrophobic core (in units of $k_B T$). Introducing a positive dimensionless parameter b_3 as

$$b_3 \equiv (4\pi)^{1/3}\gamma_0[3\upsilon(n_C+1)]^{2/3}/k_B T\,, \tag{9.201}$$

we may present Eq. (9.200) as

$$W_n^{\mathrm{L}} = b_3 n^{2/3}\,. \tag{9.202}$$

Equation (9.202) yields the inequality $W_n^{\mathrm{L}} > 0$. Positive values of the Laplace contribution W_n^{L} to the work W_n impede the formation of molecular aggregates in a micellar solution.

Let us now consider the contribution W_n^{p} of polar groups. The forced approach of the polar groups due to the addition of the monomers into the molecular aggregate results in an interaction, whose most typical part is the mutual electrostatic repulsion of dipoles. We denote this electrical contribution to the work W_n by W_n^{el} and consider the case when the electrostatic component characterizes rather well the total interaction of polar groups: $W_n^{\mathrm{el}} \approx W_n^{\mathrm{p}}$. Because the molecular aggregates are formed in a solution at constant temperature and external pressure, W_n^{el} is nothing else but the Gibbs electric energy of a capacitor formed by the hydrophilic parts of the surfactant molecules in the molecular aggregate. Assuming that the capacitor formed by the hydrophilic parts of the surfactant molecules in the molecular aggregate possesses spherical symmetry, we arrive in $k_B T$ units at [5, 7]

$$W_n^{\mathrm{el}} = \frac{(zen)^2\,\delta}{8\pi k_B T \varepsilon_0 \varepsilon\,(r+\Delta l)\,(r+\Delta l+\delta)}\,. \tag{9.203}$$

Here, ze is the electric charge of a single hydrophilic part of a surfactant molecule in the dipole (e is the elementary charge); δ is the length of the dipole of the hydrophilic part, i.e., the capacitor thickness; ε is the effective permittivity of a capacitor medium; ε_0 is the dielectric constant; and Δl is the bond length connecting the hydrophobic part of a surfactant molecule

with its polar hydrophilic part. We assume that the inequality $r + \Delta l \gg \delta$ holds (which, according to Eqs. (9.179) and (9.180), is valid at $n_C \gg 1$ and $n \gg 1$). Assuming further the inequalities $r \gg \delta$ and $r \gg \Delta l$ to be valid at $n_C \gg 1$ and $n \gg 1$, we can rewrite Eq. (9.203) using Eqs. (9.179) and (9.180) as

$$W_n^{\mathrm{el}} = b_1 n^{4/3} , \tag{9.204}$$

where

$$b_1 \equiv \frac{(ze)^2 \delta}{2(4\pi)^{1/3} k_{\mathrm{B}} T \varepsilon_0 \varepsilon [3\upsilon(n_C + 1)]^{2/3}} \tag{9.205}$$

is a positive dimensionless parameter.

A positive value of the electric contribution W_n^{el} to the work W_n impedes the formation of molecular aggregates in a micellar solution. It should be mentioned that we calculated the total contribution of polar interactions from both the chemical potential and surface tension. For our purposes, there is no necessity to calculate separately the contribution of mutual repulsion of polar groups to the surface tension that results, as it is known, in a decrease of the surface tension with an increase in the micelle size. In addition to electric forces, yet more powerful forces of direct repulsion of polar groups arising at their contact, are possible under very close approach of the hydrophilic parts of surfactant molecules. Such picture is typical in the case when the molecular packing in micelles is governed by the size of polar groups. However, we focus our attention to the case when hydrocarbon chains determine the packing, and polar groups participate in the micellization only via the long-range forces of electric repulsion.

The penultimate term on the right-hand side of Eq. (9.194) can be called the concentration contribution. Combining this term with other contributions that are proportional to the aggregation number n and introducing the dimensional parameter b_2,

$$b_2 \equiv Bn_C + \frac{a\gamma_0}{k_{\mathrm{B}} T} + \ln\left(\frac{c_1}{c^\alpha}\right) = Bn_C + \frac{(4\pi)^{1/3} (3\upsilon)^{2/3} \gamma_0}{k_{\mathrm{B}} T} + \ln\left(\frac{c_1}{c^\alpha}\right) , \tag{9.206}$$

we rewrite the work of aggregate formation W_n, employing Eqs. (9.194), (9.196), (9.202), and (9.204) as [27]

$$W_n = b_1 n^{4/3} - b_2 n + b_3 n^{2/3} . \tag{9.207}$$

The terms in Eq. (9.207) are arranged in decreasing powers of n. Evidently, Eq. (9.207) is valid at $n \gg 1$.

According to Eqs. (9.205), (9.206), and (9.201), the coefficients b_1, b_2, and b_3 are the dimensionless parameters independent of the aggregation number n. In addition, the coefficients b_1 and b_3 do not depend on the concentration c_1 of surfactant monomers in solution. Equation (9.207) is consistent with the expression reported in Refs. [6, 56]. However, the coefficient at n obtained in Refs. [6, 56], does not explicitely include the dependence on the monomer concentration in the solution.

9.13 Critical Micelle Concentration and Thermodynamic Characteristics of Micellization

9.13.1 Results of Analysis of the Droplet Model

With the dependence of aggregation work W_n, given explicitly by Eq. (9.207), we are able to find all thermodynamic characteristics of micellization in the droplet model of molecular aggregates. Taking into account that the coefficients b_1, b_2, and b_3 are independent of n, Eq. (9.207) yields

$$\frac{\partial W_n}{\partial n} = \frac{4}{3} b_1 n^{1/3} - b_2 + \frac{2}{3} b_3 n^{-1/3} , \qquad \frac{\partial^2 W_n}{\partial n^2} = \frac{4}{9} b_1 n^{-2/3} - \frac{2}{9} b_3 n^{-4/3} . \quad (9.208)$$

With Eq. (9.208) we can derive the roots $n = n_c$ and $n = n_s$ of the equations

$$\left(\frac{\partial W_n}{\partial n}\right)_{n=n_c} = 0 , \qquad \left(\frac{\partial W_n}{\partial n}\right)_{n=n_s} = 0 , \quad (9.209)$$

determining the aggregation numbers n_c and n_s of critical and stable molecular aggregates, respectively. The fact that the largest root n_s corresponds to the minimum and, respectively, the smallest root n_c, to the maximum of the work W_n follows from $b_1 > 0$ and an asymptotic rise of the work W_n with an increase in the aggregation number n. The root $n = n_0$ of the equation

$$\left(\frac{\partial^2 W_n}{\partial n^2}\right)_{n=n_0} = 0 \quad (9.210)$$

determines the inflection point n_0 of the work W_n,

$$n_0 = \left(b_3 / 2b_1\right)^{3/2} . \quad (9.211)$$

According to Eqs. (9.211), (9.205), and (9.201), the inflection point n_0 of the work W_n does not depend on the monomer concentrations c_1 in the surfactant solution. Equation (9.211) allows one to reveal the constraint on the value of $\left(b_3 / 2b_1\right)^{3/2}$, at which n_0 fits the region of aggregation numbers n that is realistic for spherical molecular aggregates.

The droplet model of molecular aggregates reflects the existence of the potential maximum and potential well of the work W_n at a sufficiently high monomer concentration c_1 in the surfactant solution. We denote the monomer concentration in surfactant solutions, at which the potential maximum and potential well of the work W_n appear, by c_{10}. Since at $c_1 = c_{10}$ the maximum and minimum of the work W_n merge in its inflection point n_0, Eq. (9.209) yields

$$\left(\frac{\partial W_n}{\partial n}\right)_{c_1=c_{10}, n=n_0} = 0 . \quad (9.212)$$

Note that the concentration c_{10} is lower than the CMC, at which the potential well of the work W_n begins to play a significant role in the consumption of the total amount of surfactant from micellar solution.

Let us represent Eq. (9.206) as

$$b_2 = \ln\left(\frac{c_1}{c_{10}}\right) + \widetilde{b}_2 \,, \tag{9.213}$$

where $\widetilde{b}_2$ is no longer dependent on c_1. Using Eqs. (9.212), (9.211), and (9.208), we then arrive at

$$\widetilde{b}_2 = \frac{4}{3}\,(2b_1b_3)^{1/2} \,, \tag{9.214}$$

which, together with Eq. (9.213), gives a dependence between the coefficient b_2 and the coefficients b_1 and b_3 in Eq. (9.207). Finally, substituting Eqs. (9.213) and (9.214) into Eq. (9.207), we obtain

$$W_n = b_1 n^{4/3} - \left[\ln\left(\frac{c_1}{c_{10}}\right) + \frac{4}{3}\,(2b_1b_3)^{1/2}\right] n + b_3 n^{2/3} \,. \tag{9.215}$$

Equation (9.215) contains three parameters b_1, b_3, and c_{10}, which are independent of n and c_1. The introduction of the parameter c_{10} allows us to eliminate the dependence on B and c^α in Eq. (9.215). All three parameters b_1, b_3, and c_{10} have a clear physical meaning.

According to Eqs. (9.206), (9.213), and (9.214), the parameter c_{10} is related to the parameters B and c^α by

$$\ln\left(\frac{c_{10}}{c^\alpha}\right) = -Bn_C - \frac{(4\pi)^{1/3}\,(3v)^{2/3}\,\gamma_0}{k_{\rm B}T} + \frac{4}{3}\,(2b_1b_3)^{1/2} \,. \tag{9.216}$$

Taking into account $c^\alpha = 1/v_C$ and Eq. (9.180), we rewrite Eq. (9.216) as

$$\ln\left(vc_{10}\right) = -Bn_C - \frac{(4\pi)^{1/3}\,(3v)^{2/3}\,\gamma_0}{k_{\rm B}T} - \ln\left(n_C + 1\right) + \frac{4}{3}\,(2b_1b_3)^{1/2} \,. \tag{9.217}$$

Equations (9.215) and (9.209) show that the aggregation numbers of critical and stable molecular aggregates satisfy the following relations at $c_1 > c_{10}$:

$$\begin{aligned} n_{\rm c} \;=\; & (8b_1)^{-3}\left\{2^{5/2}\,(b_1b_3)^{1/2} + 3\ln\left(\frac{c_1}{c_{10}}\right)\right. \\ & \left. -\;\sqrt{\left[2^{5/2}\,(b_1b_3)^{1/2} + 3\ln\left(\frac{c_1}{c_{10}}\right)\right]^2 - 32b_1b_3}\right\}^3 \,, \end{aligned} \tag{9.218}$$

$$\begin{aligned} n_{\rm s} \;=\; & (8b_1)^{-3}\left\{2^{5/2}\,(b_1b_3)^{1/2} + 3\ln\left(\frac{c_1}{c_{10}}\right)\right. \\ & \left. +\;\sqrt{\left[2^{5/2}\,(b_1b_3)^{1/2} + 3\ln\left(\frac{c_1}{c_{10}}\right)\right]^2 - 32b_1b_3}\right\}^3 \,. \end{aligned} \tag{9.219}$$

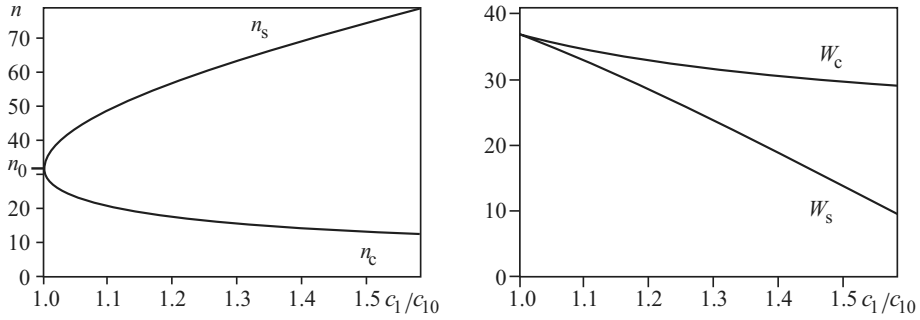

Figure 9.2: Dependences of n_c and n_s (left), and W_c and W_s (right) on the concentration ratio c_1/c_{10}

Let us calculate, now, the thermodynamic characteristics of the kinetics of micellization such as n_c, n_s, W_c, W_s, Δn_c, and Δn_s in the droplet model of a surfactant spherical molecular aggregate. We use the following values of the initial parameters of the model

$$n_C = 18\,, \qquad \gamma_0 = 30\,\frac{\text{mN}}{\text{m}}\,, \qquad \varepsilon = 30\,,$$
$$\delta = 3 \times 10^{-10}\,\text{m}\,, \qquad z = 1\,, \qquad T = 293\,\text{K}\,. \quad (9.220)$$

For the accepted value of the parameter n_C (it can be an octadecyl radical that can be completely packed into the hydrocarbon core or a fragment of a longer aliphatic hydrocarbon radical), Eq. (9.182) is reduced to $n < 108$. Results of the calculations reported below are fairly sensitive to the values of the parameters γ_0, ε, and δ. From Eqs. (9.205), (9.201), and (9.211) with the help of Eq. (9.220), we have

$$b_1 = 1.13\,, \qquad b_3 = 22.4\,, \qquad n_0 = 31.2\,. \quad (9.221)$$

Results of the calculation of the dependence of n_c and n_s on c_1/c_{10} obtained with Eqs. (9.218), (9.219), and (9.221) are shown in Fig. 9.2. At $c_1/c_{10} = 1$, the values n_c and n_s coincide and are equal to n_0. As the ratio c_1/c_{10} increases, the value n_c decreases monotonically and the value n_s increases monotonically; moreover, n_s increases faster than n_c decreases so that the curve has the form of an asymmetric loop. In this case, the constraints $n_s < 108$ and $n_c \gg 1$, which are required as the conditions of the applicability of the droplet model of molecular aggregation at $n_C = 18$, are fulfilled to increasingly lower extent. Figure 9.2 also demonstrates the dependences of W_c and W_s on the concentration ratio c_1/c_{10} obtained using Eqs. (9.215), (9.218), (9.219), and (9.221). At $c_1/c_{10} = 1$, the values W_c and W_s coincide. As the ratio c_1/c_{10} increases, the values W_c and W_s decrease monotonically; moreover, W_c decreases much slower than W_s.

Finally, the results of the calculations of the dependences of Δn_c and Δn_s on the ratio c_1/c_{10}, obtained using Eqs. (9.215), (9.218), (9.219), (9.33), and (9.221), are shown in Fig. 9.3. At $c_1/c_{10} = 1$, the values Δn_c and Δn_s tend to infinity. As the ratio c_1/c_{10} increases, the values Δn_c and Δn_s decrease monotonically; however, the inequality $\Delta n_c < \Delta n_s$ is fulfilled (the peak of the aggregation work becomes noticeably narrower than the potential well). Figures 9.2 and 9.3 agree with Fig. 9.1.

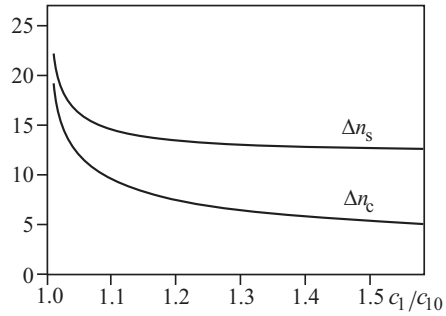

Figure 9.3: Dependences of Δn_c and Δn_s on the concentration ratio c_1/c_{10}

Let us consider further the CMC. The values at the CMC will be marked by a subscript m. Going back to the CMC in Eq. (9.120) for c_M, and using the bimodal approximation (9.118) and definition (9.137) of the degree of micellization α, we obtain [27]

$$W_{sm} = \ln\left(\pi^{1/2}\frac{1-\alpha_m}{\alpha_m} n_{sm}\Delta n_{sm}\right) . \tag{9.222}$$

As discussed earlier in Section 9.10, we take the critical degree of micellization as $\alpha_m \approx 0.1$. Possible deviations of the value α_m from 0.1 are slightly manifested in Eq. (9.222) due to weaker sensitivity of the logarithm to its argument. Substitution of Eq. (9.219) into Eq. (9.215) at $c_1 = c_{1m}$ makes it possible to express the value W_{sm} on the left-hand side of Eq. (9.222) as a known function of the ratio c_{1m}/c_{10}. Using Eqs. (9.218) and (9.215) and the second relation of Eq. (9.33) at $c_1 = c_{1m}$, we can also represent the right-hand side of Eq. (9.222) as a known function of the ratio c_{1m}/c_{10}. As a result, a transcendental equation for the determination of the ratio c_{1m}/c_{10} can be derived from Eq. (9.222) at $\alpha_m \simeq 0.1$. Solving this equation with Eq. (9.221), we have

$$c_{1m}/c_{10} = 1.58 . \tag{9.223}$$

Substituting Eqs. (9.223) and (9.221) into Eqs. (9.218) and (9.215) and into the second relation of Eq. (9.33), we find

$$n_{sm} = 79.0 , \qquad W_{sm} = 9.67 , \qquad \Delta n_{sm} = 12.6 . \tag{9.224}$$

Similarly, substituting Eqs. (9.223) and (9.221) into Eqs. (9.218) and (9.215) and into the first relation of Eq. (9.33), we obtain

$$n_{cm} = 12.3 , \qquad W_{cm} = 29.1 , \qquad \Delta n_{cm} = 4.97 . \tag{9.225}$$

As is seen from Eqs. (9.224) and (9.225), the values n_{sm} and n_{cm} for the droplet model are located at the CMC in the realistic region of aggregation numbers admitted by the constraint $n < 108$. It is also seen that the inequality $n_{sm} \gg 1$ and even the inequality $n_{cm} \gg 1$ are fulfilled, which are necessary for the applicability of the theory.

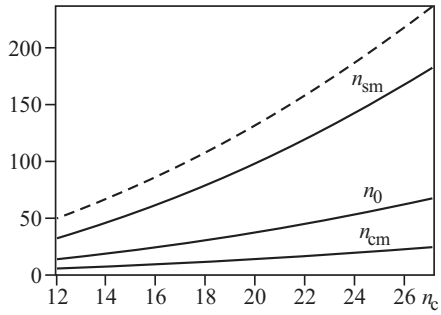

Figure 9.4: Dependences of n_{cm}, n_0, and n_{sm} on n_C. The dashed curve denotes the upper boundary of the values of the aggregation number for the spherical model of molecular aggregate corresponding to the constraint (9.182)

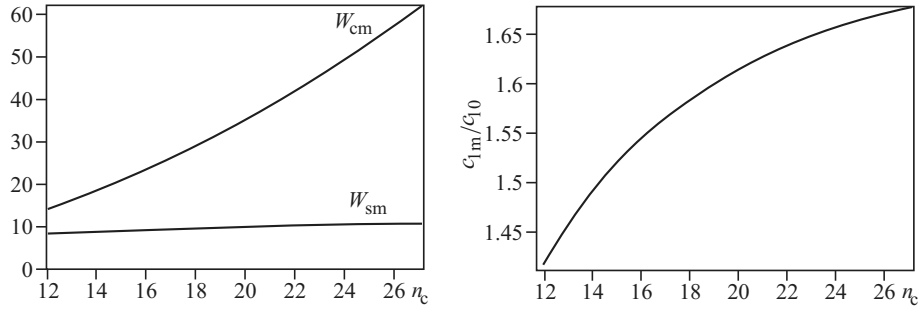

Figure 9.5: Dependences of W_{cm} and W_{sm} (left), and of the concentration ratio c_{1m}/c_{10} (right) on n_C

The dependence of the thermodynamic characteristics of micellization on the number n_C of hydrocarbon groups in the hydrophobic part of a surfactant molecule (the length of the hydrocarbon chain) is also important for any model of molecular aggregates. Figures 9.4 and 9.5 show the behavior of the values n_{cm}, n_0, and n_{sm} as well as the values W_{cm}, W_{sm}, and c_{1m}/c_{10} as functions of n_C in the range $12 \leq n_C \leq 27$. Although the number n_C in Eq. (9.220) varies in this case, the other parameters in Eq. (9.220) are assumed, for definiteness, to be constant. As is seen from Fig. 9.4, regardless of the rapid increase in the value n_{sm} with an increase in n_C, Eq. (9.182) is fulfilled at $n = n_{sm}$ rather well. This result can be explained by a quadratic increase of the right-hand side of Eq. (9.182) with an increase in n_C.

According to definitions (9.205) and (9.201), the product $b_1 b_3$ is independent of n_C. With Eqs. (9.221) and (9.217), we obtain

$$\ln(\upsilon c_{10}) = -Bn_C - \frac{(4\pi)^{1/3}(3\upsilon)^{2/3}\gamma_0}{k_B T} - \ln(n_C + 1) + 9.4\,. \tag{9.226}$$

Within the entire range $12 \leq n_C \leq 27$, the inequality $\ln(\upsilon c_{10}) < -10$ follows from Equation (9.226) and $B = 1.4$. As shown in Fig. 9.5, within the same range, the ratio c_{1m}/c_{10} is

approximately equal to 1.6. We then have $\ln(\upsilon c_{1m}) = \ln(\upsilon c_{10}) + \ln(1.6)$ with a rather high accuracy. Therefore, in addition to Eq. (9.226), the relation [27]

$$\ln(\upsilon c_{1m}) = -Bn_C - \frac{(4\pi)^{1/3}(3\upsilon)^{2/3}\gamma_0}{k_B T} - \ln(n_C + 1) + 9.9 \tag{9.227}$$

is also valid. According to Eq. (9.227), the logarithm of the concentration c_{1m}, i.e., the logarithm of the CMC, decreases with an increase in n_C almost linearly at $n_C \gg 1$. This result is confirmed by the known experimental data [6, 10, 53, 56].

9.13.2 The Quasidroplet Model

As is known from experiments [6] and the theory of the hydrophilic–hydrophobic balance [5], water molecules can partly penetrate into the depth of a micelle. In this sense, the droplet model considers the limiting version of the structure of a molecular aggregate that completely excludes water penetration into the hydrocarbon core. It is thus of interest to consider the model of a surfactant spherical molecular aggregate allowing for the maximal (in accordance with the packing rules) penetration of water molecules into the aggregate and, hence, realizing another limiting version of the structure of the hydrocarbon core. This model is called the quasidroplet model of surfactant molecular aggregates [29]. The formation of micelles from surfactant molecules begins with the appearance of molecular aggregates of two, three, or more monomers. In this case, the part of the would-be micelle is occupied by water. As new surfactant molecules are added to the aggregate, water is displaced from the space between surfactant molecules in the aggregate; however, at small aggregation numbers, water can rather deeply penetrate into the molecular aggregate.

In the quasidroplet model of molecular aggregates, shown schematically in Fig. 9.6, the hydrophobic part of each molecule constituting the aggregate is represented by two fragments. The first fragment counted from the hydrophilic part is still surrounded by water molecules. The second fragment is in the internal region of the molecular aggregate into which water molecules cannot penetrate. This region is similar to the hydrocarbon core in the droplet model of the molecular aggregate, and which explains the name "quasidroplet model." Due to mutual repulsion of the hydrophilic parts, the first fragments of monomer hydrophobic parts are located, on average, on the radii coming out from the aggregate center and are uniformly distributed over all directions in space. The angle ϕ formed by two such radii corresponding to adjacent monomers in the aggregate is determined by the aggregation number n and, at fairly large values of n, is given by the simple formula

$$\varphi = (4\pi/n)^{1/2} \qquad \text{for} \quad n \gg 1\ . \tag{9.228}$$

We bear here in mind that fairly large values are, in particular, such values of n that satisfy the inequality $\varphi/2 \ll 1$ allowing to replace the function $\sin(\varphi/2)$ by its argument. In this sense, a value $n = 10$ is no longer small.

The radius r_α of the internal (free of water molecules) region in the center of a molecular aggregate is determined by the possibility of arrangement of water molecules with the characteristic diameter d_{H_2O} between the first fragments of the hydrophobic parts of neighboring surfactant molecules in the aggregate with the characteristic cross-section diameter d. This

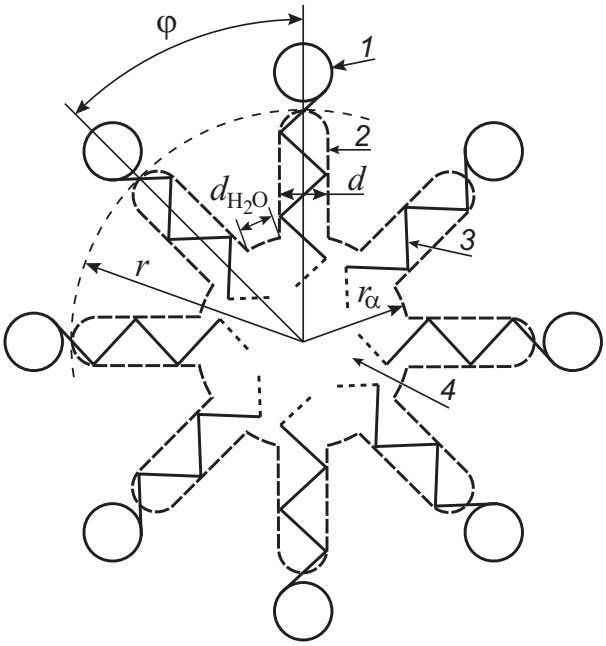

Figure 9.6: Quasidroplet model of molecular aggregates: (1) the hydrophilic part of a surfactant molecule, (2) the boundary of water penetration into the aggregate, (3) the hydrophobic part of a surfactant molecule, and (4) the hydrocarbon core of the molecular aggregate

internal region is filled with the second (in the aforementioned meaning) fragments of the hydrophobic parts of the monomers constituting the aggregate. With Eq. (9.228), we obtain

$$r_\alpha = \left(d + d_{H_2O}\right) n^{1/2} / \left(2\pi^{1/2}\right) , \tag{9.229}$$

where the approximation $\sin(\varphi/2) \approx \varphi/2$ is used. We assume here, as in the droplet model, that the second fragments of the hydrophobic parts interact with each other in such a way that they seemingly constitute the hydrocarbon phase. We will call the internal region of molecular aggregate determined as above the hydrocarbon core similar to the case of that droplet model. We use the values $d = 5.2$ Å [5] and $d_{H_2O} = 3.1$ Å for the further numerical estimates.

Let us find the number Δn_C of hydrocarbon groups in the second fragments of the hydrophobic parts of molecules, constituting the hydrocarbon core. The volume Δv_C of each fragment can be represented in the form

$$\Delta v_C = v\left(\Delta n_C + 1\right) , \tag{9.230}$$

where the fact that the terminal methyl group has a characteristic volume v_0, which is approximately twice as large as the volume v is taken into account. According to the packing rule, we have

$$\frac{4}{3}\pi r_\alpha^3 = n\Delta v_C . \tag{9.231}$$

Equations (9.230) and (9.231) with Eq. (9.229) result in

$$\Delta n_C = \left(d + d_{H_2O}\right)^3 n^{1/2} / \left(6\pi^{1/2} v\right) - 1 \, . \tag{9.232}$$

The determination of the number Δn_C from Eq. (9.232) as a continuous quantity suggests that this number is already fairly large. Let us assume that this condition is fulfilled, if

$$\Delta n_C > 4\text{–}5 \, . \tag{9.233}$$

In view of Eq. (9.232), Eq. (9.233) implies the existence of a lower bound n_1, $n > n_1$, for the aggregation numbers in the quasidroplet model. According to Eqs. (9.232) and (9.233), we obtain

$$n_1^{1/2} = (5\text{–}6)\, 6\pi^{1/2} v / \left(d + d_{H_2O}\right)^3 \, . \tag{9.234}$$

In contrast, the condition $\Delta n_C < n_C$ introduces the upper bound n_2 of aggregation numbers permissible for the applicability of the proposed model. With Eq. (9.232), the value n_2 is determined as

$$n_2^{1/2} = (n_C + 1) 6\pi^{1/2} v / \left(d + d_{H_2O}\right)^3 \, . \tag{9.235}$$

At the characteristic values of d, d_{H_2O}, and v, we have the estimate

$$6\pi^{1/2} v / \left(d + d_{H_2O}\right)^3 \approx 1/2 \, . \tag{9.236}$$

We now combine the constraints on the aggregation number in the quasidroplet model. Equations (9.234)–(9.236) allow us to conclude that the permissible values of the aggregation number n should fit the range

$$(5\text{–}6)^2 \Big/ 4 < n < (n_C + 1)^2 \Big/ 4 \, . \tag{9.237}$$

Note that the lower bound of n in Eq. (9.237) agrees with the constraint introduced in the note to Eq. (9.228).

Evidently, the first (surrounded by water molecules) fragments of the hydrophobic parts of surfactant molecules constituting the aggregate contain $n_C - \Delta n_C$ hydrocarbon groups each and have the length $(n_C - \Delta n_C)\, l_1$. Adding this length to the radius r_α, using Eqs. (9.229) and (9.232), we find the radius r of a sphere with the center in the middle of the molecular aggregate as

$$r = l_1 (n_C + 1) + \left[\left(d + d_{H_2O}\right) / \left(2\pi^{1/2}\right) - \left(d + d_{H_2O}\right)^3 l_1 / \left(6\pi^{1/2} v\right) \right] n^{1/2} \, . \tag{9.238}$$

The hydrophobic parts of surfactant molecules enter this sphere completely. According to Eq. (9.233), we have $r - r_\alpha \geq 0$. Introducing the notation

$$\alpha_{qd} = \left[\left(d + d_{H_2O}\right) / \left(2\pi^{1/2}\right) - \left(d + d_{H_2O}\right)^3 l_1 / \left(6\pi^{1/2} v\right) \right] [l_1 (n_C + 1)]^{-1} \, , \tag{9.239}$$

we rewrite Eq. (9.238) as

$$r = \ell_1 (n_C + 1) \left(1 + \alpha_{\rm qd} n^{1/2}\right) . \tag{9.240}$$

Substituting the numerical values of the parameters into Eq. (9.239), we arrive at the estimate

$$\alpha_{\rm qd} \approx -0.15/(n_C + 1) . \tag{9.241}$$

With Eq. (9.237), this estimate demonstrates that the term $\alpha_{\rm qd} n^{1/2}$ in the second round brackets on the right-hand side of Eq. (9.240) is bounded in its absolute value as

$$\left|\alpha_{\rm qd} n^{1/2}\right| \lesssim 0.08 . \tag{9.242}$$

Note that, according to Eqs. (9.238) or (9.240), the radius r decreases with an increase in the aggregation number n due to the negative value of the parameter $\alpha_{\rm qd}$. Nevertheless, the radius r is larger than the radius of the hydrocarbon core in the droplet model of surfactant molecular aggregates at each n satisfying Eq. (9.237). Equations (9.228), (9.229), and (9.240) determine the geometric parameters of the molecular aggregates in the quasidroplet model. Let us assume that the molecular aggregate is in a mechanical equilibrium at these parameters.

Taking into account the fairly small number of molecules in the molecular aggregates that are of interest to us, their geometric and thermodynamic characteristics in the quasidroplet model undergo noticeable changes on adding a new molecule to the aggregate. In particular, the hypothetical condensed phase for the substance constituting the hydrocarbon core of the molecular aggregate consists only of the second (in the meaning indicated at the beginning of this section) fragment of the hydrocarbon chains of surfactant molecules. The characteristics of such a phase changes as the length of these fragments varies with aggregation numbers.

In any phase, the molecular chemical potential is given by the standard expression (9.185). If the phase characteristics of the molecular aggregate do not change with the attachment of a surfactant monomer, then Eq. (9.189) would follow from Eq. (9.185) allowing us to determine the difference in the monomer chemical potentials in the aggregate and in the solution. We just need to take into account that, during this process, only the second fragment of the hydrophobic part of a molecule is transferred from the solution to the hydrocarbon core of the molecular aggregate.

If the surface of the hydrocarbon core is flat and the hydrophobic part of a surfactant molecule is completely transferred to the core, then the work of transfer of a single hydrophobic part from water to the bulk of the hydrocarbon phase would be equal to the value known from experiments. This value is a linear function of the number of carbon atoms constituting the hydrocarbon part with the coefficient of linear dependence B, the positive dimensionless parameter of hydrophobic interaction, determined earlier. Since in the quasidroplet model only the second fragment of the hydrophobic part of a surfactant molecule enters into the hydrocarbon core composed of Δn_C hydrocarbon groups, the relevant transfer work $w^{\beta\alpha}$ can be evidently represented as

$$w^{\beta\alpha} = -B \Delta n_C . \tag{9.243}$$

With Eq. (9.232), we can write Eq. (9.243) also in the form

$$w^{\beta\alpha} = -a_3 n^{1/2} + B , \tag{9.244}$$

where

$$a_3 \equiv B\left(d + d_{H_2O}\right)^3 / \left(6\pi^{1/2} v\right) \ . \tag{9.245}$$

The surface of a hydrocarbon core is curved and is characterized by the surface tension γ_0; therefore, the work of surfactant molecule transfer from the solution to the molecular aggregate contains a contribution w_L expressing the work required to overcome the Laplace pressure difference on this surface (the surface of polar groups will be accounted for separately). For a spherical surface (with a radius r_α) of the hydrocarbon core composed of molecular fragments with a volume Δv_C, this contribution is (instead of the third term on the right-hand side of Eq. (9.191)) given by

$$w_L = \left(\frac{2\gamma_0}{r_\alpha k_B T}\right) \Delta v_C \ . \tag{9.246}$$

Substitution of Eqs. (9.229) and (9.230) for r_α and Δv_C into Eq. (9.246) taking into account Eq. (9.232) yields

$$w_L = \left(\frac{2\gamma_0}{3k_B T}\right)\left(d + d_{H_2O}\right)^2 \ . \tag{9.247}$$

In addition, one should take into account that the surfactant molecule is not transferred as a whole into the bulk of the hydrocarbon phase but remains in a position when it intersects the aggregate dividing surface (to which the surface tension is referred) with the cross section a. Therefore, the monomer chemical potential in the aggregate also contains, as well as in the droplet model, the additional surface contribution $(-\gamma_0 a_0 / k_B T)$.

During the transfer of a surfactant molecule to the molecular aggregate, polar groups remain in the solvent medium; however, they approach each other and form the electrical double layer. The corresponding electrostatic contribution w_{el} can be estimated, as in the case of the droplet model, with the aid of the model of a spherical capacitor. We take advantage here of Eq. (9.203) for the electrostatic contribution W_n^{el}. According to Eq. (9.183), we can calculate the electrostatic contribution w_{el} by differentiating Eq. (9.203) with respect to the aggregation number n and using Eq. (9.240) for the radius r of the surface confining the hydrocarbon parts of surfactant molecules in the quasidroplet model of molecular aggregates. When writing the result and utilizing the inequalities $r \gg \delta$ and $r \gg \Delta l$ at $n_C \gg 1$ and $n \gg 1$, we ignore the second-order terms due to the small (because of the constraint (9.242)) value of $\alpha_{qd} n^{1/2}$. With Eq. (9.240), we find

$$w_{el} = 2a_1 n\left[1 - \frac{5}{2}\alpha_{qd} n^{1/2}\right] \ , \tag{9.248}$$

where

$$a_1 \equiv \frac{(ez)^2 \delta}{8\pi\varepsilon_0 \varepsilon [l_1 (n_C + 1)]^2 k_B T} \ . \tag{9.249}$$

According to above given derivation, the contribution w_{el} takes into account the change in the characteristics of the molecular aggregate (more specific, its radius r) on the attachment of

new molecules to the aggregate. Let us now take into account the contributions $w^{\beta\alpha}$ and w_{L}, as well as the concentration contribution $w_{\mathrm{conc}} = \ln(c_{1n}/c_1)$ given by the last term on the right-hand side of Eq. (9.191).

We will specify the chemical potentials of a surfactant monomer in an aggregate and the relevant contributions caused by the change in the characteristics of molecular aggregates with an accent. It follows from the above considerations that

$$w'_{\mathrm{el}} = w_{\mathrm{el}} \ . \tag{9.250}$$

As is seen from Eq. (9.232), when the next molecule is attached, the number Δn_C of hydrocarbon groups (entering into the aggregate core) of the hydrophobic part of each molecule constituting the aggregate increases. According to Eq. (9.230), the volume Δv_C (the volume of the fragments of the hydrophobic parts of surfactant molecules forming the hydrocarbon core) also increases. The increase in the number Δn_C gives rise to the energy gain from the transfer of the corresponding fragment of the hydrophobic part of surfactant molecules to the hydrocarbon core of the aggregate. Extending Eq. (9.243), we can write

$$w'^{\beta\alpha} = -B\left(\Delta n_C + n\frac{\partial \Delta n_C}{\partial n}\right) \ . \tag{9.251}$$

The factor n in front of the derivative with respect to n suggests that all n molecules in the molecular aggregate participate in the formation of the chemical potential in this aggregate. From Eq. (9.251) with Eqs. (9.232) and (9.245), we obtain

$$w'^{\beta\alpha} = -\frac{3}{2}a_3 n^{1/2} + B \ . \tag{9.252}$$

According to Eq. (9.195), the contribution $w^{\beta\alpha}$ in the droplet model is independent of the aggregation number of the molecular aggregate; however, the similar contribution $w'^{\beta\alpha}$ in the quasidroplet model increases in its absolute value with n according to Eq. (9.252). In this case, it can be shown that the contribution (9.252) is smaller in its absolute value as compared to the similar contribution for the droplet model in the lower part of the range of permissible values of aggregation numbers determined by Eqs. (9.237); in contrast, it is larger in the upper part.

During the attachment of a new molecule to the aggregate, an increase in the volume Δv_C of all second fragments of the hydrophobic parts of molecules constituting the hydrocarbon core of the aggregate tends to increase the work required for overcoming the Laplace pressure difference on the surface of the hydrocarbon core. We determine the contribution w'_{L}, which takes into account this effect, by

$$w'_{\mathrm{L}} = \frac{2\gamma_0}{r_\alpha k_{\mathrm{B}} T}\left(\Delta v_C + n\frac{\partial \Delta v_C}{\partial n}\right) \tag{9.253}$$

generalizing Eq. (9.246). Hence, combining Eqs. (9.229), (9.230), and (9.232), we arrive at

$$w'_{\mathrm{L}} = \frac{\gamma_0}{k_{\mathrm{B}} T}\left(d + d_{\mathrm{H_2O}}\right)^2 \ . \tag{9.254}$$

Equation (9.254) shows that the contribution w'_{L} is independent of the aggregation number. This circumstance distinguishes the quasidroplet model from the droplet model where a similar contribution is inversely proportional to the cubic root of n.

The molecular concentration c^{α} in the contribution w_{conc} is estimated in the case of the quasidroplet model as the concentration of the second fragments of the hydrophobic parts of surfactant molecules constituting the hydrocarbon core of the molecular aggregate. According to Eqs. (9.230) and (9.232), at the suggested dense core packing, the concentration c^{α} is then estimated by the relation

$$c^{\alpha} = [v_1 (\Delta n_C + 1)]^{-1} = \frac{6\pi^{1/2}}{n^{1/2}(d + d_{\mathrm{H_2O}})^3} \, . \tag{9.255}$$

The dependence of the concentration c^{α} on the aggregation number n (which was absent in the droplet model) requires the refinement of the contribution w_{conc}. Performing this refinement, using Eq. (9.255), and acting by analogy with Eqs. (9.251) and (9.253), we obtain

$$w'_{\mathrm{conc}} = \ln\left(\frac{c^{\alpha}}{c_1}\right) + n\frac{\partial \ln\left(c^{\alpha}/c_1\right)}{\partial n} = \ln\left[\frac{6\pi^{1/2}}{c_1 n^{1/2}(d + d_{\mathrm{H_2O}})^3}\right] - \frac{1}{2} \, . \tag{9.256}$$

For dilute solutions, the ratio c^{α}/c_1 is fairly large ($\sim 10^5$). Although Eq. (9.255) for c^{α} is a rough estimate, these values lead to practically exact expressions for $\ln(c^{\alpha}/c_1)$, which have been actually used in Eq. (9.256). Similar to Eq. (9.191), we can represent the desired chemical potential $\bar{\mu}'_{1n}$ of surfactant molecules in the molecular aggregate in the quasidroplet model as

$$\bar{\mu}'_{1n} = \bar{\mu}_1 - w'^{\beta\alpha} + w'_{\mathrm{L}} - \frac{\gamma_0 a}{k_{\mathrm{B}}T} + w'_{\mathrm{el}} + w'_{\mathrm{conc}} \, . \tag{9.257}$$

Substituting Eq. (9.257) into Eq. (9.184) and taking into account Eqs. (9.248), (9.250), (9.252), (9.254), and (9.256), we can write the expression for the aggregation work W_n in the case of the quasidroplet model at $n \gg 1$ as [29]

$$\begin{aligned} W_n \;=\; & -a_3 n^{3/2} + a_1 n^2\left(1 - 2\alpha_{\mathrm{qd}} n^{1/2}\right) - \frac{1}{2} n \, \ln n \\ & + \left\{B + \left(\frac{\gamma_0}{k_{\mathrm{B}}T}\right)\left[\left(d + d_{\mathrm{H_2O}}\right)^2 - a\right] - \ln\left[\frac{c_1\left(d + d_{\mathrm{H_2O}}\right)^3}{6\pi^{1/2}}\right]\right\} n \, . \end{aligned} \tag{9.258}$$

According to Eq. (9.258), there is a point $n = n_0$ of inflection of the work W_n in the case of the quasidroplet model. This point is independent of the concentration of the solution and satisfies Eq. (9.210) with substitution of Eq. (9.258). There is also a monomer concentration c_{10} that satisfies Eq. (9.212) with substitution of Eq. (9.258). The work W_n rises monotonically with n at $c_1 < c_{10}$. This result leads to the absence of relatively stable aggregates in the solutions at such surfactant concentrations. At $c_1 > c_{10}$, the work W_n is characterized by a local maximum at n_{c} and a local minimum at n_{s} corresponding to micelles. As c_1 increases, the points n_{c} and n_{s} move correspondingly to the left and right from the inflection point n_0. Thus, the qualitative behavior of the aggregation work W_n in the case of the quasidroplet model is similar to that in the droplet model.

Let us consider an approximation for the work W_n allowing for an analytical study. For such purposes, we omit in Eq. (9.258), according to Eq. (9.242), the terms proportional to the parameter α_{qd} and set $\ln n = \ln n_0$ (assuming that the relative deviations of n from n_0 are not

so large in the near-critical and micellar regions of aggregation numbers). Then we can rewrite Eq. (9.258) as

$$W_n = -a_3 n^{3/2} + a_1 n^2 + \left(\frac{9{a_3}^2}{32 a_1} - \ln \frac{c_1}{c_{10}} \right) n \ , \tag{9.259}$$

where Eqs. (9.258), (9.210), and (9.212) yield

$$n_0 = (3a_3/8a_1)^2 \ , \tag{9.260}$$

$$\begin{aligned} \ln \frac{c_{10} \left(d + d_{H_2O} \right)^3}{6\pi^{1/2}} &= -\frac{9}{32} \frac{{a_3}^2}{a_1} + B \\ &\quad + \frac{\gamma_0 \left[\left(d + d_{H_2O} \right)^2 - a \right]}{k_B T} - \ln \frac{3a_3}{8a_1} \ . \end{aligned} \tag{9.261}$$

Note in conclusion that the significant formal difference in the dependence of the work W_n on the aggregation number n according to Eq. (9.259) for the quasidroplet model and according to Eq. (9.215) for the droplet model is in fact that the work W_n is represented in Eq. (9.215) as the expansion in powers of the cubic root of n, whereas in Eq. (9.259) the expansion is performed in powers of the quadratic root of n. Latter result can be considered as a reflection of an almost two-dimensional structure of the surfactant molecular aggregate in the quasidroplet model with a structure similar to the rolled surfactant monolayer. A comparison of the predictions of both models in application to experimental data should demonstrate which of these models and in which cases more fully accounts for the properties of real micellar solutions.

9.13.3 Comparison of Droplet and Quasidroplet Models

We have seen in the preceding sections that both the droplet and the quasidroplet models of molecular aggregates result in different (albeit qualitatively similar) dependences of the aggregation work on the aggregation number and the concentration of surfactant monomers. At the same time, simplified assumptions concerning both the structure of the molecular aggregates and the way how the basic interactions of the surfactant molecules constitute the aggregate are taken into account introduce some uncertainty into the quantitative data obtained by using these models. It seems natural to interpret this uncertainty as the result of the insufficiently correct determination of the initial parameters of the models of the aggregates. The predictive power of the models can be increased by introducing representative experimental characteristics of micellization, provided that formulas linking the initial parameters of the models with the observable values are understood as rigorous relations.

By now, relatively reliable experimental data on the position of the potential well of the work of surfactant molecular aggregate formation on the aggregation number axis (on the mean micelle size, n_s), as well as on the half-width of this well (the average statistical scattering of micelle sizes, Δn_s), are available in literature for various micellar solutions. These data can be refined in the course of further experimental study of the equilibrium distribution with respect to the micelle aggregation numbers. Note that the value Δn_s can experimentally be found by measuring the time t_1 of fast relaxation of the micellar solution.

According to their physical meaning, the initial parameters of the droplet and quasidroplet models of molecular aggregates (represented by the coefficients in Eqs. (9.215) and (9.259)) cannot be determined directly from experiment or by molecular simulations. At the high sensitivity of the thermodynamic characteristics of micellization to these parameters, it is more convenient to initially take into account in the theory the position and half-width of the potential well of the aggregation work. As a result, this procedure allows us to relate the theory to experiment, moreover, in application to specific micellar solutions. Therefore the main aim of this section is to demonstrate how, knowing the experimental position and half-width of the potential well of the aggregation work, one can find all other thermodynamic characteristics of micellization, in particular, those referring to molecular aggregates in the premicellar (pre-critical and near-critical) regions of their sizes and those which are not easily accessible in experiment. We will follow here the approach proposed in Ref. [22]. An alternative approach based on deriving and solving the differential equations for the initial parameters of the model aggregation work was considered in Ref. [58].

It follows from Figs. 9.2 and 9.3 that the values n_s and Δn_s undergo in the droplet model only relatively small changes with concentration c_1, beginning with the CMC where the surfactant starts to be accumulated in micelles and ending with the concentrations at which almost the whole surfactant is accumulated in micelles. As we will see below, the same is true in the quasidroplet model. Along with that, taking into account Eq. (9.126) and $n_s \gg 1$, the function $\exp(-W_s)$ rapidly increases as c_1 increases from c_{1m} at the CMC. This property makes the concentrations $c_n^{(e)}$ in Eq. (9.45) sensitive to the values n_s and Δn_s, thereby decreasing the error of experimental determination of these values via Eq. (9.45). The total concentration c_M of micelles in the micellar region is determined at solution equilibrium by Eq. (9.120). Dropping the sign $\sim$ and neglecting the weak dependence of the half-width Δn_s on c_1, we get from Eqs. (9.120) and (9.126) the useful relation $\partial \ln c_M \big/ \partial c_1 = n_s \big/ c_1$, which makes it possible to determine experimentally the value n_s, provided that the dependence of c_M on c_1 is known.

Equation (9.222) relates the value W_{sm} of the aggregation work at CMC, i.e. at $c_1 = c_{1m}$, with the value n_{sm} of the aggregation number, the value Δn_{sm} of the average statistical scattering of micelle sizes, and the value α_m of the degree of micellization at $c_1 = c_{1m}$. The critical degree of micellization α_m is estimated as $\alpha_m \approx 0.1$. Then, according to Eq. (9.137), we have $n_{sm} c_{Mm}/c_{1m} \approx 1/9$ so that the relative amount of substance in the micelles at the CMC is still small, although it is already noticeable. In order to increase the ratio $n_s c_M/c_1$ approximately tenfold and, hence, for the relative amount of surfactant in micelles to exceed unity, we need to increase the concentration c_1 from c_{1m} by the value Δc_1, small compared to c_{1m}. Equations (9.120) and (9.126) result in $\Delta c_1 \big/ c_{1m} \approx \ln(10) \big/ (n_{sm} - 1)$. Note that, as we will see below, the value Δc_1 also turns out to be small as compared to the increase of $c_{1m} - c_{10}$ at the concentration c_1 required to achieve the CMC after the appearance of the potential barrier and the potential well of the work W_n. This result supports the correctness of the approximate value $\alpha_m \approx 0.1$ of the critical degree of micellization accepted and the corresponding approximate value of the CMC. Possible small deviations of the value α_m from $\alpha_m \approx 0.1$ can be only slightly manifested in Eq. (9.222) due to the low sensitivity of the logarithm in Eq. (9.222) to its argument at $n_{sm} \Delta n_{sm} \gg 1$.

Let us now analyze other thermodynamic characteristics of micellization at the CMC that may depend on the choice of the specific model of the molecular aggregates. We start with

the droplet model. The second relations in Eqs. (9.209) and (9.33) at $c_1 = c_{1m}$, $n_s = n_{sm}$, $\Delta n_s = \Delta n_{sm}$, Eqs. (9.222), (9.215) and the definition $W_{sm} \equiv W_n|_{c_1=c_{1m},n=n_{sm}}$ give three transcendental equations that allow us to analytically express three parameters b_1, b_3, and $\ln\left(c_{1m}/c_{10}\right)$ via n_{sm}, Δn_{sm}, and α_m. Solving these equations, we obtain

$$b_1 = \frac{9n_{sm}^{2/3}}{(\Delta n_{sm})^2}(1+\epsilon)\ , \qquad b_3 = \frac{9n_{sm}^{4/3}}{(\Delta n_{sm})^2}(1+2\epsilon)\ , \tag{9.262}$$

$$\ln\left(\frac{c_{1m}}{c_{10}}\right) = \frac{1.1 n_{sm}}{(\Delta n_{sm})^2}(1-1.3\epsilon)\ , \tag{9.263}$$

where the quantity ϵ depends on n_{sm}, Δn_{sm}, and α_m and is determined by

$$\epsilon = \frac{1}{3}\left(\frac{\Delta n_{sm}}{n_{sm}}\right)^2 \ln\left(\pi^{1/2}\frac{1-\alpha_m}{\alpha_m} n_{sm}\Delta n_{sm}\right)\ . \tag{9.264}$$

At $\alpha_m \approx 0.1$ and typical (by the order of magnitude) estimates $n_{sm} \sim 10^2$ and $\Delta n_{sm} \sim 10$, we get from Eq. (9.264) the result $\epsilon \sim 0.03$ so that the value of ϵ can be considered as small in comparison to 1. Therefore, we keep only the principal (linear with respect to ϵ) correction, ignoring quadratic and higher order corrections with respect to ϵ. We emphasize that the existence of a fairly small parameter $\left(\Delta n_{sm}/n_{sm}\right)^2$ is responsible for the strong inequality $\epsilon \ll 1$. Note that Eqs. (9.262) are not restricted in their validity by the constraint $\epsilon \ll 1$.

Employing Eqs. (9.215) and (9.262)–(9.263), we find the analytical dependence of the values n_{cm}, Δn_{cm}, and W_{cm} on n_{sm}, Δn_{sm}, and α_m. Taking into account only the first equations in Eqs. (9.209) and (9.33) at $c_1 = c_{1m}$, $n_c = n_{cm}$, $\Delta n_c = \Delta n_{cm}$, as well as the definition $W_{cm} \equiv W_n|_{c_1=c_{1m},n=n_{cm}}$, we arrive at

$$\begin{aligned} n_{cm} &= \frac{n_{sm}}{8}(1+3\epsilon)\ , \qquad \Delta n_{cm} = \frac{\Delta n_{sm}}{2^{3/2}}\left(1+\frac{3}{2}\epsilon\right)\ , \\ W_{cm} &= \frac{9}{16}\left(\frac{n_{sm}}{\Delta n_{sm}}\right)^2\left(1+\frac{11}{3}\epsilon\right)\ . \end{aligned} \tag{9.265}$$

Equations (9.222) and (9.263)–(9.265) express thermodynamic characteristics of micellization at the CMC via n_{sm}, Δn_{sm}, and α_m in the droplet model of molecular aggregates. Equation (9.263), together with Eq. (9.217) for the concentration c_{10}, allows us to find the experimentally measurable CMC. According to Eqs. (9.265), the inequalities $\Delta n_{cm} < \Delta n_{sm}$ and $\Delta n_{cm}/n_{cm} > \Delta n_{sm}/n_{sm}$ are valid. Hence, the scattering of aggregation numbers in the region of the potential barrier of work W_n is smaller than that of the aggregation numbers in the region of the potential well of the work W_n. However, the relative scattering of the aggregation numbers in the region of the potential barrier is larger than that of the aggregation numbers in the region of the potential well.

Let us illustrate the preceding statements by simple numerical calculations. For comparison, we consider two typical cases with $n_{sm} = 100$, $\Delta n_{sm} = 15$, and $\Delta n_{sm} = 20$ (for simplicity, we vary only Δn_{sm} out of two parameters, n_{sm} and Δn_{sm}). From Eqs. (9.222) and (9.262)–(9.264), at $\alpha_m \approx 0.1$, $n_{sm} = 100$, and $\Delta n_{sm} = 15$ we can easily find

$$W_{sm} = 10.1\ , \qquad b_1 = 0.926\ , \qquad b_3 = 21.4\ , \qquad \frac{c_{1m}}{c_{10}} = 1.61\ , \tag{9.266}$$

and for $n_{sm} = 100$ and $\Delta n_{sm} = 20$,

$$W_{sm} = 10.4\,, \qquad b_1 = 0.552\,, \qquad b_3 = 13.3\,, \qquad \frac{c_{1m}}{c_{10}} = 1.30\,. \tag{9.267}$$

Furthermore, from Eqs. (9.264)–(9.265) at $\alpha_{\rm m} \approx 0.1$, $n_{sm} = 100$, and $\Delta n_{sm} = 15$, we can easily obtain

$$n_{cm} = 15.3\,, \qquad \Delta n_{cm} = 5.90\,, \qquad W_{cm} = 31.9\,, \tag{9.268}$$

and for $n_{sm} = 100$ and $\Delta n_{sm} = 20$,

$$n_{cm} = 17.7\,, \qquad \Delta n_{cm} = 8.54\,, \qquad W_{cm} = 21.2\,. \tag{9.269}$$

Let us now recover the dependence (at the CMC) of the thermodynamic characteristics of micellization on the initial parameters b_1 and b_3 of the droplet model of molecular aggregates. It can be easily done by expressing in Eqs. (9.262) and (9.264) the parameters n_{sm} and Δn_{sm} by the pertubation theory at $\epsilon \ll 1$ via the initial parameters b_1 and b_3. As a result we obtain

$$n_{sm} = \left(\frac{b_3}{b_1}\right)^{3/2} \left(1 - \frac{3}{2}\epsilon\right)\,, \qquad \Delta n_{sm} = \frac{3{b_3}^{1/2}}{b_1}\,, \tag{9.270}$$

$$\epsilon = \frac{3b_1}{b_3^2} \ln\left(3\pi^{1/2} \frac{1-\alpha_{\rm m}}{\alpha_{\rm m}} \frac{b_3^2}{b_1^{5/2}}\right)\,. \tag{9.271}$$

The high sensitivity of the parameter n_{sm} and a lower sensitivity of the parameter Δn_{sm} to the values of the parameters b_1 and b_3 are evident. In order for Eqs. (9.270) to secure realistic estimates of $n_{sm} \sim 10^2$ and $\Delta n_{sm} \sim 10$, and correspondingly, in order for Eq. (9.271) to secure the inequality $\epsilon \ll 1$, the values of the initial parameters b_1 and b_3 of the droplet model should satisfy rather severe constraints. Equations (9.270)–(9.271), with Eqs. (9.222), (9.263), and (9.265), determine in an analytical form the desired dependence (at the CMC) of all thermodynamic characteristics of micellization on the parameters b_1 and b_3 of the droplet model of molecular aggregates. In particular, the approximations for the values n_{sm} and n_{cm},

$$n_{sm} \approx \left(\frac{b_3}{b_1}\right)^{3/2}\,, \qquad n_{cm} \approx \frac{1}{8}\left(\frac{b_3}{b_1}\right)^{3/2} \tag{9.272}$$

follow from Eqs. (9.270) and (9.265) when correction terms containing the small parameter ϵ are ignored. From Eqs. (9.211) and (9.272), we have $n_{cm}/n_0 \approx 1/2^{3/2}$ and $n_{sm}/n_0 \approx 2^{3/2}$. These relations indicate that the relative positions of maximum, inflection point, and minimum of work W_n on the aggregation number axis are independent of the parameters b_1 and b_3 in the droplet model of molecular aggregates.

Let us now turn to the quasidroplet model of molecular aggregates. The second equations in Eqs. (9.209) and (9.33) at $c_1 = c_{1m}$, $n_{\rm s} = n_{sm}$, $\Delta n_{\rm s} = \Delta n_{sm}$, Eqs. (9.222) and (9.259), and the definition $W_{sm} \equiv W_n|_{c_1 = c_{1m}, n = n_{sm}}$ give again three transcendental equations that allow us to analytically express the three parameters a_1, a_3, and $\ln(c_{1m}/c_{10})$ via n_{sm}, Δn_{sm}, and $\alpha_{\rm m}$. Solving these equations, we obtain

$$a_1 = \frac{4}{(\Delta n_{sm})^2}\,(1+\epsilon)\,, \qquad a_3 = \frac{8 n_{sm}^{1/2}}{(\Delta n_{sm})^2}\left(1 + \frac{4}{3}\epsilon\right)\,, \tag{9.273}$$

$$\ln \frac{c_{1m}}{c_{10}} = \frac{1}{2} \frac{n_{sm}}{(\Delta n_{sm})^2} (1 - \epsilon) \ , \tag{9.274}$$

where the quantity ϵ depends on n_{sm}, Δn_{sm}, and $\alpha_{\rm m}$ and is given by

$$\epsilon = \frac{3}{4} \left(\frac{\Delta n_{sm}}{n_{sm}} \right)^2 \ln \left(\pi^{1/2} \frac{1 - \alpha_{\rm m}}{\alpha_{\rm m}} n_{sm} \Delta n_{sm} \right) \ . \tag{9.275}$$

At $\alpha_{\rm m} \approx 0.1$ and typical (by the order of magnitude) estimates $n_{sm} \sim 10^2$ and $\Delta n_{sm} \sim 10$, we have from Eq. (9.275) the result $\epsilon \sim 0.07$. Thus the value of ϵ can be considered as small as possible compared to 1 in the quasidroplet model. This result allows us to keep only the principal (linear with respect to ϵ) correction, ignoring quadratic and higher order corrections with respect to ϵ. Similar to the droplet model, the existence of a fairly small parameter $\left(\Delta n_{sm} \big/ n_{sm}\right)^2$ is responsible for the strong inequality $\epsilon \ll 1$. Note that Eqs. (9.273) are not restricted in its validity to the constraint $\epsilon \ll 1$.

Using Eqs. (9.259) and (9.273)–(9.274), we find the analytical dependence of the values n_{cm}, Δn_{cm}, and W_{cm} on n_{sm}, Δn_{sm}, and $\alpha_{\rm m}$. Taking into account only the first equations in Eqs. (9.209) and (9.33) at $c_1 = c_{1m}$, $n_{\rm c} = n_{cm}$, $\Delta n_{\rm c} = \Delta n_{cm}$, as well as the definition $W_{cm} \equiv W_n|_{c_1 = c_{1m}, n = n_{cm}}$, we arrive at

$$n_{cm} = \frac{n_{sm}}{4} (1 + 2\epsilon) \ , \qquad \Delta n_{cm} = \frac{\Delta n_{sm}}{2^{1/2}} \left(1 + \frac{1}{2} \epsilon \right) \ , \tag{9.276}$$

$$W_{cm} = \frac{1}{4} \left(\frac{n_{sm}}{\Delta n_{sm}} \right)^2 \left(1 + \frac{11}{3} \epsilon \right) \ . \tag{9.277}$$

Equations (9.222), (9.274)–(9.277) express the thermodynamic characteristics of micellization at the CMC via n_{sm}, Δn_{sm}, and $\alpha_{\rm m}$ in the quasidroplet model of molecular aggregates. Equation (9.274), together with Eq. (9.261) for the concentration c_{10}, allows us to find the experimentally measurable CMC.

Let us perform a comparison of the droplet and quasidroplet models. According to Equations (9.276), the inequalities $\Delta n_{cm} < \Delta n_{sm}$ and $\Delta n_{cm}/n_{cm} > \Delta n_{sm}/n_{sm}$ are still valid in the quasidroplet model. According to Eq. (9.277), a fairly strong dependence of the value W_{cm} on the large parameter $(n_{sm}/\Delta n_{sm})^2$ still exists. However, as is now seen from a comparison of Eqs. (9.277) and (9.265), this dependence is approximately $9/4$ times weaker than in the droplet model of molecular aggregates. Correspondingly, the extremely strong dependence of $\exp(W_{cm})$ on the large parameter $(n_{sm}/\Delta n_{sm})^2$ becomes now weaker approximately by $\exp\left[(5/16)(n_{sm}/\Delta n_{sm})^2\right]$ times. Because $\exp(W_{cm})$ determines the time of slow relaxation of the micellar solution, it can be expected that, for micellar solutions where this time is not so long and, hence, $\exp(W_{cm})$ is not very large, the quasidroplet model of molecular aggregates provides the estimate $\exp(W_{cm}) \sim \exp\left[(1/4)(n_{sm}/\Delta n_{sm})^2\right]$, which seems to be preferable. On the contrary, for micellar solutions where this time is very long and, hence, $\exp(W_{cm})$ is also very large, the droplet model of molecular aggregates provides the estimate $\exp(W_{cm}) \sim \exp\left[(9/16)(n_{sm}/\Delta n_{sm})^2\right]$, which seems to be preferable in this alternative case. Note also that, in the quasidroplet model at the same values n_{sm} and Δn_{sm}, the values n_{cm} and Δn_{cm} will be approximately twice as large as in the droplet model (as is seen from

a comparison of Eqs. (9.276) and Eqs. (9.265)) and, on the contrary, the value $\ln(c_{1m}/c_{10})$ will be approximately twice as small as in the droplet model (as evident from a comparison of Eqs. (9.274) and (9.263)).

Let us illustrate the preceding considerations by simple numerical calculations, again. For comparison, we consider two typical cases with $n_{sm} = 100$, $\Delta n_{sm} = 10$, and $\Delta n_{sm} = 15$ (for simplicity, we vary only Δn_{sm} out of two parameters, n_{sm} and Δn_{sm}). From Eqs. (9.222) and (9.273)–(9.275), at $\alpha_{\mathrm{m}} \approx 0.1$, $n_{sm} = 100$, and $\Delta n_{sm} = 15$, we can easily find

$$W_{sm} = 9.68\,, \qquad a_1 = 0.0429\,, \qquad a_3 = 0.877\,, \qquad \frac{c_{1m}}{c_{10}} = 1.59\,, \tag{9.278}$$

and for $n_{sm} = 100$ and $\Delta n_{sm} = 15$

$$W_{sm} = 10.1\,, \qquad a_1 = 0.0208\,, \qquad a_3 = 0.436\,, \qquad \frac{c_{1m}}{c_{10}} = 1.20\,. \tag{9.279}$$

Furthermore, from Eqs. (9.275)–(9.277) at $\alpha_{\mathrm{m}} \approx 0.1$, $n_{sm} = 100$ and $\Delta n_{sm} = 10$, we can easily obtain

$$n_{cm} = 28.6\,, \qquad \Delta n_{cm} = 7.33\,, \qquad W_{cm} = 31.7\,, \tag{9.280}$$

and for $n_{sm} = 100$ and $\Delta n_{sm} = 15$

$$n_{cm} = 33.5\,, \qquad \Delta n_{cm} = 11.5\,, \qquad W_{cm} = 18.0\,. \tag{9.281}$$

Let us now recover the dependence on the initial parameters a_1 and a_3 in the quasidroplet model. From Eqs. (9.273) and (9.275), by the perturbation method at $\epsilon \ll 1$, we obtain

$$n_{sm} = \left(\frac{a_3}{2a_1}\right)^2 \left(1 - \frac{2}{3}\epsilon\right)\,, \qquad \Delta n_{sm} = \frac{2}{a_1^{1/2}}\left(1 + \frac{1}{2}\epsilon\right)\,, \tag{9.282}$$

$$\epsilon = \frac{48a_1^3}{a_3^4} \ln\left(\pi^{1/2} \frac{1-\alpha_{\mathrm{m}}}{\alpha_{\mathrm{m}}} \frac{a_3^2}{2a_1^{5/2}}\right)\,. \tag{9.283}$$

The high sensitivity of the parameter n_{sm} to the parameters a_1 and a_3 and lower sensitivity of the parameter Δn_{sm} to the parameter a_1 are evident. In order for Eqs. (9.282) to provide realistic estimates of $n_{sm} \sim 10^2$ and $\Delta n_{sm} \sim 10$, and correspondingly, in order for Eq. (9.283) to provide the inequality $\epsilon \ll 1$, the values of the initial parameters a_1 and a_3 of the quasidroplet model should satisfy rather severe constraints. Equations (9.282)–(9.283), with Eqs. (9.222), (9.274), and (9.276)–(9.277), determine in an analytical form the desired dependence (at the CMC) of all thermodynamic characteristics of micellization on the parameters a_1 and a_3 of the quasidroplet model of molecular aggregates. In particular, the approximations for values n_{sm} and n_{cm},

$$n_{sm} \approx \left(\frac{a_3}{2a_1}\right)^2\,, \qquad n_{cm} \approx \left(\frac{a_3}{4a_1}\right)^2 \tag{9.284}$$

follow from Eqs. (9.282) and (9.276) when corrections due to terms containing the small parameter ϵ are ignored. From Eqs. (9.260) and (9.284), we have $n_{cm}/n_0 \approx (2/3)^2$, $n_{sm}/n_0 \approx$

$(4/3)^2$. These relations indicate that the relative positions of maximum, point of inflection and minimum of the work W_n on the aggregation number axis are independent of the parameters a_1 and a_3 in the quasidroplet model of molecular aggregates.

Let us now derive formulas for the thermodynamic characteristics of micellization in the droplet and quasidroplet models of molecular aggregates that are valid in the region $c_1 > c_{1m}$ of monomer concentration c_1. It is natural that within the framework of the models, all conclusions will be referred only to the region of concentrations where micelles still retain their spherical shape. As will be shown below, this concentration region can be considered, even on the accumulation (in micelles) of almost the entire surfactant in the micellar solution (when the degree of micellization is close to unity and the total surfactant concentration is much higher than the CMC), as so narrow that the relations

$$n_{\rm c} \approx n_{cm} \ , \qquad n_{\rm s} \approx n_{sm} \ , \qquad \Delta n_{\rm c} \approx \Delta n_{cm} \ , \qquad \Delta n_{\rm s} \approx \Delta n_{sm} \tag{9.285}$$

hold in this region with a high accuracy with an error that does not exceed several percent. It follows from Eq. (9.142) that, even at

$$c_M/c_{Mm} \lesssim 10^3 \ , \tag{9.286}$$

the inequality

$$c_1/c_{1m} < 1 + (6.91/n_{sm}) \tag{9.287}$$

is valid. According to Eq. (9.137) and $\alpha_{\rm m} \simeq 0.1$, we have $\alpha \simeq 0.99$ at the upper limit of inequalities (9.286) and (9.287). This result implies that micelles already accumulate the main part of the entire surfactant in micellar solution. Hereafter, we assume that Eqs. (9.286) and (9.287), which indicate the narrowness of the concentration region $c_1 > c_{1m}$, are fulfilled.

For the droplet model of molecular aggregates we can find with Eqs. (9.208), (9.33) and (9.215) the dependence of the values $n_{\rm c}$, $n_{\rm s}$, $\Delta n_{\rm c}$, and $\Delta n_{\rm s}$ on the concentration c_1 via $\ln\left(c_1\big/c_{10}\right)$ even in an analytical form. Equations (9.287) and (9.263) show that, at the upper limit of the constraint (9.287), we have

$$\frac{\ln\left(c_1/c_{10}\right)\ln\left(c_{1m}/c_{10}\right)}{\ln\left(c_{1m}/c_{10}\right)} \simeq 6.28\left(\frac{\Delta n_{sm}}{n_{sm}}\right)^2 \ . \tag{9.288}$$

For simplicity, we ignore here and below the correction terms of order ϵ. Thus we see that the deviation of the value of $\ln\left(c_1/c_{10}\right)$ from its magnitude at the CMC is relatively small at $(\Delta n_{sm}/n_{sm})^2 \sim 10^{-2}$. Then, retaining the principal (with respect to this deviation) contributions to the dependences of $n_{\rm c}$, $n_{\rm s}$, $\Delta n_{\rm c}$, and $\Delta n_{\rm s}$ on $\ln\left(c_1/c_{10}\right)$ and taking into account Eqs. (9.262)–(9.263), (9.265), and (9.288), we obtain

$$\begin{aligned} n_{\rm c} &\simeq n_{cm}\left[1 - 3.45\left(\frac{\Delta n_{sm}}{n_{sm}}\right)^2\right] \ , \\ n_{\rm s} &\simeq n_{sm}\left[1 + 3.45\left(\frac{\Delta n_{sm}}{n_{sm}}\right)^2\right] \ , \\ \Delta n_{\rm c} &\simeq \Delta n_{cm}\left[1 - 3.45\left(\Delta n_{sm}/n_{sm}\right)^2\right] \end{aligned} \tag{9.289}$$

$$\Delta n_{\rm s} \simeq \Delta n_{sm}\left\{1-\left[0.77\ln\left(\frac{\pi^{1/2}(1-\alpha_{\rm m})}{\alpha_{\rm m}}n_{sm}\Delta n_{sm}\right)-2.65\right]\times\left(\frac{\Delta n_{sm}}{n_{sm}}\right)^4\right\}. \tag{9.290}$$

The same approach can be used for the quasidroplet model. Here Eqs. (9.208), (9.33), and (9.259) allow us to determine the dependence of $n_{\rm c}$, $n_{\rm s}$, $\Delta n_{\rm c}$, and $\Delta n_{\rm s}$ on the concentration c_1 via $\ln\left(c_1/c_{10}\right)$ (again, in an analytical form). As follows from Eqs. (9.287) and (9.274), we have at the upper limit of the constraint (9.287) in the quasidroplet model the result

$$\frac{\ln\left(c_1/c_{10}\right)-\ln\left(c_{1m}/c_{10}\right)}{\ln\left(c_{1m}/c_{10}\right)}\simeq 13.8\left(\frac{\Delta n_{sm}}{n_{sm}}\right)^2. \tag{9.291}$$

We see that the deviation of $\ln\left(c_1/c_{10}\right)$ from its value at the CMC is still relatively small. Then, retaining principal (with respect to this deviation) contributions to the dependences of $n_{\rm c}$, $n_{\rm s}$, $\Delta n_{\rm c}$, and $\Delta n_{\rm s}$ on $\ln\left(c_1/c_{10}\right)$ and taking into account Eqs. (9.273)–(9.274), (9.276), and (9.291), we obtain in the quasidroplet model

$$n_{\rm c}\simeq n_{cm}\left[1-6.91\left(\frac{\Delta n_{sm}}{n_{sm}}\right)^2\right],\qquad n_{\rm s}\simeq n_{sm}\left[1+3.45\left(\frac{\Delta n_{sm}}{n_{sm}}\right)^2\right], \tag{9.292}$$

$$\begin{aligned}\Delta n_{\rm c} &\simeq \Delta n_{cm}\left[1-5.18\left(\frac{\Delta n_{sm}}{n_{sm}}\right)^2\right],\\ \Delta n_{\rm s} &\simeq \Delta n_{sm}\left[1-2.59\left(\frac{\Delta n_{sm}}{n_{sm}}\right)^2\right].\end{aligned} \tag{9.293}$$

It follows from Eqs. (9.289)–(9.290) and (9.292)–(9.293) at $\left(\Delta n_{sm}/n_{sm}\right)^2 \sim 10^{-2}$ that Eqs. (9.285) are fulfilled with high accuracy at the upper limit of the constraint (9.287). Evidently, this statement is valid throughout the concentration region $c_1 > c_{1m}$ admitted by the constraint (9.287). The existence of the small parameter $\left(\Delta n_{sm}/n_{sm}\right)^2$ is responsible for the fulfillment of Eqs. (9.285) in the droplet and quasidroplet models of molecular aggregates.

Note also the following circumstance. According to Eq. (9.287), a relative increase in monomer concentration c_1 that is needed to accumulate almost the whole surfactants in micelles after reaching the CMC turned out to be still markedly lower than the relative increase in the monomer concentration $c_1$estimated by Eqs. (9.266), (9.267), (9.278), and (9.279) that is necessary to reach the CMC after the appearance of the potential barrier and potential well of the work W_n at $c_1 = c_{10}$. This results confirm all statements that have been made above concerning the physical meaning of the CMC.

Acknowledgements

This work was supported by the Russian Foundation for Basic Research (grant no. 04-03-32134) and the National Science Foundation (grant no. CHE-0313563).

References

[1] R. Becker, *Theorie der Wärme* (Springer, Berlin, 1955).

[2] D. Kashchiev, *Nucleation: Basic Theory with Applications* (Butterworth-Heinemann, Oxford, 2000).

[3] K. Shinoda and E.J. Hutchinson, Phys. Chem. **66**, 577 (1962).

[4] D.G. Hall, Faraday Trans. Royal Soc. II **68**, 668 (1972).

[5] A.I. Rusanov, *Micellization in Surfactant Solutions* (Harwood Academic, Reading, MA, 1997).

[6] C. Tanford, *The Hydrophobic Effect: Formation of Micelles and Biological Membranes* (Wiley, Toronto, 1980), 2nd ed.; J. Phys. Chem. **78**, 2469 (1974).

[7] J.N. Israelachvili, D.J. Mitchell, and B.W. Ninham, J. Chem. Soc. Faraday Trans. II **72**, 1525 (1976).

[8] E. Ruckenstein and R. Nagarajan, Thermodynamics of amphiphilar aggregation into micelles and vesicles, in *Micellization, Solubilization and Microemulsions*, edited by K.L. Mittal (Plenum, New York, 1977), pp. 133–149.

[9] R. Nagarajan and E. Ruckenstein, J. Colloid Interface Sci. **71**, 580 (1979).

[10] R. Nagarajan and E. Ruckenstein, Langmuir **7**, 2934 (1991).

[11] R. Nagarajan and E. Ruckenstein, Self-assembled systems, in *Equations of State for Fluids and Fluid Mixtures*, edited by J.V. Sengers et al. (IUPAC, 2000), pp. 589–749.

[12] B. Fodi and R. Hetschke, Langmuir **16**, 1626 (2000).

[13] E.A.G. Aniansson and S.N. Wall, J. Phys. Chem. **78**, 1024 (1974).

[14] M. Almgren, E.A.G. Aniansson, and K. Holmaker, Chem. Phys. **19**, 1 (1977).

[15] E.A.G. Aniansson, Ber. Bunsenges. Phys. Chem. **82**, 981 (1978).

[16] E.A.G. Aniansson, A Treatment of the kinetics of micelles, in *Techniques and Applications of Fast Reactions in Solution*, edited by W.J. Gettins and E. Wyn-Jones (Reidel, Dordrecht, 1979), pp. 249–258.

[17] R. Nagarajan and E. Ruckenstein, J. Colloid Interface Sci. **60**, 221 (1977).

[18] A.I. Rusanov, F.M. Kuni, and A.K. Shchekin, Colloids Surfaces A **128**, 13 (1997).

[19] F.M. Kuni, A.K. Shchekin, A.P. Grinin, and A.I. Rusanov, Colloid J. **62**, 172 (2000).

[20] F.M. Kuni and A.P. Grinin, Vestn. Leningr. Univ. **22**, 10 (1982).

[21] F.M. Kuni, A.K. Shchekin, and A.P. Grinin, Physics-Usp. **44**, 331 (2001).

[22] F.M. Kuni, A.K. Shchekin, A.P. Grinin, and A.I. Rusanov, Colloid J. **65**, 459 (2003).

[23] A.I. Rusanov, F.M. Kuni, and A.K. Shchekin, Colloid J. **62**, 167 (2000).

[24] F.M. Kuni, A.P. Grinin, A.K. Shchekin, and A.I. Rusanov, Colloid J. **62**, 451 (2000).

[25] F.M. Kuni, A.P. Grinin, A.K. Shchekin, and A.I. Rusanov, Colloid J. **63**, 197 (2001).

[26] F.M. Kuni, A.K. Shchekin, A.P. Grinin, and A.I. Rusanov, Colloid J. **63**, 723 (2001).

[27] A.I. Rusanov, F.M. Kuni, A.P. Grinin, and A.K. Shchekin, Colloid J. **64**, 605 (2002).

[28] A.I. Rusanov, A.P. Grinin, F.M. Kuni, and A.K. Shchekin, J. Gen. Chem. **72**, 607 (2002).

[29] A.P. Grinin, A.I. Rusanov, F.M. Kuni, and A.K. Shchekin, Colloid J. **65**, 145 (2003).

[30] J. Bilingham and P.V. Coveney, J. Chem. Soc. Faraday Trans. **90**, 1953 (1994).

[31] P.V. Coveney and J.A.D. Wattis, Proc. R. Soc. London A **452**, 2079 (1996).

[32] G. Waton, J. Phys. Chem. B **101**, 9727 (1997).
[33] P.V. Coveney and J.A.D. Wattis, J. Chem. Soc., Faraday Trans. **94**, 233 (1998).
[34] P. Mukerjee, J. Phys. Chem. **76**, 565 (1972).
[35] K. Binder, Phys. Rev. B **15**, 4425 (1977).
[36] F.M. Kuni and A.P. Grinin, Kolloid. Zh. **46**, 23 (1984).
[37] E.A.G. Aniansson, S.N. Wall, M. Almgren, H. Hoffman, I. Kielmann, W. Ulbricht, R. Zana, J. Lang, and C. Tondre, J. Phys. Chem. **80**, 905 (1976).
[38] H. Hoffmann, R. Nagel, G. Platz, and W. Ulbricht, Colloid Polymer Sci. **254**, 812 (1976).
[39] H. Hoffmann, Progr. Colloid Polymer Sci. **65**, 148 (1978).
[40] S. Wall and C. Elvingson, J. Phys. Chem. **89**, 2695 (1985).
[41] J. Gormally, W.J. Gettins, and E. Wyn-Jones, Micellization in surfactants, in *Molecular Interactions*, edited by H. Ratajczak and N.I. Orvil-Thomas (Wiley-Interscience, New York, 1981), Vol. 20.
[42] T. Telgmann and U. Kaatze, J. Phys. Chem. B **101**, 7758 (1997).
[43] T. Telgmann and U. Kaatze, J. Phys. Chem. B **101**, 7766 (1997).
[44] E.V. Chertkov, A.A. Saidov, and P.K. Khabibullaev, Colloids Surf. A **168**, 185 (2000).
[45] S.N. Wall and E.A.G. Aniansson, J. Phys. Chem. **84**, 727 (1980).
[46] A.P. Grinin and D.S. Grebenkov, Colloid J. **65**, 603 (2003).
[47] S.J. Marrink, D.P. Tieleman, and A.E. Mark, J. Phys. Chem. **104**, 12165 (2000).
[48] N.M. van Os, B. Smit, and S. Karaborni, Recl. Trav. Chim. Pays-Bas **101**, 181 (1994).
[49] H. Wennerstrom, Curr. Opin. Colloid Interface Sci. **1**, 370 (1996).
[50] D. Blankschtein, A. Shiloach, and N. Zoeller, Curr. Opin. Colloid Interface Sci. **2**, 294 (1997).
[51] R. Nagarajan, Colloids Surf. A **71**, 39 (1993).
[52] R. Nagarajan, Langmuir **10**, 2028 (1994).
[53] R. Nagarajan, Theory of micelle formation. Quantitative approach to predicting the micellar properties from surfactant molecular structure, in *Structure-Performance Relationships in Surfactants*, edited by K. Esumi and M. Ueno (Dekker, New York, 1997), pp. 1–81.
[54] E. Ruckenstein and R. Nagarajan, J. Phys. Chem. **79**, 2622 (1975).
[55] E. Ruckenstein and R. Nagarajan, J. Colloid Interface Sci. **57**, 388 (1976).
[56] R. Nagarajan and E. Ruckenstein, J. Colloid Interface Sci. **91**, 500 (1983).
[57] A.I. Rusanov, *Phasengleichgewichte und Grenzflächenerscheinungen* (Akademie-Verlag, Berlin, 1978).
[58] D.S. Grebenkov, J. Colloid Interface Sci. **249**, 162 (2002).

10 Nucleation in a Concentration Gradient

Andriy M. Gusak and Fiqiri Hodaj

Nothing has such power to broaden the mind
as the ability to investigate systematically and truly all
that comes under your observation in life.
Marcus Aurelius

A detailed analysis of the thermodynamics and kinetics of nucleation in solid solutions in the presence of concentration gradients is presented. Different modes of intermediate phase nucleation in the vicinity of the initial contact interface of a diffusion couple and their competition are considered. The possibility of a temporary suppression of certain phases as well as of oscillatory nucleation regimes is demonstrated.

10.1 Introduction

The present review is devoted to the modeling and theoretical description of the "Big Bang" of solid-state reactions, the very initial stages including nucleation. The evident nanotrend of materials science makes the initial stages of solid-state reactions (a true nanoprocess) a very important issue. Till the 1980s, the diffusion community, occupied mainly with diffusion and reactions in macrosamples, treated the initial stages of these processes as some exotic problem, basically, as a theoretical one. The reason was that the initial stage is usually being "forgotten" by the system in the further course of its evolution (in accordance with basic principles of nonequilibrium thermodynamics and statistical mechanics), when the diffusion zone reaches several micrometers [1, 2]. In the case of reactive diffusion, the "initial stage" means the period till the formation and parabolic growth of all stable intermediate phases. It includes, in principle, the following substages:

(i) nucleation of intermediate phases, i.e., the formation of supercritical nuclei (islands) of the new phase at or in the vicinity of the initial contact interface [2–8].

(ii) Growth of new phase islands and competition (for space and material) between them till the formation of phase layers with a more or less planar geometry [9–11]. In the case of ternary and multicomponent systems, two-phase layers can be formed as well.

(iii) Overcoming interfacial barriers (if they exist) [1, 12] and/or relaxation of the vacancy subsystem.

For the first time, a practical interest in the analysis of the initial stages of solid-state reactions arose in connection with the investigation of reactive diffusion in thin films. The usually observed one-by-one (sequential) phase growth led to the conclusion that the initial stage of evolution might well be for some phases simultaneously the final stage. If, for example, the evolution of the intermediate phase A_1B_2 is suppressed by some reason during the growth of the phase A_2B_1 till the consumption of pure B, this phase will never appear at all. Yet, even for

Nucleation Theory and Applications. edited by J. W. P. Schmelzer

ISBN: 3-527-40469-4

explaining phase suppression, people tried to avoid the consideration of nucleation processes. Instead, the suppression has been explained in terms of interplay of diffusion and interfacial barriers. The most successful theory of this type was developed by Goesele and Tu [12]. Introducing some rather arbitrary rate constants for fluxes across interfaces, they managed to derive expressions for the critical thicknesses of suppressing phases and delay periods of suppressed phases. Nucleation issues, in terms of the standard nucleation approach but in application to solid-state reactions, have been discussed first by d'Heurle in 1986 [3].

The situation became even more intriguing with the discovery of the solid-state amorphizing reactions [13, 14] demonstrating the growth of metastable amorphous layers without any evidence of stable phase formation till the amorphous layer has reached a certain critical thickness of hundreds of nanometers. It looked like as if nucleation and/or growth of stable phases has been suppressed not just by low temperatures, but by the growing metastable phase. Detailed differential scanning calometry investigations of solid-state reactions in multilayers by the groups of Barmak and Gas [9, 15, 16] demonstrated the possibility of two heat-release maxima for the same phase. Such feature can be explained in terms of some kind of two-stage phase formation (the first stage being possibly the lateral growth of new phase islands). Recently, Schmitz et al. used an atom-probe tomography method to investigate the very initial stage of solid-state reactions [17, 18]. This method, with a resolution of a few angstroms, provides us with the three-dimensional distribution of atoms of the reacting species. These experiments clearly show that usually even the first islands of the first phase to grow do not form immediately after contact. Thus, indeed, the "nanovector" of solid-state reactions makes it more and more important to properly take the nucleation stage into account.

In 1982, one of the authors (A.G.), jointly with his teacher, the late Professor Cyrill Gurov (Institute for Metallurgy, Moscow), presented a simple (even "naive," as we realize it today) model of phase competition taking into account the nucleation stage of each phase ([4], see also [19]). Actually, the only concept that had been taken in Ref. [4] from nucleation theory was the existence of a critical nucleus. Such critical nuclei appear due to some "miraculous process" called heterophase fluctuations, which are stochastic events and cannot be described by any deterministic model. The initial idea was just that each phase cannot start from zero thickness; it should start, in contrast, from some well-defined critical size of the particle (of the order of nanometers). In contrast to the standard nucleation theory, critical nuclei of intermediate phases during reactive diffusion are formed in a strongly inhomogeneous region, the interfacial zone between other phases. Therefore, from the very beginning they have to let diffusion fluxes pass through themselves. Evidently, such fluxes will change abruptly when passing across each newly formed boundary of the newly born nuclei, and thus speed up the boundary motion.

The picture of interface movement due to flux steps described above is well known from the analysis of diffusion couples where it is called the Stephan problem and means diffusive interactions between neighboring phases. Yet, including nucleation events into the description, the initial width of each phase is taken now to be equal to the critical nucleus size (instead of zero). The peculiarity of the initial stage is just the possibility that the width of some new-phase nucleus (the distance between left and right boundaries), *can decrease* as well as increase. If it decreases, then the nucleus becomes subcritical, and should disappear. Usually it happens if the neighboring phases have a larger diffusivity and comparative thickness. Then these neighbors ("vampires" or "sharks") will destroy and consume all of the newly forming

nuclei, making the new phase to be present only virtually in the form of constantly forming (due to heterophase fluctuations) and vanishing (due to diffusive suppression by the neighbors) embryos. Based on these ideas, a simple mathematical scheme was developed allowing one to predict the sequence of phase formation and incubation periods, provided one knows the integrated Wagner diffusivities and sizes of critical nuclei for each phase. One of the most simple examples of this scheme is presented in Sect. 10.2. This scheme was then applied to competition with solid solutions [5], to phase growth under strong electric currents [20], to reactive diffusion in ternary systems [21], and to phase competition in reacting powder systems [7, 22]. Applications to the electric field case demonstrated that the phase spectrum of the reaction zone can be influenced and even controlled by a strong enough current density. Large current densities have been expected then to become a real possibility of affecting the processes under study due to the miniaturization of integrated schemes and the introduction of the flip-chip technology [23]. Recent results on reactive diffusion in under-bump metallization (UBM)-solder contacts under a strong current crowding confirm this point of view.

Later we realized that in our naive model of phase competition we had taken into account the inhomogeneity of the nucleation region only partially. Namely, we treated the diffusive interactions of the newly born nuclei, but we did not consider the possible change of the nucleation barrier, size and shape, caused by the very fact of existence of sharp concentration gradients. Thus, we had to reconsider the thermodynamics of nucleation in a concentration gradient. The very first version of such theory was presented at the All-Union Conference *Defects and Diffusion 1989* (DD-89) in Russia and first published in May 1990 [6] (see also [19]). The main idea was that if prior to intermediate phase formation a narrow layer of a metastable solid solution or amorphous alloy has been formed at the base of the initial interface, the sharp concentration gradient inside this layer provides a decrease of the total bulk driving force of nucleation and a corresponding increase of the nucleation barrier. Nuclei were taken to be spheres, appearing in the strongly inhomogeneous concentration profile of the parent phase, so that the local driving force of transformation could change significantly from the left to the right along the diameter of the nucleus. This effect appeared to be nonnegligible, since usually the intermediate phases have a very strong concentration dependence in the Gibbs energy. The main result of this analysis was the new type of size dependence of the Gibbs energy containing now in addition to the terms of second order (surface energy, positive) and third order (bulk driving force, negative), a new term proportional to the fifth order of size R and the concentration gradient (∇C) squared, i.e.,

$$\Delta G\,(R) = \alpha R^2 - \beta R^3 + \gamma\ (\nabla C)^2\, R^5\ . \tag{10.1}$$

Here the parameter γ is positive and proportional to the second-order derivative of the new phase Gibbs energy with respect to the concentration. Equation (10.1) implies that for a large enough gradients $\nabla C > \nabla C^{\text{crit}}$ (typically $\nabla C^{\text{crit}} \cong 10^8\ \text{m}^{-1}$) the dependence $\Delta G\,(R)$ becomes a monotonically increasing function of R (infinitely high nucleation barrier) resulting in a thermodynamic suppression of nucleation by very sharp concentration gradients. Thus, according to our model, at the very initial stage of reactive diffusion nucleation can be suppressed even without diffusive competition, just due to too narrow space regions favorable for the transformation.

Independently similar results were published by Desre et al. in 1990 and 1991 [24, 25]. This approach was applied then to a description of solid-state amorphizing reactions [24–27],

explaining why stable intermetallics are formed in a diffusion zone only after the amorphous layer exceeds some critical thickness. Despite the similarity of the results, the models of nucleation in a sharp concentration gradient, outlined in Refs. [6,19] and [24,25] assumed quite different possible mechanisms of phase formation (different nucleation modes). In Refs. [6, 19], a *polymorphous mode* was suggested on the basis of the following picture: Initially diffusion is assumed to lead to the formation and growth of a metastable parent solution with a sharp concentration profile. When this profile becomes smooth enough to provide sufficient space for compositions favorable for a new intermediate phase, this very phase nucleates just by reconstruction of atomic order without changing immediately the concentration profile (i.e., at "frozen-in" diffusion). Such model treats the process essentially as a polymorphic transformation.

In Refs. [24, 25], the *transversal nucleation mode* was suggested on the basis of the following picture of the process. It is assumed here that each thin slice of the newly formed nucleus, perpendicular to the direction of the concentration gradient, is considered to be the result of decomposition in the corresponding thin infinite slice of the parent solution, leading, of course, to a redistribution of atoms among new and old phases. In this transversal mode, the redistribution proceeds within each slice, independently of the other ones.

In Ref. [28], one more mechanism of phase formation was proposed (and analyzed in more detail in Refs. [29, 30]), the *total mixing (longitudinal) nucleation mode*, when the redistribution of atoms proceeds during nucleation, but only inside the newly forming nucleus. In contrast to the two previous modes, in this case the concentration gradient assists nucleation since in Eq. (10.1) the coefficient γ is negative. The above-mentioned approach was generalized taking into account shape optimization [31–34], the effect of stresses [35], ternary systems [36], and heterogenous nucleation at grain boundaries [32]. Most simple models in the frame of this approach are presented in Section 10.3.

It is quite "natural" to expect that nature will use the mechanism with the lowest nucleation barrier, i.e., the total mixing mode. However, nucleation is governed not only by thermodynamics but also by kinetics. Thermodynamics of nucleation with constraints indicates only some probable paths of evolution. The real path is determined by the kinetics of the process, taking into account not only the free energy profit but also the different "mobilities" along each path.

All the above-mentioned models treat the case when the system, prior to nucleation, can form a metastable parent phase with a broad concentration range, overlapping the equilibrium concentration range of the new stable phase (Fig. 10.1). Yet, in most cases the solid-state reactions proceed in couples with small mutual solubilities even in metastable states (Fig. 10.2). In the case of phase γ nucleation between α and β, these phases, in the absence of phase γ, have metastable solubilities $C_{\alpha\gamma}$ and $1 - C_{\beta\gamma}$. Prior to nucleation the interdiffusion should lead to a step-like concentration profile that has a concentration gap $\left(C_{\alpha\gamma}, C_{\beta\gamma}\right)$ and, therefore, is not overlapping the phase γ concentration range. Of course, in this case the polymorphic mode of transformation is impossible. The transversal mode, in contrast, is quite possible here and should be realized as a simultaneous decomposition of metastable nonhomogeneous solutions within the concentration intervals $\left(C_{\alpha\gamma}, C_{\alpha\beta}\right)$ and $\left(C_{\beta\alpha}, C_{\beta\gamma}\right)$ on both the sides of the interface. Some aspects of this problem, concerning the nucleus shape, have been treated in Refs. [37, 38]. The nucleus shape, being an important factor of nucleation in a concentration gradient, is not a decisive one [29]. Therefore, in our present analysis in Sect. 10.4 (see

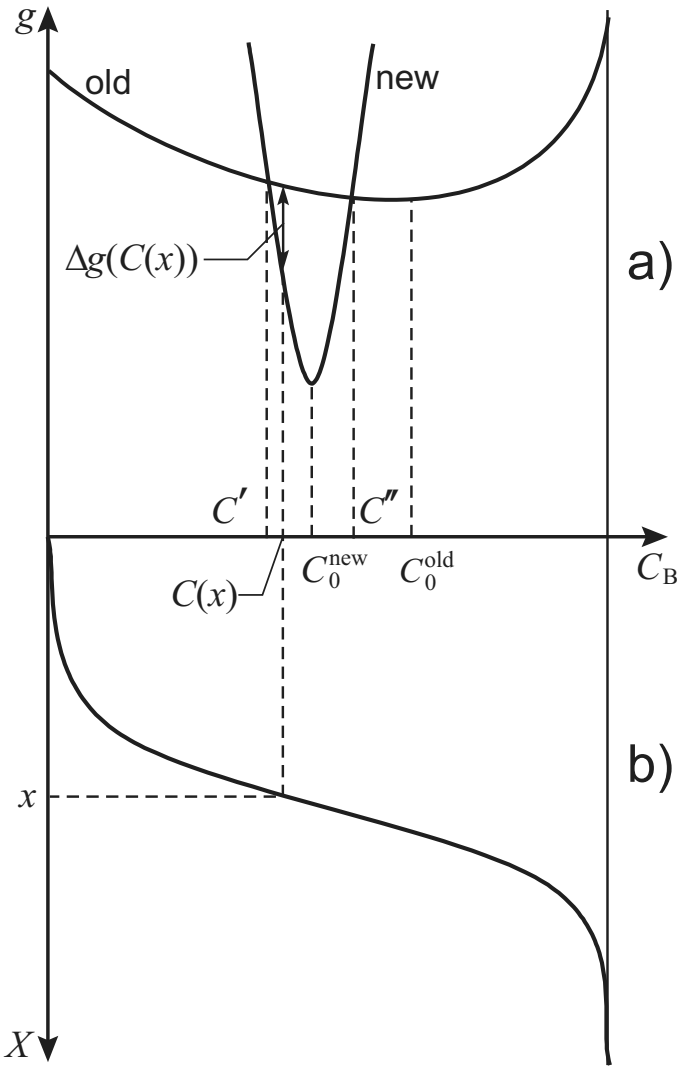

Figure 10.1: Illustration of nucleation by the polymorphic transformation mode at a frozen-in concentration profile. (a): Composition dependences of the Gibbs free energy per atom in the old and new phases. (b): Frozen-in concentration profile in the diffusion couple being approximately linear in the nucleation region

also [39]) we, so far, have left the shape problem aside, concentrating on "gradient effects" on the nucleation barrier.

The main idea, developed in Sect. 10.4, is that the effect of concentration gradients (or, better, chemical potential gradients) should be especially important for nucleation in systems with limited solubility, especially when at least one intermediate phase is already growing. It is

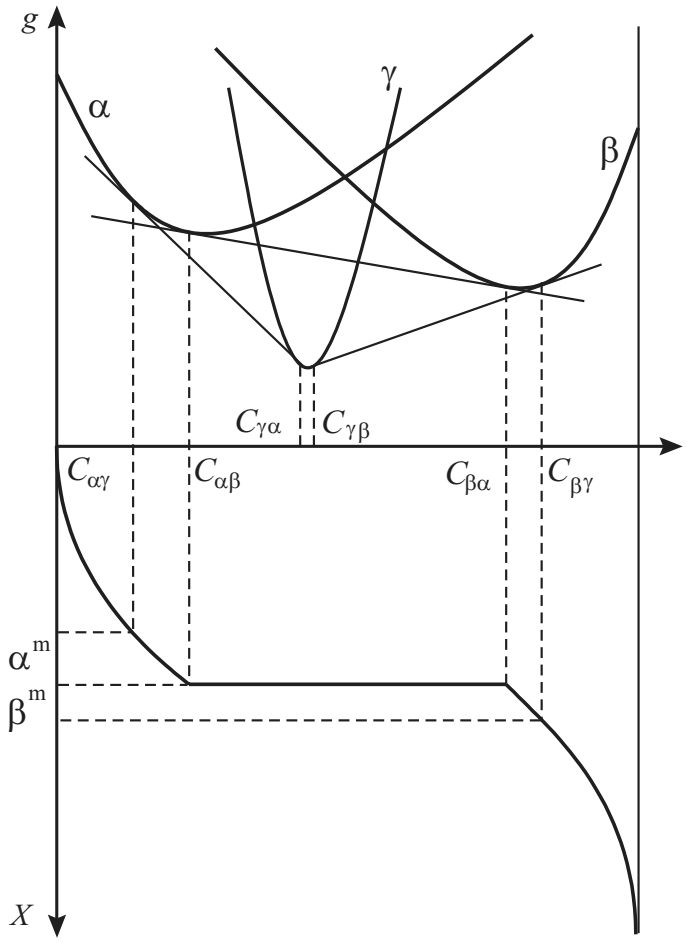

Figure 10.2: Stable and metastable equilibria in a binary system with a limited solubility of the ambient solid solution. A composition in the intervals $(C_{\alpha\gamma}, C_{\alpha\beta})$ and $(C_{\beta\alpha}, C_{\beta\gamma})$ allows nucleation of the γ-phase

quite possible that in this case, the "gradient approach" can give a key for the understanding of a sequential phase growth. We analyze the general case of phase "i" nucleation at the interface between nonhomogenous (with gradients of concentration and of chemical potentials) phase layers L and R. We apply this general formalism, respectively, to nucleation at the interface between (a) two diluted solutions α and β, (b) two already growing intermediate phases (1) and (3), and (c) growing phase (1) and diluted solution β.

As mentioned above, thermodynamic profit is a necessary but not sufficient condition for successful nucleation and growth. Kinetics can be a decisive factor as well. To describe theoretically the nucleation kinetics, we use the Fokker–Planck approach, applied widely in the nucleation theory after the classical work of Zeldovich [40]. Our contribution to this approach

is just taking into account that the driving force depends on the concentration gradient, which in turn depends on time according to diffusion laws. It has been shown in Ref. [30] that the relative contribution of each mechanism depends on the ratio of atomic mobilities in the parent and nucleating phases. If the atomic mobility in the new phase is much lower than that in the parent one, we can forget about the total mixing mode. In the opposite case (high mobility inside the new phase), nucleation will proceed via total mixing and very fast ("fast is the first"). As will be shown, one of the "raisins" of the total mixing (assisting) mode is that the easily formed nuclei, if not growing too fast in comparison with the decrease of the concentration gradient, after some period of time can find themselves to be subcritical and will be destroyed again. The main results will be briefly reviewed in Sect. 10.5.

10.2 Phase Competition under Unlimited Nucleation

What do we mean by phase competition during solid-state reactions? Let us consider a diffusion couple consisting of two partially soluble species A and B diffusing into each other and forming the intermediate phases and possibly the solid solutions. Let the binary system A–B has three stable intermetallic phases 1, 2, 3, a metastable compound 4, and a metastable amorphous phase 5. The composition dependences of the Gibbs free energy for these phases are shown in Fig. 10.3. According to the standard theory, for sufficiently long annealing times, three stable planar phase layers should grow according to parabolic laws. Very often the real situation is, however, different, only one stable phase grows, only the metastable crystalline phase grows, or an amorphous one is found. Thus, phases compete with each other, as well as different regimes of reactive diffusion.

It has been well known for several decades that the reactive diffusion in thin films usually demonstrates "one by one" (sequential) phase formation [41, 42]. Despite the existence of several stable intermediate phases at the phase equilibrium diagram, only one growing phase layer is usually observed. The next phase appears, or at least becomes visible, only after one of the terminal materials has been consumed, so that the first phase has no more material for further growth, become itself a material for second phase formation, and so on. Such sequential growth has, at least, three possible explanations:

(i) *"Just slow growth"* The first phase to grow usually has the maximum diffusivity and, hence, grows fast (according to d'Heurle [42], "fast is the first" or "first is fast"). Other phases, with less diffusivities, grow even slower than they could do alone, without a fast growing neighbor. For example, in the case of two simultaneously growing phases 1 and 2 with significantly different integrated Wagner diffusivities $D_1 \Delta C_1 \gg D_2 \Delta C_2$, where

$$D_i \Delta C_i = \int_{C_{iL}}^{C_{iR}} \widetilde{D}\,(C)\,\mathrm{d}C\ , \quad C_{iR} - C_{iL} = \Delta C_i\ ,$$

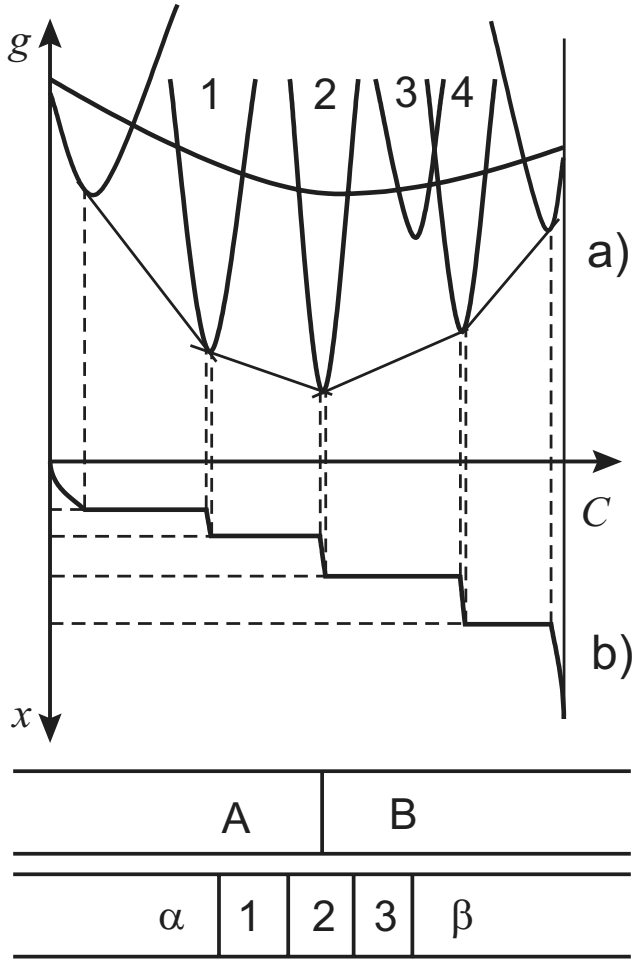

Figure 10.3: Phase spectrum of a binary system: (a) schematic composition dependences of the Gibbs free energy per atom of the intermediate phases and (b) phase spectrum of the diffusion zone for long annealing times

ΔC_i is the homogeneity interval, C is the atomic fraction of the B-component, and $\widetilde{D}\,(C)$ is the interdiffusion coefficient [2,43,44]; their thickness ΔX_i obeys the following parabolic laws (omitting factors of the order of unity):

$$\Delta X_1 \approx \sqrt{2D_1 \Delta C_1}\, t^{1/2}\,, \quad \Delta X_2 \approx \frac{2D_2 \Delta C_2}{\sqrt{2D_1 \Delta C_1}}\, t^{1/2}\,,$$

so that

$$\frac{\Delta X_2}{\Delta X_1} \approx \frac{D_2 \Delta C_2}{D_1 \Delta C_1}$$

holds. Note that in the absence of the fast phase 1, the second phase would grow much faster as

$$\Delta X_2^{\text{single}} \approx \sqrt{2D_2\Delta C_2 t}^{1/2} .$$

Thus, according to this first explanation, other phases exist and grow, but too slowly, and their layers are so thin that it is just difficult to detect them.

(ii) *Interfacial barriers and competition*[12] Interfacial barriers are believed to cause the initial linear phase growth. In the case of single phase formation the interfacial barriers simply slow down the rate of formation, making it linear instead of parabolic. In the case of two phases the barriers can make the growth rate of some phase formally negative even for zero thickness, which means that this phase will be totally absent. The model, as outlined in Ref. [12], is nice, but the constants of the interfacial kinetics are, to our knowledge, adjusting parameters.

(iii) *Diffusive suppression of critical nuclei* [4–7] Any phase can start growing only from the nuclei of some critical size l_{cr}. Yet, since these nuclei (born as a result of inevitable heterophase fluctuations) are from the very beginning situated in the sharply inhomogeneous system and, hence, take part in diffusive interactions, they can shrink to subcritical (unstable with respect to dissolution) sizes due to diffusive suppression by a neighboring, fast growing phase.

To simplify the analysis, let us consider a binary diffusion couple A–B with two intermediate phases 1 and 2. Let the layer of phase 1 grow according to the law

$$\Delta x_1 = \sqrt{\frac{2D_1\Delta C_1}{C_1(1-C_1)}t} \tag{10.2}$$

and the phase 2 form a critical nucleus with a longitudinal size l_2 at the moving interface 1-B due to heterophase fluctuations (so that there are no thermodynamic constraints). As will be shown in Sect. 10.3, sharp concentration gradients lead to a plate-like shape of the nuclei (leaving aside the total mixing mode up to the last section). Therefore one can consider left and right boundaries of the nucleus as being nearly flat. Drops of the diffusion fluxes at these boundaries generate their evolution according to the laws

$$\begin{aligned}(C_2 - C_1)\frac{\mathrm{d}x_{2L}}{\mathrm{d}t} &= \frac{D_1\Delta C_1}{\Delta x_1} - \frac{D_2\Delta C_2}{l_2} ,\\ (1-C_2)\frac{\mathrm{d}x_{2R}}{\mathrm{d}t} &= \frac{D_2\Delta C_2}{l_2} - 0 .\end{aligned} \tag{10.3}$$

We neglect here the solubility of A in B. Hence, the rate of change of the width of the critical nucleus is equal to

$$\left.\frac{\mathrm{d}\Delta x_2}{\mathrm{d}t}\right|_{l_2} = \frac{\mathrm{d}x_{2R}}{\mathrm{d}t} - \frac{\mathrm{d}x_{2L}}{\mathrm{d}t} = \frac{1}{C_2 - C_1}\left(-\frac{D_1\Delta C_1}{\Delta x_1} + \frac{1-C_1}{1-C_2}\frac{D_2\Delta C_2}{l_2}\right) . \tag{10.4}$$

One can easily see that this expression is positive for large values of Δx_1, but can be negative for small values of Δx_1. If

$$\Delta x_1 < \Delta x_1^* = \frac{1 - C_2}{1 - C_1} \frac{D_1 \Delta C_1}{D_2 \Delta C_2} l_2 \,,$$

then $(\mathrm{d}\Delta x_2/\mathrm{d}t)|_{l_2} < 0$ holds, so that every critical nucleus decreases (being "eaten" by the rapidly growing neighbor phase 1) and therefore becomes a subcritical (unstable) embryo and will be dissolved. Such unsuccessful attempts of phase 2 nucleation will be repeated during the "incubation period"

$$\tau = \frac{C_1 (1 - C_1)}{2 D_1 \Delta C_1} \left(\Delta x_1^*\right)^2 = \frac{C_1 (1 - C_2)^2}{2 (1 - C_1)} \frac{D_1 \Delta C_1}{(D_2 \Delta C_2)^2} l_2^2 \,. \tag{10.5}$$

In order to determine which of the phases will grow first, one has to consider the diffusional interaction between two initial layers of critical nuclei of both phases. One can easily check that

$$\begin{aligned} \left.\frac{\mathrm{d}\Delta x_1}{\mathrm{d}t}\right|_{l_1} &= \frac{1}{C_2 - C_1} \left(\frac{C_2}{C_1} \frac{D_1 \Delta C_1}{l_1} - \frac{D_2 \Delta C_2}{l_2} \right) \,, \\ \left.\frac{\mathrm{d}\Delta x_2}{\mathrm{d}t}\right|_{l_2} &= \frac{1}{C_2 - C_1} \left(-\frac{D_1 \Delta C_1}{l_1} + \frac{1 - C_1}{1 - C_2} \frac{D_2 \Delta C_2}{l_2} \right) \end{aligned} \tag{10.6}$$

hold. Here we have three possibilities:

(i) Phase 2 ("vampire") starts growing, "eating" the nuclei of phase 1 at

$$\frac{D_1 \Delta C_1}{D_2 \Delta C_2} \frac{l_2}{l_1} < \frac{C_1}{C_2} \Rightarrow \left.\frac{\mathrm{d}\Delta x_1}{\mathrm{d}t}\right|_{l_1} < 0 \,, \quad \left.\frac{\mathrm{d}\Delta x_2}{\mathrm{d}t}\right|_{l_2} > 0 \,.$$

(ii) Both phases grow from the moment of nucleation at

$$\frac{C_1}{C_2} < \frac{D_1 \Delta C_1}{D_2 \Delta C_2} \frac{l_2}{l_1} < \frac{1 - C_1}{1 - C_2} \Rightarrow \left.\frac{\mathrm{d}\Delta x_1}{\mathrm{d}t}\right|_{l_1} > 0 \,, \quad \left.\frac{\mathrm{d}\Delta x_2}{\mathrm{d}t}\right|_{l_2} > 0 \,.$$

(iii) Phase 1 ("vampire") starts growing, "eating" the nuclei of phase 2 at

$$\frac{D_1 \Delta C_1}{D_2 \Delta C_2} \frac{l_2}{l_1} > \frac{1 - C_1}{1 - C_2} \,.$$

Such a simple approach can be easily generalized to an arbitrary number of intermediate phases [8].

10.3 Thermodynamics of Nucleation in Concentration Gradients: Case of Full Metastable Solubility

10.3.1 General Aspects

In the previous section, we considered the formation of critical nuclei as an unlimited source of candidates for further growth. Problems appeared only when these critical nuclei entered the competition process. Of course, such simplified picture is too naive. The existence of a sharp concentration gradient in the vicinity of a nucleation site should change the thermodynamics of nucleation. Nucleation barriers (saddle points) for intermediate phase formation in the diffusion zone have to be computed in a more rigorous approach, taking into account the redistribution of components outside the newly born nucleus. The parent inhomogeneous phase (or two adjacent phases) are metastable with respect to new-phase formation, but simultaneously it is (they are) unstable with respect to further interdiffusion. Therefore, at fixed size and composition of the nucleus the optimal distribution for outside parent phase(s) will be reached only after full homogenization. Obviously, the nucleus will not "wait" for the completion of this process. It means that true minimization of the Gibbs potential for nucleation during diffusion is impossible. Therefore, the problem of nucleation in an inhomogeneous system has to be solved under certain constraints, which are determined by the kinetics of the diffusion processes. Depending on the type of constraints one can distinguish between different nucleation modes. We can point out at least three possible different nucleation modes:

1. *The polymorphic mode* (Gusak [6,19]): This mode is possible if the parent metastable (for example, amorphous) phase can exist in a concentration range advantageous for a new intermediate phase. First, interdiffusion forms a concentration profile in the parent phase overlapping the concentration interval where the new intermediate phase has a lower Gibbs potential (Fig. 10.1). Then the polymorphic transformation takes place in a limited region forming the lattice of a new phase at a frozen-in concentration gradient. After this step, diffusion proceeds and the newly born nucleus interacts with the parent phase due to a step-like change of the diffusion fluxes at its boundaries. The role of the parent phase can be played by the metastable solid solution or a previously formed amorphous layer. Obviously, in order that this mode may determine the process, the rate of lattice reconstruction has to be much higher than the rate of diffusion in the parent phase.

2. *The transversal mode* (Desre [24, 25]): This mode is possible for both cases shown in Figs. 10.2 and 10.3. In the case shown in Fig. 10.3, interdiffusion prior to the formation of an i-phase nucleus leads to "meta-quasiequilibrium" $\alpha - \beta$ with metastable concentration ranges $\left(C_{\alpha\gamma}, C_{\alpha\beta}\right)$ and $\left(C_{\beta\alpha}, C_{\beta\gamma}\right)$, unstable with respect to decomposition into $\alpha + \gamma$ and $\beta + \gamma$. According to the model developed by Desre [25], during nucleus formation in a concentration gradient (in the x-direction) each thin slice $(x, x + \mathrm{d}x)$ of this nucleus forms by unlimited redistribution of the components inside this slice independently of other slices. The concentration $C^{\mathrm{new}}(x)$ in this nucleus slice is determined by the concentration $C^{\mathrm{old}}(x)$ in the surrounding phase (for the same slice) according to the rule of parallel tangents (not the joint tangent) via

$$\frac{\partial g^{\mathrm{new}}}{\partial C^{\mathrm{new}}} = \frac{\partial g^{\mathrm{old}}}{\partial C^{\mathrm{old}}} \,.$$

Obviously, to make the transversal mode real, the diffusivity in the parent phase(s) has to be much larger than that in the new phase ($D_m \gg D_i$).

3. *Total mixing (longitudinal) mode* (Hodaj, Desre [28]): This mode supposes nucleus formation only by cost of the transformed region of the parent phase, hereby the concentration distribution outside the nucleus is assumed to be unchanged. Obviously, to make this mode real, the diffusivity in the evolving phase has to be much larger than that in the parent phase ($D_i \gg D_m$).

In the general case, all these modes (and, may be, some others) will operate simultaneously. Which of them dominates, is a problem of the kinetics and will be discussed in Sect. 10.5. In the subsequent analysis, we will discuss first in detail the thermodynamics of each of these modes.

10.3.2 The Polymorphic Nucleation Mode

Let the nucleus of the intermediate phase appear in the frozen-in concentration profile formed by interdiffusion in the metastable continuous phase (solid solution or amorphous phase; Fig. 10.1). The change of the Gibbs free energy caused by the formation of the nucleus is then given by

$$\Delta G = n \int \left(g^{\text{new}} \left(C \left(x \right) \right) - g^{\text{old}} \left(C \left(x \right) \right) \right) S \left(x \right) \mathrm{d}x + \sigma S \, . \tag{10.7}$$

Here we neglect volume changes (atomic density $n_1 \approx n_2 = n$) and the corresponding stresses (such effects will be discussed below). S is the area of the newly formed interfacial surface, σ is its surface energy per unit area, $S(x)$ is the area of the nucleus cross section with the plane x perpendicular to the concentration gradient, and g is the Gibbs free energy per atom. To make the mathematics simpler, the following approximations are employed in the further analysis:

$$g^{\text{old}} \left(C \right) = g_0^{\text{old}} + \frac{\alpha^{\text{old}}}{2} \left(C - C_0^{\text{old}} \right)^2 \, , \tag{10.8}$$

$$g^{\text{new}} \left(C \right) = g_0^{\text{new}} + \frac{\alpha^{\text{new}}}{2} \left(C - C_0^{\text{new}} \right)^2 \, , \tag{10.9}$$

$$C \left(x \right) \cong C \left(0 \right) + x \nabla C \, . \tag{10.10}$$

Taking into account Eqs. (10.8)–(10.10), one obtains

$$\Delta G = n \int \left(A_0 + A_1 \nabla C \cdot x + A_2 \left(\nabla C \right)^2 x^2 \right) S(x) \, \mathrm{d}x + \sigma S$$

with

$$\begin{aligned} A_0 &= - \left(g_0^{\text{old}} - g_0^{\text{new}} + \frac{\alpha^{\text{old}} \left(C \left(0 \right) - C_0^{\text{old}} \right)^2}{2} - \frac{\alpha^{\text{new}} \left(C \left(0 \right) - C_0^{\text{new}} \right)^2}{2} \right) , \\ A_1 &= \alpha^{\text{new}} \left(C \left(0 \right) - C_0^{\text{new}} \right) - \alpha^{\text{old}} \left(C \left(0 \right) - C_0^{\text{old}} \right) \, , \\ A_2 &= \frac{\alpha^{\text{new}} - \alpha^{\text{old}}}{2} \, . \end{aligned} \tag{10.11}$$

Spherical Nuclei

Let the nucleus be a sphere with the center at some point x_c, so that the relation

$$S(x) = \pi \left(R^2 - (x - x_c)^2 \right)$$

holds. Then simple algebra transforms Eq. (10.7) into

$$\Delta G = \sigma 4\pi R^2 + n\pi \left(B_0 \tfrac{4}{3} R^3 + B_2 \tfrac{4}{15} R^5 \right) , \tag{10.12}$$

with

$$B_0 = A_0 + A_1 x_c \nabla C + A_2 x_c^2 (\nabla C)^2 , \quad B_2 = A_2 (\nabla C)^2 . \tag{10.13}$$

First of all one has to determine the optimal place for nucleation from the conditions

$$\begin{aligned} &\frac{\partial \Delta G}{\partial x_c} = 0 , \quad \frac{\partial^2 \Delta C}{\partial x_c^2} > 0 , \\ &x_c = -\frac{A_1}{2A_2 \nabla C} = \frac{\alpha^{\text{old}} \left(C(0) - C_0^{\text{old}} \right) - \alpha^{\text{new}} \left(C(0) - C_0^{\text{new}} \right)}{\left(\alpha^{\text{new}} - \alpha^{\text{old}} \right) \nabla C} . \end{aligned} \tag{10.14}$$

The above conditions correspond to a minimum if the inequality $\alpha^{\text{new}} > \alpha^{\text{old}}$ holds. Thus, when the concentration gradient changes with time, the optimal place of nucleation shifts but the corresponding concentration in the center

$$C(0) + x_c \nabla C = C(0) - \frac{A_1}{2A_2}$$

remains the same.

Furthermore we restrict ourselves to nuclei forming in the optimal place. In this case the size dependence of ΔG has the simple form

$$\Delta G(R) = \alpha R^2 - \beta R^3 + \gamma (\nabla C)^2 R^5 , \tag{10.15}$$

where

$$\begin{aligned} &\alpha = 4\pi\sigma , \quad \gamma = \frac{4\pi n}{15} \left(\frac{\alpha^{\text{new}} - \alpha^{\text{old}}}{2} \right) , \quad \beta = \frac{4\pi n}{3} \left(\frac{A_1^2}{4A_2} - A_0 \right) , \\ &\beta = \frac{4\pi n}{3} \left(g_0^{\text{old}} - g_0^{\text{new}} + \frac{\alpha^{\text{new}} \alpha^{\text{old}}}{2 \left(\alpha^{\text{new}} - \alpha^{\text{old}} \right)} \left(C_0^{\text{old}} - C_0^{\text{new}} \right)^2 \right) . \end{aligned} \tag{10.16}$$

The coefficient β fulfills the inequality $\beta > 0$ if the curve $g^{\text{new}}(C)$ intersects the curve $g^{\text{old}}(C)$. As follows from Eq. (10.15), the dependence $\Delta G(R)$ can be monotonically increasing or nonmonotonic in R, depending on the magnitude of the concentration gradient (Fig. 10.4).

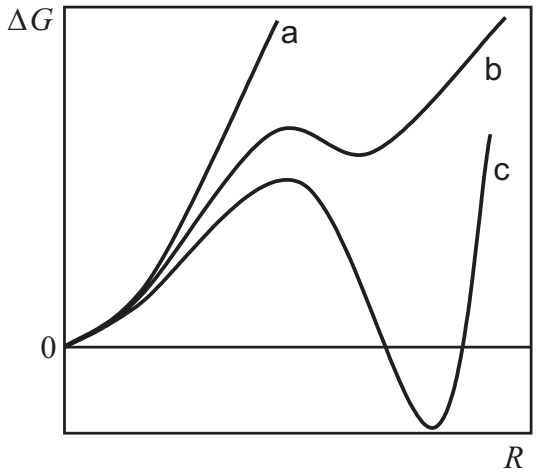

Figure 10.4: Size dependence of the Gibbs free energy due to the formation of a spherical particle in a concentration gradient (see text). (a) Nucleation is forbidden thermodynamically. (b) Metastable nuclei can be formed. (c) Nucleation is possible

Case (a) in Fig. 10.4 corresponds to full suppression of nucleation at sharp concentration gradients. It is found for

$$\nabla C > (\nabla C)_2^{\text{crit}} = \frac{\beta}{\alpha}\sqrt{\frac{\beta}{5\gamma}} \, .$$

Case (b) implies a possibility of metastable nucleus formation. It is realized if the conditions

$$(\nabla C)_2^{\text{crit}} > (\nabla C) > (\nabla C)_1^{\text{crit}} = \frac{\beta}{\alpha}\sqrt{\frac{4\beta}{27\gamma}}$$

hold. Case (c) allows the possibility of forming a stable particle of the new phase, the size of which will increase with decreasing (with time, due to interdiffusion) concentration gradients. It is realized for

$$\nabla C < (\nabla C)_1^{\text{crit}} \, .$$

Hereby simple algebra gives the following expressions for the critical values of the concentration gradient $(\nabla C)_{1,2}^{\text{crit}}$, corresponding to crossovers $c \leftrightarrow b$ and $b \leftrightarrow a$, respectively:

$$(\nabla C)_1^{\text{crit}} = \frac{\beta}{\alpha}\sqrt{\frac{4\beta}{27\gamma}} \, , \quad (\nabla C)_2^{\text{crit}} = \frac{\beta}{\alpha}\sqrt{\frac{\beta}{5\gamma}} \, . \tag{10.17}$$

One can see that the values of $(\nabla C)_1^{\text{crit}}$ and $(\nabla C)_2^{\text{crit}}$ are rather close, so that the regime of metastable nucleation is difficult to detect. Moreover, we shall see below that the shape optimization excludes this regime (if one does not take stresses into account).

Spheroidal Nuclei

Evidently, since concentration gradients suppress nucleus growth in the longitudinal direction, nature will find alternative possibilities of increasing the nucleus volume (and decreasing the Gibbs free energy) by transversal growth. This statement means that nuclei forming in the diffusion zone should be of nonspherical shapes. For each fixed nucleus volume, one has to take into account a shape optimization. A first attempt in this direction was made in 1991 [31]. Nuclei (embryos) were supposed to be spheroids, with a (rotational) symmetry axis directed along the ∇C-direction with parameters $R_{\|}$ ($\| x$) and $R_{\perp}$ ($\perp x$). In this case, ΔG is a function of two arguments, the volume V and the shape parameter $\eta = (R_{\perp}/R_{||})$ at a fixed concentration gradient $\nabla C = (1/L)$. One gets

$$\frac{\Delta G(R_{||}, R_{\perp})}{2\pi n} = -\frac{2}{3}\left\{\Delta g_0 R_{||} R_{\perp}^2 + \frac{g''}{15L^2} R_{||}^3 R_{\perp}^2 + \frac{2\sigma}{n}\left[\frac{R_{\perp}^2}{2} + \frac{R_{||} R_{\perp}^2}{2\sqrt{\left|R_{||}^2 - R_{\perp}^2\right|}}\right.\right.$$
$$\times \left\{\begin{array}{l} \ln\left(\sqrt{\left(\frac{R_{\perp}}{R_{||}}\right)^2 - 1} + \frac{R_{\perp}}{R_{||}}\right)\Bigg]\Bigg\}, \quad \frac{R_{\perp}}{R_{||}} > 1 \\ \arcsin\left(\sqrt{1 - \left(\frac{R_{\perp}}{R_{||}}\right)^2}\right)\Bigg]\Bigg\}, \quad \frac{R_{\perp}}{R_{||}} < 1\,, \end{array}\right. \tag{10.18}$$

where

$$R_{||} = \left(\frac{3V}{4\pi}\right)^{\frac{1}{3}} \eta^{-\frac{2}{3}}\,, \quad R_{\perp} = \left(\frac{3V}{4\pi}\right)^{\frac{1}{3}} \eta^{\frac{1}{3}}\,.$$

At any fixed volume V, the optimal shape $\eta\,(V)$ is found by minimizing the function $\Delta G\,(\eta|V)$. The function $\eta_{\mathrm{opt}}\,(V)$ increases to infinity at some value V^* (Figure 10.5), which is determined by the concentration gradient (the larger the ∇C, the less the V^*). The dependence $\Delta G(V, \eta_{\mathrm{opt}}(V))$ looks different for sharp and smooth concentration gradients (Figs. 10.5(a) and (b)).

Thus, the main result of the previous paragraph, the existence of a concentration gradient above which nucleation of an intermediate phase is forbidden, is reestablished. Yet, the possibility of metastable nuclei formation disappeared due to shape optimization. New results of the analysis are (i) the formation of plate-like nuclei (of course, this result is not valid if the critical value of ΔG is much higher than $60k_{\mathrm{B}}T$) and (ii) the decrease of the nucleation barrier and a corresponding increase of the value of the critical concentration gradient due to shape optimization.

Of course, the assumption of a spheroidal shape of the nucleus has to be justified as well. To verify this assumption and the validity of the above-mentioned results, we will present the results of the Monte Carlo (MC) simulation of nucleus formation in the following section.

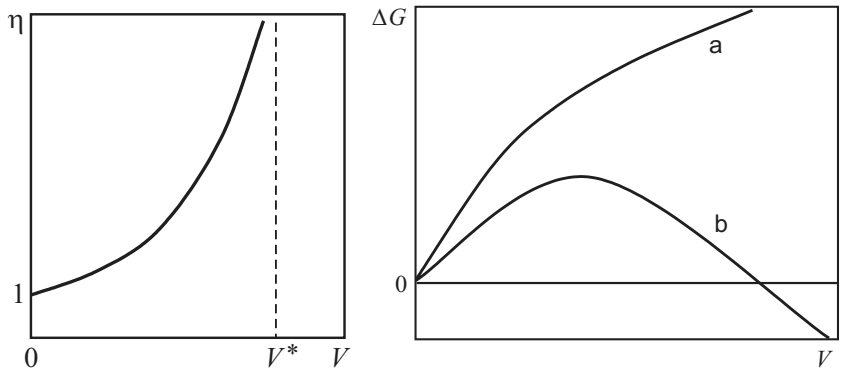

Figure 10.5: Left: Dependence of the optimal shape on the nucleus volume. Right: Dependence of the Gibbs free energy on the volume of the nucleus with optimized shape for (a) $\nabla C > (\nabla C)^{\text{crit}}$ and (b) $\nabla C < (\nabla C)^{\text{crit}}$

MC Simulation of Nucleus Shapes

Let the interdiffusion in the binary A–B couple lead to the formation of a metastable parent phase (solid solution or amorphous phase) with a concentration gradient inversely proportional to $\sqrt{Dt}$, where D is the diffusivity in the parent phase. We investigate the possible nucleation of the stable intermediate phase in this gradient. Let the concentration dependences of the Gibbs potential for both phases are approximately parabolic with minima at $C_0^{\text{new}} = C_0^{\text{old}} = (1/2)$ (latter approximation is important only for comparison with analytical solutions and is not required for the Monte Carlo simulation). The concentration profile in the parent phase in the vicinity of the forming nucleus is approximated by a linear dependence.

Here we limit ourselves to the polymorphic mode suggesting that nucleation proceeds fast in the frozen-in concentration gradient and concentration changes start due to diffusion after nucleation. We divide the homogeneous alloy into "elementary" cells, each of them can transform from the old to the new phase and vice versa, depending on thermodynamic profit that is determined by the bulk driving force and the number of neighboring cells with different phase states. The *simulation procedure* is anticipated as follows: Each cell is assumed to exist in one of two phase states, the old and new ones. The change of the state in the cell leads to a change of both bulk and surface energy terms. For example, if the cell transforms from the old to the new state then the change of the Gibbs potential for the system is equal to

$$\Delta G = \left(g^{\text{new}}(C) - g^{\text{old}}(C)\right) a^3 n + \sigma \Delta N a^2 \,. \tag{10.19}$$

Here C is the concentration in the cell depending on its position (x-coordinate, if the concentration gradient is parallel to x), n is the atomic density, a is the cell size, σ is the surface tension between old and new phases, ΔN is the change of the number of neighboring cells with different states (it is an even number ranging from -6 to $+6$). If ΔG is negative the transformation is accepted, otherwise the acceptance probability is given by $\exp(-\Delta G/k_B T)$ (Metropolis algorithm).

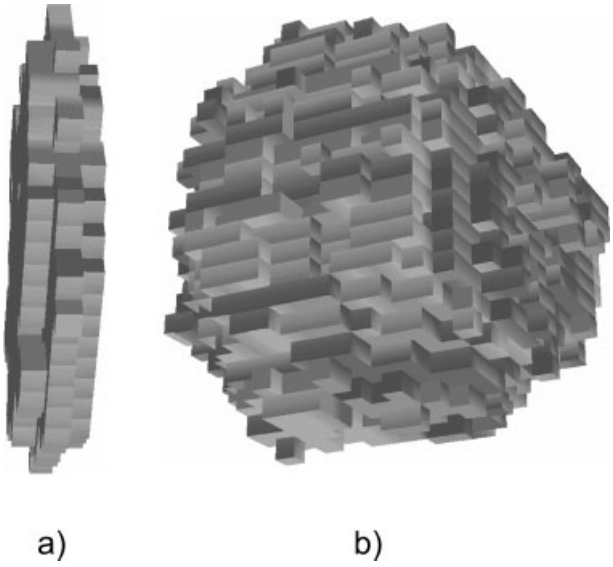

Figure 10.6: Examples of nucleus shape simulation results for sharp (a) $\nabla C = 10^9$ m^{-1} and smooth (b) $\nabla C = 10^7$ m^{-1} concentration gradients. The parameters employed in the simulation are $\sigma = 0.15$ J m^{-2}, $a = 1.5 \times 10^{-10}$ m, $n = 10^{29}$ m^{-3}, $(\partial^2 g/\partial C^2) = 7.77 \times 10^{-19}$ J, $g_0^{\text{old}} - g_0^{\text{new}} = 7.48 \times 10^{-21}$ J

In order to make the Monte Carlo procedure time saving we restrict changes of the state to cells in the boundary layer of the evolving nucleus. The following algorithm has been realized: (0) In the initial state, all cells belong to the old phase. Randomly, we choose one cell as a nucleation site and try its transformation according to the Metropolis procedure ($\Delta N = 6$). (1) One of the boundary cells is chosen randomly (the cell belongs to the boundary set if it belongs to the nucleus and has at least one neighbor of the old phase). (2) Furthermore, the cluster consisting of the chosen boundary cell and its six neighbors is analyzed. One of the seven cells of this cluster is chosen randomly. This choice is accepted if the chosen cell is central (transformation $new \rightarrow old$) or if it is a neighbor belonging to the old phase (transformation $old \rightarrow new$). Otherwise, the attempt is repeated. (3) The change of the Gibbs potential for a possible transformation is calculated according to Eq. (10.19) and the decision on acceptance/nonacceptance is made according to the Metropolis procedure. Step (2) of the above-mentioned algorithm artificially increases the probability of nucleus growth. Otherwise the subcritical embryo would be most probably destroyed and the formation of a supercritical nucleus would require a very long computation time. The results of the simulation are presented for sharp and smooth concentration gradients in Fig. 10.6.

Effect of Elastic Stresses

In the previous analysis, the difference of molar volumes of the new and parent phases leading to stresses and additional energy terms have been neglected. The influence of stresses on

intermediate phase nucleation was studied in detail in Ref. [35]; the respective results will be summarized here. We consider the case that the lattice of the intermediate phase differs from the parent lattice to such extent that the interface nucleus phase is incoherent from the very beginning. Taking into account elastic stresses, one can represent the change of the Gibbs free energy due to nucleation in the following form:

$$\Delta G = \Delta G_{\text{bulk}} + \Delta G_{\text{surf}} + \Delta G_{\text{elastic}} \,, \tag{10.20}$$

where the first two terms have been described above; the elastic term is written under the assumption of a spheroidal nucleus shape employing the Nabarro model

$$\Delta G_{\text{elastic}} = \frac{2}{3}\mu\Gamma^2 nV E\left(\frac{R_\perp}{R_{||}}\right) .$$

Here Γ is the dilatation ($\Gamma = (v^{\text{p}} - v^{\text{i}})/v^{\text{p}}$, where v^{i} and v^{p} are the atomic volumes of the intermediate and parent phases), V is the volume of the nucleus, E is the Nabarro function (see below), $2R_1$ is the longitudinal size, $2R_2$ is the transversal size, and μ is the shear modulus of the parent phase.

The Nabarro function is quite well approximated by the polynomial

$$E(x) = \tfrac{3}{4}\pi x - 3\left(\frac{\pi}{2} - 1\right)x^2 + \left(\tfrac{3}{4}\pi - 2\right)x^3 .$$

Employing the above given relations, a simple algebra leads to the following dependence of the Gibbs potential on the nucleus volume and shape factor $\varphi = (R_\perp/R_{||})$,

$$\begin{aligned}\Delta G(V,\varphi) = {} & -n\Delta g_m V + C_3\left(\frac{1}{\varphi}\right)^{\frac{4}{3}} V^{\frac{5}{3}} \\ & + C_4\left(\varphi^{\frac{2}{3}} + \frac{\ln\left(\sqrt{\varphi^2-1}+\varphi\right)}{\sqrt{\varphi^2-1}}\left(\frac{1}{\varphi}\right)^{\frac{1}{3}}\right) V^{\frac{2}{3}} + \tfrac{2}{3}\mu\frac{\left(v^{\text{i}}-v^{\text{p}}\right)^2}{v^{\text{p}}} E\left(\frac{1}{\varphi}\right) nV \,,\end{aligned} \tag{10.21}$$

where

$$C_3 = \frac{\pi n g''}{10\left(\frac{4}{3}\pi\right)^{\frac{2}{3}}} \,, \quad C_4 = \frac{2\pi\sigma}{\left(\frac{4}{3}\pi\right)^{\frac{2}{3}}} \,.$$

The shape is optimized at every fixed volume and then the dependence $\Delta G(V)$ for the optimized shape is investigated. As follows from a detailed analyis, taking account into the elastic energy changes the main results only quantitatively. The critical gradient still exists, but slightly decreases. Calculations have been carried out for the following parameters: $\alpha^{\text{new}} = 7.77 \times 10^{-19}$ J, $\Delta g_{\max} \equiv g_0^{\text{new}} - g_0^{\text{old}} = 7.77 \times 10^{-21}$ J, $\sigma = 0.15$ J m^{-2}, $\mu = 5 \times 10^{10}$ N m^{-2}. The dilatation was varied from 0 to 0.1. The dependences of the nucleation barrier on the concentration gradients for different dilatations are shown in Fig. 10.7.

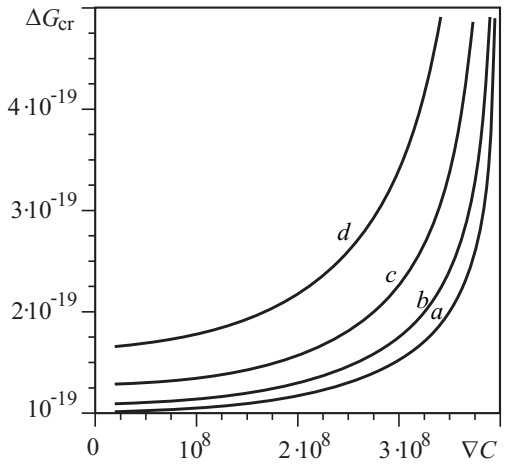

Figure 10.7: Dependence of the intermediate phase nucleation barrier ΔG_{cr} on the concentration gradient ∇C (in m^{-1}) for different values of dilatation: (a) $\Gamma = 0.00$, (b) $\Gamma = 0.01$, (c) $\Gamma = 0.03$, and (d) $\Gamma = 0.05$

Nucleation is practically suppressed for a sufficiently high nucleation barrier $\Delta G_{\mathrm{cr}} > 60 k_{\mathrm{B}} T$. We took $T = 600$ K (at which solid-state amorphizing reactions take place in the system Ni–Zr). One can see that the value of the critical gradient changes slightly, but the height of the nucleation barrier for gradients near the critical value can change significantly. For example, at a concentration gradient $\nabla C = 3 \times 10^8\ \mathrm{m}^{-1}$ the dilatation $\Gamma = 0.05$ increases the nucleation barrier by 65% and the nucleation probability decreases by 3×10^6 times. Stresses influence the nucleus shape as well (Fig. 10.7). Both factors – concentration gradient and stress – lead to plate-like nuclei. Thus, stresses arising due to nucleation of intermediate phases can influence the nucleation probability if the concentration gradient is close to the critical value (above which nucleation is totally forbidden).

Shape Optimization for Clusters with Rotational Symmetry: Rigorous Analytical Approach

Nucleation of phase 1 from the parent phase is considered at a first stage as a nondiffusive transformation without compositional changes involving only the reconstruction of the lattice. The change of the Gibbs free energy caused by nucleation can be expressed as

$$\Delta G = n \int_{x=-R_{||}}^{x=R_{||}} \Delta g\,(C(x))\,\pi\, y(x)^2\,\mathrm{d}x + \sigma \int_{x=-R_{||}}^{x=R_{||}} 2\pi\, y(x) \sqrt{1 + \left(\frac{\mathrm{d}y}{\mathrm{d}x}\right)^2}\,\mathrm{d}x\ , \quad (10.22)$$

if one neglects stresses and crystal peculiarities and considers the nucleus to be a body of revolution with arbitrary boundary shape $y(x)$. The second term is the ordinary surface energy. The first term shows the gain in the bulk Gibbs free energy at nucleation taking into account

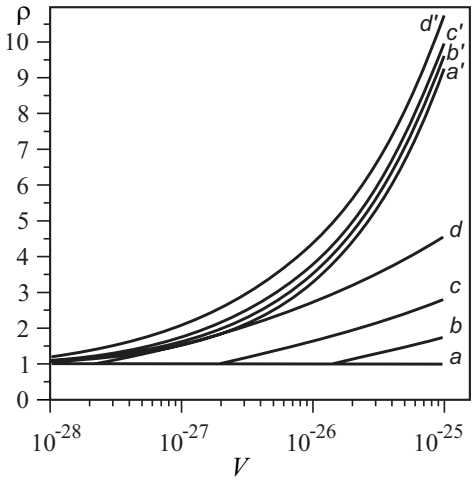

Figure 10.8: Shape parameter $\rho = R_{\perp}/R_{||}$ versus the nucleus volume V (in m^{-3}) at dilatations $\Gamma = 0.0, 0.05, 0.07, 0.10$ and a concentration gradient $\nabla C = 2.2 \times 10^8\ \mathrm{m}^{-1}$ (curves a', b', c', d') and without gradient (curves a, b, c, d)

the nonuniformity of the driving force. In the case of a constant value of Δg the first term would depend only on the volume, not on the shape. The shape would be determined by the minimization of the second term and would be spherical. If the concentration gradient exists the first term depends on the shape as well. The shape can be found from the variation problem for $\Delta G\,(y\,(x)\,, V)$ at every fixed volume V. Then one can build the dependence $\Delta G\,(V)$ considering the shape to be optimized for every V. Omitting rather tricky mathematics and the details of the numeric algorithm (cf. [32]), we review here only the main results.

We found the existence of a scale invariance: The nucleus shape depends on the volume and concentration gradient via the ratio V/L^2 (strictly speaking, via the parameter $P = (C_1 V/C_2 L^2)$, where $C_1 = (ng''/2\,(2\pi)^{\frac{2}{3}})$, $C_2 = (2\pi\sigma/\,(2\pi)^{\frac{2}{3}})$). We determined the optimal nucleus shape and the dependence $\Delta G\,(V)$ for values of P varying from 0 to 20. For larger values of P the convergence interval becomes very narrow and to get into this interval one must take very small steps ΔV.

As mentioned above the nucleus shape is determined only by the parameter P. At first, both longitudinal and transversal sizes increase, but the transversal size increases faster, so that deviations from spherical shape also increase. Yet the shape differs substantially from spheroidal: the corresponding coefficient of variation increases with P (0.5% at $P = 0.5$ and 21% at $P = 15.8$). Thus, according to our calculations, if the nucleus can grow, it must form almost flat "pancake" like islands. The dependence of the change of the Gibbs potential on the nucleus volume is determined by the concentration gradient or by the parameter L. At $L < L^*$ this dependence appeared to be monotonic (Fig. 10.8(a)), which implies a thermodynamic prohibition of the new intermediate phase formation at a sharp concentration gradient (initial stage of reactive diffusion). At $L < L^*$, the dependence $\Delta G\,(V)$ has a familiar form with a maximum corresponding to the critical nucleus. In contrast to the result obtained for the case

of spherical nuclei, a second extremum – a minimum – is absent. This result implies that in the absence of stresses the transversal growth of nuclei is restricted only by other nuclei and/or by sample borders.

Completing the analysis, we give below a summary of results for the polymorphic nucleation mode:

1. Nucleation of an intermediate phase is thermodynamically forbidden if the diffusion zone is too narrow:

$$\left(\frac{\partial C}{\partial x} > \frac{1}{L^*}\right) .$$

2. If nucleation is possible at

$$\left(\frac{\partial C}{\partial x} < \frac{1}{L^*}\right) ,$$

the nucleus has a nonspherical shape which differs substantially from a spheroidal one. Its shape is determined by the ratio (V/L^2).

3. The nucleus grows mainly in a direction transversal to the concentration gradient; the ratio $(R_\perp/R_{||})$ tends rapidly to infinity with increasing volume and can be restricted only by other nuclei or sample borders or by composition fluctuations.

4. Nucleation at the grain boundary changes the results only quantitatively.

5. Taking into account elastic stresses practically does not change the critical value of the concentration gradient but changes the nucleation barriers.

10.3.3 Transversal Nucleation Mode

The transversal nucleation mode was first introduced by Desre and Yavari [24] for cubic nuclei without shape optimization. In 1998 shape optimization was performed by Hodaj, Gusak, and Desre [15] for the simplest case of parallelepipeds in the following way. Let an embryo (nucleus) in the form of a parallelepiped $2h \times 2h \times 2r$ be formed in the concentration gradient ∇C of a metastable parent phase ($2r$ along ∇C). Every thin slice $2h \times 2h \times \mathrm{d}x$ with a concentration $C^{\mathrm{new}}(x)$ forms at the cost of the slice $\infty \times \infty \times \mathrm{d}x$ with the concentration $C^{\mathrm{old}}(x)$ according to the rule of parallel tangents (Fig. 10.9).

To avoid the misunderstanding, we will prove this rule. Consider a small volume ΔV of the new phase with a concentration C^{new} and components B, formed in a large volume V_0 of the old phase with an initial concentration C^{old} ($V_0 \gg \Delta V$). The formation of the new phase slightly changes the concentration of the old phase, so that $\Delta C = (C^{\mathrm{old}} - C^{\mathrm{new}}/V_0 - \Delta V)\Delta V$ (taking conservation of matter into account). The change of the Gibbs free energy due to new phase formation is then given by

$$\Delta G = \sigma S + n\left[g^{\mathrm{new}}\left(C^{\mathrm{new}}\right)\Delta V + g^{\mathrm{old}}\left(C^{\mathrm{old}} + \Delta C\right)(V_0 - \Delta V) - g^{\mathrm{old}}\left(C^{\mathrm{old}}\right)V_0\right] ,$$

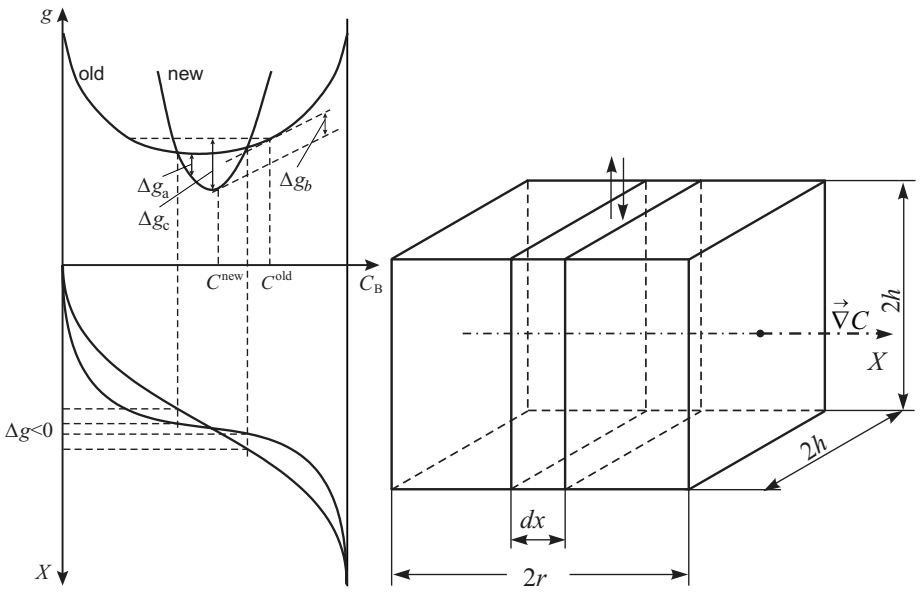

Figure 10.9: Left: Scheme of driving forces per atom of the nucleus for (a) polymorphic, (b) transversal and (c) total mixing modes. Right: Scheme of transversal nucleation modes; vertical arrows show the direction of redistribution in the slice dx

with

$$g^{\mathrm{old}}\left(C^{\mathrm{old}}+\Delta C\right)\approx g^{\mathrm{old}}\left(C^{\mathrm{old}}\right)+\frac{\partial g^{\mathrm{old}}}{\partial C}\Delta C\ .$$

Here S is the interface area, and σ is the surface tension. Substituting ΔC from the condition of conservation of mass, one obtains

$$\begin{aligned}\Delta G&=\sigma S-\Delta V n\left(g^{\mathrm{old}}\left(C^{\mathrm{old}}\right)+\frac{\partial g^{\mathrm{old}}}{\partial C^{\mathrm{old}}}\left(C^{\mathrm{new}}-C^{\mathrm{old}}\right)-g^{\mathrm{new}}\left(C^{\mathrm{new}}\right)\right)\\&=\sigma S-N\Delta g\ .\end{aligned}$$

The value ΔG is minimal for such C^{new}, for which

$$\frac{\partial\Delta G}{\partial C^{\mathrm{new}}}=0=-\Delta V\left(\frac{\partial g^{\mathrm{old}}}{\partial C^{\mathrm{old}}}-\frac{\partial g^{\mathrm{new}}}{\partial C^{\mathrm{new}}}\right)$$

holds. Thus, a maximal decrease of the Gibbs free energy (and the corresponding maximal formation probability) is reached for C^{new}, satisfying the rule of parallel tangents. The driving force *per atom of the nucleus* (not of the total system) is equal to

$$\Delta g_b=g^{\mathrm{old}}\left(C^{\mathrm{old}}\right)+\frac{\partial g}{\partial C}\left(C^{\mathrm{new}}-C^{\mathrm{old}}\right)-g^{\mathrm{new}}\left(C^{\mathrm{new}}\right)\ ,$$

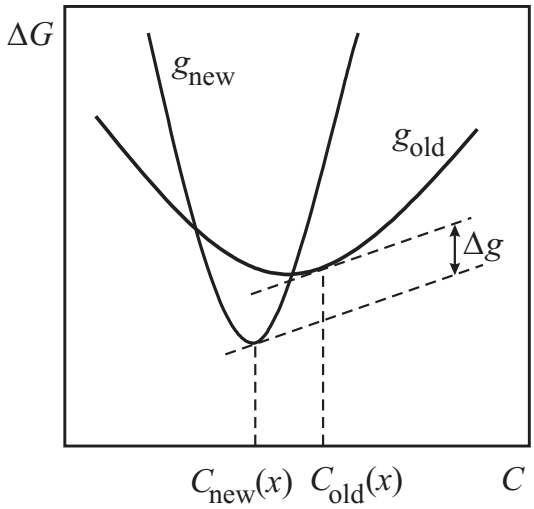

Figure 10.10: Rule of parallel tangents

and is determined by the vertical interval between two parallel tangents as shown in Fig. 10.10.

Using the rule of parallel tangents for each thin slice dx of the parallelepiped, one obtains

$$\Delta G = -n \int_{x_c-r}^{x_c+r} \Delta g \left(C^{\text{old}}(x) \longrightarrow C^{\text{new}}(x) \right) 4h^2 \, \mathrm{d}x + 2\sigma_1 4h^2 + 4\sigma_2 4hr \ ,$$

where

$$C^{\text{old}}(x) = C(0) + x\nabla C \ , \quad C^{\text{new}}(x) = C_0^{\text{new}} + \frac{\alpha^{\text{old}}}{\alpha^{\text{new}}} \left(C^{\text{old}}(x) - C_0^{\text{new}}(x) \right) \ .$$

Here σ_1 and σ_2 are the surface tensions for phases located perpendicular and parallel to the concentration gradient. Rather simple algebra, analogous to that in Sect. 10.3, shows that the optimal center for nucleation is determined by

$$C_{\text{opt}} = x_c \nabla C + C(0) = C_0^{\text{old}} + \frac{C_0^{\text{new}} - C_0^{\text{old}}}{1 - \dfrac{\alpha^{\text{old}}}{\alpha^{\text{new}}}} \ . \tag{10.23}$$

In this case

$$\Delta G = -\alpha 8h^2 r + \gamma \ (\nabla C)^2 \, h^2 r^3 + 8 \left(\sigma_1 h^2 + 2\sigma_2 hr \right) \tag{10.24}$$

holds, where

$$\alpha = n\left(g_0^{\text{old}} - g_0^{\text{new}} + \frac{\alpha^{\text{old}}}{2\left(1-\dfrac{\alpha^{\text{old}}}{\alpha^{\text{new}}}\right)}\left(C_0^{\text{new}} - C_0^{\text{old}}\right)^2\right) ,$$
$$\gamma = \frac{4\pi n}{3}\alpha^{\text{old}}\left(1-\frac{\alpha^{\text{old}}}{\alpha^{\text{new}}}\right) . \tag{10.25}$$

It is convenient to express ΔG as a function of the volume $V = 8h^2 r$ and the shape parameter

$$\varphi = \frac{h}{r} , \quad r = \frac{1}{2}V^{\frac{1}{3}}\varphi^{-\frac{2}{3}} , \quad h = \frac{1}{2}V^{\frac{1}{3}}\varphi^{\frac{1}{3}} ,$$

resulting in

$$\Delta G\,(V,\varphi) = -aV^1 + \frac{(\nabla C)^2\,\gamma}{32}\varphi^{-\frac{3}{2}}V^{\frac{5}{3}} + 2\sigma_1\left(\varphi^{\frac{2}{3}} + 2s\varphi^{-\frac{1}{3}}\right)V^{\frac{2}{3}} , \tag{10.26}$$

where $s = (\sigma_2/\sigma_1)$ is the Wulff parameter. The function $\Delta G\,(V \mid \varphi)$ has, at every fixed volume, one minimum, which is determined by the condition $(\partial G/\partial\varphi) = 0$, which gives the following expression for the optimal shape:

$$\varphi_{\text{opt}} = \left(\frac{h}{r}\right)_{\text{opt}} = \frac{s}{2} + \sqrt{\frac{s^2}{4} + \frac{\gamma\,(\nabla C)^2 V}{32\sigma_1}} . \tag{10.27}$$

For small volumes it leads to the Wulff rule

$$\varphi_{\text{opt}}\,(V \to 0) = s = \frac{\sigma_2}{\sigma_1} . \tag{10.28}$$

For large volumes, the shape parameter tends to infinity as $V^{\frac{1}{2}}$, i.e.,

$$\varphi_{\text{opt}}\,(V \to \infty) \approx \left(\nabla C^2 V\right)^{\frac{1}{2}}\left(\frac{\gamma}{32\sigma_1}\right)^{\frac{1}{2}} , \tag{10.29}$$

which implies a plate-like shape – the concentration gradient limits the longitudinal size,

$$r_{V\to\infty} \to r_{\max} = \left(\frac{4\sigma_1}{\gamma\,(\nabla C)^2}\right)^{\frac{1}{3}} \sim (\nabla C)^{-\frac{2}{3}} , \tag{10.30}$$

but does not limit the transversal growth,

$$h_{V\to\infty} \sim V^{\frac{1}{3}}\left(V^{\frac{1}{2}}\right)^{\frac{1}{3}} = V^{\frac{1}{2}} \to \infty .$$

One can see that the shape parameter depends on the product $(\nabla C)^2\,V$, which implies some kind of scale invariance.

Thus, the volume dependence of ΔG for optimized shapes is given by

$$\Delta G = -\alpha V^1 + \frac{\gamma\,(\nabla C)^2}{32}\left[\frac{s}{2} + \left(\frac{s^2}{4} + \frac{\gamma\,(\nabla C)^2\,V}{32\sigma_1}\right)^{\frac{1}{2}}\right]^{-\frac{4}{3}} V^{\frac{5}{3}} + 2\sigma_1\left\{\left[\frac{s}{2} + \left(\frac{s^2}{4} + \frac{\gamma\,(\nabla C)^2\,V}{32\sigma_1}\right)^{\frac{1}{2}}\right]^{\frac{2}{3}} + 2s\left[\frac{s}{2} + \left(\frac{s^2}{4} + \frac{\gamma\,(\nabla C)^2\,V}{32\sigma_1}\right)^{\frac{1}{2}}\right]^{-\frac{1}{3}}\right\} V^{\frac{2}{3}}\,. \quad (10.31)$$

In the limiting cases of small and large volumes, we have

$$\begin{aligned}\Delta G\,(V \to 0) &\approx 6\left(\sigma_1\sigma_2^2\right)^{\frac{1}{3}} V^{\frac{2}{3}}\,,\\ \Delta G\,(V \to \infty) &\approx \left[-\alpha + (\nabla C)^{\frac{2}{3}}\,\frac{3}{2}\left(\frac{\sigma_1^2\gamma}{4}\right)^{\frac{1}{3}}\right] V^1\,,\end{aligned} \quad (10.32)$$

respectively. One can easily see that, depending on the value of the concentration gradient, ΔG can be a monotonically increasing function or nonmonotonic with a maximum (nucleation barrier). For

$$\nabla C > (\nabla C)^{\mathrm{crit}} = \frac{4\alpha}{3\sigma_1}\left(\frac{2}{3}\frac{a}{\gamma}\right)^{\frac{1}{2}}$$

nucleation is forbidden; for

$$\nabla C < (\nabla C)^{\mathrm{crit}}$$

nucleation is possible. Thus, the transversal mode under the condition of shape optimization, gives qualitatively the same results as the polymorphic mode:

1. Nuclei should be more plate-like – the more the volume, the more the concentration gradient – the shape being determined by their product $(\nabla C)^2\,V$.
2. Nucleation is forbidden if the concentration gradient exceeds a certain critical value about 10^8–$10^9\ \mathrm{m}^{-1}$.

10.3.4 Total Mixing Mode of Nucleation

Another possibility of nucleation in a fixed gradient is a redistribution of components only inside the forming nucleus resulting in a constant concentration C^{new} and a new lattice, and

an unchanged gradient outside the nucleus. In this case, the change of the Gibbs free energy due to formation of the nucleus of the parallelepipedal shape $2h \times 2h \times 2r$ is given by the following expression:

$$\Delta G = 4\left(2\sigma_1 h^2 + 4\sigma_2 hr\right) + n4h^2 \int_{x_c - r}^{x_c + r} \left\{ g^{\text{new}}\left[C^{\text{new}}(x) - g^{\text{old}}\left(C^{\text{old}}(x)\right)\right]\right\} \mathrm{d}x \ , \quad (10.33)$$

where x_c is the coordinate of the nucleus center,

$$C^{\text{old}}(x) = C(0) + x\nabla C \ , \quad C^{\text{new}}(x) = C(0) + x\nabla C = \text{const} \ ,$$

and g^{new} and g^{old} are parabolic as in previous sections. Optimization of the place of nucleation x_c gives

$$C\,(0) + x_{\text{c}}\nabla C = \frac{C_0^{\text{new}} - C_0^{\text{old}}}{1 - \dfrac{\alpha^{\text{old}}}{\alpha^{\text{new}}}} + C_0^{\text{old}} \ . \quad (10.34)$$

For this optimal place of nucleation simple mathematics leads to the relation

$$\Delta G = 4\left(2\sigma_1 h^2 + 4\sigma_2 hr\right) - \alpha 8h^2 r + \gamma_{||}\left(\nabla C\right)^2 h^2 r^3 \ , \quad (10.35)$$

where

$$\alpha = n\left(g_0^{\text{old}} - g_0^{\text{new}} + \frac{\alpha^{\text{old}}}{2}\frac{\left(C_0^{\text{new}} - C_0^{\text{old}}\right)^2}{1 - \dfrac{\alpha^{\text{old}}}{\alpha^{\text{new}}}}\right) \ , \quad \gamma_{||} = -\frac{4n}{3}\alpha^{\text{old}} \ . \quad (10.36)$$

The main peculiarity here is the negative sign of $\gamma_{||}$. This property implies that, in contrast to the polymorphic and transversal modes, in the case of operating the total mixing mode the concentration gradient *favors* nucleation. Therefore, at any concentration gradient nucleation via the total mixing mode is always possible in thermodynamic sense. As we will see at the end of this chapter, kinetics can nevertheless suppress such nucleation mode.

The most interesting feature in the case of total mixing mode is the behavior of the shape of the nuclei. The dependence $\Delta G\,(\varphi)$ is, at fixed volumes, nonmonotonic with one minimum and one maximum for small volumes (Fig. 10.11(a)) and monotonically increasing for large volumes (Fig. 10.11(b)). The extremum condition $(\partial G/\partial\varphi)$ leads to

$$\varphi^2 - S\varphi + \frac{\gamma_{||}\left(\nabla C\right)^2 V}{32\sigma_1} = 0$$

with two solutions

$$\varphi_{1,2} = \frac{S}{2} \pm \sqrt{\frac{S^2}{4} - \gamma_{||}\frac{\left(\nabla C\right)^2 V}{32\sigma_1}} \ .$$

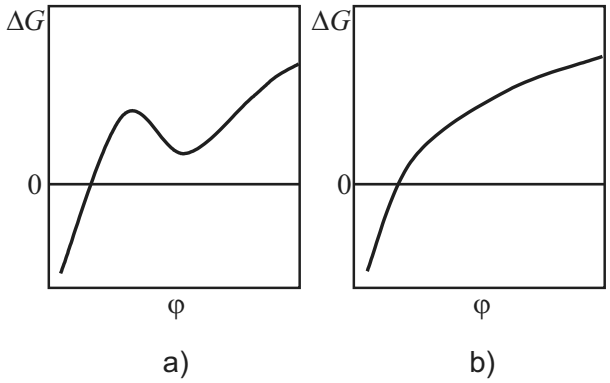

Figure 10.11: Dependence of ΔG on the shape parameter φ for the total mixing mode at small ((a) $(\nabla C)^2 V < (8S^2\sigma_1/\gamma_{||})$) and large ((b) $(\nabla C)^2 V > (8S^2\sigma_1/\gamma_{||})$) values of $(\nabla C)^2 V$

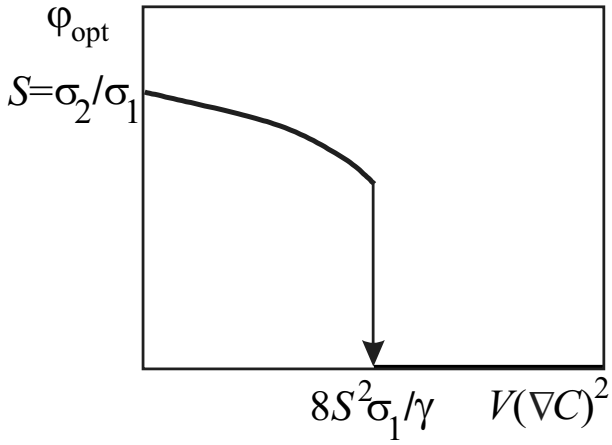

Figure 10.12: "Phase shape transition" for the total mixing mode

The first solution corresponds to a metastable minimum and the second to a maximum. These solutions disappear for $(\nabla C)^2 V > (8S^2\sigma_1/\gamma_{||})$, so that the nucleus should rapidly transform into a needle-like structure (see Fig. 10.12). Thus, one has something like a shape phase transition. Obviously all above-mentioned considerations are valid only for $\nabla C = \text{const}$ along the nucleus, so that the needle cannot exceed the size of the diffusion zone. Of course, the total mixing mode should operate as well if the redistribution in the transversal direction in the parent phase is absent. For this case, the diffusivity of the new phase should be much larger than that of the old one.

10.4 Thermodynamics of Nucleation at the Interface: The Case of Limited Metastable Solubility

10.4.1 Nucleation of Line Compounds at the Interface during Interdiffusion

Let us consider now the case that phases L and R have already developed some concentration profiles $C_L(X)$ and $C_R(X)$ with a concentration gap (C_{LR}, C_{RL}) and metastable regions (C_{Li}, C_{RL}) and (C_{LR}, C_{Ri}), favorable for nucleation of a line compound "i" (Fig. 10.13). Let us find the change of the Gibbs free energy due to nucleation (by transversal mode) of a parallelepiped $2h \times 2h \times 2r$ of the new phase with $2h$ being the size in the lateral (axes Y, Z) directions under the influence of a concentration gradient in the longitudinal (axis X) direc-

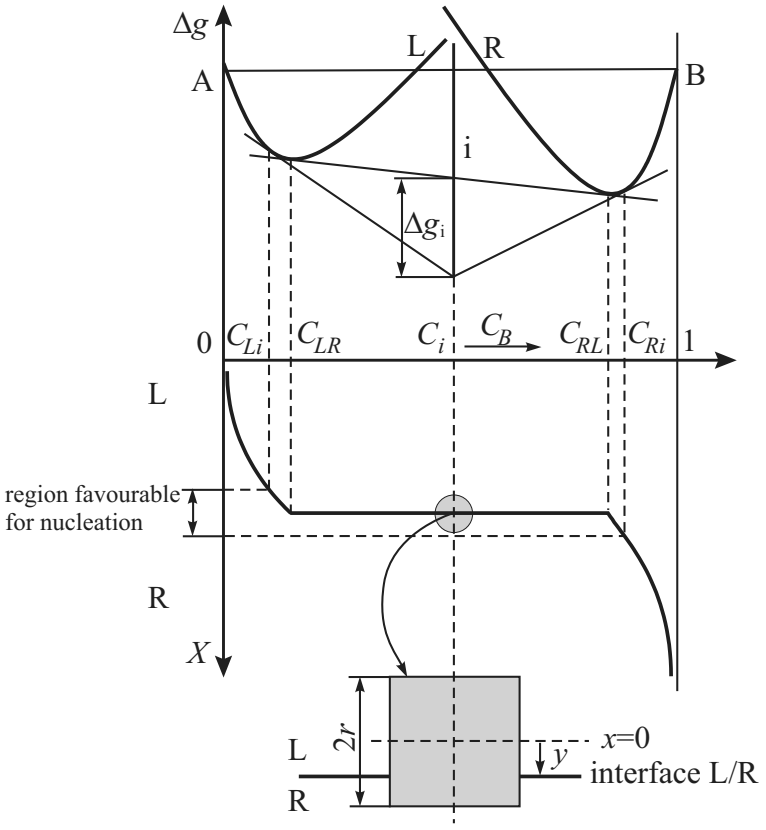

Figure 10.13: Schematic representation of intermediate phase nucleation at the L/R interface with L and R being the parent phases. Δg_i is the driving force per mole of atoms for the $L + R \rightarrow i$ reaction. The distribution of the nucleus volume among the phases is determined by an additional optimization procedure

tion. The longitudinal size $2r$ consists of parts overlapping the phases L and R and originated from these phases, i.e., $2r = r_L + r_R$. Then we get

$$\Delta G = 4h^2\left(\sigma_{iL} + \sigma_{iR} - \sigma_{LR}\right) + 4(2h)\left(r_L\sigma_{iL} + r_R\sigma_{iR}\right) + \frac{1}{\Omega}\int\limits_{y-r_L}^{y} \Delta g\left(C_L(X) \longrightarrow C_i\right) 4h^2\,\mathrm{d}X + \frac{1}{\Omega}\int\limits_{y}^{y+r_R} \Delta g\left(C_R(X) \longrightarrow C_i\right) 4h^2\,\mathrm{d}X\ . \tag{10.37}$$

Here Ω is the atomic volume of phase "i", σ_{iL}, σ_{iR}, and σ_{LR} are the corresponding surface tensions, and y specifies the position of the L/R interface with respect to the x-axis ($x = 0$ is located at the center of the embryo). The driving forces per atom of the nucleus for $L^{\text{metast}} \longrightarrow i$ and $R^{\text{metast}} \longrightarrow i$ precipitation are expressed by the "parallel tangents rule" (not to confuse with the "common tangent rule"); for $L^{\text{metast}} \longrightarrow i$, we get

$$-\Delta g\left(C_L\left(X\right) \longrightarrow C_i\right) = g_L\left(C_L\left(X\right)\right) - g_i - \left(C_L\left(X\right) - C_i\right)\left.\frac{\partial g_L}{\partial C}\right|_{C=C_L(X)} \tag{10.38}$$

and a similar expression for $R^{\text{metast}} \longrightarrow i$ by analogy. Further we employ expansions into Taylor series both for concentrations and for Gibbs free energies per atom, resulting in

$$\begin{aligned} C_L\left(X\right) &\approx C_L\left(y\right) + \left(X - y\right)\nabla C_L|_{X=y-0} \quad \text{for} \quad X < y\ , \\ C_R\left(X\right) &\approx C_R\left(y\right) + \left(X - y\right)\nabla C_R|_{X=y+0} \quad \text{for} \quad X > y\ , \end{aligned} \tag{10.39}$$

$$\begin{aligned} g_L\left(C_L\right) &\approx g_L\left(C_{LR}\right) + \left(C_L - C_{LR}\right) g'_L + \frac{\left(C_L - C_{LR}\right)^2}{2} g''_L\ , \\ g_R\left(C_R\right) &\approx g_R\left(C_{RL}\right) + \left(C_R - C_{RL}\right) g'_R + \frac{\left(C_R - C_{RL}\right)^2}{2} g''_R\ . \end{aligned} \tag{10.40}$$

Here the first- and second-order derivatives with respect to the concentration are taken at the metaequilibrium compositions C_{LR} and C_{RL} (see Fig. 10.13). Substitution of Eqs. (10.39)–(10.40) into Eq. (10.38), and then Eq. (10.38) into Eq. (10.37) gives, after simple but extended algebra,

$$\begin{aligned} \Delta G = \left[4h^2\left(\sigma_{iL} + \sigma_{iR} - \sigma_{LR}\right) + 42h\left(r_L\sigma_{iL} + r_R\sigma_{iR}\right)\right] + \Delta g_i \frac{4h^2}{\Omega}\left(r_L + r_R\right) \\ + \frac{2h^2}{\Omega}\left[\left(C_i - C_{LR}\right) g''_L \nabla C_L r_L^2 + \left(C_{RL} - C_i\right) g''_R \nabla C_R r_R^2\right] \\ + \frac{2h^2}{3\Omega}\left[g''_L\left(\nabla C_L\right)^2 r_L^3 + g''_R\left(\nabla C_R\right)^2 r_R^3\right]\ . \end{aligned} \tag{10.41}$$

Here $(-\Delta g_i)$ is the driving force of the reaction $L + R \longrightarrow i$ per atom of i.

The first two terms in Eq. (10.41) represent the classical model of heterogeneous nucleation $\Delta G^{\text{classic}}$ (yet, without taking into account Young's equilibrium conditions at the three-phase junctions – otherwise we would have a nonsymmetrical cap with much less transparent

mathematics for the gradient effects). The gradient effect is represented here both by linear ∇C terms and by quadratic $(\nabla C)^2$ terms providing, respectively, a fourth and fifth order power size dependence. In the case of total metastable solubility, the optimization of the nucleation place had led to elimination of the linear terms in the concentration gradient (Sect. 10.3). In the case of limited solubility, they remain and, moreover, may play a decisive role. Indeed, $r_L \nabla C_L$ is evidently less than the metastable composition range $\Delta C_L = C_{LR} - C_{Li}$ of the L-phase and $r_R \nabla C_r < \Delta C = C_{Ri} - C_{RL}$. If we consider as parent only those phases with small mutual solubility (as we do here!), then we can neglect the terms $(\nabla C)^2 r^3$ in comparison with $(\nabla C)^1 r^2$, since $\nabla C r \ll 1$. In this case, we arrive at

$$\Delta G = \Delta G^{\text{classic}} + \frac{2h^2}{\Omega}\left[(C_i - C_{LR})\, g''_L \nabla C_L r_L^2 + (C_{RL} - C_i)\, g''_R \nabla C_R r_R^2\right] . \quad (10.42)$$

Equation (10.42) is the basic one for the further analysis.

Minimization of ΔG with respect to r_L or r_R (with fixed sum $2r$) results, in the particular case of equal surface tensions σ for all interfaces, in

$$r_L = 2r\frac{\Lambda}{1+\Lambda} , \quad r_R = 2r\frac{1}{1+\Lambda} \quad (10.43)$$

with

$$\Lambda = \frac{(C_{RL} - C_i)\, g''_R \nabla C_R}{(C_i - C_{LR})\, g''_L \nabla C_L} . \quad (10.44)$$

Substituting Eqs. (10.43)–(10.44) into Eq. (10.42), one has the following expression for the change of the Gibbs free energy due to nucleation,

$$\Delta G = \Delta G^{\text{classic}} + \frac{8h^2 r^2}{\Omega}\frac{A_L A_R}{A_L + A_R} \quad (10.45)$$

with

$$A_L = (C_i - C_{LR})\, g''_L \nabla C_L , \quad A_R = (C_{RL} - C_i)\, g''_R \nabla C_R .$$

The values of the products $g''\nabla C$ are the most important parameters for the further estimates. Let us take them as known.

From Eqs. (10.43)–(10.44) it is evident that the nucleus will prefer to overlap more with the smaller gradient term $g''\nabla C$. Also from Eq. (10.45) one can conclude that the gradient contribution to the change of the Gibbs free energy is controlled by the smaller of the two terms A_L and A_R and determined by $g''\nabla C$ (differences of compositions are of the order of unity). Note that for the simplest case of a cubic shape, $h = r$, one has, for a limited solubility within the parent phase (instead of Eq. (10.1) for full solubility within the parent phases), the relation

$$\Delta G\,(r) = \Delta G^{\text{classic}} + qr^4 = \alpha r^2 - \beta r^3 + qr^4 \quad (10.46)$$

with

$$\alpha = 20\sigma , \quad \beta = \frac{8\Delta g_i}{\Omega} , \quad q = \frac{8}{\Omega}\frac{A_L A_R}{A_L + A_R} . \quad (10.47)$$

Depending on the value of q, the $\Delta G(r)$ dependence can be monotonically increasing (large q, nucleation forbidden), or with a metastable minimum (intermediate values of q), or with a stable minimum (small q, nucleation possible) in analogy with the results presented in Fig. 10.4. A crossover to possible nucleation (second minimum at zero level) means

$$\left.\frac{\partial \Delta G}{\partial r}\right|_{r^*} = 0 \,, \quad \Delta G\left(r^*\right) = 0 \,. \tag{10.48}$$

It gives

$$r^* = \frac{2\alpha}{\beta} = 5\frac{\sigma\Omega}{\Delta g_i} \,, \quad q^{\text{crit}} = \frac{\beta^2}{4\alpha} = \frac{4\left(\Delta g_i\right)^2}{5\sigma\Omega^2} \tag{10.49}$$

or

$$\left[\frac{A_L A_R}{A_L + A_R}\right]^{\text{crit}} = \frac{\left(\Delta g_i\right)^2}{10\sigma\Omega} \,. \tag{10.50}$$

The intermediate phase suppression criterion is then

$$\frac{A_L A_R}{A_L + A_R} > \frac{\left(\Delta g_i\right)^2}{10\sigma\Omega} \,. \tag{10.51}$$

Let us recall that $(-\Delta g_i)$ is the driving force of the reaction $L + R \longrightarrow i$ per atom of i. Below we will apply the just developed formalism to different types of adjacent phases L and R.

10.4.2 Nucleation between Two Growing Intermediate Phase Layers

Let L and R be the intermediate phases 1 and 3, growing simultaneously between mutually almost insoluble materials A and B. We study here nucleation of phase 2 at the interface 1/3 (cf. Fig. 10.14). We suppose that 1, 2, and 3 are line compounds. In this case it is more convenient to treat chemical potential gradients instead of concentration gradients. Mathematically it can be done via

$$\begin{aligned} g_1'' \nabla C_1 = \frac{\partial}{\partial X}\left(\frac{\partial g_1}{\partial C}\right) &\approx \frac{\left.\frac{\partial g_1}{\partial C}\right|_{13} - \left.\frac{\partial g_1}{\partial C}\right|_{1\alpha}}{\Delta X_1} = \frac{\frac{g_3 - g_1}{C_3 - C_1} - \frac{g_1 - g_\alpha^m}{C_1 - 0}}{\Delta X_1} \\ &= \frac{C_3}{C_1\left(C_3 - C_1\right)}\frac{(-\Delta g_{10})}{\Delta X_1} \,, \end{aligned} \tag{10.52}$$

where $(-\Delta g_{10})$ is a driving force of the reaction $A + 3 \longrightarrow 1$ (see Fig. 10.14). Similarly,

$$g_3'' \nabla C_3 = \frac{1 - C_1}{\left(1 - C_3\right)\left(C_3 - C_1\right)}\frac{(-\Delta g_{30})}{\Delta X_3} \,, \tag{10.53}$$

where $(-\Delta g_{30})$ is a driving force of reaction $1 + B \longrightarrow 3$. Thus, in this case, we have

$$A_L = A_1 = w_1\frac{(-\Delta g_{10})}{\Delta X_1} \,, \quad A_R = A_3 = w_3\frac{(-\Delta g_{30})}{\Delta X_3} \,, \tag{10.54}$$

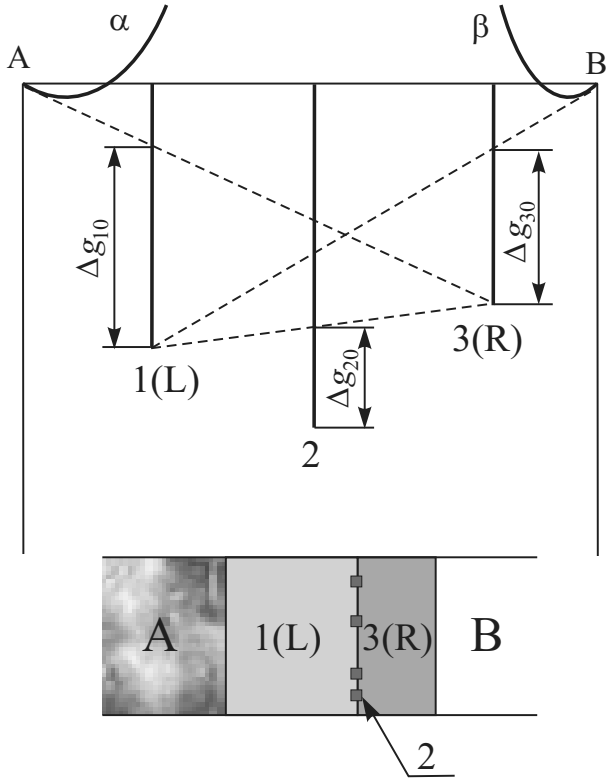

Figure 10.14: Schematic representation of phase 2 nucleation between phases 1 and 3 already growing in an A/B couple. Δg_{10}, Δg_{30}, and Δg_{20} are the driving forces per mole of atoms for the reactions $A + B \to 1$, $A + B \to 3$, and $1 + 3 \to 2$, respectively

where

$$w_1 = \frac{(C_2 - C_1)\, C_3}{C_1\, (C_3 - C_1)}\,, \quad w_3 = \frac{(1 - C_1)\, (C_3 - C_2)}{(1 - C_3)\, (C_3 - C_1)}\,. \tag{10.55}$$

Then, the phase 2 suppression criterion (10.51) can be easily reduced to the following form:

$$\frac{\Delta g_{10}}{\Delta g_{30}} \frac{\xi_3}{w_3} + \frac{\Delta g_{30}}{\Delta g_{10}} \frac{\xi_1}{w_1} < 5 \frac{\Delta g_{10} \Delta g_{30}}{(\Delta g_{20})^2}\,, \tag{10.56}$$

where

$$\xi_1 = \frac{\Delta X_1}{\left(\frac{2\sigma\Omega}{\Delta g_{10}}\right)} = \frac{\Delta X_1}{l_1^{\mathrm{cr}}}\,, \quad \xi_3 = \frac{\Delta X_3}{\left(\frac{2\sigma\Omega}{\Delta g_{30}}\right)} = \frac{\Delta X_3}{l_3^{\mathrm{cr}}}\,. \tag{10.57}$$

Note that w_1 and w_3 are of the order of unity.

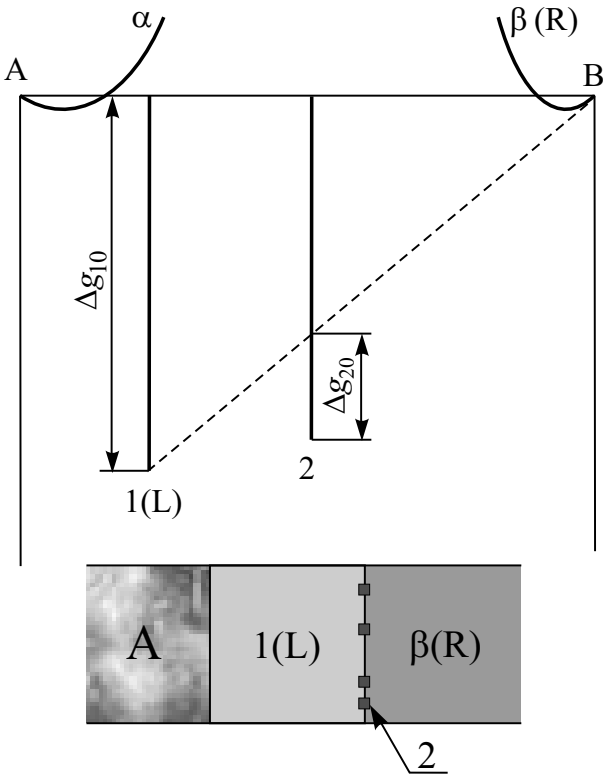

Figure 10.15: Schematic representation of phase 2 nucleation between intermediate phase 1 and the diluted solution, β, already growing in an A/B couple. Δg_{10} and Δg_{20} are the driving forces per mole of atoms for the reactions $A + B \rightarrow 1$ and $1 + \beta \rightarrow 2$, respectively

If phases 1 and 3 are mutually symmetric ($\Delta g_{10} = \Delta g_{30},\ w_1 = w_3$), then the criterion Eq. (10.51) is reduced to

$$\frac{\Delta X_1}{l_1^{\mathrm{cr}}} + \frac{\Delta X_3}{l_3^{\mathrm{cr}}} < 5\frac{(\Delta g_{10})^2}{(\Delta g_{20})^2}\,. \tag{10.58}$$

Δg_{20} is a driving force of the reaction $1(L) + 3(R) \longrightarrow 2$ (see Fig. 10.14).

If phase 1 is much wider than phase 3, i.e.,

$$\frac{\Delta X_1}{\Delta X_3} \gg \left(\frac{\Delta g_{10}}{\Delta g_{30}}\right)^2\,,$$

then one can show that nucleation of phase 2 is preferable at the side of phase 1 ($r_R \approx 0$), and the criterion (10.58) is reduced to

$$\frac{\Delta X_1}{l_1^{\mathrm{cr}}} < 5\frac{(\Delta g_{10})^2}{(\Delta g_{20})^2}\,. \tag{10.59}$$

The estimates (10.58) and (10.59) are very important. They demonstrate that the critical thickness of the first (and fast) growing phase can be rather large, since the driving force of the second phase formation (from already growing phases 1 and 3) is often significantly less than that of the first phase formation from one compound and one pure element (see Fig. 10.14).

10.4.3 Nucleation between Growing Intermediate Phase and Dilute Solution

Let L and R be respectively the growing phase 1 and the diluted solution of A in B (β). In this case the phase 2 suppression criterion is

$$\left(\frac{A_1 A_\beta}{A_1 + A_\beta}\right) > \frac{(\Delta g_{20})^2}{10\sigma\Omega} \tag{10.60}$$

with, as before,

$$A_1 = (C_2 - C_1)\, g_1'' \nabla C_1 = w_1 \tag{10.61}$$

and

$$A_\beta = \left(C_{\beta 1} - C_2\right) g_\beta'' \nabla C_\beta \approx (1 - C_2)\, \frac{k_B T}{1 - C_\beta} \nabla C_\beta \,. \tag{10.62}$$

In the above equations, Δg_{10} and Δg_{20} are the driving forces of the reactions $A + B \to 1$ and $1(L) + B(R) \to 2$, respectively (see Fig. 10.15).

To express the gradient in a diluted solution in the presence of a growing intermediate phase, one has to solve the following set of algebraic equations for simultaneous parabolic growth of the phase 1 layer and of the β-solution with parabolic movement of interfaces $A/1$ and $1/\beta$

$$C_1 \frac{k_{A1}}{2} = -\frac{D_1 \Delta C_1}{k_{1\beta} - k_{A1}} \,, \tag{10.63}$$

$$(1 - C_1)\, \frac{k_{1\beta}}{2} = \frac{D_1 \Delta C_1}{k_{1\beta} - k_{A1}} - \sqrt{\frac{D_\beta}{\pi}}\, \left(1 - C_{\beta 1}\right) \frac{\exp\left(-\dfrac{k_{1\beta}^2}{4D_\beta}\right)}{1 - \operatorname{erf}\left(\dfrac{k_{1\beta}}{2\sqrt{D_\beta}}\right)} \,, \tag{10.64}$$

where $y_{A1} = k_{A1}\sqrt{t}$ and $y_{1\beta} = k_{1\beta}\sqrt{t}$. Analytically, we can treat the limiting case (which is most often encountered) given by the conditions $D_\beta \ll D_1 \Delta C_1$ (very low diffusivity in solution, which is common for high melting B). Omitting elementary algebra and expansions into Taylor series, we will immediately get the results, i.e.,

$$\begin{aligned} k_{1\beta} &\approx \sqrt{\frac{C_1}{1 - C_1}} \sqrt{2 D_1 \Delta C_1} \,, \quad \Delta X_1 \approx \sqrt{\frac{1}{C_1 (1 - C_1)}} \sqrt{2 D_1 \Delta C_1 t} \,, \\ \nabla C_\beta &\approx \left(1 - C_\beta\right) \sqrt{\frac{C_1}{1 - C_1}} \sqrt{\frac{2 D_1 \Delta C_1}{2 D_\beta^2 t}} \,, \end{aligned} \tag{10.65}$$

so that

$$A_\beta \approx (1 - C_2)\sqrt{\frac{C_1}{1 - C_1}}\sqrt{2D_1 \Delta C_1}\frac{k_B T}{2D_\beta \sqrt{t}}$$

and

$$\frac{A_1}{A_\beta} = \frac{C_2 - C_1}{C_1 (1 - C_2)}\frac{\Delta g_{10}}{k_B T}\frac{D_\beta}{D_1 \Delta C_1} \ll 1 \tag{10.66}$$

holds. By the above given conditions, the relation $(A_1 A_\beta / A_1 - A_\beta) \approx A_1$ is fulfilled and the suppression criterion is

$$\frac{\Delta X_1}{l_1^{\mathrm{cr}}} < 5\frac{C_2 - C_1}{C_1 (1 - C_1)}\left(\frac{\Delta g_{10}}{\Delta g_{20}}\right)^2 . \tag{10.67}$$

Thus, in the case of a smaller driving force for the second phase and low diffusivity in B the thermodynamic suppression of phase 2 may be rather significant. Consequently, the best candidates for the suppression of the second phase by chemical potential gradients are the systems with a large difference in melting temperature between the constituents. More probably, the first phase to grow will be that phase which is more close to the low-melting-point element. Then, for the second phase we will have the situation as analyzed in this section.

10.5 Kinetics of Nucleation in a Concentration Gradient

The thermodynamic possibility of nucleation does not guarantee new phase formation due to kinetic constraints, caused by finite rates at interfaces and, first of all, by diffusional interactions between the newly born and parent phases. For this reason, we will analyze, in addition to the thermodynamic factors discussed before, peculiarities of the kinetics of nucleation in concentration gradients.

10.5.1 Kinetics of Intermediate Phase Nucleation in Concentration Gradients: Polymorphic Mode

As we have seen in Sections 10.3 and 10.4, in fact, nucleation can be inhibited by too sharp concentration gradients. Therefore, the system should wait and prepare sufficiently smooth concentration profiles in the contact zone as a prerequisite for subsequent nucleation.

According to the classical nucleation theory, nucleation is some kind of a miracle (proceeding in violation of the second law of thermodynamics) and consists of sequential elementary miracles of one-by-one attachment events. Following the classical approach [40], one can describe the statistics of such miracles in the framework of a Fokker–Planck approach. Let us start with the assumption that at the initial stage of nucleus formation, the rearrangement of the lattice can take place without a modification of composition, i.e., let us assume a polymorphic transformation. The appropriate generalization of the Gibbs theory of nucleation for this case was developed already in Sect. 10.3 and will be employed now.

The evolution of the system of aggregates of the new phase will be described in terms of the continuous distribution function $f(N,t)$ (cf. also Chapter 3). Here $f(N,t)\,\mathrm{d}N$ is the number of aggregates in the range of cluster sizes N, $N+\mathrm{d}N$ at time t. The distribution function $f\,(N,t)$ for the nuclei of a new phase is determined by the Fokker–Planck equation

$$\frac{\partial f\,(N,t)}{\partial t} = \frac{\partial}{\partial N}\left(\Delta\nu f\right) + \frac{\partial^2}{\partial N^2}\left(\bar{\nu} f\right) = -\frac{\partial j}{\partial N}\,, \tag{10.68}$$

where the "density of fluxes" j in size space consists of drift term $\Delta\nu f$ and the "diffusional," purely stochastic term $\bar{\nu} f$, which makes the very process of nucleation possible.

In the present analysis, $\bar{\nu} = ((\nu_+ + \nu_-)/2)$ is assumed to have a constant value, where $\nu_\pm$ are the frequencies of increase (or decrease) of the number N of atoms or molecules in a cluster by one A-atom joining (leaving) the embryo lattice (in combination with k B-atoms required for preserving the stoichiometry $A_1 B_k$). $\Delta\nu = \nu_+ - \nu_-$ depends on the thermodynamic driving force via

$$\Delta\nu = -\frac{1}{k_\mathrm{B}T}\frac{\partial G}{\partial N}\bar{\nu}\,. \tag{10.69}$$

In the case of phase formation by the polymorphic mode, the gradient term is positive (the concentration gradient inhibits nucleation). Assuming a spherical nucleus shape, the dependence of the Gibbs free energy on the number of atoms in the nucleus has the following form:

$$\Delta G\,(N) = \Delta g_m N + \left(\frac{3}{4\pi n}\right)^{\frac{2}{3}}\frac{g''}{10}\left(\nabla C\right)^2 N^{\frac{5}{3}} + \left(\frac{3}{4\pi n}\right)^{\frac{2}{3}} 4\pi\sigma N^{\frac{2}{3}}\,. \tag{10.70}$$

Here g'' is the second-order derivative of the Gibbs free energy per atom with respect to the concentration of the new phase. If the concentration gradient in the nucleation place changes according to a parabolic law via

$$\left(\nabla C\right)^2 = \frac{1}{4\pi D_\mathrm{parent} t}\,, \tag{10.71}$$

then the drift term in the Fokker–Planck equation explicitly depends on time. Physically such dependence results in the lowering of the nucleation barrier due to interdiffusion in the parent phase(s).

For the further analysis, it is convenient to employ the dimensionless variables

$$\tau \equiv \bar{\nu} t\,, \quad \alpha \equiv \frac{\Delta g_m}{k_\mathrm{B}T} < 0\,, \quad \beta = C_3\frac{g''\dfrac{\bar{\nu}}{k_\mathrm{B}T}}{24\pi D_\mathrm{parent}}\,, \quad \gamma \equiv C_3\frac{8\pi\sigma}{3k_\mathrm{B}T}\,, \tag{10.72}$$

where $C_3 = (3/4\pi n)^{\frac{2}{3}}$ holds. Treating $\bar{\nu}$ approximately as a constant, we have

$$\frac{\partial f\,(N,t)}{\partial \tau} = \frac{\partial^2 f}{\partial N^2} + \frac{\partial}{\partial N}\left[f\left(\alpha + \beta\frac{N^{\frac{2}{3}}}{\tau} + \frac{\gamma}{N^{\frac{1}{3}}}\right)\right]\,. \tag{10.73}$$

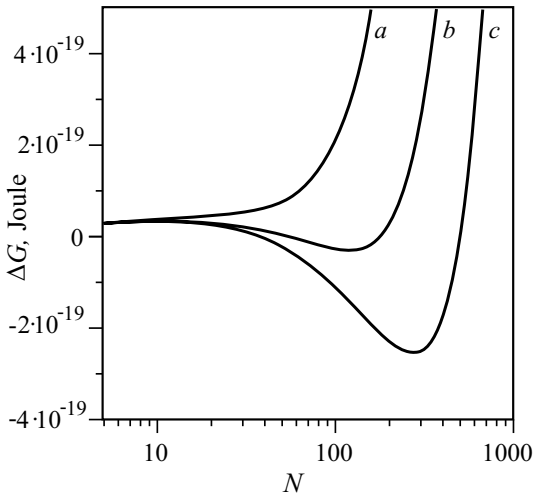

Figure 10.16: Dependence $\Delta G(N)$ for sharp concentration gradients ∇C (small annealing times)

A numerical solution of the latter equation has been obtained for a fixed total number of nucleation sites (heterogeneous nucleation)

$$\int f(N,t)\,\mathrm{d}N = \text{const}\,. \tag{10.74}$$

The evolution in time of the size distribution $f(N,t)$ corresponds to the evolution of the potential field $\Delta G(N)$ but is shifted in time. For small annealing times, when the concentration gradient remains sharp enough, the dependence $\Delta G(N)$ monotonically increases so that nucleation is thermodynamically forbidden (cf. Fig. 10.16). During this period, the distribution $f\,(N)$ remains monotonically decreasing. After a certain thermodynamic "incubation time," when the concentration gradient in the parent phase becomes less than the critical value, nucleation becomes thermodynamically possible ($\Delta G(N)$ becomes nonmonotonic with a maximum corresponding to the nucleation barrier). Yet, the distribution function $f(N)$ reveals a maximum not immediately, but after a certain "kinetic incubation period" (Fig. 10.17).

We define an incubation time as a period of peak formation for the size distribution function $f(N)$ (not counting an initial peak at $N = N_{\min}$). Obviously, in a dimensionless time scale τ, the incubation time (τ_{inc}) should depend on the ratio of two kinetic parameters, $\bar{\nu}$ and D_{parent}.

The dependences $\tau_{\text{inc}}\left(D_{\text{parent}}/\bar{\nu}\right)$ are shown for different values of the surface tensions in Fig. 10.18. To evaluate the realistic range of the ratio $(D/\bar{\nu})$ one should take into account that the frequency ν can be estimated as

$$\nu \sim N^{\frac{2}{3}}\frac{D_{\text{boundary}}}{\lambda^2}\,,$$

where D_{boundary} is the diffusivity at the interface between the new and old phases, N is the number of atoms in the nucleus, and λ is the characteristic length of random walk of the atom

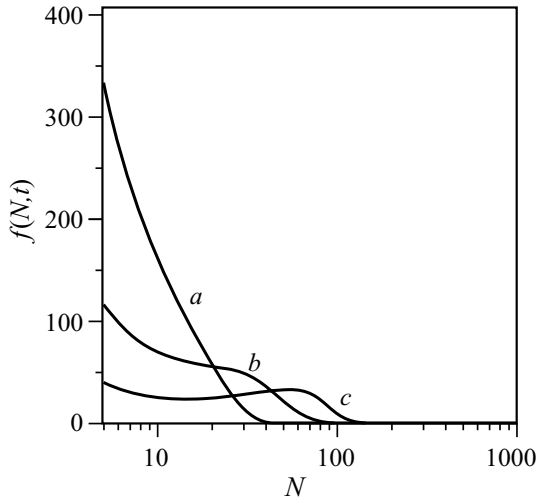

Figure 10.17: Evolution of the size distribution function for nuclei of the intermediate phase. The different curves refer to reduced times $\tau = 50$ (a), $\tau = 100$ (b), and $\tau = 150$ (c). The parameter values are $D_{\text{parent}} = 10^{-20}$ m^2 s^{-1}, $\Delta g_m = -7.48 \times 10^{-21}$ J, $g'' = (\partial^2 g/\partial C^2) = 7.77 \times 10^{-19}$ J, $n = 10^{29}$ m^{-3}, $T = 600$ K, $\sigma = 0.15$ J m^{-2}

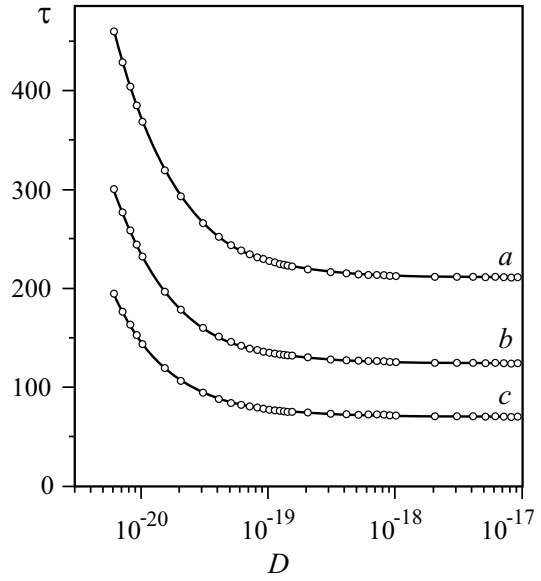

Figure 10.18: Dependence of the dimensionless incubation time, $\tau_{\text{inc}} = \bar{\nu} t_{\text{inc}}$, on the ratio $D/\bar{\nu}$ for different values of the surface tension (in J m^{-2}): (a) $\sigma = 0.11$, (b) $\sigma = 0.10$, (c) $\sigma = 0.09$

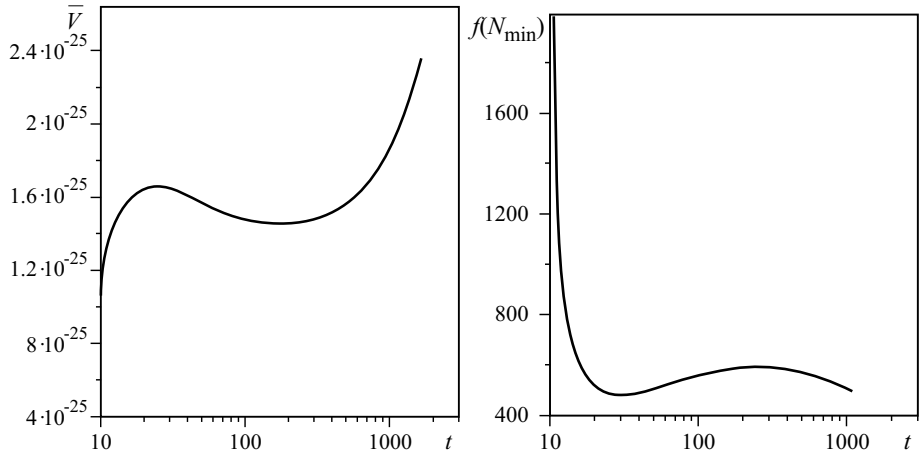

Figure 10.19: Left: Time dependence of the new phase volume in the case of the total mixing mode for $\sigma = 0.20$ J m^{-2}. Right: Time dependence of the number of smallest new phase embryos ($N_{\min} = 5$) for heterogeneous nucleation via the total mixing mode for a value of the surface tension equal to $\sigma = 0.15$ J m^{-2}

looking for a suitable place of joining the new phase. It is reasonable to suppose that the conditions $D_{\text{boundary}} > D_{\text{parent}}$ and $\lambda > a$ hold, where a is an atomic distance. If $N \sim 30$, then $\lambda \sim 10^{-10}$–10^{-8} m and $(D/\bar{\nu})$ has values in the range 10^{-17}–10^{-21} m^2. One can notice that with growing diffusivity of the parent phase, the dimensionless incubation time decreases to some asymptotic level. It means that this level represents the time for nuclei growth even when gradient effects do not hinder nucleation. Then we may consider the difference $\tau - \tau_{\min}$ as a time of "concentration preparation."

10.5.2 Kinetics of Nucleation via the Total Mixing Mode

For the total mixing mode, the gradient term (factor γ) in Eq. (10.73) is negative, i.e., the concentration gradient ∇C supports the nucleation process. For this reason, the results of the calculation for the total mixing mode differ substantially from those for the polymorphic mode. First of all, nucleation is never suppressed. Moreover, the nucleation behavior may be oscillatory as well. For a certain range of parameters the time evolution of the new phase volume is nonmonotonic (see Fig. 10.19). A similar nonmonotonic behavior is observed as well for the number of smallest embryos (in our case $N_{\min} = 5$) for the same thermodynamic parameters except surface tension (Fig. 10.19).

Why are the embryos generated intensively at the very first stage and then are partially dissolved? Our answer is the following: For the total mixing mode the gradient term supports nucleation. At first the gradient is large making the nucleation barrier low and the nucleation process easy. With time the gradient decreases, and the nucleation barrier and the critical nucleus size increase. Therefore, particles that had been generated earlier as supercritical and which did not manage to reach the new critical size find themselves to be subcritical and are

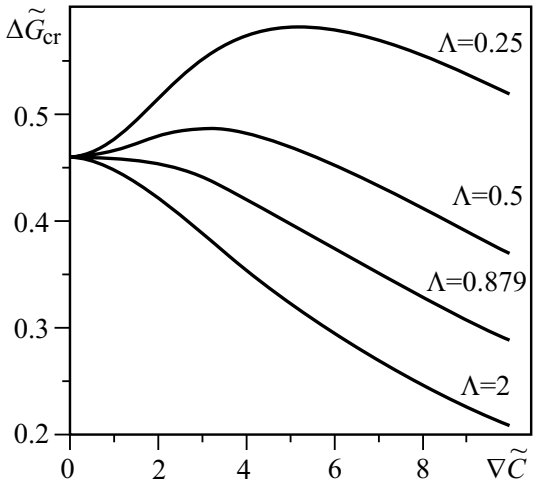

Figure 10.20: Dependence of the effective nucleation barrier for the critical nucleus on the dimensionless concentration gradient for different ratios of the diffusivities in the new and parent phases

dissolved. In other words, if the growth rate of the particles is less than the rate of the critical size growth (due to decreasing concentration gradient), these particles will be disintegrated. We observed such nonmonotonic behavior of new phase formation during interdiffusion also by Monte Carlo simulations both for second-order and first-order phase transitions in a concentration gradient [45, 46].

10.5.3 Interference of Nucleation Modes

As we have just seen, nucleation of an intermediate phase during reactive diffusion can proceed via different "modes," each being characterized by its own nucleation barrier, own frequency factor, and own shape/volume dependence. We restricted ourselves to a special shape, to parallelepipeds, retaining only one free shape parameter $\varphi = (h/r)$, where $2h$ and $2r$ are the nucleus sizes in transversal and longitudinal directions. In general, every mode has its own velocity determined by diffusivities and embryo shape.

In Ref. [30], we considered the interference of two modes – transversal and total mixing. Nucleation modes operate simultaneously with different rates

$$\nu_{+/-}(N) = \nu^{(b)}_{+/-}(N) + \nu^{(c)}_{+/-}(N) \ . \tag{10.75}$$

Rather tricky mathematics, using the steady-state solutions of the Fokker–Planck equation with additive contributions to frequencies from two modes, demonstrated that interference leads to a dependence of the effective nucleation barrier on the ratio of the kinetic parameters – the larger the diffusivity of the new phase, the lower the effective nucleation barrier.

The specific form of the function $\Delta\widetilde{G}_{\rm cr}\left(\widetilde{\nabla}c\right)$ (reduced to a dimensionless form) depends on the ratio

$$\Lambda = \frac{D_i}{4D}\exp\left(-\frac{\Delta\bar{G}^{(c)} - \Delta\bar{G}^{(b)}}{\theta}\right),$$

including the ratio of diffusivities in intermediate and parent phases. At $\Lambda < \Lambda^*$, the function $\Delta\widetilde{G}_{\rm cr}(\widetilde{\nabla}c)$ is nonmonotonic with a maximum (Fig. 10.20), which shifts to zero $\widetilde{\nabla}c$ with increasing Λ to Λ^*. With decreasing to zero values of Λ this maximum $\Delta G_{\rm cr}^{\max}$ tends to infinity (the transversal mode is overwhelming). At $\Lambda > \Lambda^*$, the function $\Delta\widetilde{G}_{\rm cr}\left(\widetilde{\nabla}c\right)$ is monotonic – the sharper the concentration gradient, the less the nucleation barrier (total mixing mode is overwhelming). Thus, strictly speaking, there is no critical gradient in the general case, and nucleation of an intermediate phase is possible at any gradient due to the possibility of the total mixing mode. Instead of a critical gradient, above which nucleation would be impossible, a characteristic gradient exists at which the probability of nucleation has its smallest values.

In the process of interdiffusion, in the parent phase the concentration gradient decreases and the nucleation barrier increases first. It means that the nuclei of the new phase, formed at the very beginning, can become subcritical at a later stage (if they had no time for growth). Therefore, an oscillatory regime of intermediate phase formation can be possible. Thus, the kinetic constraints and the interference of different nucleation modes lead to effective nucleation barriers depending on the ratio of diffusivities as well as on usual thermodynamic factors.

Acknowledgements

This work was supported by INTAS (Grant 784) and in part by CRDF (Grant UE1-2523-CK-03). The authors appreciate the assistance of Ihor Sobchenko at the stage of manuscript preparation.

References

[1] Ya.E. Geguzin, *Diffusion Zone*, (Nauka, Moscow, 1981) (in Russian).
[2] C.P. Gurov, B.A. Kartashkin, and Yu.E. Ugaste, *Interdiffusion in Multiphase Metallic Systems*, (Nauka, Moscow, 1981).
[3] F.M. d'Heurle, J. Mater., Res. **3**, 167 (1988).
[4] A.M. Gusak and K.P. Gurov, Fiz. Met. Metallovedenie (USSR) **53**, 842 (1982) (in Russian).
[5] K.P. Gurov and A.M. Gusak, Izv. Acad. Sci. (USSR), Met. **1**, 163 (1990) (in Russian).
[6] A.M. Gusak, Ukr. Phys. J. **5**, 725 (1990) (in Russian).
[7] A.M. Gusak and G.V. Lucenko, Acta Mater. **46**, 3343 (1998).
[8] A.M. Gusak, A.O. Bogatyrev, T.V. Zaporozhets et al., *Models of Solid State Reactions*, (Cherkasy National University, 2004).
[9] C. Michaelsen, K. Barmak, and T.P. Weihs, J. Phys. D: Appl. Phys. **30**, 3167 (1997).
[10] L. Klinger, Y. Brechet, and G. Purdy, Acta Mater. **46**, 2617 (1998).
[11] G. Lucenko and A.M. Gusak, Bull. Cherkasy State Univ. Phys. **37–38**, 145 (2001–2002).

[12] U. Goesele and K.N. Tu, J. Appl. Phys. **53**, 3252 (1982).
[13] W.L. Johnson, J. Mater. Sci. **30**, 81 (1986).
[14] V. Vieregge and Chr. Herzig, J. Nucl. Mater. **175**, 29 (1990).
[15] E. Emeric, P. Gas, G. Clugnet, and C. Bergman, Microelectron. Eng. **50**, 285 (2000).
[16] E. Emeric, Etude des Reactions a l'etat Solide dans des Multicouches Al/Co, Ph.D. thesis, Marseille, 1998.
[17] T. Jeske and G. Schmitz, Scripta Mater. **45**, 555 (2001).
[18] F. Hartung and G. Schmitz, Phys. Rev. B **64**, 245418 (2001).
[19] A.M. Gusak and K.P. Gurov, Solid State Phenomena **23–24**, 117 (1992).
[20] A.M. Gusak and K.P. Gurov, Fiz. Met. Metalloved. (USSR) **53**, 848 (1982) (in Russian).
[21] A.M. Gusak and Yu.A. Lyashenko, Phys. Chemi. Mater. Process. (Fizika i Khimiya Obrabotky Materialov) **5**, 140 (1993) (in Russian).
[22] A.M. Gusak, Poroshk. Metall. (Powder Metall., USSR)**3**, 39 (1989) (in Russian).
[23] K.N. Tu, A.M. Gusak, and M. Li, J. Appl. Phys. **93**, 1335 (2003).
[24] P.J. Desre and A.P. Yavari, Phys. Rev. Lett. **64**, 1553 (1990).
[25] P.J. Desre, Acta Metall. **39**, 2309 (1991).
[26] A.M. Gusak and A.V. Nazarov, Metallofizika (Metal Physics, USSR) **12**, 48 (1990) (in Russian).
[27] A.M. Gusak and A.V. Nazarov, J. Phys.: Condens. Matter 4, 4753 (1992).
[28] F. Hodaj and P.J. Desre, Acta Mater. **44**, 4485 (1996).
[29] F. Hodaj, A.M. Gusak, and P.J. Desre, Phil. Mag. A **77**, 1471 (1998).
[30] A.M. Gusak, F. Hodaj, and A.O. Bogatyrev, J. Phys.: Condens. Matter **13**, 2767 (2001).
[31] A.M. Gusak, O.V. Dubiy, and S.V. Kornienko, Ukr. Phys. J. **36**, 286 (1991), (in Russian).
[32] A.M. Gusak and A.O. Bogatyrev, Metallofiz. Noveishi. Technol. (Metal Phys. Adv. Technol.) **16**, 28 (1994) (in Russian).
[33] A.M. Gusak, Yu.A. Lyashenko, and A.O. Bogatyrev, in Nucleation at the interphase interface in the process of reactive diffusion, *Solid to Solid Phase Transformations*, edited by W.C. Johnson, J.M. Howe, D.E. Laughlin, W.A. Soffa (TMS, USA, 1994), p. 1171.
[34] A.M. Gusak, Yu. A. Lyashenko, and A.O. Bogatyrev, Defect Diffus. Forum **129–130**, 95 (1996).
[35] A.O. Bogatyrev and A.M. Gusak, Metallofiz. Noveish. Technol. (Metal Phys. Adv. Technol.) **18**, 897 (2000).
[36] A.M. Gusak, Yu. A. Lyashenko, and S.V. Kornienko, Funct. Mater. **6**, 242 (1999).
[37] J.J. Hoyt and L.N. Brush, J. Appl. Phys. **78**, 1589 (1995).
[38] A.O. Bogatyrev, Ph.D. thesis, Institute for Metal Physics, Kiev, 1999.
[39] F. Hodaj and A.M. Gusak, Acta Mater. **52**, 4305 (2004).
[40] Ya.B. Zeldovich, Acta Physicochim. **18**, 1 (1943).
[41] K.N. Tu and J.W. Mayer, in Silicide formation, edited by J.M. Poate, K.N. Tu, J.W. Mayer, *Thin Films – Interdiffusion and Reactions* (Wiley, New York, 1978), Chapter 10.
[42] P. Gas and F.M. d'Heurle, in Diffusion in silicides: Basic Approach and Practical Applications, edited by L. Miglio and F.M. d'Heurle *Silicides: Fundamentals and Applications* (World Scientific, Singapore, 2000), p. 34.

[43] F.J.J. van Loo, Prog. Solid State Chem. **20**, 47 (1990).

[44] A.M. Gusak and M.V. Yarmolenko, J. Appl. Phys. **73**, 4881 (1993).

[45] A.M. Gusak and A.O. Kovalchuk, Phys. Rev. B **58**, 2551 (1998).

[46] A.M. Gusak, A.O. Bogatyrev, and A.O. Kovalchuk, in *Initial Stage of Reactive Diffusion: Nucleation and Avrami Kinetics*, Defect and Diffusion Forum 194-199 (DIMAT-2000, Paris, 2000), p. 1625.

11 Is Gibbs' Thermodynamic Theory of Heterogeneous Systems Really Perfect?

Jürn W. P. Schmelzer, Grey Sh. Boltachev, and Vladimir G. Baidakov

The strongest arguments prove nothing
so long as the conclusions are not verified by experience.
Experimental science is the queen of sciences
and the goal of all speculation.
Roger Bacon

The important thing in science is not so much
to obtain new facts
as to discover new ways of thinking about them.
Sir William Bragg

The theory determines what can be measured.
Albert Einstein

Results of a critical analysis of the advantages and shortcomings of the classical Gibbs' approach to the description of heterogeneous systems in application to the determination of the parameters of the critical clusters and the work of critical cluster formation in nucleation theory are outlined. A generalization of Gibbs' classical approach is developed allowing us to give a theoretically well-founded description not only of thermodynamic equilibrium but also of thermodynamic nonequilibrium states consisting of a cluster or ensembles of clusters of, in general, arbitrary sizes and composition in the otherwise homogeneous ambient phase. Most importantly, the generalization of Gibbs' approach allows us to incorporate into the description a dependence of the surface tension of the clusters of arbitrary sizes on the state parameters of both coexisting phases. In application to the determination of the parameters of the critical clusters, the generalized Gibbs' approach results in relations different, in general, from the equilibrium conditions as derived by Gibbs. For macroscopic phases (large sizes of the critical clusters), the results coincide. However, for clusters of nanometric sizes, the generalized Gibbs' approach leads to different results for the determination of the state parameters of the critical clusters and the work of critical cluster formation as compared with the classical Gibbs' method. As one of the highly important consequences, the results of the generalized Gibbs' approach turn out to be in qualitative and partly even quantitative agreement with the van der Waals square gradient and more advanced density functional computations of the parameters of the critical clusters and the work of critical cluster formation. The generalized Gibbs' approach allows us to advance, in addition, the hypothesis that the clusters of critical sizes have different temperatures as compared with the ambient phase. If this result will be confirmed by further independent methods it follows that nucleation is, in principle, a nonisothermal process. Taking into account this principal nonisothermal character of nucleation

Nucleation Theory and Applications. edited by J. W. P. Schmelzer

ISBN: 3-527-40469-4

will result then in a variety of additional consequences with respect to the determination of the parameters of the critical clusters and the work of critical cluster formation.

11.1 Introduction

Despite many years of intensive research, the theoretical description of the kinetics of nucleation and the subsequent growth is still a challenging topic of research. One of the basic problems one is confronted with the analysis of these phenomena is the description of the state of the clusters evolving in the course of the nucleation-growth process and, in particular, the determination of the state of the critical clusters and the work of critical cluster formation. The work of critical cluster formation determines, in almost all existing theoretical approaches to nucleation, essentially the steady-state nucleation rate (see, e.g. [1–10], Chapters 4 and 5).

In order to determine the state of the critical clusters and the work of critical cluster formation, up to now predominantly Gibbs' classical thermodynamic theory of heterogeneous systems is employed [11] either in order to predict, making certain additional assumptions, the work of critical cluster formation or, once this quantity is determined via alternative approaches such as density functional computations of different levels of sophistication, in order to determine the properties of critical clusters [12–16]. Hereby it is commonly believed that Gibbs' theory is not only the first comprehensive theory but also the most perfect thermodynamic theory of heterogeneous systems.

Indeed, already Gibbs, when analyzing his thermodynamic approach, came to a similar quite optimistic conclusion. He wrote (cited after [17]): "Although my results were in a large measure such as had been previously obtained by other methods, yet, as I readily obtained those which were to me before unknown, or by vaguely known, I was confirmed in my belief in the suitableness of the method adopted." The power of Gibbs' method was demonstrated also in the further application of Gibbs' theory for more than hundred years, now.

On the other hand, when applied to the description of critical clusters (of systems of nanometric sizes) the question has been advanced from time to time whether Gibbs' theory is really as perfect for this particular application as assumed or whether it has to be modified in one or the other way leaving it untouched in the analysis of problems where it has demonstrated convincingly its power. Some of such examples are the extended discussions on the necessity of taking into account translational and rotational degrees of freedom in the description of the work of critical cluster formation [18–20] and the analysis of a topic termed recently [21] the Renninger–Wilemski problem [22–25]. To some extent, this discussion is directed to the problem whether Gibbs' method allows an appropriate description of the bulk properties of critical clusters or not.

A detailed analysis shows that Gibbs' classical approach does not give, in general, an appropriate description of the bulk properties of critical clusters [15,26,27]. This shortcoming is, as we believe, the major reason for the problems occuring in its application in nucleation theory aimed at the interpretation of nucleation experiments [28–30]. Here one is confronted partly with grave deviations between experimental results and theoretical predictions with respect to the values of the nucleation rate [31,32]. To a certain degree, these problems can be overcome by the introduction of appropriate dependences for the curvature dependence

of the surface tension. However, proceeding in such a way other internal contradictions may arise [29, 31].

Another problem inherent to Gibbs' approach consists in the restriction to an analysis of *equilibria of heterogeneous substances* (cf. the title of his paper [11]). This restriction allows us to avoid some highly nontrivial problems in the development of the thermodynamic theory but results in a grave limitation as well. For example, it does not allow us – without the introduction of more or less founded additional assumptions – to describe clusters or ensembles of clusters in the ambient phase for nonequilibrium states, when the necessary thermodynamic equilibrium conditions are not fulfilled (i.e., for sub- or supercritical clusters). Here it is commonly widely assumed – without having at ones disposal a sound theoretical basis allowing the estimate of the accuracy of such assumption – that the properties of such clusters refer widely to the properties of the newly evolving macroscopic phase. This lack of theoretical foundation is highly unfortunate per se but even more taking into account the growing interest in the properties of matter at nanoscale sizes. So, with respect to both nucleation and the description of the evolution of clusters and cluster ensembles of sub- and supercritical sizes a generalization of Gibbs' thermodynamic approach is highly desirable. Such a generalized thermodynamic theory could serve then as a sound basis for more detailed approaches in the analysis of the structure of matter at the nanometer length scales.

Attempts of a generalization of Gibbs' thermodynamic theory have been advanced by different authors and with different methods and results (see, e.g., [33–36] for an overview). In all these analyses, however, Gibbs' fundamental equation for the superficial (or interfacial) parameters was basically not changed. As a result, also the form of the thermodynamic equilibrium conditions, as derived by Gibbs in his approach, has remained unchanged. In recent years, a new approach to the determination of the work of critical cluster formation in nucleation theory has been developed [26–30, 37–46]. It was demonstrated for quite different applications that by employing this approach, Gibbs' [11] and van der Waals' [12, 13] (or more advanced density functional [14–16]) approaches to the description of the work of critical cluster formation can be reconciled, i.e., the newly developed method leads to qualitatively and partly even quantitatively similar results with respect to this quantity and with respect to the description of the properties of critical clusters as compared with density functional computations. In particular, the newly developed method leads to a vanishing of the work of critical cluster formation in the vicinity of the spinodal. In performing the respective analysis, only the knowledge of the bulk properties of the respective phases and the values of the interfacial tension for an equilibrium coexistence of the respective phases at planar interfaces have to be known in order to compute the respective quantities for clusters of critical sizes. The thermodynamic approach, underlying the mentioned new developments, leads to different expressions for the determination of the size parameters and the state of the critical clusters as compared with Gibbs' original method. For this reason, an intensive analysis of Gibbs' thermodynamic theory has been performed. This analysis leads to the conclusion that Gibbs' theory has to be modified, indeed, in order to give an adequate description both of the state of critical clusters, the processes of their formation (i.e., the state of subcritical clusters) and of the subsequent growth of supercritical clusters [28–30]. Similar conclusions were drawn with respect to critical cluster formation recently in [21] by a different argumentation as well. We would like to underline that both approaches – the classical Gibbs' method and its generalization – lead to equivalent results for phase coexistence at planar interfaces. Thus,

the methods and results of the description of macroscopic phase equilibria are not affected by the generalization of Gibbs' method.

The aim of the present analysis consists in a comprehensive outline of the respective generalization of Gibbs' theory and the derivation of some further consequences for the description of nucleation processes not discussed so far. In particular, it is shown that the condition of equality of temperatures of the critical cluster and the ambient phase – as derived via Gibbs' classical approach – has to be modified, in general, as well. The chapter is organized as follows: In Section 11.2, the essential ideas of Gibbs' classical approach are summarized as the basis for the subsequent generalization performed in Section 11.3. Some important consequences are analyzed in Section 11.4. A discussion of the results and some further possible developments (Section 11.5) completes the chapter.

11.2 Gibbs' Classical Approach

11.2.1 Basic Assumptions

The first comprehensive thermodynamic theory of heterogeneous systems was developed by J.W. Gibbs [11]. In Gibbs' theory, the real system, consisting of the homogeneous bulk phases and the interfacial region between the coexisting phases, is replaced by an idealized model system. This model system is formed out of two homogeneous subsystems divided by a mathematical surface, representing the interfacial zone. The deviations from additivity of the thermodynamic quantities are expressed through the introduction of superficial quantities formally attributed to this mathematical surface (*postulate 1*). In particular, for the internal energy U, the entropy S and the mole or particle numbers of the different components, n_j, $j = 1, 2, \ldots, k$, of the whole system, we get

$$U = U_1 + U_2 + U_\sigma \ , \quad S = S_1 + S_2 + S_\sigma \ , \quad n_j = n_{j1} + n_{j2} + n_{j\sigma} \ . \tag{11.1}$$

For the bulk contributions to the thermodynamic quantities, specified here by the subscripts (1) and (2), the common postulates and results of the thermodynamics of homogeneous phases are assumed to hold. In other words, both bulk phases are assumed to be in an internal thermodynamic equilibrium. The so-called superficial quantities U_σ, S_σ, and $n_{j\sigma}$, introduced to account for the deviations from additivity, depend both on the properties of the interfacial region and on the choice of the dividing surface. They may be both positive and negative.

The superficial quantities obey – following Gibbs' original approach [11] – a relation similar to the fundamental equation of bulk phases (*postulate 2*)

$$\mathrm{d}U_\sigma = T_\sigma \, \mathrm{d}S_\sigma + \sum_{j=1}^{k} \mu_{j\sigma} \, \mathrm{d}n_{j\sigma} + \sigma \, \mathrm{d}A + C_1 \, \mathrm{d}c_1 + C_2 \, \mathrm{d}c_2 \ . \tag{11.2}$$

Here A is the surface or interfacial area, σ is the interfacial tension or specific interfacial energy, c_1 and c_2 are the principal curvatures of the considered surface element, while the parameters C_1 and C_2 describe the variation of the internal energy connected with changes of the curvature of the surface element. T_σ and $\mu_{j\sigma}$ are the values of the temperature and chemical potentials assigned to the interface.

As noted by Gibbs [11], he supposed his theory to be valid generally *when applied to cases in which the surface of discontinuity is spherical however small the radius may be*. For small nonsperical clusters, limitations of the applicability of his theory have to be taken into consideration as pointed out by himself. In order to avoid these additional difficulties and to concentrate the analysis on the principal aspects, here we consider therefore the case of formation of spherically shaped drops or bubbles (denoted further, in general, as clusters) leaving straightforward generalizations to a future analysis. If one restricts, as we will do, the considerations to spherical interfaces, then Eq. (11.2) is further simplified ($c_1 = c_2 = c$, $C_1 + C_2 = C$) to

$$\mathrm{d}U_\sigma = T_\sigma \,\mathrm{d}S_\sigma + \sum_{j=1}^{k} \mu_{j\sigma} \,\mathrm{d}n_{j\sigma} + \sigma \,\mathrm{d}A + C \,\mathrm{d}c \,. \tag{11.3}$$

An integration of this equation results in

$$U_\sigma = T_\sigma S_\sigma + \sum_{j=1}^{k} \mu_{j\sigma} n_{j\sigma} + \sigma A \,. \tag{11.4}$$

The form of Eq. (11.4) is independent of the particular choice of the dividing surface; the different quantities entering this equation do depend on this choice, of course.

A derivation of Eq. (11.4) and comparison with Eq. (11.3) yields then the well-known Gibbs adsorption equation in the general form

$$S_\sigma \,\mathrm{d}T_\sigma + A \,\mathrm{d}\sigma + \sum_{j=1}^{k} n_{j\sigma} \,\mathrm{d}\mu_{j\sigma} = C \,\mathrm{d}c \,. \tag{11.5}$$

Thus, in Gibbs' approach an explicite dependence of the thermodynamic properties on the curvature is incorporated into the description, in general. However, it was also shown already by Gibbs [11] that for a definite choice of the dividing surface, the parameter C in Eq. (11.5) becomes equal to zero. In such situation, the size dependence remains but enters the description implicitly via a possible size dependence of T_σ and $\mu_{j\sigma}$. The particular dividing surface, corresponding to $C = 0$, is, following Gibbs' notation, denoted as the surface of tension [11]. This particular dividing surface is chosen in the majority of applications of Gibbs' theory to processes of nucleation.

Equation (11.5) describes in Gibbs' classical approach the change of the surface tension with variations of the state parameters of the system. However, in order to allow definite conclusions, the quantities T_σ and $\mu_{j\sigma}$ have to be specified. Such procedure has been performed by Gibbs for phase coexistence in equilibrium states, exclusively (remember that the title of Gibbs' fundamental work [11] is "On the equilibrium of heterogeneous substances"). A brief rederivation of Gibbs' equilibrium conditions is given in the following section.

11.2.2 Equilibrium Conditions for Clusters in the Ambient Phase

As a particular application of Gibbs' theory, we will consider now processes of formation of a cluster (drop or bubble, for example) in an ambient phase. Then we will calculate the change

of the characteristic thermodynamic potential connected with such process in dependence on the parameters specifying the state of the cluster. Specifying, for the considered application, the quantities describing the cluster phase by the subscript α, the characteristics of the ambient phase by β, and the superficial quantities further by σ, one obtains

$$\begin{aligned} U &= T_\alpha S_\alpha - p_\alpha V_\alpha + \sum_{j=1}^{k} \mu_{j\alpha} n_{j\alpha} + T_\beta S_\beta - p_\beta V_\beta \\ &\quad + \sum_{j=1}^{k} \mu_{j\beta} n_{j\beta} + \sigma A + T_\sigma S_\sigma + \sum_{j=1}^{k} \mu_{j\sigma} n_{j\sigma} \ , \end{aligned} \tag{11.6}$$

$$\begin{aligned} \mathrm{d}U &= T_\alpha \, \mathrm{d}S_\alpha - p_\alpha \, \mathrm{d}V_\alpha + \sum_{j=1}^{k} \mu_{j\alpha} \, \mathrm{d}n_{j\alpha} + T_\beta \, \mathrm{d}S_\beta \\ &\quad - p_\beta \, \mathrm{d}V_\beta + \sum_{j=1}^{k} \mu_{j\beta} \, \mathrm{d}n_{j\beta} + T_\sigma \, \mathrm{d}S_\sigma + \sigma \, \mathrm{d}A + C \, \mathrm{d}c + \sum_{j=1}^{k} \mu_{j\sigma} \, \mathrm{d}n_{j\sigma} \ . \end{aligned} \tag{11.7}$$

Here V is the volume and p is the pressure. For an isolated system with the boundary conditions

$$\begin{aligned} V = V_\alpha + V_\beta &= \text{const}, \quad S = S_\alpha + S_\beta + S_\sigma = \text{const}, \\ n_j &= n_{j\alpha} + n_{j\beta} + n_\sigma = \text{const}, \end{aligned} \tag{11.8}$$

the general thermodynamic equilibrium condition $(\mathrm{d}U)_{S,V,\{n\}} = 0$ [11] reads

$$\begin{aligned} (\mathrm{d}U)_{S,V,\{n\}} &= (T_\alpha - T_\sigma) \, \mathrm{d}S_\alpha + \left(T_\beta - T_\sigma\right) \mathrm{d}S_\beta \\ &\quad - (p_\alpha - p_\beta) \, \mathrm{d}V_\alpha + \sigma \, \mathrm{d}A + C \, \mathrm{d}c \\ &\quad + \sum_{j=1}^{k} (\mu_{j\alpha} - \mu_{j\sigma}) \, \mathrm{d}n_{j\alpha} + \sum_{j=1}^{k} (\mu_{j\beta} - \mu_{j\sigma}) \, \mathrm{d}n_{j\beta} = 0 \ . \end{aligned} \tag{11.9}$$

Considering possible variations of the independent variables (chosen here to be given by the set of quantities S_α, S_β, $n_{j\alpha}$, $n_{j\beta}$, and V_α) and taking into account that for a spherical cluster, the surface area, the curvature, and the volume of the cluster are dependent quantities, Eq. (11.9) yields

$$\mu_{j\alpha}\left(T_\alpha, p_\alpha, \{x_\alpha\}\right) = \mu_{j\beta}\left(T_\beta, p_\beta, \{x_\beta\}\right) = \mu_{j\sigma} \ , \quad j = 1, 2, \ldots, k \ , \tag{11.10}$$

$$T_\alpha = T_\beta = T_\sigma \ , \tag{11.11}$$

$$p_\alpha - p_\beta = \frac{2\sigma}{R} + C \frac{\mathrm{d}c}{\mathrm{d}V_\alpha} \ . \tag{11.12}$$

Here R is the radius of the critical cluster for any of the possible choices of the dividing surface (the position of the dividing surface has to be well defined, but a number of different definitions can be employed). $\{x\}$ denotes the sets of molar fractions of the different components that have to be taken into account for a characterization of the state of both bulk phases. Thus, so far

we assume that the state of both bulk phases is described by pressure, temperature, and the set of independent molar fractions of the different components. Later we will employ alternative sets of variables for the description of the state of the cluster and ambient phases as well, e.g., the set of particle densities of the different components $\{\rho\}$ and the entropy density, s.

Equations (11.10)–(11.12) are a direct consequence of Gibbs' classical approach. As evident from the considerations given above, their derivation requires exclusively the expressions for the change of the internal energy of both bulk phases, Gibbs' expression for the superficial quantities (Eq. (11.3)), and the general thermodynamic equlibrium conditions $(\mathrm{d}U)_{S,V,\{n\}} = 0$. No further additional assumptions are employed. Moreover, Eqs. (11.10) and (11.11) allow the following additional conclusion. Provided one knows the dependence of the chemical potentials of the different components in both bulk phases on an appropriate set of state parameters, the knowledge of the state of the ambient phase allows us to determine uniquely the bulk state parameters of the cluster phase. Hereby these reference bulk state parameters of the cluster phase are independent of the choice of the dividing surface. In addition, employing again Eqs. (11.10) and (11.11), we can now replace T_σ and $\mu_{j\sigma}$ in Gibbs' adsorption equation (11.5). This relation describes then, how the surface tension is varied if the system goes over from one equilibrium state to a neighboring one. For such variations of the state of the considered two-phase systems, the surface tension is uniquely defined by either the state parameters of the ambient phase or those of the cluster phase (both sets of parameters are connected uniquely by Gibbs' equilibrium conditions (11.10) and (11.11)).

In contrast to the bulk properties of the critical clusters – following Gibbs' classical approach – both the size of a cluster and the value of the surface tension depend, in general, on the choice of the dividing surface. If we choose, for example, the surface of tension (specified by a subscript s) as the dividing surface, then for any state of the ambient phase Eq. (11.12) uniquely determines the ratio $\sigma_\mathrm{s}/R_\mathrm{s}$. Consequently, for any given state of the ambient phase one can determine the value of the radius of the surface of tension provided one knows the value of the surface tension, referred to the surface of tension, for this given equilibrium state. This knowledge is sufficient for the determination of the values of the surface tension for any other well-defined dividing surface and the respective cluster radius as well. Indeed, as shown by Ono and Kondo [47], the term $C(\mathrm{d}c/\mathrm{d}V_\alpha)$ can be expressed generally via the notional derivative $[\mathrm{d}\sigma/\mathrm{d}R]$ as $C(\mathrm{d}c/\mathrm{d}V_\alpha) = [\mathrm{d}\sigma/\mathrm{d}R]$. Latter expression $[\mathrm{d}\sigma/\mathrm{d}R]$ means a variation of the position of the dividing surface, the physical state of the system being remained unchanged. In particular, for the equimolecular dividing surface in one-component systems (defined via $n_\sigma = 0$ and characterized by the radius R_e and the surface tension σ_e), the relation $[\mathrm{d}\sigma/\mathrm{d}R] = \mathrm{d}\sigma_\mathrm{e}/\mathrm{d}R_\mathrm{e}$ holds. For multicomponent systems, such property holds for a dividing surface introduced first by König [48] and denoted recently as König's dividing surface [49]. In any case, provided one knows the dependence of the surface tension, referred to the surface of tension, σ_s, on the radius of the surface of tension, R_s, one can determine directly both the surface tension, σ, and the radius of the dividing surface, R, for any other well-defined dividing surface via the relation [47]

$$\frac{\sigma(R)}{\sigma_\mathrm{s}(R_\mathrm{s})} = \frac{R_\mathrm{s}^2}{3R^2} + \frac{2R}{3R_\mathrm{s}} \,. \tag{11.13}$$

Consequently, in order to determine the size of the critical clusters, we have to know – following Gibbs' classical approach – the dependence of the surface tension, referred to the surface

of tension, on the state parameters of one of the bulk phases (or any equivalent information) for the respective unstable equilibrium states.

However, in the search for extrema and saddle points (where the necessary equilibrium conditions are fulfilled) of the characteristic thermodynamic potential, we have to compare not different equilibrium states but different nonequilibrium states (where the state parameters of the cluster phase and, in particular, the surface tension are not determined by the equilibrium conditions) and to search for the singular points (extrema or saddle points) then. For thermodynamic nonequilibrium states – consisting of single clusters (or ensembles of such objects) in the homogeneous ambient phase – the surface tension has to depend, in general, on both the states of the ambient and the newly evolving phases. Such dependence cannot be incorporated into the description in Gibbs' classical approach. Indeed, according to Gibbs' adsorption equation (11.5), σ can be considered as a function of curvature c and $(k+1)$ additional independent state parameters. The number of independent parameters, required to determine the intensive state parameters of some given bulk phase, is equal to $(k+1)$. Consequently, in order to incorporate into the description a dependence of the surface tension on the state parameters of both coexisting bulk phases (two times $(k+1)$ variables), Gibbs' fundamental equation has to be generalized.

Summarizing these results, we conclude that Gibbs' original treatment is well suited to describe variations of the state parameters, including, for example, thermodynamical potentials and the surface tension, for reversible, quasiequilibrium processes, proceeding via a sequence of equilibrium states. It does not allow us in its original version to describe nonequilibrium states. For this reason, it does not give the appropriate tool for the search of saddle points or extrema of the thermodynamic potentials modeling cluster formation in nucleation and growth processes. We will return to this crucial point shortly.

11.2.3 The Work of Critical Cluster Formation

The change of the internal energy in cluster formation, ΔU, can be written – following Gibbs' approach – generally as (e.g., [10])

$$\begin{aligned}\Delta U &= U_{\text{het}} - U_{\text{hom}} = T_\alpha S_\alpha + T_\beta S_\beta + T_\sigma S_\sigma - TS - p_\alpha V_\alpha - p_\beta V_\beta + \sigma A \\ &\quad + pV + \sum \mu_{j\alpha} n_{j\alpha} + \sum \mu_{j\beta} n_{j\beta} + \sum \mu_{j\sigma} n_{j\sigma} - \sum \mu_j n_j \ . \end{aligned} \tag{11.14}$$

Neglecting changes of the state of the ambient phase in cluster formation (i.e., if the system is sufficiently large as compared with the size of the cluster), we have $p = p_\beta$, $\mu_j = \mu_{j\beta}$, and $T = T_\beta$ (p, T, and μ_j are the pressure, temperature, and chemical potential in the homogeneous initial state, respectively). Taking further into account the boundary conditions (11.8), Eq. (11.14) is simplified to

$$\begin{aligned}\Delta U &= S_\alpha (T_\alpha - T_\beta) + S_\sigma (T_\sigma - T_\beta) + (p_\beta - p_\alpha) V_\alpha + \sigma A \\ &\quad + \sum n_{j\alpha} (\mu_{j\alpha} - \mu_{j\beta}) + \sum n_{j\sigma} (\mu_{j\sigma} - \mu_{j\beta}) \ . \end{aligned} \tag{11.15}$$

Equation (11.15) gives a formal solution of the problem of determination of the change of the internal energy in cluster formation. However, this equation cannot be employed as far as the values of the superficial parameters, in particular, of T_σ and $\mu_{i\sigma}$ and the state parameters of the cluster phase are not specified. This problem is, as already mentioned, not analyzed by

Gibbs. He restricted his analysis to equilibrium states. For equilibrium states, latter problems are resolved immediately. Indeed, with Gibbs' equilibrium conditions (11.10) and (11.11), we then get the following general expression for the work, W_*, of critical cluster formation:

$$W_* = (p_\beta - p_\alpha)V_\alpha + \sigma A \ . \tag{11.16}$$

The state parameters of the cluster phase are determined here uniquely via a subset of Gibbs' equilibrium conditions (11.10) and (11.11). Equation (11.16) holds widely independent of the boundary conditions employed provided (as we assumed) the state of the ambient phase is not changed in the course of formation of the critical cluster, i.e., if the system is sufficiently large. For systems of finite size, additional terms have to be accounted for and the form of these additional terms depends on the boundary conditions employed [21, 33, 34, 50–52]. Thus, for clusters of critical sizes, fulfilling the necessary equilibrium conditions as derived via Gibbs' original treatment, the change of the thermodynamic potential in critical cluster formation can be determined uniquely provided the value of the surface tension is known in dependence on the state of the ambient phase. Moreover, employing the equation for pressure equilibrium (Eq. (11.12)), we generally get

$$W_* = \frac{1}{3}\sigma A - V_\alpha \left\{ C \frac{\mathrm{d}c}{\mathrm{d}V_\alpha} \right\} = \frac{1}{3}\sigma A - V_\alpha \left[\frac{\mathrm{d}\sigma}{\mathrm{d}R} \right] \ . \tag{11.17}$$

For the surface of tension, we get, as a special case, the following general result:

$$W_* = \frac{1}{3}\sigma A = \frac{16\pi}{3} \frac{\sigma^3}{\left(p_\alpha - p_\beta\right)^2} \ . \tag{11.18}$$

Thus, for any value of the work of critical cluster formation it is always possible to find a value of the surface tension such that above equation is fulfilled. However, following Gibbs' original approach, we have no possibility (without introducing further assumptions) of formulating expressions for the thermodynamic potentials of thermodynamic nonequilibrium states. Thus, the problem arises, how Gibbs' theory can be extended to allow a description of clusters of arbitrary sizes in the otherwise homogeneous ambient phase (see also [33–36]).

11.2.4 Extension of Gibbs' Classical Approach to Nonequilibrium States

In order to determine the thermodynamic potentials for nonequilibrium states in the framework of Gibbs' classical approach, one of the problems one has to solve – according to the considerations given in the previous section – consists in the determination of the values of $\mu_{j\sigma}$ and T_σ in Eq. (11.15). In accordance with an intensive analysis of such problems by Defay et al. [53], Prigogine and Bellemans ([54], *a surface phase has no real autonomy, in general*), and Rowlinson and Widom ([14], *we cannot measure or define unambigously the thermodynamic properties of the surface phase*), we developed some time ago the postulate that the superficial quantities have to be set equal to the respective parameters of one of the coexisting macrophases [33, 34]. In application to cluster formation, we demand (the alternative possibility will be analyzed somewhat later) as an additional postulate (*postulate 3*) that

the superficial parameters T_σ and $\mu_{j\sigma}$ have to be set equal to the respective quantities of the ambient phase (see also [14])

$$T_\sigma = T_\beta \ , \quad \mu_{j\sigma} = \mu_{j\beta} \ . \tag{11.19}$$

With these conditions, Eq. (11.15) is simplified to

$$\Delta U = S_\alpha (T_\alpha - T_\beta) + (p_\beta - p_\alpha) V_\alpha + \sigma A + \sum n_{j\alpha} (\mu_{j\alpha} - \mu_{j\beta}) \tag{11.20}$$

and becomes well defined. Note that this relation is valid independent of the choice of the state parameters of the reference phase for the description of the bulk properties of the cluster. Other thermodynamic potentials of nonequilibrium states, appropriate for the respective alternative boundary conditions, can be derived from this relation straightforwardly (e.g., [14, 33–38]).

11.3 A Generalization of Gibbs' Thermodynamic Theory

11.3.1 A Generalization of Gibbs' Fundamental Equation for the Superficial Parameters

Equation (11.20) allows us to compute the thermodynamic potentials of thermodynamic systems consisting of a cluster or ensembles of clusters in the otherwise homogeneous ambient phase providing us in this way with a first step in the generalization of Gibbs' classical approach. However, the final solution of such task should include, as outlined earlier, an incorporation into the theory of the possible dependence of the surface tension of the state parameters not only of one phase but also of both of the coexisting bulk phases. As will be shown in the further analysis, in order to solve such task, Gibbs' fundamental equation for the superficial parameters has to be generalized. Indeed, if one follows further Gibbs' classical procedure, then the additional relations (11.19) lead to the conclusion that the surface or interfacial tension is determined by the properties of the ambient phase exclusively (and, in general, on the curvature). Indeed, a substitution of Eqs. (11.19) into Gibbs' adsorption equation (11.5) yields

$$S_\sigma \, \mathrm{d}T_\beta + A \, \mathrm{d}\sigma + \sum_{j=1}^{k} n_{j\sigma} \, \mathrm{d}\mu_{j\beta} = C \, \mathrm{d}c \ , \tag{11.21}$$

verifying this statement. However, for thermodynamic nonequilibrium states (if we are interested in variations of the interfacial tension if the system is transferred to a state slightly different from the initial state), the surface tension has to depend, in general, on the state parameters of both the ambient and the newly evolving phases. Consequently, variations of the interfacial tension should depend on changes of the thermodynamic state of both bulk phases. Thus, we have to analyze how such property can be incorporated properly into the description modifying the classical Gibbs' treatment not more than absolutely necessary.

In order to resolve mentioned problems, let us analyze more carefully Gibbs' fundamental equation for the superficial quantities (Eq. (11.2)) resulting in Gibbs' adsorption equation (11.5). The right-hand side of Eq. (11.2) consists of two parts. One group of terms ($\sigma \, \mathrm{d}A + C_1 \, \mathrm{d}c_1 + C_2 \, \mathrm{d}c_2$) accounts for the work done by changing the shape and surface

area of the considered surface element. The second group ($T_\sigma \, \mathrm{d}S_\sigma + \sum \mu_{j\sigma} \, \mathrm{d}n_{j\sigma}$) describes variations of the thermodynamic state parameters of the interfacial region or the parameters describing it in Gibbs' model approach. Thus, employing Gibbs' fundamental equation (11.2), it is assumed that the thermodynamic state of the interface can be described by $(k + 1)$ independent parameters (e.g., T_σ and $\mu_{j\sigma}$, $j = 1, 2, \ldots, k$). However, for a two-phase system in a thermodynamic nonequilibrium state, the total number of degrees of freedom of both bulk phases is $2(k + 1)$, i.e., for each of the bulk phases $(k + 1)$ variables may vary independently (Gibbs' phase rule). Each of the independent variables may affect then the properties of the interfacial region. It follows as a consequence that Gibbs' fundamental equation cannot give, in principle, a complete description of the possible variations of the state of the interface in dependence on the state parameters of the coexisting bulk phases for nonequilibrium states of the considered systems. The number of independent variables is too small. A complete description requires, consequently, a dependence of U_σ on $2(k + 1)$ thermodynamic state parameters supplemented by appropriate work terms accounting for the change of the shape and surface area of the considered surface element.

The above-mentioned requirements are fulfilled by the following generalization of Gibbs' classical approach. In this generalization, we employ Gibbs' method of dividing surfaces, again, and define the different superficial parameters via Eqs. (11.1) or similar relations. However, in contrast to Gibbs' classical method, we generalize the fundamental equation (11.2) as

$$\mathrm{d}U_\sigma = T_\sigma \, \mathrm{d}S_\sigma + \sum_{j=1}^{k} \mu_{j\sigma} \, \mathrm{d}n_{j\sigma} + \sigma \, \mathrm{d}A + C \, \mathrm{d}c + \sum_{i=1}^{k+1} \phi_{i\alpha} \, \mathrm{d}\varphi_{i\alpha} \, , \tag{11.22}$$

retaining the additional conditions as given by Eq. (11.19). In Eq. (11.22), $\{\varphi_{i\alpha}\}$ is a complete set of intensive variables, specifying the bulk state of the cluster phase. The restriction to intensive variables $\{\varphi_{i\alpha}\}$ in the specification of above dependence is a consequence from the fact that the surface tension of a given surface element cannot depend on the spatial extensions of the cluster phase but only on the intensive thermodynamic state parameters. The coefficients $\phi_{i\alpha}$ are a measure of the effect of variations of the thermodynamic state parameters $\varphi_{i\alpha}$ of the cluster phase on U_σ for a given state of the ambient phase and surface area and, in general, for a given value of the curvature of the surface element. Of course, in order to realize, a reversible process as described by Eq. (11.22) certain well-defined constraints have to be introduced to prevent irreversible flow processes (cf. Refs. [21, 36]).

Since all state parameters $\varphi_{i\alpha}$ are intensive variables, an integration of Eq. (11.22) results in Eq. (11.4) again. It follows as a first consequence that the expressions for the thermodynamic potentials remain formally unchanged as compared with Gibbs' original method. In particular, for the change of the internal energy in cluster formation we get Eq. (11.15) again, and taking into account Eq. (11.19) an expression identical to Eq. (11.21). As a result, we can also determine any other thermodynamic potentials for any nonequilibrium states of the considered type. The respective expressions are identical to those that one obtains in the extension of the classical Gibbs' approach to nonequilibrium states as we discussed before.

However, the generalization of Gibbs' fundamental equation for the superficial quantities (Eq. (11.22)) reads now

$$\mathrm{d}U_\sigma = T_\beta \,\mathrm{d}S_\sigma + \sum_{j=1}^{k} \mu_{j\beta} \,\mathrm{d}n_{j\sigma} + \sigma \,\mathrm{d}A + C \,\mathrm{d}c + \sum_{i=1}^{k+1} \phi_{i\alpha} \,\mathrm{d}\varphi_{i\alpha} \ . \tag{11.23}$$

The generalized Gibbs' adsorption equation then gets the form

$$S_\sigma \,\mathrm{d}T_\beta + A \,\mathrm{d}\sigma + \sum_{j=1}^{k} n_{j\sigma} \,\mathrm{d}\mu_{j\beta} = C \,\mathrm{d}c + \sum_{i=1}^{k+1} \phi_{i\alpha} \,\mathrm{d}\varphi_{i\alpha} \ . \tag{11.24}$$

It leads to the consequence that the surface tension has to be considered, in general, as a function of the state parameters of both the ambient and the cluster phases. This result is the basic difference between the classical and the generalized Gibbs' approaches as discussed here. Taking $(T_\beta, \{\rho_\beta\})$ as the set of independent variables for the description of the state of the ambient phase, we have

$$\phi_{i\alpha} = A \left(\frac{\partial \sigma}{\partial \varphi_{i\alpha}} \right)_{\{\rho_{j\beta}\}, T_\beta, c} \tag{11.25}$$

as one of the possible expressions for the determination of the coefficients $\phi_{i\alpha}$. Defining the surface of tension in the generalized approach – similar to Gibbs' original approach – via $C = 0$, again, the condition of constancy of c in Eq. (11.25) may be omitted.

11.3.2 The Equilibrium Conditions in the Generalization of Gibbs' Approach

While the form of the expressions for the thermodynamic potentials is the same in the classical and the generalized Gibbs' approaches, the form of the equilibrium conditions is changed. With $\mathrm{d}U = \mathrm{d}U_\alpha + \mathrm{d}U_\beta + \mathrm{d}U_\sigma$ and Eq. (11.23), we get

$$\begin{aligned} \mathrm{d}U \quad = \quad & \left(T_\alpha - T_\beta\right) \mathrm{d}S_\alpha + \left(p_\beta - p_\alpha + \sigma \frac{\mathrm{d}A}{\mathrm{d}V_\alpha} + C \frac{\mathrm{d}c}{\mathrm{d}V_\alpha} \right) \mathrm{d}V_\alpha \\ & + \sum_{j=1}^{k} \left(\mu_{j\alpha} - \mu_{j\beta}\right) \mathrm{d}n_{j\alpha} \\ & + \sum_{i=1}^{k+1} \phi_{j\alpha} \,\mathrm{d}\varphi_{j\alpha} + (\cdots) \,\mathrm{d}S + (\cdots) \,\mathrm{d}V + \sum_{i=1}^{k} (\cdots) \,\mathrm{d}n_i \ . \end{aligned} \tag{11.26}$$

The terms containing brackets $(\cdots)$ will have no effect on the results of the further derivations and are not given explicitely here. In order to employ the general equilibrium conditions $(\mathrm{d}U)_{S,V,\{n\}} = 0$, we choose – as one possible set of independent variables for the description of the bulk properties of the cluster phase – the variables $\{\varphi_{i\alpha}\} = (s_\alpha, \rho_{1\alpha}, \rho_{2\alpha}, \ldots, \rho_{k\alpha})$ with $s_\alpha = (S_\alpha / V_\alpha)$ and $\rho_{i\alpha} = (n_{i\alpha} / V_\alpha)$. We then obtain

$$(\mathrm{d}U)_{S,V,\{n\}} \quad = \quad \left[\left(T_\alpha - T_\beta\right) s_\alpha + \left(p_\beta - p_\alpha\right) + \sigma \frac{\mathrm{d}A}{\mathrm{d}V_\alpha} + C \frac{\mathrm{d}c}{\mathrm{d}V_\alpha} \right.$$

$$+\sum_{j=1}^{k}\rho_{j\alpha}\left(\mu_{j\alpha}-\mu_{j\beta}\right)\Bigg]\mathrm{d}V_\alpha \tag{11.27}$$
$$+\sum_{j=1}^{k}\left[\left(\mu_{j\alpha}-\mu_{j\beta}\right)V_\alpha+\phi_{j\alpha}\right]\mathrm{d}\rho_{j\alpha}$$
$$+\left[\left(T_\alpha-T_\beta\right)V_\alpha+\phi_{s\alpha}\right]\mathrm{d}s_\alpha=0\,.$$

For other choices of the set of independent variables, the form of the resulting expressions can be different, but the final results with respect to the properties of the critical clusters have to be, of course, the same.

In the derivation of Eq. (11.27), again, only the expressions for the changes of the internal energies of both the bulk phases, the generalization of Gibbs' fundamental equation (11.24), and the general equilibrium conditions are employed. Equation (11.27) then results (with Eqs. (11.25)) originally in the following set of equilibrium conditions:

$$\left(T_\alpha-T_\beta\right)s_\alpha+\left(p_\beta-p_\alpha\right)+\sigma\frac{\mathrm{d}A}{\mathrm{d}V_\alpha}+C\frac{\mathrm{d}c}{\mathrm{d}V_\alpha}+\sum_{j=1}^{k}\rho_{j\alpha}\left(\mu_{j\alpha}-\mu_{j\beta}\right)=0\,, \tag{11.28}$$

$$\left(\mu_{j\alpha}-\mu_{j\beta}\right)V_\alpha+\phi_{j\alpha}=0\quad\text{or}\quad\left(\mu_{j\beta}-\mu_{j\alpha}\right)=\frac{3}{R}\left(\frac{\partial\sigma}{\partial\rho_{j\alpha}}\right)_{\{\rho_{i\beta}\},T_\beta,c}\,, \tag{11.29}$$

$$\left(T_\alpha-T_\beta\right)V_\alpha+\phi_{s\alpha}=0\quad\text{or}\quad\left(T_\beta-T_\alpha\right)=\frac{3}{R}\left(\frac{\partial\sigma}{\partial s_\alpha}\right)_{\{\rho_{i\beta}\},T_\beta,c}\,. \tag{11.30}$$

For the surface of tension – defined again via $C=0$ – we then get the more simple results

$$\left(T_\alpha-T_\beta\right)s_\alpha+\left(p_\beta-p_\alpha\right)+\sigma\frac{\mathrm{d}A}{\mathrm{d}V_\alpha}+\sum_{j=1}^{k}\rho_{j\alpha}\left(\mu_{j\alpha}-\mu_{j\beta}\right)=0\,, \tag{11.31}$$

$$\left(\mu_{j\beta}-\mu_{j\alpha}\right)=\frac{3}{R_\mathrm{s}}\left(\frac{\partial\sigma}{\partial\rho_{j\alpha}}\right)_{\{\rho_{i\beta}\},T_\beta}\,, \tag{11.32}$$

$$\left(T_\beta-T_\alpha\right)=\frac{3}{R_\mathrm{s}}\left(\frac{\partial\sigma}{\partial s_\alpha}\right)_{\{\rho_{i\beta}\},T_\beta}\,. \tag{11.33}$$

Evidently, Eqs. (11.28)–(11.33) are reduced to Gibbs' classical expressions (11.10)–(11.12) again, if the possible (and essential) dependence of the surface tension on the state parameters of the cluster phase is neglected in the analysis. Substitution of the equilibrium conditions (11.28)–(11.30) into the general expression for the change of the internal energy in cluster formation (Eq. (11.20)) yields

$$\Delta U_*=\frac{1}{3}\sigma A-V_\alpha\left\{C\frac{\mathrm{d}c}{\mathrm{d}V_\alpha}\right\}\,. \tag{11.34}$$

For the generalized surface of tension (defined via $C = 0$, again) this relation is simplified to the conventional expression

$$\Delta U_* = \frac{1}{3}\sigma A \ . \tag{11.35}$$

The subscript $*$ in Eqs. (11.34) and (11.35) specifies the values of the internal energy of the critical clusters. Thus, the general equations for the determination of the work of critical cluster formation in the generalized Gibbs' approach are identical to the results of the classical Gibbs' method. Differences in the values of this quantity in dependence on supersaturation are due thus exclusively to differences in the bulk parameters of the critical clusters the corresponding values of the surface tension and the size f the critical clusters.

With the above given considerations, the general thermodynamic formalism of the generalization of Gibbs' approach is completed. The further analysis will be directed now to a discussion of possible methods of application of this theoretical schema and of some basic results.

11.3.3 Determination of the Dependence of the Surface Tension on the State Parameters of the Coexisting Phases

In order to employ the newly developed expressions (11.28)–(11.33) for the determination of the state properties of the critical clusters, we have to know – as one of the prerequisites of the analysis – the dependence of the interfacial tension on the state parameters of both coexisting phases. We will perform the respective analysis for the generalized surface of tension, determined similar to Gibbs' classical approach via $C = 0$. In such a case, an explicite dependence of the surface tension on the curvature does not occur. Implicitely, the surface tension may change in dependence on the cluster size due to the dependence of the cluster bulk properties on the size of the clusters. Thus, the choice of the surface of tension has the unique advantage that it allows us to employ dependences for the surface tension obtained for macroscopic samples to the determination of the properties of clusters.

The surface tension, referred to the surface of tension in the generalized Gibbs' approach, can be considered (according to the generalization of Gibbs' fundamental equation (11.24)) as a function of well defined sets of the intensive state parameters of both coexisting phases. We demand, moreover, that the surface tension has to depend generally on the sets of differences of the intensive state parameters of the two considered bulk phases. Denoting the respective sets as $\{\varphi_{i\alpha}\}$ and $\{\varphi_{i\beta}\}$, respectively, we get

$$\sigma_{\alpha,\beta} = \sigma_{\alpha,\beta}\left((\varphi_{1\alpha} - \varphi_{1\beta}), (\varphi_{2\alpha} - \varphi_{2\beta}), \ldots, (\varphi_{k+1,\alpha} - \varphi_{k+1,\beta})\right) \ . \tag{11.36}$$

By choosing the dependence in such a form, the limiting condition $\sigma \to 0$ for $(\{\varphi_{j\alpha} - \varphi_{j\beta}\} \to 0,\ j = 1, 2, \ldots, k+1)$ has to be fulfilled (i.e., when both phases become identical, the surface tension should be equal to zero). A truncated Taylor expansion of $\sigma_{\alpha,\beta}$ with respect to the differences $\{(\varphi_{j\alpha} - \varphi_{j\beta})\}$ reads then initially

$$\sigma_{\alpha,\beta} = \sum_{j=1}^{k+1} \Theta_j \left(\varphi_{j\alpha} - \varphi_{j\beta}\right) + \sum_{i,j=1}^{k+1} \Theta_{ij} \left(\varphi_{i\alpha} - \varphi_{i\beta}\right)\left(\varphi_{j\alpha} - \varphi_{j\beta}\right) + \cdots \ . \tag{11.37}$$

The quantity $\sigma_{\alpha,\beta}$ denotes the value of the surface tension, when a cluster (with parameters specified by α) is formed in an ambient phase (specified by the subscript β). However, since $\sigma_{\alpha,\beta}$ is, by the above given derivation, independent of the phase which forms the cluster, and that represents the surrounding bulk and is equal to the respective value for a planar coexistence of both phases, the symmetry relation $\sigma_{\alpha,\beta} = \sigma_{\beta,\alpha} = \sigma$ has to be fulfilled. It follows that the linear terms with respect to the density differences and, more generally, any odd terms vanish. Instead of Eq. (11.37), we then obtain in the lowest approximation

$$\sigma = \sum_{i,j=1}^{k+1} \Theta_{ij} \left(\varphi_{i\alpha} - \varphi_{i\beta}\right) \left(\varphi_{j\alpha} - \varphi_{j\beta}\right) + \cdots . \tag{11.38}$$

In order to employ this relation, we have to determine the independent parameters Θ_{ij}. This task can be performed by measuring the value of the surface tension for a planar coexistence of the two phases for different sets of state parameters of the ambient phase. Since only the sums $\Theta_{ij} + \Theta_{ji}$ (for $i \neq j$) can be determined uniquely, we may assume without loss of generality $\Theta_{ij} = \Theta_{ji}$. In order the surface tension to be positive semidefinite, hereby well-defined conditions have to be fulfilled concerning possible values of the parameters (cf., e.g., [39,41,44,46]). We can specify in more detail the kinds of intensive variables the surface energy has to depend on. The surface energy can be expected to be determined – according to the approach developed – by the volume densities of particle numbers and entropies (or temperatures) in both coexisting phases, i.e., by the local conditions in the vicinity of the interface. For this reason, we derived here the equilibrium conditions for these sets of independent variables.

For one-component systems, dependences similar to Eq. (11.38) are widely used for the description of the interfacial tension for liquid–gas phase coexistence (e.g., Macleod's and similar equations [14,41,55]) and for phase separation processes in solutions (Becker's equation [39,56]). Generalizations of such types of dependences to phase coexistence in multicomponent systems have been advanced – in the framework of Gibbs' original approach (where their application is, however, partly questionable by above-discussed reasons) – already as well [57]. Thus, the above-described method of specification of the dependence of the surface tension on the state parameters of both phases can be considered as well-founded and will be employed in the further analysis.

11.3.4 Analysis of an Alternative Version

In connection with the proposed here method of generalization of Gibbs' theory to nonequilibrium states the question may arise whether or not the alternative possibility

$$T_\sigma = T_\alpha \ , \quad \mu_{j\sigma} = \mu_{j\alpha} \ . \tag{11.39}$$

is utilized instead of Eq. (11.19). As a first general argument in favor of Eq. (11.19) instead of Eq. (11.39), one can advance the preposition that the properties T_σ and $\mu_{i\sigma}$ of the interface have to be determined mainly by the properties of the macroscopic ambient phase. However, as shown below, one may also develop an even more conclusive additional argument in favor of Eq. (11.19). Indeed, following the same procedure as earlier but employing this time Eq. (11.39), we get instead of Eq. (11.20)

$$\Delta U \quad = \quad \widetilde{S}_\alpha (T_\alpha - T_\beta) + (p_\beta - p_\alpha) V_\alpha + \sigma A + \sum \widetilde{n}_{j\alpha} (\mu_{j\alpha} - \mu_{j\beta}) \ ,$$

$$\widetilde{S}_\alpha = S_\alpha + S_\sigma \ , \quad \widetilde{n}_{j\alpha} = n_{j\alpha} + n_{j\sigma} \ . \tag{11.40}$$

This relation gives a well-defined expression for the internal energy as well. It is less convenient, however, as compared with Eq. (11.20) since here U is, in part, not expressed directly via the parameters of the cluster phase, $n_{j\alpha}$, S_α but via $\widetilde{n}_{j\alpha}$ and $\widetilde{S}_\alpha$.

Similar to Eq. (11.40), the generalizations of Gibbs' fundamental and Gibbs' adsorption equations (Eqs. (11.22) and (11.24)) read now

$$\mathrm{d}U_\sigma = T_\alpha \, \mathrm{d}S_\sigma + \sum_{j=1}^{k} \mu_{j\alpha} \, \mathrm{d}n_{j\sigma} + \sigma \, \mathrm{d}A + C \, \mathrm{d}c + \sum_{i=1}^{k+1} \phi_{i\beta} \, \mathrm{d}\varphi_{i\beta} \ . \tag{11.41}$$

$$S_\sigma \, \mathrm{d}T_\alpha + A \, \mathrm{d}\sigma + \sum_{j=1}^{k} n_{j\sigma} \, \mathrm{d}\mu_{j\alpha} = C \, \mathrm{d}c + \sum_{i=1}^{k+1} \phi_{i\beta} \, \mathrm{d}\varphi_{i\beta} \ . \tag{11.42}$$

Taking $(T_\alpha, \{\rho_\alpha\})$ as the set of independent variables for the description of the state of the cluster phase, we get the following expression for the coefficients $\phi_{i\beta}$:

$$\phi_{i\beta} = A \left(\frac{\partial \sigma}{\partial \varphi_{i\beta}} \right)_{\{\rho_{j\alpha}\}, T_\alpha, c} \ . \tag{11.43}$$

The general equilibrium condition reads, now, instead of Eq. (11.27),

$$\begin{aligned} (\mathrm{d}U)_{S,V,\{n\}} &= \left(T_\alpha - T_\beta\right) \mathrm{d}\widetilde{S}_\alpha + \left[\left(p_\beta - p_\alpha\right) + \sigma \frac{\mathrm{d}A}{\mathrm{d}V_\alpha} + C \frac{\mathrm{d}c}{\mathrm{d}V_\alpha} \right] \mathrm{d}V_\alpha \\ &\quad + \sum_{j=1}^{k} \left(\mu_{j\alpha} - \mu_{j\beta}\right) \mathrm{d}\widetilde{n}_{j\alpha} + \sum_{i=1}^{k+1} \phi_{j\beta} \, \mathrm{d}\varphi_{j\beta} = 0 \ . \end{aligned} \tag{11.44}$$

However, in any variations of the state parameters of the cluster (volume, entropy, particle numbers), the state parameters of the ambient phase remain constant. We consider, as outlined earlier, a sufficiently large system where the formation of a cluster does not affect the state parameters of the ambient phase. Therefore, $\mathrm{d}\varphi_{i\beta} = 0$ holds and we obtain the conventional Gibbs' adsorption equation (Eq. (11.42) becomes equivalent to Eq. (11.5)) and the conventional Gibbs' equilibrium conditions (Eq. (11.44) leads to Eqs. (11.10)–(11.12)).

It turns out that the alternative possibility of determining the properties of heterogeneous systems in nonequilibrium states, utilizing Eqs. (11.39) instead of Eqs. (11.19), does not lead to any modifications of the basic equations, the properties of the critical clusters, and the work of critical cluster formation as compared with Gibbs' classical approach. Indeed, with the condition $\mathrm{d}\varphi_{i\beta} \cong 0$, Eq. (11.41) becomes equivalent to the fundamental equation as employed by Gibbs [11]. Therefore, only the condition introduced with Eq. (11.19) allows one to incorporate into the description the required dependence of the surface tension of the state parameters of both the ambient and the newly evolving phases. For this reason, condition (11.19) is preferable to Eq. (11.39).

11.4 Applications: Condensation and Boiling in One-Component Fluids

11.4.1 Nucleation at Isothermal Conditions

In order to illustrate the consequences of the above-developed theory, we consider here the case of formation of droplets and bubbles in a van der Waals fluid first for isothermal conditions, i.e., we suppose that the temperature in the whole system is kept constant by some appropriate mechanism. The results are compared with van der Waals' square gradient density functional computations. The equations employed and the method of computations are outlined in detail in [27, 41, 44] (see also the Appendix). Therefore, we can concentrate here the attention immediately on the results.

For isothermal conditions and one-component systems, liquid and gas are distinguished by the density, ρ, or the specific volume, v. Following Eqs. (11.33) and (11.38), the surface tension has to be written then (in a first approximation) in the form

$$\sigma = \Theta(\theta)\left(\rho_{\mathrm{l}} - \rho_{\mathrm{g}}\right)^{\chi} \tag{11.45}$$

with $\chi = 2$. For any arbitrary value of the temperature θ, the parameter Θ can be determined then from the knowledge of the densities at the liquid and vapor branches of the binodal curves and the value of the surface tension for an equilibrium coexistence of both phases at planar interfaces (for the method of determination of the macroscopic value of σ as employed in our analysis, see [27]). In Fig. 11.1, the binodal and spinodal curves of a van der Waals fluid are given in reduced variables $\theta = T/T_{\mathrm{c}}$ and $\omega = v/v_{\mathrm{c}}$ (here T_{c} is the critical temperature and v_{c} the critical volume of the fluid).

We first consider condensation and bubble formation at a temperature $\theta = 0.7$. The supersaturation is changed then by variations of the specific volume of the ambient phase between the respective binodal and spinodal curves. In Fig. 11.2, the specific volume of the liquid in the droplet of critical size and the specific volume of the gas in the bubble of critical size are shown. The dotted curves refer to the values of these parameters, when Gibbs' original method is used. The dashed curve presents the results obtained via the generalized Gibbs' approach employing Eq. (11.45) with $\chi = 2$. The full curves refer to the respective results, when the van der Waals square gradient method is employed for the computations of the work of critical cluster formation and the results are then used to compute the respective quantities as determined via Gibbs' original method (via Eqs. (11.10), (11.12), and (11.18)). Similarly, in Fig. 11.3, the sizes of the critical clusters are shown when the surface of tension is chosen as the dividing surface. Finally, in Fig. 11.4, the work of critical cluster formation is presented for condensation and boiling as obtained by the different methods of computation. Similar results were obtained in already cited papers [27, 41, 44]; however, there the parameter χ was set equal to $\chi = 2.5$. Such choice made there was motivated by experimentally observed dependences of the surface tension on the state parameters of the coexisting phases. The results obtained with Eq. (11.45) but assuming $\chi = 2.5$ are given in Figs. 11.2–11.4 by the dashed-dotted curves.

Analyzing the results presented in Figs. 11.1–11.4, we come to the following conclusions (for a more detailed analysis see [41, 44, 45]):

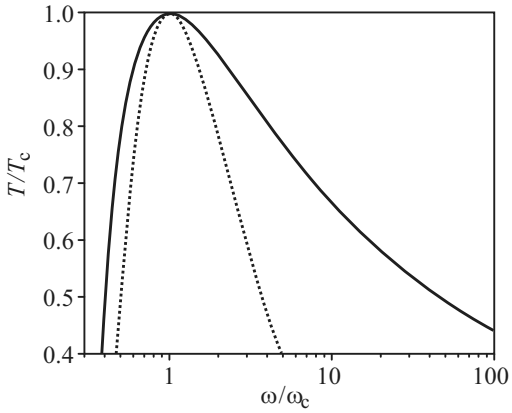

Figure 11.1: Binodal (full line) and spinodal (dotted line) curves of the van der Waals fluid. The phase transformation proceeds via nucleation and growth processes for initial states located between the binodal and spinodal curves. For the process of condensation of gases by nucleation and growth, the initial states are located between the right-hand side branches of both curves. Similarly, bubble formation occurs for initial states between the left-hand side branches of the curves

(i) Gibbs' classical approach does not give a correct description of the bulk properties of the cluster phase (Fig. 11.2). In contrast, the generalized Gibbs' approach is in, at least, qualitative agreement with the results of density functional computations, in particular, for high supersaturations.

(ii) The radius of the critical cluster, referred to the surface of tension, has, for small and moderate supersaturations similar values, when (a) the classical Gibbs approach is used for its determination supplemented by the capillarity approximation and (b) when the respective size parameter is computed via the generalized Gibbs' approach. Only for initial supersaturations near the spinodal, approaches (a) and (b) lead to different results. Here the radius of the surface of tension, computed via the generalized Gibbs' approach, diverges (in agreement with density functional computations of characteristic size parameters of the critical clusters). In contrast, the radius of the surface of tension, determined via the classical Gibbs' method employing the van der Waals computations for the work of critical cluster formation, tends here to zero. The radius of the surface of tension, determined via the generalized Gibbs' approach, gives in this way a much more realistic description of the real spatial dimensions of the critical clusters as the respective quantity determined via the combined van der Waals–Gibbs method.

(iii) The size of the critical clusters, determined via the methods (a) and (b), remains nearly constant for intermediate supersaturations. This range of intermediate supersaturations corresponds commonly to the range of experimental observations of nucleation processes. It follows as a consequence that the size of the critical clusters should be of the same order of magnitude independent of the degree of supersaturation reached in a specific

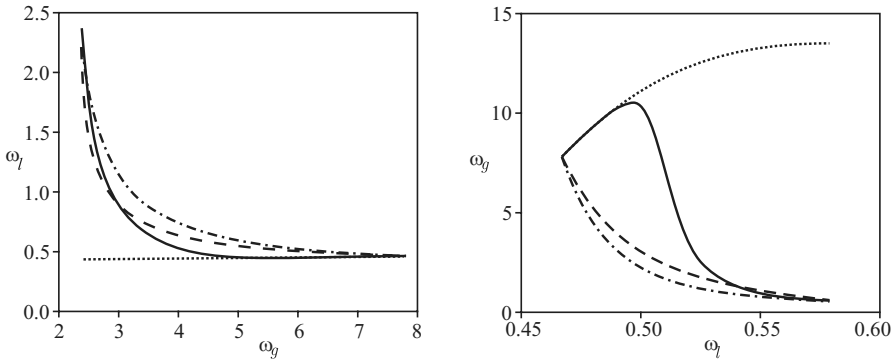

Figure 11.2: Dependence of the specific volumes of the liquid, ω_{l}, in the drops and of the gas, ω_{g}, in the bubbles of critical sizes, employed as reference states for the description of the bulk contributions to the thermodynamic potential, on the initial supersaturation. For condensation (left part of this and subsequent figures), the supersaturation is determined by the value of the specific volume of the gas, ω_{g}. For bubble formation (right part of the figures), the supersaturation may be expressed via the molar volume of the liquid, ω_{l}. The dotted curves refer here and later on to the respective values of the molar volumes as determined via Gibbs' original approach. The dashed curves correspond to the newly developed generalized Gibbs' approach utilizing Eq. (11.45) with $\chi = 2$, while the dashed-dotted curves correspond to similar results obtained with a value of χ equal to $\chi = 2.5$. The full curves represent the results of calculations of the specific volumes in the center of the critical clusters performed via the van der Waals square gradient approximation. In both cases (condensation and boiling), the temperature is set equal to $T = 0.7\,T_{\mathrm{c}}$ and is assumed to be the same in both the ambient and the newly evolving phases

experiment. Similar results have been obtained also for segregation in solid and liquid solutions and bubble formation in liquid–gas solutions [26, 39, 46]. Thus, such feature of the nucleation process seems to be of widely universal nature.

(iv) Both the van der Waals and the generalized Gibbs' approach lead, for moderate and high values of the initial supersaturation, to lower values of the work of critical cluster formation as compared with the classical Gibbs' method when in its application the capillarity approximation is employed. However, while the dependences of the critical cluster composition and the critical cluster size on supersaturation in the generalized Gibbs' approach behave in a qualitatively similar way, the dependence of the work of critical cluster formation on supersaturation is qualitatively different for the cases $\chi = 2$ and $\chi = 2.5$, respectively. As shown earlier [37, 41], near the spinodal the work of critical cluster formation tends to zero for values of the parameter $\chi > 2$, only. For $\chi = 2$, we get small but finite values of the work at the spinodal. In the case considered, this value is near $k_{\mathrm{B}}T$.

Nevertheless, we can prolong the curve for the dependence of the work of critical cluster formation on supersaturation to zero also for the case $\chi = 2$. This possibility is due to the following circumstances (see also [30]): For any value of the initial supersaturation, in the

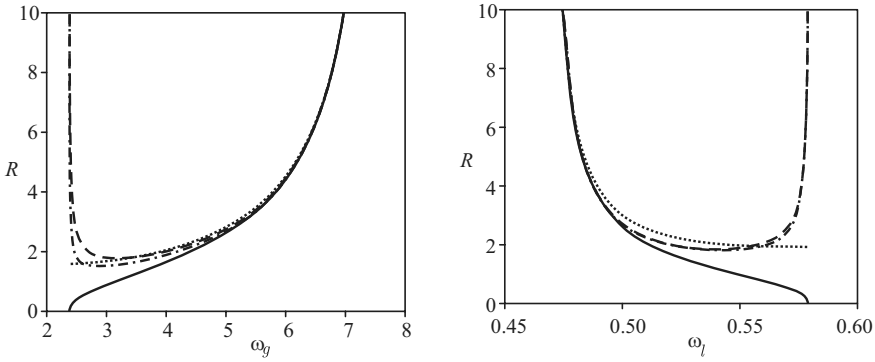

Figure 11.3: Dependence of the size of the critical clusters (referred to the surface of tension) on the initial supersaturation. The dotted curves refer to the respective values as determined via Gibbs' approach (employing the capillarity approximation). The dashed curves refer to the newly developed generalized Gibbs' approach utilizing Eq. (11.31) with $\chi = 2$. The dashed-dotted curves show similar results but for a value of the parameter χ equal to $\chi = 2.5$. The full curves represent the results of calculations performed via the van der Waals square gradient approximation used then for the determination of the respective quantities introduced via Gibbs' classical approach. It is assumed here again that the temperature is the same in both the ambient and the newly evolving phases

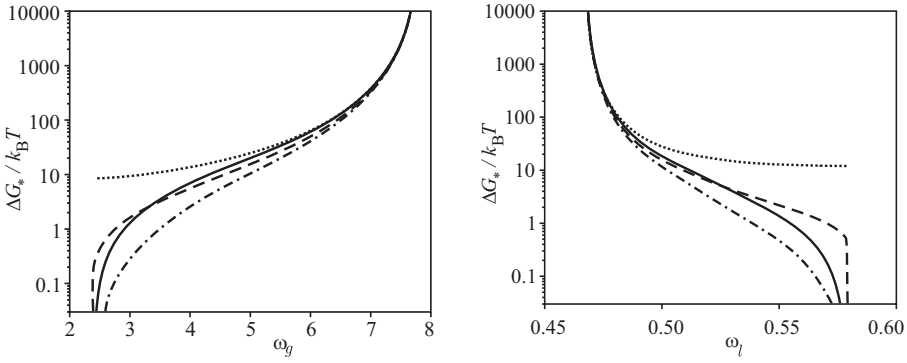

Figure 11.4: Dependence of the work of critical cluster formation on the initial supersaturation. The dotted curves refer to the respective values as determined via Gibbs' original approach if the capillarity approximation is employed. The dashed curves refer to the newly developed generalized Gibbs' approach utilizing Eq. (11.45) with $\chi = 2$. The dashed-dotted curves show similar results but for a value of the parameter χ equal to $\chi = 2.5$. The full curves represent the results of calculations performed via the van der Waals square gradient approximation. It is assumed here again that the temperature is the same in both the ambient and the newly evolving phases

range between binodal and spinodal ($\omega_{\rm bin} \leq \omega \leq \omega_{\rm spin}$), the equilibrium conditions (11.31)–(11.33) lead to two different solutions. In addition to the results shown in Fig. 11.2 there exists a second solution $\omega_{\rm cluster} = \omega$, i.e., the specific volume of the critical cluster is equal to the specific volume of the ambient phase. This solution is physically meaningless for $\omega_{\rm bin} \leq \omega \leq \omega_{\rm spin}$ (it leads to negative values of the critical cluster size), but it is the only solution for $\omega > \omega_{\rm spin}$. Here it results in values of the work of critical cluster formation identically equal to zero. Thus, for $\chi = 2$ we get finite values for the work of critical cluster formation at the spinodal, but, as soon as we consider initial states inside the unstable region, the theory predicts values of the work of critical cluster formation equal to zero (independent of the value of the parameter χ in the range $\chi \geq 2$). Moreover, it can be seen that Eq. (11.45) with $\chi = 2$ leads to a better agreement with the results for the work of critical cluster formation between the generalized Gibbs' and the van der Waals square gradient approaches as compared with the assumption $\chi = 2.5$ (cf. also [27]). One may suppose that this correlation is connected with the similarity of the square gradient van der Waals approach employed and the method leading to the relation for the dependence of the surface tension on the state parameters of both coexisting phases: Both approaches employ Taylor expansions truncated at the quadratic terms. However, this correlation and its possible origin require some further detailed analysis.

11.4.2 Analysis of the General Case

The above-discussed results rely on one additional assumption. It is assumed that the temperature in the critical droplet or the bubble of critical size is equal to the temperature of the ambient phase. This assumption is widely employed in the theoretical analysis of nucleation phenomena. It is founded by Gibbs' classical approach (cf. Eq. (11.11)) if one assumes, as is usually done, that the evolution to the new phase proceeds via the saddle point of the appropriate thermodynamic potential. However, according to the generalized Gibbs' approach the assumption of equality of temperatures of both phases (the ambient phase and the reference phase employed for the description of the bulk properties of the critical clusters) is, in general, not correct (cf. Eqs. (11.30) and (11.33)). In the following analysis, we will try to establish an estimate of the temperature differences of the critical cluster as compared with the ambient phase and compare the results concerning the parameters of the critical clusters with those obtained under the assumption that nucleation proceeds at isothermal conditions (restricting here the analysis to the case $\chi = 2$).

In order to determine the dependence of the surface tension on the state parameters of both phases in the general situation, we employ Eq. (11.38). Utilizing this equation, we have to know, for example, the dependence of the surface tension not only on the differences of the volume, mass or particle densities of the different components but also on the differences of the volume densities of the entropies, s, of the different phases. The surface tension can be expressed then (according to Eq. (11.38)) generally as

$$\sigma = \Theta_\rho \left(\rho_\alpha - \rho_\beta\right)^2 + \Theta_{\rho,s} \left(\rho_\alpha - \rho_\beta\right)\left(s_\alpha - s_\beta\right) + \Theta_s \left(s_\alpha - s_\beta\right)^2 \cdots . \tag{11.46}$$

In order to employ this equation, we have to determine the values of the coefficients Θ_ρ, $\Theta_{\rho,s}$, and Θ_s. However, we have at our disposal only one relation connecting the values of the

surface tension at the planar interface at some given temperature (here $T/T_c = 0.7$) with the equilibrium particle and entropy densities of the coexisting phases $\rho_\alpha^{(eq)}$, $\rho_\beta^{(eq)}$, $s_\alpha^{(eq)}$, and $s_\beta^{(eq)}$.

In order to get some first insight into the possible dependences, we parametrize Eq. (11.46) and analyze the resulting dependences for different parameter values. Hereby, we have to realize that the parameters Θ or their equivalents have to obey the conditions

$$\Theta_\rho \geq 0\,, \quad \Theta_s \geq 0\,, \quad |\Theta_{\rho,s}| \leq \sqrt{\Theta_s \Theta_\rho} \tag{11.47}$$

in order to get positive values of the surface tension independent of the differences of the state parameters. As a first dependence, we employ the relation

$$\frac{\sigma}{\sigma_\infty} = \alpha \left(\frac{\rho_\alpha - \rho_\beta}{\rho_\alpha^{(eq)} - \rho_\beta^{(eq)}} \right)^2 + (1-\alpha) \left(\frac{s_\alpha - s_\beta}{s_\alpha^{(eq)} - s_\beta^{(eq)}} \right)^2 , \quad 0 \leq \alpha \leq 1\,. \tag{11.48}$$

It realizes the limit $\Theta_{\rho,s} = 0$. We write the second parametric dependence for the surface tension in the form

$$\begin{aligned} \frac{\sigma}{\sigma_\infty} \;=\; & \beta^2 \left(\frac{\rho_\alpha - \rho_\beta}{\rho_\alpha^{(eq)} - \rho_\beta^{(eq)}} \right)^2 + 2\beta(1-\beta) \left(\frac{s_\alpha - s_\beta}{s_\alpha^{(eq)} - s_\beta^{(eq)}} \right) \left(\frac{\rho_\alpha - \rho_\beta}{\rho_\alpha^{(eq)} - \rho_\beta^{(eq)}} \right) \\ & + (1-\beta)^2 \left(\frac{s_\alpha - s_\beta}{s_\alpha^{(eq)} - s_\beta^{(eq)}} \right)^2 . \end{aligned} \tag{11.49}$$

It realizes the limit $\Theta_{\rho,s} = \sqrt{\Theta_s \Theta_\rho}$ for values of β in the range $0 < \beta < 1$ and $\Theta_{\rho,s} = -\sqrt{\Theta_s \Theta_\rho}$ for values of β in the range $1 < \beta$. The constancy of ρ_β and T_β in Eq. (11.33) implies that also s_β can be considered as constant. Consequently, for our purposes we may rewrite Eq. (11.33) as

$$\left(T_\beta - T_\alpha\right) = \frac{3}{R_s} \left(\frac{\partial \sigma}{\partial s_\alpha} \right)_{\rho_\beta, s_\beta} . \tag{11.50}$$

Generally, the values of the coefficients Θ do not depend on whether condensation or boiling is analyzed. Consequently, in general, the thermal effect on nucleation – as follows from the generalized Gibbs' approach – will be asymmetric for both considered cases of phase formation.

In order to proceed with the computations, we have to know the location of the binodal curve, the entropy density, and the value of the surface tension of a van der Waals fluid analyzed here as the model system. The respective derivations and results are given in the Appendix. Employing these results, we can now determine quantitatively the changes in temperature in the critical cluster as compared with the temperature in the ambient phase. The respective results for condensation and boiling of a van der Waals fluid are shown in Fig. 11.5. In Fig. 11.5, the temperature in the ambient phase is chosen equal to $T/T_c = 0.7$, again. The solid curves correspond to a dependence of the surface tension on the state parameters of both phases as described by Eq. (11.48) with (1): $\alpha = 0.8$ and (2): $\alpha = 0.5$. The dashed and dotted

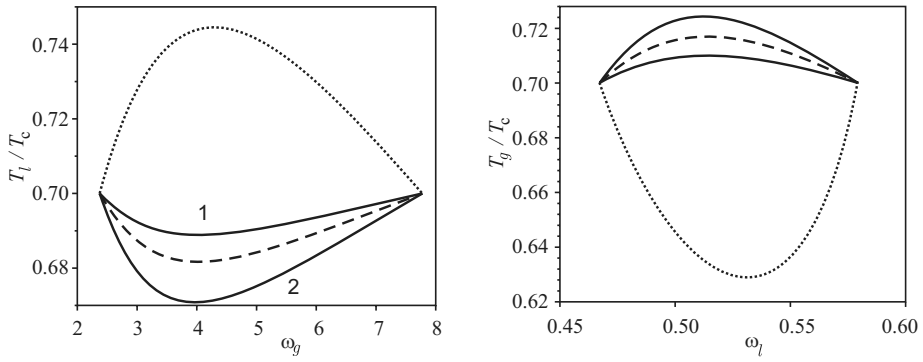

Figure 11.5: Change of the temperature in a droplet (left curve) and a bubble (right curve) of critical sizes in dependence on supersaturation. The temperature in the ambient phase is equal to $T/T_c = 0.7$, again. The full curves correspond to a dependence of the surface tension as described by Eq. (11.48) with (1): $\alpha = 0.8$ and (2): $\alpha = 0.5$. The dashed and dotted curves refer to a dependence of the surface tension on the state parameters as described by Eq. (11.49) with $\beta = 2/3$ (dashed) and $\beta = 2$ (dotted curve)

curves refer to a dependence of the surface tension on the state parameters as described by Eq. (11.49) with $\beta = 2/3$ (dashed) and $\beta = 2$ (dotted curve). It turns out that the sign of the difference may vary in dependence on the relation employed for the dependence of the surface tension on the state parameters of both phases.

Taking into account the differences in temperature of the critical cluster and the ambient phase, the dependence of the size of the critical clusters (drops or bubbles) and the work of critical cluster formation on supersaturation will be different as compared with the results obtained via the assumption of isothermal nucleation. These differences are illustrated in Figs. 11.6 and 11.7. In the computations for the isothermal case (full curve), the parameter χ in Eq. (11.45) was set equal to $\chi = 2$. The dashed curve shows the results for the critical cluster size and the work of critical cluster formation utilizing Eq. (11.48) with a value of the parameter α equal to $\alpha = 0.5$.

The above-given results show that the deviations of the temperature of the critical cluster from the respective values of the ambient phase can be significant. Moreover, the temperatures can deviate in different directions in dependence on the particular expression employed for the dependence of the surface tension on the state parameters. Thus, in order to apply the theory to the description of nucleation, methods of determination of the dependence of the surface tension on the state parameters on both phases have to be advanced in the future analysis.

11.5 Discussion

According to the predictions of the generalized Gibbs' approach, the temperatures in the critical cluster and the vapor have, in general, to differ. This difference may lead to significant variations in the size of the critical clusters and the value of the work of critical cluster forma-

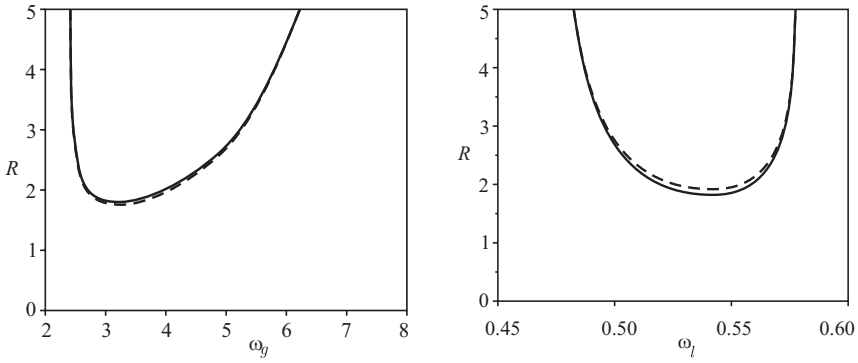

Figure 11.6: Effect of change of temperature on the size of the critical clusters. The temperature in the ambient phase is chosen equal to$T/T_c = 0.7$, again. The full curves correspond to the isothermal case, while the dashed curve gives the results when the dependence of the surface tension on the state parameters of both phases is described by Eq. (11.48) with $\alpha = 0.5$

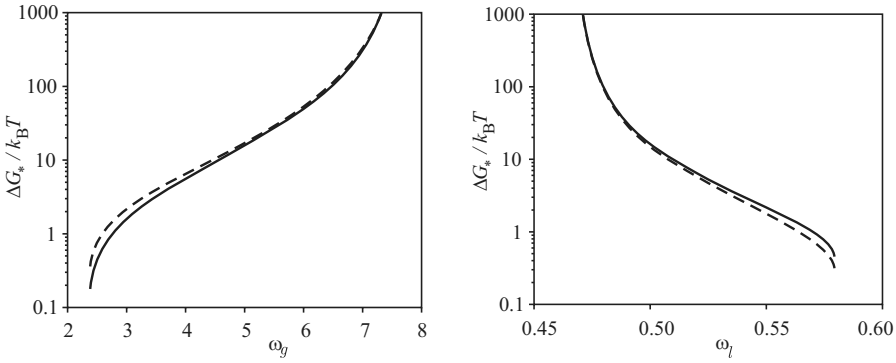

Figure 11.7: Effect of change of temperature on the work of critical cluster formation. The temperature in the ambient phase is chosen equal to $T/T_c = 0.7$, again. The full curves correspond to the isothermal case, while the dashed curve gives the results when the dependence of the surface tension on the state parameters of both phases is described by Eq. (11.48) with $\alpha = 0.5$

tion as compared with the case when equal values of the temperature are assumed; however, for the considered case the resulting variations occurred to be of minor importance. In general, it may serve as an additional factor the implementation of which may improve the agreement between experimental and theoretical results on nucleation kinetics. It is planned to check the predictions of the generalized Gibbs' approach with respect to the temperature of the critical clusters by independent methods. Here molecular dynamics is one possible tool allowing us to come to some definite conclusions. It is planned to extend existing work [58] in this direction to an analysis of this problem. An alternative theoretical method to verify the predictions of the generalized Gibbs' approach is possibly the application of the methods of small systems' statistical physics (e.g., [59]). It is expected that the research along this line will also allow us

to specify more definitely the form of the dependence of the surface tension on the state parameters of both coexisting phases. Since the generalized Gibbs' approach has shown its power in the prediction of the bulk properties of the critical clusters [21,26,27,46], it can be expected that the predictions with respect to temperature will be verified as well. In the alternative case, one would have to suppose – modifying slightly the generalized Gibbs' approach as outlined here – that, with respect to temperature, the conditions $T_\alpha = T_\sigma$ (cf. Eqs. (11.39)) are fulfilled leaving the conditions for the chemical potentials ($\mu_{j\sigma} = \mu_{j\beta}$) untouched (cf. Eq. (11.19)). In such a case, Eqs. (11.30) and (11.33) should be replaced by equality of temperatures as in the original Gibbs' approach. However, so far we cannot see any reason why it should be necessary to make such a distinction.

Note that the newly developed modified Gibbs' approach has some further significant advantage as compared with Gibbs' original method (and existing density functional calculations as well): It allows us to determine theoretically the state of clusters not only of critical sizes but – employing some generally rather weak additional assumption (see [29, 30]) – the state of clusters of sub- and supercritical clusters as well. An analysis of this topic in application to condensation and bubble formation will be performed in a forthcoming paper. However, this particular problem is only one of the broad spectra of possible future directions of research, where the generalized Gibbs' approach is expected to lead to new highly interesting results.

11.6 Appendix

The thermal equation of state for one mole of a van der Waals fluid is given by

$$\left(p + \frac{a}{v^2}\right)(v - b) = R_\mathrm{g} T \ . \tag{11.51}$$

Here p is the pressure, v is the molar volume, T is the temperature, and R_g is the universal gas constant. a and b are two parameters reflecting specific properties of the system under consideration. The parameters a, b and the universal gas constant R_g may be expressed via the molar volume, v_c, the pressure, p_c, and the temperature, T_c, at the critical point. We get

$$a = 3 p_\mathrm{c} v_\mathrm{c}^2 \ , \quad b = \frac{1}{3} v_\mathrm{c} \ , \quad R_\mathrm{g} = \frac{8}{3} \frac{p_\mathrm{c} v_\mathrm{c}}{T_\mathrm{c}} \ . \tag{11.52}$$

Employing Eq. (11.52), Eq. (11.51) can be written in the form of a law of corresponding states as

$$\left(\Pi + \frac{3}{\omega^2}\right)(3\omega - 1) = 8\theta \tag{11.53}$$

with

$$\Pi = \frac{p}{p_\mathrm{c}} \ , \quad \omega = \frac{v}{v_\mathrm{c}} \ , \quad \theta = \frac{T}{T_\mathrm{c}} \ . \tag{11.54}$$

The position of the classical spinodal curve can be found via the determination of the extrema of the thermal equation of state $\Pi(\omega, \theta)$ (Eqs. (11.51) and (11.53)) considering the

temperature θ as constant. By taking the derivative of $\Pi(\omega)$ with respect to ω, we obtain from Eq. (11.53) the result

$$\frac{\partial \Pi(\omega)}{\partial \omega} = -6\left[\frac{4\theta}{(3\omega-1)^2} - \frac{1}{\omega^3}\right] = 0\ , \quad \frac{(3\omega-1)^2}{\omega^3} = 4\theta\ . \tag{11.55}$$

For $\theta < 1$ this equation has two positive solutions $\omega_{\mathrm{Sp}}^{(\mathrm{left})}$ and $\omega_{\mathrm{Sp}}^{(\mathrm{right})}$ for ω corresponding to the specific volumes of both the macrophases at the spinodal curves (or at the limits of metastability).

Similarly, the binodal curves give for $\theta \leq 1$ the values of the specific volumes of the liquid and the gas phases coexisting in thermal equilibrium at a planar interface ($\omega_{\mathrm{l}}^{(\mathrm{eq})}(\theta) = \omega_{\mathrm{B}}^{(\mathrm{left})}$: specific volume of the liquid phase, $\omega_{\mathrm{g}}^{(\mathrm{eq})}(\theta) = \omega_{\mathrm{B}}^{(\mathrm{right})}$: specific volume of the gas). For $\theta = 1$, both solutions coincide at the critical point ($\omega_{\mathrm{l}}^{(\mathrm{eq})} = \omega_{\mathrm{g}}^{(\mathrm{eq})} = \omega_{\mathrm{c}} = 1$), again. The location of the binodal curve may be determined from the necessary thermodynamic equilibrium conditions (for planar interfaces) – equality of pressure and chemical potentials – via the solution of the set of equations

$$\Pi_{\mathrm{l}}(\omega_{\mathrm{l}}, \theta) = \Pi_{\mathrm{g}}(\omega_{\mathrm{g}}, \theta)\ , \quad \mu_1(\omega_{\mathrm{l}}, \theta) = \mu_{\mathrm{g}}(\omega_{\mathrm{g}}, \theta)\ . \tag{11.56}$$

Here μ denotes the chemical potential of the atoms or molecules in the liquid (l) and the gas (g). For a van der Waals fluid, we have generally [41]

$$\left(\frac{\mu(\omega,\theta)}{p_{\mathrm{c}} v_{\mathrm{c}}}\right) = -\frac{8\theta}{3}\ln(3\omega-1) + \frac{8\theta\omega}{3\omega-1} - \frac{6}{\omega} + \chi(\theta)\ . \tag{11.57}$$

Here $\chi(\theta)$ is some well-defined function only of temperature. The binodal and spinodal curves for a van der Waals gas are shown in Fig. 11.1. For a reduced temperature $\theta = 0.7$, the position of the binodal curves is given by $\omega_{\mathrm{B}}^{(\mathrm{left})} = 0.467$, $\omega_{\mathrm{B}}^{(\mathrm{right})} = 7.811$; the respective parts of the spinodal curves are located at $\omega_{\mathrm{Sp}}^{(\mathrm{left})} = 0.579$; $\omega_{\mathrm{Sp}}^{(\mathrm{right})} = 2.376$.

Further, the Helmholtz free energy per mole, f, of a van der Waals fluid is given by [41]

$$\left(\frac{f}{p_{\mathrm{c}} v_{\mathrm{c}}}\right) = -\frac{8\theta}{3}\ln(3\omega-1) - \frac{3}{\omega} + \chi(\theta)\ , \tag{11.58}$$

where (if the isochoric heat capacity, c_{v}, is supposed to be constant) the function $\chi(\theta)$ may be written as

$$\chi(\theta) = -\frac{8}{3}\frac{c_{\mathrm{v}}}{R_{\mathrm{g}}}\theta\ln(\theta) + \frac{8}{3}\theta\alpha_1^0 + \frac{8}{3}\alpha_2^0\ . \tag{11.59}$$

The constant α_2^0 is not significant for the computations, and the constant α_1^0 can be determined knowing the value of entropy S_0^{id} of a perfect gas at some reference state (T_0, ρ_0). We then get

$$\alpha_1^0 = \frac{c_{\mathrm{v}}}{R_{\mathrm{g}}} - \frac{S_0^{\mathrm{id}}(T_0,\rho_0)}{R_{\mathrm{g}}} + \ln\left(\frac{\rho_{\mathrm{c}}}{\rho_0}\right) - \frac{c_{\mathrm{v}}}{R_{\mathrm{g}}}\ln\left(\frac{T_{\mathrm{c}}}{T_0}\right)\ . \tag{11.60}$$

The statistical analysis of a monoatomic perfect gas ($c_v = 1.5 R_g$) gives

$$\frac{S_0^{id}}{R_g} = 2.5 + \ln\left[g \left(\frac{M R_g T_0}{2\pi (N_A h_p)^2} \right)^{3/2} \frac{R_g T_0}{N_A p_0} \right] . \tag{11.61}$$

N_A is the Avogadro number, and $h = 2\pi h_p$ is Planck's constant. The theoretical determination of the entropy S_0^{id} was performed for $p_0 = 0.101325$ MPa, $T_0 = 298.15$ K for argon. The following additional parameter values were employed: molar mass $M = 39.948$ (g/mol), spin degeneracy $g = 1$, critical parameters $T_c = 150.687$ K, $p_c = 4.863$ MPa, $\rho_c = 13.407$ mol/dm^3.

With $\mathrm{d}f = -s\,\mathrm{d}T - p\,\mathrm{d}v$ and Eq. (11.52), we arrive further at

$$s = -\frac{T_c}{p_c v_c} \left(\frac{\partial f}{\partial \theta} \right)_\omega = R_g \ln(3\omega - 1) - \frac{p_c v_c}{T_c} \left(\frac{\partial \chi}{\partial \theta} \right)_\omega . \tag{11.62}$$

The knowledge of the binodal curve allows one to determine the specific volumes of both coexisting phases in dependence on temperature. Equation (11.62) yields then the respective values of the entropy per mole in both the coexisting phases.

Acknowledgements

The authors would like to express their gratitude to the Deutsche Forschungsgemeinschaft (DFG, Grants SCHM 937/8-1; 436 RUS 113/605/0-1; RO 905/26-1 & 26-2), the Brazilian Research Foundation FAPESP (Grant No. 03/12617-0), and the Russian Foundation for Basic Research (Grant No. 01-02-04014) for financial support.

References

[1] M. Volmer, *Kinetik der Phasenbildung* (Th. Steinkopff, Dresden, Leipzig, 1939).

[2] Ya.I. Frenkel, *Kinetic Theory of Liquids* (Oxford University Press, Oxford, 1946).

[3] V.P. Skripov, *Metastable Liquids* (Nauka, Moscow, 1972 (in Russian); Wiley, New York, 1974 (in English)).

[4] A.C. Zettlemoyer (Ed.), *Nucleation* (Dekker, New York, 1969); *Nucleation Phenomena*, Adv. Colloid Interf. Sci. **7**, (1977).

[5] J.D. Gunton, M. San Miguel, and P.S. Sahni, The dynamics of first-order phase transitions, in *Phase Transitions and Critical Phenomena*, edited by C. Domb and J.L. Lebowitz (Academic Press, London, New York, 1983), Vol. 8.

[6] I. Gutzow and J. Schmelzer, *The Vitreous State: Thermodynamics, Structure, Rheology, and Crystallization* (Springer, Berlin, 1995).

[7] P.G. Debenedetti, *Metastable Liquids: Concepts and Principles* (Princeton University Press, Princeton, NJ, 1996).

[8] M. Kulmala and P.E. Wagner (Eds.), *Nucleation and Atmospheric Aerosols 1996*, *Proc. 14th Int. Conf. on Nucleation and Atmospheric Aerosols, Helsinki, 26–30 August, 1996* (Pergamon, London, 1996).

[9] B. Hale and M. Kulmala (Eds.), *Proc. 15th Int. Conf. on Nucleation and Atmospheric Aerosols*, *Rolla, MO, USA, August 6–11, 2000* (Melville, New York, 2000) AIP Conference Proceedings, Vol. 534.

[10] J.W.P. Schmelzer, J. Colloid Interf. Sci. **242**, 354 (2001).

[11] J.W. Gibbs, On the equilibrium of heterogeneous substances, Trans. Connecticut Acad. Sci. **3**, 3, 108, 343 (1875–78); see also J.W. Gibbs, *The Collected Works* (Longmans-Green, New York, London, Toronto, 1928), Vol. 1.

[12] J.D. van der Waals, *Die Kontinuität des gasförmigen und flüssigen Zustandes* (Johann-Ambrosius-Barth Verlag, Leipzig, 1899–1900), 2nd ed.

[13] J.D. van der Waals and Ph. Kohnstamm, *Lehrbuch der Thermodynamik* (Johann-Ambrosius-Barth Verlag, Leipzig und Amsterdam, 1908).

[14] J.S. Rowlinson and B. Widom, *Molecular Theory of Capillarity* (Clarendon, Oxford, 1982).

[15] D.W. Oxtoby, Acc. Chem. Res. **31**, 91 (1998).

[16] V.G. Baidakov, *Interfacial Structure of Simple and Quantum Liquids* (Russian Academy of Sciences Press, Ural Branch, Ekaterinburg, Russia, 1994).

[17] M. Rukeyser, *Willard Gibbs* (Doubleday, Doran & Company, New York, 1942).

[18] J. Lothe and G.M. Pound, J. Chem. Phys. **36**, 2080 (1962).

[19] H. Reiss, J.L. Katz, and E.R. Cohen, J. Chem. Phys. **48**, 5553 (1968).

[20] B. Senger, P. Schaaf, D.S. Corti, R. Bowles, J.-C. Voegel, D. Pointu, and H. Reiss, J. Chem. Phys. **110**, 6421, 6438 (1999).

[21] D. Reguera and H. Reiss, J. Chem. Phys. **119**, 1533 (2003).

[22] G.J. Doyle, J. Chem. Phys. **35**, 795 (1961); **75**, 1585 (1981).

[23] R.G. Renninger, F.C. Hiller, and R.C. Bone, J. Chem. Phys. **75**, 1584 (1981).

[24] G. Wilemski, J. Chem. Phys. **80**, 1370 (1984); **88**, 5134 (1988).

[25] G. Wilemski, J. Phys. Chem. **91**, 2492 (1987).

[26] V.G. Baidakov, G.Sh. Boltachev, and J.W.P. Schmelzer, J. Colloid Interf. Sci. **231**, 312 (2000).

[27] J.W.P. Schmelzer and V.G. Baidakov, J. Phys. Chem. B **105**, 11595 (2001).

[28] J.W.P. Schmelzer, J. Phys. Chem. Glasses **45**, No. 2, 116 (2004).

[29] J.W.P. Schmelzer, A.R. Gokhman, and V.M. Fokin, J. Colloid Interface Sci. **172**, 109 (2004).

[30] J.W.P. Schmelzer, A.S. Abyzov, and J. Möller, J. Chem. Phys. **121**, 6900 (2004)

[31] E.D. Zanotto and V.M. Fokin, Phil. Trans. R. Soc. A **361**, 591 (2003).

[32] J. Wölk, R. Strey, C.H. Heath, and B.E. Wyslouzil, J. Chem. Phys. **117**, 4954 (2003).

[33] J.W.P. Schmelzer, Thermodynamik finiter Systeme und die Kinetik von thermodynamischen Phasenübergängen 1. Art, Dissertation B, University of Rostock, Germany, 1985.

[34] H. Ulbricht, J. Schmelzer, R. Mahnke, and F. Schweitzer, *Thermodynamics of Finite Systems and the Kinetics of First-Order Phase Transitions* (Teubner, Leipzig, 1988).

[35] K. Nishioka and I. Kusaka, J. Chem. Phys. **96**, 5370 (1992).

[36] P.G. Debenedetti and H. Reiss, J. Chem. Phys. **108**, 5498 (1998).

[37] J.W.P. Schmelzer, J. Schmelzer, Jr., and I. Gutzow, Reconciling Gibbs and van der Waals: a new approach to nucleation theory, published as a preprint in [38], pp. 237–289.

[38] J.W.P. Schmelzer, G. Röpke, and V.B. Priezzhev, *Nucleation Theory and Applications* (Joint Institute for Nuclear Research Publishing House, Dubna, Russia, 1999).

[39] J.W.P. Schmelzer, J. Schmelzer, Jr., and I. Gutzow, J. Chem. Phys. **112**, 3820 (2000).

[40] J.W.P. Schmelzer, Reconciling Gibbs and van der Waals: a new approach to nucleation theory, in *15th Int. Conf. on Nucleation and Atmospheric Aerosols, Rolla, MO, USA, August 6–11, 2000*, AIP Conference Proceedings 534, edited by B. Hale and M. Kulmala (Melville, New York, 2000), pp. 155–180.

[41] J.W.P. Schmelzer and J. Schmelzer, Jr., J. Chem. Phys. **114**, 5180 (2001).

[42] J.W.P. Schmelzer and J. Schmelzer, Jr., Kinetics of Bubble Formation and the Tensile Strength of Liquids, published as a preprint in [43], pp. 88–119.

[43] J.W.P. Schmelzer, G. Röpke, and V.B. Priezzhev, *Nucleation Theory and Applications* (Joint Institute for Nuclear Research Publishing House, Dubna, Russia, 2002).

[44] J.W.P. Schmelzer and J. Schmelzer, Jr., Atmos. Res. **1085**, 31 (2002).

[45] J.W.P. Schmelzer, V.G. Baidakov, and G.Sh. Boltachev, Kinetics of boiling in binary liquid–gas solutions, published as a preprint in [43], pp. 120–145.

[46] J.W.P. Schmelzer, V.G. Baidakov, and G.Sh. Boltachev, J. Chem. Phys. **119**, 6166 (2003).

[47] B. Ono and S. Kondo, Molecular theory of surface tension in liquids, in *Handbuch der Physik*, edited by S. Flügge (Springer, Berlin, 1960), Vol. 10.

[48] F.O. König, J. Chem. Phys. **18**, 449 (1950).

[49] V.G. Baidakov, G.Sh. Boltachev, and J.W.P. Schmelzer, J. Colloid Interface Sci. **264**, 228 (2003).

[50] A.I. Rusanov, *Phasengleichgewichte und Grenzflächenerscheinungen* (Akademie-Verlag, Berlin, 1978).

[51] J.W.P. Schmelzer and F. Schweitzer, Z. Phys. Chemie **271**, 565 (1990).

[52] D. Reguera, R.K. Bowles, Y. Djikaev, and H. Reiss, J. Chem. Phys. **118**, 340 (2003).

[53] R. Defay, I. Prigogine, R. Bellemans, and D.H. Everett, *Surface Tension and Adsorption* (Longmans, Green & Co., London, 1966).

[54] I. Prigogine and A. Bellemans, Statistical mechanics of surface tension and adsorption, in *Adhesion and Adsorption of Polymers*, edited by L.H. Lee (Plenum, New York, 1980), Part A.

[55] D.B. Macleod, Trans. Faraday Soc. **19**, 38 (1923).

[56] R. Becker, Ann. Phys., Lpz. **51**, 66 (1938).

[57] C. Flageollet-Daniel, J.P. Garnier, and P. Mirabel, J. Chem. Phys. **78**, 2600 (1983) and references cited therein.

[58] S. Wonczak, Molekulardynamische Simulationen von Argon-Clustern, Ph.D. thesis, Universität Köln, 2002; Cuvillier Publ., Göttingen, 2002.

[59] D.H.E. Gross, *Microcanonical Thermodynamics: Phase Transitions in "Small" Systems*, Lecture Notes in Physics (World Scientific, Singapore, 2001), Vol. 66.

12 Summary and Outlook

Jürn W.P. Schmelzer

The first principle is that you must not fool yourself; and you are the easiest person to fool.
Richard Feynman

Pleasure in the job puts perfection in the work.
Aristotle

Finally, the task formulated in the introduction is fulfilled and an overview on a number of different current topics of research in the wide field of theory and applications of first-order phase transitions is outlined. It was (not always but in most of the time) a pleasure for the authors to prepare the respective chapters and for the editor to bring them into the final form. In the course of this work, also some other necessary first principles have been taken permanently into account (see above) which should facilitate the desired standard. Whether such desire could be realized, has to be evaluated already and exclusively by the reader.

Coming to the completion stage of the present book, the question immediately arises what will be the possible further developments in the field of research considered in the next years. Of course, making predictions in this respect is always a dangerous endeavor connected with high uncertainties and affected by personal preferences. Thus, here only one possible further development will be sketched which has already shown to some extent its possible value in the analysis of nucleation and growth processes.

As mentioned already in the introduction, in the theoretical description of nucleation-growth processes presently Gibbs' classical thermodynamic theory of heterogeneous systems is employed predominantly for the description of the properties of the critical clusters. The validity of this statement can be proven easily by having a close look at the contributions given in the present monograph.

The analyses of the properties of the critical clusters and the determination of the work of critical cluster formation, based on the classical Gibbs' approach, can be supplemented by different versions of density functional computations. In most of such approaches, the interaction potentials between the particles of the considered systems have to be known. As it turns out, the results allow a qualitative analysis of the dependence of the work of critical cluster formation on supersaturation. However, quantitatively the results depend very sensitively on the choice of the interaction potentials, this way these methods encounter here serious problems when applied to the analysis of experimental data on nucleation motivating the search for new approaches (cf. e.g. [1–3]). The van der Waals' density functional computations, as employed in Chapter 5 in application to boiling in binary liquid–gas solutions, have the significant advantages that they require exclusively the knowledge of data on the thermodynamic bulk properties of the systems under consideration and the interfacial properties for planar interfaces. This way, the problems with the choice of the interaction potentials do not occur here. However, they have certain well-known limitations as well.

Nucleation Theory and Applications. Edited by J. W. P. Schmelzer

ISBN: 3527-40469-4

In order to overcome the mentioned shortcomings, in recent years a generalization of Gibbs' classical approach has been developed and used for the description of nucleation processes (cf. Refs. [2, 3] and Chapter 11). This generalization of Gibbs' classical method leads, for a variety of different applications discussed, to dependences of the work of critical cluster formation on supersaturation that are qualitatively and widely even quantitatively in agreement with density functional computations. Moreover, the generalized Gibbs' approach has the similar advantage as van der Waals' density functional computations, in order to employ this method only the knowledge of the bulk properties of the respective substances and the values of the specific interfacial energy for coexistence of the respective phases at planar interfaces have to be known. The generalized Gibbs' approach employs Gibbs' method of dividing surfaces as well. However, Gibbs' fundamental equation for the superficial or surface quantities is generalized allowing to introduce into the description the dependence of the surface tension on the state parameters of both coexisting phases. In this theory, first the thermodynamic potentials for the respective nonequilibrium states are formulated. After this task is performed, the general equilibrium conditions are derived. They coincide with Gibbs' expressions for phase coexistence at planar interfaces, they lead, however, to different equations for the determination of the properties of the critical clusters and the work of critical cluster formation for critical clusters of finite sizes.

An example of the resulting differences is shown in Fig. 12.1. In this figure, the parameters of the critical clusters are given in dependence on supersaturation [3]. As a particular application, boiling in helium–nitrogen solutions is considered. For the chosen value of temperature the density $\rho_{\mathrm{liq}} = 24.7\,\mathrm{kmol\,m^{-3}}$ corresponds to the binodal curve, while the density $\rho_{\mathrm{liq}} = 22.48\,\mathrm{kmol\,m^{-3}}$ refers to the spinodal curve. In Fig. 12.1, x is the molar fraction of helium in the critical bubble, Π is a measure of the thermodynamic driving force, R is a measure of the size of the critical bubble, and W_* is the work of critical bubble formation. The results as obtained via Gibbs' classical approach employing in addition the capillarity approximation are given by the dotted curves, the results obtained via the generalized Gibbs' approach by the full curves, and the results of van der Waals' density-functional computations are given by the dashed curves (for more details see Ref. [3]). It is evident that the generalized Gibbs' approach leads to results widely equivalent to those of density-functional computations. In particular, it leads to vanishing values of the work of critical cluster formation for initial states near the spinodal. It turns out that the generalized Gibbs' approach allows one to describe the parameters of the critical clusters not only in one-component (as discussed in detail, for example, in Chapter 11) but also in multicomponent systems in a way that is, at least, qualitatively in agreement with density functional computations.

It follows as one of the consequences of the preceding analysis that the clusters of critical sizes have properties that are widely different, in general, from the properties of the newly evolving macroscopic phases. By this reason, also the properties of sub- and supercritical clusters will depend, in general, both on supersaturation and cluster size. In order to develop, consequently, an appropriate description of the course of the phase transitions, one has to develop a method to establish the dependence of composition of clusters of arbitrary sizes on mentioned parameters. As a first step in this direction, we developed in Refs. [4, 5] the proposal that the clusters will evolve in such a way as to follow the valley of the appropriate thermodynamic potential on a path of evolution passing the critical point (similarly to a ball moving in a force field or a river following the valley of some landscape). In application to

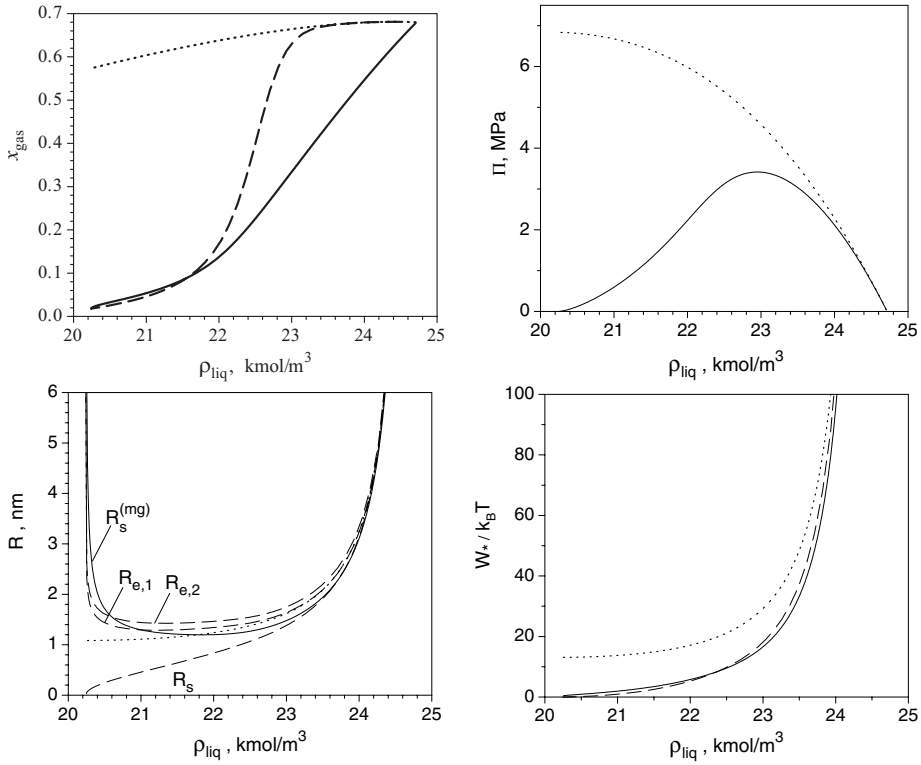

Figure 12.1: Composition of the critical cluster x, thermodynamic driving force of nucleation Π, the radius R of the critical cluster for different definitions of this parameter and the work of critical cluster formation, W_*, for bubble formation in a binary liquid-gas solution (for details see Ref. [3] and text)

segregation in binary solutions, one can then determine the change of the state of the cluster in dependence on its sizes as illustrated in Fig. 12.2 (cf. also Chapter 3).

The change of the composition of the clusters in dependence of their sizes leads to a size-dependence of almost all thermodynamic (in particular, the driving force and the surface tension) and kinetic parameters (diffusion coefficients and growth rates) determining the course of the phase transition (for details, see again Ref. [4]). Note that this size dependence is connected with changes of the bulk properties of the clusters. An explicit size dependence of some of the thermodynamic parameters – like the growth rate – connected with interfacial contributions to the thermodynamic potentials may be of significance in addition as well.

Here we would like to draw the attention to one additional point which is discussed in detail in Ref. [6]. Following the thermodynamic analysis in the framework of the generalized Gibbs' approach, as done here, we come to the conclusion that the kinetics of nucleation and growth in solutions does not proceed according to the classical picture but exhibits features typical for spinodal decomposition. According to the results of the analysis as illustrated in

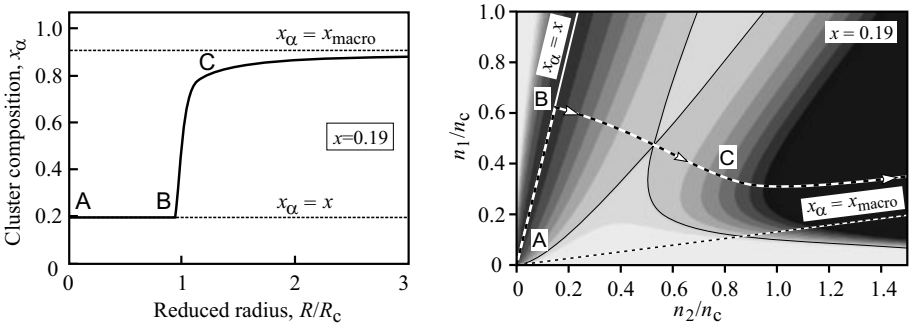

Figure 12.2: Change of the composition, x_α, of the cluster in dependence on its size, R/R_c (left side) and path of the evolution in the space of particle numbers in the clusters n_1 and n_2. Here R_c and n_c are the critical radius and the total number of particles in the critical cluster, respectively. The computations are performed for segregation in a regular solution (for details see Ref. [4])

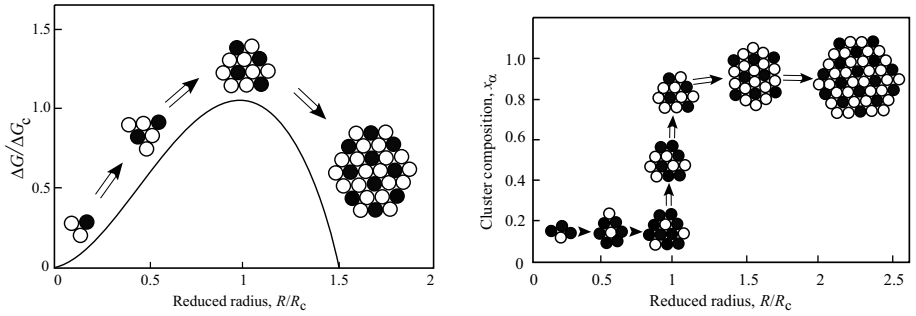

Figure 12.3: Comparison of the classical model of phase separation in multicomponent solutions (left side) with the scenario as developed based on the generalized Gibbs' approach (right side; see text)

Figs. 12.2 and 12.3, nucleation proceeds as follows. In a part of the ambient phase with a radius near to the critical one (both R_c and the ratio R/R_c depend on supersaturation [6]), the composition is changed until the properties of the newly evolving macroscopic phase are reached. Only afterwards, the classical picture – growth in size of aggregates with nearly constant composition – reflects the situation correctly. The classical model does not give a correct description for the stage of nucleation. Note that this result is confirmed by the statistical-mechanical analyses of model systems [7,8] giving this way an additional confirmation of the validity of the generalized Gibbs' approach employed here.

The determination of the trajectory of evolution by purely thermodynamic arguments (evolution along the valley of the thermodynamic potential), as employed in Fig. 12.2, has one disadvantage mentioned already in Ref. [4], it does not account for the specific features of the kinetics of the processes of cluster growth and its possible effects on the choice of the

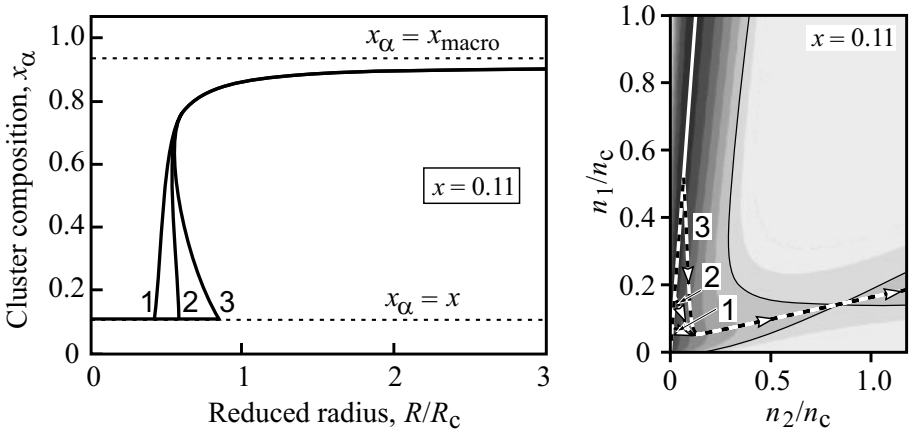

Figure 12.4: Change of the composition, x_α, of the cluster in dependence on its size, R/R_c (left side) and path of the evolution in the space of particle numbers in the clusters, n_1 and n_2. Here R_c and n_c are the critical radius and the total number of particles in the critical cluster. The computations are performed for segregation in a regular solution. In generalization of the results as given in Fig. 12.2, here also the effects of the kinetics are incorporated. Different evolution paths are obtained for different values of the ratio of the diffusion coefficients of both components (for details see Ref. [6])

trajectory of cluster evolution. Moreover, the question remains partly open, which set of thermodynamic variables is most suited to be employed in the determination of the preferred path of evolution. These shortcomings have been overcome in generalization of the thermodynamic criterion as developed in Ref. [6]. According to this generalization, the preferred path of evolution of the clusters is determined by the deterministic equations of motion of cluster growth starting with initial states slightly above and below the critical cluster size. As evident from Fig. 12.4, the incorporation of such kinetic effects may modify the above-discussed scenario quantitatively but not qualitatively.

This way, the generalized Gibbs' approach is able to lead to a variety of new insights into the course of first-order phase transformations. In addition to the mentioned results, it allows a new interpretation of the problem of existence or non-existence of metastable phases in crystallization of different glass-forming melts and the evolution of bimodal cluster size distributions for intermediate stages of segregation processes (cf. Ref. [4] and Chapter 4) and the behavior of phase separating systems near the classical spinodal curve (cf. Ref. [6]). In particular, it is shown that ridge crossing nucleation may be the dominating mechanism of phase formation not only in metastable but also in unstable initial states near the spinodal curve. As a further consequence, it leads to the conclusion that, not merely as an exception but as the rule, the temperature in the critical cluster has to be different from the temperature of the ambient phase (cf. Chapter 11). Such effects are expected to be of considerable importance for the understanding of the course of first-order phase transitions and require partly a quite different approach as compared with the classical methods. Some of such possible modifications have been already discussed in Chapter 3, but, as it seems, this will be only the beginning of such a

process of revision of classical methods. This way, it is believed that the further development of the generalized Gibbs' approach in application to nucleation and growth processes and its consequences may serve as a quite powerful tool in order to resolve problems in the comparison of experimental results and theoretical predictions which have not found a satisfactory solution so far.

References

[1] D. Reguera and H. Reiss, *EMLD-DNT Approach to Nucleation: A New Theory*, submitted for publication, and cited there references.

[2] J.W.P. Schmelzer et al., J. Chem. Phys. **112**, 3820 (2000); **114**, 5180 (2001), **119**, 6166 (2003).

[3] J.W.P. Schmelzer, V.G. Baidakov, and G.Sh. Boltachev, J. Chem. Phys. **119**, 6166 (2004).

[4] J.W.P. Schmelzer, A.R. Gokhman and V.M. Fokin, J. Colloid Interface Sci. **272**, 109 (2004).

[5] J.W.P. Schmelzer, Phys. Chem. Glasses **45**(2), 116 (2004).

[6] J.W.P. Schmelzer, A.S. Abyzov, and J. Möller, J. Chem. Physics **121**, 6900 (2004).

[7] J.D. Gunton, San M. Miguel, and P.S. Sahni, The dynamics of first-order phase transitions, in *Phase Transitions and Critical Phenomena*, edited by C. Domb and J.L. Lebowitz (Academic Press, London, New York, 1983), Vol. 8.

[8] K. Binder, Rep. Prog. Phys. **50**, 783 (1987).

Index

Nucleation Theory and Applications. Edited by J. W. P. Schmelzer

ISBN: 3527-40469-4